2012

Cosmology

Sponsored by

. CNRS (Centre National de la Recherche Scientifique)
. CEA (Commissariat à l'Énergie Atomique)
. IN2P3 (Institut National de Physique Nucléaire et de Physique des Particules)

XLVIIth Rencontres de Moriond
La Thuile, Aosta Valley, Italy – March 10-17, 2012

2012 Cosmology

web

Proceedings of the XLVIIth RENCONTRES DE MORIOND

Cosmology

La Thuile, Aosta Valley Italy *March 10-17, 2012*

2012

Cosmology

edited by

Etienne Augé,
Jacques Dumarchez
and
Jean Trân Thanh Vân

The XLVIIth Rencontres de Moriond

2012 Cosmology

was organized by :

Etienne Augé (IN2P3, Paris)
Jacques Dumarchez (LPNHE, Paris)

with the active collaboration of :

R. Ansari (Orsay)
P. Astier (Paris)
F. Bernardeau (Saclay)
Ch. Charmousis (Orsay)
K. Ganga (Paris)
Y. Giraud-Héraud (Paris)
Ch. Magneville (Saclay)
H. McCracken (Paris)
J. Silk (Oxford)
B. Wandelt (Paris)

2012 RENCONTRES DE MORIOND

The XLVIIth Rencontres de Moriond were held in La Thuile, Valle d'Aosta, Italy.

The first meeting took place at Moriond in the French Alps in 1966. There, experimental as well as theoretical physicists not only shared their scientific preoccupations, but also the household chores. The participants in the first meeting were mainly french physicists interested in electromagnetic interactions. In subsequent years, a session on high energy strong interactions was added.

The main purpose of these meetings is to discuss recent developments in contemporary physics and also to promote effective collaboration between experimentalists and theorists in the field of elementary particle physics. By bringing together a relatively small number of participants, the meeting helps develop better human relations as well as more thorough and detailed discussion of the contributions.

Our wish to develop and to experiment with new channels of communication and dialogue, which was the driving force behind the original Moriond meetings, led us to organize a parallel meeting of biologists on Cell Differentiation (1980) and to create the Moriond Astrophysics Meeting (1981). In the same spirit, we started a new series on Condensed Matter physics in January 1994. Meetings between biologists, astrophysicists, condensed matter physicists and high energy physicists are organized to study how the progress in one field can lead to new developments in the others. We trust that these conferences and lively discussions will lead to new analytical methods and new mathematical languages.

The XLVIIth Rencontres de Moriond in 2012 comprised three physics sessions:

- March 3 - 10: "Electroweak Interactions and Unified Theories"
- March 10 - 17: "QCD and High Energy Hadronic Interactions"
- March 10 - 17: "Cosmology"

We thank the organizers of the XLVIIth Rencontres de Moriond:

- A. Abada, E. Armengaud, J. Conrad, S. Davidson, P. Fayet, J.-M. Frère, P. Hernandez, L. Iconomidou-Fayard, P. Janot, M. Knecht, J. P. Lees, S. Loucatos, F. Montanet, L. Okun, J. Orloff, A. Pich, S. Pokorski, D. Wood for the "Electroweak Interactions and Unified Theories" session,

- E. Augé, E. Berger, S. Bethke, A. Capella, A. Czarnecki, D. Denegri, N. Glover, B. Klima, M. Krawczyk, L. McLerran, B. Pietrzyk, L. Schoeffel, Chung-I Tan, J. Trân Thanh Vân, U. Wiedemann for the "QCD and High Energy Hadronic Interactions" session,

- R. Ansari, P. Astier, F. Bernardeau, Ch. Charmousis, J. Dumarchez, K. Ganga, Y. Giraud-Héraud, Ch. Magneville, H. McCracken, J. Silk, B. Wandelt for the "Cosmology" session

and the conference secretariat and technical staff:

V. de Sá-Varanda and C. Bareille, I. Cossin, G. Dreneau, D. Fligiel, N. Ribet, S. Vydelingum.

We are also grateful to Andrea Righetto, Gioacchino Romani,Matteo Tuzzi, Roberta Musio and the Planibel Hotel staff who contributed through their hospitality and cooperation to the well-being of the participants, enabling them to work in a relaxed atmosphere.

The Rencontres were sponsored by the Centre National de la Recherche Scientifique, the Institut National de Physique Nucléaire et de Physique des Particules (IN2P3-CNRS), the Commissariat à l'Energie Atomique (DSM and IRFU), the Fonds de la Recherche Scientifique (FRS-FNRS), the Belgium Science Policy and the National Science Foundation. We would like to express our thanks for their encouraging support.

It is our sincere hope that a fruitful exchange and an efficient collaboration between the physicists and the astrophysicists will arise from these Rencontres as from previous ones.

E. Augé, J. Dumarchez and J. Trân Thanh Vân

Contents

5. Lensing

6. Dark Matter: direct and indirect detection

7. Neutrinos and Cosmology

8. Posters

1.
Methodology

CMB, lensing, and non-Gaussianities

Antony Lewis
Department of Physics & Astronomy, University of Sussex, Brighton BN1 9QH, UK

Abstract

The CMB is still by far the cleanest and most powerful way to measure many cosmological parameters and constrain early universe physics. Information in the power spectrum is partially limited by degeneracies, however these can be broken by using non-Gaussian information from CMB lensing which has just started to be measured with useful accuracy. Primordial non-Gaussianitics are also a powerful way to constrain or rule out inflationary models. I show what the various possible signals might look like, and how they can be measured.

1 Introduction

Observations of the CMB can provide accurate constraints on cosmological models given various fairly weak assumptions. However certain cosmological parameter combinations cannot be distinguished from the linear CMB anisotropies alone. The primary CMB anisotropies are generated around recombination and what we observe is a projection of conditions on the last-scattering surface. If we keep the physical densities in baryons, cold dark matter and the number of (massless) neutrinos fixed, the pre-recombination physics is unchanged. Since the mapping of physical scales at last-scattering to observed angular scales depends only on the angular-diameter distance to last-scattering, there are generally degenerate combinations of "late-time" parameters (such as the curvature parameter Ω_K and expansion rate today H_0) that yield very nearly the same power spectra of primary anisotropies [1, 2, 3]. This is the well-known 'geometrical degeneracy'

As is well-known, CMB lensing (for reviews see Refs. [4, 5]) can break the geometrical degeneracy since the lensing deflections are sourced all along the line of sight, and hence are sensitive to both the geometry and growth of structure after recombination [6, 7, 8, 9]. The effect of lensing on the power spectra has recently been used to constrain dark energy using only CMB data from ACT [8] and SPT [10].

However lensing also induces non-Gaussianities [11], because it induces shear and convergence modulations of the observed last-scattering surface. This can yield further information and must also be carefully distinguished from primordial non-Gaussianities. There has recently been great progress, with the lensing non-Gaussianity being measured at high-significance by SPT [10], and Planck should improve this further, especially at lower multipoles.

Primordial non-Gaussianity is also of great interest as a probe of inflation (and other) models. As the power spectrum becomes increasingly well measured with Planck, future CMB observations will be mainly of interest as a powerful probe of B-mode inflation and non-Gaussianites, both primordial and lensing. I will describe what some of these signals might look like; the presentation here is based largely on Ref. [12].

2 Gaussianity and the power spectrum

Before discussing non-Gaussianity, it is worth quickly remembering the key features of Gaussian fields. In particular we are usually interested is statistically isotropic and homogenous universe models, and hence in fields that have these symmetries. For simplicity I shall focus mainly on scalar fields 2D flat space, for example a slice through the matter density field or a small patch of the CMB, but almost everything generalizes to other cases such as full-sky observations.

Assuming we can measure a field $T(\mathbf{x})$ as a function of position, in flat space these can be Fourier transformed and written as

$$T(\mathbf{x}) = \frac{1}{(2\pi)^{N/2}} \int \mathrm{d}\mathbf{k}\, T(\mathbf{k}) e^{i\mathbf{k}\cdot\mathbf{x}} \tag{1}$$

where N is the number of dimensions. Statistical homogeneity and isotropy means that the statistical properties of the field must be unchanged under translations and rotations $T(\mathbf{x}) \to T(\mathbf{x}')$, so $\langle T(\mathbf{x})T(\mathbf{x}')\rangle$ can only be a function of the invariant separation between the points $|\mathbf{x} - \mathbf{x}'|$. This implies that the covariance of the field is determined by a power spectrum depending only on $k \equiv |\mathbf{k}|$:

$$\langle T(\mathbf{k}_1)T(\mathbf{k}_2)\rangle = \delta(\mathbf{k}_1 + \mathbf{k}_2)P(k_1). \tag{2}$$

For a small patch of the CMB, the power spectrum is just C_l, where $l = k$. The delta function says that modes with different wavevectors are completely uncorrelated: knowing the sign of $T(\mathbf{k}_1)$ tells you nothing about the likely sign of $T(\mathbf{k}_2)$. From the power spectrum the only thing we know is the variance of each individual mode, which from the assumption of isotropy is the same independent of the orientation of the mode.

A purely Gaussian statistically homogeneous and isotropic field is fully described statistically by its power spectrum. However more interesting fields are possible that are also statistically homogeneous and isotropic, with the non-Gaussian statistics described by a series of higher-point correlation functions.

3 Bispectrum

The first non-Gaussian signal to consider is a bispectrum, corresponding to a three-point correlation, or in Fourier space a correlation between three different mode wavevectors. We are still interested in statistically homogeneous and isotropic fields, which implies the statistics are described by a reduced bispectrum $b(k_1, k_2, k_3)$ that depends only the lengths of the wavevectors:

$$\langle T(\mathbf{k}_1)T(\mathbf{k}_2)T(\mathbf{k}_3)\rangle = \frac{1}{(2\pi)^{N/2}}\delta(\mathbf{k}_1 + \mathbf{k}_2 + \mathbf{k}_3)b(k_1, k_2, k_3). \tag{3}$$

From now on when referring to the bispectrum I will mean the reduced bispectrum as defined here; an analogous definition applies on the full sky. The delta-function here means that the 3-mode correlation is zero unless the wavevectors sum to zero: they form a triangle. If there is a non-zero bispectrum, modes with different wavevectors are not independent: if we measure $T(\mathbf{k}_1)$ and $T(\mathbf{k}_2)$, the sign of the bispectrum $b(k_1, k_2, k_3)$ then tells us which sign of $T(\mathbf{k}_3)$ is more likely. Positive sign gives positive skewness (tail of very high values), negative sign gives negative skewness (tail of very low values). What this looks like in real space depends on the shape of the triangle (the relative lengths of the different wavevectors).

3.1 *Equilateral and flattened (folded) triangles*

The first case I consider is equilateral triangles, where the lengths of the three sides of the triangle are the same, $k_1 = k_2 = k_3$. If there's a non-zero equilateral bispectrum, what does the field look like in real space? To answer this we can consider taking the $T(\mathbf{k}_1)$ and $T(\mathbf{k}_2)$ components of the field, and then ask what the bispectrum tells us about $T(\mathbf{k}_3)$. Depending on the relative sign of $T(\mathbf{k}_3)$, a field consisting of these three modes looks rather different — see Fig. 1. The sign of the bispectrum tells us which sign of $T(\mathbf{k}_3)$ is more likely, in other words whether we are more likely to have small regions of concentrated overdensity ($b > 0$) or regions of concentrated underdensity ($b < 0$). As can easily be imagined, such patterns can be obtained by locally moving matter around, for example concentrated overdensities can form by

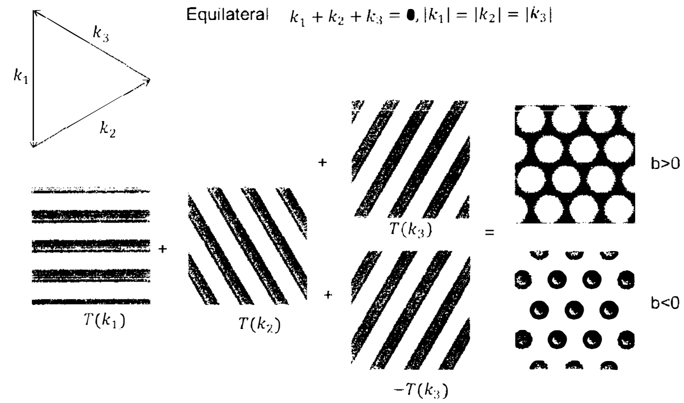

Figure 1: Equilateral bispectrum: a field can be decomposed into plane-wave modes, and the three components with wavevectors that form an equilateral triangle may have different relative signs. The sign of the bispectrum tells you which combination of signs is more likely (on average gives a positive or negative product of the three modes). A positive reduced bispectrum corresponds to being likely to have waves combining to have strong overdensities surrounded by larger areas of milder underdensity. A negative equilateral bispectrum corresponds to being likely to have concentrated underdensities surrounded by areas of milder overdensity. Note that in 3D the figures extend into the page, and hence the positive bispectrum corresponds to concentrated overdense filaments surrounded by larger areas of milder underdensity.

gravitational collapse, and thus equilateral non-Gaussianity is likely to be present in any field undergoing local non-linear dynamical processes.

A bispectrum is determined by three wavevectors which always lie in a plane. In 3D, the modes we are considering correspond to plane waves, and the concentrated overdensities correspond to filaments. These are precisely what form during the growth of large-scale structure. Since it is the overdensities that are concentrated, not the underdensities, the non-linear large-scale structure density field will have a large positive equilateral component to its bispectrum (for a perturbation theory calculation see Ref. [13]).

Of course exactly equilateral triangles are a very special case, but there are many shapes that are close to equilateral and these will also look similar, but correspond to slightly elliptical concentrated overdensities or underdensities. As the bispectrum triangle becomes more flattened, these turn into a line, or in 3D concentrated overdensity or underdensity pancakes (planes); see Fig. 2. Note that shapes that are qualitatively distinct in 3D may not be after projection into 2D: for example if an purely equilateral shape is present in 3D, projecting down to 2D will give flattened contributions when the line of sight lies close to the plane of the triangle (slicing a 3D filament along its length gives a line of overdensity).

Since equilateral-form non-Gaussianity involves wavevectors of roughly the same magnitude, these modes would have left the horizon during inflation at roughly the same time. Non-linear dynamics prior to horizon exit during inflation can therefore generate a bispectrum with a significant equilateral bispectrum component. By an analogy with large-scale structure growth, one might imagine than any non-linear growth prior to horizon exit would require a low sound speed for the perturbations[a]; however in standard single-field inflation the rest-frame sound speed

[a]The sound speed, given by $c_s^2 \equiv \delta p/\delta\rho$, measures the pressure perturbation δp induced by a given density perturbation $\delta\rho$. In structure growth pressures prevent gravitational collapse. The sound horizon roughly determines the Jeans scale below which pressure prevents collapse, so a low sound speed is required in order to have much growth on small sub-horizon scales.

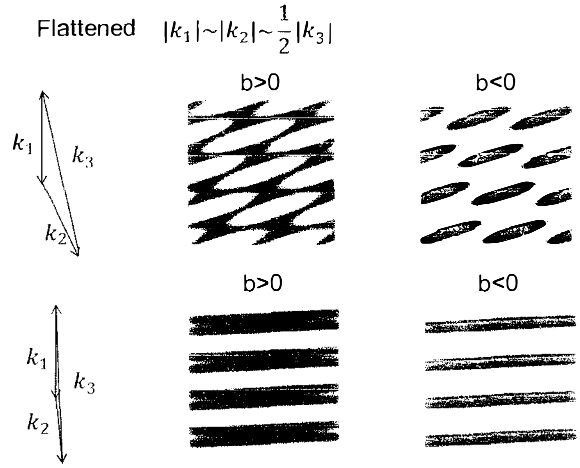

Figure 2: As an approximately equilateral bispectrum triangle flattens, the round areas of overdensity become flattened into pancakes. In 3D a positive flattened bispectrum with $k_1 = k_2 = k_3/2$ corresponds to being likely to have overdense pancakes with larger mildly underdense planes in between.

of the perturbations is exactly the speed of light. This prevents significant non-Gaussianity developing. However in extended models the speed of sound can be much lower, and in such cases significant equilateral non-Gaussianity can develop [14]. Non-linear dynamics after horizon re-entry will of course also generate equilateral non-Gaussianity, for example second-order effects prior to recombination. Though small compared to the strongly non-linear growth of structure at lower redshifts, these signals might present an important source of possible confusion for small inflationary signals [15].

3.2 Squeezed triangles

Squeezed triangles correspond to having one wavevector much shorter than the other two: in other words one large-scale mode and two much shorter-scale modes. The bispectrum is invariant under permutations of k_1, k_2, k_3, so for squeezed triangles it is convenient to adopt the convention that we permute indices so that $k_1 \leq k_2 \leq k_3$, and k_1 therefore always labels the large-scale mode. Sometimes people refer to the "squeezed-limit", meaning the limit as $k_1 \to 0$, but this is not really observationally relevant as very super-horizon modes are unobservable. By squeezed I will mean triangles with $k_2, k_3 \gg k_1$, but the wavelength of k_1 not much larger than the horizon size today, so that the mode is still observationally relevant.

First it is helpful to consider what a combination of two small-scale modes with $\mathbf{k}_2 \sim -\mathbf{k}_3$ looks like: the waves destructively interfere in some regions leaving little small-scale structure, but in other regions they reinforce each other giving a large small-scale signal. So this looks like a large-scale modulation in the small-scale power, where the wavevector of the modulation is given by $-(\mathbf{k}_2 + \mathbf{k}_3)$. In a Gaussian field the signs of all the modes are independent, so of course there is no modulation on average. However if there is a non-zero squeezed bispectrum, there is a correlation between this modulation and the large-scale modes; for example see Fig. 3. A positive squeezed bispectrum means that where there's a large-scale overdensity there's likely to be more small-scale structure, and where there is an large-scale underdensity there is likely to be less small-scale structure.

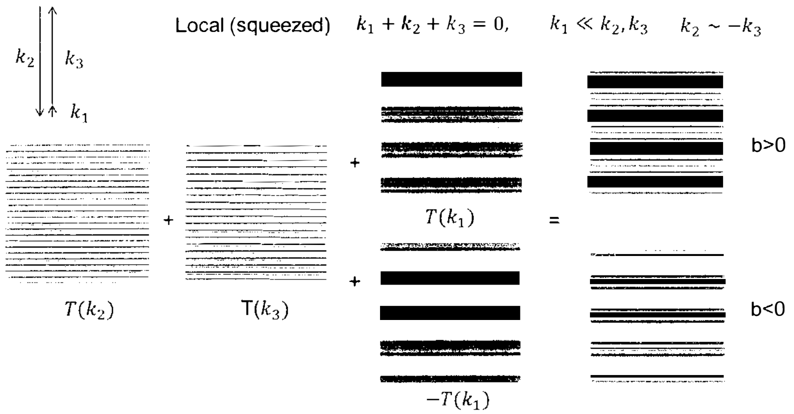

Figure 3: Squeezed bispectrum: two small-scale modes with nearly-equal wavelength ($k_2 \sim k_3$) interfere with each other, giving some regions with lots of small-scale power and others with destructive interference giving little small-scale power. The sign of the bispectrum tells you whether a region of high small-scale power is more likely to be associated with a large-scale overdensity or a large-scale underdensity.

For squeezed bispectra, the small-scale modes leave the horizon during inflation significantly later than the large-scale modes. The large-scale modes therefore effectively modify the background seen by the small-scale modes as they leave the horizon and beyond. In single-field inflation there is a one-to-one mapping between the background Hubble parameter and field values, so the conditions on the surface where a small-scale mode leaves the horizon at $k_{\rm phys} = H$ are locally identical to what they would be without the large-scale mode [16, 17]. However when we observe angular scales on the sky, we can look at many different Hubble patches; since these patches all have slightly different large-scale field values they have undergone slightly different expansion histories: there is a local perturbation to the scale factor in each patch, and this affects the observed angular scales (for an explicit calculation see Ref. [18]). This signal is easily calculated and fairly small: any detected modulation beyond this would be rule out essentially all single-field inflation models [16]. However in models with multiple fields the super-horizon evolution can be modulated in more significant ways by auxiliary fields, and larger squeezed non-Gaussian signals are possible (for a review see Ref. [19]).

CMB lensing also produces a squeezed bispectrum, due to correlation of large-scale lenses with the Integrated Sachs-Wolfe effect [20, 22]. It projects onto $f_{\rm NL} \sim 9$, but has a rather different anisotropic shape and can easily be distinguished.

4 Trispectrum

The trispectrum is the harmonic four-point function. As with the bispectrum, statistical isotropy and homogeneity means that the four wavevectors must sum to zero, and for a parity invariant ensemble the shape is fully determined by the lengths of six lines joining the four points. Gaussian fields have a trivial four-point function given by products of the power spectrum, so the trispectrum $\mathcal{T}$ is defined as the more interesting connected part:

$$\langle T(\mathbf{k}_1)T(\mathbf{k}_2)T(\mathbf{k}_3)T(\mathbf{k}_4)\rangle_C \propto \delta(\mathbf{k}_1 + \mathbf{k}_2 + \mathbf{k}_3 + \mathbf{k}_4)\mathcal{T}(k_1, k_2, k_3, k_4; K_{12}, K_{23}). \tag{4}$$

Here $k_1..k_4$ are the lengths of the wavevectors, and K_{12}, K_{23} are the lengths of the two 'diagonals'.

CMB lensing only induces a significant bispectrum because the lenses are correlated with the integrated Sachs-Wolfe. However the power spectrum of the lensing potential is quite large, and this gives rise to a much more easily detectable trispectrum. This can be used to reconstruct the lensing potential, and hence measure the lensing potential power spectrum. I will discuss this equivalently using a slightly different interpretation below in terms of statistical anisotropy estimators.

5 Statistical anisotropy and modulation reconstruction

We've seen that large-scale modulating fields can give rise to a squeezed bispectrum and trispectrum when we average over all possible field values. However we could ask a slightly different question: in our universe there must be a particular realization of the large-scale modulation field, can we learn what it is? Looking at Fig. 3 how to do this seems obvious: the small-scale power is modulated, so if we estimate the power spectrum in different places, the spatial dependence of the power spectrum should trace out the modulation.

Imagine that there are modulation scalar modes X that we want to learn about. If they are large-scale modes, we can make the approximation that products of small-scale fields only depend linearly on X (but possibly non-linearly on all the other fields. For a pair of small-scale modes we therefore have

$$\tilde{T}(\mathbf{k}_2)\tilde{T}(\mathbf{k}_3) \approx \tilde{T}(\mathbf{k}_2)\tilde{T}(\mathbf{k}_3)|_{X=0} + \int \mathrm{d}\mathbf{K} X(\mathbf{K})^* \frac{\delta}{\delta X(\mathbf{K})^*}\left(\tilde{T}(\mathbf{k}_2)\tilde{T}(\mathbf{k}_3)\right). \tag{5}$$

If we then average over the conditional distribution for the fields given fixed X, for $\mathbf{k}_2 \neq -\mathbf{k}_3$ we have

$$\langle \tilde{T}(\mathbf{k}_2)\tilde{T}(\mathbf{k}_3)\rangle_{P(\tilde{T}|X)} \approx \int \mathrm{d}\mathbf{K} X(\mathbf{K})^* \left\langle \frac{\delta}{\delta X(\mathbf{K})^*}\left(\tilde{T}(\mathbf{k}_2)\tilde{T}(\mathbf{k}_3)\right)\right\rangle, \tag{6}$$

where for a result to linear order in $X(\mathbf{K})$ the expectation on the right hand side can be evaluated averaging over all the fields. If we correlate this with $T(\mathbf{k}_1)$ and average over X this recovers the general form of the squeezed bispectrum. From statistical homogeneity the wavevectors in the expectation value over all fields must form a triangle, so this term is proportional to a delta-function, and we can define

$$\left\langle \frac{\delta}{\delta X(\mathbf{K})^*}\left(\tilde{T}(\mathbf{k}_2)\tilde{T}(\mathbf{k}_3)\right)\right\rangle \equiv \mathcal{A}(K, k_2, k_3)\delta(K + k_2 + k_3), \tag{7}$$

where $\mathcal{A}(K, k_2, k_3)$ encodes how the small-scale modes change with the large-scale modulation. Hence averaging over all the other modes recovers something just proportional to the modulation $X(\mathbf{K})$ [23, 22]:

$$\langle \tilde{T}(\mathbf{k}_2)\tilde{T}(\mathbf{k}_3)\rangle_{P(\tilde{T}|X)} \approx \mathcal{A}(K, k_2, k_3)\; X(\mathbf{K})^*|_{\mathbf{K}=-\mathbf{k}_2-\mathbf{k}_3}\,. \tag{8}$$

This tells us that by averaging over a quadratic combination of all the observed small-scale modes (which all see the same large-scale modulation realization), we can construct an estimator $\hat{X}$ of the modulation field X. This is the more formal statement of the obvious idea that measuring the small-scale power as a function of position should trace out the large-scale modulation. The use of such quadratic estimators has proved useful in CMB studies for reconstructing fields in wide classes of statistically anisotropic models [24, 25], and for lensing reconstruction (where the modulation field is the large-scale lensing potential [26, 27]; for reviews see Refs. [4, 5]). Of course in observations there are only a finite number of small-scale modes to average over, and this leads to a cosmic variance reconstruction 'noise': random fluctuations in an isotropic field will look anisotropic, which is hard to distinguish from a modulation-induced anisotropy with only a small number of observed modes. The CMB lensing signal is large enough to be relatively easily detected (as seen recently by ACT and SPT [28, 10]; see [27] for other forecasts), but primordial signals are much more difficult since only the very largest-scale modulations are not swamped by reconstruction noise.

6 Conclusions

The CMB power spectrum is well measured, and Planck will measure the temperature spectrum almost to the limits of cosmic variance and astrophysical confusion. However non-Gaussianities could yield far more information, both about primordial physics and the matter fluctuations and geometry that describe the CMB lensing signal. Squeezed-shape non-Gaussianities, such as local primordial non-Gaussianity and lensing, give rise to modulations of the observed small-scale CMB power, and we can use this signal to reconstruct the modulation field. In the case of CMB lensing this allows us to measure the lensing potential, which can then be used to learn about dark energy and the growth of structure.

7 Acknowledgements

I acknowledge support from the Science and Technology Facilities Council [grant number ST/I000976/1].

References

[1] Matias Zaldarriaga, David N. Spergel, and Uros Seljak. Microwave background constraints on cosmological parameters. *Astrophys. J.*, 488:1–13, 1997.

[2] J.R. Bond, G. Efstathiou, and M. Tegmark. Forecasting cosmic parameter errors from microwave background anisotropy experiments. *Mon.Not.Roy.Astron.Soc.*, 291:L33–L41, 1997.

[3] G. Efstathiou and J.R. Bond. Cosmic confusion: Degeneracies among cosmological parameters derived from measurements of microwave background anisotropies. *Mon.Not.Roy.Astron.Soc.*, 304:75–97, 1999.

[4] Antony Lewis and Anthony Challinor. Weak gravitational lensing of the cmb. *Phys. Rept.*, 429:1–65, 2006.

[5] Duncan Hanson, Anthony Challinor, and Antony Lewis. Weak lensing of the CMB. *General Relativity and Gravitation*, 42:2197–2218, 2010.

[6] R. Stompor and G. Efstathiou. Gravitational lensing of cosmic microwave background anisotropies and cosmological parameter estimation. *Mon. Not. Roy. Astron. Soc.*, 302:735, 1999.

[7] Kendrick M. Smith, Wayne Hu, and Manoj Kaplinghat. Cosmological information from lensed cmb power spectra. *Phys. Rev.*, D74:123002, 2006.

[8] Blake D. Sherwin, Joanna Dunkley, Sudeep Das, John W. Appel, J.Richard Bond, et al. Evidence for dark energy from the cosmic microwave background alone using the Atacama Cosmology Telescope lensing measurements. *Phys.Rev.Lett.*, 107:021302, 2011.

[9] Cullan Howlett, Antony Lewis, Alex Hall, and Anthony Challinor. CMB power spectrum parameter degeneracies in the era of precision cosmology. *JCAP*, 1204:027, 2012.

[10] A. van Engelen, R. Keisler, O. Zahn, K.A. Aird, B.A. Benson, et al. A measurement of gravitational lensing of the microwave background using South Pole Telescope data. 2012.

[11] Wayne Hu. Angular trispectrum of the cosmic microwave background. *Phys. Rev.*, D64:083005, 2001.

[12] Antony Lewis. The real shape of non-Gaussianities. *JCAP*, 1110:026, 2011.

[13] James N. Fry. The Galaxy correlation hierarchy in perturbation theory. *Astrophys. J.*, 279:499–510, 1984.

[14] Leonardo Senatore, Kendrick M. Smith, and Matias Zaldarriaga. Non-Gaussianities in Single Field Inflation and their Optimal Limits from the WMAP 5-year Data. *JCAP*, 1001:028, 2010.

[15] Cyril Pitrou, Jean-Philippe Uzan, and Francis Bernardeau. The cosmic microwave background bispectrum from the non- linear evolution of the cosmological perturbations. *JCAP*, 1007:003, 2010.

[16] Juan Martin Maldacena. Non-Gaussian features of primordial fluctuations in single field inflationary models. *JHEP*, 05:013, 2003.

[17] Paolo Creminelli, Guido D'Amico, Marcello Musso, and Jorge Norena. The (not so) squeezed limit of the primordial 3-point function. *JCAP*, 1111:038, 2011.

[18] Antony Lewis. The full squeezed CMB bispectrum from inflation. 2012.

[19] Christian T. Byrnes and Ki-Young Choi. Review of local non-Gaussianity from multi-field inflation. *Adv. Astron.*, 2010:724525, 2010.

[20] Uros Seljak and Matias Zaldarriaga. Direct signature of evolving gravitational potential from cosmic microwave background. *Phys. Rev.*, D60:043504, 1999.

[21]

[22] Antony Lewis, Anthony Challinor, and Duncan Hanson. The shape of the CMB lensing bispectrum. *JCAP*, 1103:018, 2011.

[23] Wayne Hu and Takemi Okamoto. Mass reconstruction with CMB polarization. *Astrophys. J.*, 574:566–574, 2002.

[24] Anthony R. Pullen and Marc Kamionkowski. Cosmic Microwave Background Statistics for a Direction- Dependent Primordial Power Spectrum. *Phys. Rev.*, D76:103529, 2007.

[25] Duncan Hanson and Antony Lewis. Estimators for CMB Statistical Anisotropy. *Phys. Rev.*, D80:063004, 2009.

[26] Matias Zaldarriaga and Uros Seljak. Reconstructing projected matter density from cosmic microwave background. *Phys. Rev.*, D59:123507, 1999.

[27] Takemi Okamoto and Wayne Hu. CMB lensing reconstruction of the full sky. *Phys. Rev.*, D67:083002, 2003.

[28] Sudeep Das, Blake D. Sherwin, Paula Aguirre, John W. Appel, J.Richard Bond, et al. Detection of the Power Spectrum of Cosmic Microwave Background Lensing by the Atacama Cosmology Telescope. *Phys.Rev.Lett.*, 107:021301, 2011.

Bayesian Large Scale Structure Inference

J. Jasche[1], B.D. Wandelt[2,1,3,4]
[1] *CNRS, UMR7095, Institut d'Astrophysique de Paris, F-75014, Paris, France*
[2] *UPMC Univ Paris 06, UMR7095, Institut d'Astrophysique de Paris, F-75014, Paris, France*
[3] *Department of Physics, 1110 W Green Street, University of Illinois at Urbana-Champaign, Urbana, IL 61801, USA*
[4] *Department of Astronomy, 1002 N Gregory Street, University of Illinois at Urbana-Champaign, Urbana, IL 61801, USA*

Comparison between observations and theories is often hampered due to the many systematic and statistical uncertainties typically involved in observations. All these effects need to be accounted for carefully in modern statistical analyses in order not to misinterpret finally inferred quantities such as cosmological parameters. Here we present the Bayesian large scale structure inference code HADES, which accounts for all these effects and permits thorough analyses of the three dimensional large scale structure and corresponding uncertainties. The present algorithm represents the first step towards an all-embracing full Bayesian large scale structure inference framework.

1 Introduction

The formation of the cosmic large scale structure (LSS) is governed by a variety of different physical processes ranging from inflation at the beginning of the Universe to the dynamics of dark and luminous matter as well as dark energy. For this reason, observations of the LSS provide important information to test and refine our current picture of the origin and evolution of the Universe. Unfortunately, contact between theory and observations cannot be established directly, since data is subject to a variety of systematics and statistical uncertainties. Most notably of those are survey geometries, selection effects, galaxy bias, redshift distortions, noise and cosmic variance. All these effects have to be accounted for accurately in order not to draw false conclusions on the finally inferred quantities such as cosmological parameters. Additional complications arise from the fact that the presently observed large scale structure is highly non-linear and thus requires modern and numerical efficient non-linear and non-Gaussian methods to analyze observations. Additionally, mapping and characterizing the three dimensional LSS requires thorough statistical approaches to deal with the often joint uncertainties of all effects involved.

To address these problems we developed the full Bayesian large scale structure inference framework HADES (Hamiltonian Density Estimation and Sampling), which accounts for all the aforementioned observational effects and at the same time permits to accurately quantify joint and correlated uncertainties involved in the inference process [2] [3]. This is achieved by numerical efficient exploration, via efficient Markov Chain Monte Carlo methods, of the joint posterior distribution of all parameters involved, such as the three dimensional density field and the true radial locations of galaxies, when dealing with galaxy surveys with highly uncertain redshift estimates.

As a scientific result our method provides a numerical representation of the LSS posterior distribution, which permits to report any desired statistical summary such as mean, mode or variance for all inferred parameters such as the 3d density field. In this fashion, the application of the HADES algorithm to data permits to construct highly detailed cosmographic descriptions of the three dimensional large scale structures, in terms of density maps and corresponding uncertainties. Based on these results a variety of subsequent scientific analyses can be performed ranging from testing current models of structure formation, studying relations between galaxy properties and large scale structure as well as measuring power-spectra and analyzing the dynamic nature of dark energy. Application of the HADES algorithm to Sloan Digital Sky Survey data [8] yielded a highly detailed map of the matter distribution and the possibility to accurately quantify its significance [3]. Furthermore, the HADES algorithm is able to account for radial uncertainties in the locations of galaxies. This ability will be of increasing importance for the analysis of present and future photometric redshift surveys, which probe large volumes to deep redshifts for the expense of low redshift accuracies. By exploring the joint posterior distribution of the three dimensional density field and the radial locations of galaxies conditional on observations, the algorithm exploits joint information to mutually enhance the inference of all quantities involved. In particular, the code provides improved redshifts for galaxies and accurate density fields when inferring them from galaxy surveys with uncertain radial positions of galaxies. In this fashion, the HADES algorithm represents the basic step towards a all-encompassing full Bayesian LSS inference framework.

2 Bayesian Inference

Particularly due to statistical uncertainties, as described in the introduction, a unique recovery of the three dimensional density field from observations is not possible. There will always be a set of possible solutions for particular three dimensional large scale structure configurations, that are compatible with the observations within the allowed uncertainty ranges. For this reason, we aim at answering the question:'What are these possible 3d density fields, that are compatible with the observations?'. In a Bayesian framework, this question can be best answered by providing the posterior distribution for the signal to be analyzed. In our case this yields the following large scale structure posterior distribution:

$$\mathcal{P}(\delta|d) = \mathcal{P}(\delta)\frac{\mathcal{P}(d|\delta)}{\mathcal{P}(d)} \tag{1}$$

where the prior $\mathcal{P}(\delta)$ describes our a priori knowledge on the three dimensional density field δ, the likelihood $\mathcal{P}(d|\delta)$ describes the statistical process by which the observations d where generated given a specific realization of the matter field δ and $P(d)$ is the evidence normalizing the probability distribution. The posterior distribution generally contains all information which are important for a scientific analysis. It contains all the information on the three dimensional density field, which can be extracted from the data, and at the same time, since it is a probability distribution, quantifies corresponding uncertainties. Given such a posterior distribution for the three dimensional density field a variety of interesting scientific analyses can be performed:

1. parameter space studies
2. model selection
3. report any desired statistical summary, such as mean mode or variance

Additionally, given the posterior distribution it is possible to perform non-linear and non-Gaussian error propagation to any finally inferred quantity. For these reasons, our work aims at

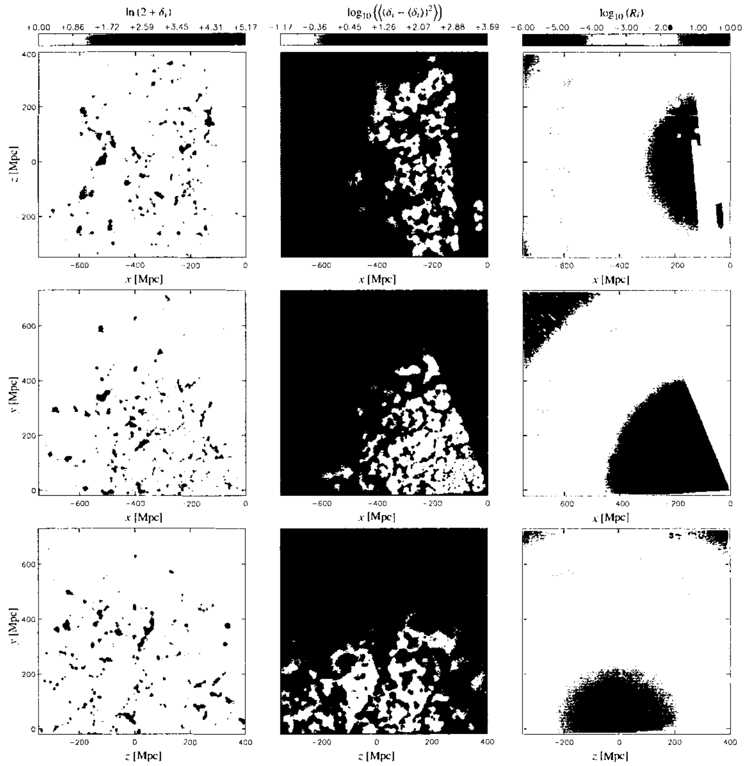

Figure 1: Three different slices from different sides through ensemble mean density (left panels), ensemble variance (middle panels) and the three dimensional response operator R_i, which is the product of survey geometry and radial selection function, (right panels). Especially the variance plots demonstrate, that the method accounted for the full Poisonian noise structure introduced by the galaxy sample. One can also see the correlation between high density regions and high variance regions, as expected for Poissonian noise.

providing numerical representations of the posterior distributions for the full three dimensional density fields, which will permit thorough scientific analyses in the linear and non-linear regimes.

3 Non-linear density field inference

With our work we aim at inferring the density field in the mildly non-linear and non-linear regimes. In these regimes the statistical behavior of the present day density field does not obey Gaussian statistics any longer, since gravitational interaction introduced mode coupling and phase correlations to the density field. The exact statistical behavior of the non-linear density field in terms of a probability distribution is not known. However, there exist phenomenological approaches such as the log normal distribution for the evolved density field. The log normal distribution can be justified via theoretical arguments[12] and has been demonstrated to fit results obtained from numerical large scale structure simulations with reasonable accuracy[1]. The log normal distribution therefore seems a logical choice as a prior distribution for Bayesian inference in the non-linear regime. Also note, that from a Bayesian perspective a log normal prior is well justified, since it is a maximum entropy prior on a logarithmic scale and as such represents the least informative prior for a positive three dimensional density field, once the mean and the covariance matrix are specified. In addition, to the log normal prior we were also interested in treating the statistical noise more accurate than in previous Gaussian approximations, such as Wiener filtering [4 14 15 16]. In particular, we focused on treating the local noise structure of the galaxy distribution and hence the large scale structure depended noise. These effects can be modeled in a Poissonian picture of structure formation, in which the galaxy distribution is considered to arise from an inhomogeneous Poisson process [13]. The resultant log normal Poissonian distribution is highly non-linear and non-Gaussian. This fact considerably complicates density field inference in the non-linear regime, since numerically efficient non-Gaussian and non-linear methods are required to explore the corresponding parameter spaces. Typically the analysis comprises on the order of 10^7 degrees of freedom which correspond to the density amplitudes stored at the grid nodes of an equidistant Cartesian grid which subdivides the analysis domain into voxels [2 3].

Unlike, as in the Gaussian Gibbs sampling approach to density field inference [4], there exists no known way to directly draw samples from the log normal Poissonian distribution. Generally, in situations like this, one has to rely on Metropolis-Hastings techniques to explore the posterior distribution. However, the Metropolis-Hastings has the numerical disadvantage that not every sample will be accepted. A low acceptance rate can therefore result in a prohibitive numerical scaling for the method, especially since we are interested in estimating full three dimensional matter fields which usually have about 10^7 or more parameters. Such a high rejection rate is due to the fact, that conventional Markov Chain Monte Carlo (MCMC) methods move through the parameter space by a random walk and therefore require a prohibitive amount of samples to explore high-dimensional spaces. Given this situation, we proposed to employ Hybrid Monte Carlo methods, which in the absence of numerical errors, would yield an acceptance rate of unity [6]. The so called Hamiltonian Monte Carlo (HMC) method exploits techniques developed to follow classical dynamical particle motion in potentials [6]. In this fashion the Markov sampler follows a persistent motion through the parameter space, greatly suppressing random walk behavior, yielding reasonable efficiencies to explore high dimensional parameter spaces [7].

Our implementation of the HMC algorithm is the HADES (Hamiltonian Density Estimation and Sampling) code [2 3] which forms the heart of a growing Bayesian large scale structure inference framework. The HADES algorithm aims at performing full non-linear and non-Gaussian Bayesian analyses of three dimensional density fields from galaxy observations.

3.1 Large scale structure inference with the SDSS

Applications of the HADES algorithm to data yield highly detailed three dimensional maps of the matter distribution, which permit to study various aspects of structure and galaxy formation. In particular, we performed an analysis of the Sloan Digital Sky Survey (SDSS) Data Release 7 main sample [8]. The aim of this analysis is to provide a numerical representation of the large scale structure posterior distribution in the SDSS volume. These results then permit to estimate detailed three dimensional maps and to quantify corresponding uncertainties, which are essential for any subsequent scientific analysis. The density inference is performed on a Cartesian equidistant box of side length 750 Mpc and $256^3 \sim 10^7$ grid nodes which correspond to the degrees of freedom of the problem to analyze [3]. The resultant resolution for the inferred density field then amounts to about ~ 3 Mpc [3]. The application of the HADES algorithm to the SDSS data yielded about 3 TB of data in the form of 4×10^4 matter field realizations drawn, conditionally on the data, from the posterior distribution. This set of posterior samples constitutes a numerical representation of the target log normal Poissonian distribution described above [3]. Based on these results we may report any desired statistical summary such as mean, mode or variance. Figure 1 displays slices through the three dimensional ensemble

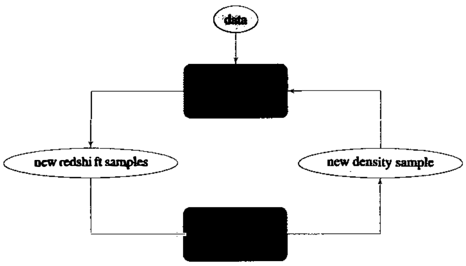

Figure 2: Flow-chart depicting the two step iterative block sampling procedure. First a set of galaxy redshift reconstructions is sampled conditional on the last density field. In a second step, a density field sample is generated conditional on the new galaxy redshifts, assuming them to be related to the density field through log-normal Poisson statistics.

mean and standard deviations estimated from the 4×10^4 density field realizations [3]. One can nicely see the detailed filamentary structure of the cosmic web as predicted by current models of large scale structure formation. Also note, that movies of different posterior realizations and of tomographic slices through the full three dimensional ensemble mean density field are available on-line [a]. Furthermore, figure 1 demonstrates that the HADES algorithm also permits to accurately quantify statistical uncertainties in general as demonstrated by the middle panels which depict the corresponding standard deviations. It should be remarked, that we are not restricted to purely Gaussian error quantification, since with the set of posterior samples we also posses information on non-linear and Non-Gaussian errors. This fact is of particular interest for propagating uncertainties to any finally inferred quantity.

4 Photometric redshift inference

The HADES algorithm forms the heart of a general large scale structure inference framework. As described above the HADES code accounts for systematic uncertainties such as selection effects, biases and survey geometry as well as statistical uncertainties such as the noise of the galaxy population and cosmic variance. In general real galaxy observations suffer from a variety of additional uncertainties. Of particular relevance for the study of cosmological parameters are uncertainties in radial distance estimates [17 18 19]. These uncertainties will become increasingly important for present and future photometric redshift surveys, which probe large volumes to deep redshifts for the prize of low redshift accuracy. Typically these redshift distortions can amount up to a radial uncertainty of about 100 Mpc along the line of sight. For the sake of density field inference, these redshift uncertainties can have pronounced effects since they yield elongated structures along the line of sight, when naively estimating the density field from such a galaxy sample. This immediately clarifies that uncertainties in the locations of galaxies will yield spatial uncertainties in the estimated density field. Consequently, the inferred density field is not only subject uncertainties stemming from galaxy shot noise but also due to redshift uncertainties. Uncertainties in the density field are therefore correlated in many ways. On the other hand, galaxies are not arbitrarily distributed in three dimensional space. According to the current paradigm of structure formation we believe, that galaxies form predominantly in high density regions and are less likely to be found in low density regimes. Therefore, naively one expects the probability of finding a galaxy in three dimensional space to be roughly proportional

[a] Movies of tomographic slices through the inferred 3d density field and random realizations of the posterior distribution can be found at http://www.mpa-garching.mpg.de/mpa/research/current_research/hl2009-12/hl2009-12-en-print.html.

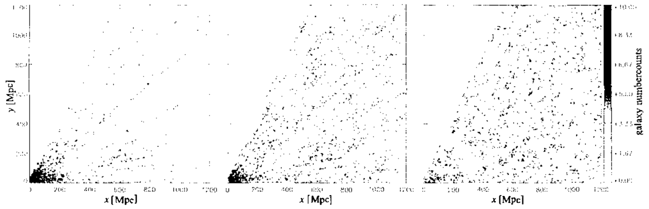

Figure 3: Slices through three successive galaxy count samples, first sample (left panel), fifth sample middle panel and 100th sample (right panel). The first sample shows prominent redshift smearing which quickly decay in subsequent samples.

to the amplitude of the underlying three dimensional matter distribution. This naive guess turns out to be essentially correct in a Poissonian picture of galaxy formation [5]. Therefore, given the underlying density field it is possible to constrain the radial locations of galaxies. In reality however, we have no knowledge on the true underlying three dimensional density field. Nevertheless, the above discussion demonstrates, that the accuracy of the three dimensional density field will improve with more accurate redshift estimates while inference of radial galaxy positions will improve given some knowledge on the underlying density field. Inference of the density field and galaxy redshifts thus is tightly coupled and involves correlated uncertainties, which generally require a joint approach. On the other hand simultaneous inference of all quantities may improve their mutual inference. We therefore propose to extent the previously presented HADES algorithm by a redshift sampling procedure to jointly infer three dimensional density fields and radial locations of galaxies from galaxy observation with uncertain radial positions of galaxies[5]. More specifically, we aim at exploring the joint posterior $\mathcal{P}(\delta, z|z_{obs}, \phi, \theta)$ of the three dimensional density field δ and the true galaxy redshifts z conditional on the observed redshifts z_{obs} and the angles in the sky ϕ and θ [5]. In order to perform such a full joint Bayesian analysis the framework of a multiple block Metropolis-Hastings sampler permits to break up the high dimensional problem in a set of lower dimensional problems which can then be treated iteratively [9]. Particularly, we may perform iterative sampling from the following two conditional distributions [5]:

$$\begin{aligned} &1) \quad z^{i+1} \leftarrow \mathcal{P}(z|\delta^{i}, z_{obs}, \phi, \theta)\,, \\ &2) \quad \delta^{i+1} \leftarrow \mathcal{P}(\delta|z^{i+1}, z_{obs}, \phi, \theta)\,. \end{aligned} \tag{2}$$

Thus, one can explore the joint posterior distribution by iterative sampling from the two conditional distributions where in the first step one draws a random realization of radial galaxy positions z and in a second step we generate a three dimensional density field sample δ. The iteration of these two random processes will provide samples of the joint posterior distribution. A schematic description of the sampling procedure is depicted in figure 2.

This sampling approach permits us to produce data-constrained samples of the three dimensional density field and galaxy redshifts for photo-z surveys with tens of millions of galaxies in a numerically efficient way.

4.1 redshift sampling from artificial galaxy surveys

Full Bayesian analyses in high dimensional parameter spaces are numerically challenging tasks. To provide a proof of concept we performed a joint analysis of the three dimensional density field and the true radial locations of galaxies in an artificial test scenario. An artificial galaxy observation was build on a matter field realization calculated by the tree-PM code GADGET-2 [10]. The details of this simulation are described in [11]. To generate an artificial galaxy catalog, the

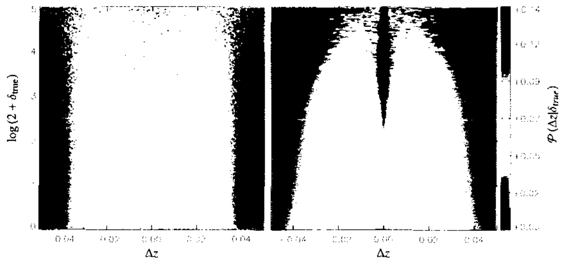

Figure 4: Probability distribution for the difference Δz between measured and true redshift conditional on the true underlying density field δ_{true}. The left panel shows the initial Gaussian redshift likelihood, as measured from the initial particle distribution, which is conditionally independent of the true underlying density field. The right panel shows the a posteriori conditional probability density distribution for Δz estimated from the Markov samples. It can be seen that the accuracy of inferred redshifts depends on the true underlying density field. Also note that the resulting probability distribution is non-Gaussian.

simulated matter density field has been estimated on a 256^3 Cartesian equidistant grid with side length of 1200 Mpc, followed by a Poisson sampling process to generate the galaxy distribution [5]. The radial galaxy positions have been distorted corresponding to a truncated Gaussian distribution with dispersion of $\sigma_z = 0.03$, which amounts to a radial uncertainty of about ~ 100 Mpc. In total we generate about 2×10^7 galaxies. Together with the number of grid nodes, used to infer the density field, this amounts to about 3×10^7 parameters for the present inference problem. The application of the two step sampling process, depicted in figure 2, then provides samples from the joint density and redshift posterior distribution. In figure 3, we depict slices through successive galaxy number count samples during the initial burn-in phase of the Markov sampler. While initially the galaxy sample exhibits strong redshift distortions, in subsequent samples these effects get iteratively corrected when galaxies move towards their true redshift positions. In figure 4, we show the comparison of the distributions of deviations from the true underlying redshift Δz before and after the application of our algorithm. Also note, since it is expected that the algorithm performs better in high density regions, where many galaxy measurements are available, than in low density regions, we plotted the distribution of Δz conditional on the true underlying matter density field. It can be nicely seen that the initial Δz distribution is essentially a Gaussian and that it is strictly independent of the underlying density field. After the application of our algorithm, the Δz is generally sharper than the original distribution. In particular galaxy redshifts in high density regimes can be accurately recovered [5]. As expected, the improvement in the low density regime is less prominent. Nevertheless, generally galaxy redshifts in all density regimes are improved. To quantify the accuracy of the inferred density field we compare the ensemble mean density field $\langle\delta\rangle$ to the true underlying density field δ_{true}, smoothed on different scales, via cross correlation. The density fields are smoothed with a spherical top hat filter in Fourier space with different filter radii k_{th}. The corresponding correlation coefficient for the different filter thresholds k_{th} are then given as [5]:

$$r(k_{th}) = \frac{\left\langle \delta_{true}^{k_{th}} \, \langle\delta\rangle^{k_{th}} \right\rangle}{\sqrt{\left\langle \left(\delta_{true}^{k_{th}}\right)^2 \right\rangle} \sqrt{\left\langle \left(\langle\delta\rangle^{k_{th}}\right)^2 \right\rangle}} \,. \tag{3}$$

The results of this analysis are depicted in the right panel of figure 5. To further study density dependent effects, we repeated the analysis for various thresholds in the true underlying density field. These results demonstrate that at the highest densities the density field can be recovered very well with a correlation of about 90 per cent even at the target resolution of about 5

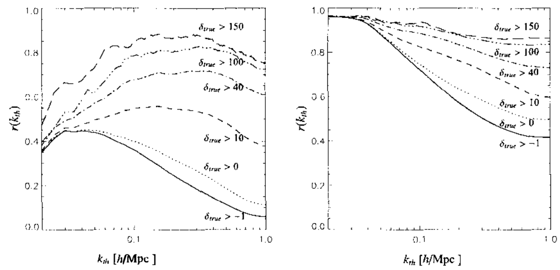

Figure 5: Correlation coefficient $r(k_{th})$ as a function of filter scale k_{th} for different density amplitude thresholds δ_{th} as indicated in the plot. The left panel correspond to the correlations between the initial density contrast, estimated from the galaxy counts, and the true density field, while the right panel depicts the correlation between the amplitudes of the true underlying and the ensemble mean density field. It can be seen that the correlation between amplitudes in the true underlying density field and the inferred ensemble mean density field increases on all filter scales with increasing density thresholds $\delta_{true} > \delta_{th}$. Also note the improved correlation at the large scales due to the correction of observational effects such as survey geometry and selection effects.

Mpc. With decreasing density amplitude the correlation between inferred and true density field decreases to a minimal value of about 40 per cent. For comparison, we performed the same analysis with a density field naively estimated from the redshift distorted galaxy survey, which we depicted in the left panel of figure 5. It can be seen, that the HADES algorithm greatly improves the density field inference on all scales and all density regimes [5].

5 Summary and Conclusion

Although the three dimensional large scale structure hosts a plenitude of information to test our current physical picture of cosmological structure formation, contact between observations and theory can not be established directly. Observational data are generally subject to a variety of systematic and statistical uncertainties such as survey geometries, selection effects, biases, redshift distortions and noise. These effects have to be accurately accounted for in order not to draw false conclusions on the finally inferred quantities. In addition, particularly due to statistical uncertainties, it is not possible to uniquely infer the three dimensional density field from observations. There will always be a set of possible three dimensional large scale structure configurations that are compatible with the observations within the range of uncertainty. To address this problem we developed the full Bayesian large scale structure inference framework HADES, which explores the large scale structure posterior distribution via an efficient implementation of a Markov Chain Monte Carlo algorithm, while accounting for all the afore mentioned systematics and uncertainties. Specifically HADES provides samples from the log-normal Poissonian posterior distribution conditioned on observations. In this fashion, HADES permits to estimate highly detailed three dimensional maps of the matter distribution from observations and to quantify corresponding statistical uncertainties. The algorithm has further been extended to account for redshift uncertainties, inherent to present and future photometric redshift surveys. It has been demonstrated that a joint inference of the three dimensional density field and the true locations of galaxies from redshift surveys with uncertain radial locations of galaxies can greatly improve the mutual inference of density field and galaxy positions. Particularly, the redshifts of galaxies in high density regimes can be accurately recovered. Being a full Bayesian method the HADES algorithm also accounts for all joint and correlated uncertainties of all quantities involved in the inference process. This permits highly accurate estimates for the significance of all finally inferred quantities, such as cosmological parameters. In summary, the HADES algorithm forms the basis for a full Bayesian large scale structure inference framework, which has the potential to greatly contribute to the era of precision cosmology.

Acknowledgments

JJ is partially supported by a Feodor Lynen Fellowship by the Alexander von Humboldt foundation. BDW acknowledges support from NSF grants AST 07-08849 and AST 09-08693 ARRA, and a Chaire d'Excellence from the Agence Nationale de Recherche and computational resources provided through XSEDE grant AST100029.

References

1. I. Kayo *et al*, *ApJ* **561**, 22 (34).
2. J. Jasche and F.S. Kitaura, *MNRAS* **407**, 29 (42).
3. J. Jasche *et al*, *MNRAS* **409**, 355 (370).
4. J. Jasche *et al*, *MNRAS* **406**, 60 (85).
5. J. Jasche and B.D. Wandelt, *ArXiv e-prints* **1106.2757**, ().
6. S. Duane *et al*, *Phys. Lett.* B **195**, 216 (222).
7. K.M. Hanson, *Society of Photo-Optical Instrumentation Engineers (SPIE) Conference Series* **4322**, 456 (467).
8. K.N. Abazajian, *ApJs* **182**, 543 (558).
9. W.K. Hastings, *Biometrika* **57**, 97 (109).
10. V. Springel, *MNRAS* **364**, 1105 (1134).
11. A. Pillepich *et al*, *MNRAS* **402**, 192 (206).
12. P. Coles and B. Jones, *MNRAS* **248**, 1 (13).
13. V.J. Martínez and E. Saar, *Chapman & Hall/CRC* Statistics of the Galaxy Distribution 2002.
14. F.S. Kitaura *et al*, *MNRAS* **400**, 183 (203).
15. P. Erdoğdu *et al*, *MNRAS* **352**, 939 (960).
16. S. Zaroubi, *MNRAS* **331**, 901 (908).
17. D. Huterer *et al*, *MNRAS* **366**, 101 (114).
18. G. Bernstein and B. Jain, *ApJ* **600**, 17 (25).
19. M. Ishak, *MNRAS* **363**, 469 (478).

DETECTING CANDIDATE COSMIC BUBBLE COLLISIONS WITH OPTIMAL FILTERS

J. D. MCEWEN[1], S. M. FEENEY[1], M. C. JOHNSON[2], H. V. PEIRIS[1]
[1]*Department of Physics and Astronomy, University College London, London WC1E 6BT, U.K.*
[2]*Perimeter Institute for Theoretical Physics, Waterloo, Ontario N2L 2Y5, Canada*

Abstract

We review an optimal-filter-based algorithm for detecting candidate sources of unknown and differing size embedded in a stochastic background, and its application to detecting candidate cosmic bubble collision signatures in Wilkinson Microwave Anisotropy Probe (WMAP) 7-year observations. The algorithm provides an enhancement in sensitivity over previous methods by a factor of approximately two. Moreover, it is optimal in the sense that no other filter-based approach can provide a superior enhancement of these signatures. Applying this algorithm to WMAP 7-year observations, eight new candidate bubble collision signatures are detected for follow-up analysis.

1 Introduction

The standard ΛCDM concordance cosmological model is now well supported by observational evidence. However, there are many theoretically well-motivated extensions of ΛCDM that predict detectable secondary signals in the cosmic microwave background (CMB) that are subdominant and consistent with current observational constraints. One such example is the signature of cosmic bubble collisions which arise in models of eternal inflation[1]. The most unambiguous way to test cosmic bubble collision scenarios is to determine the full posterior probability distribution of the global parameters defining the theory. However, the enormous size of modern CMB datasets, such as Wilkinson Microwave Anisotropy Probe[2] (WMAP) and Planck[3] observations, make a full-sky evaluation of the posterior at full resolution computationally impractical. Recently, however, a method for approximating the full posterior has been developed[4,5]. This approach requires preprocessing of the data to recover a set of candidate sources which are most likely to give the largest contribution to the marginalized likelihood used in the calculation of the posterior. The preprocessing stage of this method is thus crucial to its overall effectiveness. Candidate source detection aims to minimise the number of false detections while remaining sensitive to a weak signal; a manageable number of false detections is thus tolerated, as false detections will not significantly contribute to the marginalized likelihood. In these proceedings we review the recent work by McEwen *et al.* (2012)[6], where we developed an optimal-filter-based candidate source detection algorithm that we applied to detect candidate bubble collision signatures in WMAP data.

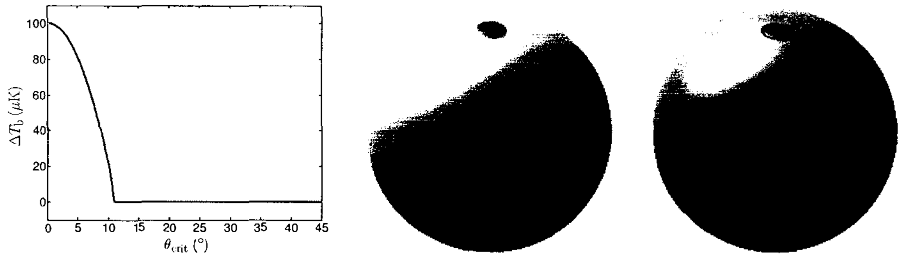

(a) Radial profile (b) Signature on the sphere (c) Matched filter

Figure 1: Panels (a) and (b) show the radial profile and spherical plot, respectively, of a bubble collision signature with parameters $\{z_0, \theta_{\rm crit}, \theta_0, \varphi_0\} = \{100\ \mu\text{K}, 10^\circ, 0^\circ, 0^\circ\}$. In panel (c) the corresponding matched filter is shown for the case where the background noise is specified by the CMB.

2 Optimal detection of candidate bubble collisions

Bubble collisions induce a modulative and additive contribution to the temperature fluctuations of the CMB[4,7], however the modulative component is second order and may be safely ignored. The additive contribution induced in the CMB by a bubble collision is given by the azimuthally-symmetric profile

$$\Delta T_{\rm b}(\theta, \varphi) = [c_0 + c_1 \cos(\theta)]\, s(\theta; \theta_{\rm crit})\,, \tag{1}$$

when centered on the North pole, where $(\theta, \varphi) \in \mathrm{S}^2$ denote the spherical coordinates of the unit sphere S^2, with colatitude $\theta \in [0, \pi]$ and longitude $\varphi \in [0, 2\pi)$, c_0 and c_1 are free parameters, $s(\theta; \theta_{\rm crit})$ denotes a "Schwartz" step function (an infinitely continuous step function that approximates the Heaviside step function) and $\theta_{\rm crit}$ is the size of the bubble collision signature. Bubble collision signatures may occur at any position on the sky (θ_0, φ_0) and at a range of sizes $\theta_{\rm crit}$ and amplitudes $z_0 = c_0 + c_1$ (we restrict our attention to bubble signatures with zero amplitude at their causal boundaries due to theoretical motivations[8,9], *i.e.* $z_{\rm crit} = c_0 + c_1 \cos(\theta_{\rm crit}) \sim 0\ \mu K$). A typical bubble collision signature is illustrated in Fig. 1.

We first construct matched filters to detect candidate bubble collision signatures for a known source size, before describing an algorithm for detecting multiple candidate bubble collision signatures of unknown and differing sizes. Matched filters are constructed on the sphere for a given candidate signature size $\theta_{\rm crit}$ following the methodology derived by Schaefer *et al.* (2006)[10] and McEwen *et al.* (2008)[11]. The matched filter corresponding to a typical bubble signature embedded in the CMB is shown in Fig. 1. We construct and apply matched filters for a grid of scales $\theta_{\rm crit}$ and then construct significance maps from each filtered field using simulated noise realisations. Potential candidate sources are recovered from the local peaks of thresholded significance maps. We then look across scales and eliminate potential detections if a stronger potential detection is made on an adjacent scale. In this manner we are able to detect candidate bubble collision signatures of unknown and differing size. Further details on the algorithm are given by McEwen *et al.* (2012)[6], where the approach is shown to perform well on simulations.

3 Bubble collision candidates in WMAP 7-year observations

The algorithm described previously to detect candidate bubble collision signatures was applied[6] to foreground-cleaned WMAP 7-year W-band observations, once it was calibrated to realistic WMAP observations. The analysis was calibrated using 3,000 Gaussian CMB WMAP simulations with W-band beam and anisotropic instrumental noise to compute the background mean

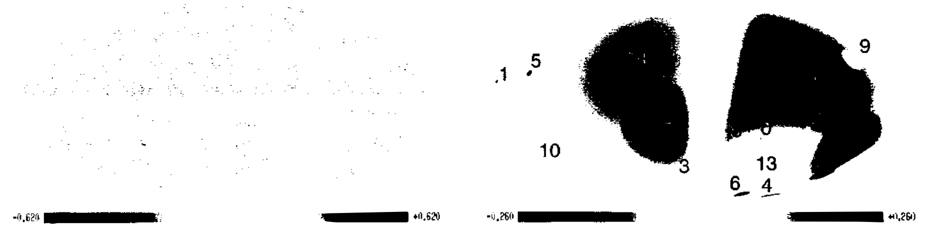

(a) WMAP 7-year W-band observations

(b) Candidate bubble collision signatures

Figure 2: WMAP data analysed by the bubble collision detection algorithm are shown in panel (a) and the resulting candidate bubble collision signatures detected are shown in panel (b) (in units of mK).

and variance required to compute significance maps, for each filter scale. The threshold levels for each scale were calibrated from a realistic WMAP simulation that did not contain bubble collision signatures. The thresholds were chosen to allow a manageable number of false detections while remaining sensitive to weak bubble collision signatures. For this calibration a complete end-to-end simulation of the WMAP experiment provided by the WMAP Science Team[12] was used. Throughout the calibration the WMAP KQ75 mask[12] was adopted.

The calibrated bubble collision detection algorithm was applied[6] to foreground-cleaned WMAP 7-year W-band observations[13], with the conservative KQ75 mask[12] applied. The WMAP W-band data that were analysed and the detected candidates are plotted on the full-sky in Fig. 2. Sixteen candidate bubble collision signatures were detected, including eight new candidates that have not been reported by previous studies. The parameters of the detected candidate signatures are reported by McEwen *et al.* (2012)[6].

4 Conclusions

We have reviewed the work by McEwen *et al.* (2012)[6], where an algorithm for detecting candidate cosmic bubble collision signatures in CMB observations was developed and applied. The algorithm is based on the application of optimal filters on the sphere and thus it is optimal in the sense that no other filter-based approach can provide a superior enhancement of bubble collision signatures. Furthermore, the approach is general and applicable to the detection of other sources on the sphere embedded in a stochastic background. After calibrating the algorithm on realistic WMAP simulations, it was applied to WMAP 7-year observations. Sixteen candidate bubble collision signatures were detected, including eight new candidates that have not been reported by previous studies. To ascertain whether these detections are indeed bubble collision signatures or merely rare ΛCDM fluctuations, it is necessary to use the candidates detected by the optimal-filter-based algorithm to construct the full posterior[4,5] and perform a robust model selection analysis; this is the focus on ongoing work.

Acknowledgments

We thank Daniel Mortlock for useful discussions. SMF thanks David Spergel for an interesting related conversation. We are very grateful to Eiichiro Komatsu and the WMAP Science Team for supplying the end-to-end WMAP simulations used in our null tests. This work was partially supported by a grant from the Foundational Questions Institute (FQXi) Fund, a donor-advised fund of the Silicon Valley Community Foundation on the basis of proposal FQXi-RFP3-1015 to the Foundational Questions Institute. JDM was supported by a Leverhulme Early Career Fellowship from the Leverhulme Trust throughout the completion of this work and is now supported by a Newton International Fellowship from the Royal Society and the British Academy. SMF is supported by the Perren Fund and STFC. Research at Perimeter Institute is supported by the Government of Canada through Industry Canada and by the Province of Ontario through the Ministry of Research and Innovation. HVP is supported by STFC and the Leverhulme Trust. We acknowledge use of the `HEALPix` package and the Legacy Archive for Microwave Background Data Analysis (LAMBDA). Support for LAMBDA is provided by the NASA Office of Space Science.

References

1. Anthony Aguirre, Matthew C Johnson, and Assaf Shomer. Towards observable signatures of other bubble universes. *Phys. Rev. D.*, D76:063509, 2007.
2. C. L. Bennett, M. Bay, M. Halpern, G. Hinshaw, C. Jackson, N. Jarosik, A. Kogut, M. Limon, S. S. Meyer, L. Page, D. N. Spergel, G. S. Tucker, D. T. Wilkinson, E. Wollack, and E. L. Wright. The Microwave Anisotropy Probe Mission. *Astrophys. J.*, 583:1–23, January 2003.
3. J. A. Tauber, N. Mandolesi, J.-L. Puget, et al. Planck pre-launch status: The Planck mission. *Astron. & Astrophys.*, 520, September 2010.
4. Stephen M. Feeney, Matthew C. Johnson, Daniel J. Mortlock, and Hiranya V. Peiris. First observational tests of eternal inflation: Analysis methods and wmap 7-year results. *Phys. Rev. D.*, D84:043507, 2011.
5. Stephen M. Feeney, Matthew C. Johnson, Daniel J. Mortlock, and Hiranya V. Peiris. First observational tests of eternal inflation. *Phys. Rev. Lett.*, 107:071301, 2011.
6. J. D. McEwen, S. M. Feeney, M. C. Johnson, and H. V. Peiris. Optimal filters for detecting cosmic bubble collisions. *Phys. Rev. D.*, in press, 2012.
7. Spencer Chang, Matthew Kleban, and Thomas S. Levi. Watching Worlds Collide: Effects on the CMB from Cosmological Bubble Collisions. *JCAP*, 0904:025, 2009.
8. Roberto Gobbetti and Matthew Kleban. Analyzing Cosmic Bubble Collisions. 2012.
9. Matthew Kleban, Thomas S. Levi, and Kris Sigurdson. Observing the Multiverse with Cosmic Wakes. 2011.
10. Bjoern Malte Schaefer, Christoph Pfrommer, Reinhard M. Hell, and Matthias Bartelmann. Detecting Sunyaev-Zel'dovich clusters with Planck: II. Foreground components and optimised filtering schemes. *Mon. Not. Roy. Astron. Soc.*, 370:1713–1736, August 2006.
11. J. D. McEwen, M. P. Hobson, and A. N. Lasenby. Optimal filters on the sphere. *IEEE Trans. Sig. Proc.*, 56(8):3813–3823, 2008.
12. B. Gold, N. Odegard, J. L. Weiland, R. S. Hill, A. Kogut, C. L. Bennett, G. Hinshaw, X. Chen, J. Dunkley, M. Halpern, N. Jarosik, E. Komatsu, D. Larson, M. Limon, S. S. Meyer, M. R. Nolta, L. Page, K. M. Smith, D. N. Spergel, G. S. Tucker, E. Wollack, and E. L. Wright. Seven-year Wilkinson Microwave Anisotropy Probe (WMAP) Observations: Galactic Foreground Emission. *Astrophys. J. Supp.*, 192:15, February 2011.
13. N. Jarosik, C. L. Bennett, J. Dunkley, B. Gold, M. R. Greason, M. Halpern, R. S. Hill, G. Hinshaw, A. Kogut, E. Komatsu, D. Larson, M. Limon, S. S. Meyer, M. R. Nolta, N. Odegard, L. Page, K. M. Smith, D. N. Spergel, G. S. Tucker, J. L. Weiland, E. Wollack, and E. L. Wright. Seven-year Wilkinson Microwave Anisotropy Probe (WMAP) Observations: Sky Maps, Systematic Errors, and Basic Results. *Astrophys. J. Supp.*, 192:14, February 2011.

RELATIVISTIC EFFECTS IN GALAXY SURVEYS

C. BONVIN
Kavli Institute for Cosmology Cambridge and Institute of Astronomy, Madingley Road, Cambridge CB3 OHA, England
and
DAMTP, Centre for Mathematical Sciences, Wilberforce Road, Cambridge CB3 OWA, England

We derive a general relativistic expression for the galaxy number density in a perturbed universe. We take into account all linear effects that modify the observed position and redshift of galaxies. We find that besides matter density and redshift-space distortion, the distribution of galaxies is affected by gravitational lensing, Doppler effects and gravitational potential effects. We compute the angular power spectrum of the galaxy number density and we compare the relative importance of the new relativistic terms for various redshift and angular separations.

1 Introduction

Galaxy surveys provide information on the distribution of galaxies as a function of redshift and direction. Perturbations in the observed number density of galaxies can be used to infer the matter power spectrum and learn about the growth rate of structure. At small sub-horizon scales, the distribution of galaxies reflects accurately the underlying distribution of dark matter (providing that the bias is well understood). Observations can therefore be straightforwardly interpreted and used to constrain cosmological parameters. However at large scales, the relation between the galaxy distribution and the matter distribution becomes more complicated. Observations are affected by changes in the energy and the trajectory of light between the source and the observer. Consequently, perturbations in the galaxy number density depend not only on the matter density fluctuations at the source position, but also on velocities and metric perturbations along the geodesics. In this work, we derive a gauge invariant expression for the galaxy number density perturbations, taking into account all the relevant effects up to first order in perturbation theory. We show that in addition to the well-known redshift-space distortion, galaxy number density is affected by gravitational lensing, Doppler effects and gravitational potential effects. We then compute the angular power spectrum of this observable and we compare the amplitude and shape of the various terms. Since the galaxy distribution is three-dimensional we are interested in both the angular power spectrum at a fixed redshift and the radial power spectrum correlating distributions at different redshifts. We find that the importance of the new terms depends on the angular and redshift separation.

2 Galaxy number density in redshift space

In a galaxy redshift survey, observers measure the number density of galaxies $N(\mathbf{n}, z)d\Omega_{\mathbf{n}}dz$ in direction $\mathbf{n}$ and at redshift z. They then average over the direction $\mathbf{n}$ to obtain the redshift distribution $\langle N\rangle(z)dz$. The perturbation in the number density of galaxies is defined as

$$\Delta(\mathbf{n},z)\equiv\frac{N(\mathbf{n},z)-\langle N\rangle(z)}{\langle N\rangle(z)}\ . \tag{1}$$

Neglecting the bias, we can relate the number density of galaxies to the matter density ρ with $N(\mathbf{n},z)=\rho(\mathbf{n},z)V(\mathbf{n},z)$, where $V(\mathbf{n},z)$ is the physical volume density per redshift bin and per solid angle. Since both the energy and the trajectory of light are affected by inhomogeneities between the source and the observer, the redshift z and the volume $V(\mathbf{n},z)$ are perturbed quantities. Denoting by δz and δV their respective perturbation, we find at linear order

$$\Delta(\mathbf{n},z)=\delta(\mathbf{n},z)-3\frac{\delta z}{1+z}+\frac{\delta V(\mathbf{n},z)}{V(z)}\ , \tag{2}$$

where $\delta=\delta\rho/\rho$ denotes the matter density fluctuation. Note that as required for an observable quantity, the above combination of terms in Δ is gauge invariant. In this paper we present the calculation in the longitudinal (newtonian) gauge[a] for which the metric reads

$$ds^2=a^2(\eta)\Big[-(1+2\Psi(\mathbf{x},\eta))+(1-2\Phi(\mathbf{x},\eta))\Big]\ , \tag{3}$$

where η is the conformal time.

Let us first compute the redshift perturbation. We consider a photon, emitted by a galaxy at $\eta=\eta_S$, and moving toward us in direction $\mathbf{n}$. The observer receives the photon redshifted by a factor $1+z_S=(n\cdot u)_S/(n\cdot u)_O$, where u_S and u_O denote the 4-velocity of the source, respectively the observer. Solving the null geodesic equation to obtain the photon momentum n^μ and using that $u=a^{-1}(1-\Psi,\mathbf{v})$, where $\mathbf{v}$ is the peculiar velocity we find for the redshift

$$1+z_S=\frac{a_O}{a_S}\left[1+\Psi_O-\Psi_S+\mathbf{n}(\mathbf{v}_O-\mathbf{v}_S)-\int_0^{r_S}dr(\dot\Phi+\dot\Psi)\right]\ . \tag{4}$$

Here $r_S=\eta_O-\eta_S$ is the galaxy radial coordinate and a dot means derivative with respect to η.

To calculate the perturbations in the volume of observation, we consider a small spatial volume element, $dV=\sqrt{-g}\ \epsilon_{\mu\nu\alpha\beta}\ u^\mu dx^\nu dx^\alpha dx^\beta$, seen by a source with 4-velocity u^μ. Perturbations in the photon trajectory generate perturbations in dV. Denoting by $\delta\theta$ and $\delta\varphi$ the perturbations in the angles of observation and by δr the perturbation in the radial distance, we find for the perturbed volume element at linear order (for a more detailed derivation see[1])

$$\begin{aligned}\frac{\delta V(\mathbf{n},z)}{V(z)} &= -3\Phi+\left(\cot\theta_O+\frac{\partial}{\partial\theta}\right)\delta\theta+\frac{\partial\delta\varphi}{\partial\varphi}-\mathbf{v}\cdot\mathbf{n}+\frac{2\delta r}{r}\\ &- \frac{d\delta r}{dr}+\frac{1}{\mathcal{H}(1+z)}\frac{d\delta z}{dr}+\left(4-\frac{2}{r\mathcal{H}}-\frac{\dot{\mathcal{H}}}{\mathcal{H}^2}\right)\frac{\delta z}{1+z}.\end{aligned} \tag{5}$$

Using the null geodesic equation to obtain $\delta\theta$, $\delta\varphi$ and δr, we find for Δ (see also[1 2 3])

$$\begin{aligned}\Delta(\mathbf{n},z) &= D_s+\frac{1}{\mathcal{H}}\partial_r(\mathbf{v}\cdot\mathbf{n})-\int_0^{r_S}dr\frac{r_S-r}{rr_S}\Delta_\Omega(\Phi+\Psi)+\left(\frac{\dot{\mathcal{H}}}{\mathcal{H}^2}+\frac{2}{r_S\mathcal{H}}\right)\mathbf{v}\cdot\mathbf{n}\\ &+ \Psi-2\Phi+\frac{1}{\mathcal{H}}\dot\Phi+\left(\frac{\dot{\mathcal{H}}}{\mathcal{H}^2}+\frac{2}{r_S\mathcal{H}}\right)\left(\Psi+\int_0^{r_S}dr(\dot\Phi+\dot\Psi)\right)+\frac{2}{r_S}\int_0^{r_S}dr(\Phi+\Psi)\ ,\end{aligned} \tag{6}$$

where D_s is the gauge invariant density fluctuation in Newtonian gauge and Δ_Ω denotes the transverse Laplacian. The first and second terms in Eq. (6) are the standard density perturbation and redshift-space distortion. The third term is a lensing contribution, which deforms the solid angle of observation; and the fourth one, proportional to the peculiar velocity along the line of sight, is the Doppler contribution. The second line gathers all the gravitational potential contributions.

[a] Note that in[1] we performed the calculation without fixing the gauge and therefore we explicitly demonstrated that Δ is gauge invariant

3 Results

Since $\Delta(\mathbf{n}, z_S)$ is a function on the sphere, we can expand it in spherical harmonics and compute its angular power spectrum. We have

$$\Delta(\mathbf{n}, z_S) = \sum_{\ell m} a_{\ell m}(z_S) Y_{\ell m}(\mathbf{n}), \qquad C_\ell(z_S, z_{S'}) = \langle a_{\ell m}(z_S) a^*_{\ell m}(z_{S'}) \rangle \ , \tag{7}$$

where the angular power spectrum C_ℓ can be evaluated either at a fixed redshift value $z_S = z_{S'}$ or as a cross-correlation between two different redshift slices $z_S \neq z_{S'}$. In the following we show the angular power spectrum computed in a ΛCDM universe. We assume gaussian adiabatic initial conditions with a flat power spectrum. In Fig. 1 we plot the various contributions to the

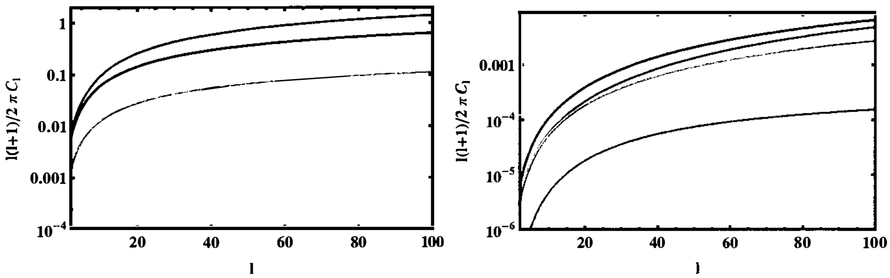

Figure 1: The various contributions to the angular power spectrum as a function of multipole ℓ, at $z_S = 0.1$ (left) and $z_S = 3$ (right). The different curves are: density (red), redshift-space distortion (green), correlation between density and redshift-space distortion (blue), lensing (magenta) and Doppler term (cyan).

angular power spectrum, for a fixed redshift value $z_S = z_{S'}$ and as a function of multipole ℓ. We see that the signal is strongly dominated by the standard terms, which are enhanced (at small scales) by at least a factor $(k/\mathcal{H})^2$ with respect to the new contributions. At small redshift (left panel) the Doppler term is enhanced by its prefactor $\propto 1/r_S^2$. On the other hand, since light deflections accumulate along the trajectory, the lensing contribution is enhanced at large redshift (right panel). In Fig. 2 we plot the angular power spectrum at different redshifts,

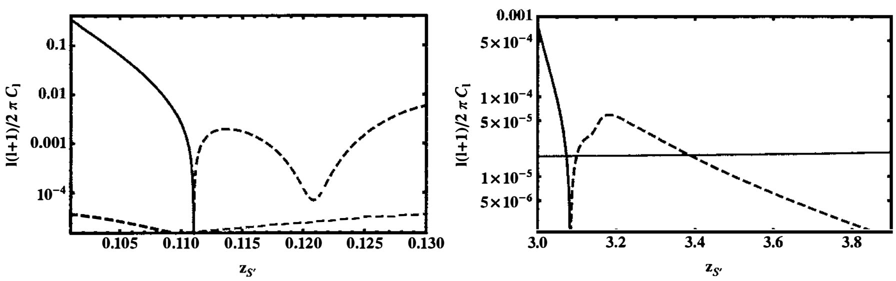

Figure 2: The angular power spectrum at $\ell = 20$, plotted as a function of $z_{S'}$ for $z_S = 0.1$ (left panel) and $z_S = 3$ (right panel). The different curves are: standard terms (blue), lensing (magenta), Doppler term (cyan) and potential terms (black). Solid lines denote positive contribution and dashed lines denote negative contributions.

which interestingly is more sensitive to the new contributions. We see that for some redshift separation, the Doppler term dominates over the standard one at small redshifts (left panel) and the lensing term dominates over the standard one at large redshift (right panel). This

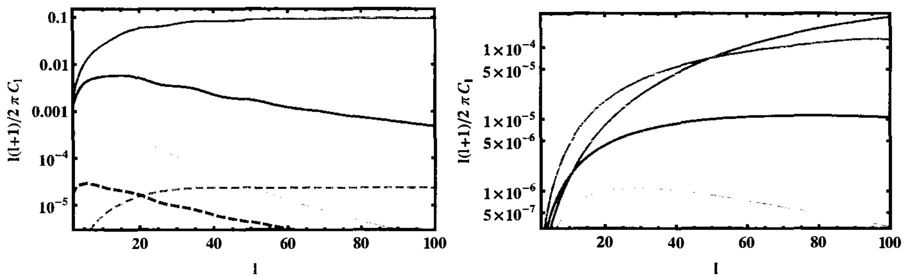

Figure 3: The various contributions to the binned angular power spectrum as a function of ℓ, with a 10 % window function at $z_S = 0.1$ (left) and $z_S = 3$ (right). The different curves are: density (red), redshift distortion (green), density-redshift distortion correlation (blue), lensing (magenta), Doppler (cyan) and potential terms (black).

follows from the fact that the density and redshift-space distortion are strongly dominated by small scales, that contribute less at different redshifts. Consequently the amplitude of the standard term decreases very quickly as the redshift difference increases. On the other hand, the Doppler term and the potential terms are suppressed by a factor $(\mathcal{H}/k)^2$, respectively $(\mathcal{H}/k)^4$, with respect to the standard terms. The integrals over k in the angular power spectrum receive therefore contributions from larger scales, that are correlated over a wider redshift range. Finally, since the lensing term is an integrated effect, it is almost insensitive to the redshift difference, as seen in the right panel of Fig. 2. Hence by looking at various redshift separations, we can in principle disentangle the new relativistic contributions from the standard terms. Finally in Fig. 3 we plot the angular power spectrum averaged over a redshift bin. We model the redshift bin with a gaussian window function with 10 percent width. Due again to the difference in scaling of the standard and new terms, the binning in redshift enhances the importance of the new terms with respect to the standard ones.

4 Conclusions

We have derived an expression for the quantity which is truly measured in galaxy surveys, namely the number density of galaxies as a function of direction and redshift. We have then computed the angular power spectrum of this observable in various configurations, i.e. for different angular and redshift separations. We have seen that by looking at different multipoles and redshift differences, we can measure different combinations of terms which depend on cosmological parameters in a variety of ways. Our results will be most significant for future galaxy surveys, like BOSS, DES and especially Euclid, that will span very large areas of the sky and observe up to high redshifts, allowing to probe relativistic scales.

Acknowledgments

CB supported by a Herchel Smith Postdoctoral Fellowship and by King's College Cambridge.

References

1. C. Bonvin and R. Durrer, Phys. Rev. **D84**, 063505 (2011).
2. A. Challinor and A. Lewis, Phys. Rev. **D84**, 043516 (2011).
3. J. Yoo, M. Zaldarriaga and L. Hernquist, Phys. Rev. **D81**, 123006 (2010);
   J. Yoo, Phys. Rev. **D82**, 083508 (2010) .

Biases on cosmological parameters by general relativity effects

Laura Lopez-Honorez
Max-Planck-Institut für Kernphysik, Saupfercheckweg 1, 69117 Heidelberg, Germany

General relativistic corrections to the galaxy power spectrum appearing at the horizon scale, if neglected, may induce biases on the measured values of the cosmological parameters. We analyze the impact of general relativistic effects on standard cosmology and in a scenario with a coupling between the dark energy and the dark matter fluids. We then explore whether general relativistic corrections affect future constraints on cosmological parameters in the case of a constant dark energy equation of state.

1 Introduction

In these proceedings, we study the effect of general relativistic corrections [1,2] in two different cosmological models presented in Sec. 2. We also analyze the expected errors and biases on the cosmological parameters in a constant dark energy equation of state scenario from a future Euclid-like galaxy survey by means of a Fisher matrix analysis, comparing the results with and without general relativistic corrections in the matter power spectrum, for more details, see Ref. [3].

Following the results of Refs. [4,1,2,5,6], we briefly summarize the treatment of the observed galaxy power spectrum in redshift space. In linear perturbation theory, the observed (matter) density $\rho_{\rm m}$ at a given redshift is defined as a function of the density fluctuation $\delta_{\rm m}$ and the background (matter) density $\bar{\rho}_{\rm m}$: $\rho_{\rm m} \equiv \bar{\rho}_{\rm m}(\bar{z})(1+\delta_{\rm m})$. The observed redshift of a given source, z, actually differs from the background one due to the matter/gravity fluctuations that the photon encounters between the emitter and the observer positions. The observed (perturbed) redshift z reads $1 + z \equiv 1 + \bar{z} + \delta z$. Expressing the matter density in terms of the observed redshift, instead of the unobservable background one, one obtains:

$$\rho_{\rm m} = \bar{\rho}_{\rm m}(z)\left(1+\delta_{\rm m} - \frac{d\bar{\rho}_{\rm m}}{dz}\frac{\delta z}{\bar{\rho}_{\rm m}}\right) \equiv \bar{\rho}_{\rm m}(z)\,(1+\Delta_z)\ , \tag{1}$$

with the background matter density $\bar{\rho}_m(z)$ function of the observed redshift z. While the density contrast $\delta_{\rm m}$ and the redshift fluctuation δz are gauge dependent quantities, their combination Δ_z is, instead, gauge invariant. Notice, however, that the truly observed quantity is the galaxy number density perturbation [1,5,6] corresponding to:

$$\Delta_{obs} = \frac{\delta N}{\overline{N}} \equiv \frac{N(z) - \overline{N}(z)}{\overline{N}(z)} = \Delta_z + \frac{\delta {\rm Vol}}{\overline{\rm Vol}}\ , \tag{2}$$

where an extra contribution from the physical survey volume perturbation appears. Being the volume density perturbation, δVol, a gauge invariant quantity, Δ_{obs} is automatically gauge invariant, as it should be for any observable quantity.

In the Newtonian gauge, the density perturbation Δ_{obs} read respectively:

$$\begin{aligned}\Delta_{obs} &= \delta_{\rm m}^{N} + \frac{1}{\mathcal{H}}\mathbf{n}\cdot\partial_r\mathbf{v} - 2\kappa + \Psi_N - 2\Phi_N + \frac{1}{\mathcal{H}}\dot{\Phi}_N \\ &+ \left(\frac{2}{r_s\mathcal{H}} + \frac{\dot{\mathcal{H}}}{\mathcal{H}^2}\right)\left[\mathbf{n}\cdot\mathbf{v} + \Psi_N + \int_0^{r_s} d\lambda\left(\dot{\Psi}_N + \dot{\Phi}_N\right)\right] + \frac{2}{r_s}\int_0^{r_s} d\lambda\,(\Psi_N + \Phi_N)\ , \quad (3)\end{aligned}$$

where κ is the lensing convergence, Ψ_N and Φ_N are the scalar perturbations of the metric in the Newtonian gauge and the partial derivative $\partial_r = e_r^i\partial_i = -n^i\partial_i$ with e_r^i indicating the source position. With δ_m^N and $\mathbf{v}$, we refer to the matter density and peculiar velocity perturbation in the Newtonian gauge and $r_s = \int_{\tau_o}^{\tau_s} d\tau$ corresponds to the comoving distance between the source and the observer. Notice that Eq. (3) holds in the case of a conserved matter energy density. Slight modifications in the expression of (3) appear in the case of coupled cosmologies, see Sec. 2 and Ref[3] for more details.

In the standard Newtonian approximation, the galaxy number density perturbation, Δ_{st}, only gets contributions from the three first terms of Eq. (3), namely from the matter density perturbation, the redshift space distortion term and from the convergence term. We consider that, neglecting the bias between galaxy and matter overdensities, the associated standard Newtonian power spectrum is related to the matter power spectrum evaluated in the synchronous gauge in the following way: $P_{\Delta_{st}} = P_{\rm m}^{S}\left(1 + f_{\rm eff}\mu_k^2\right)^2$. The latter is typically used for calculating the power spectrum when relativistic contributions can be safely neglected (i.e. for scales much smaller than the horizon scale). The index S refers to the synchronous comoving gauge, $f_{\rm eff}$ is the linear growth function and μ_k is the cosine of the angle between the line of sight and the wave vector k.

2 Cosmological scenarios

We first consider a cosmological model including standard cold dark matter and a dark energy fluid characterized by a constant equation of state w. The left panel of Fig. 1 shows the dark matter power spectra $P_{\Delta_{obs}}(k,\mu_k)$ and $P_{\Delta_{st}}(k,\mu_k)$ for the transverse ($\mu_k = 0$) modes at $z = 0.5$ for several values of w. The modifications in the shape of the power spectra when relativistic effects are considered barely change when the dark energy equation of state is varied. In addition, the new features on the power spectrum induced by the general relativity terms appear only at very large scales: consequently, one would not expect much improvement on the measurement of w when relativistic effects are included. For the same reason, the bias induced on the dark energy equation of state w when the data are fitted to $P_{\Delta_{st}}$ (instead of using the full description given by $P_{\Delta_{obs}}$) is expected to be negligible.

Let us also briefly discuss the case of coupled cosmologies. As an illustration, we parameterize the dark matter-dark energy interactions at the level of the stress-energy tensor conservation equations [7]: $\nabla_\mu T^\mu_{(\rm dm)\nu} = Q_\nu$ and $\nabla_\mu T^\mu_{(\rm de)\nu} = -Q_\nu$, with $Q_\nu = \xi\mathcal{H}\rho_{\rm de}u_\nu^{\rm dm}/a$. $u_\nu^{\rm dm}$ is the cold dark matter four velocity and ξ is a dimensionless coupling, considered negative in order to avoid early time non adiabatic instabilities [8]. Coupled cosmologies imply some extra terms in the expression of the gauge invariant matter fluctuation. Indeed, in the case of the coupled models studied here $\frac{d\rho_{\rm dm}}{dz} = 3\frac{\rho_{\rm dm}}{1+z} - \xi\frac{\rho_{\rm de}}{1+z}$, which directly affects the expressions for Δ_m and Δ_z. In the right panel of Fig. 1, we show the resulting matter power spectra. As in the case of the dark energy equation of state, no strong biases are expected in constraining the coupling when these new general relativistic terms are included in the analysis: the shape of the different curves including relativistic corrections barely changes when the coupling is varied.

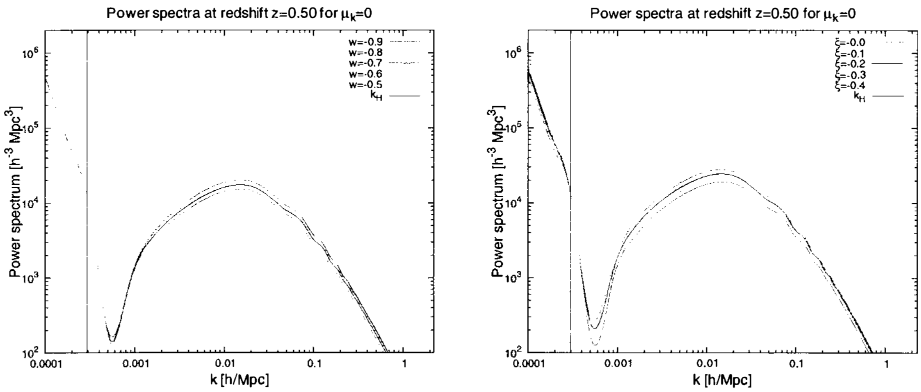

Figure 1: $P_{\Delta_{obs}}(k)$ *(solid lines) and* $P_{\Delta_{st}}(k)$ *(dashed lines) for* $\mu_k = 0$. *The vertical line corresponds to the horizon scale* k_H. *In the left panel, the dark energy equation of state* w *is assumed to be constant and has been varied between* -0.9 *and* -0.5. *The right panel depicts the power spectra for coupled models with an interaction term proportional to* $u_\nu^{\rm dm}$ *and for different values of the coupling* ξ.

3 Cosmological parameter forecasts and biases

In this section we explore if the measurement of the different cosmological parameters in a standard cosmological scenario with a constant dark energy equation of state is affected by relativistic corrections. We present constraints from future galaxy survey measurements, making use of the Fisher matrix formalism. Then, we compare the cosmological parameter errors with and without general relativistic corrections. In addition to the marginalized parameter errors, the biases[9,3] induced in the cosmological parameters when data are wrongly fitted to the standard Newtonian power spectrum, neglecting general relativity corrections, are also computed. We exploit here an enlarged version of the future Euclid galaxy survey experiment, with an area of 20000 deg^2, 24 redshift slices between $z = 0.15$ and $z = 2.55$ and a mean galaxy density of 1.56×10^{-3}, see Refs.[10,11]. The model is described by the physical baryon and cold dark matter densities, $\Omega_{\rm b}h^2$ and $\Omega_{\rm dm}h^2$, the scalar spectral index, $n_{\rm s}$, h, the dimensionless amplitude of the primordial curvature perturbations, $A_{\rm s}$ and w.

Parameter	$P_{\Delta_{st}}(k,\mu_k)$	$P_{\Delta_{obs}}(k,\mu_k)$	Biases
$\Delta(\Omega_{\rm dm}h^2)$	0.0035	0.0057	$7.0\,10^{-5}$
$\Delta(\Omega_{\rm b}h^2)$	0.0010	0.0016	$-8.0\,10^{-5}$
$\Delta A_{\rm s}$	0.021	0.036	$1.1\,10^{-5}$
Δh	0.010	0.017	$1.3\,10^{-4}$
$\Delta n_{\rm s}$	0.012	0.016	$-4.3\,10^{-3}$
Δw	0.015	0.010	$7.7\,10^{-3}$

Table 1: 1–σ marginalized errors from the Euclid-like survey considered here for a fiducial cosmology with a constant dark energy equation of state, with a fiducial value $w = -1$. The third row illustrates the biases induced in the cosmological parameters when general relativistic corrections are (wrongly) neglected. The error on the amplitude of the primordial fluctuations $\Delta A_{\rm s}$ is quoted in units of $2.64 \cdot 10^{-9}$.

Table 1 contains the 1–σ marginalized errors on the cosmological parameters for a fiducial cosmology with constant dark energy equation of state $w = -1$. Two results are illustrated: those obtained with the standard Newtonian power spectrum and those obtained with general relativistic corrections included. Note that the errors obtained in the standard Newtonian prescription are generally 40% smaller than those obtained with general relativistic one, except for the w parameter in which case the tendency is reversed. The biases on the cosmological parameters are also presented in Tab. 1. Note that their size is always smaller than the $1-\sigma$ marginalized errors and therefore these biases will barely interfere with the extraction of the cosmological parameters.

4 Conclusion

The complete general relativistic description of the observed matter power spectrum at large scales is significantly different than the standard Newtonian one. In these proceedings, we have studied the role of relativistic effects in the extraction of different cosmological parameters with the galaxy power spectrum measurements that will be available from future surveys. We find that general relativistic corrections will not interfere with the extraction of the standard cosmological parameters. The biases induced in the different cosmological parameters when neglecting these relativistic effects are also negligible. We conclude that the measurement of the cosmological parameters will not be compromised by the presence of general relativistic effects, once they will be included in the analysis.

Acknowledgments

I would like to thank the organizers of the Rencontres de Moriond conference for giving me the opportunity to present my work in the Cosmology Session this year. The results presented here were obtained in collaboration with O. Mena and S. Rigolin in Ref. [3].

References

1. Jaiyul Yoo, A. Liam Fitzpatrick, and Matias Zaldarriaga. A New Perspective on Galaxy Clustering as a Cosmological Probe: General Relativistic Effects. *Phys. Rev.*, D80:083514, 2009.
2. Jaiyul Yoo. General Relativistic Description of the Observed Galaxy Power Spectrum: Do We Understand What We Measure? *Phys. Rev.*, D82:083508, 2010.
3. L. Lopez-Honorez, O. Mena, and S. Rigolin. Biases on cosmological parameters by general relativity effects. *Phys.Rev.*, D85:023511, 2012.
4. Camille Bonvin, Ruth Durrer, and M. Alice Gasparini. Fluctuations of the luminosity distance. *Phys. Rev.*, D73:023523, 2006.
5. Camille Bonvin and Ruth Durrer. What galaxy surveys really measure. 2011.
6. Anthony Challinor and Antony Lewis. The linear power spectrum of observed source number counts. 2011.
7. M. B. Gavela, L. Lopez Honorez, O. Mena, and S. Rigolin. Dark Coupling and Gauge Invariance. *JCAP*, 1011:044, 2010.
8. M. B. Gavela, D. Hernandez, L. Lopez Honorez, O. Mena, and S. Rigolin. Dark coupling. *JCAP*, 0907:034, 2009.
9. Roland de Putter and Eric V. Linder. To Bin or Not To Bin: Decorrelating the Cosmic Equation of State. *Astropart.Phys.*, 29:424–441, 2008.
10. A. Refregier, O. Boulade, Y. Mellier, B. Milliard, R. Pain, et al. DUNE: The Dark Universe Explorer. 2006.
11. A. Refregier, A. Amara, T.D. Kitching, A. Rassat, R. Scaramella, et al. Euclid Imaging Consortium Science Book. 2010.

The Sunyaev-Zel'dovich effect in WMAP

J.M. Diego
Instituto de Fisica de Cantabria, Universidad de Cantabria-CSIC,
Avda. Los Castros s/n. 39005 Santander, Spain

Using WMAP 5 year data, we look for the average Sunyaev-Zel'dovich effect (SZE) signal from clusters of galaxies by stacking the regions around hundreds of known X-ray clusters. We conclude that the observed SZE seems to be less than the expected signal derived from X-ray measurements when a standard β-model is assumed for the gas distribution. Models with steeper profiles are able to simultaneously fit both X-ray and WMAP data better than a β-model. A model assuming point source contamination in SZE clusters renders a better fit to the one-dimensional SZE profiles thus suggesting that contamination from point sources could be contributing to a diminution of the SZE signal.

1 Introduction

In the last few years years, there has been an ongoing debate about the possibility that we do not yet quite understand the physics involved in the interaction between the gas inside galaxy clusters and the cosmic microwave background (or CMB) known as the Sunyaev-Zel'dovich effect (or SZE hereafter; Sunyaev & Zel'dovich 1972). The motivation for this debate is the apparent weaker strength of the SZE signal in galaxy clusters than expected from X-ray observations of the same clusters (Lieu et al. 2006, Afshordi et al. 2007, Atrio-Barandela et al. 2008). On the other hand, other works claim that there is no missing signal and that the interaction between galaxy clusters and the CMB can be well described in terms of the SZE once a realistic model for the gas distribution is considered. Understanding the SZE is important also for cosmological studies based on clusters and the SZE (see for instance Bartlett & Silk 1993, Diego et al 2002b)

We follow previous works and revisit the debate, but also perform a different analysis using the most accurate CMB data to date, namely the five year WMAP data (Hinsaw et al. 2009). We use a large sample of known X-ray clusters and stack the CMB data in an area around each one of them. The stacking procedure effectively reduces the contributions of instrumental noise and fluctuations in the CMB itself relative to the SZE making it possible to *see* the clusters (or their average signal) in WMAP data. Using the X-ray fluxes we are able to predict the SZE for each cluster (and hence, the average signal when the SZE signal of all clusters is added together) and compare the average predicted SZE with the observations. We find that the expected SZE signal depends strongly on the assumptions made about the internal distribution of the cluster gas. Our results neither strongly contradict nor strongly confirm the findings in some previous works where a lack of signal from clusters at mm wavelengths was found. Our results still show a lack of SZE signal in galaxy clusters but the disagreement between the observed signal and the expected one is significantly less than previously reported by Lieu et al (2006). A detailed discussion of the results of this work can be found in Diego & Partridge (2010).

2 X-ray cluster catalogs

There are a variety of cluster catalogs. For the purpose of this work the most interesting ones are those based on an X-ray selection. For this work, we build a large cluster catalog combining three catalogs: the Bright Cluster Sample (or BCS Ebeling et al. 1998), the extended Bright Cluster Sample (or eBCS Ebeling et al. 2000) and the ROSAT-ESO Flux-Limited X-Ray catalog (or REFLEX; Böhringer et al. 2004). These catalogs are X-ray selected using data from the ROSAT All Sky Survey (or RASS). The combined catalog covers both the north and south Galactic hemispheres for Galactic latitudes roughly above 20° and below -20°. There are 750 clusters in our combined catalog outside the Galactic exclusion zones. The combined catalog contains measured redshifts, X-ray fluxes, temperatures (for some clusters) and luminosities for the brightest X-ray clusters observed with ROSAT. In the case of REFLEX clusters, the catalog does not contain temperature estimates, but these can be derived from scaling relations as described below. A scaling relation was also used by Ebeling et al. (2000) to derive temperatures for some of the clusters in the eBCS catalog.

We focus on having a large sample of clusters (even if their profiles are not resolved) rather than a small but well defined sample of clusters. Instead of fitting the profile of a few dozen clusters we fit the average flux of a much wider sample of hundreds of clusters. Taking a large sample of clusters is crucial for reducing the CMB and instrumental noise fluctuations that contaminate the SZE signal. We use the X-ray observed flux in every cluster to *normalize* the gas model.

Average properties can usually be described by scaling relations, and are powerful tools that have allowed us to set constraints on cosmological models using galaxy cluster observations. Some of these scaling relations show very tight correlations between cluster properties. The best studied so far use X-ray data. In particular, one of the most famous is the correlation between the X-ray luminosity (L_x) and the plasma temperature (T) or $L_x - T$ relation (David et al. 1993, Mushotzky & Scharf 1997). N-body simulations, as well as analytical models, predict similar correlations between quantities derived from SZE observations. Scaling relations are representative of the average properties of clusters and we use them to model the average signal observed by two very different experiments, ROSAT and WMAP. A relation between the X-ray luminosity and physical core size of the cluster can be obtained from the above $L_x - T$ relation

3 Results

Through a stacking procedure we reduce the contribution of the CMB and instrumental noise since these two signals should average to zero for a sufficiently large number of stacked fields.

In our stacking procedure we first construct full sky maps of the data to be stacked (in those cases where the all sky maps are not already available). An area (or field of view, FOV hereafter) of $2.5° \times 2.5°$ is then selected around each galaxy cluster in our combined catalog and the area is projected into a plane using an orthographic projection. We sample the FOV of 2.5 degrees with

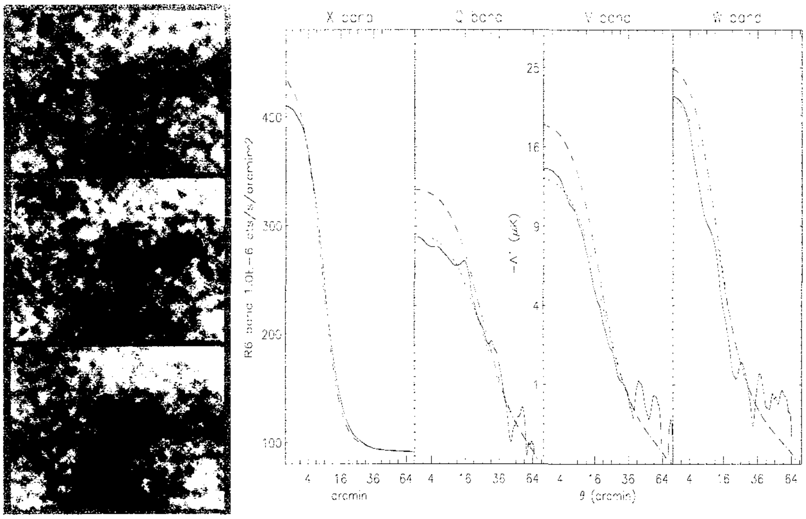

Figure 1: **Left**. SZ in WMAP data. From top to bottom, W, V and Q bands. Each panel shows the average signal obtained after stacking an area of $2.51° \times 2.51°$ around the clusters in the X-ray catalog. Those clusters with bright radio sources have been masked. Note the very clear decrement in the W band. The decrement can still be seeing in the V and Q bands but with less intensity due to the beam smearing. **Right**.One dimensional profiles (solid lines) compared with the best fitting model (dashed line). From left to right, X-ray RASS profile, Q, V and W WMAP profiles. The dotted lines in the Q, V and W bands show the model minus the contribution of a point source at the center of the cluster with fluxes of 16, 26 and 18 mJy in Q, V and W bands respectively.

256×256 pixels (i.e a pixel size of ≈ 0.6 arcmin). Due to the random orientations introduced by the stacking procedure, the original pixels in the all-sky maps take random orientations and do not align with other pixels in different FOVs. The stacking procedure introduces an average pixel resulting from the average of all the possible orientations of the original pixel. In the next section we will discuss how to estimate this effect quantitatively, using the X-ray data as an example.

We use three of the WMAP frequency bands, Q (at 41 GHz), V (at 61 GHz) and W (at 94 GHz) to search for the signal from known galaxy clusters in the average stacked map. A more detailed description of the WMAP five year data and its main results can be found in Hinsaw et al. (2009). Due to beam dilution effects, we expect to have the strongest SZE signal in the W band which has superior angular resolution.

4 Conclusions

By stacking WMAP 5 year data we are able to see the average SZE signal from a large sample of galaxy clusters. These clusters are X-ray selected.

A comparison of models with the average X-ray profile and the average SZE profile allows us to narrow down the range of possible models. Standard β-models are harder to reconcile with both data sets. A steeper profile, like the one suggested by Ascasibar & Diego (2008) renders a better fit to the data. None of the models considered is able to perfectly fit both data sets. We find a best fitting model that predicts a signal close to the observed ones (in X-rays and SZE) and also leaves room for point source contamination at roughly the level expected from radio and infrared extrapolations. We conclude that the X-ray and SZE measurements are consistent once a careful modeling of both data sets and a realistic level of point source contamination are taken into account. Based on the predictions made by the *concordance* model, we compare the SZE and X-ray fluxes and find a tight correlation between them. These kinds of correlations have been predicted in the past but never observed with a large sample of clusters. Future SZE data like Planck, and also high resolution experiments like ACT or SPT, will help answer some of the questions raised in this paper and further develop this new and exciting field.

Acknowledgments

JMD acknowledges support for a Ministerio de Ciencia e Innovación grant JC2008-00104 from the Jose Castillejo program. JMD would like to thank Haverford College for its hospitality during the duration of this project. BP's research is supported in part by NSF grant AST-0606975 to Haverford College.

References

1. Ascasibar Y., Diego J.M. 2008, MNRAS, 383, 369
2. Afshordi N. Lin Y-T., Nagai D. Sanderson A.J.R. 2007, MNRAS, 378, 293
3. Atrio-Barandela F., Kashlinsky A., Kocevski D., Ebeling H. 2008, ApJ, 675, L57
4. Bartlett J. G., Silk J. 1993, ApJ, 407, L45.
5. Böhringer et al. (more than 8 authors). 2004, A&A, 425, 367
6. Diego J.M., Martínez-González E., Sanz J.L., Cayón L., Silk J. 2001, MNRAS, 325, 1533.
7. Diego J.M., Martínez-González E.; Sanz J.L., Benitez N., Silk, J. 2002, MNRAS, 331, 556
8. Diego, J. M.; Silk, J.; Sliwa, W. 2003, MNRAS, 346, 940
9. Diego J.M., Ascasibar Y. 2008, MNRAS, 389, 1805
10. Diego J.M & Partridge B. 2010, MNRAS, 402, 1179
11. Ebeling H., Edge A.C., Böhringer H., Allen S.W., Crawford C.S., Fabian A.C., Voges W., Huchra J.P., 1998, MNRAS, 301, 881
12. Ebeling H., Edge A.C., Allen S.W., Crawford C.S., Fabian A.C., Huchra J.P. 2000, MNRAS, 318, 333
13. Hinshaw G. et al. (more than 8 authors) 2009, ApJS, 180, 225
14. Lieu R., Mittaz J.P.D., Zhang S.N., 2006, ApJ, 648, 176
15. Mushotzky R.F., Scharf C.A., 1997, 1997, ApJ, 482, L13
16. Sunyaev R.A. & Zel'dovich Ya.B., 1972, A&A, 20, 189

2.
CMB, Clusters, SZ

SZ CLUSTERS IN THE PLANCK SURVEY

E. Pointecouteau [1,2]
on behalf of the *Planck* Consortium
[1] *CNRS; IRAP; 14 avenue Edouard Belin, F–31400 Toulouse, France ;*
[2] *Université de Toulouse; UPS-OMP; IRAP; Toulouse, France*
etienne.pointecouteau@irap.omp.eu

The *Planck* mission has surveyed the whole sky more than four times. We have released the early SZ sample of 189 clusters detected via the Sunyaev-Zel'dovich effect with high signal-to-noise clusters and is highly reliable from the first survey. The Planck collaboration has published various early and intermediate results on clusters: SZ detection, new detected clusters, ongoing follow-up programs, constraints on SZ scaling relations, etc. I review will search for clusters in the *Planck* surveys and the results on galaxy clusters.

1 Introduction

The observation of clusters of galaxies through the Sunyaev-Zeldovich (SZ) effect, the inverse Compton scattering of cosmic microwave photon by hot intra-cluster electrons [1], have proven to be an efficient way to search for new clusters [2,3,4]. The total SZ signal is closely related to the cluster mass (e.g. [5]), and its surface brightness insensitive to distance. Therefore, SZ surveys can potentially be used to built unbiased close to mass selected cluster samples up to high redshift. Such samples will be of tremendous help for structure formation studies and to provide CMB independent cosmological constraints. However, this requires a precise understanding of the statistical properties of the cluster population and furthermore a precise calibration of scaling relations between clusters physical properties and their mass.

The *Planck*[a] satellite has been surveying the sky in the microwave bands since August 2009 [6]. Although, its spatial resolution is moderate with respect to ground based SZ surveys (e.g., [2,3]), it possesses a unique nine-band coverage from 30 to 857 GHz and, most crucially, it covers an exceptionally large survey volume. Indeed *Planck* is the first all-sky survey capable of blind cluster detections since the *ROSAT* All-Sky Survey (RASS, in the X-ray domain). Early *Planck* results on galaxy clusters were recently pub-

[a] *Planck* (http://www.esa.int/Planck) is a project of the European Space Agency (ESA) with instruments provided by two scientific consortia funded by ESA member states (in particular the lead countries: France and Italy) with contributions from NASA (USA), and telescope reflectors provided in a collaboration between ESA and a scientific consortium led and funded by Denmark.

lished in [7,4,8,9,10,11]. These results include the publication of the high signal-to-noise ratio (S/N > 6) Early SZ (ESZ) cluster sample [7]

In the following I review the status of the search for clusters in the *Planck* surveys, I describe the methodology for their validation and I detail the follow-up programme meu undergone by the *Planck* collaboration to confirm and characterize SZ sources. I then briefly review the some other results on the SZ effect and clusters of galaxies published form the *Planck* data.

2 The Planck mission

Planck [12,6] is the third generation space mission to measure the anisotropy of the cosmic microwave background (CMB). It observes the sky in nine frequency bands covering 30–857 GHz with high sensitivity and angular resolution from 31 to 5 arcmin. The Low Frequency Instrument (LFI; [13,14,15]) covers the 30, 44, and 70 GHz bands with amplifiers cooled to 20 K. The High Frequency Instrument (HFI; [16,17]) covers the 100, 143, 217, 353, 545, and 857 GHz bands with bolometers cooled to 0.1 K. Polarisation is measured in all but the highest two bands [18,19]. A combination of radiative cooling and three mechanical coolers produces the temperatures needed for the detectors and optics [20]. Two Data Processing Centers (DPCs) check and calibrate the data and make maps of the sky [21,22]. *Planck*'s sensitivity, angular resolution, and frequency coverage make it a powerful instrument for Galactic and extragalactic astrophysics as well as cosmology. Early astrophysics results are given in Planck Collaboration VIII– XXVI 2011, based on data taken between 13 August 2009 and 7 June 2010. Intermediate astrophysics results are now being presented in a series of papers based on data taken between 13 August 2009 and 27 Novcmber 2010.

3 Detection of galaxy clusters in the Planck survey

The surface brightness of the SZ effect is proportional to the thermal pressure integrated along the line of sight:

$$y = \frac{\sigma_T}{m_e c^2} \int P(l) dl \tag{1}$$

where σ_T is the Thomson cross-section, m_e the mass of the electron and c the speed of light. P is the thermal pressure and is the genuine product of the gas temperature and density.

We adopted the 'universal' pressure profile provided by [23] as a baseline model. We parametrised it with the scale radius, R_{500}, and the integrated Compton parameter, Y_{500}, as shape and normalisation parameter respectively. Here Y_{500} is defined as follow:

$$Y_{500} = \int_{\Omega_{500}} y(\Omega)\, d\Omega \tag{2}$$

We implemented this model in different detection methods based on (i) matched multi-frequency filter algorithms [24,25] or (ii) a Powell-Snakes algorithm [26,27]. The algorithms further assume the spectral dependance of the SZ effect formalised by [1]. We run a blind cluster search on the whole *Planck* sky. Output lists are then merged and candidates then undergo an internal SZ quality check in order to trim spurious detection (e.g., association with artefacts or galactic sources). We assess the quality of the SZ signal from both the the number of redundant blind detection across methods, the signal-to-noise ratio ad visual inspection.

To further consolidate the list of candidate each were processed through a validation chain starting with the cross-correlations with existing catalogues of clusters in X-rays (e.g., NORAS, REFLEX, BCS, MACS, NEP, EMSS, 400sd, etc) making use of the meta-catalogue of X-ray clusters [28], and in the optical (e.g., ABELL, ZWICKY, SDSS based catalogues, etc). We cross-checked our sources with those from other SZ experiments (e.g., OVRO, BIMA, SPT, ACT, SZA, etc). We ran a systematic search in RASS at the location of each target and queried the digital sky survey database looking for photons and galaxies overdensities respectively. We searched the logs of X-ray and optical observatories in order to associate sources potentially already targeted by other facilities.

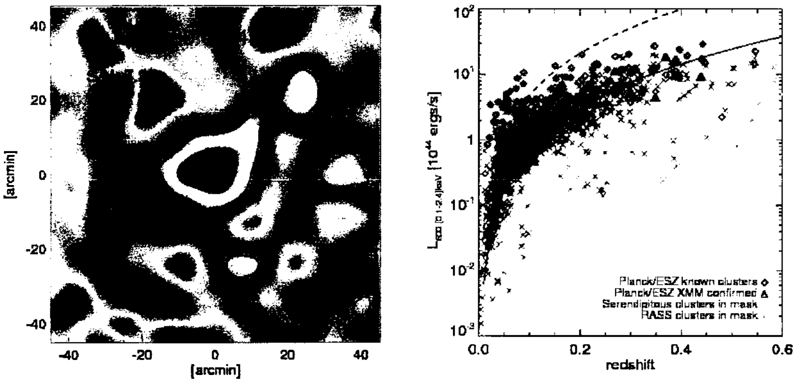

Figure1: *(left)* Exampleofablindnewdetectedcluster.ThemapshowsthereconstructedSZsignalfromthelinearcombinationofthe *Planck*-HFIsixfrequency. *(right)* The158clustersfromthe *Planck* ESZsampleidenti fiedwithknownX-rayclusters inredshiftluminosityspace,comparedwith serendipitousandRASSclusters[7].

FortheEarlycatalogue,weassembledasampleof189SZclustersoutofwhich20arenewsources blindlydetectedby *Planck*.For80%ofthe169identi fiedclusters,weprovidedthe firstSZmeasurements. 162oftheidenti fiedclusterswereobservedinX-rays.TheconstructionoftheESZsampleisfullydetailed in[7].

4 Validation and follow-ups

ThePlanckcollaborationisrunningamulti-wavelengthsfollow-upprogramforvalidation.Theaimis threefolds:(1)con firmthesourceasaclusterofgalaxies;(2)obtainameasurementofitsredshift;(3) provideanmeantodoublecheckthe *Planck* performancesforSZobservations,thusforclusterscience.

Thisprogrammeincludesopticalfollow-upswithnumerousfacilities,amongwhichENO /INT,ENO/WHT, NOT,ESO /MPG-2.2m,ESO /NTT,RTT,etc.ComplementarySZobservationsarerunat15Ghzwiththe ArcminuteMicrokelvinImager[29].Furthermore,X-rayobservationwith *XMM-Newton* constitutesthe backboneofthisfollow-upprogramme.Indeed,X-rayobservationsprovideastraightforwardasabove theGalacticPlane,thedetectionofextendedX–rayemissionisanunambiguoussignatureofacluster. *XMM-Newton* [30]isperfectly fittedforfollowingupnewly-detected *Planck* clustersuptohighredshift. Snapshotsexposureof10ksecsu fficetocon firmany *Planck* clustercandidateatleastupto $z = 1.5$, andwhenstatisticsallowsit,providesthesourceredshiftfromtheironKline.Alsoclustersdetectedby *Planck* areexpectedtobelargerthan1arcmin(nearbyand /ormassive),scalesatwhich *XMM-Newton* spatialresolutionissu fficienttodiscriminatebetweenapointsourceandextendedemission.

ViaanagreementbetweentheESA *XMM-Newton* and *Planck* projectscientists,the *Planck* collaborationbene fited500ksof *XMM-Newton* Director'sDiscretionaryTimeinordertomakeuseofthesynergy betweenthetwomissionstobetterunderstandtheSZsignal,andhelptocharacteriseandvalidatethe *Planck* SZsourcesinviewofthepublicdeliverytothescienti ficcommunity.

Thefull *XMM-Newton* validationfollow-upprogrammecomprises51observationsof *Planck* cluster candidatesoutofwhich43SZcandidatesareassociatedwithclustersand8arefalsedetections.We confirmed51 *bonafide* newclusters,includingfourdoublesystemsandtwotriplesystems.Thesehigh fractionofmultiplesystemsillustratestheconfusionproblemduetothe *Planck* beamsize.Foreachcluster,itallowedustoprovidea firstphysicalcharacterisation(e.g.,globalmeasurementsfortheluminosity, temperature,mass,etc).TheeightfalsecandidateswereallfoundatS /N < 5.Theystresstheimportance ofouroverallvalidationprocess.

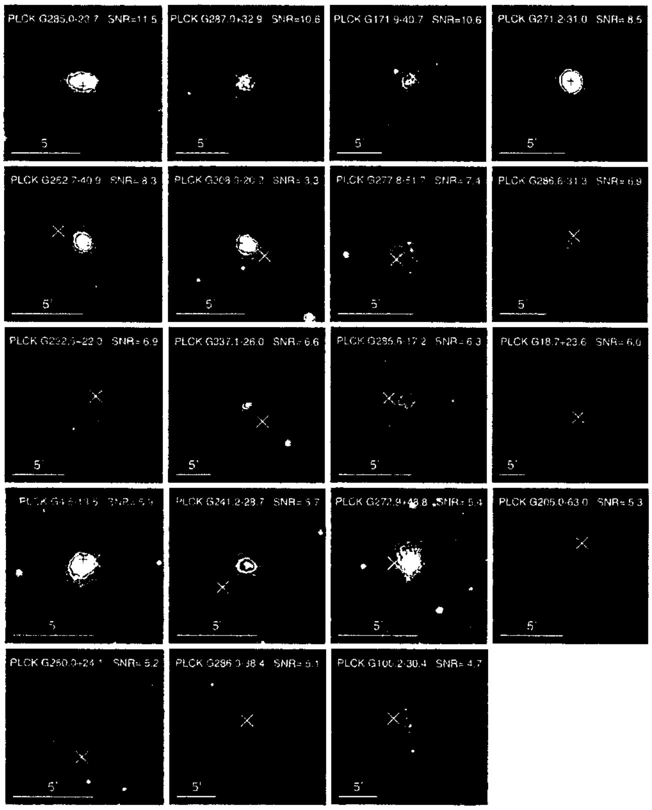

Figure 2: *XMM-Newton* images in the [0.3–2] keV energy band of all confirmed cluster candidates (except for the two triple systems) from validation runs 1 & 2. Image sizes are $3 \times \theta_{500}$ on a side, where θ_{500} is estimated from the M_{500}–Y_X relation [23]). The majority of the objects show evidence for significant morphological disturbance. A yellow cross indicates the *Planck* position and a red/green plus sign the position of a RASS-BSC/FSC source.

Thirty-two of the 51 individual clusters have high quality redshift measurements from the Fe K line. The new clusters span a large redshift range, i.e., [0.09 – 1], more than one decade in Y_{500}, i.e., ([0.29 – 3.0]$\times 10^{-3}$] arcmin^2 and the masses M_{500} of single systems ranges within the interval [0.25–1.6]$\times 10^{15}$ $M_\odot$. The actual mass threshold depends on redshift, but *Planck* can detect systems with $M_{500} > 5 \times 10^{14}$ $M_\odot$ at $z > 0.5$. The gallery of *XMM-Newton* images for the single and double systems of the two first runs is presented on Fig. 2.

In summary, our *Planck* SZ cluster candidates are detected in the *Planck* survey at $4.0 < S/N < 6.1$. The newly-detected clusters follow the Y_X–Y_{500} derived from other *Planck* studies [9, 10]. These results are consistent with other works [31, 32], bringing complementary redshift coverage and increased precision on SZ scaling relations. On average, new clusters are under-luminous compared to X-ray selected clusters, and more morphologically disturbed. This population of clusters might be under-represented in X-ray surveys. Consequently, the scatter about the $M - L_X$ might be larger than previously thought. This may have implications for statistical studies of X-ray selected samples for cosmology and/or for the physics of structure formation as discussed in detail by [33].

Furthermore the *XMM-Newton* follow-ups confirmed the *Planck* sensitivity and show that *Planck* can detect clusters well below the X-ray flux limit of RASS based catalogues, ten times lower than REFLEX

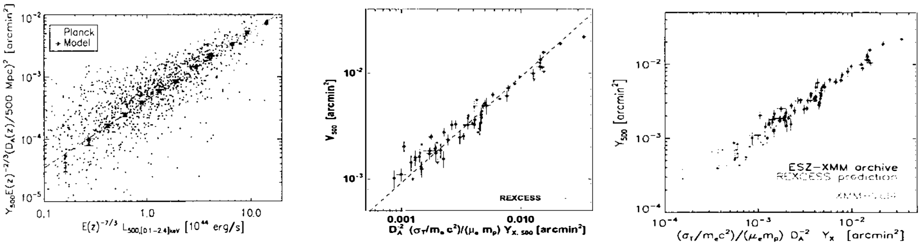

Figure 3: *(left)* Scaling relation between Planck SZ measurements and X-ray luminosity for ~ 1600 MCXC clusters. Individual measurements are shown by the black dots and the corresponding bin averaged values by the red diamonds. Thick bars give the statistical errors, while the thin bars are bootstrap uncertainties. The X-ray based model is shown as a solid blue line, and the bin-averaged SZ cluster signal it predicts is shown by the blue stars. The red dot-dashed line shows the best fitting power-law to the data [9]. *(middle)* SZ flux vs X-ray prediction. Blue stars indicate cool core systems. Left panel: Relation plotted in units of arcmin^2. The dashed line is the prediction from REXCESS X-ray observations [23]. See [10]. *(right)* Relation between apparent SZ signal (Y_{500}) and the corresponding normalised Y_X parameter. Black points show clusters in the *Planck*-ESZ sample with *XMM-Newton* archival data as presented in [10]; green and red points represent Planck clusters confirmed with *XMM-Newton* validation programme [4,34,35]. The blue lines denote the Y_{500} scaling relations predicted from the REXCESS X-ray observations [23]. The grey area corresponds to median Y_{500} values in Y_X bins with $\pm 1\sigma$ standard deviation. [9,34,35]

at high z, and below the limit of the most sensitive RASS survey, i.e., MACS.

These results illustrate the potential of the all-sky *Planck* survey to detect the most massive clusters in the Universe. Their characterisation, and the determination of their detailed physical properties, depends on a vigorous follow-up programme, which we are currently undertaking.

5 Further *Planck* results

Beyond the search, validation and first characterisation of clusters in the all-sky *Planck* survey, the *Planck* consortium has carried out specific studies of clusters and of the SZ signal. Noticeably:

- The statistical combination of ~ 1600 MCXC clusters ($0.01 < z < 1$) with the all-sky *Planck* data led to a precise measurement of the correlation between the SZ signal and the X-ray luminosity. Averaging SZ fluxes in bins of X–ray luminosity, L_X, the SZ signal detected at very high significance. This *Planck* observed signal is consistent with X-ray based predictions over two decades in X–ray luminosity, down to $L_X = 10^{43}\,\mathrm{erg/s} \lesssim L_{500}E(z)^{-7/3} \lesssim 2\times10^{45}\,\mathrm{erg/s}$. Consequently no evidence for any deficit in SZ flux with respect to the X–rays, underlining the robustness and consistency of our overall view of intra-cluster medium properties (left panel of Fig. 3). See [9].
- A study on 62 massive clusters detected by *Planck* at a high signal-to-noise ratio and also observed by *XMM-Newton* allowed to investigate the scaling relations between the SZ signal, $D_A^2\,Y_{500}$, and the X-ray-derived properties (i.e., gas mass $M_{g,500}$, temperature T_X, luminosity $L_{500,[0.1-2.4]\mathrm{keV}}$, SZ signal analogue $Y_{X,500} = M_{g,500}\times T_X$, and total mass M_{500}). The derived results are in excellent agreement with both X-ray predictions and recently-published ground-based data derived from smaller samples (see middle panel of Fig. 3). See [10].
- We investigated the relation between the *Planck* SZ signal and the the galaxy cluster mass from (i) weak lensing (WL) measurements (Subaru Telescope observations) and (ii) X–ray data assuming the hydrostatic equilibrium (HE; *XMM-Newton* observation). If the M_{WL}–D_A^2Y relation is consistent with previous determinations using WL masses, we found an offset in normalisation with respect to relations based on HE X-ray masses. Because our SZ data are consistent with previous *Planck* measurements, we are left, for the present sample, with an average ratio of the HE X-ray masses 22 ± 8 percent larger than the WL masses. This discrepancy is driven by a differences in

mass concentration and centre offset are measured and defined by X-ray and WL analysis discrepancies are enhanced in dynamically disturbed systems. See [36].

Further intermediate results are currently being published providing further insights on the clusters of galaxies. The nominal *Planck* mission, which includes 15th months of data corresponding to two full sky surveys is to be released early 2013 to the community. It will have a tremendous legacy value for the coming decades.

Acknowledgments – I am grateful to the organisers of the conference for inviting me to present the *Planck* results on clusters of galaxies at the Moriond's meeting. EP acknowledges the support from grant ANR-11-BD56-015.

References

1. R. A Sunyaev and Ya. B Zeldovich. *Comments on Astrophysics and Space Physics*, 4:173, Nov 1972.
2. T. A. Marriage, et al. *ApJ*, 731:100, April 2011.
3. J. E. Carlstrom, et al. *P. A. S. P.*, 123:568–581, May 2011.
4. Planck Collaboration IX. *A&A*, 536:A9, 2011.
5. A C da Silva, et al. *MNRAS*, 348:1401–1408, 2004.
6. Planck Collaboration I. *A&A*, 536:A1, 2011.
7. Planck Collaboration VIII. *A&A*, 536:A8, 2011.
8. Planck Collaboration XXVI. *A&A*, 536:A26, 2011.
9. Planck Collaboration X. *A&A*, 536:A10, 2011.
10. Planck Collaboration XI. *A&A*, 536:A11, 2011.
11. Planck Collaboration XII. *A&A*, 536:A12, 2011.
12. J. A. Tauber, et al. *A&A*, 520:A1 +, September 2010.
13. N. Mandolesi, et al. *A&A*, 520:A3 +, September 2010.
14. M. Bersanelli, et al. *A&A*, 520:A4 +, September 2010.
15. A. Mennella, et al. *A&A*, 536:A3, 2011.
16. J.-M. Lamarre, et al. *A&A*, 520:A9 +, September 2010.
17. Planck HFI Core Team. *A&A*, 536:A4, 2011.
18. J. P. Leahy, et al. *A&A*, 520:A8 +, September 2010.
19. C. Rosset, et al. *A&A*, 520:A13 +, September 2010.
20. Planck Collaboration II. *A&A*, 536:A2, 2011.
21. Planck HFI Core Team. *A&A*, 536:A6, 2011.
22. A. Zacchei, et al. *A&A*, 536:A5, 2011.
23. M. Arnaud, et al. *A&A*, 517:A92, July 2010.
24. D. Herranz, et al. *MNRAS*, 336:1057–1068, November 2002.
25. J.-B. Melin, J. G. Bartlett, and J. Delabrouille. *A&A*, 459:341–352, November 2006.
26. P. Carvalho, G. Rocha, and M. P. Hobson. *MNRAS*, 393:681–702, March 2009.
27. P. Carvalho, et al. *ArXiv e-prints*, December 2011.
28. R. Piffaretti, et al. *A&A*, 534:A109 +, October 2011.
29. J. T. L. Zwart, et al. *MNRAS*, 418:2754–2772, December 2011.
30. F. Jansen, et al. *A&A*, 365:L1–L6, January 2001.
31. K. Andersson, et al. *ApJ*, 738:48– +, September 2011.
32. C. Sifon, et al. *ArXiv e-prints*, January 2012.
33. R. E. Angulo, et al. *ArXiv e-prints*, March 2012.
34. Planck Collaboration I. Submitted to *A&A*, [arXiv:astro-ph/1112.5595], 2012.
35. Planck Collaboration IV. Submitted to *A&A*, [arXiv:astro-ph/1205.3376], 2012.
36. Planck Collaboration III. Submitted to *A&A*, [arXiv:astro-ph/1204.2743?], 2012.

An update from the Arcminute Microkelvin Imager – New results and ongoing SZ science

Michel P. SCHAMMEL
Astrophysics Group, Cavendish Laboratory, University of Cambridge, JJ. Thomson Avenue, Cambridge CB3 0HE, United Kingdom

We present a summary of the two recent SZ investigations from the Arcminute Microkelvin Imager (AMI). First we investigate the total masses of a subset of LoCuSS clusters as measured by AMI (with *no* X-ray information) and by weak-lensing or X-ray; we find consistency between $M_{\mathrm{T,AMI}}(r_{200})$ and $M_{\mathrm{T,lensing}}(r_{200})$, but at lower radius we find $M_{\mathrm{T,X}}(r_{500})/M_{\mathrm{T,AMI}(r_{500})} = 1.7 \pm 0.2$. The cause of the X-ray – AMI discrepancy appears to be that strong mergers make n^2 weighted X-ray temperatures higher than n weighted SZ temperatures even at high radius. Secondly, we present the status of the blind SZ survey carried out by AMI with the first blind detection of a large, complex SZ structure detected. Our Bayesian analysis tool fits a two component system and measures a total mass of $M_{\mathrm{T,200}} = 5.5^{+1.2}_{-1.3} \times 10^{14} h_{70}^{-1} M_{\odot}$ for the lower component and $M_{\mathrm{T,200}} = 3.5^{+0.9}_{-0.9} \times 10^{14} h_{70}^{-1} M_{\odot}$ for the upper component. By simply fitting for the temperature decrement of this structure, we find a temperature decrement of $-295^{+36}_{-15}\mu$K and $-302^{+70}_{-27}\mu$K respectively.

1 The Sunyaev-Zel'dovich (SZ) effect

The SZ [1,2,3] effect is the intensity change δI_{ν} of the CMB seen toward a galaxy cluster due to inverse Compton scattering by the hot cluster plasma:

$$\delta I_{\nu} = T_{\mathrm{CMB}}\, y\, f(\nu) \frac{\partial B_{\nu}}{\partial T}\bigg|_{T=T_{\mathrm{CMB}}} \quad \text{and} \quad y = \frac{\sigma_T}{m_e c^2} \int_{-\infty}^{+\infty} n_e(r) k_b T_e(r) dl, \qquad (1)$$

where $\mathrm{T_{CMB}}$ is the temperature of the CMB blackbody spectrum, f is the frequency dependence of thermal SZ signal, B_{ν} is the CMB intensity and the dimensionless parameter y is the Comptonisation parameter along the line of sight l determined by n_e, the electron number density at radius r, T_e is the electron gas plasma temperature, σ_T is the Thomson scattering cross-section, m_e is the electron mass, c is the speed of light.

2 The Arcminute Microkelvin Imager (AMI)

The Arcminute Microkelvin Imager (AMI [4]) is a dual interferometric array consisting of eight 12.8-m antennas, the Large Array (LA) and ten 3.7-m dishes, the Small Array (SA). Both arrays observe over a frequency range of 14-18 GHz at which δI_{ν} is negative. The SA is the primary SZ array with finely tuned baselines of 200–1000λ for observing out to the virial radii of clusters at $z \gtrsim 0.2$, whereas the LA with baselines of 1–5 kλ is used to investigate the source environment around the SZ target to subtract its contribution to the SA data.

3 Data Analysis

We use the Bayesian data analysis tool McADAM [5] to take account of radio sources, primordial CMB power spectrum, and instrument noise, plus the potential presence of one or more clusters. This methodology has many advantages.[6] To model the cluster, we have used a physical parameterisation of an isothermal β model, based on the assumption of spherical symmetry and a mass-temperature scaling relationship, but we are now gradually moving to a new, analytical model [8]. This parameterisation uses a NFW dark matter halo distribution and a GNFW pressure profile for the cluster gas and overcomes many of the limitations of the previous model.

4 The LoCuSS subsample [7]

To permit a joint X-ray and SZ comparison of galaxy clusters forming part of the LoCuSS [9,10] sample, we selected a sub-sample of 19 clusters with $L_X \geq 7 \times 10^{37}$W ($0.1 - 2.4$ keV, restframe, $h_{50} = 1$; we assume $h_{70} = 1$ from now on), above declination 20° and with no sources brighter than 10 mJy/beam within 10′ of the X-ray cluster centre. We emphasise that LoCuSS sample has a narrow redshift range ($0.142 \leq z \leq 0.295$), hence the cosmic evolution is minimised.

AMI is sensitive to radii out to $r \approx r_{200}$ (the radius internal to which the average density is 200 times to closure density), $\approx$ the classical virial radius. To exploit this, we have compared SZ masses (obtained assuming a virial relation between total mass $M_{\rm T}(r_{200})$ and (isothermal) plasma temperature) with the few other $M_{\rm T}(r_{200})$ estimates we can find for our subsample clusters – weak-lensing for five clusters and X-ray (SUZAKU) for one cluster. Agreement seems good although the statistics are poor. When we improve statistics by going to the more commonly studied $M_{\rm T}(r_{500})$, agreement remains between AMI and weak lensing, but goes away between AMI and X-ray: *in fact* $M_{\rm T,X}/M_{\rm T,AMI} = 1.7 \pm 0.2$ *within* r_{500}.

Some indication as to the cause of the $M_{\rm T,X}$ *vs* $M_{\rm T,AMI}$ discrepancy comes from Figure 2. This shows the AMI mean temperatures versus X-ray temperatures at $r \approx$ 500kpc taken from CHANDRA and SUZAKU data where they exist for our subsample. For most of the analysed clusters, the correspondence is reasonable; the most inconsistent data points (A773, RXJ0142+2131 and A1758a) pertain to (strongly) merging clusters. Also shown is a second X-ray measurement [16], labeled A611* of Abell 611 over 450-750 kpc with 68% confidence bars.

Smith [18] investigate the scatter between lensing masses within $\leq$ 500 kpc with CHANDRA X-ray temperatures averaged over 0.1–2 Mpc for ten clusters and also find that disturbed systems have higher temperatures. However, Marrone [19] measure the relationship between SZ-$Y_{\rm sph}$ and lensing masses within 350 kpc for 14 clusters and found no segregation between disturbed and relaxed systems. Kravtsov et al. [20] analysed a cluster sample extracted from cosmological simulations and noticed that X-ray temperatures of disturbed clusters were biased high, while the X-ray analogue of SZ-$Y_{\rm sph}$, did not depend strongly on cluster structure. The combination of these literature results with Figure 2 implies that even at small distances from the core, SZ-based mass (or temperature) is a less sensitive indicator of disturbance disturbance than is X-ray-based mass.

Major mergers in our sample have large-radius X-ray temperatures (at $\approx$ 500 kpc) *higher* than the SZ temperatures (averaged over the whole cluster). This suggests that the mergers affect the n^2-weighted X-ray temperatures more than the n-weighted SZ temperatures and do so out to large radius. This is evidence for shocking or clumping or both *at large radius* in mergers. Hydrodynamical simulations [21] have shown that gas clumping can indeed introduce a large bias in large-r X-ray measurements.

5 Blind surveys [24]

The AMI Consortium is carrying out a blind survey comprising 12 different fields of each 1 deg^2. The aim is to find low mass clusters ($M \geq 2 \times 10^{14} h_{70}^{-1} M_\bullet$) via deep integration of every individual field, down to a typical sensitivity of $\approx 100\mu$Jy per SA beam, in contrast to other SZ surveying strategies. Fields were chosen to contain no previously detected galaxy clusters by cross-matching with the ROSAT All Sky Survey and Abell catalogues.

Here, we present the first blind detection and refer the reader to the publication [24] for details on data reduction and analysis techniques. Figure 3 shows a large, complex SZ structure both

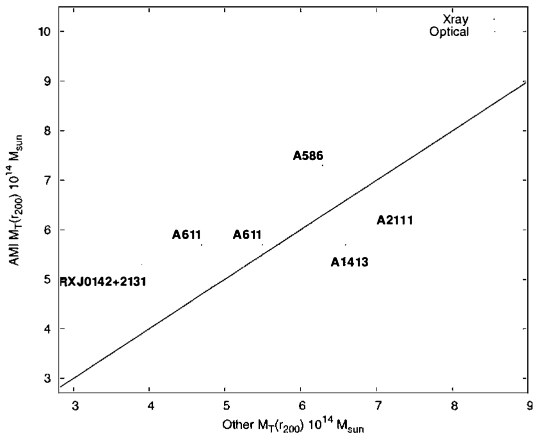

Figure 1: Comparison of AMI $M_{\mathrm{T}}(r_{200})$ measurements with others. Methods used for estimating $M_{\mathrm{T}}(r_{200})$ are given in the legend. Mass is given in units of $\times 10^{14} M_{\odot}$. The *ratio* between the AMI results axis and the other one is 0.63 and a line of gradient one has been included to aid comparison. The references are as follows: Abell 586 [11], Abell 611 [11,12,13] Abell 1413 [15], Abell 2111 [13] and RXJ0142+2131 [11]. In general, there is good agreement between both measurements.

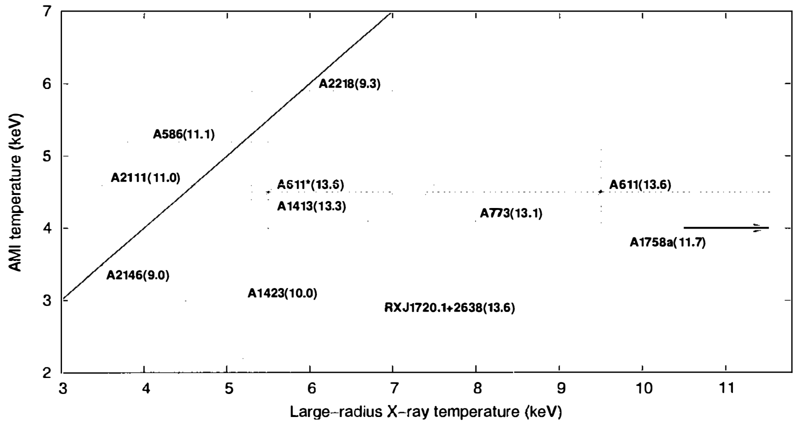

Figure 2: The AMI mean temperature within r_{200} versus the X-ray temperature. Each point is labeled with the cluster name and X-ray luminosity. Most of the X-ray measurements are large-radius temperatures from the *ACCEPT* [16] archive with 90% confidence bars. The radius of the measurements taken from the *ACCEPT* archive are 400-600 kpc for Abell 586, 300-700 kpc for Abell 611, 300-600 kpc for Abell 773, 450-700 kpc for Abell 1423, 500-1000 kpc for Abell 2111, 450-550 for Abell 2218 and for RXJ1720.1+2638, r = 550-700 kpc. The Abell 611* temperature is the 450-750kpc value with 68% confidence bars [18]. The Abell 2146 [17] temperature measurement has 68% confidence bars. The Abell 1413 X-ray temperature is estimated from the 700-1200 kpc SUZAKU measurements [15]; this value is consistent with [22,23]. The *ACCEPT* archive temperature for Abell 1758A is 16±7keV at r = 475-550 kpc, and with SZ temperature 4.5±0.5, is off the right-hand edge of this plot. Abell 611 is shown using dashed blue lines to emphasize that this cluster has two X-ray-derived large-r temperatures. The black diagonal solid line is the 1:1 line and the *ratio* between the AMI values axis and the other one is 0.86.

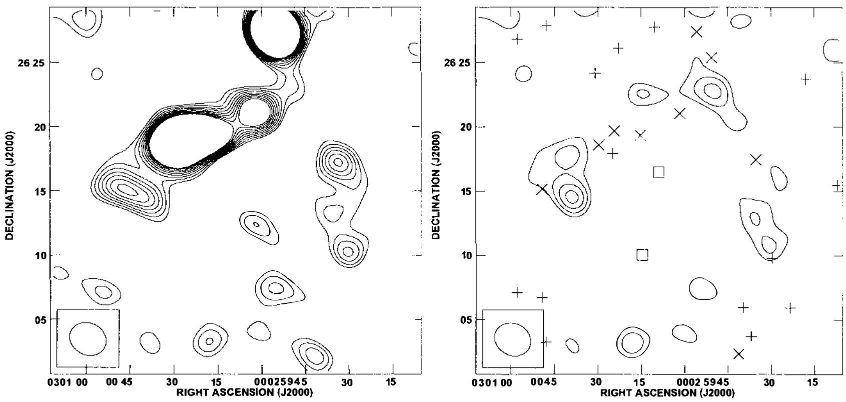

Figure 3: Maps of the first blind detection. On the LHS, we show the map without any source-subtraction. Positive contours are solid lines in black where as negative contours are shown in red, dashed lines. Contour lines scale in multiples of the noise level, omitting the 1 σ contour. The crosses on the right map denote the positions of these sources that have been subtracted where as the two boxes show the positions of the two component system fitted to the data. The synthesised beam is shown in the frame on the lower left side.

before doing any source subtraction (left) and after subtracting radio sources.

Our Bayesian analysis fits two components to the SZ structure and measures a mass of complex SZ structure detected and measures a mass of $M_{\mathrm{T},200} = 5.5^{+1.2}_{-1.3}\times\ 10^{14}h_{70}^{-1}M_{\odot}$ for the lower component and $M_{\mathrm{T},200} = 3.5^{+0.9}_{-0.9} \times 10^{14}h_{70}^{-1}M_{\odot}$ for the upper component respectively. By simply fitting for the temperature decrement of this structure, we find a temperature decrement of $-295^{+36}_{-15}\mu$K and $-302^{+70}_{-27}\mu$K.

References

1. Sunyaev R. A., & Zel'dovich Y. B., 1970, Comments on Astrophysics and Space, 2, 66
2. Birkinshaw M., 1999, Physics Reports, 310, 97
3. Carlstrom J. E., Holder G. P., Reese E. D., 2002, ARA&A, 40, 643
4. AMI Consortium: Zwart J. T. L. et al., 2008, MNRAS, 391, 1545
5. Marshall P. J., et al., 2003, MNRAS, 346, 489
6. AMI Consortium: Zwart J. T. L., et al., 2011, MNRAS, 418, 2754
7. AMI Consortium: Rodríguez-Gonzálvez, C., et al., 2012, submitted to MNRAS
8. Olamaie M., et al., 2011, arXiv, arXiv:1109.2834
9. Smith G. P., et al., 2003, ApJ, 590, L79
10. Smith G. P., et al., 2005, MNRAS, 359, 417
11. Okabe N., et al., 2010, PASJ, 62, 811
12. Romano A., et al., 2010, A&A, 514, A88
13. AMI Consortium: Hurley-Walker N., et al., 2011, arXiv, arXiv:1101.5912
14. Voit G. M.,2005, RvMP, 77, 207
15. Hoshino A., et al., 2010, PASJ, 62, 371
16. Cavagnolo K. W.,et al., 2009, ApJS, 182, 12
17. Russell, H.R., et al., 2010, MNRAS
18. Donnarumma A., et al., 2010, arXiv:1002.1625
19. Marrone D. P., et al., 2009, ApJ, 701, L114
20. Kravtsov A. V., et al., 2006, ApJ, 650, 128
21. Nagai D., Lau E. T., 2011, ApJ, 731, L10
22. Vikhlinin A., et al., 2005, ApJ, 628, 655-672
23. Snowden, S. L., et al., 2008, A&A, 478, 615
24. AMI Consortium: Shimwell, T. W., et al., 2010, arXiv, arXiv:1012.4441

TESTING COSMOLOGY WITH EXTREME GALAXY CLUSTERS

Ian Harrison
School of Physics & Astronomy, Cardiff University,
5 The Parade, Cardiff, CF24 3AA, United Kingdom

The current concordance model of cosmology makes definite predictions for the number density of massive gravitationally bound objects (visible as galaxy clusters) in the Universe and how this distribution evolves with redshift. It has been suggested that some recently observed objects are too massive at too early a time to exist within a standard model universe, hinting that modifications may be necessary. It is possible to consider this problem within the framework of Extreme Value Statistics (EVS): are any of theses objects more extreme than the most unusual objects we expect to observe? The current answer appears to be 'no' and so the standard model currently passes this particular test. However, it is plausible that future observations will observe objects too extreme for the concordance model; it may then also be possible to perform model selection between different models of enhanced structure formation using these extreme clusters.

1 The Problem of Big Clusters

Cosmology in 2012 has a 'concordance' or standard model which, amongst other things, allows us to predict how structures should form and grow in the Universe. In particular, we can predict the co-moving number density of collapsed Cold Dark Matter haloes (visible via the galaxy clusters which reside within them) at a given mass and redshift: $n(m, z)$, the halo mass function. This distribution is expected to have a very steep cutoff at higher masses ($m \gtrsim 10^{15} M_{\odot}$), the steepness and evolution of which is sensitive to the initial conditions of the CDM density field, nature of gravitational collapse and background expansion rate. Hence, the abundance of massive objects in our universe has the potential to constrain primordial non-Gaussianity, modified gravity and the nature of dark energy.

In recent years new experiments such as XMM-Newton, ACT, SPT and Planck have begun to observe the Universe with sufficient sensitivity to see the most massive objects at appreciable redshifts ($z \sim$ 1-2), allowing us to probe structure formation at these times. As these surveys have been ongoing, a number of analyses have calculated the expected abundance of the most massive objects found within them [1]. All of these analyses found galay clusters with masses and redshifts which meant they appeared "too-big, too-early" to exist naturally within a ΛCDM universe, indicating new physics away from the concordance model may be necessary. Furthermore, some suggested the inclusion of primordial non-Gaussianity on of $f_{NL} \sim$ 300-500 could ease this tension, 1-2 orders of magnitude greater than what is observed in the CMB.

Unfortunately, these analyses have been shown to contain a bias [2] which, when accounted for, causes the tension with the concordance model to disappear. However, we have currently only surveyed a small portion of the sky with the sensitivity to detect such clusters, and so it may be reasonable to suppose a 'ΛCDM-killer' may still be waiting for us to observe it. If so, it is desirable that we have statistical machinery available in order to be able to truly determine how 'extreme' a given cluster is without the biases present in previous methods.

2 Extreme Value Statistics of Galaxy Clusters

Rather than making inference using the mean of a sample from a probability distribution, Extreme Values Statistics (EVS) [3] seeks to make inference using sample *extrema* (i.e. the greatest or least value within a sample). If N i.i.d. random deviates are drawn from and underlying cumulative distribution function $F(m)$ then the probability that the largest $M_{max} \leq m$ is simply the product that each individual draw is $\leq m$, allowing us to find the probability and cumulative distribution functions:

$$\begin{aligned} \Phi(M_{\max} \leq m; N) &= F^N(m) && (1) \\ \phi(M_{\max} = m; N) &= N f(m) \left[F(m)\right]^{N-1}. && (2) \end{aligned}$$

It is a seminal result in EVS that, in analogy with the central limit theorem for sample means, in the $N \to \infty$ limit the distribution of sample extremes will tend to an asymptotic distribution, the Generalised Extreme Value (GEV) distribution:

$$P_{GEV}(M_{max} \leq m; \alpha, \beta, \gamma) = \exp\left\{ - \left[1 + \gamma\left(\frac{m-\alpha}{\beta}\right)\right]^{-1/\gamma} \right\} \quad (3)$$

where α and β are location and scale parameters and γ is the shape parameter, which depends on the underlying distribution. For some distributions it is possible to analytically determine the asymptotic behaviour; for a Gaussian distribution, $\gamma = 0$ is the aymptotic value. However, if we wish to make predictions for EVS of galaxy clusters residing in CDM haloes, we can make use of the exact distribution (1) by forming the underlying distribution from the halo mass function $n(m, z)$.

3 Results

3.1 Null Tests

Figure 1 shows probability contours calculated using EVS for the mass of most massive galaxy cluster in a ΛCDM universe at each redshift, along with several of the most massive galaxy clusters so far observed. As can be seen, no currently observed cluster lies above the 99% region of this plot and so the concordance model survives this test [4].

If, in the future, a galaxy cluster is observed in the area above this region ruling out ΛCDM, we can also consider whether it is possible to exclude or allow different models of enhanced structure formation. To this end, we construct the EVS of galaxy clusters within two alternative cosmologies:

1. Primordial non-Gaussianity of the local type, parameterised by f_{NL} and included as an alteration to the lcdm halo mass function via a non-Gaussian correction factor $\mathcal{R}(f_{\rm NL})$.
2. 'SUGRA003' in which a quintessence dark energy field is coupled to the dark matter particles and has a supergravity-motivated potential. The presence of a global minimum in this potential means that the evolution of the scalar field will change sign at a particular redshift z_{bounce}, with structure formation being enhance above z_{bounce} and depleted below it.

In order to account for the full non-linear behaviour of these cosmologies we make use of the publicly available CoDECs N-body simulations[5]. As can be seen in figure 2, observations of 'too massive' clusters at different redshifts can favour or disfavour different alternative models.

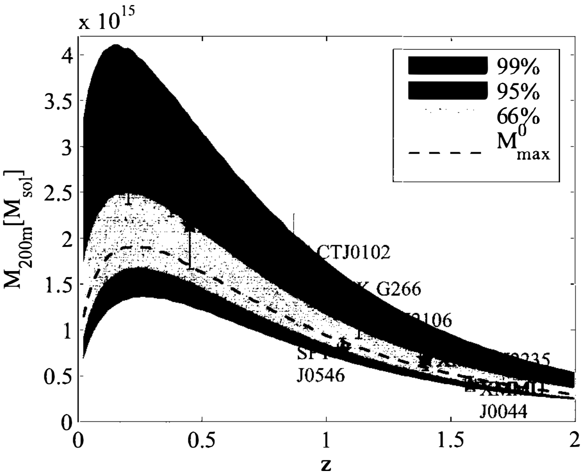

Figure 1: 66%, 95% and 99% confidence regions for the mass of the most massive cluster at a given redshift in a ΛCDM universe, along with the most massive high and low redshift clusters so far observed.

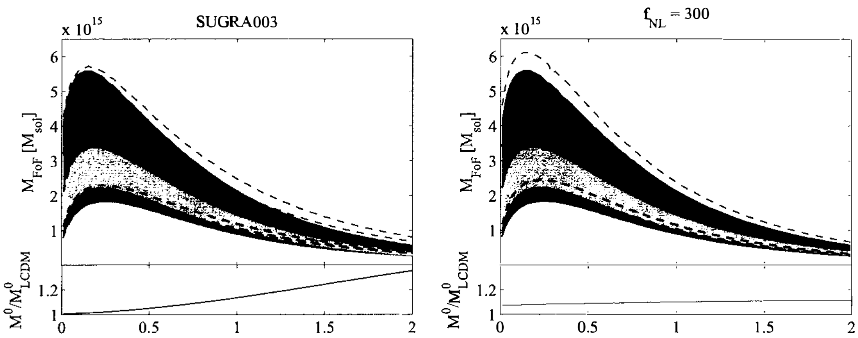

Figure 2: Shaded regions are as figure 1 for a ΛCDM simulation, dashed lines are the edges of these contours in the two alternative models. Lower panels show the enhancement in $\langle M_{max} \rangle$

3.2 Parameter Estimation

Whilst it is possible to rule out individual models using such null tests, a more efficient search technique for new physics is to parameterise away from the fiducial model and attempt to constrain these parameters. In order to place both upper and lower bounds on a parameter using extreme galaxy clusters, it is necessary to guarantee that there is no more massive cluster in the sky which has merely been missed by an observational survey. This requires a truly mass-limited survey. Fortunately, surveys which select clusters using the thermal Sunyaev-Zel'dovich (tSZ) effect are capable of approaching this ideal.

The South Pole Telescope has recently conducted a tSZ cluster survey over 2500deg^2 of the sky [6] and present the 26 clusters with highest tSZ S/N in the region. Unfortunately, S/N does not correlate directly with mass and the survey is not epected to be truly complete. However, we make the approximation that these 26 are in fact the most massive which exist within the survey region, intepolating between a current experiment and a future one with a mass threshold low enough to ensure the contours in Figure 1 lie completely above it. We then divide the redshift intervals interval into bins, and assert that, if a bin is empty of clusters, the most massive cluster in that bin is *not more massive* than the lowest of these 26 clusters. We can then form a likelihood over e.g. the f_{NL} parameter, as shown in Figure 3.

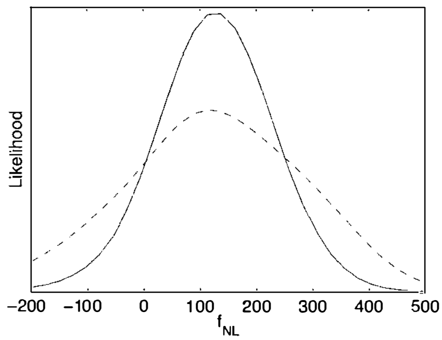

Figure 3: Limits on f_{NL} from the 26 extreme clusters in the idealised experiment described in the text. The solid line represents a sharp prior on σ_8, whilst the dashed one marginalises over the WMAP7 prior.

References

1. Cayón, L., Gordon, C., Silk, J., MNRAS **415**, 849 (2011). arXiv:1006.1950
   Holz, D. E., Perlmutter, S., ArXiv e-prints , (2010). arXiv:1004.5349
   Hoyle, B., Jimenez, R., Verde, L., Phys. Rev. D **83**, 10 (2011). arXiv:1009.3884
   Jimenez, R., Verde, L., Phys. Rev. D **80**, 12 (2009). arXiv:0909.0403
   Mortonson, M. J., Hu, W., Huterer, D., Phys. Rev. D **83**, 2 (2011). arXiv:1011.0004
2. Hotchkiss, S., JCAP **7**, 4 (2011). arXiv:1105.3630
3. E. Gumbel, *Statistics of Extremes*, (Columbia University Press, 1958).
4. Harrison, I., Coles, P., MNRAS **421**, L29 (2012). arXiv:1111.1184
5. Baldi, M., 2011, ArXiv e-prints, arXiv:1109.5695
6. Williamson *et al*, Astrophys. J. **738**, 2 (2011). arXiv:1101.1290

THE QUEST FOR GRAVITY WAVE B-MODES

CLEMENT PRYKE
University of Minnesota Physics, 116 Church Street S.E.,
Minneapolis, MN, 55455, USA

One of the most exciting quests in all of contemporary science is to find hints that in the first tiny fraction of a second after the Big-Bang the Universe hyper-inflated by a factor of $\sim 10^{60}$. Such inflation will have injected gravity waves into the fabric of spacetime which will in turn have left a faint imprint in the polarization pattern of the Cosmic Microwave Background. This paper describes the history of polarization measurement, the experimental optimization of this latest search for the gravity wave imprint, and the current round of experiments and their various approaches to the challenge.

1 Introduction

The study of the anisotropy of the Cosmic Microwave Background (CMB) has taught us much about the origin, content and fate of the Universe in which we find ourselves, and is one of the cornerstones of what has come to be called the standard cosmological model (LCDM). In this model the Universe began in a hot "Big-Bang" approximately 14 billion years ago and has been expanding and cooling ever since — around 400,000 years after the beginning it made the transition from plasma (opaque) to neutral gas (transparent) and the CMB is the highly re-shifted hot-object (black-body) light which has been freely streaming through the Universe ever since. It therefore offers us a snapshot of the density pattern at this time of "last scattering" on a spherical shell around the location where our galaxy would later form. Measurements of the total intensity (T) pattern by ground-based and balloon-borne instruments had by 2003 resulted in stringent cosmological constraints [1], which were confirmed by the WMAP spacecraft, and will shortly be further improved upon by the Planck space mission.

Meanwhile efforts to observe the predicted polarization of the CMB intensified and in 2002 the DASI experiment announced the first detection [2]. The "headless vector" polarization pattern on the sphere can be broken down into two scalar quantities dubbed E-modes and B-modes [3]. If the electrons at last scattering are exposed to radiation fields which have a quadrupolar component then Thompson scattering results in a net polarization. Flows of material generate such quadrupoles via Doppler shifts along the direction of flow resulting in a "pure gradient" or E-mode pattern. Since those flows are sourced by the density perturbations, correlations between the T and E patterns also naturally result. After last scattering the purity of the initial E-mode pattern is slightly disrupted by small gravitational deflections of the CMB photons as they travel to us through the forming large scale structure. This leads to a B-mode within the base model which is referred to as the "lensing B-mode".

While the basic LCDM model is enormously successful it leaves several fundamental questions unanswered. From the earliest calculations it was conventional to assume a flat power law initial perturbation spectrum coming out of the Big-Bang [4]. There was no real reason to do so other than simplicity, but, quite remarkably, recent CMB observations have proven it to be very close to the truth! Later the cosmo-genic theory known as Inflation was invented [5] which naturally predicts such an initial perturbation spectrum and also makes several other predictions which have subsequently proven to be true, such as the global flatness of space ($\Omega_{tot} = 1$) and the small degree of large scale anisotropy.

However Inflation is a radical theory positing expansion of space by a vast factor ($\sim 10^{60}$) occurring at an incredibly early time ($\sim 10^{-35}$ s), and hence at energies ($\sim 10^{16}$ GeV) far, far above anything probed by terrestrial experiment. Such radical ideas must be tested in all possible ways. Fortunately inflation makes an additional prediction — it injects a background of gravitational waves (aka tensor perturbations) into the Universe which have been propagating through it ever since. These distortions of the fabric of spacetime will induce additional quadrupolar moments in the radiation field incident on the electrons at last scattering which will in turn result in both E-mode and B-mode polarization — see figure 1. The magnitude of the gravity wave component is conventionally described by the tensor to scalar ratio denoted by r.

The motivations for making measurements of CMB polarization can be summarized as follows:

- Measuring the E and TE spectra tests the basic LCDM paradigm. At larger angular scales there is additional information to be had regarding the process of reionization [6].
- Measuring lensing B-modes at smaller angular scales can provide information about structure formation, and in particular neutrino mass.
- Measuring B-modes at intermediate and large angular scales holds out the tantalizing possibility of detecting Inflationary gravity waves — this has been referred to as the "smoking gun of inflation".
- The TB and EB spectra are identically zero in the standard paradigm. However alternate Lorentz violating models might produce a signal here [7].

2 Review of CMB Polarization Measurements to Date

The first detection of CMB polarization was reported by the DASI experiment in 2002 [2]. Measuring over a broad range of angular scales around $\ell \sim 200$ the E-mode was found to be consistent with the LCDM expectation and inconsistent with zero at around the $\sim 5\sigma$ level, whereas the B-mode was consistent with zero as expected.

In 2003 WMAP reported high significance detections of TE correlation and the somewhat surprising result of a strong reionization contribution at large angular scales [6], although this result was later partially retracted.

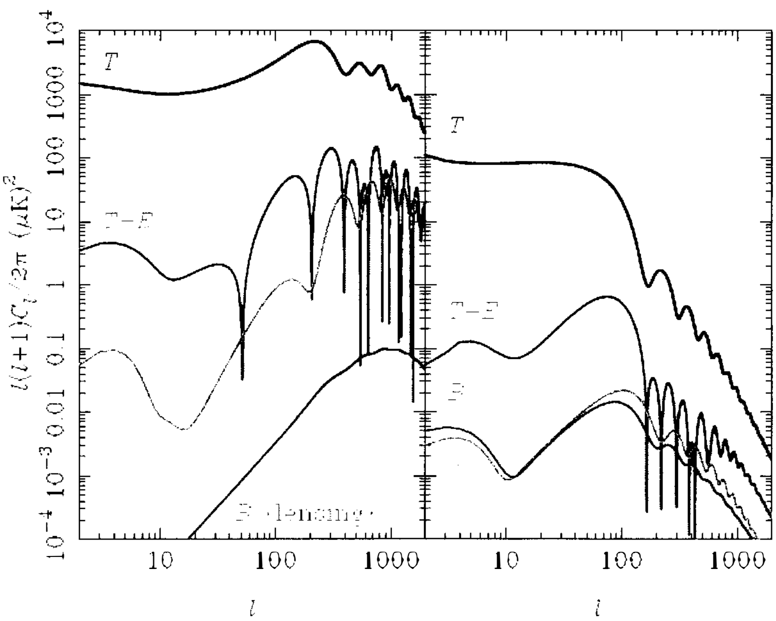

Figure 1: Theoretical CMB power spectra showing the basic T, E and TE contributions from density perturbations at left, along with the B-mode resulting from lensing of that initial E-mode. The tensor contribution from inflationary gravity waves to each spectrum is shown at right for $r = 0.2$. We see that the inflationary B-mode at $\ell \lesssim 100$ is potentially detectable. (Figure courtesy of A. Challinor)

To date $\sim$ 10 experiments have reported detections of E and TE with only upper limits on B-modes to date — Figure 2 shows the current situation. At the moment the QUAD [8] and BICEP1 [9] experiments lead the field at smaller and intermediate angular scales respectively, with WMAP providing the only available information at the largest scales.

3 Optimizing the Quest for Gravity Wave B-modes

The current best limit is $r < 0.17$ [10] from WMAP7+SPT temperature data [a]. However such T based limits are now cosmic variance limited and to go further we must search for B-modes. As we see in figure 1 there are two regions where the detectability is maximized: the "recombination bump" around $\ell \sim 80$ and the "reionization bump" at $\ell < 10$. Clearly the recombination bump is potentially lost in the rapidly rising lensing induced B-mode. However to measure low multipoles one must use a large fraction of the celestial sphere — and much of it is obscured by foreground emission from our own galaxy. There is hence a complex trade-off between sky area and observing frequencies when deciding how best to target this experimental goal.

3.1 Galactic foregrounds and optimum observing frequency

At low (< 30 GHz) frequencies the sky brightness is dominated by synchrotron radiation from relativistic electrons spiraling in the magnetic fields of the galactic ISM (inter stellar medium).

[a] As we see in Figure 1 gravity waves will add power to all spectra including T.

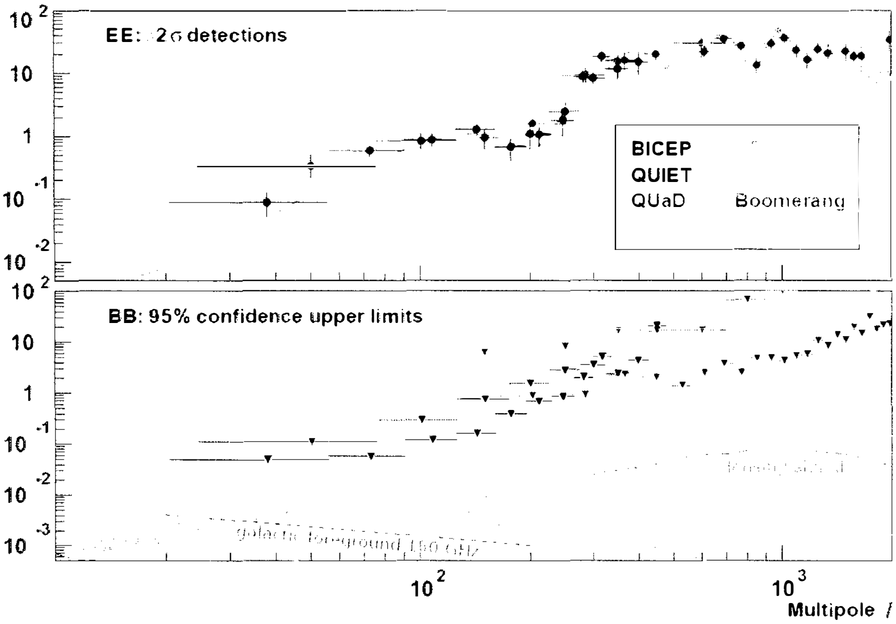

Figure 2: Current results on CMB polarization. The upper panel shows E-mode results compared to the standard LCDM expectation. The lower panel shows 95% upper limits on B-modes, with the dashed gray lines indicating B-mode signals from lensing and a possible gravity wave signal with $r = 0.1$; the solid gray line is the sum of these two signals. The dashed blue line indicates an estimate of the B-mode signal from Galactic foregrounds (both synchrotron and dust) at 150 GHz in a small, clean patch of sky. (Adapted from Chiang et al. (2009) with the addition of more recent points from the QUIET experiment and the foreground projections.)

At higher (> 300 GHz) frequencies emission from galactic dust is dominant. Since the dust is cold it is confined to a thin disk, whereas the high energy electrons have a much larger scale height and fill the galactic halo. It is a fortunate accident that the peak brightness of the 2.7 K CMB black body radiation at $\sim$ 150 GHz is close to the minimum of the total galactic emission.

It is very important to note that the maximum of the ratio of CMB brightness to sync+dust is a function of galactic latitude — close to the disk one wants to go to lower frequencies to get away from dust, whereas at high latitude the optimum frequency shifts up as we see in Figure 3. One must therefore be very careful of statements implying there is a single best observing frequency — such statements always carry an implicit assumption as to the required sky area.

Moving from total intensity to polarization leads to additional complications since the polarization fraction differs between synchrotron and dust, and with position on the sky. To connect the two requires (highly uncertain) modeling of the galactic magnetic field — see for example[12]. The best current information comes from WMAP at low frequencies and from extrapolations from IRAS at high frequencies. Figure 3 shows a projection — information from Planck will shortly massively increase our knowledge of polarized foregrounds.

3.2 Small patch or big patch?

If one decides to target the reionization bump there is no choice as to sky coverage — to resolve modes at $\ell < 10$ one needs as large a fraction of the sky as possible. Since we already know

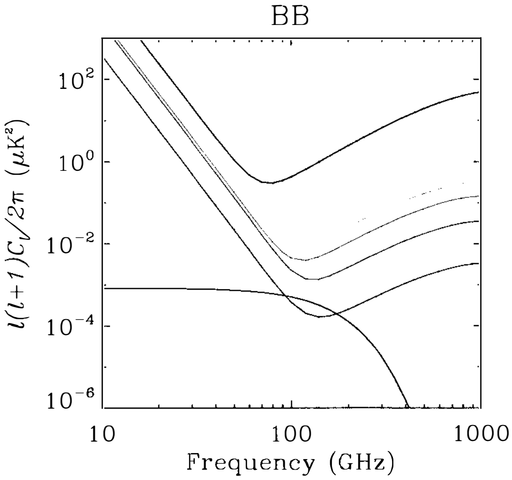

Figure 3: The colored lines show the total projected polarized galactic emission at angular scales of $80 < \ell < 120$ as a function of frequency for sky coverage: from top to bottom, full, galactic latitude greater than 10, 30, and 50 degrees, and for a clean patch with radius of 10 degrees. The lower black line shows the inflationary B-mode for $r = 0.01$. We see the asymmetry between dust and synchrotron foregrounds — (high frequency) dust emission falls much more rapidly with increasing galactic latitude causing the optimum frequency of observation to shift up from < 100 GHz towards 150 GHz. (Reproduced from Dunkley et al. (2008).)

$r \lesssim 0.2$ this means that heavy foreground "cleaning" will be required to reach the cosmological signal. This dictates making measurements at several frequencies and decomposing them as sums of multiple components — a well established technique in WMAP (and now Planck) analysis. The ultimate limitations of cleaning are hard to predict but the prospect of pulling out "ghost-like" $\ell < 10$ cosmological B-modes which are submerged by many orders of magnitude beneath galactic foreground is daunting to say the least. Nevertheless the projected ability to set limits of $r \lesssim 0.03$ with Planck has been claimed [13]. Measuring close to the whole sky at many frequencies is something that many would claim is only possible in space [b].

If one instead chooses to target the recombination bump there is a huge benefit — we can focus on small patches of sky at high galactic latitude which have foreground contamination at least an order of magnitude lower. From a simplistic signal-to-noise point of view when aiming for an initial detection one wants to concentrate the available sensitivity onto as small a patch of sky as possible. The lower limit is then set by the need for the patch to be at least as big as the largest angular scale of interest. Since the E and B mode patterns are non-local in practice one needs a patch several times larger than this to maintain separability [14]. In practice when targeting the $\ell \sim 80$ recombination bump a patch of area ~ 500 square degrees is appropriate.

3.3 Angular resolution

Once one has decided the observing frequency, and patch of sky to be observed, the remaining variable is the size of the telescope aperture — the angular resolution. In principle the requirement is modest — the angular scale corresponding to $\ell \sim 80$ is adequately resolved by a 25 cm aperture at 150 GHz.

However if higher angular resolution and sufficient sensitivity are available then the lensing

[b]But see the PIPER and CLASS experiments in Section 4.

contribution at larger angular scales can be computed and subtracted in a map sense — the lensing component can be cleaned out. From Figure 2 we see that this becomes necessary around $r \sim 0.01$. In addition, of course, measuring the lensing B-modes is an important goal in of itself allowing several scientific results including constraints on the neutrino mass.

3.4 Detector Technologies

The two main detector technologies used for CMB detection are bolometers (photons go to heat) and coherent amplifiers (photons go to voltage on a wire). Either of these can be used in direct imaging (telescope beam scans around on the sky) or interferometric systems (multiple telescopes "stare" at the sky and outputs are cross correlated). The DASI and CBI experiments were 30 GHz interferometers based on (coherent) HEMT amplifiers. The WMAP, CAPMAP and QUIET experiments were direct imaging HEMT based systems. The other experiments shown in Figure 2 (Boomerang, QUaD and BICEP) were direct imaging bolometer systems. To date bolometer experiments have held the edge in terms of per detector sensitivity.

3.5 Polarization Modulation and Beam Systematics

To measure linear polarization anisotropy in a direct imaging experiment one needs to measure brightness differences scanning across the sky with detectors sensitive to different polarization directions. Even from the best sites on the ground one is looking at the CMB through a "glowing screen" whose brightness variations are many times the size of the CMB anisotropies (think clouds). This problem is mostly alleviated on balloons or in space, but all detectors are subject to intrinsic fluctuations ($1/f$ noise) at low frequencies which have a similar practical effect. However the atmospheric emission is largely unpolarized and $1/f$ noise largely common mode between co-located detectors. Therefore one can overcome these effects by either fast modulation of the polarization sensitivity direction of a single detector (faster than the $1/f$ and scan rate), or by simultaneous differencing of orthogonal pairs of detectors (combined with later re-observation at another angle with the same, or another, pair of detectors) [c].

When modulating the modulator must not change the beam position and shape on the sky. When pair-differencing each half of the pair must have the same beam position and shape on the sky. Inasmuch as these conditions are violated then leakage from the much stronger T and E-mode spectra will occur into the B-mode spectrum.

In general beam imperfections are a fraction of the beam width so they are much more critical for the big beam (small aperture) experiments. However many of the effects at least partially cancel by rotating the telescope with respect to the sky and repeating the observations. Such rotation may take place due to the rotation of the Earth (at non-polar sites) and/or by including an additional line-of-sight (LOS) axis into the telescope mount. For some pair differencing experiments a major problem is "A/B centroid mismatch" where the beams of the orthogonal pair are offset from one another on the sky. This causes leakage from the gradient of T into polarization. However consider rotating by 180 degrees — now the sense of the leakage is reversed and under co-addition it cancels.

Some beam imperfections do not cancel under rotation of the telescope. For this reason some pair-differencing experiments also incorporate a slow (stepped) polarization modulator. So long as the behavior of the upstream optics is polarization independent (a property always required of a modulator) then one can achieve cancellation of beam systematics by repeating the observations at a set of discrete modulation angles.

Analysis mitigation is also possible — if one has knowledge of the beam imperfections and a T map (from another or the same experiment) one can compute the leakage and subtract it

[c] Pair differencing is popular — of all the bolometer experiments mentioned in Table 1 EBEX and PIPER may be the only ones which do not have co-located pairs of detectors.

out. Going further one can instead "project out" the potentially contaminated modes and avoid having to know the beam imperfections a priori. Many frequently referenced estimates of the needed degree of beam performance ignore such observation and analysis based mitigation and hence conclude that much higher beam purity is needed than is in fact the case [15].

3.6 Ground/Balloon/Space

Observing from the ground modern detectors are "background limited" meaning that photon arrival statistics of the atmospheric emission dominate the statistical noise. Thus when observing from above the Earth's atmosphere dramatically better per detector performance can be achieved. However even "long duration" balloon flights are currently $\lesssim 10$ days whereas ground based experiments can and do observe for up to ~ 1000 days. Historically both techniques have delivered final results of comparable quality when equipped with similar numbers of detectors.

Observing from space is a different matter — now one has the low noise level *and* years of exposure. However note that while in principle a CMB spacecraft could concentrate this awesome sensitivity on a small patch of clean sky, in practice — because they have the unique capability to observe the whole sky — they always do. Therefore the deepest small patch maps at any given time are always those from ground/balloon experiments.

4 Current/Future Experimental Efforts

There are a large number of experimental efforts focused on CMB polarization. Table 1 summarizes these with some additional information on each given below.

4.1 Space and Balloon

Planck is a 1.5 m aperture ESA space mission that launched in 2009. The High Frequency Instrument used bolometer detectors similar to those used in the Boomerang, BICEP1 and QUaD experiments, and completed operation in early 2012. The Low Frequency Instrument uses HEMT amplifiers and is still operating. Planck makes full sky maps and improves over WMAP in terms of frequency coverage (9 versus 5 channels), angular resolution ($\sim 3\times$) and sensitivity ($\sim 10\times$). Initial CMB results are expected in early 2013 with polarization results not expected until early 2014.

EBEX is a 1.5 m aperture balloon based experiment funded by NASA which has been under preparation for several years. Its first science flight will be a ~ 10 day circumpolar ("long duration" or LD) flight in Anarctica in late 2012. EBEX has 1500 TES bolometer detectors modulated by a continuously spinning half wave plate at 150, 250 and 410 GHz.

SPIDER is a balloon based array of 0.3 m aperture telescopes funded by NASA. The telescope optics and focal planes are very similar to BICEP2 and Keck-Array. A circumpolar flight is planned for late 2013 with focal planes at 90, 150 and 280 GHz and a total of ~ 2000 TES detectors.

PIPER is a third NASA funded balloon program emphasizing high frequencies (200, 270, 350, 600 GHz) with smaller resolution (~ 0.3 meter) apertures and large numbers of TES detectors (5000 per frequency). Only one frequencies will be active in any given flight and eight "standard duration" (SD) flights are planned split between northern and southern hemispheres. The goal is to cover a large fraction of the sky and target the reionization bump.

4.2 Ground Based in Chile

All the following experiments are (largely) funded by the US NSF and located at various sites in the Atacama desert in Chile.

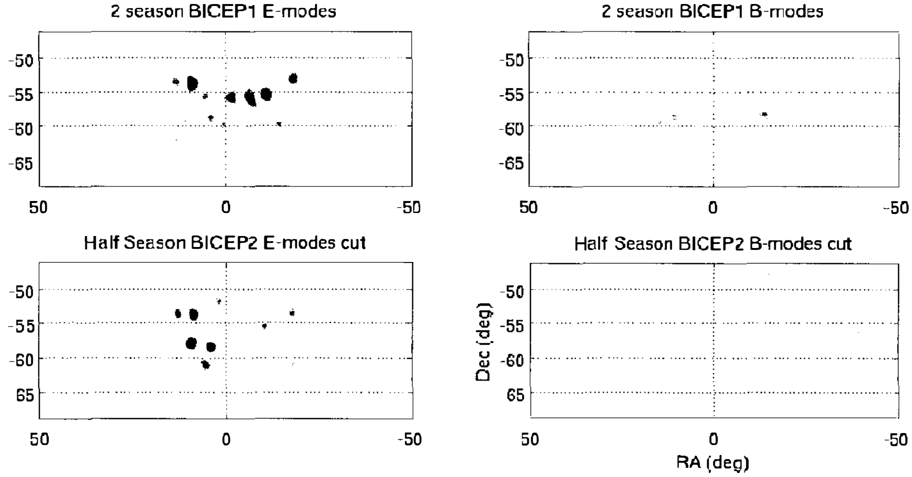

Figure 4: Maps of the CMB polarization E-mode and B-mode filtered to the angular scale range where the inflationary gravity wave signal is expected to be most prominent ($50 < \ell < 120$). The upper maps are the published BICEP1 results which hold the current world record in terms of sensitivity ($r < 0.72$, Chiang et al. (2010)). The lower maps are new preliminary BICEP2 results using half a season of data. The E-mode maps were already signal dominated for BICEP1 and so show little change going to BICEP2. However the BICEP2 B-mode maps show a large decrease in noise due to the much higher sensitivity of the BICEP2 instrument.

QUIET is 1.4 m aperture telescope utilizing HEMT amplifiers. It has released 43 GHz results (see Figure 2), and 90 GHz results are expected soon. It is currently unclear if the QUIET program will continue.

POLARBEAR is a 2.5 m aperture telescope. Deployment was completed in early 2012 and the focal plane is equipped with $\sim$ 1300 TES detectors operating at 150 GHz.

ABS is a 0.3 m all cold reflecting telescope. It has $\sim$ 500 TES detectors at 150 GHz and has been running since early 2012. ABS has a warm waveplate outside the cryostat which spins at 2.5 Hz.

ACTpol is a polarized receiver for the existing 6 m ACT telescope which will deploy in late 2012. ACTpol is *not* emphasizing inflationary B-mode detection.

CLASS is unique amongst ground based experiments in that it is targeting the reionization bump. It will observe at 40, 90 and 150 GHz and deployment is planned to start in 2013.

4.3 Ground Based at South Pole

The following experiments are (largely) funded by the US NSF and located at the South Pole station in Antarctica.

SPTpol is a polarized receiver for the existing 10 m SPT telescope which deployed in early 2012 and is now operating. It has 1500 total TES detectors at 100 and 150 GHz.

BICEP2 is a 0.3 m refracting telescope with 500 TES detectors at 150 GHz. As of mid 2012 it is midway through its third and final season of observation. The proven on sky sensitivity of BICEP2 is $\sim 10\times$ higher than that of BICEP1 — comparable to that of the Planck spacecraft but concentrated on a small patch of ultra clean sky. Figure 4 shows E and B-mode maps from BICEP2.

Keck-Array (aka SPUD) is an array of BICEP2 like telescopes. It operated through the 2011 season with three receivers at 150 GHz, and is operating for 2012 with five such receivers. For future seasons some receivers may be reconfigured to 90 and/or 220 GHz.

Table 1: Parameters of current and upcoming CMB telescopes.

Name	Type	Deploy/Fly	Aperture	Freq. (GHz)	Detectors	Modulation[a]
Planck	Space	2009	1.5 m	30–860		PD/LOS
EBEX	LD Balloon	late 2012	1.5 m	150/250/410	1500 TES	SR/FM
SPIDER	LD Balloon	late 2013	0.3 m	90/150/280	2000 TES	SR/PD/SM
PIPER	SD Balloon	9/2013	~ 0.3 m	200/270/350/600	5000 TES	SR/FM
QUIET-I	Chile	2008–10	1.4 m	40/90	19/90 HEMT	SR/FM/LOS
POLARBEAR	Chile	early 2012	2.5 m	150	1300 TES	SR/PD/SM
ABS	Chile	early 2012	0.3 m	150	500 TES	SR/PD/FM
ACTpol	Chile	late 2012	6 m	90/150	3000 TES	SR/PD
CLASS	Chile	late 2013	?	40/90/150	?	SR/?
SPTpol	South Pole	early 2012	10 m	100/150	1500 TES	PD
BICEP2	South Pole	early 2010	0.3 m	150	500 TES	PD/LOS
Keck-Array	South Pole	early 2011	0.3 m	150	2500 TES	PD/LOS

[a] SR = sky-rotation, FM/SM = fast/slow modulator (HWP, VPM or phase-switch), PD = pair-difference, LOS = line-of-sight rotation of whole telescope.

4.4 Future Space Mission?

The 2007 Bpol proposal to ESA consisted of an array of small refracting telescopes and was not selected. The US 2010 Decadal Survey recommended that NASA reconsider a future CMB space mission mid-decade. In 2010 the European community tried again with the more ambitious 1.2 m 6000 detector COrE mission which incorporated a large reflective polarization modulator. This was rated just below the selection cutoff for further study.

5 Conclusion

Inflation is often talked about as a part of the "standard cosmological model". It is perhaps more correct to say that this audacious theory is compatible with observations — it naturally produces the sort of Universe in which we find ourselves: spatially flat, isotropic and with scale-free, adiabatic initial conditions. It is therefore of critical importance to search for the final, and so far unobserved, prediction of Inflation — a background of primordial gravitational waves. If such waves exist at the time when the CMB photons last scatter they will imprint a very specific B-mode polarization pattern.

This paper has described the optimizations and trade-offs necessary to search for the gravitational wave signal in terms of frequency, sky-coverage, detector technology, modulation and experiment location. The current experimental "landscape" has also been summarized: many groups are pushing hard to detect this possible signal using a range of approaches, and emphasizing different parts of the problem. If nature is kind, and $r \geq 0.02$ then we should detect it soon!

Acknowledgments

The author wishes to thank his collaborators and many other members of the CMB community for useful discussions, the NSF (grant number ANT-1110087) for funding, and the conference organizers.

References

1. X. Wang, M. Tegmark, B. Jain and M. Zaldarriaga, *Phys. Rev.* D **68**, 123001 (2003). astro-ph/0212417
2. J. Kovac, E. Leitch, C. Pryke, J. Carlstrom, W. Holzapfel, *Nature* **420**, 772 (2002). astro-ph/0209478
3. M. Zaldarriaga and U. Seljak, *Phys. Rev.* D **55**, 1830 (1997). astro-ph/9609170
4. P. Peebles and J. Yu, *ApJ* **162**, 815 (1970).
5. A. Guth and S. Pi, *Phys. Rev. Lett.* **49**, 1110 (1982).
6. A. Kogut et al., *ApJS* **148**, 161 (2003). astro-ph/0302213
7. B. Feng, H. Li, M. Li and X. Zhang, *Phys. Lett.* B **620**, 27 (2005). hep-ph/0406269
8. M. Brown et al., *ApJ* **705**, 978 (2009). arxiv/0906.1003
9. C. Chiang et al., *ApJ* **711**, 1123 (2010). arxiv/0906.1181
10. R. Keisler et al., *ApJ* **743**, 28 (2011). arxiv/1105.3182
11. J. Dunkley et al., *AIP Conf. Proc.* **1141**, 222 (2008). arxiv/0811.3915
12. D. O'Dea et al., *Monthly Notices of the Royal Astr. Soc.* **417**, 1795 (2012). arxiv/1107.4612
13. G. Efstathiou and S. Gratton, *Jour. of Cosmology and Astropart. Phys.* **6**, 11 (2009). arxiv/0903.0345
14. A. Ferte, these proceedings.
15. W. Hu, M. Hedman and M. Zaldarriaga, *Phys. Rev.* D **67**, 043004 (2003). astro-ph/0210096

THE POLARBEAR EXPERIMENT

H. NISHINO[1], P. ADE[2], A. ANTHONY[3], K. ARNOLD[1], D. BARRON[4], D. BOETTGER[4], J. BORRIL[5,6], S. CHAPMAN[7], Y. CHINONE[8], M. A. DOBBS[9] J. ERRARD[10], G. FABBIAN[10], D. FLANIGAN[1], G. FULLER[4], A. GHRIBI[1], W. GRAINGER[2], N. HALVERSON[3], M. HASEGAWA[8], K. HATTORI[8], M. HAZUMI[8], W. L. HOLZAPFEL[1], J. HOWARD[1], P. HYLAND[11], A. JAFFE[12] M. LE JEUNE[10], B. KEATING[4], Z. D. KERMISH[1], T. KISNER[13], A. T. LEE[1,13], E. LINDER[13], M. LUNGU[1], F. MATSUDA[4], T. MATSUMURA[8], N. MILLER[4], H. MORII[8], S. MOYERMAN[4], M. J. MYERS[1], H. PAAR[4], C. REICHARDT[1], C. ROSS[7], I. SCHANNING[4], A. SHIMIZU[8], C. SHIMMIN[1], M. SHIMON[4], M. SHOLL[13], P. SIRITANASAK[4], H. SPIELER[13], N. STEBOR[4], B. STEINBACH[1], R. STOMPOR[10], A. SUZUKI[1], T. TOMARU[8], C. TUCKER[2], E. QUEALY[1], P. L. RICHARDS[1], AND ●. ZHAN[13,14]

Department of Physics, University of California, Berkeley, USA[1]
School of Physics and Astronomy, University of Cardiff, UK[2]
Department of Astrophysical and Planetary Science, University of Colorado, USA[3]
Physics Department, University of California, San Diego, USA[4]
Computational Cosmology Center, Lawrence Berkeley National Laboratory, USA[5]
Space Sciences Laboratory, University of California, Berkeley, USA[6]
Department of Physics and Atmospheric Science, Dalhousie University, Canada[7]
High Energy Accelerator Research Organization (KEK), Japan[8]
Physics Department, McGill University, Canada[9]
Laboratoire AstroParticule et Cosmologie (APC), Université Paris 7, France[10]
Physics Department, Austin College, USA[11]
Department of Physics, Imperial College, UK[12]
Physics Division, Lawrence Berkeley National Lab, USA[13]
Berkeley Center for Cosmological Physics (BCCP), University of California, Berkeley, USA[14]

POLARBEAR is a ground-based experiment in the Atacama desert in Chile, designed to measure the polarization of the Cosmic Microwave Background (CMB) radiation. The main science goals of POLARBEAR are to discover B-mode polarization of the CMB due to gravitational waves produced during the epoch of cosmological inflation. Detection of the B-mode polarization pattern in the CMB would provide strong evidence for inflationary cosmological models while the non-detection of B-modes by POLARBEAR would rule out a majority of single-field, slow-roll inflationary models. POLARBEAR will observe 700 square-degrees of the sky at 150 GHz with an array of 1,274 polarized antenna-coupled Transition Edge Sensor (TES) bolometers. POLARBEAR is expected to reach a sensitivity to the tensor-to-scalar ratio r = 0.025 at 95% confidence level, using the data from 2-years of operation. The beam size of 3.5 arcminutes makes it possible to also detect B-mode polarization signals at small-angular scales. These signals originate from weak gravitational lensing and are therefore sensitive to dark energy and the summed masses of neutrinos. POLARBEAR will be able to measure the sum of neutrino masses with a sensitivity of 75 meV, at 68%C.L., when our data are combined with the forthcoming data from Planck HFI. POLARBEAR was deployed in September 2011 and achieved "first-light" four months later, in January 2012. We will report the current status and the future prospects of POLARBEAR.

1 Introduction

Measurements of the Cosmic Microwave Background (CMB) have provided us rich information on the early universe and played a key role in establishing the standard model of cosmology by giving stringent constraints on cosmological parameters. Polarization measurements of the CMB have the potential to bring new insight into the epoch of inflationary cosmology. Inflation predicts the existence of primordial gravitational waves, which could be observable via a "curl-like" polarization pattern in the CMB called the B-mode [1]. POLARBEAR was built to probe for B-modes by measuring CMB polarization with unprecedented levels of sensitivity. For a tensor-to-scalar ratio, r, of 0.025, POLARBEAR will reach a 95% confidence level after 2 years of taking data[a]. POLARBEAR is designed to simultaneously probe for not only the primoridial B-modes, but also for lensing B-modes. The lensing B-modes are due to gravitational lensing of the CMB by large scale structure, and are expected to be present at the arcminute scale. This lensing effect is sensitive to the sum of the neutrino masses, and therefore by combining POLARBEAR's high-precision polarization data with Planck HFI's all-sky survery data, the expected sensitivity for a measurement of Σm_ν will be 75 meV at 68% confidence level.

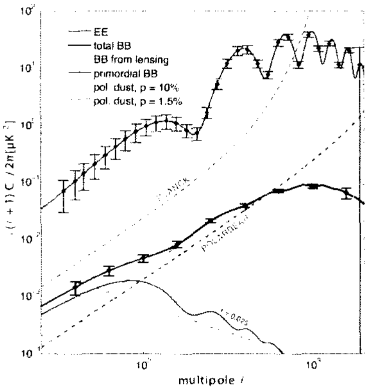

Figure 1: Expected POLARBEAR sensitivity (8μK-arcmin) (blue thick dashed line) from 2 years of observation and B-mode signal from primordial gravitational wave ($r = 0.025$) (magenta) and weak lensing (orange).

2 Instrument

The Huan Tran Telescope, which is used for the POLARBEAR experiment, is located at the James Ax Observatory in the Atacama desert of Chile, at 5200m altitude near Cerro Toco, as shown in Fig. 2. The telescope has off axis Gregorian Dragone optics with a 3.5m diameter primary mirror consisting of a monolithic 2.5m high accuracy panel and a guard ring. The telescope also has a comoving ground-shield to suppress sidelobe response. With a beam size of 3.5 arcminutes at 150 GHz, POLARBEAR is sensitive to both the primordial B-modes as well as the weak lensing B-modes. A rotating half-wave plate installed in the receiver periodically modulates polarized signals from the sky.

Fig. 3 shows the POLARBEAR focal plane, which consists of 7 modular arrays with a total of 1,274 antenna-coupled Transition Edge Sensor (TES) bolometers [2]. The focal plane is cooled to 260 mK by the combination of a pulse tube cooler and a helium multi stage sorption refrigerator

[a] r is proportional to the amplitude of the B-mode signal and the energy scale of inflation

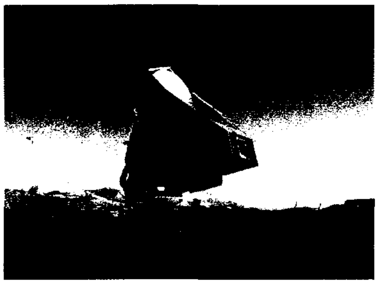

Figure 2: Photograph of the Huan Tran Telescope deployed at the Atacama desert in Chile.

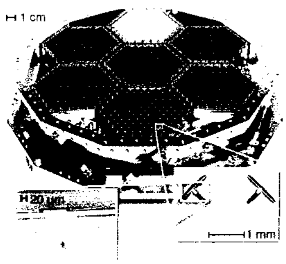

Figure 3: Focal plane of POLARBEAR. Six wafers have silicon lenstlets, while a wafer has alminua lenslets (white). There is no significant difference in performance between them.

in the receiver. Each of the 7 arrays, or wafers, on the focal plane has 91 pixels, and each individual pixel has two Al/Ti TES bolometers with a crossed polarization double-slot antenna and microstrip filters which define the 150 GHz observational band. The large number of bolometers is read out by a digital frequency domain multiplexed readout system (DfMux)[3], which can read out 8 bolometer channels with a single SQUID[b] amplifier. The expected sensitivity in NET per bolometer is about 480 $\mu K\sqrt{s}$. Given the expected yield, this gives an array sensitivity of 16 $\mu K\sqrt{s}$, which is comparable to that of Planck HFI[4]. Details of the POLARBEAR instruments can be found in Arnold et al (2010)[5].

3 Results from the Engineering Run

During the summer 2010, we performed an end-to-end test of all the systems of POLARBEAR in California at CARMA (Combined Array for Research in Millimeter-wave Astronomy) site at 2200m altitude. This included a test of the telescope, bolometers, readout systems, cryogenics, data acquisition, and Quicklook software. A modified focal plane, with only 3 wafers in place of 7, was installed, and an end-to-end system check was performed. We validated POLARBEAR's performance via noise power spectra, and beam maps of polarized and unpolarized sources.

The measured beam size and shape were consistent with optics simulation. One crucial systematic for POLARBEAR is due to mismatched beams between two detectors in a single pixel. If there are any beam differences between a pixel's two detectors, the intensity signal can be leaked into a polarization signal when the two detectors are differenced, mimicking B-mode polarization. The engineering run allowed us to measure the POLARBEAR differential beam properties, and show that our beams satisfy the requirement[6] for detection of a tensor-to-scalar ratio, r, of 0.025.

From the measured noise power spectra, we see common mode noise which was substantially reduced when a pair of orthogonally sensitive detectors was differenced. For the pixel difference spectra, our 1/f knee was roughly 100 mHz. Also, the low noise levels indicate that POLARBEAR will be able to meet its goals of measuring the physics targets of both primordial gravitational wave B-modes and weak lensing B-modes. We achieved predicted NET of 1 $mK\sqrt{s}$ per bolometer in the non-optimal atmosphere in California.

One of the polarized sources which we observed during the engineering run was Tau A, a supernova remnant at the heart of the Crab nebula which is polarized by synchrotron emission.

[b]superconducting quantum interference device

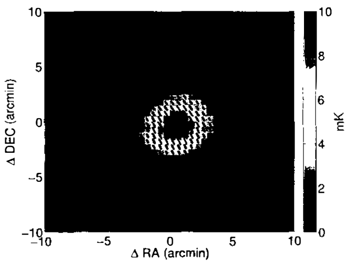

Figure 4: Polarization Map of TauA measured in the engineering run at California. Bars in each pixel indicate orientations of polarization.

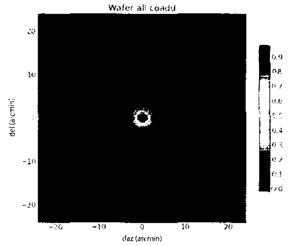

Figure 5: Beam map from the Saturn observation in Chile. This is a coadded map of all the pixels on the array.

Figure 4 shows the polarization results of our Tau A observations, specifically the polarization $\sqrt{Q^2 + U^2}$, of the source. Our results agree well at 150 GHz with the result published by Aumont *et al*[7], which was carried out with the IRAM 30m telescope at 90 GHz.

4 Current Status

After our successful engineering run in California in 2010, the telescope was shipped to Chile and reassembled starting in mid-September 2011. We achieved "first light" on January 10, 2012, only four months after we broke ground and laid the foundation in Chile.

Fig. 5 shows the beam map from a preliminary Saturn observation in Chile. The beam map is fairly circular, which shows successful installation of the entire system.

The detailed optimization of observation patches is in progress. Our basic plan is to observe three 15 × 15 degree^2 patches in the cleanest dust region in the southern sky. The sky coverage will be 700 square degrees in total. The planned observation patches have been chosen to overlap with other experiments, QUIET, EBEX, SPIDER and Planck HFI, which can help us to understand foregrounds contamination in the observation patches. Lower-freqeuency data are available from the QUIET Q band observations[8] at 43 GHz, and we anticipate gaining access to higher frequency (HFI) data from the Planck satellite mission in the near future, both of which will help to constrain dust emission with sufficient precision.

With our successful engineering run in California and commissioning in Chile, we have proven that POLARBEAR works as expected. POLARBEAR will start CMB observation shortly and give us exciting scientific results in the near future.

References

1. U. Seljak, and M. Zaldarriaga, *Phys. Rev. Lett.* **78**, 2054 (1997)
2. M. Myers *et al*, *Applied Physics Letters* **86**, 114103 (2005)
3. M. Dobbs and E. Bissonnette, and H. Spieler, *IEEE Trans. on Nucl. Sci.* **55**, 21 (2008)
4. J.-M. Lamarre *et al*, *Astronomy & Astrophysics* A **9**, 520 (2010)
5. K. Arnold *et al*, *Proc. SPIE* **7741**, 77411E (2010)
6. M. Shimon, B. G. Keating, N. Ponthieu, and E. Hivon, *Phys. Rev.* D **77**, 083003 (2008); N. J. Miller, M. Shimon, and B. G. Keating, *Phys. Rev.* D **79**, 063008 (2009); N. J. Miller, M. Shimon, and B. G. Keating, *Phys. Rev.* D **79**, 103002 (2009)
7. J. Aumont *et al*, *Astronomy & Astrophysics* A **514**, 70 (2010)
8. C. Bischoff *et al*, *Astrophysical Journal* **741**, 111 (2011)

Primordial tensor-to-scalar ratio constraints from CMB B-mode polarization observations in the presence of polarized astrophysical foregrounds

J. ERRARD
AstroParticule et Cosmologie, Univ Paris Diderot, CNRS/IN2P3, CEA/Irfu, Obs de Paris, Sorbonne Paris Cité, France

We study the impact of astrophysical foregrounds on the ability of Cosmic Microwave Background (CMB) B-mode polarization experiments to constrain the primordial tensor-to-scalar ratio, r. Our work is based on a formalism for performance forecasting and optimization of future CMB experiments [?]. We consider nearly full sky, multifrequency, B-mode polarization observations, and take into account statistical uncertainties due to the CMB sky statistics, instrumental noise, as well as the presence of two diffuse polarized foreground components, dust and synchrotron. To clean them we use parametric, maximum likelihood component separation technique and study cases with and without calibration errors, spatial variability of the foreground properties, and partial or complete B-mode lensing signal removal [?]. We find that, in the limit of an arbitrarily low noise level and in the absence of instrumental or modeling systematic effects, the foreground residuals do not impose a limit on the lowest detectable value of r, which can however arise if the lensing signal is not perfectly removed. We show that the need to control the foreground residuals will be a main factor in determining the minimal noise levels necessary to permit a robust detection of r, typically leading to requirements well below the statistical ones. For noise levels corresponding to current and proposed experiments, the foreground residuals are found to be non-negligible and can significantly restrict our ability to set constraints on r. Our conclusions are found to be independent on the assumed overall normalization of the foregrounds.

1 Introduction

Cosmic Microwave Background (CMB) B-mode observations are expected to be a primary source of information about the physics of the very early Universe, potentially providing an unambiguous proof of existence of the primordial gravity waves, considered as a telltale signature of inflation. Consequently, the CMB B-mode observations are a very dynamic area of the current research in cosmology, with multiple observatories being designed, built, and deployed. Besides the observation-specific issues, related to instrumental hardware or its operations, lensing-induced B-mode signal and astrophysical foregrounds, have come to the fore, both deemed as capable of setting some ultimate limitations to the exploitation of the CMB B-mode potential.

We study in this work the impact of astrophysical foregrounds on the ability of CMB polarization experiments to constrain the tensor-to-scalar ratio r, which parametrizes the amplitude of primordial B-modes signal. From a perspective of the parametric component separation technique, we consider only three polarized signals: CMB, dust and synchrotron, each of these two latter being parametrized by one parameter, called hereafter spectral indices. More detailed explanations can be found in Errard and Stompor [?].

2 Method

Parametric component separation. The fiducial data set we consider hereafter is made of multiple-single frequency maps of Q and U Stokes parameters, with an instrumental noise assumed to be uncorrelated, both between the detectors and channels, pixel-independent, and characterized by its variance, $\mathbf{N}$. The corresponding data model we use hereafter then reads,

$$\mathbf{d}_p = \mathbf{B}\,(\beta,\omega)\;\mathbf{s}_p\,+\,\mathbf{n}_p \equiv \mathbf{\Omega}\,(\omega)\;\mathbf{A}\,(\beta)\;\mathbf{s}_p\,+\,\mathbf{n}_p, \tag{1}$$

where for each pixel p, $\mathbf{A}$ is a mixing matrix parametrized by the spectral indices, β, $\mathbf{s}_p$ – a vector of sky signals to be recovered and $\mathbf{n}_p$ – instrumental noise. $\mathbf{\Omega}$ is a pixel-independent, diagonal matrix where the diagonal elements, $\omega_i \equiv \mathbf{\Omega}_{ii}$, correspond to the calibration factors for each of the channels, as introduced in Stompor et al. ?.

Residual computation. The computation of the residuals involves two steps. First, we obtain the error of the estimation of the spectral parameters. As shown in Errard and Stompor ?, this is done using a generalization of Eq. (5) of Errard et al. ?, allowing for calibration errors ?, and derived as a Fisher matrix, $\mathbf{\Sigma}_{ij}$, given by

$$\mathbf{\Sigma}_{ij}^{-1} = n_{pix} \operatorname{tr} \left\{ \left[\mathbf{B}_{,i}^t \mathbf{N}^{-1} \mathbf{B} \left(\mathbf{B}^t \mathbf{N}^{-1} \mathbf{B} \right)^{-1} \mathbf{B}^t \mathbf{N}^{-1} \mathbf{B}_{,j} - \mathbf{B}_{,i}^t \mathbf{N}^{-1} \mathbf{B}_{,j} \right] \hat{\mathbf{F}} \right\} + \left[(\omega - \bar{\omega})^t \, \mathbf{\Xi}^{-1} \, (\omega - \bar{\omega}) \right]_{,ij} \Big|_{\hat{\gamma}}, \quad (2)$$

which has to be evaluated at the true values of the parameters, i.e. $\gamma = \hat{\gamma}$ where γ stands for either β or ω, $_{,i} \equiv \partial / \partial \gamma_i$, and the matrix $\hat{\mathbf{F}}$, defined as $\hat{\mathbf{F}} \equiv n_{pix}^{-1} \sum_p \mathbf{s}_p \, \mathbf{s}_p{}^t$, encapsulates all the information about the sky components needed for the parameter errors estimation. Calibration uncertainty is described by an error matrix, $\mathbf{\Xi}$, which for simplicity is assumed to be proportional to the identity matrix, i.e., $\mathbf{\Xi}_{ij} \equiv \sigma_\omega^{-2} \, \delta_i^j$. In the following we will be removing the contribution to $\mathbf{\Sigma}$ related to the mode describing an overall miscalibration of the final CMB map. RMS of which is given by σ_ω, introducing a similar error in our determination of r – however, this is typically much smaller than the statistical uncertainty, i.e. $\delta r / r \gtrsim 0.01 \gtrsim \sigma_\omega^2$ for $r \lesssim 0.1$, and thus negligible.

Secondly, after estimating the error on the spectral parameters, we use the recipe of Stivoli et al. ? to compute the power spectra of the typical noise-free foreground residuals, $\mathbf{C}_\ell^\Delta$, which are defined as a linear combination of the true sky signals power spectra $\hat{\mathbf{C}}_\ell^{jj'}$ and weighted by the $\mathbf{\Sigma}$ elements:

$$\mathbf{C}_\ell^\Delta \equiv \sum_{k,k'} \sum_{j,j'} \mathbf{\Sigma}_{kk'} \, \alpha_k^{0j} \, \alpha_{k'}^{0j'} \, \hat{\mathbf{C}}_\ell^{jj'}. \quad (3)$$

Residuals significance. We quantify the importance of the residuals by defining the quantity:

$$\sigma_\alpha^{-1} = \left[f_{sky} \sum_\ell^{\ell_{max}} \frac{(2\ell + 1) C_\ell^\Delta}{C_\ell^{\mathrm{prim}}(r) + \eta \, C_\ell^{\mathrm{lens}} + C_\ell^{\mathrm{noise}}} \right]^{\frac{1}{2}}. \quad (4)$$

It expresses the statistical significance with which the residuals template could be detected, had it been known, given the instrumental noise, C_ℓ^{noise}, and the CMB signal, $C_\ell^{\mathrm{prim}}(r) + \eta C_\ell^{\mathrm{lens}}$. η denotes the fraction of the lensing signal left after its potential removal. Whenever σ_α^{-1} is large, the residuals can not be neglected in an analysis of the CMB map. Otherwise, the foreground residuals will be irrelevant for the estimation of r.

Experiment optimization. Following the approach described in Errard et al. ?, we assume a fixed, though arbitrary, focal plane area during the optimization and restrict frequencies of the observational channel bands to range from 30 to 400 GHz. The detector noise, expressed in antenna temperature units, is assumed to be constant among the frequency channels. The optimization then tries to minimize the effective r value as proposed in Amblard et al. ?, given by $\sum_\ell^{\ell_{max}} C_\ell^{prim}(r_{\mathrm{eff}}) = \sum_\ell^{\ell_{max}} C_\ell^\Delta$: this criterion reflects the fact that we want to minimize the effects of the foreground residuals and thus keep their amplitude as low as possible. The resulting experiment setup includes 5 frequency bands: $\nu = [30, 40, 130, 300, 400]$ GHz occupying, respectively, a fraction $f_{\mathrm{p}} = [9, 21, 36, 25, 9]$ % of the focal plane area.

3 Results

Hereafter we will use the noise level of the recovered CMB map, $\sigma^2_{\rm CMB}$, as a measure of the sensitivity of the considered experimental setups. This is given by

$$\sigma^2_{\rm CMB} \equiv \left[\left(\mathbf{B}\left(\hat{\gamma}\right)^t\,\mathbf{N}^{-1}\,\mathbf{B}\left(\hat{\gamma}\right)\right)^{-1}\right]_{00}, \tag{5}$$

where we assume that CMB is the zeroth component recovered in the separation procedure. Given the diagonal elements of the correlation matrix, $\mathbf{N}$, expressing the noise level of each frequency channel, one can show that for the experimental setup we consider, we can write numerically

$$\frac{\sigma_{\rm CMB}}{\mu{\rm K_{cmb}\,arcmin}} \simeq 2.6\;10^{-3}\,\frac{\sigma_{NET}}{\mu{\rm K_{ant}}}\,\sqrt{\frac{f_{\rm sky}}{0.82}\,\frac{1{\rm GHz}^{-2}}{A_{\rm fp}}\,\frac{2{\rm yrs}}{T_{\rm obs}}}. \tag{6}$$

The major features of σ_α^{-1}, defined in Eq. ??, as a function of the noise level, $\sigma_{\rm CMB}$, can be tracked back to the behavior of the parameter errors, $\mathbf{\Sigma}$, and foreground residuals expressions. In particular, in the low-noise regime, the value of σ_α^{-1} increases $\propto \sigma^2_{\rm CMB}$ whenever no calibration uncertainty is present or the contribution of the overall miscalibration mode is suppressed, leading to a self-calibrating property of the considered system, thanks to the assumed scaling laws spanning the entire range of considered frequency bands.

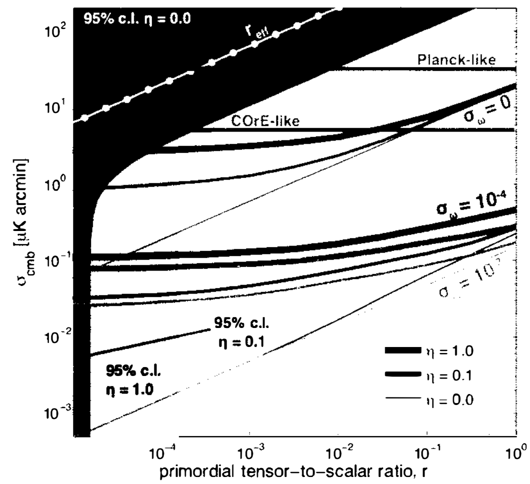

Figure 1: Upper limits on the map noise levels, $\sigma_{\rm CMB}$, which ensure that the foreground residuals are statistically irrelevant, are shown with solid lines. Each set of three lines corresponds to a different assumptions about the calibration errors as marked in the figure. In each set the lines depict the cases with no (heavy), 90% (medium), and perfect (thin) cleaning efficiency. The thick dots show the analogous noise limits based on an alternative criterion, r_{eff}. The shaded areas depict statistical 2σ limits due to the noise and sky signal for three lensing cleaning efficiencies $\eta = 1.0$, 0.1, and 0.0 (light to dark grey). The noise levels for Planck and COrE-like experiments are also shown as a reference.

Moreover, by solving the relation $\sigma_\alpha^{-1}\left(r, \sigma_{\rm CMB}\right) = \sigma_\alpha^{-1}|_{crit}$, we can set limits on $\sigma_{\rm CMB}$, as shown in Fig. ??. We used here $\sigma_\alpha^{-1}|_{crit} = 1$, corresponding to a "$1\sigma$" detection of the residuals on the map level. In general, this value should be adjusted, and the curves in the figure rescaled by a factor $\propto \sigma_\alpha|_{crit}^{-1/2}$, given a specific application envisaged for the output maps and 1 is used here as an illustration. For a given r value, each curve, computed for specific assumptions about the experiment and/or foregrounds, provides an upper limit on the experiments sensitivity so the foreground residuals will be found irrelevant for the analysis of the obtained CMB map. The gray-shaded areas show the statistical uncertainties, corresponding to a different level of gravitational lensing signal cleaning. We note that the foreground residual limits do not prevent detecting arbitrarily low value of r assuming that a sufficiently sensitive observation can be performed. Instead, the lower limit on r can arise due to a residual level of the lensing-induced B-mode signal left over from some cleaning procedure [?,?,?]. This remains true when the calibration errors are included but also when spatial variability of the foregrounds is allowed for [?], and will hold at least as long as no significant deviation from the assumed component scaling laws is observed. However, we show that effects of the spatial variability of the polarized foregrounds spectral indices lead to a tightening of the noise constraints.

The results obtained here demonstrate that in an absence of post-component separation processing and with calibration uncertainties as typically present in actual experiments the noise levels required for an unambiguous and robust determination of r are $\sim 10^{-1}\mu$K arcmin, significantly below the noise levels for the currently considered satellite mission concepts. Moreover, if the lensing contribution left over after its cleaning is higher than $\sim 10\%$ of its initial value, the dependence of the noise levels on the targeted value of r is rather weak. This emphasizes that once the sufficient noise level is indeed attained, the measurable values of r would be limited only by the statistical uncertainties. On the contrary, a failure to reach such a noise level may render the experiment incapable of setting any constraints on r of current interest. If the lensing could be cleaned nearly perfectly, $\eta \lesssim 10\%$, lower noise levels lead to a progressively lower limit on the detectable r.

4 Conclusions

We have studied the importance of the foreground residuals left over from the maximum likelihood parametric component separation procedure on the detection of the primordial tensor-to-scalar ratio coefficient, r, by nearly full-sky CMB B-mode experiments. We have found that though the foreground residuals are likely to be a major driver in defining the sensitivity requirements for such experiments, they do not on their own lead to any fundamental lower limits on detectable r, at least as long as sufficiently precise frequency scaling models are available. These will be rather set by the uncertainty due to the lensing signal present in the maps after its cleaning. We note that the latter may also in turn depend on the presence of foregrounds and instrumental noise [?,?], an issue we will address in a future work.

References

1. J. Errard et al., *Phys. Rev.* D **84**, 063005 (2011)
2. J. Errard and R. Stompor, *Phys. Rev.* D **85**, 083006 (2012).
3. R. Stompor et al., MNRAS **392**, 216 (2009), 0804.2645.
4. F. Stivoli et al., MNRAS **408**, 2319 (2010), 1004.4756.
5. A. Amblard et al., *Phys. Rev.* D **75**, 083508 (2007), arXiv:astro-ph/0610829.
6. L. Knox and Y.-S. Song, *Phys. Rev. Lett.* **89**, 011303 (2002), arXiv:astro-ph/0202286.
7. M. Kesden et al. *Phys. Rev. Lett.* **89**, 011304 (2002), arXiv:astro-ph/0202434.
8. U. Seljak and C. M. Hirata, *Phys. Rev.* D **69**, 043005 (2004), arXiv:astro-ph/0310163.
9. V. Stolyarov et al. MNRAS **357**, 145 (2005), arXiv:astro-ph/0405494.
10. W. Hu and T. Okamoto, ApJ **574**, 566 (2002), arXiv:astro-ph/0111606.
11. K.M. Smith et al., American Institute of Physics Conference Series, **vol. 1141**, pp. 121-178 (2009), 0811.3916.

A template of atmospheric O_2 circularly polarized emission for CMB experiments

G. Fabbian[1], S. Spinelli[2], M. Gervasi[2], A. Tartari[1,2], M. Zannoni[2]
[1] *AstroParticule et Cosmologie, Univ Paris Diderot, CNRS/IN2P3, CEA/Irfu, Obs de Paris, Sorbonne Paris Cité, France*
[2] *Dipartimento di Fisica "G. Occhialini", Università di Milano Bicocca, Piazza della Scienza 3, 20126, Milano*

We compute the polarized signal from atmospheric molecular oxygen due to Zeeman effect in the Earth magnetic field for various sites suitable for CMB measurements such as South Pole, Dome C (Antarctica) and Atacama desert (Chile). We present maps of this signal for those sites and show their typical elevation and azimuth dependencies. We find a typical circularly polarized signal (V Stokes parameter) of 50 – 300 μK at 90 GHz looking at the zenith while Dome C site presents the lowest gradient in polarized temperature: 0.3 $\mu K/\text{o}$ at 90 GHz. The accuracy and robustness of the template are tested with respect to actual knowledge of the Earth magnetic field, to its variability and to atmospheric parameters.

1 Motivation

In the last 15 years several experiments managed to successfully observe CMB anisotropies from the ground in the atmospheric windows far from the emission lines of most abundant molecules of the atmosphere. For next generation of ground experiment, which will be able to map CMB polarization at high resolution and with high sensitivity, an evaluation of atmospheric emission is required. As pointed out first by Hanany *et al.*[6], the main atmospheric contaminant for this kind of measurements is the circularly polarized Zeeman emission of molecular oxygen (O_2). Such signal can in fact be converted into linear polarization through non idealities of the instrument and thus generate spurious Q and U quantities.
In second instance the circular polarization of CMB itself has a cosmological interest and a theoretical effort is undergoing to investigate the mechanisms which can produce such signal either at last scattering surface or at later epoch (see for example Giovannini,[7] Cooray *et al.*[3] and references in Spinelli *et al.*[1]). In this perspective any dedicated future measurement aiming to update the current constraint on V Stokes parameter[9] has to face the presence of atmospheric molecular oxygen as a foreground.

2 Polarized emission theory

O_2 is the only abundant molecule in the atmosphere having a non-negligible magnetic dipole moment since its electronic configuration set two parallel coupled spin electrons in the highest energy level. This characteristic together with the presence of the Earth magnetic field allows the Zeeman splitting of its roto-vibrational lines in the millimeter region of the electromagnetic spectrum. In particular we notice that O_2 has a single intense line around $\nu \simeq 118.75$GHz and a forest of lines in the range 50–70 GHz. Selection rules corresponding to transitions $\Delta m_j = 0, \pm 1$ identify three different type of Zeeman lines (π, $\sigma_\pm$ respectively) having polarization direction and intensity properties varying as a function of the angle θ between the line of sight (los) and the Earth magnetic field.
The polarized intensity for each line can be evaluated through their coherency matrices ρ; the total coherency matrix $\mathbf{A}_{tot}$ is given by the superposition of those for all the different lines weighted by two factors taking into account the transition dependence on pressure and temperature ($C(\nu, P, T)$) and the line broadening and mixing, $F(\nu, \nu_k, \Delta\nu_c)$.[5]

$$\mathbf{A}_{tot} = C(\nu, P, T) \sum_{\Delta m_j=-1}^{+1} \rho_{\Delta m_j} \sum_{m_j=-j}^{+j} P_{trans}(S, L, m_j, \Delta j, \Delta m_j) F(\nu, \nu_k, \Delta\nu_c) \qquad (1)$$

P_{trans} denotes the transition probability for each line as predicted by quantum mechanics, and fixes their relative intensities. Taking into account all these relations the final matrix has the following form:

$$\mathbf{A}_{tot} = a\rho_{\sigma_-} + b\rho_{\sigma_+} + c\rho_\pi = \begin{pmatrix} a+b & i(a-b)\cos\theta \\ -i(a-b)\cos\theta & (a+b)\cos^2\theta + c\sin^2\theta \end{pmatrix} \tag{2}$$

We notice that the precence of non vanishing and purely conjugate imaginary off-diagonal terms means that radiation is only circularly polarized ($V \neq 0, U = 0$) with a circular polarization stronger when the los is aligned with the Earth magnetic field ($V \propto \cos\theta$). On the other hand, diagonal terms are different and thus a small fraction of Q-like linear polarization is produced which is stronger when the los is orthogonal to the Earth magnetic field ($Q \propto (a+b-c)\sin^2\theta$). Nevertheless the ratio of linear to circular polarization intensity is very low ($\approx 10^{-4}$) and the first can be neglected.[6]

3 Signal computation

Once $\mathbf{A}$ matrix is computed for a given pressure and temperature at a given altitude, we use the tensor radiative transfer approach for isothermal layers[8,4] to propagate the signal through the atmosphere. According to this theory the signal emerging from one isothermal layer is a weighted sum of the physical temperatures of the layer itself. The weight function encodes all the information about transfer properties and is a function of the total coherency matrix $\mathbf{A}$.
For the signal computation we used vertical profiles for atmospheric pressure and temperature available in literature [2] and the IGRF-2010 model for the Earth magnetic field. The latter describes the geomagnetic field up to an angular scale of $\simeq 15^\circ$, corresponding to a typical wavelength of 3000 km along the surface. Smaller scale correction due to magnetized rocks in the crust are not accounted for.

4 Results

4.1 *Frequency templates*

We computed the circularly polarized emission for various sites suitable for mm astronomy (Chajnantor in Atacama desert, South Pole, Dome C, Testa Grigia) at the zenith as a function of frequency (fig. 1). Differences among various sites are mainly due to the difference of altitudes between them (lower layers of the atmosphere, having an higher pressure, are in fact the major contributors to the signal) and amplitude and direction of Earth magnetic field, since the signal depends on the scalar product between the latter and the los. We notice that both right handed ($V > 0$) and left handed ($V < 0$) circular polarization are produced and that a sign reversal takes place at frequencies $\nu \simeq 100$, 160 GHz.

4.2 *Angular templates*

We produced maps of the signal at the various sites in local alt-azimuthal coordinates at 90 GHz (see figure 2 and Spinelli *et al.*). Both right handed and left handed circular polarization is produced varying the los. In some cases a null signal direction is present and corresponds to the angular position where magnetic field and los are orthogonal. As expected, the observed signal depends on a combination between the atmospheric thickness (elevation scans have a zenith secant dependence law) and the magnetic field direction (see fig. 3). Such dependency can lead the two effects to combine to roughly compensate each other and produce a nearly constant signal on a large part of the visible sky (see Dome C case in fig. 2), or to enhance the signal

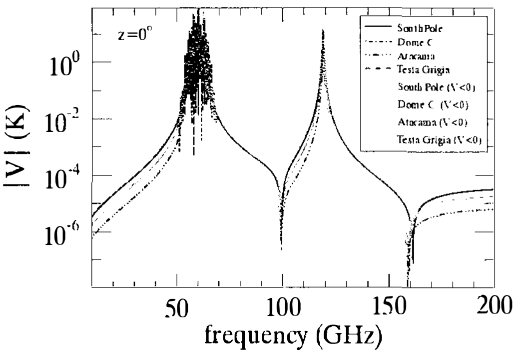

Figure 1: Absolute value of polarized atmospheric signal at the zenith for various sites as a function of frequency. Colored lines denote negative values.

gradient where the magnetic field is nearly horizontal, as in Atacama case.
Typical signal variation at 90 GHz for North-South elevation scans ranges between $70\mu K$ (Dome C) and $500\mu K$ (Atacama) while for a full 360° azimuthal scan at $el = 45°$ varies between $50\mu K$ (Dome C) and $270\mu K$ (Atacama). We also computed the signal gradient for both type of scans

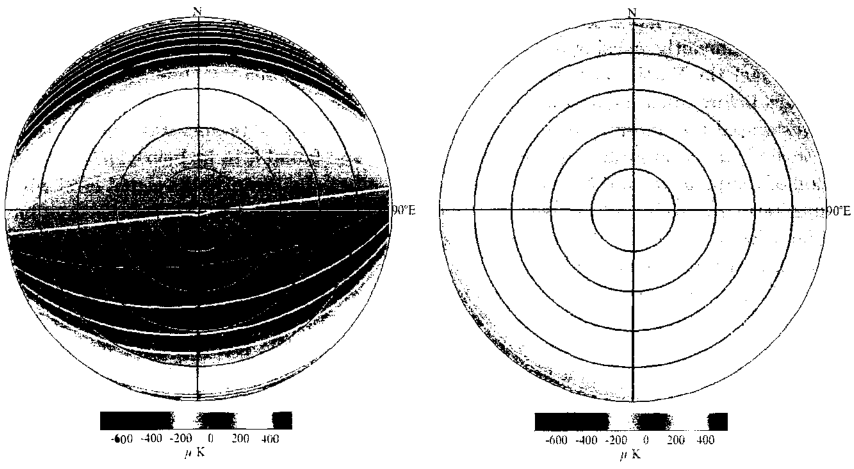

Figure 2: Map of atmospheric O_2 circularly polarized signal at ν = 90 GHz for Atacama (left) and Dome C (right) in Lambert projection centered on the zenith. Black circles denote elevation intervals of 15°; white (red) contours denote intervals of $50\mu K$ in brightness temperature (null signal level).

in order to give a better description of the signal angular dependence. The maximum value of the gradient takes values in a range $0.3 - 5.1\mu K/°$ for elevation scans while for azimuth scans it varies between $0.4 - 2.5\mu K/°$ with minimum and maximum values at Dome-C and Atacama respectively.

Dome C presents the smoother pattern for O_2 polarized signal which thus can be minimized for any kind of differential scanning strategy. We note however that for real experiment the signal computed in our template has to be integrated with the bandwidth efficiency and convolved with the beam profile.

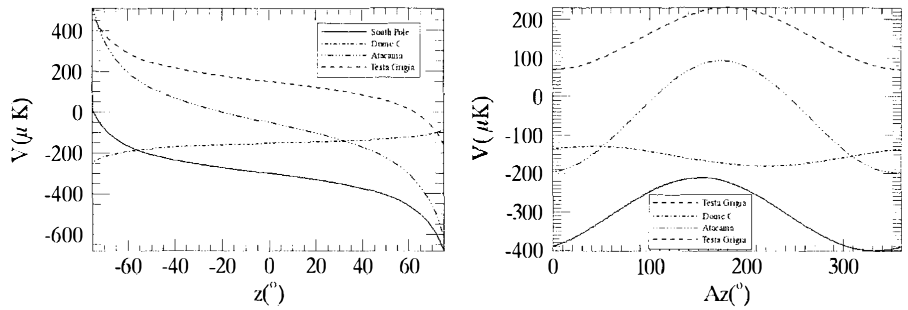

Figure 3: North-South elevation scans (left) and azimuthal scans at constant elevation $el = 45°$ (right) of the oxygen polarized signal for different sites at $\nu = 90$ GHz.

5 Accuracy

The accuracy of the 90GHz templates has been estimated taking into account uncertainties and typical variability of the main parameters of the model through Monte Carlo techniques. In particular the influence of uncertainties in the magnetic field model direction and magnitude and secular variation (SV) have been found negligible for all sites ($\delta V_{rms} < 0.2\mu K$, $\frac{\delta V_{sv}}{\delta t} < 0.5\mu K/y$). A violent and rapid event like a solar magnetic storm conversely can affect the accuracy of the template more significantly, causing a variation of $2 - 9\mu K$ on the level of the V signal. During those events in fact the Earth magnetic field strength can vary as much as $1000nT$ for no more than a few days before quiet conditions are established again.
We then investigated the uncertainty with respect to the accuracy of temperature and pressure profiles for several sites using values quoted in literature[2], and found it to be below $2\mu K$. Day to day variation of temperature and pressure profiles don't affect significantly the signal level while seasonal long term variability of atmospheric parameters affects the accuracy of the template only for polar sites ($3 - 14\mu K$), where it concerns the whole air column and not only the lowest layers of the atmosphere like e.g. Atacama case.
We note also that the line transition frequencies are known with negligible error bars but the Oxygen absorption parameters, which are crucial to compute the line profiles, have error bars of at least 5% at 90 GHz. This accuracy applies up to $\approx$ 120 GHz but at higher frequencies, where models and values of Oxygen absorption are not yet validated, results should be used with caution.

References

1. Spinelli, S., Fabbian, G., Tartari, A., Zannoni, M., & Gervasi, M. 2011, *MNRAS , 414, 3272*
2. *Tomasi, C., Petkov, B., Benedetti, E., et al. 2006,* Journal of Geophysical Research (Atmospheres), 111, 20305
3. Cooray, A., Melchiorri, A., & Silk, J. 2003, Physics Letters B, 554, 1
4. Lenoir, W. B. 1968, *Journal of Geophysical Research , 73, 361*
5. *Rosenkranz, P. W., & Staelin, D. H. 1988, Radio Science, 23, 721*
6. *Hanany, S., & Rosenkranz, P. 2003,* New Astr. Rev , 47, 1159
7. Giovannini, M. 2009, *Phys. Rev.* D, 80, 123013
8. Lenoir, W. B. 1967, Journal of Applied Physics, 38, 5283
9. Partridge, R. B., Nowakowski, J., & Martin, H. M. 1988, *Nature , 331, 146*

QUBIC: THE QU BOLOMETRIC INTERFEROMETER FOR COSMOLOGY

M.-A. BIGOT-SAZY on behalf of the QUBIC collaboration
Université Paris Diderot, Laboratoire Astroparticule et Cosmologie (APC), UMR 7164, 75013, Paris

The quest of B-mode polarisation of the cosmic background is one of the scientific priorities of the observational cosmology today. An important experimental effort aiming at the detection of the B-mode is in progress. The QUBIC instrument is one of the many experiments dedicated to this purpose, it is based on a novel technology: bolometric interferometry. We present the design of this instrument and we will focus on a new specific procedure of calibration: the self-calibration.

1 Introduction

Observing the B-mode is the most direct way to constrain the period of inflation. The detection of such a weak signal is however a real experimental challenge. In addition to a high statistical sensitivity (huge number of horns and bolometers required), future experiments will need an excellent quality of foreground removal and an unprecedented control of systematics.

Currently, most of the projects are based on the experimental concept of an imager. This technology allows to have a good sensitivity with large array of bolometers and large bandwidth. However, a number of sources of systematic effects are hard to control (ground pickup, time varying systematics). An alternative approach to the imager is interferometry. Two interferometers, DASI and CBI have been the first experiments to detect E-mode polarization of the cosmic background (Kovac et al., 2002 and Readhead et al., 2002). Interferometers provide a direct measurement of the Fourier modes of the sky while imagers measure maps of the cosmic background. Interferometers offer advantages for controlling systematic effects (sensitivity to 1/f noise, clean optics). On the other hand, it is limited by the complexity to construct a large bandwidth N-elements correlator.

The goal of bolometric interferometry is to combine the advantages of an interferometer with the ones of an imager. This novel concept is the project of the QUBIC instrument. QUBIC is a collaboration between France (APC Paris, CESR Toulouse, CSNSM Orsay, IAS Orsay), Ireland (Maynooth University), Italy (Universita di Roma La Sapienza, Universita di Milano Bicocca), United Kingdom (University of Manchester) and USA (University of Wisconsin, Brown University, Richmond University).

A first module is planned to be installed at the Franco-Italian Concordia station in Dome C, Antarctica within two years. This module will consist of an array of 400 horns operating at 150 GHz with 25% bandwidth and 14 degree (FWHM) primary beams. The optical combiner will have a focal length of about 30 cm and each of the two focal planes will comprise arrays of 30x30 bare TES bolometers of 3 mm size. The full instrument will include 6 modules at three different frequencies (90, 150, 220 GHz) and will constrain a tensor to scalar ratio of 0.01 in one year of data taking at the 90% confidence level.

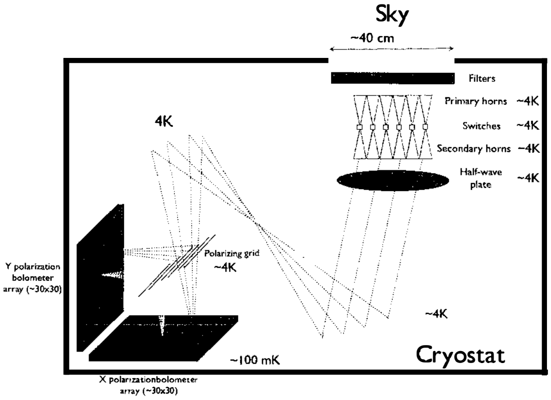

Figure 1: QUBIC concept

2 QUBIC design

The bolometric interferometer proposed with the QUBIC instrument is the millimetric equivalent of the first interferometer dedicated to astronomy: the Fizeau interferometer.

The receptors are two arrays of horns: the primary and secondary horns back to back on a squared array behind the optical window of a cryostat. Filters and switches are placed in front and between the horns array. The switches will be used only during the calibration phase, they are metal shutters which close the waveguide section between the back-to-back horns. The polarization of the incoming field is modulated using a half-wave plate located after the back horns. Signals will be correlated together using an optical combiner. The interference fringe patterns arising from all pairs of horns, with a given angle, are focused to a single point on the focal plane. Finally, a polarizing grid splits the signal into x and y polarisations, each being focused on a focal plane equipped with bolometers. These bolometers measure a linear combination of the Stokes parameters modulated by the half-wave plate.

The image we observe on the focal plane is the synthetic image, making the QUBIC instrument a synthetic imager. The electric fields from all pairs of horns are added, squared and averaged in time using bolometers contrary to radio-interferometers, where the signals (visibilities) are obtained by multiplying the electric fields from pairs of receivers.

3 QUBIC observables

The observables measured by the QUBIC bolometric interferometer are the synthesized images. A bolometer q, in the focal plane of the beam combiner, measures the following power:

$$S_q(t) = S_q^I \pm cos(4wt)S_q^Q \pm sin(4wt)S_q^U \tag{1}$$

where S_q^X are the dirty images on the focal plane for each Stokes parameter $X = \{I,Q,U\}$ (images of the sky filtered by the horns array), and where the cosine and sine coefficients come from the modulation induced by the rotating half-wave plate (whose angular frequency is w).

These dirty images, recovered after demodulation, are the convolution of the Stokes parameters with the synthesized beam $B_s^q(\widehat{n_p})$ pointing towards $\widehat{n_p}$:

$$S_q^X = \int X(\widehat{n_p}) B_s^q(\widehat{n_p}) d\widehat{n_p} \tag{2}$$

The synthesized image is the image of the sky seen through the synthesized beam which is approximately given by the discrete Fourier transform of the horns distribution. This beam has much more structure than a Gaussian function as it is built from the combination of a finite number of baselines of the primary horns array.

4 Self-Calibration

4.1 Principles

The expected weakness of the B-mode implies that the instrument needs to have a good handle on systematic effects. Instrument-induced effects include, for example, beam errors (mismatching and cross-polarization), gain errors (pointing and detector miscalibration), coupling (due to instrumental polarization, misalignment of polarization angles)... .

This self-calibration technique is inspired by traditional interferometry (Pearson and Readhead, 1984) and is based on the redundancy of the receiver array (Wieringa, 1991). It uses the fact that in absence of systematic effects, equivalent baselines of the interferometer should measure exactly the same quantity. For an ideal instrument, the measurements will be the same, for a real instrument they will be different because of systematics. The self-calibration relies on comparing all the redundant baselines with each others and permits to calibrate parameters that characterize completely the instrument at the same time for each channel.

4.2 Observables

When the baseline (i, j) is open, the bolometer k measures the synthesized images for each Stokes parameter $X = \{I, Q, U\}$:

$$S_{ijqp}(\widehat{n_p}) = C_{iq}(\widehat{n_p}) + C_{jq}(\widehat{n_p}) + 2Re(\alpha_{iq}\alpha^*_{jq}\beta_i(\widehat{n_p})\beta^*_j(\widehat{n_p})X(\widehat{n_p})) \tag{3}$$

where $C_{iq}(\widehat{n_p})$ and $C_{jq}(\widehat{n_p})$ are the powers respectively measured with only switch i or switch j open which can be writted as: $C_{iq}(\widehat{n_p}) =\mid \alpha_{iq} \mid^2\mid \beta_i(\widehat{n_p}) \mid^2 X(\widehat{n_p})$.

We introduce the coefficients α_{iq} and $\beta_i(\widehat{n_p})$. The coefficients α_{iq} are defined for each channel of horns-bolometers and include the geometrical phases induced by the beam combiner, the beams of the secondary horns $B_{sec}(\overrightarrow{d_q})$ and the gain g_q of the bolometer q:

$$\alpha^{ideal}_{iq} = g_q \int B_{sec}(\overrightarrow{d_q})exp[i2\pi\frac{\overrightarrow{x}_i}{\lambda}\frac{\overrightarrow{d_q}}{D_f}]J(\nu)\Theta(\overrightarrow{d} - \overrightarrow{d_q})d\nu d\overrightarrow{d_q} \tag{4}$$

where f_D is the focal length of the beam combiner, $\Theta(\overrightarrow{d})$ describes the bolometer geometry, $\overrightarrow{x}_i$ is the position of a pair of back-to-back horn i in the aperture plane, the detectors location is given by $\overrightarrow{d_q}$, λ is the wavelength of the instrument and ν is the frequency. The integrations are over the surface of each individual bolometer and on bandwidth.

The coefficients $\beta_i(\widehat{n_p})$ are defined for each channel of pointings-horns and include the primary beam $A^X_i(\widehat{n_p})$, the horns position $\overrightarrow{x_i}$ and the pointings direction $\widehat{n_p}$:

$$\beta^{ideal}_i(\widehat{n_p}) = B_{prim,i}(\widehat{n_p})exp(i2\pi\overrightarrow{x_i}\widehat{n_p}) \tag{5}$$

During the calibration phase, using the switches, one can modulate on/off a single pair of horns while leaving all the others open in order to access the synthesized images and the powers measured by bolometers. By repeating this with a subset of all baselines, with all bolometers and different pointings, one can construct a system of equations whose unknowns are the coefficients α_{iq}, the primary beam $B_{prim,i}$, the horns location $\overrightarrow{x_i}$, the pointings direction $\widehat{n_p}$ and the Stokes parameters $X(\widehat{n_p})$. For a square grid array of $N_h \geq 6$ horns, the problem becomes overdetermined and can be solved with a least squares fit.

4.3 Simulation

We have implemented numerically the method to check if the nonlinear system could be inverted. We generate the instrument and the systematic parameters (horns location errors, pointings errors, assymetries of beams, bolometers location errors, gain errors). We compute the corrupted synthesized images and add statistic noise. We solve the non-linear system with a standard non-linear least-squares method based on a Levenberg-Marquardt algorithm. The coefficients without systematic errors are used as starting guess for the different parameters. We run the simulation for an array of 9 primary horns, 16 bolometers and 36 pointings.

Fig.2 shows that the corrupted parameters are well-reconstructed.

parameters	rms(ideal-corrupted)	rms(corrupted-recovered)
α_{iq}	0.0029	0.0007
$B_{prim,i}(\widehat{n_p})$	0.0090	0.0005
$\widehat{n_p}$	0.0082	0.0009
$\vec{x_i}$ (x1000)	0.0983	0.0114
$X(\widehat{n_p})$	0.9951	0.0057

Figure 2: *This is the table of the root mean square of the different recovered parameters. On the second column there is the values of the relative error between the ideal and corrupted parameters and on the third column between the corrupted and recovered parameters.*

Conclusion

The QUBIC instrument is a bolometric interferometer. It combines the signals from an array of wide entry horns using a cold telescope as an optical combiner to form interference fringes of I, Q and U Stokes parameters (modulated with a half-wave plate) on a bolometer array.

The statistical sensitivity of QUBIC is comparable to that of an imager with the same number of horns covering the same sky fraction. Furthermore, the control of the systematic effects with the self-calibration technique appears to be a strong argument in favor of bolometric interferometry. It allows to determine accurately the systematic effects for each of the channels of the instrument.

Acknowledgments

This work was supported by Agence Nationale de la Recherche (ANR), Centre National dEtudes Spatiales (CNES), Centre National de la Recherche Scientifique (CNRS), Science and Technology Facilities Council (STFC), the National Science Foundation (NSF), the National Aeronautics and Space Administration (NASA), Instititut Paul Emile Victor (IPEV), Programma Nazionale Ricerche in Antartide (PNRA) and Science Foundation Ireland (SFI).

References

1. The QUBIC Collaboration, *Astroparticle Physics* 34 (2011).
2. R. Charlassier, PhD, University Paris-Diderot (2010).
3. J. Kovac, *et al*, *Nature*, 420 772 (2002).
4. A.C.S. Readhead, *et al*, *Science*, 306, 836 (2002).
5. M. Wieringa, Ast. Soc. of the Pacific Conf. series, vol. 19:192-196 (1991).
6. A.C.S Readhead and P.N. Wilkinson, ApJ 223:25-36 (1978).

The CMB bispectrum from secondary anisotropies: the Lensing-Integrated Sachs Wolfe-Rees Sciama contribution

Anna Mangilli
Institut d'Astrophysique de Paris, 98bis boulevard Arago 75014 Paris (France) and UPMC

We investigated the CMB bispectrum signal arising from the cross correlation between lensing and the Integrated Sachs Wolfe/Rees Sciama effects. The ISW and RS effects arise because of time varying gravitational potential due, respectively, to the linear and non-linear growth of structure in the evolving universe. Both the lensing and the ISW-RS effects are related to the matter gravitational potential and thus are correlated phenomena, giving rise to a non-vanishing three points correlation function. The LRS signal is expected to be detected at high statistical significance from ongoing and future CMB experiments and, being a late time effect, it can be a powerful probe of the late time universe. Moreover, we showed that this bispectrum signal, if not accounted properly, can bias the estimation of the amplitude and variance of the local primordial non-Gaussianity. Finally we built CMB simulations with the LRS signal and we implemented and tested the optimal estimator for this specific bispectrum.

1 Introduction

One of the most relevant mechanism that can generate non-Gaussianity from secondary Cosmic Microwave Background (CMB) anisotropies is the coupling between weak lensing and the Integrated Sachs Wolfe (ISW) [1] Rees Sciama (RS) [2] effects. This is in fact the leading contribution to the CMB secondary bispectrum with a blackbody frequency dependence [3,4,5]. Weak lensing of the CMB is caused by gradients in the matter gravitational potential that distorts the CMB photon geodesics. The ISW and RS effects on the other hand arise because of time varying gravitational potential due, respectively, to the linear and non-linear growth of structure in the evolving universe. Both the lensing and the ISW-RS effect are then related to the matter gravitational potential and thus are correlated phenomena. This gives rise to a non-vanishing three points correlation function or, analogously, a non-vanishing bispectrum, its Fourier counterpart. Further, lensing and the RS effect are related to non-linear processes which are therefore highly non-Gaussian. The CMB bispectrum signal arising from the cross correlation between lensing and ISW/RS (from now on referred as LRS) is expected to have an high signal-to-noise from ongoing and future CMB experiments so that it will be detectable in the near future with an high statistical significance [4, 5, 6, 7, 8]. This will open the possibility to exploit the cosmological information related to the late time evolution encoded in the LRS signal. Moreover the LRS bispectrum can be a problem for the estimation of the primary local non-Gaussianity from future data since it can be a serious contaminant [7, 9].

Ongoing CMB experiments like e.g. Planck and future experiments like CORE will then require a detailed reconstruction of the Lensing-ISW RS bispectrum either to be able to separate out correctly the LRS contribution when estimating the local primary non-Gaussian parameter f_{NL} or to exploit the cosmological information encoded in the signal.

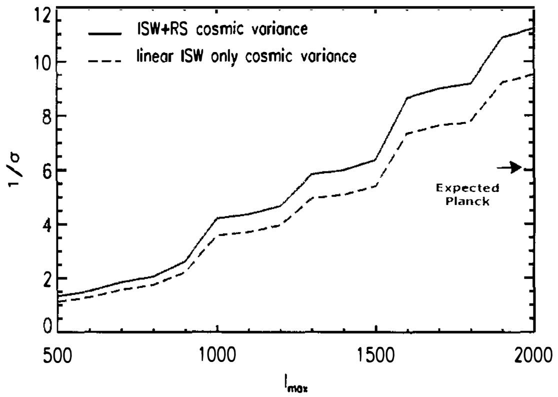

Figure 1: Expected statistical detection significance of the LRS bispectrum in the case of a cosmic variance limited full sky experiment as a function of the maximum multipole ℓ_{max}. The red arrow indicates a more realistic statistical detection significance expected for Planck at $\ell_{max} = 2000$.

2 The Lensing-ISW-RS bispectrum signal

The CMB Lensing-ISW-Rees Sciama bispectrum takes the form[3,4,7]:

$$B^{m_1m_2m_3}_{\ell_1\ell_2\ell_3} \equiv \langle a^{m_1}_{\ell_1} a^{m_2}_{\ell_2} a^{m_3}_{\ell_3}\rangle = \langle a^{m_1 P}_{\ell_1} a^{m_2 L}_{\ell_2} a^{m_3 RS}_{\ell_3}\rangle + 5 \text{ Permutations}. \tag{1}$$

This becomes: $B^{m_1m_2m_3\,(L-RS)}_{\ell_1\ell_2\ell_3} = \mathcal{G}^{m_1m_2m_3}_{\ell_1\ell_2\ell_3} b^{L-ISW/RS}_{\ell_1\ell_2\ell_3}$, where $\mathcal{G}^{m_1m_2m_3}_{\ell_1\ell_2l_3}$ is the Gaunt integral and the reduced bispectrum is given by

$$b^{L-ISW/RS}_{\ell_1\ell_2\ell_3} = \left[\frac{\ell_1(\ell_1+1) - \ell_2(\ell_2+1) + l_3(\ell_3+1)}{2} C^P_{\ell_1} q_{\ell_3} + (5\ perm.)\right], \tag{2}$$

Here C^P_ℓ is the primary angular CMB temperature power spectrum and q_ℓ are the coefficients which express the statistical expectation of the correlation between the lensing and the ISW-RS effect:

$$q_\ell \equiv \langle \phi^{*m}_{L\ell} a^{RSm}_\ell\rangle \simeq 2\int_0^{z_{ls}} \frac{r(z_{ls}) - r(z)}{r(z_{ls})r(z)^3}\left[\frac{\partial}{\partial z}P_\phi(k,z)\right]_{k=\frac{\ell}{r(z)}} dz. \tag{3}$$

Here P_ϕ is the gravitational potential power spectrum and the above equation accounts for both the linear ISW and the non-linear Rees-Sciama effect.

Fig.1 shows the statistical detection significance S/N expected for the LRS bispectrum signal as a function of the maximum multipole ℓ_{max}:

$$\text{S/N} = \sqrt{\sum_{\ell_{min}\le\ell_1\le\ell_2\le\ell_3}^{\ell_{max}} \frac{B^{L-RS}_{\ell_1\ell_2\ell_3} B^{L-RS}_{\ell_1\ell_2\ell_3}}{\Delta_{\ell_1\ell_2\ell_3} C_{\ell_1}C_{\ell_2}C_{\ell_3}}}. \tag{4}$$

3 The bias to the primary local Non-Gaussianity

The LRS bias to primary local f_{NL} is given by:

$$\hat{f}_{NL} = \frac{\hat{S}}{N}, \text{ where } \hat{S} = \sum_{2\le\ell_1\ell_2\ell_3} \frac{B^{L-RS}_{\ell_1\ell_2\ell_3} B^P_{\ell_1\ell_2\ell_3}}{C_{\ell_1}C_{\ell_2}C_{\ell_3}} \text{ and } N = \sum_{2\le\ell_1\ell_2\ell_3} \frac{(B^P_{\ell_1\ell_2\ell_3})^2}{C_{\ell_1}C_{\ell_2}C_{\ell_3}}. \tag{5}$$

We find that a bispectrum estimator optimized for constraining primordial non-Gaussianity of the local type would measure an effective $f_{NL} = 10$ for $\ell_{max} = 1000$ due to the presence of the primary-lensing-Rees-Sciama correlation. If not accounted for, this introduces a contamination in the constraints on primordial non-Gaussianity from the CMB bispectrum. For forthcoming data this bias will be larger than the $1-\sigma$ error and thus non-negligible.

4 Optimal estimator and simulations

Estimator

Here we are interested in the L-RS case, for which the angular bispectrum, parametrized by the amplitude parameter f_{NL}^{LRS}, is:

$$\langle a_{\ell_1 m_1} a_{\ell_2 m_2} a_{\ell_3 m_3} \rangle = \mathcal{G}_{\ell_1 \ell_2 l_3}^{m_1 m_2 m_3} f_{NL}^{LRS} b_{\ell_1 \ell_2 \ell_3}^{LRS}, \tag{6}$$

where $\mathcal{G}_{\ell_1 \ell_2 l_3}^{m_1 m_2 m_3}$ is the Gaunt integral, $b_{\ell_1 \ell_2 \ell_3}^{LRS}$ is the LRS reduced bispectrum as defined in equation (2) and $q_\ell \equiv \langle \phi_{\ell m}^{*L} a_{\ell m}^{RS} \rangle$ are the lensing-ISW/RS cross-correlation coefficients (which account for both the linear ISW and the non-linear Rees-Sciama effect) of equation (3).

It is then possible to build an optimal estimator for f_{NL}^{LRS} by maximizing the PDF with respect to this parameter. So, by solving $d \ln P / d f_{\rm NL}^{L-RS} = 0$, this is given by:

$$f_{NL}^{L-RS} = (F^{-1}) S_{LRS}, \tag{7}$$

where (F^{-1}) is the inverse of the L-RS Fisher matrix.

Assuming that the only NG contribution is coming from the L-RS term, S_{L-RS} is given by the data as:

$$S_{L-RS} \equiv \frac{1}{6} \sum_{all\ \ell m} \mathcal{G}_{\ell_1 \ell_2 \ell_3}^{m_1 m_2 m_3} b_{\ell_1 \ell_2 \ell_3}^{L-RS} \left[(C^{-1}a)_{\ell_1 m_1} (C^{-1}a)_{\ell_2 m_2} (C^{-1}a)_{\ell_3 m_3} - 3 (C^{-1})_{\ell_1 m_1, \ell_2 m_2} (C^{-1}a)_{\ell_3 m_3} \right], \tag{8}$$

Simulations: the separable mode expansion method

Following[10] and[11], the non-Gaussian part of the CMB angular coefficients can be defined starting from a given CMB power spectrum C_ℓ and reduced bispectrum $b_{\ell_1 \ell_2 \ell_3}$. For the LRS bispectrum these take the form:

$$[a_{\ell m}^{NG}]_{LRS} = \int d^2\hat{\mathbf{n}} \sum_{\ell_2 m_2 \ell_3 m_3} b_{\ell \ell_2 \ell_3}^{LRS} Y_\ell^{m*}(\hat{\mathbf{n}}) \frac{a_{\ell_2 m_2}^G Y_{\ell_2}^{m_2}(\hat{\mathbf{n}})}{C_{\ell_2}} \frac{a_{\ell_3 m_3}^G Y_{\ell_3}^{m_3}(\hat{\mathbf{n}})}{C_{\ell_3}}, \tag{9}$$

where, again, $b_{\ell \ell_2 \ell_3}^{LRS}$ is the reduced bispectrum of eq.(2). The angular coefficients containing the wanted signal will then be: $a_{\ell m} = a_{\ell m}^G + [a_{\ell m}^{NG}]_{LRS}$, where $a_{\ell m}^G$ is the Gaussian part.

Results

I tested the estimator and the LRS coefficients built with the separable modes expansion method with 100 runs at full resolution ($N_{side} = 2048$) and up to $\ell_{max} = 1000$. According to the definition of f_{NL}^{LRS} the expected value is 1 with 1-σ error predicted from theory for $\ell_{max} = 1000$ of $\simeq 0.25$. The simulations give $f_{NL}^{LRS} = 1.11$ with averaged 1-σ error 0.36 as shown in Fig.2.

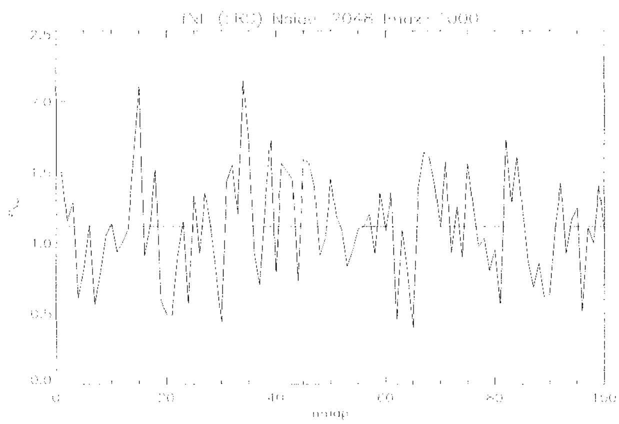

Figure 2: f_{NL}^{LRS} (eq. 7) obtained by testing the LRS estimator (cfr eq. 8) on 100 CMB maps (full sky and cosmic variance limited, $N_{side} = 2048$) containing the LRS signal simulated by using the separable mode expansion method (cfr eq. 9).

5 Conclusions

In this work we studied the LRS bispectrum signal. We showed that it can be a significant contaminant to the bispectrum signal from primordial non-Gaussianity of the local type. In particular both signals are frequency-independent and are maximized for nearly squeezed configurations, which in fact are the configurations that contribute the most to the S/N. If not included in the modeling, the primary-lensing-Rees-Sciama contribution yields an effective f_{NL} of 10 when using a bispectrum estimator optimized for local non-Gaussianity. Considering that expected 1-σ errors on f_{NL} are < 10 from forthcoming experiments, the contribution from this signal must be included in future constraints on f_{NL} from the Cosmic Microwave Background bispectrum. Within this picture it is extremely important to be able to model the LRS bispectrum either to be able to avoid contaminations either for exploiting it as a cosmological observable in view of future data. I presented the formalism and the numerical implementation for generating CMB non-gaussian maps which contain the LRS signal. I also implemented and tested numerically the Non-gaussian estimator optimized for the LRS bispectrum.

References

1. R. K.Sachs and A. M.Wolfe,APJ **147**, 73 (1967)
2. M. J. Rees and D. W. Sciama, Nature **217**, 511 (1968).
3. D. N. Spergel and D. M. Goldberg, Physical Review D **59**, 103001 (1999) and D. M. Goldberg and D. N. Spergel, Physical Review D **59**, 103002 (1999)
4. L. Verde and D. N. Spergel, Physical Review D **65**, 043007 (2002), arXiv:astro-ph/0108179.
5. F. Giovi, C. Baccigalupi, and F. Perrotta, Physical Review D **71**, 103009 (2005)
6. W.Hu, Physical Review D **62** 043007 (2000)
7. A. Mangilli and L. Verde, Physical Review D **80**, 123007 (2009)
8. A. Lewis et al. JCAP, 03(2011)018
9. D. Hanson et al.Physical Review D **80** :083004 (2009)
10. J.R. Fergusson, M. Liguori and E. P. S. Shellard, Physical Review **D**,82, 023502 (07/2010)
11. K.M. Smith and M. Zaldarriaga arXiv:astro-ph/0612571v1 (2006)

CONSTRAINTS ON THE TOPOLOGY OF THE UNIVERSE DERIVED FROM THE 7-YEAR WMAP CMB DATA AND PERSPECTIVES OF CONSTRAINING THE TOPOLOGY USING CMB POLARISATION MAPS

P. BIELEWICZ[1,2], A.J. BANDAY[1,2], K.M. GÓRSKI[3,4]

[1] *Université de Toulouse, UPS-OMP, Institut de Recherche en Astrophysique et Planétologie, Toulouse, France*

[2] *CNRS, IRAP, 9 Av. colonel Roche, BP 44346, F 31028 Toulouse cedex 4, France*

[3] *Jet Propulsion Laboratory, M/S 169/327, 4800 Oak Grove Drive, Pasadena CA 91109*

[4] *Warsaw University Observatory, Aleje Ujazdowskie 4, 00-478 Warszawa, Poland*

We impose constraints on the topology of the Universe determined from a search for matched circles in the cosmic microwave background (CMB) temperature anisotropy patterns of the 7-year *WMAP* data. We pay special attention to the sensitivity of the method to residual foreground contamination of the sky maps. A search for pairs of matched back-to-back circles in the higher resolution *WMAP* W-band map allows tighter constraints to be imposed on topology. Our results rule out universes with topologies that predict pairs of such circles with radii larger than $\alpha_{\rm min} \approx 10^\circ$. This places a lower bound on the size of the fundamental domain for a flat universe of about 27.9 Gpc. We study also the possibility for constraining the topology of the Universe by means of the matched circles statistic applied to polarised CMB anisotropy maps. The advantages of using the CMB polarisation maps in studies of the topology over simply analysing the temperature data as has been done to-date are clearly demonstrated. It is found that the noise levels of both Planck and next generation CMB experiments data are no longer prohibitive and should be low enough to enable the use of the polarisation maps for such studies.

1 Introduction

According to General Relativity, the pseudo-Riemannian manifold with signature (3,1) is a mathematical model of spacetime. The local properties of spacetime geometry are described by the Einstein gravitational field equations. However, they do not specify the global spatial geometry of the universe, i.e. its topology. This can only be constrained by observations. The concordance cosmological model assumes that the universe possesses a simply-connected topology, yet various anomalies observed on the largest angular scales in the *WMAP* data in the last decade suggest that it may be multiply-connected. Evidence of such anomalies comes from the suppression of the quadrupole moment and an alignment between the preferred axes of the quadrupole and the octopole (Copi *et al.* [1], de Oliveira-Costa *et al.* [2]).

We constrained the topology of the Universe (Bielewicz and Banday [3]) using the method of matched circles proposed by Cornish *et al.* [4] and applied it to the 7-year *WMAP* data (Jarosik *et al.* [5]). In contrast to the majority of previous studies, we paid special attention to the impact of Galactic foreground residuals on the constraints. The method was applied to higher resolution maps than previously, which implies a lower level of false detection and therefore tighter constraints on the size of the Universe. As a result of computational limitations, we restricted the analysis to a search for back-to-back circle pairs[a].

[a] pairs of circles centred around antipodal points

The method of matched circles is not inherently limited to temperature anisotropy studies. It can also be applied to the CMB polarisation data (Bielewicz *et al.*[6]). We investigate also such an application of the method. We test it on simulated CMB maps for a flat universe with the topology of a 3-torus, and explicitly consider the possibility for the detection of matching circle pairs for data with an angular resolution and noise level characteristic of the Planck and COrE data. The latter is treated as a reference mission for the next generation of CMB experiments.

2 Statistic for the matched circles

If light had sufficient time to cross the fundamental cell, an observer would see multiple copies of a single astronomical object. To have the best chance of seeing 'around the universe' we should look for multiple images of distant objects. Searching for multiple images of the last scattering surface is then a powerful way to constrain topology. Because the surface of last scattering is a sphere centred on the observer, each copy of the observer will come with a copy of the last scattering surface, and if the copies are separated by a distance less than the diameter of the last scattering surface, then they will intersect along circles. These are visible by both copies of the observer, but from opposite sides. The two copies are really one observer so if space is sufficiently small, the CMB radiation from the last scattering surface will contain a pattern of hot and cold spots that match around the circles.

The idea of using such circles to study topology is due to Cornish *et al.* [4]. Therein, a statistical tool was developed to detect correlated circles in all sky maps of the CMB anisotropy – the circle comparison statistic

$$S^{\pm}_{p,r}(\alpha, \phi_*) = \frac{\langle 2\, X_p(\pm\phi) X_r(\phi + \phi_*)\rangle}{\langle X_p(\phi)^2 + X_r(\phi)^2\rangle}\ , \tag{1}$$

where $\langle\rangle = \int_0^{2\pi} d\phi$ and $X_p(\pm\phi)$, $X_r(\phi + \phi_*)$ are temperature (or polarisation) fluctuations around two circles of angular radius α centered at different points, p and r, on the sky with relative phase ϕ_*. The sign $\pm$ depends on whether the points along both circles are ordered in a clockwise direction (phased, sign $+$) or alternately whether along one of the circles the points are ordered in an anti-clockwise direction (anti-phased, sign $-$). This allows the detection of both orientable and non-orientable topologies. For orientable topologies the matched circles have anti-phased correlations while for non-orientable topologies they have a mixture of anti-phased and phased correlations. To find correlated circles for each radius α, the maximum value $S^{\pm}_{\max}(\alpha) = \max\limits_{p,r,\phi_*} S^{\pm}_{p,r}(\alpha, \phi_*)$ is determined. In case of anticorrelated circles the maximum value of $-S^{\pm}_{p,r}(\alpha, \phi_*)$ is used. In the original paper by Cornish *et al.*[4] the above statistic was applied exclusively to temperature anisotropy maps. However, it can also be applied to polarisation data and in this work, we focus on its application to the E-mode map. In this case, the X map is simply the map of the E-mode.

To draw any conclusions from an analysis based on the statistic $S^{\pm}_{\max}(\alpha)$ it is important to correctly estimate the threshold for a statistically significant match of the circle pairs. We used simulations of the maps with the same noise properties and smoothing scales as the data to establish the threshold such that fewer than 1 in 100 simulations would yield a false event.

3 Constraints on the topology of the Universe derived from 7-year WMAP data

In order to decrease the false detection level and be able to detect matched circles with smaller radius, we analyzed the *WMAP* data with the highest angular resolution i.e. the W-band map, corrected for Galactic foregrounds and smoothed with a Gaussian beam profile of the Full Width

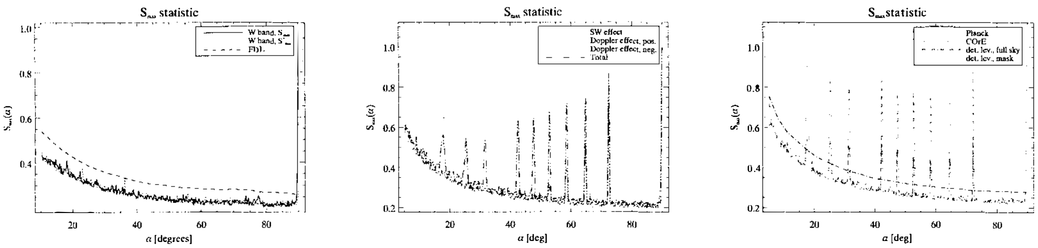

Figure 1: In the left figure, $S^{\pm}_{\rm max}$ statistic for the *WMAP* 7-year W-band map. Solid and dotted lines show the statistics $S^{-}_{\rm max}$ and $S^{+}_{\rm max}$, respectively, for the W-band map masked with the KQ85y7 mask. The dashed line is the false detection level estimated from 100 MC simulations. The peak at 90° corresponds to a match between two copies of the same circle of radius 90° centered around two antipodal points. In the middle and right figures, examples of the $S^{-}_{\rm max}$ statistics for simulated CMB temperature and polarisation anisotropy maps, respectively, of universe with the topology of a cubic 3-torus with dimensions $L = 2\ c/H_0$. In the middle figure, the dotted, solid, dashed and three dot-dashed lines show the statistic for CMB maps of the Sachs-Wolfe (SW) effect, the positive and negative correlations of the Doppler effect and total anisotropy, respectively. In the right figure, the solid and dashed lines show the statistic for simulated polarisation maps with angular resolution and noise level corresponding to the Planck and COrE data, respectively. The dot-dashed and three dot-dashed lines show the false detection levels for the statistic estimated from 100 Monte Carlo simulations of the Planck coadded 100, 143 and 217 GHz frequency polarisation maps for the full sky and cut sky analysis, respectively.

at Half Maximum (FWHM) 20′ to decrease the noise level. The statistic for this map analysed with the KQ85y7 mask is shown in Fig. 1.

We did not find any statistically significant correlation of circle pairs in the map. As shown in Bielewicz and Banday [3], the minimum radius at which the peaks expected for the matching statistic are larger than the false detection level is about $\alpha_{\rm min} \approx 10°$ for the W-band map. Thus, we can exclude any topology that predicts matching pairs of back-to-back circles larger than this radius. This implies that in a flat universe described otherwise by the best-fit 7-year *WMAP* cosmological parameters, a lower bound on the size of the fundamental domain is $d = 2\,R_{\rm LSS}\cos(\alpha_{\rm min}) \simeq 27.9$ Gpc, where $R_{\rm LSS}$ is the distance to the last scattering surface. However, one has to keep in mind that this constraint concerns only those universes with such dimensions and orientation of the fundamental domain with respect to the mask that allow the detection of pairs of matched circles.

4 Prospects of constraining the topology using CMB polarisation maps

4.1 Discussion of degrading effects for temperature maps

Since the signatures of topology are imprinted on the surface of last scattering, any effects that dilute this image will also degrade the ability to detect such signatures by means of the matched circles statistic. In the case of the temperature fluctuations, there are two sources of anisotropy generated at the last scattering surface: the combination of the internal photon density fluctuations and the Sachs-Wolfe (SW) effect and the Doppler effect. In the latter case, the correlations for pairs of matched circles can be negative in universes with multi-connected topology. For pairs of back-to-back circles with a radius smaller than 45° the Doppler term becomes increasingly anticorrelated. The consequences of these degrading effects are weaker constraints on the topology of the Universe obtained from the matched circle statistic. As we can see in Fig. 1, use of the CMB map without both of the degrading effects would allow us to impose lower bounds on the minimum radius of the correlated circles which can be detected much below the present constraints $\alpha_{\rm min} \approx 10°$ (Bielewicz and Banday [3]).

4.2 Search of matched circles in polarisation maps

A polarisation map at small angular scales can be considered as a snapshot of the last scattering surface. Theoretically, then, the polarisation provides a better opportunity for the detection of multi-connected topology signatures than a temperature anisotropy map. The only serious issues preventing its use in studies of topology are instrumental noise and the correction of the polarised data for the Galactic foreground.

The $S^{-}_{\max}$ statistic for the simulated maps is shown in Fig. 1. As expected the amplitudes of the peaks do not decrease with the radius of the circles as in the case of the temperature anisotropy maps. We see that pairs of matched circles can be detected for the Planck coadded 100, 143 and 217 GHz frequency polarisation maps. However, comparing with figure for the temperature anisotropy one should notice that the relative amplitude of the peaks with respect to the average correlation level for the circles with small radius is not bigger than for the temperature map. Thus, the constraints on topology will not be much tighter than those derived from an analysis of temperature maps. A much better perspective arises for the COrE maps. The signal of the multi-connected topologies is very pronounced in this case enabling the detection of matched circles with very small radius thus providing tighter constraints on the topology of the Universe.

Acknowledgments

We acknowledge use of CAMB[b] [7] and the HEALPIX[c] software Górski *et al.*[8] and analysis package for deriving the results in this paper. We acknowledge the use of the Legacy Archive for Microwave Background Data Analysis (LAMBDA). Support for LAMBDA is provided by the NASA Office of Space Science. The authors acknowledge the use of version 1.6.6 of the Planck Sky Model, developed by the Component Separation Working Group (WG2) of the *Planck* Collaboration (Leach *et al.*[9], Betoule *et al.*[10]). Part of the computations were performed at Interdisciplinary Center for Mathematical and Computational Modeling at Warsaw University within a grant of computing time no. G27-13.

References

1. C. J. Copi, D. Huterer, G. D. Starkman, *Phys. Rev.* D **70**, 043515 (2004).
2. A. de Oliveira-Costa, M. Tegmark, M. Zaldarriaga, A. Hamilton, *Phys. Rev.* D **69**, 063516 (2004).
3. P. Bielewicz and A. J. Banday, *MNRAS* **412**, 2104 (2011).
4. N. J. Cornish, D. N. Spergel, G. D. Starkman, *CQGra* **15**, 2657 (1998).
5. N. Jarosik *et al*, *ApJS* **192**, 14 (2011).
6. P. Bielewicz, A. J. Banday, K. M. Górski, *MNRAS* **421**, 1064 (2012).
7. A. Lewis, A. Challinor, A. Lasenby, *ApJ* **538**, 473 (2000).
8. K. M. Górski, E. Hivon, A. J. Banday, B. D. Wandelt, F. K. Hansen, M. Reinecke, M. Bartelmann, *ApJ* **622**, 759 (2005).
9. S. M. Leach *et al*, *A&A* **491**, 597 (2008).
10. M. Betoule, E. Pierpaoli, J. Delabrouille, M. Le Jeune, J. F. Cardoso, *A&A* **503**, 691 (2009).

[b] http://camb.info/
[c] http://healpix.jpl.nasa.gov

Parity in the CMB: Space Oddity

Assaf Ben-David[1], Ely D. Kovetz[1,2] and Nissan Itzhaki[1]
[1]*Raymond and Beverly Sackler Faculty of Exact Sciences, School of Physics and Astronomy, Tel-Aviv University, Ramat-Aviv, 69978, Israel*
[2]*Theory Group, Department of Physics and Texas Cosmology Center, The University of Texas at Austin, Texas 78712, USA*

We search the CMB sky for a direction that exhibits parity symmetry under reflections through a plane. We mask outlying regions in the Galactic plane and find a distinct direction of odd parity at a significance level of above 3.5σ.

1 Introduction

A basic assumption in cosmology is that at large enough scales, the universe is homogeneous and isotropic. When this assumption is confronted with the data, the ΛCDM theory emerges as a very good fit. However, the largest scales, for which the cosmic variance is large, still show some unexpected features that could indicate the breaking of isotropy at those scales.

In this work, based on Ben-David et al.,[1] we focus on a simple question: does the Cosmic Microwave Background (CMB) radiation at the largest scales behave as expected with respect to a mirror parity transformation? While this question was studied before,[2,3,4,5] previous works concentrated on specific aspects, such as the parity of galactic foregrounds or the relation to the apparent alignment of the $\ell = 2, 3$ multipoles. Here we study the parity symmetry of the CMB data with respect to all directions in the sky and check for anomalous parity directions.

2 Full Sky Analysis

2.1 Parity Estimator

We would like to check the CMB temperature fluctuations map for parity symmetry with respect to reflections through a plane, i.e. $\mathcal{P}_{\hat{\mathbf{n}}} : \hat{\mathbf{r}} \to \hat{\mathbf{r}} - 2\,(\hat{\mathbf{r}} \cdot \hat{\mathbf{n}})\,\hat{\mathbf{n}}$, where $\hat{\mathbf{n}}$ is the normal to the plane. This symmetry was tested by de Oliveira-Costa et al.[2,3] using a straightforward statistic in pixel space. We take a different approach and define our statistic in harmonic space, where statistically there are no two-point cross-correlations, and the scale can easily be controlled. Since under reflections through the plane normal to the $\hat{\mathbf{z}}$ axis the spherical harmonics transform as

$$Y_{\ell m}(\mathcal{P}_{\hat{\mathbf{z}}}(\hat{\mathbf{n}})) = (-1)^{\ell+m} Y_{\ell m}(\hat{\mathbf{n}})\,, \tag{1}$$

a natural strategy is for each direction $\hat{\mathbf{n}}$, to compare the distribution of power in each multipole ℓ between even and odd $\ell + m$ modes. Hence we define our estimator to be

$$S(\hat{\mathbf{n}}) = \sum_{\ell=2}^{\ell_{\max}} \left[\sum_{m=-\ell}^{\ell} (-1)^{\ell+m} \frac{|a_{\ell m}(\hat{\mathbf{n}})|^2}{\hat{C}_\ell} - 1 \right], \tag{2}$$

(a)

(b)

Figure 1: (a) The parity estimator calculated on the full sky 7-year WMAP ILC map, with $\ell_{\max} = 5$. The maximum lies in the direction of the "axis-of-evil". (b) The parity estimator calculated on the ILC map with 12% of the sky masked as described in the text.

where $a_{\ell m}(\hat{\mathbf{n}})$ are the multipole coefficients calculated in a coordinate system in which $\hat{\mathbf{n}}$ is the $\hat{\mathbf{z}}$ axis and $\hat{C}_\ell = \frac{1}{2\ell+1}\sum_m |a_{\ell m}|^2$ is the total observed power for the ℓ multipole. The more $S(\hat{\mathbf{n}})$ is positive (negative) the more the temperature map is parity-even (odd) in the $\hat{\mathbf{n}}$ direction. We have normalized $S(\hat{\mathbf{n}})$ so that in ΛCDM the ensemble average vanishes.

2.2 Results

We calculate our statistic (2) on the WMAP 7-year Internal Linear Combination (ILC) map. The results for $\ell_{\max} = 5$ are shown in Fig. 1(a). As can be seen, the maximum lies at $(l, b) = (260°, 48°)$, the direction found in de Oliveira-Costa et al.[3] of the alignment of the quadrupole and octupole, the anomaly known as the "Axis of Evil". Since the alignment of the multipoles is directly related to their planarity (corresponding to large $m = \pm\ell$ modes), this can be seen as a special case of an even parity symmetry (large even $\ell + m$ modes). The minimum of the map, signifying odd parity, lies at $(l, b) = (266°, -19°)$. In the full sky score map both extrema do not appear to be significant with respect to the other directions.

3 Cut Sky Analysis

3.1 Masking Scheme

In order to disregard galactic foreground contamination, we should mask out the galactic plane. Naively, one would simply calculate the harmonic coefficients by integrating only on the masked sky. This approach, however, suffers from the fact that the spherical harmonic functions are not orthogonal on the masked sky, resulting in calculated $a_{\ell m}$ coefficients that are cross-correlated. We therefore use the covariance inversion method,[6,7,8] where higher-ℓ correlations are used to reconstruct the coefficients on the masked sky. The covariance matrix is built from the power spectrum C_ℓ of ΛCDM, with $\ell > \ell_{\max}$.

Conservatively, we would like to use the full WMAP KQ75 or KQ85 masks. Unfortunately, these masks cover roughly 30% and 20% of the sky, respectively. Such extremely large masks induce significant errors in the calculations of the multipole coefficients and render the parity estimator unreliable. In an attempt to overcome this issue, we would like to define a mask that is as small as possible (and so it can be used to calculate multipole coefficients) but is still efficient in removing local outlying regions and so enables to test large scale physics. We examine the squared temperature map after smoothing it by 20° (see Fig. 2(a)).[a] The most intense areas in the map lie in small patches around the galactic plane. We therefore choose a fixed total

[a]This is motivated by Bennett et al.,[9] where this map of anisotropy power was used to manually define localized regions and check the sensitivity of the alignment of $\ell = 2, 3$ to their removal.

(a) (b)

Figure 2: (a) The squared smoothed ILC map. The prominent regions lie close to the galactic plane, or inside it. (b) Masks that cover the most powerful pixels of the squared, smoothed ILC map. The masks cover 2.5% (*black*), 5% (*red*), 7.5% (*orange*) and 10% (*yellow*) of the sky. The KQ75 galactic mask is also shown (in light gray).

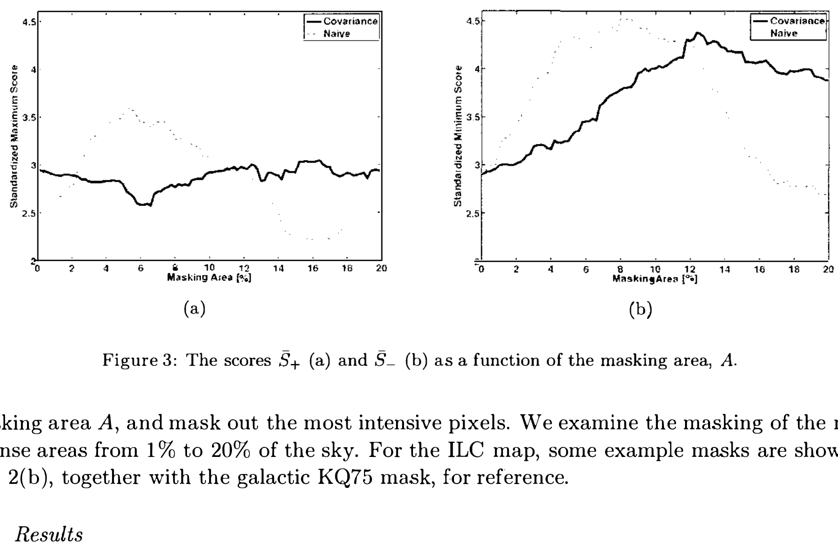

(a) (b)

Figure 3: The scores $\bar{S}_+$ (a) and $\bar{S}_-$ (b) as a function of the masking area, A.

masking area A, and mask out the most intensive pixels. We examine the masking of the most intense areas from 1% to 20% of the sky. For the ILC map, some example masks are shown in Fig. 2(b), together with the galactic KQ75 mask, for reference.

3.2 Results

We can now apply our parity estimator (2) on the masked data, after choosing the masking area A and reconstructing the $a_{\ell m}$ coefficients appropriately. The resulting score map for $A = 12\%$ as an example is shown in Fig. 1(b). Comparing the results to the full sky map (Fig. 1(a)), we can see that the location of the maximum has shifted by almost 40°, to $(l, b) = (198°, 55°)$. It now stands out relative to the other positive peaks, but it does not appear significant. The result for the minimum of the map (which signifies maximal odd parity) is more compelling. Its location has shifted by no more than a few degrees when applying the masks and remains stable under further cuts (including the full KQ85 or KQ75 masks). Furthermore, it now appears much more significant, as we discuss below.

In order to estimate the significance of our findings we normalize the extremal scores for each A and define

$$\bar{S}_{\pm}(A) = \left| \frac{S_{\pm}(A) - \mu(A)}{\sigma(A)} \right| , \tag{3}$$

where $S_{\pm}(A)$ are the maximum and minimum of the score map, and $\mu(A)$ and $\sigma(A)$ are its mean and standard deviation, respectively. These scores, for the ILC map, are plotted in Fig. 3.

The score for the even parity direction (Fig. 3(a)) almost does not change with A. This is not the expected behavior of an anomalous direction. The one for the odd parity direction

(Fig. 3(b)), however, appears as we would expect from an anomalous direction. As we increase A, the score increases, since more and more galactic noise is removed. Eventually, as we keep on increasing A, the reconstruction noise grows and at some point it is bound to dominate and lower $\bar{S}$. We can therefore take the peak score at $A = 12\%$ as an indicator for the underlying strength of the anomaly.

We can now compare these standardized scores to the values of $\bar{S}_{\pm}(A)$ calculated for random simulations. We generate random maps using the 7-year WMAP power spectrum, apply the same masking procedure described above for the ILC, and calculate the score. Indeed, if we compare the typical value for the even direction, $\bar{S}_{+}(A) \sim 3$, to random simulations, 12% get a higher score. In contrast, comparing the peak score for the odd direction to random simulations, the significance is 3.6σ, as 0.03% of 500,000 randoms get a higher score. It is important to note that the odd parity direction remains significant not only for the choice of $\ell_{\max} = 5$, but for 6 and 7 as well. In fact, for $\ell_{\max} = 6$ it reaches as high as 4.3σ. For larger values of $\ell_{\max}$ the significance starts to drop.[b] Finally, to support the possibility of a cosmological origin for our findings, we checked our cut sky estimator directly on the WMAP V and W frequency band maps as well. For these maps we have no choice but to use the entire KQ85 galactic mask instead of the smaller masks discussed above, potentially introducing significant reconstruction errors. Nevertheless, both bands show very similar odd and even parity signals, at the same locations.

4 Conclusions

We have found strong evidence for odd parity in the WMAP data. In addition, there appears to be a parity-even direction that does not appear significant. These results were achieved using a novel masking scheme, that is a compromise between reducing remaining outliers in the low foreground ILC full sky map and avoiding reconstruction noise.

Planck is expected to see better than WMAP though the Galactic noise. Thus the significance of the parity-odd and even directions we found is likely to change. Since we are already reporting at least a 3.6σ effect, if the significance increases further, we believe that this will be a real challenge to ΛCDM, one that calls for either a systematic or cosmological explanation.

Acknowledgments

This work is supported in part by the Israel Science Foundation (grant number 1362/08) and by the European Research Council (grant number 203247).

References

1. A. Ben-David, E. D. Kovetz and N. Itzhaki, Astrophys. J. **748**, 39 (2012)
2. A. de Oliveira-Costa, G. F. Smoot and A. A. Starobinsky, Astrophys. J. **468**, 457 (1996)
3. A. de Oliveira-Costa, M. Tegmark, M. Zaldarriaga and A. Hamilton, Phys. Rev. D **69**, 063516 (2004)
4. K. Land and J. Magueijo, Phys. Rev. Lett. **95**, 071301 (2005)
5. P. Naselsky, M. Hansen and J. Kim, JCAP **1109**, 012 (2011)
6. A. de Oliveira-Costa and M. Tegmark, Phys. Rev. D **74**, 023005 (2006)
7. G. Efstathiou, Y. Z. Ma and D. Hanson, arXiv:0911.5399 [astro-ph.CO]
8. R. Aurich and S. Lustig, Mon. Not. Roy. Astron. Soc. **411**, 124 (2011)
9. C. L. Bennett *et al.*, Astrophys. J. Suppl. **192**, 17 (2011)

[b] While this is a natural result of a pre-inflationary effect, it might also stem from the fact that the errors in the reconstruction method grow quickly with ℓ.[6,7,8]

TESTING ISOTROPY OF LIGHT PROPAGATION WITH CMB POLARIZATION DATA

G. GUBITOSI
CEA, Institut de Physique Théorique, 91191 Gif-sur-Yvette cédex, France

Lorentz symmetry violations are expected to emerge when spacetime is probed on very short distance scales, of the order of the Planck length ($\sim 10^{-35}m$), and can produce anomalous light propagation. CMB photons provide a way to test spacetime on these very small scales thanks to their long propagation time, during which propagation anomalies can accumulate. Here we concentrate on a quite generic model for Lorentz-violating electrodynamics, leading to energy-dependent birefringence, whose amount varies with the propagation direction of radiation if space isotropy is also violated. We present the current constraints on isotropic birefringence and show that data gathered by the PLANCK satellite will reach the sensitivity required to test spacetime symmetries up to the Planck-scale. Moreover, we show that the availability of an almost full-sky coverage can allow to perform also accurate tests on non-isotropic birefringence effects. This report is mainly based on works by the author and collaborators. [1,2,3]

1 Motivations and theoretical framework

One of the main open problems in modern physics is finding a description for phenomena taking place at scales where both gravitational and quantum effects are significant. The characteristic scale of quantum gravity can be heuristically set observing that combining the three main fundamental constants of gravitational and quantum physics, *i.e.* the Newton constant G, the speed of light c and the Planck constant $\hbar$, it is possible to construct another constant with dimensions of a length, the Planck length $L_P \equiv \sqrt{\frac{\hbar G}{c^3}} \sim 10^{-35}m$. Of course invariance of physics under Lorentz transformations is not compatible with the presence of a constant length scale, so its existence leads to question the reliability of Lorentz symmetries in the description of physics at scales where that length is non-negligible.

Among the many approaches to quantum gravity, most of which present indeed violations of Lorentz symmetries, here we are going to concentrate on an effective field theory framework. The effects of physics at the Planck scale on low energy (long wavelength) physics can be described through the addition to the Standard Model Lagrangian of non-renormalizable operators, with coupling constants given by the dimensionally appropriate power of the Planck length. To encode the violation of standard spacetime symmetries these operators will explicitly break Lorentz invariance through a coupling between the standard matter fields and some fixed constant vector.[a]

[a]Note that explicit Lorentz symmetry breaking violates the invariance of physics as seen by different inertial observers, introducing a preferential frame. It is also possible to consider scenarios in which the Poincaré group is deformed[4], so that the equivalence between inertial observers is preserved, but the laws of transformation between different reference frames are modified.

Modifications of the electrodynamics Lagrangian can in particular affect propagation of light, and can in principle be constrained through observations of CMB radiation. In fact, even if CMB radiation is characterized by quite a long wavelength with respect to the Planck length, it has been propagating for very long times, so that it is potentially subject to a large accumulation of new physics effects affecting photons propagation.

To the lowest order in the Planck length, it was shown a few years ago [5] that the most generic electrodynamics Lagrangian is of the form:

$$\mathcal{L}_{QG} = -\frac{1}{4}F_{\mu\nu}F^{\mu\nu} + \frac{1}{2}L_P n^\alpha F_{\alpha\delta} n^\sigma \partial_\sigma (n_\beta \varepsilon^{\beta\delta\gamma\lambda} F_{\gamma\lambda}) \ , \tag{1}$$

where n^α is the symmetry-breaking four-vector and the coupling constant between the electromagnetic field and the vector is given by the Planck length, so setting the appearance of new physics at that scale, if $n^\alpha \sim 1$.

It can be shown [2] that this Lagrangian leads to a modified photon dispersion relation, producing a birefringent behavior during propagation, whose amount can also depend on the propagation direction if the symmetry-breaking vector has a non-zero spatial component.

As a consequence, the linear polarization direction of CMB radiation would rotate during propagation, with rotation angle given by [3]:

$$\alpha(\theta, \phi) = L_P |\vec{p}|^2 \left(n_0 - |\vec{n}| \left(\sin\theta \sin\theta_n \cos(\phi - \phi_n) + \cos\theta \cos\theta_n\right)\right)^3 t. \tag{2}$$

Here θ and ϕ indicate the observation direction of CMB radiation ($\{\theta_n, \phi_n\}$ is the direction pointed out by the spatial part of n^α), n_0 and $\vec{n}$ refer respectively to the time and space components of the symmetry-breaking vector. Note that the amount of rotation increases linearly with propagation time, t, and quadratically with the photons energy p.

At each point in the sky, the polarization rotation produces a mixing between the Stokes parameters of CMB radiation, whose amount, for each given $\vec{n}$, depends on the observation direction and at the first order in the rotation angle α is:

$$\begin{aligned} Q'(\theta, \phi) &= Q(\theta, \phi) + 2\alpha(\theta, \phi) U(\theta, \phi) \\ U'(\theta, \phi) &= U(\theta, \phi) - 2\alpha(\theta, \phi) Q(\theta, \phi) \end{aligned} \tag{3}$$

If n^α has only the time component different from zero, then the polarization rotation angle is constant,

$$\alpha = \alpha_0 = L_P |\vec{p}|^2 n_0^3 t, \tag{4}$$

and the cross-correlation power spectra of CMB polarization are also mixed in a peculiar way [1]. At linear order in α_0 the only modified spectra are:

$$\begin{aligned} (C_\ell^{EB})' &= -2\alpha_0 \left(C_\ell^{BB} - C_\ell^{EE}\right) \\ (C_\ell^{TB})' &= 2\alpha_0 C_\ell^{TE} \end{aligned} \tag{5}$$

If, on the other hand, n^μ has zero time component, then the full-sky cross correlation spectra won't change.[3] An intuitive way to understand why this happens is to realize that, for n^μ purely space-like, the rotation angle α of eq. 2 takes opposite signs in opposite directions in the sky. Essentially, the modifications to the power spectra coming from one hemisphere of the sky compensate the modifications, of opposite sign, coming from the other hemisphere, and full-sky spectra are not affected by the polarization rotation. In the following we will concentrate on these two extremal cases of $\vec{n} = 0$ and $n_0 = 0$, showing how in both cases it is possible to constrain the model. Intermediate cases will need to use a mix of the two techniques we are going to describe, but this is quite straightforward.

2 Spatially isotropic birefringence

Constraints on isotropic birefringence using CMB data have been the topic of already quite a wide literature [6], even if only a few papers [1,7], by the present author and collaborators, focused on the specific model described above, whose peculiarity is a quadratic energy dependence of the birefringent effect. So here we will only recall very briefly the method used to analyze the data and the results obtained, to focus more on the most innovative part of the work we want to present, which is the non-isotropic case.

Using the relations 5, we can perform a standard best-fit analysis on CMB power spectra, adding n_0 to the standard set of cosmological parameters to be estimated. It's necessary to jointly estimate all the parameters, since the energy redshift due to the Universe expansion makes α (eq. 4) dependent on the cosmological model. Note also that, because of the energy dependence of α, we have to be careful when combining results from different experiments sensitive to different frequencies of CMB radiation. It does not make sense to give joint constraints on the rotation angle α, while the correct parameter to use in joint constraints is n_0.

Analyzing BOOMERang and WMAP5 data, we get [1,7], respectively, $n_0^3 = -0.09 \pm 0.12$ and $n_0^3 = -0.123 \pm 0.096$ with one-sigma errors, corresponding to a rotation angle of, respectively, $\alpha_0 = -1.6 \pm 2.1$ and $\alpha_0 = -5.2 \pm 4.0$. The joint constraint on the time component of the symmetry-breaking vector is $n_0^3 = -0.110 \pm 0.075$. As explained in the previous section, being able to probe n_0 at less than order one level means that we are able to probe physics at the Planck scale. Exploiting the availability of multi-channel data coming from the PLANCK experiment, it will be possible to improve the constraint of two orders of magnitude [1,7], up to $\sigma(n_0^3) = 8.5 \cdot 10^{-4}$.

The model of this section was also tested in several astrophysical contexts, leading to very stringent constraints [8]. But these bounds exploit significantly the spatial isotropy regained by the *ad hoc* choice of having a purely timelike symmetry-violating four-vector. This assumption can be limiting in two ways. Constraints on one single component of a four vector derived in different reference frames (like the rest frame of two different astrophysical sources) cannot be compared without any information on the other components of the four-vector. Moreover [2] the limits placed assuming the four-vector to be purely timelike and using one single point-source do not give reliable information on the most general case in which the four-vector has all the components different from zero, since in that case there can be significantly big regions of the sky where we would expect to see no effect. In the case of point-like astrophysical sources one would need to do some statistical analysis of the information coming from many sources (which is not presently available) and combine it with the information on the state of motion of these sources with respect to some fixed reference frame, like the one of CMB, which is also very difficult to obtain. This should make clear why it is very useful to rely on CMB analysis (which gives an almost full-sky information) when trying to constrain non-isotropic Lorentz breaking models like the one we are dealing with here. In the following section we show how to put constraints in the case of purely spacelike symmetry breaking vector.

3 Non-isotropic birefringence

The most relevant characteristic of the model described in this section is that anomalous light behavior depends on its propagation direction with respect to a preferred direction codified within the spatial part $\vec{n}$ of the symmetry-breaking vector n^α.

In this case, as was explained in the first section of this paper, the peculiar space-dependence of the birefringence effect, which from eq. 2 we write as:

$$\begin{aligned} \alpha(\theta,\phi) &= \alpha_{max}\left(\sin\theta\sin\theta_n\cos(\phi-\phi_n)+\cos\theta\cos\theta_n\right)^3 \qquad (6) \\ \alpha_{max} &= -L_P|\vec{p}|^2|\vec{n}|^3 t, \end{aligned}$$

is such that the polarization rotation can not be detected exploiting the standard tool of full-sky cross-correlation power spectra, which instead was shown to be valuable for constraining the isotropic rotation effect studied in the previous section.

A crucial observation to overcome this problem is that the rotation angle (2) is a slowly varying function of θ and ϕ in a neighborhood of θ_n and ϕ_n. So if we consider a small circular region of the sky centered at $\{\theta_n, \phi_n\}$, there we can approximate the rotation as constant, and the power spectra estimated on the region are rotated according to Eqs. 5 by an angle $\alpha_0 = A \times \alpha_{max}$, where A is given by the average of the function $(\sin\theta \sin\theta_n \cos(\phi - \phi_n) + \cos\theta \cos\theta_n)^3$ over the region.

So our method consists in generating a set of 1000 masks, to select, out of a CMB map, disks of angular radius 20° and centers $\{\theta_c, \phi_c\}$ distributed randomly in one half of the sky ($\theta_c \in [0°, 90°]$, $\phi_c \in [0°, 360°]$). In correspondence of each of these disks there is another one centered in the opposite direction. In this way we cover the entire available sky allowing for a certain degree of superposition among the disks. Then we can test the hypothesis that a disk is centered in the direction of maximum rotation. For this purpose we estimate the polarized power spectra out of each of them. [3] Then for each couple of opposite disks we perform a best-fit analysis on the reduced power spectra in a similar way as described in the previous section for the full-sky case. We just have to take into account the fact that opposite disks will se the same rotation effect, but for a flip of sign.

We end up with an estimate of α_0 for each region and we project these values onto a sky map. Our estimate of α_{max} is the maximum value found on this α_0 map, rescaled by the correction factor A. The uncertainties on α_{max} can be assessed via Monte Carlo simulations. From the estimate on α_{max} it is straightforward to deduce the constraints on $\vec{n}$.

To derive an estimate of the direction of the symmetry breaking vector, $\{\bar{\theta}_n, \bar{\phi}_n\}$, and the confidence intervals associated to it, we take the direction of the maximum value of the α_0 map as the best-fit of $\{\theta_n, \phi_n\}$ and we derive the uncertainty on this estimate by slicing the function $\alpha_0(\theta, \phi)$ in correspondence of the 1 and 2σ errors on α_0.

With this method it is possible [3] to analyze data coming from the *Planck* satellite and constrain anomalous non-isotropic light propagation with a sensitivity of 0.2 degrees on α_{max} and also identify the special direction pointed by the symmetry breaking vector with an uncertainty of roughly 40 degrees on the θ angle and 60 degrees on the ϕ angle.

References

1. G. Gubitosi, L. Pagano, G. Amelino-Camelia, A. Melchiorri and A. Cooray, JCAP **0908** (2009) 021 [arXiv:0904.3201 [astro-ph.CO]].
2. G. Gubitosi, G. Genovese, G. Amelino-Camelia and A. Melchiorri, Phys. Rev. D **82** (2010) 024013 [arXiv:1003.0878 [gr-qc]].
3. G. Gubitosi, M. Migliaccio, L. Pagano, G. Amelino-Camelia, A. Melchiorri, P. Natoli and G. Polenta, JCAP **1111** (2011) 003 [arXiv:1106.6049 [astro-ph.CO]].
4. G. Amelino-Camelia, arXiv:0806.0339 [gr-qc].
5. R. C. Myers and M. Pospelov, Phys. Rev. Lett. **90** (2003) 211601 [hep-ph/0301124].
6. See, for example, the following papers and references therein:
   B. Feng, M. Li, J. Q. Xia, X. Chen and X. Zhang, Phys. Rev. Lett. **96** (2006) 221302 [arXiv:astro-ph/0601095], E. Komatsu *et al.* [WMAP Collaboration], Astrophys. J. Suppl. **192** (2011) 18 [arXiv:1001.4538 [astro-ph.CO]].
7. L. Pagano, P. de Bernardis, G. De Troia, G. Gubitosi, S. Masi, A. Melchiorri, P. Natoli and F. Piacentini *et al.*, Phys. Rev. D **80** (2009) 043522 [arXiv:0905.1651 [astro-ph.CO]].
8. The most recent work is P. Laurent, D. Gotz, P. Binetruy, S. Covino and A. Fernandez-Soto, arXiv:1106.1068 [astro-ph.HE].

MEASURING THE FEATURES IN THE PRIMORDIAL POWER SPECTRUM

Zhiqi Huang
CEA, Institut de Physique Théorique, 91191 Gif-sur-Yvette cédex, France
CNRS, URA 2306, F-91191 Gif-sur-Yvette, France

Using a MCMC analysis, we compare the power of the CMB with that of the combination of CMB and galaxy survey data, to constrain the primordial power spectrum. The analysis is based on the Planck satellite and a spectroscopic redshift survey with configuration parameters close to those of the Euclid mission as examples. We found that the inclusion of large scale structure (LSS) data is crucial for measuring sharp features in the power spectrum, as CMB only measures a projected 2D angular power spectrum where sharp features are suppressed. We also used the current CMB data (WMAP + ACT) to study the axion monodromy model, which predicts cosine oscillations in the power spectrum. In contrast to the recent studies by Aich *et al* and Meerburg *et al*, we found no detection or hint of the oscillations. We pointed out that the CAMB code modified by Aich *et al* does not have sufficient numerical accuracy.

1 Introduction

Inflation [1,2,3] is a successful paradigm to explain the observed CMB anisotropies [4]. Single-field inflation models predict a slightly titled primordial (scalar) power spectrum of the metric fluctuations, which is consistent with the current CMB and large scale structure data [4,5]. However, this prediction only relies on the flatness of the potential $V(\phi)$. Thus, it is difficult to learn about the underlying physics of this class of model. On the other hand, local signatures in the power spectrum can arise from models that are less "natural", for instance, a inflation potential with sharp features [6], a transition between different stages in the inflation evolution [7,8], multiple-field models [9,10], particle production during inflation [11,12], modulated preheating [13], and models motivated by monodromy in the extra dimensions [14,15]. These features represent an important window on new physics because they are often related to UV scale phenomena inaccessible in the lab.

The angular power spectrum of CMB anisotropies is a projected 2D spectrum. Sharp features are expected to be suppressed due to the projection from the 3D power spectrum into 2D. The power of constraining the features hence degrades as sharper features are considered. In the case of large scale structure survey where redshift information is available, for instance, a spectroscopic redshift survey, the 3D power spectrum is directly measured, although complication arises due to redshift distortion [16] and the redshift-dependence of the bias. In this work we compare the two probes by taking the Planck satellite mission [17] and a spectroscopic redshift survey with configuration parameters close to those of the Euclid mission [18,19] as examples. For the specification of these experiments and the description of the likelihood, the reader is referred to our recent work [20]. We perform a Markov Chain Monte Carlo (MCMC) analysis, which does not rely on the assumption that the likelihood is approximately Gaussian, which should not be taken for granted for models with sharp features in the spectrum.

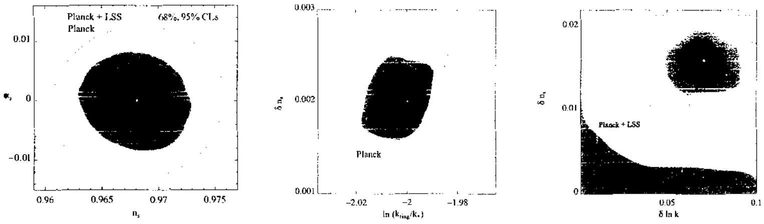

Figure 1: Marginalized posterior contours with 68.3% and 95.4% confidence levels.

Recently "hints" (significant improvement of χ^2-fit) of cosine oscillations in the primordial power spectrum $\mathcal{P}(k)$, the prediction of the axion monodromy model[14], were found by Aich *et al*[21] and Meerburg *et al*[22]. However, caution should be taken when computing the CMB angular power spectrum C_ℓ for models with sharp features in $\mathcal{P}(k)$. The C_ℓ's should be computed in an ℓ-by-ℓ way, instead of using the interpolation method that implicitly assumes the smoothness in $\mathcal{P}(k)$. Moreover, the stepsize in k should be adaptively changed when performing the numerical integration, depending on the width of the feature and the mutipole ℓ. Using a new CMB code that is optimized for this task [23], we found that the C_ℓ spectrum computed in Aich *et al* is inaccurate.

2 The CMB and LSS Forecast

2.1 Smooth $\mathcal{P}(k)$

For a smooth power spectrum we expand $\ln \mathcal{P}(k)$ around the pivot scale $k_* = 0.05\,\mathrm{Mpc}^{-1}$ as a quadratic function of $\ln k$. The spectral index and the running of the spectral index are defined at the pivot as $n_s \equiv 1 + d\ln\mathcal{P}(k)/d\ln k$ and $\alpha_s = dn_s/d\ln k$, respectively. To produce the mock data we take a fiducial quadratic inflation potential $V = \frac{1}{2}m^2\phi^2$, which predicts $n_s \approx 0.968$ and $\alpha_s \approx 0.00$. The forecasted constraints n_s and α_s are shown in the first panel of Fig. 1, from which we conclude that future LSS data can only mildly improve the CMB constraint.

2.2 Starobinsky Potential

As an example of model of inflation predicting a feature in the power spectrum we consider the model first presented by Starobinsky in [6], which is defined as

$$M_p\frac{dV}{d\phi} = \begin{cases} V_{1,-} & \text{if } \phi < \phi_\pm \ , \\ V_{1,+} & \text{if } \phi > \phi_\pm \ , \end{cases} \tag{1}$$

where $V_{1,-}$ and $V_{1,+}$ are constants, and M_p the reduced Planck Mass. We construct the following parameters from $V_{1,-}$, $V_{1,+}$ and $\phi_\pm$ and $V_* \equiv V|_{\mathrm{aH=k_*}}$,

$$A_s \equiv \frac{V_*^3}{6\pi^2 M_p^4(V_{1,-}^2 + V_{1,+}^2)} \ , \ n_s \equiv 1 - \frac{3}{2}\left[\left(\frac{V_{1,-}}{V_*}\right)^2 + \left(\frac{V_m 1,+}{V_*}\right)^2\right], \tag{2}$$

which approximate the average of the amplitude and spectral index of the spectrum, respectively, and

$$\delta n_s \equiv \frac{3}{2}\left[\left(\frac{V_{1,-}}{V_*}\right)^2 - \left(\frac{V_{1,+}}{V_*}\right)^2\right] \ , \ \ln(k_{\mathrm{ring}}/k_*) \equiv \phi_\pm\sqrt{\frac{3}{1-\tilde{n}_s}}, \tag{3}$$

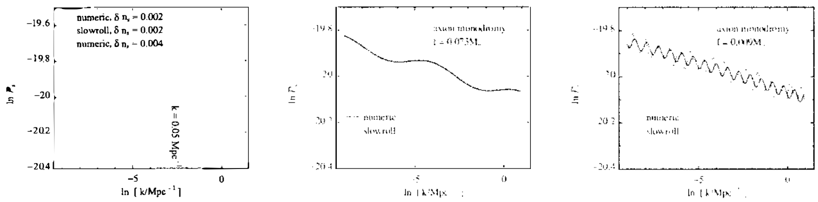

Figure 2: Primordial power spectrum for different models.

which parameterize the variation of the spectral index and the position where the feature is produced. As an example, in the left panel of Fig. 2 we show the scalar power spectrum calculated by numerically solving the evolution equations for scalar perturbations. The solid red line corresponds to the case $\ln \tilde{A}_s = 3.02$, $\tilde{n}_s = 0.975$, $\delta n_s = 0.002$ and $\ln(k_{\rm ring}/k_*) = -2$, which will be studied below. The slow-roll approximation [24] is also shown for comparison and as a check of the numerical accuracy. To see the effect of varying δn_s on the power spectrum, in the same plot we also show the case for $\delta n_s = 0.004$ in cyan.

The constraint on δn_s and $\ln(k_{\rm ring}/k_*)$ are shown in the middle panel of Fig. 1. Again the inclusion of LSS data does not improve the constraint by much, because the width of the feature in this model is large – typically of $O(1)$ [20].

2.3 Axion Monodromy Model

For the axion monodromy model the inflation potential is[25],

$$V(\phi) = \mu^3 \left[\phi + bf \cos\left(\frac{\phi + \phi_f}{f}\right)\right] , \tag{4}$$

where μ parameterizes the scale of inflation, b is a small parameter, f is a typically sub-Planckian scale, and ϕ_f is a phase parameter which need to be marginalized over. We use ϕ_* to denote the value of the field when the pivot scale exits the Hubble radius, which for 60 e-folds of inflation is $\phi_* \approx 11 M_p$

We parameterize the primordial power spectrum using the analytical approximation [25],

$$\mathcal{P}(k) = A_s \left(\frac{k}{k_*}\right)^{n_s - 1} \left[1 + \delta n_s \cos\left(\frac{\ln k}{\delta \ln k} + \varphi\right)\right] , \tag{5}$$

where A_s, δn_s, $\delta \ln k$, and φ can be related to μ, f and b, and ϕ_f [20,25].

Examples of $\mathcal{P}(k)$ for different choices of f and b are shown in the middle and right panels in Fig. 2. For models with $\delta \ln k >\sim 0.1$, we again found no significant improvement upon the constraint due to the inclusion of LSS data. However, when we use a fiducial $\delta \ln k = 0.01$, we found significant improvement as shown in the right panel of Fig. 1. This is because such sharp features are almost completely smeared out due to the projection from the 3D spectrum $\mathcal{P}(k)$ to the 2D CMB angular power spectrum C_ℓ.

3 Hints of Axion Monodromy in Current Data?

In Aich *et al*[21] the authors used their modified CAMB to compute the CMB power spectrum. Such a modification is not trivial for small $\delta \ln k$. Since the best-fit $\delta \ln k$ they found is tiny – $\delta \ln k \approx 0.005$, it is necessary to exam the numerical accuracy. For $\delta \ln k \approx 0.005$, the modulation period in $\ln k$ is $T_{\ln k} = 2\pi\delta \ln k \approx 0.03$. In the CMB power spectrum one should see same

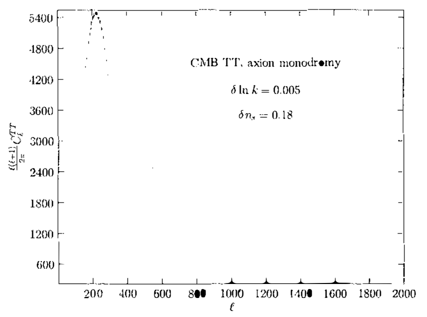

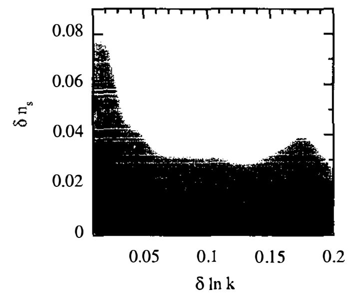

Figure 3: Left Panel: the CMB power spectrum for the best-fit model in Aich et al. Right Panel: The marginalized 68.3% and 95.4% confidence level contours of δn_s and $\delta \ln k$ for axion monodromy model.

modulation period in $\ln \ell$, i.e., $T_{\ln \ell} = T_{\ln k} \approx 0.03$. However, in Figure 5 of Aich *et al* the "oscillations" in C_ℓ seems to be random, which might just be numerical noise. In the left panel of Fig. 3 we show the CMB temperature angular power spectrum computed using our CMB code [23], where the parameters are chosen to be close to the ones used in Figure 5 of Aich *et al.* Qualitative difference can be seen between the two figures. In the left panel of Fig. 3 the C_ℓ spectrum presents clear modulations that agrees with the $\delta \ln k$ value, while the modified CAMB used in Aich *et al* failed to produce the expected modulations.

We present the marginalized 68.3% and 95.4% confidence-level posterior contours in the right panel of Figure 3. WMAP-7yr and ACT data are used. CMB angular power spectrum are computed up to $\ell = 4000$ with CMB lensing effect included. We used uniform priors $0.003 \leq \delta \ln k \leq 0.2$ and $0 \leq n_s \leq 0.2$. No detection of axion monodromy oscillations are found since zero amplitude of oscillations ($\delta n_s = 0$) is consistent with the data.

4 Conclusion

While interesting physics can manifests itself in the form of glitches in the primordial power spectrum, we found that future LSS survey can significantly improve the constraint on these models – if the predicted features are sharp $\delta \ln k <\sim 0.01$.

Using our CMB code [23] that optimized for computing the CMB power spectrum for models with sharp features in $\mathcal{P}(k)$, we found that the recently claimed "hint" of axion monodromy in current WMAP and ACT data is erroneous. The error is due to insufficient accuracy in their modified CAMB code.

Acknowledgment

I thank Filippo Vernizzi and Licia Verde, as some results presented in this proceeding are taken from my paper with them [20]. I would also like to thank Xingang Chen, Cyril Pitrou, Julien Lesgourgues and Emiliano Sefusatti for useful advice and discussions.

1. A. H. Guth. Inflationary universe: A possible solution to the horizon and flatness problems. *Phys. Rev. D*, 23:347–356, January 1981.
2. A. H. Guth and S.-Y. Pi. Fluctuations in the new inflationary universe. *Physical Review Letters*, 49:1110–1113, October 1982.
3. A. A. Starobinsky. Dynamics of phase transition in the new inflationary universe scenario and generation of perturbations. *Physics Letters B*, 117:175–178, November 1982.

4. E. Komatsu, K. M. Smith, J. Dunkley, C. L. Bennett, B. Gold, G. Hinshaw, N. Jarosik, D. Larson, M. R. Nolta, L. Page, D. N. Spergel, M. Halpern, R. S. Hill, A. Kogut, M. Limon, S. S. Meyer, N. Odegard, G. S. Tucker, J. L. Weiland, E. Wollack, and E. L. Wright. Seven-year Wilkinson Microwave Anisotropy Probe (WMAP) Observations: Cosmological Interpretation. *Astrophys. J., Suppl.*, 192:18–+, February 2011.
5. A. G. Sanchez, C. G. Scoccola, A. J. Ross, W. Percival, M. Manera, F. Montesano, X. Mazzalay, A. J. Cuesta, D. J. Eisenstein, E. Kazin, C. K. McBride, K. Mehta, A. D. Montero-Dorta, N. Padmanabhan, F. Prada, J. A. Rubino-Martin, R. Tojeiro, X. Xu, M. Vargas Magana, E. Aubourg, N. A. Bahcall, S. Bailey, D. Bizyaev, A. S. Bolton, H. Brewington, J. Brinkmann, J. R. Brownstein, J. R. Gott, III, J. C. Hamilton, S. Ho, K. Honscheid, A. Labatie, E. Malanushenko, V. Malanushenko, C. Maraston, D. Muna, R. C. Nichol, D. Oravetz, K. Pan, N. P. Ross, N. A. Roe, B. A. Reid, D. J. Schlegel, A. Shelden, D. P. Schneider, A. Simmons, R. Skibba, S. Snedden, D. Thomas, J. Tinker, D. A. Wake, B. A. Weaver, D. H. Weinberg, M. White, I. Zehavi, and G. Zhao. The clustering of galaxies in the SDSS-III Baryon Oscillation Spectroscopic Survey: cosmological implications of the large-scale two-point correlation function. *ArXiv e-prints*, March 2012.
6. A. A. Starobinsky. Spectrum of adiabatic perturbations in the universe in the presence of singularities in the inflation potential. *Pis ma Zhurnal Eksperimental noi i Teoreticheskoi Fiziki*, 55:477–482, May 1992.
7. C. R. Contaldi, M. Peloso, L. Kofman, and A. Linde. Suppressing the lower multipoles in the CMB anisotropies. *Journal of Cosmology and Astro-Particle Physics*, 7:2, July 2003.
8. J. M. Cline, P. Crotty, and J. Lesgourgues. Does the small CMB quadrupole moment suggest new physics? *Journal of Cosmology and Astro-Particle Physics*, 9:10–+, September 2003.
9. D. Polarski and A. A. Starobinsky. Spectra of perturbations produced by double inflation with an intermediate matter-dominated stage. *Nuclear Physics B*, 385:623–650, October 1992.
10. D. Langlois and F. Vernizzi. From heaviness to lightness during inflation. *Journal of Cosmology and Astro-Particle Physics*, 1:2, January 2005.
11. N. Barnaby, Z. Huang, L. Kofman, and D. Pogosyan. Cosmological fluctuations from infrared cascading during inflation. *Phys. Rev. D*, 80:043501–+, August 2009.
12. Neil Barnaby and Zhiqi Huang. Particle production during inflation: Observational constraints and signatures. *Phys. Rev. D*, 80:126018, Dec 2009.
13. J. R. Bond, A. V. Frolov, Z. Huang, and L. Kofman. Non-Gaussian Curvature Spikes from Chaotic Billiards in Inflation Preheating. *Physical Review Letters*, 103:071301–+, August 2009.
14. E. Silverstein and A. Westphal. Monodromy in the CMB: Gravity waves and string inflation. *Phys. Rev. D*, 78:106003–+, November 2008.
15. R. Bean, X. Chen, G. Hailu, S.-H. H. Tye, and J. Xu. Duality cascade in brane inflation. *Journal of Cosmology and Astro-Particle Physics*, 3:26–+, March 2008.
16. N. Kaiser. Clustering in real space and in redshift space. *Mon. Not. R. Astron. Soc.*, 227:1–21, July 1987.
17. Planck Science Team. *Planck: The Scientific Programme (Blue Book). ESA-SCI (2005)-1. Version 2*. European Space Agency., 2009.
18. R. Laureijs. Euclid Assessment Study Report for the ESA Cosmic Visions. *ArXiv e-prints*, December 2009.
19. R. Laureijs, J. Amiaux, S. Arduini, J. . Augueres, J. Brinchmann, R. Cole, M. Cropper, C. Dabin, L. Duvet, A. Ealet, and et al. Euclid Definition Study Report. *ArXiv e-prints*, October 2011.
20. Z. Huang, L. Verde, and F. Vernizzi. Constraining inflation with future galaxy redshift

survcys. *Journal of Cosmology and Astro-Particle Physics*, 4:5, April 2012.
21. M. Aich, D. K. Hazra, L. Sriramkumar, and T. Souradeep. Oscillations in the inflaton potential: Exact numerical analysis and comparison with the recent and forthcoming CMB datasets. *ArXiv e-prints*, June 2011.
22. P. D. Meerburg, R. A. M. J. Wijers, and J. P. van der Schaar. WMAP7 constraints on oscillations in the primordial power spectrum. *Mon. Not. R. Astron. Soc.*, page 2297, January 2012.
23. Z. Huang. A Cosmology Forecast Toolkit – CosmoLib. *ArXiv e-prints*, January 2012.
24. E. D. Stewart and D. H. Lyth. A more accurate analytic calculation of the spectrum of cosmological perturbations produced during inflation. *Physics Letters B*, 302:171–175, March 1993.
25. R. Flauger, L. McAllister, E. Pajer, A. Westphal, and G. Xu. Oscillations in the CMB from axion monodromy inflation. *Journal of Cosmology and Astro-Particle Physics*, 6:9–+, June 2010.

THE IMPRINT OF SUPERSTRUCTURES ON THE COSMIC MICROWAVE BACKGROUND

Stéphane Ilić, Mathieu Langer, Marian Douspis
Université Paris-Sud, Institut d'Astrophysique Spatiale, UMR8617, Orsay, F-91405 & CNRS, Orsay, F-91405

We present here an analysis of the integrated Sachs-Wolfe effect produced by large scale structures in the Universe, focusing on supervoids. We study the results of a previous work by Granett et al.[1] (2008), known to be at odds with Λ-CDM predictions. We perform statistical tests on these results and compute our own theoretical predictions obtained with the use of the LTB metric of General Relativity. We are able to reproduce the observed structures and compute their expected ISW effect. We also find discrepancies between the expected and reported value of the effect, although we argue that these are most likely not sufficient to completely discard the Λ-CDM model.

1 Introduction

More than a decade after its discovery, the nature of the Dark Energy (DE) still eludes us. Among its several probes, the integrated Sachs-Wolfe (ISW) effect represents in principle a robust and independent test of its existence and properties. The ISW effect is the impact of large-scale structures on Cosmic Microwave Background (CMB) photons through gravitationnal effects. In a DE-dominated universe, gravitationnal potentials are stretched by the accelerated expansion : CMB photons that fall into these structures then climb out of shallower potentials and therefore carry more energy when they exit the potentials. The effect is reversed when the photons cross underdense regions in the Universe.

This ISW effect shows in the power spectrum of the CMB temperature anisotropies at large angular scales but its small amplitude and the cosmic variance at those multipoles make its direct measurement very challenging, if not impossible, when using only the CMB itself. To circumvent this limitation, we usually exploit the link between this imprint on the CMB and the large-scale structures causing the ISW effect, by cross-correlating the CMB with matter density maps (galaxy surveys in practice) and then comparing the results to a null hypothesis and to what is expected from theory.

During the last decade or so, a growing interest has risen in this field thanks to the development of galaxy surveys in many wavelengths. However, this method has yet to produce a definitive and conclusive detection of the ISW effect from current surveys, with significances ranging so far from negligible up to more than 4σ, and with sometimes conflicting results throughout the literature while being based on the very same data (see e.g. the meta-analysis of Dupé et al.[2]). Although future large scale surveys (Euclid, Pan-STARRS, etc.) will improve these studies, some possible alternatives for galaxy surveys were also recently explored (eg. the Cosmic Infrared Background [3]) with promising results.

In this short report of our work presented in Ilić et al.[4] (2012), we consider an alternative method for the study of the ISW effect, namely the effect of single superstructures on the CMB temperature. First we investigate the results of a previous study on this subject by Granett et al., 2008 [1](G08), focusing here on the supervoids they identified in the Sloan Digital Sky Survey (SDSS). We confront their results to our expectations about the ISW effect through several consistency checks. We then proceed to develop a method to reproduce these structures, and fully compute the expected ISW effect from these objects.

2 Voids in the SDSS data

G08 identified hundreds of clusters and voids using a sample of 1.1 million Luminous Red Galaxies (LRGs) from the SDSS data, covering 7500 square degrees about the North Galactic pole, and spanning a redshift $0.4 < z < 0.75$. These LRGs are thought to be good tracers of the cosmic matter distribution on scales greater than 10 Mpc ; nevertheless, one must bear in mind that only the brightest –therefore rarest– of these galaxies are observed at those redshifts, therefore inducing a sparsity in their spatial distribution, which might in return bias the detection of structures, especially voids (see e.g. P. Sutter, in these proceedings).

From their preliminary search, G08 then selected the 50 most significant supervoids and 50 superclusters, and subsequently cut and stacked patches of the CMB (from WMAP5) at the positions of these structures. They measured this way a 4σ temperature deviation in the full stacked CMB image with an amplitude of 9.6μK ($+7.9\mu$K for clusters, -11.3μK for voids), independent of the considered fequencies (the Q,V and W band of WMAP). They conclude that the most likely explanation for this observation is a detection of the ISW effect.

On the other hand, considering the characteristics of the G08 structures, the Λ-CDM model predicts a lower expected value for the temperature deviation due to the ISW effect – whether it comes from perturbation theory [5] (1-2 μK) or from large cosmological simulations such as Millenium [6] (4.2 μK). In the following section, we take a closer look on the G08 results to find clues about their reported disagreement with theory.

3 Exploring the catalogue

Let us recall a few general intuitions about the ISW effect and its characteristics :

- supposedly, the larger a structure (void or cluster), the bigger its expected imprint on the CMB temperature, since the photon travel time within it is longer, thus undergoing a stronger ISW effect
- similarly, the strucutres that are the closest to us (therefore the most recent) are supposed to contribute the most to the ISW effect, their evolution being more DE-dominated.

Unfortunately, checking the aforementionned statements for each void of G08 is impossible due to the dominant background noise – the CMB itself. As a workaround we adopt an approach similar to "Jacknife" methods : We construct ten of thousands sets of n randomly selected voids among the 50 of the sample, and compute each time the mean redshift, mean radius, and associated stacked ISW flux.

The results (for $n = 10$ void sets) of this tests are shown on Fig. 1. Contrary to our expectations, here the amplitude of the ISW effect does not show any correlation neither to the radius nor the redshift of the observed structures. Moreover, a non-negligible part of the created voids sets produces a positive ISW effect, contrary to our expectations. On the other hand, some of the sets produce a strong negative effect as low as $\sim -30\mu$K, accounting for most of the final observed signal – an issue briefly noticed in G08. This raises different kinds of interrogations, first regarding the data itself which might contain some unseen systematics biasing the observations. There might also be some fortuitous peculiarity in the data, such as compensations between redshift and radius effects which could account for these results. Finally, our first assumptions about the ISW effect may be too naive and require a deeper and more

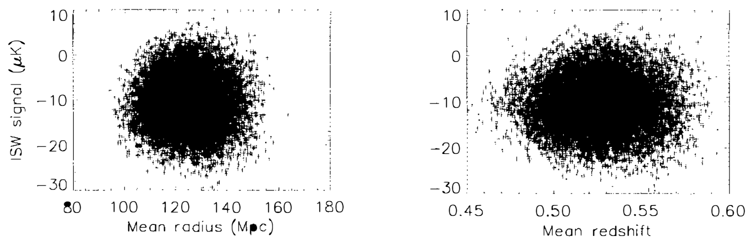

Figure 1: ISW signal for random sets of 10 voids from G08 sample, as a function of mean radius (*left pannel*) and mean redshift (*right pannel*) of the sets.

rigorous understanding of its workings. We address the last question in the next section, where we develop a way to compute the exact ISW effect generated by structures with characteristics similar to those of G08.

4 Modelling voids

As a first step towards this, we have to be able to compute the full exact evolution of an over/underdensity, from some early time (e.g. $z = 1100$) until now ($z = 0$). One of the simplest ways to precisely achieve this task is to use the most generic metric of General Relativity (GR) with spherical symmetry and pressureless dust, the Lemaître-Tolman-Bondi (LTB) metric :

$$ds^2 = dt^2 - \frac{R_{,r}{}^2}{1+2E(r)}dr^2 - R(r,t)^2 d\Omega^2$$

We therefore restrict ourselves to the modelling of spherical structures. This metric has two free functions, $M(r)$ and $E(r)$, which are the analogs to a mass profile and a curvature profile respectively. In order to determine them, we start from an initial density profile and assume that the considered structures are compensated, and that they connect smoothly with an FLRW background ; these conditions are sufficient to compute the full history of the perturbation and all its relevant functions. Once these are calculated, we use the geodesic equations of GR to compute the path of a photon travelling through the perturbation, while keeping track of its energy. We then compare it to the path of a photon evolving simultaneously in the FLRW background ; the relative difference in energy between these two photons gives us an estimate of the ISW effect generated by the structure.

Using this framework, we first made an exploration of our parameter space, fixing the cosmology to Λ-CDM ; we tested many different realistic density profiles, playing with the initial density contrast at the center of the void (from about $\delta = -0.001$ to -0.01) and its initial radius. We also chose the mean redshift of the G08 voids as the time of crossing of the photon. By doing so, we got an overview of the ISW levels that are realistically attainable. We could observe that the amplitudes reported (-11.3μK) are plausible, as they sit well within our calculated range that extend from about -0.1 to -100μK, depending on the initial conditions.

In the next step, we were able to repoduce all of voids used by G08, with the same properties (radius, depth, etc.) at their redshift of observation. Using radial photons, we then calculated the theoretical ISW effect associated with them. The results of this study are shown in Fig. 2. We first notice that the predicted mean ISW effect (red dashed line), which is a good estimate of the stacked ISW effect, is again weaker (around -3μK) than the reported value of G08 (-11.3μK) ; this agrees with the trend observed in other theoretical results in the literature[5 6].

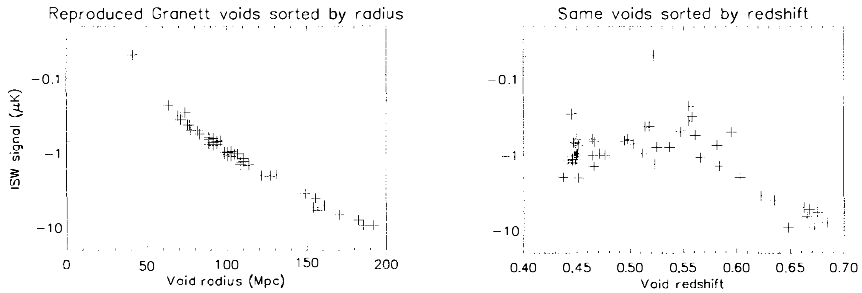

Figure 2: ISW signal associated with the 50 reproduced voids from G08 sample as a function of their radius (*left pannel*) and redshift (*right pannel*). The red dashed line marks the mean ISW temperature of all these voids.

We also find a clear correlation between the void sizes and their associated ISW amplitude, as expected from our initial idea about the behaviour of the ISW effect. We note that a few (around 10, below the mean value) voids contribute for the most important part of the predicted signal : these also happen to be the largest ones in the sample. We find them again in the ISW-redshift graph, at the highest redshifts of the sample : This seems to indicate an correlation between the size and distance of these voids. The largest ones are therefore found at the far edge of the survey, which points towards a bias in the detection of these voids, maybe due to "border" effetcs.

Besides, we identify these most (theoretically) contributing voids in the catalogue, then go back to the data used in G08 and redo the stacking having removed them. This supposedly should have a significant impact, but in pratice, we get almost no modification of the resulting ISW flux, again a counterintuitive fact.

5 Conclusions and perspectives

At this point of the study, we still have discrepancies that need to be solved or explained, but many leads and ways for improvement are yet to be explored. Among others things, we compute (see Ilić et al.[4], 2012) the full radial profile of the ISW effect created by our voids in order to account for all possible effects such as overlaps. Indeed, some of the structures of G08 are found to be close to each other in the projected sky, which could bias the stacked image. These profiles are also necessary to study the possible chance alignements of other voids on the line of sight.

Furthermore, we also consider testing other cosmological models to see if they are better fits to the observed data. There could either be some unexpected effect which slows down the accelerated expansion at the lowest redshifts and results in a relatively stronger ISW effect in the past or, more probably, some of the reported voids are likely to be misidentified due to the sparsity of the chosen tracers. That is why one might also question the data itself, first concerning the robustness of the detection of these strucutres – especially regarding the sparsity of the LRGs it is based on – but also the significance of its mere 50 structures. This last point incites us to do the same kind of analysis on other – maybe more adapted - surveys of galaxies. In the end, the observed signal of G08 may very well be indeed a detection of the ISW effect but it would be unreasonable to invalidate the Λ-CDM model yet.

References

1. B R Granett, M C Neyrinck and I Szapudi, 2008, ApJ. 683, L99-L102 (G08)
2. F X Dupé, A Rassat, J L Starck and M J Fadili, 2011, A&A 534, A51
3. S Ilić, M Douspis, M Langer, A Pénin and G Lagache, 2011, MNRAS, 416, 2688-2696
4. S Ilić, M Langer, M Douspis, 2012, in prep.
5. S Nadathur, S Hotchkiss, S Sarkar, 2011, arxiv :1109.4126
6. V Springel et al., 2005, Nature, 435, 629

3.
Dark Energy

SNLS 3-YEAR: RESULTS AND IMPROVEMENT PROSPECTS

M. BETOULE, for the SNLS collaboration
LPNHE, CNRS-IN2P3 and Université Paris 6 & 7, 4 place Jussieu, Paris Cedex 05, France
PCCP, CNRS-IN2P3, 10 rue Alice Domond et Léonie Duquet, 75205 Paris Cedex 13, France

The recent results from the analysis of the Supernova Legacy Survey 3-year data sample have settled the most stringent constraints to date on the dark energy equation of state. When combined with baryon acoustic oscillation measurements from the Sloan Digital Sky Survey (SDSS) and measurements of the cosmic microwave background power spectrum from the WMAP-7 year data, SNe data delivers a measurement of the dark energy equation of state $w = -1.068 \pm 0.08$, assuming a flat universe. The major part of this uncertainty is related to systematic uncertainties in the analysis. We discuss the origin of these systematics and describe ongoing work to decrease their amplitude and further improve the cosmological constraints.

1 Introduction

The measurement of the evolution of type Ia supernova (SNe Ia) luminosity distances with redshift delivered, about 14 years ago, the first evidences[1,2] that the expansion of the universe is actually accelerating. The discovery has since been confirmed by other probes of the expansion history such as baryon acoustic oscillations (BAOs), and the available data offers a consistent picture of a universe currently undergoing an accelerated expansion hypothetically driven by an unknown component called "dark-energy". The nature of this dark energy remains a crucial and open question in the current cosmological model.

Probing more precisely the history of the expansion gives an opportunity to discriminate between different hypothesis by constraining the equation of state of the dark component: $w = p_X/\rho_X$. Available data is, at this stage, compatible with the cosmological constant model (Λ-CDM) that requires $w = -1$. Among the cosmological probes, the measurement of the luminosity distance of SNe-Ia accounts, up to now, as the most constraining for dark energy.

In this contribution, we review the recent release and analysis of the data gathered during the first 3 years of the Supernova Legacy Survey (SNLS)[3]. The emphasis shall be put on the systematics of the analysis as they actually limit the accuracy of the cosmological result. If left at the current level, systematic uncertainties would prevent the analysis of the full 5 year SNLS sample to bring a net improvement of the current cosmological result. We also discuss how these uncertainties can be further reduced. We quote ongoing work addressing the photometric calibration accuracy that currently constitutes the limiting factor of the analysis.

2 The SuperNova Legacy Survey

The SNLS is a five years program completed in August 2008, targeting the discovery and follow-up of SNe-Ia in the 4 one square-degree deep fields of the Canada France Hawaï Telescope Legacy Survey (CFHTLS). The 4 pointings of the deep survey are evenly distributed in right ascension, so that observations with a single instrument can occur continuously over the year. The project has two components: an imaging survey, repeatedly imaging the same fields every 3 days to detect the supernovae and monitor their lightcurves, and a spectroscopic program, to confirm the nature of the candidates, and measure their redshift.

2.1 The Imaging Survey

The imaging component of the SNLS was conducted on the 3.6m Canada France Hawaï Telescope (CFHT) using the one square degree camera MegaCam[4]. The observations were sequenced in a way that enables, from the same data, the detection of supernovae as well as the monitoring of their luminosity evolution (light-curves). Such an observation strategy, usually called rolling search or rolling survey, proved to be an efficient way to discover and monitor distant supernovae.

Each field stayed visible during 5 to 7 consecutive lunation. The observations occurred during dark time every lunation, and visible fields were imaged at roughly equally spaced epochs (every 3 or 4 days) in the four photometric bands g_M, r_M, i_M and z_M. Observations lost due to poor atmospheric conditions remained queued up until the next clear observing opportunity. The observations and the pre-processing of images are conducted by the CFHT staff using the Elixir reduction pipeline[5].

2.2 The Spectroscopic Survey

A spectroscopic follow-up is needed to confirm SN-Ia candidates and obtain their redshifts. The faintness of these distant objects requires observations on 8-10 meter class telescopes. The SNLS was allocated 60 hours / semester at the European Southern Observatory Very Large Telescope, and 60 hours / semester at Gemini-North and South. Some spectroscopic time was also obtained at Keck-I and Keck-II.

The number of transient discovered in the search largely exceeded what can be observed spectroscopically. A pre-selection of candidates was conducted by attempting a photometric identification and discarding known variable objects. Over the 5 years of the survey, more than 450 type-Ia supernovae were discovered and spectroscopically confirmed. The first three years of the spectroscopic data sample are published in Bronder *et al.*(2008)[6] and Balland et al. (2009).[7]

3 The SNLS 3 year analysis

The cosmological analysis of the 3 year SNLS sample has been published in a set of three papers. The first paper by Guy et al. (2010)[8] details the photometric properties and distance measurements for every SN in the selected sample. The SNLS sample is combined to lower and higher redshift samples in Conley et al. (2011)[9], to fill the Hubble diagram in the range $0.02 < z < 1.2$ and yield meaningful constraints on the expansion history of the universe from SNe-Ia alone. The constraints obtained when combining the Supernovae with other cosmological probes are discussed in Sullivan *et al.* (2011)[10].

With respect to the first year analysis from Astier et al. (2006)[3], the 3 year analysis relies on a spectroscopic sample of supernovae nearly four times as large. Another important characteristic of the entire analysis is its large emphasis on a careful estimation of systematic uncertainties. In particular, all steps of the processing have been duplicated with different algorithmic choices in an attempt to identify systematics related to peculiar modeling choices and propagate them to the cosmological result.

In this section, we briefly recall the main ingredients of the analysis leading to the cosmological result.

3.1 Cosmology with supernovae

The constraints on cosmological model parameters arise from the adjustment of the predicted Hubble diagram (luminosity as a function of redshift) to the measurements of supernovae. In the absence of covariances between measurements, the χ^2 of the model would write:

$$\chi^2 = \sum_{\text{SNe}} \frac{(m_B - m_{\text{mod}})^2}{\sigma^2}, \tag{1}$$

where m_B is the rest-frame peak B band magnitude of a supernova and m_{mod} is the predicted magnitude of the SN given the cosmological model. The uncertainty term σ includes both contributions from the measurement error on m_B and the model uncertainty m_{mod}. In addition to the cosmological parameters that predict the luminosity distance $\mathcal{D}_L$, two other quantities (a shape parameter S and a color $\mathcal{C}$) which describe the light-curve of the particular SN intervene in the prediction of the supernovae luminosity:

$$m_{\text{mod}} = 5\log_{10} \mathcal{D}_L\left(z_{\text{hel}}, z_{\text{cmb}}, w, \Omega_{\text{M}}, \Omega_{DE}\right) - \alpha S + \beta \mathcal{C} + \mathcal{M}. \tag{2}$$

The dependency of supernova luminosity with color β and stretch α, as well as the intrinsic luminosity $\mathcal{M}$ attributed to supernovae are nuisance parameters adjusted at the same time as the selected set of cosmological parameters (*e.g.* $w, \Omega_{\text{M}}, \Omega_{DE}$). Deviations of individual supernovae from this model amounts typically at 15% rms and is the first contribution to the σ term. With the large number of supernovae measured today, other error sources correlated between measurements are becoming predominant.

3.2 *Differential photometry*

The photometry of supernovae is at the heart of the cosmological measurement. As long as spectroscopic redshifts are available for the majority of the events, the accuracy on the photometry is what limits the constraining power of the Hubble diagram.

Interestingly, as the intrinsic luminosity of supernovae is affected by a large variation (say 15% rms) from one object to another, the precision on individual measurements is not a crucial issue. The important matter is that the flux measurement is made without bias on average. There are some obstacles to this process, one of them is the contribution of the supernova host galaxy to the measured flux.

The survey being a rolling search, large numbers of images on the same field are accumulated before and/or long after the supernova explosion. Those can be used to obtain an accurate model of the galaxy flux contaminating the supernova measurement.

Another issue is the unavoidable variation of the effective instrument throughput, from one exposure to another. To overcome this difficulty the measurement of SN flux is made relatively to the flux of selected surrounding stars (called tertiary standards). Those stars are selected to be non variable so that in average they constitute an excellent flux reference.

Two photometry methods exploiting these properties have been developed and run independently on the same data. They deliver light-curves for point like objects such as the stars and supernovae from the successive images of each field. Full description of the methods can be found in Astier *et al.* (2006)[3] and Guy et al. (2010)[8]. The important point is that the difficulties of the measurement, among which the variation of the PSF and pixel frames between different images or the modeling of the galactic flux, are handled differently by each algorithm. The comparison of the two methods confirmed that the first one (Astier *et al.*, 2006)[3] was free from host subtraction biases with an accuracy of 1 to 3 mmag (depending on the band), which has negligible consequences on the cosmological result.

3.3 *Photometric calibration*

Differential photometry of SNe deliver broadband flux measurements relative to the flux of selected surrounding stars (the tertiary standards). The purpose of photometric calibration is to provide calibrated measurements of broadband flux for those stars. This enables the comparison between flux measurements in different photometric bands (and made by different instruments), and thus between supernovae at different redshifts.

The SNLS3 calibration[11] is a two step process. The magnitude of the tertiary standards (typically a few thousand objects per field) are first anchored to the set of secondary standards established by Landolt[12]. Those stars are spread in selected regions (the Selected Areas) along the celestial equator and have very uniform magnitudes in the UBVRI photometric system. The anchoring to these secondary standards is accomplished by regularly observing concomitantly the science fields (hosting the tertiaries and the SN) and the Selected Areas (hosting the secondary standards). As already mentioned, the throughput of the instrument is susceptible to vary between the science and the calibration exposure. The main (unavoidable for ground-based experiment) contributors to this variation are small changes in the atmospheric transmission. Even on clear nights this variation limits the accuracy of flux ratio measurement between distant exposures to about 1 or 2%. Those variations are however expected to be uncorrelated from one night to another so that it is possible to reach the required sub-percent accuracy by the repetition of the measurement. Typically 20 nights in each photometric band were accumulated to transfer the Landolt calibration to the SNLS fields in this release.

In a second step, the flux scale of the consistent magnitude system defined by the tertiary standards has to be set. This is readily done by delivering the corresponding magnitudes in this system of a star of known spectral energy distribution. Such a star is called a primary spectrophotometric standard in what follows. The best set of spectrophotometric standards available is provided by the space-constituted CALSPEC database. The HST/STIS spectrograph was used to transfer the flux calibration defined by the modeling of 3 pure-hydrogen white dwarfs[13], to several other stars among which the F-subdwarf BD +17 4708[14]. Most of those stars are in practice too bright to be observed with MegaCam. However, BD +17 4708 was accurately measured in the Landolt UBVRI system[15]. The MegaCam magnitudes of this star can be inferred from these measurements as the MegaCam observations of the Landolt equatorial standards measure precisely the transformation between the two systems. The transfer of the calibration of the HST primary standard to the SNLS tertiary is thus made through Landolt observations in the UBVRI system.

In this calibration transfer, one instrumental issue has to be carefully handled: the uniformity of the photometric response of the wide field camera. This is notoriously difficult to ensure, because the usual "flat-fielding" solutions[a] are generally polluted by various optical effects as internal reflection of light on the various optical elements. The impact of residual non uniformities on the SNLS calibration is exacerbated by the fact that secondary standards are preferentially observed at the center of the focal plane, while tertiary stars (and SN-Ia) are spread over the entire area.

The effective response of MegaCam was repeatedly mapped over the course of the survey, using dedicated observation sequences of dense stellar fields (the "grid" observation in the CFHT parlance). During these dedicated observations the camera is moved over dense stellar fields, delivering measurements of the same stars at different positions on the focal plane. Such data enables to solve for the instrumental response at a limited spatial resolution (2 arcmin).

Another difficulty accounted for in the SNLS 3 calibration is the variation of the effective instrument passband as a function of the position on the focal plane. Most of the effect is related to the manufacturing of the interference filters and details in the deposit of coatings. The mapping of the effective response variation can also be achieved on the grid observation at a slightly coarser resolution ($5'$).

The calibration accuracy reached with this procedure is expected to be 0.3, 0.5, 0.7 and 1.9% in band $g_M r_M i_M z_M$ respectively, with some correlations between bands, reported in Regnault *et al.* (2009).[11].

3.4 Light-curve modeling

The photometry of the 3 year sample yields photometric measurements of the supernova at several epochs (or phase p, approximately regularly spaced) and in at least two photometric bands. One relies on a parametric model of the time-spectral sequence followed by supernovae to interpolate between those measurements and estimate the supernova characteristics.

The 3 year analysis makes use of two light-curve models (SALT2 and SIFTO) that are different in their basic assumptions. Both are describing (ultimately) the supernova observations with three parameters: 1) a normalization parameter chosen to be the apparent flux of the supernova at its maximum in one fiducial rest-frame band[b], as well as 2 other parameters that are known to correlate with the luminosity, one describing the shape of the light curve (roughly its stretching with time) and the other one the color of the supernova at maximum. Beside this common framework, the parameterization used by SALT and SIFTO are fairly different.

The SALT2 model[16] is based on a description of the SN spectral sequence (function of the phase p and the wavelength λ) $M(p, \lambda)$ in term of two additive components corrected by a color law. Specifically:

$$M(p, \lambda; x_0, x_1, c) = x_0[M_0(p, \lambda) + x_1 M_1(p, \lambda)] \exp(cCL(\lambda)) \tag{3}$$

The color law CL and the two components M_0 and M_1 are adjusted to provide the best description of a spectrophotometric SNe-Ia data sample (the training sample). The adjustment of this model to the photometric light curves of the science sample yields the determination of the relevant parameters for each supernova: x_0, x_1 and c respectively play the role of the luminosity parameter, the shape parameter and the color parameter.

In contrast SIFTO[17] assumes that each supernova sequence is purely a time-stretched (with a wavelength dependent stretch) version of a given spectral sequence:

$$M(p, \lambda; s_B) = M(p/(s(\lambda, s_B) - 1), \lambda) \tag{4}$$

Amplitude of the light-curve are adjusted independently for each photometric band (observer frame). The color (rest-frame B-V) and luminosity (rest-frame B) of the supernova at maximum are then inferred from the fitted observer frame magnitudes at maximum.

Again, the spectral sequence and its stretching law s, as well as the relations allowing the estimate the B-V color are trained to describe best a large training sample. In both cases, the training sample includes high-z data from the SNLS which provides well calibrated observations (in the visible domain) of the UV part of the SN spectrum. This makes the resulting model in the UV less sensitive to potential problems in the ground-based UV observations.

3.5 Cosmological constraints

To provide meaningful constraints on the expansion history, the measurement of the brightness evolution with redshift provided by the 242 high-z supernovae in the SNLS sample has to be completed by measurements of

[a] Such as the observation of twilight assumed to deliver a uniform enlightenment of the focal plan.
[b] Conventionally the B photometric band.

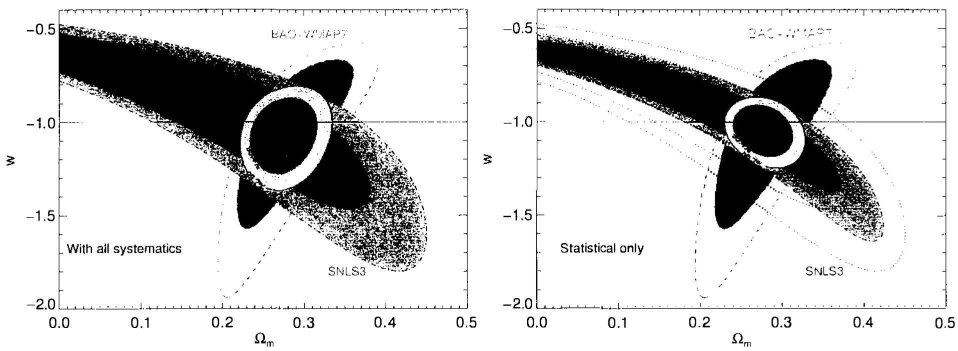

Figure 1: Confidence contours in the cosmological parameters Ω_M and w arising from fits to the combined SNLS3 SN-Ia sample published in Sullivan *et al.* (2011). In both panels, the SNLS3 SN Ia contours are shown in blue, and combined BAO/WMAP7 constraints from Percival *et al.* (2010) and Komatsu *et al.* (2011) in green. The combined constraints are shown in grey. The contours enclose 68.3%, 95.4% and 99.7% of the probability. *left*: The baseline fit, where the SNLS3 contours include statistical and all identified systematic uncertainties. *Right*: The filled SNLS3 contours include statistical uncertainties only; the dotted open contours refer to the baseline fit with all systematics included.

supernovae at other redshifts (especially nearby supernovae) collected by other experiments. The full sample used to build the Hubble diagram presented in the 3 year analysis includes 14 supernovae at higher redshift from the HST[18], 93 supernova at intermediate redshift ($0.1 < z < 0.4$) from the Sloan Digital Sky Survey (SDSS) supernova survey[19], and an heterogeneous combination of 123 nearby supernovae ($z < 0.2$) provided by non-rolling surveys.

Light-curves were fitted with both SALT2 and SIFTO and the difference between the two was taken as an estimate of the uncertainty to be propagated to the cosmological result. The main cosmological result is obtained by combining the SN sample to the SDSS DR7 BAO measurement from Percival *et al.* (2010)[23] and the WMAP7 measurement of the CMB from Larson et al. (2011)[24]. The cosmological constraints obtained for a FwCDM model are summarized on the left panel of Fig. 1. The corresponding best fit value for w is $w = 1.021^{+0.078}_{-0.079}$. The current data sample does not bring meaningful constraints on the potential time evolution of this parameter.

4 Propagation of uncertainties

4.1 The systematic error budget

A thorough review of the uncertainty sources and systematic errors affecting the measurements was conducted for all survey entering in the constitution of the Hubble diagram. Estimates for their respective amplitudes were propagated to the cosmological results using a Fisher analysis. It is interesting to deliver hints about the relative importance of the various uncertainty sources. The contribution to the uncertainty on w under the assumption of a FwCDM universe, when using the priors from CMB and BAO, can be used as a figure of merit to this purpose. An illustrative summary of the main contributions is given in table 1.

What is generally dubbed as the "sytematics" of the analysis are uncertainty sources susceptible to affect the *average* measurement of luminosity distances in a way dependent on the redshift. Their importance is to be compared to the statistical constraining power of the sample, which is ultimately limited by the uncertainty on the intrinsic luminosity of individual events. Without any breakthrough in the understanding of type IA supernova physic, the only improvement on this subject can come from an increased number of measured supernovae. This "statistical" uncertainty is readily estimated from the dispersion of the Hubble diagram. Would the measurement be only affected by this noise component, the 472 events that entered in the Hubble diagram yield a measurement of w with a precision of 5.4%. As illustrated by the comparison between the left and right panels in Figure 1, the uncertainty is actually dominated by systematics.

4.2 Uncertainties on the photometric calibration

The limited accuracy of the photometric calibration can be seen to be the main issue. It contributes to the degradation of the cosmological result by a factor of about 2. Its origin (for what concern the calibration of

Table 1: Error budget in the SNLS3 analysis. The right column displays the contribution (in %) to the uncertainty on w under the assumption of a FwCDM universe, when using the priors from CMB and BAO.

Uncertainty source	Induced error on w
Statistical	5.4%
Calibration	5.4%
light curve modeling	3%
Evolution of supernovae	$< 1\%$
Host-galaxy	$< 1\%$
Correction of Malmquist bias[22]	$< 1\%$
Peculiar velocity of low-z	$< 1\%$
Core collapse contamination	$< 1\%$

SNLS) is detailed in Regnault et al. (2009)[11]. It is interesting to distinguish the calibration uncertainties affecting the SED of the primary standard star itself from the uncertainties introduced when transferring this calibration to the supernovae measurements.

The uncertainty on the calibration reference has two potential origins. The first is the uncertainty on the STIS measurements that were used to transfer the white dwarfs fundamental standards to our primary standard star BD +17 4708. It amounts to a few mmag depending on the band (from 1 mmag in band g_M to 6 mmag in band z_M). The second is the white dwarf modeling uncertainty that affects the calibration of fundamental standards. It is thought to be negligible at this stage but is harder to estimate.

Most of the calibration error actually arises in the calibration transfer to the SNLS tertiaries. The trickiest part is the transformation of the BD +17 4708 measurement from their UBVRI system to the MegaCam natural system. The loss of precision due to the limited accuracy of this transformation is expected to range from 2 mmag in band g_M to 18 mmag in band z_M.

4.3 Light-curve models

The impact on cosmological parameter estimates of the modeling choice made within the light-curve fitters is estimated from the difference between the two light-curve models presented above. It can be seen to be fairly acceptable at this stage, being subdominant with respect to the statistical uncertainty.

A specificity of the SNLS is to provide accurate photometry in the 3 photometric bands $g_M r_M i_M$. This enables the comparison of the luminosity in the rest-frame range 2900–6400Å for supernovae in the redshift range $0.2 < z < 0.7$. Besides this range, the V-band information is lost, and the comparison became more dependent on the specificity of the spectral-sequence model to extrapolate the $U-B$ color to a $B-V$ estimate. A net improvement on this situation can be expected from an increased sensitivity of the photometry in the infrared, which should be provided by future surveys (such as DES).

4.4 Evolution of supernovae

Other important issues are related to the evolution with redshift of environmental parameters, like metallicity that may impact the supernova. A sensitive test, that can be conducted at this stage, is the comparison of events at similar redshifts occurring in different environments. Such analysis were conducted and the most relevant effect empirically discovered at this time are some kind of relations between the SN luminosity and quantities related to the mass (age, metallicity) of its host galaxy. For example, using SNLS data, Sullivan et al. (2010)[21] showed that supernovae in massive galaxies (thus statistically older) appear to have a larger intrinsic luminosity (once corrected for stretch).

This effect was accounted for in the analysis by adjusting separately the intrinsic luminosity of supernovae in massive (M_{stellar} $10^{10}\,M_\bullet$) and smaller galaxies. It would have constituted our first source of error if neglected.

Upper bounds were set on other evolution effects (such as potential evolution of the color-luminosity relation) and their impact on cosmology was found to be small. It is included in the systematic error budget.

5 Improvement prospects

5.1 The final supernova sample

The complete 5 year sample of the Supernova Legacy survey contains about 450 spectroscopically confirmed and well measured type Ia supernova. In addition, the SDSS-II supernova survey gathered a similar data sample of roughly 500 supernovae at lower redshift. To benefit from the increased statistical power of such an extended sample, another significant step on reducing systematic uncertainties must be accomplished. In this part we discuss preliminary work on the release of the final SNLS sample. Peculiar attention was paid to the dominant systematic which is the uncertainty on photometric calibration.

5.2 Improving the photometric calibration of SNLS

An important advance can be achieved in the photometric calibration of the SNLS by observing directly the primary photometric standards in the MegaCam system. The major uncertainty in the current calibration transfer was indeed related to the transformation of the primary standard measurements made in a different photometric system to the native MegaCam system. While most of the spectrophotometric standard stars used to be too bright to be observed with MegaCam at the 3.6m CFHT, the CALSPEC database was recently extended to incorporate fainter and redder G-type stars.[20] Among those new standards, 3 stars (P177D, P330E and SNAP2) are conveniently observable along with an SNLS field (D3). A short observation program was undertaken at CFHT to anchor (without intermediary) measurements of those three primary standards to the magnitude system defined by the SNLS tertiary standards.

Another hard point of the MegaCam calibration is the uniformity of the instrument response. With the extension of the data sample, and several more independent determinations of the response maps, it can now be demonstrated that the repeated determinations of the response maps throughout the life of the survey deliver a consistent picture of the calibration. This is illustrated on the left panel of Fig. 2. Each data point corresponds to an independent realization of the survey calibration. In particular different data points involve independently determined response maps. All points can be seen to agree with a rms below 3 mmag in all bands.

5.3 Direct cross-calibration with the SDSS

The relevant cosmological constraints arise from the comparison between nearby and distant supernovae. In the current situation, they are measured with different instruments, and the comparison of the measured flux involves the absolute calibration of each survey. Relative calibration between similar surveys is actually much easier to obtain than the absolute calibration. Such a shortcut was realized for the SNLS and the SDSS supernova survey by anchoring sub-samples of their respective tertiary standards together with a short MegaCam observation program.

The gathered data sample brings several improvements to the calibration. First it shortens the cross-calibration path and enables the comparison of SNLS and SDSS measurements with a greater accuracy. Second it delivers a way to investigate both instrument systematics (e.g. uniformity of the photometry). Third it delivers a cross-check of the independent calibration relative to the HST of the two surveys. Last point is illustrated in the right panel of Fig. 2 that shows in each photometric band the relative calibration offsets between the three now available calibration paths: the historical SNLS calibration relying on Landolt observation of BD +17 4708 (the snls5 line in the plot), the calibration set by the direct observation of HST standards with MegaCam (the sa line) and the calibration set by the comparison to SDSS independently calibrated tertiary standards (the sdss line). They can be seen to agree within 1%. Combination of these results improves over the individual calibration, leaving the uncertainty of the HST calibration the dominant contribution to the calibration error.

6 Conclusion

The first 3 years of the SNLS survey represent about 1500 hours of observation on the 3.6m Canada France Hawaï Telescope. They enabled the discovery and spectroscopic identification of 242 high redshift supernovae. Such a sample yields a measurement of the dark energy equation of state parameter w with an accuracy of 8% when combined with nearby SNe-Ia and the CMB data. This makes the observation of supernovae the most efficient probe for dark energy science at this stage. The analysis is however hindered by systematic uncertainties that now dominate the intrinsic uncertainty of the probe.

Further work on systematics had to be undertaken as their relative importance will be exacerbated with the full SNLS and SDSS samples as they should increase the number of supernovae populating the Hubble diagram by a factor of two. Preliminary work to improve the calibration accuracy of the photometric measurements, which constitutes the limiting point in current data, was presented. It enables the exploitation of the full potential of the SNLS sample.

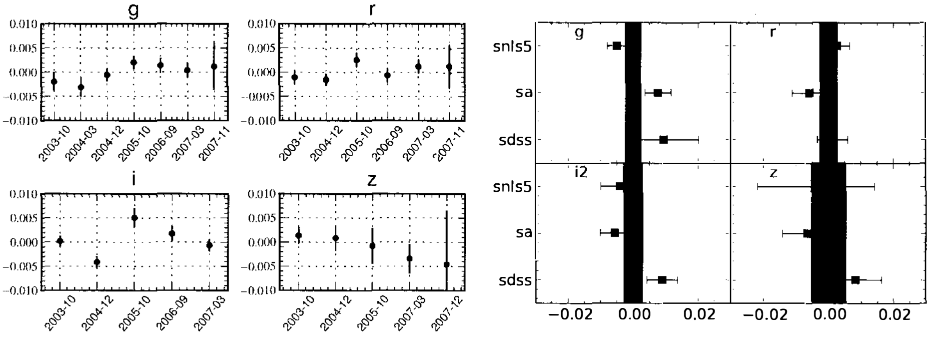

Figure 2: *Left*: Agreement between independent realizations of the SNLS calibration. Each point is the calibration offset for a given period with respect to the average calibration over the full survey. *Right:* Calibration offsets when anchoring SNLS to the HST using three independent sets of observation: via Landolt standards (snls5), via direct observation of HST solar analogs (sa) or via the observation of a subset of SDSS calibrated tertiary standards (sdss). All numbers are magnitudes.

Upcoming surveys will also benefit from the large ongoing effort aiming at the reduction of the various systematics. In particular, noticeable improvements on the photometric calibration are to be expected from the advent of man-made calibration sources and better survey designs. We also advocate that other uncertainty sources are likely to be reduced by extended data samples with an improved sensitivity in the infrared.

References

1. S. Perlmutter et al, *Astrophysical Journal* **116**, 1009 (1998)
2. A. G. Riess et al, *Astronomical Journal* **116**, 1009 (1998)
3. Astier, P.; Guy, J.; Regnault, N. *et al. Astronomy and Astrophysics* **447**, 31 (2006)
4. Boulade, O. *et al., Proceedings of SPIE* **4081**, 72 (2003)
5. Magnier, E. *Publications of the Astronomical Society of the Pacific* **116**, 449 (2004)
6. Bronder, T. J.; Hook, I. M. *Astronomy and Astrophysics* **477**, 717 (2008)
7. Balland, C.; Baumont, S.; Basa, S. *et al. Astronomy and Astrophysics* **507**, 85 (2009)
8. Guy, J.; Sullivan, M.; Conley, A. *et al. Astronomy and Astrophysics* **523**, (2010)
9. Conley, A.; Guy, J.; Sullivan, M. *et al. Astrophysical Journal, Supplement* **192**, (2011)
10. Sullivan, M.; Guy, J.; Conley, A. *et al. Astrophysical Journal* **737**, ? (2011)
11. Regnault, N.; Conley, A.; Guy, J. *et al. Astronomy and Astrophysics* **506**, (2009)
12. Landolt, A. U. *Astronomical Journal* **104**, 340 (1992)
13. Bohlin, R. C. *Astronomical Journal* **120**, 437 (2000)
14. Bohlin, R. C., Gilliland, R. L. *Astronomical Journal* **128**, 3053 (2004)
15. Landolt, A. U., Uomoto, A. K. *Astronomical Journal* **133**, 768 (2007)
16. Guy, J.; Astier, P.; Baumont, S. *et al. Astronomy and Astrophysics* **466**, 11 (2007)
17. Conley, A.; Sullivan, M.; Hsiao, E. Y. *et al. Astrophysical Journal* **681**, 482 (2008)
18. Riess, A. G.; Strolger, L.-G.; Casertano, S. *et al. Astrophysical Journal* **659**, 98 (2007)
19. Kessler, R.; Becker, A. C.; Cinabro, D. *et al. Astrophysical Journal, Supplement* **185**, 32 (2009)
20. Bohlin, R. C. *Astronomical Journal* **139**, 1515 (2010)
21. Sullivan, M.; Conley, A.; Howell, D. A. *et al. Monthly Notices of the Royal Atronomical Society* **406**, 782 (2010)
22. Perret, K.; Balam, D.; Sullivan, M. *Astronomical Journal* **140**, 518 (2010)
23. Percival, W. J.; Reid, B. A.; Eisenstein, D. J. *et al. Monthly Notices of the Royal Atronomical Society* **401**, 2148 (2010)
24. Larson, D.; Dunkley, J.: Hinshaw, G. *et al. Astrophysical Journal, Supplement* **192**, 16 (2011)
25. `http://cfht.hawaii.edu/Science/CFHTLS`

Constraints on SNe Ia color and extinction with the SNfactory data sample

Arnaud Canto
LPNHE -Barre 12-22 1er etage, 4 place Jussieu 75252 PARIS CEDEX 05

Type Ia Supernovae (hereafter SNe Ia) has been proven to be effective as standardizable canddles to measure cosmological distances [1]. Yet some systematics errors due to the objects environment still prevent some improvement for the measurement of the acceleration of the Universe's expansion. In order to reduce systematic errors for the low redshift SNe Ia and to have a better understanding of the mechanism of those objects, the SNfactory experiment has been taking spectral time series of SNe Ia since 2004. Using this sample, we will investigate further one of the source of the systematics : the color of the object, trying to determine the contribution of intrinsic and extrinsic components. The extrinsic color component will be studied through the Na ID absorption feature and the close dust environment of the SNe Ia wil be studied as well.

1 Colors and redenning in type Ia Supernovae

In order to model the dispersion of SNe Ia observed on Hubble fits, one can parametrize the corrected Hubble residual as :

$$\Delta M_b^{corr} = \Delta M_b + \alpha x1 - \beta c \tag{1}$$

where x1=1-stretch accounts for the intrinsic luminosity evolution effects of the objects whether c accounts for the colorof the objects. In what follows, we will focus only on the c parameter and try to identifiate the different origins of the color of the object and their contribution. As shown in previous results (see [2]) an intrinsic contribution of the color can be extracted from the spectral analysis of wide velocity range absorption features such as Ca II. On the other hand, an extrinsic part of the color also exists and is mostly due to the several absorption process encountered by the SN photons along the line of sight while crossing different dust medium. The absorption can be modeled using the column density of the surrounding dust ($F_{SN}^{abs} = F_{SN}e^{-\tau\lambda}$ where τ is the column density, F_{SN}^{abs} the absorbed SN flux). The color excess of SNe Ia between different bands as been deeply investigated as well, leading to several relations (see [3]) which describe the evolution of extinction in function of wavelength. The investigations of those relations can lead to crucial informations concerning host galaxies dust medium properties hence the need of extended SNe Ia spectrometry surveys.

2 Color components in SNfactory data sample

2.1 SNFactory data

The SNfactory experiment has been collecting SNe Ia spectral time series for 8 years. This data was obtained using the SNIFS (SuperNovae Integral Field Spectrometer) mounted on the

UH-88 Telescope on Mauna Kea, an IFU spectrograph consisting in two spectrometry channels (B channel with a 3100-5100 Å range and R channel with a 4900-10000Å range) as well as a photometry channel used for the flux calibration.The resolution is 2.5Å and 2.93Å for the blue and the red channel respectively. The first aim of the survey is to reduce systematic errors observed on Hubble residual data for low redshift SNe Ia as well as to have a better understanding of the physics occuring in SNe Ia objects. Hence, the current collected dataset consists in more than 2730 spectra taken between -15 to +40 days according to B band maximum luminosity making it a complete time sampled spectral catalogue for 250 SNe Ia (with a redshift range $0.001 \leq z \leq 0.12$). In order to study the SNe Ia physical properties the whole sample has been split into several subsamples to permit different kinds of analysis mainly based on flux quality criteria and goodness of lightcurve's fit. The dust medium analysis presented next has been released using a subsample of 177 SNe Ia spectral time series consisting in overluminous and underluminous objects as well as normal type SNe Ia for a better understanding of the overall SNe Ia landscape.

2.2 Interstellar Dust Medium

We will now focus on the extrinsic part of the color of SNe Ia using a deep analysis of the interstellar dust medium. The host Galaxy dust effects on SNe Ia spectra can be spotted studying the reduced velocity range spectral features (around several hundredth of $km.s^{-1}$, appearing as 20Å on SNIFS spectra). As shown in previous papers, one of the most efficient probe for host galaxy dust medium is the Na ID doublet absorption feature (5889.Å and 5895.Å). In what follows, we will use the EW to characterize the amount of Na ID in the dust medium defined as:

$$EW = \frac{\int_{\lambda_1}^{\lambda_2} cont_{SN}\ (\lambda)\ F_{SN}\ (\lambda)\ d\lambda}{\int_{\lambda_1}^{\lambda_2} cont_{SN}\ (\lambda)\ d\lambda} \tag{2}$$

Where $cont_{SN}$ is the estimated continuum of the SN on the considered wavelength range and F_{SN} is the flux of the spectra on the feature wavelength range. Previous correlations have already been established between the extinction and the amount of Na ID detected (see [4], [5], [6]). Using 177 objects from the SNfactory datasample, we compare Na ID and Salt2 model color of the objects (see 1). Though no clear correlation appears, one can notice that the reddest objects contain a significant amount of Na ID and that the mean of the color distribution is higher for objects containing Na ID (upper right panel). A step further is to compare the host type ith the amount of dust since elliptical galaxies are supposed to be less active and have a lower amount of interstellar dust material than spirals. Using a spectroscopic galaxy typing, we can see that most of the detection of Na ID (and all Na ID detections over 5σ) occurs for objects within spiral hosts (see fig 2), for further details, an extended anaysis of Na ID lines profile in function of host type has been presented in [7].

One finally would like to know if the markers of intrinsic color have an influence on observed Hubble residuals. We therefore used 120 SNe Ia based ofter a flux quality cut to build the Hubble residual relations shown on fig 3. The evolution of Hubble residual in function of Na ID EW and salt2 color parameter are depicted (respectively on upper and lower panels). The residuals are plotted before and after correction (respectively left-hand panels and right-hand panels). Notice that Hubble residual vs salt 2 color figures are displayed as aqn indicator for color correction. Though the correlation is not as strong as for the salt2 color before correction, one can notice a slight trend for the Hubble residual in function of Na ID EW suggesting that a part of the color driven by the host galactic medium of the object might not be entirely corrected for by the usual color parameter. We will now attempt to analyse more deeply the spectral time series in order to search for information concerning the local dust environment of the objects.

2.3 Circumstellar medium

The circumstellar medium (hereafter CSM) consists in all te dust material in the surroundings of the SNe Ia (typically within a several U.A. radius from the object). Due to its closeness and to its dust properties, this environment can evolve due to several photoionization processes from the SN Ia itself. Indeed, arounf 20 days before B band maximum luminosity, a UV flash can occur which will ionize a part of this close dust medium. Notice that this UV flash is less energetic for SNe Ia than for Type II SNe permitting this ionization process to occur just for reduced distances. After the UV flash comes a period during which the ionized dust medium will recombine into former material form (in our case Na ID). One will then expect to see an increase of Na ID amount along time on spectra in the case of such a phenomenon. As observed in some papers displaying high resolution spectroscopy results ([8], [9]), CSM detections can be made through the observation of Na ID EW ime variations. We hereby used the overall SNfactory time series sample to look for additionnal data on this matter. In spite of the moderate resolution of SNIFS, the amount of data allowed to confirm the previously published time evolution of Na ID amount for SN2006X (for which we find similar EW Na ID evolution from 0 to +15 days as in [10]) and SN2007le as shown on 4 as well as for 3 additional objects (see SN2007bc example on fig 4).

3 Conclusions

The improvement of Hubble residuals needs a better understanding of the color of SNe Ia. This color can be split into an intrinsic (directly related to the SN) and an extrinsic part (due to galaxy dust environment). The extrinsic part can be efficiently related to the amount of certain dust markers dislayed on spectra, more precisely Na ID spectral feature. Using the SNfactory data sample, we have shown that the reddest objects contain a significant amount of Na ID and that the mean of the color distribution for objects with Na ID is sightly higher than for other objects. The study of host stypes also shows that most of the objects with Na ID are located within spiral galaxies (as expected). A slight trend seems to arise between the Na ID EW and the Huble residual of objects as well when considering the residuals corrected from color parameter suggesting an extrinsic contribution non accounted for by the color parameter. Eventually, the Na ID features time variations can be used to track local environment and allowed us to find 3 additional evidence of CSM detections accounting for the single degenerate scenario.

References

1. S. Perlmutter, G. Aldering, S. Deustua, S. Fabbro, G. Goldhaber, D. E Groom, A. G Kim, M. Y Kim, R. A Knop, P. Nugent, C. R Pennypacker, A. Goobar, R. Pain, I. M Hook, C. Lidman, R. S Ellis, M. Irwin, R. G McMahon, P. Ruiz-Lapuente, N. Walton, B. Schaefer, B. J Boyle, A. V Filippenko, T. Matheson, A. S Fruchter, N. Panagia, H. J. M Newberg, and W. J Couch. Cosmology from type ia supernovae. *arXiv:astro-ph/9812473*, December 1998. Bull.Am.Astron.Soc.29:1351,1997.
2. N. Chotard, E. Gangler, G. Aldering, P. Antilogus, C. Aragon, S. Bailey, C. Baltay, S. Bongard, C. Buton, A. Canto, M. Childress, Y. Copin, H. K. Fakhouri, E. Y. Hsiao, M. Kerschhaggl, M. Kowalski, S. Loken, P. Nugent, K. Paech, R. Pain, E. Pecontal, R. Pereira, S. Perlmutter, D. Rabinowitz, K. Runge, R. Scalzo, G. Smadja, C. Tao, R. C. Thomas, B. A. Weaver, and C. Wu. The reddening law of type ia supernovae: separating intrinsic variability from dust using equivalent widths. *arXiv:1103.5300*, March 2011.
3. Jason A. Cardelli, Geoffrey C. Clayton, and John S. Mathis. The relationship between infrared, optical, and ultraviolet extinction. *The Astrophysical Journal*, 345:245, October

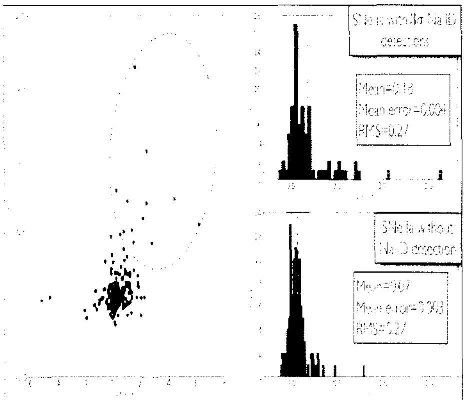

Figure 1: Links between Na ID EW for 177 objects. The left hand-side of the plot shows the direct correlation figure between the amount of Na ID and the object color (objects in red are those for which Na ID is detected at a $3\sigma level$). The two right hand panels show the salt2 color distribution for objects with and without significant NaID (upper and lower panels respectively).

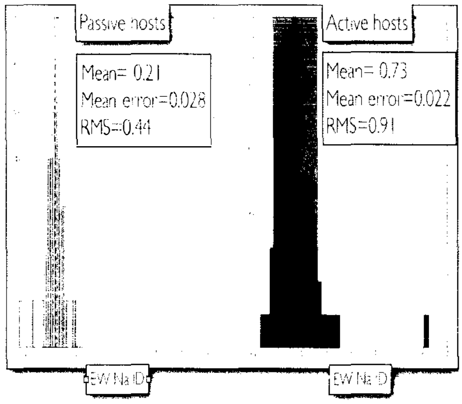

Figure 2: Distributions of Na ID EW for passive (left panel) and active hosts types (right panel) for the 177 SNe Ia from the SNfactory sample.

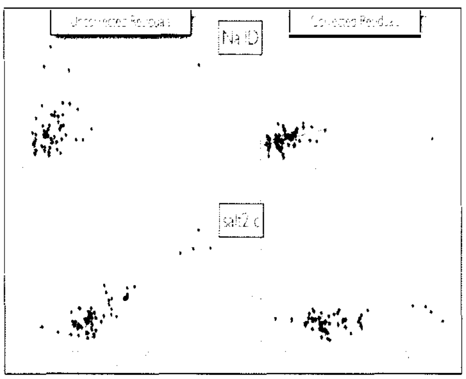

Figure 3: Hubble residual relation with Na ID. For each pannel, the y axis displays the Hubble residal values. The left-hand pannels show the evolution of HR in function of Na ID EW (upper pannel) and Salt2 color parameter (lower pannel) before any correction. The same figures are displayed on right-hand pannels after correction of the Hubble residuals.

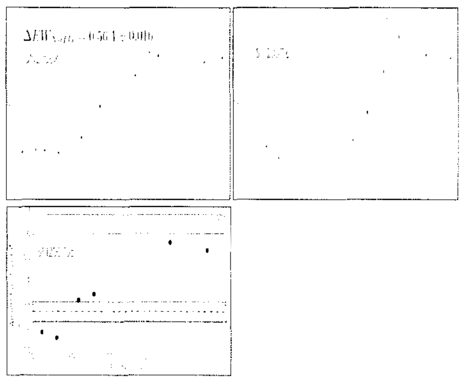

Figure 4: Three examples of Na ID EW time variations in the SNfactory sample. For each figure the x axis is the phase in days regarding B band maximum luminosity, the y axis is the Na ID EW.

1989.

4. Massimo Turatto. Classification of supernovae. *arXiv:astro-ph/0301107*, January 2003.
5. U. Munari and T. Zwitter. Equivalent width of NA i and k i lines and reddening. *Astronomy and Astrophysics*, 318:269–274, February 1997.
6. R. Barbon, S. Benetti, L. Rosino, E. Cappellaro, and M. Turatto. Type IA supernova 1989B in NGC 3627. *Astronomy and Astrophysics*, 237:79–90, October 1990.
7. Assaf Sternberg, Avishay Gal-Yam, Josh D Simon, Douglas C Leonard, Robert M Quimby, Mark M Phillips, Nidia Morrell, Ian B Thompson, Inese Ivans, Jennifer L Marshall, Alexei V Filippenko, Geoffrey W Marcy, Josh S Bloom, Ferdinando Patat, Ryan J Foley, David Yong, Bryan E Penprase, Daniel J Beeler, Carlos Allende Prieto, and Guy S Stringfellow. Circumstellar material in type ia supernovae via sodium absorption features. *arXiv:1108.3664*, August 2011. Science 333, 856 (2011).
8. F. Patat, P. Chandra, R. Chevalier, S. Justham, Ph Podsiadlowski, C. Wolf, A. Gal-Yam, L. Pasquini, I. A Crawford, P. A Mazzali, A. W. A Pauldrach, K. Nomoto, S. Benetti, E. Cappellaro, N. Elias-Rosa, W. Hillebrandt, D. C Leonard, A. Pastorello, A. Renzini, F. Sabbadin, J. D Simon, and M. Turatto. Detection of circumstellar material in a normal type ia supernova. *arXiv:0707.2793*, July 2007.
9. Joshua D Simon, Avishay Gal-Yam, Orly Gnat, Robert M Quimby, Mohan Ganeshalingam, Jeffrey M Silverman, Stephane Blondin, Weidong Li, Alexei V Filippenko, J. Craig Wheeler, Robert P Kirshner, Ferdinando Patat, Peter Nugent, Ryan J Foley, Steven S Vogt, R. Paul Butler, Kathryn M. G Peek, Erik Rosolowsky, Gregory J Herczeg, Daniel N Sauer, and Paolo A Mazzali. Variable sodium absorption in a low-extinction type ia supernova. *arXiv:0907.1083*, July 2009. Astrophys.J.702:1157-1170,2009.
10. S. Blondin, J. L Prieto, F. Patat, P. Challis, M. Hicken, R. P Kirshner, T. Matheson, and M. Modjaz. A second case of variable na i d lines in a highly-reddened type ia supernova. *arXiv:0811.0002*, October 2008. Astrophys.J.693:207-215,2009.

PROBING THE NATURE OF DARK MATTER WITH THE SKA

S. COLAFRANCESCO
SKA Research Chair, University of the Witwatersrand, Johannesburg (South Africa).
Email: sergio.colafrancesco@wits.ac.za

The Square Kilometre Array (SKA) is the most ambitious radio telescope ever planned, and it is a unique multi-disciplinary experiment. The SKA, in its original conception, has been dedicated to constrain the fundamental physics aspects on dark energy, gravitation and magnetism. However, much more scientific investigation could be done with its configuration: the exploration of the nature of Dark Matter, that we discuss here, is one of the most important additional scientific themes.

1 The SKA

With a collecting area of about one square kilometer, the SKA will be about fifty times more sensitive than the currently most powerful radio interferometer, the Expanded Very Large Array (EVLA). The SKA will continuously cover most of the frequency range accessible from ground, from 70 MHz to 10 GHz in the first (SKA-1) and second (SKA-2) phases, and it will be later extended to at least 25 GHz. The SKA will have an enormously wide field of view, ranging from 200 square degrees at 70 MHz to at least 1 square degree at 1.4 GHz. The speed to survey a large part of the sky, particularly at the lower frequencies, will hence be 10^4 to 10^6 times faster than what is possible today.

The SKA is a radio interferometer consisting of many antennas (see Fig.1) which will be spread over a large area to obtain high resolving power. The SKA central region will contain about 50% of the total collecting area and comprises i) separate core stations of 5 km diameter each for the dish antennas and the two types of aperture arrays, ii) the mid-region out to about 180 km radius from the core with dishes and aperture array antennas aggregated into stations distributed on a spiral arm pattern, and iii) remote stations with about 20 dish antennas each one out to distances of at least 3000 km from the core, and located on continuations of the spiral arm pattern. The overall extent of the array determines the angular resolution, which will be ~ 0.1 arcsec at 100 MHz and ~ 0.001 arcsec at 10 GHz. To meet these ambitious specifications in a sustainable way, the planning and construction of the SKA requires many technological innovations such as light and low-cost antennas, detector arrays with a wide field of view, low-noise amplifiers, high-capacity data transfer, high-speed parallel-processing computers and high capacity data storage units. The enormous data rates of the SKA will require online image production with automatic software pipelines.

The SKA frequency range that is spanning more than two decades cannot be realized with one single antenna design, so this will be achieved with a combination of different types of antennas. Under investigation are the following designs for the low and mid-frequency ranges: 1) An aperture array of simple dipole antennas with wide spacings (a sparse aperture array) for

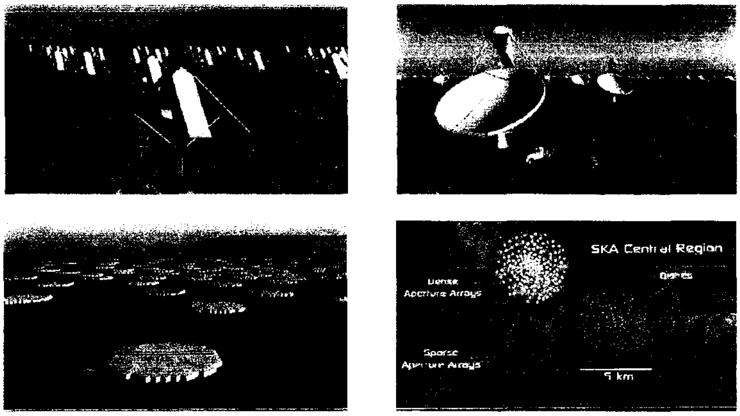

Figure 1: A graphical rendering of the SKA antennac: SKA aperture array station of dipole elements for about 70-450MHz (top left): SKA dishes for about 0.45-3GHz (top right); SKA aperture array station made up of 3m × 3m *tiles* for about 0.5-1GHz (bottom left); SKA central region with separate core stations for the aperture arrays for low and mid frequencies and for the dish array (bottom right). Figures from the SKA Project Office (SPO).

the low-frequency range (~ 70-450 MHz). This is a software telescope with no moving parts, steered solely by electronic phase delays. It has a large field of view and can observe towards several directions simultaneously.
2) An array of several thousand parabolic dishes of about 15 meters diameter each for the medium-frequency range (~ 0.45-3 GHz), each equipped with a wide-bandwidth single-pixel feed. The surface accuracy of these dishes will allow a later receiver upgrade to higher frequencies.

As an Advanced Instrumentation Programme for the full SKA, two additional technologies for substantially enhancing the field of view in the 0.5-1 GHz range are under development: aperture arrays with dense spacings, forming an almost circular station 60m across and phased-array feeds for the parabolic dishes.

Technical developments of the SKA project around the world are being coordinated by the SKA Science and Engineering Committee and its executive arm, the SKA Project Office. The technical work itself is funded from national and regional sources, and is being carried out via a series of verification programs. The global coordination is supported by funds from the European Commission under a program called PrepSKA, the Preparatory Phase for SKA, whose primary goals are to provide a costed system design and an implementation plan for the telescope by the end of 2012. A number of SKA Pathfinder telescopes provide examples of low frequency arrays, such as LOFAR (Low Frequency Array) telescope, with its core in the Netherlands, MWA (Murchison Widefield Array) in Australia, PAPER (Precision Array to Probe the Epoch of Reionization), both in South Africa and in Australia, LWA (LongWavelength Array) in the USA. All these low-frequency telescopes are software telescopes steered by electronic phase delays (phased aperture array). Examples of dishes with a single-pixel feed are under development in South Africa (MeerKAT, Karoo Array Telescope KAT-7). Dense aperture arrays comprise up to millions of receiving elements in planar arrays on the ground which can be phased together to point in any direction on the sky. Due to the large reception pattern of the basic elements, the field of view can be up to 250 square degrees. This technology can also be adapted to the focal plane of parabolic dishes. Prototypes of such wide-field cameras are under construction in various countries participating the SKA.

The data from all stations have to be transmitted to a central computer and processed online. Compared to LOFAR - with a data rate of about 150 Gigabits per second and a central processing power of 27 Tflops - the SKA will produce at least one hundred times more data and need much more processing power.

On 25 May 2012 the Members of the SKA Organisation announced that the SKA telescope would be split over Africa and Australia, with a major share of the telescope destined to be built in South Africa. The scheme in Fig.1 shows the distribution of the SKA components across the African and Australian continents (see http://www.ska.ac.za/releases/20120530.php) The detailed design for low and mid frequencies will be ready by 2013. The development of

SKA Phase 1 (about 10% of the total SKA)	
South Africa	**Australia**
South Africa's precursor array - the 64-dish MeerKAT telescope - will be integrated into Phase 1. An additional 190 mid-frequency dish-shaped antennas, each about 15 m high will be built	Australia's 36-dish SKA Pathfinder (ASKAP) will be integrated into Phase 1. An additional 60 mid-frequency dish-shaped antennas, each about 15 m high, will be built, as well as a large number of small, low-frequency antennas - each about 1,5 m high
SKA Phase 2	
South Africa & African partners Telescope will extend to long baselines of 3 000 km or more	**Australia** Telescope extends over a baseline of 200 km
A total of about three thousand mid-frequency dishes, with the highest concentration in the Northern Cape, South Africa, but some dishes in Namibia, Botswana, Zambia, Mozambique, Kenya, Ghana, Madagascar and Mauritius. In addition, a large number of flat mid-frequency antennas, each about 60 m in diameter (number to be determined).	Up to 10 times more of the low-frequency antennas - each about 1,5 m high.

technologies for the high-frequency band (about 3-25GHz) will start in 2013. Construction of the SKA-2 is planned to start in 2016. In the first phase (until 2019) about 10% of the SKA will be erected (SKA-1) (Garrett et al. 2010), with completion of construction at the low and mid frequency bands by about 2023, followed by construction at the high-ν band.

Apart from the many expected technological spin-offs, five main science questions (Key Science Projects) have driven the SKA design (see, e.g., Carilli & Rawlings 2004).

- **Probing the dark ages**. The SKA will use the emission of neutral hydrogen to observe the most distant objects in the Universe and probe the Epoch of Reionization. The energy output from the first stars and AGNs started to heat the neutral gas, forming bubbles of ionized gas as structure emerged. The signatures from this exciting transition phase should still be observable with help of the redshifted HI (21-cm) line. The lowest SKA frequency will allow to detect HI at redshifts of up to 20, to search for the transition from a neutral to an ionized Universe, and hence provide a test of our cosmological model.

- **Galaxy evolution, cosmology, and dark energy**. The expansion of the Universe is currently accelerating, a not understood phenomenon, that is often referred to be produced by dark energy (DE). One important method of distinguishing between the various explanations is to compare the distribution of galaxies at different epochs in the evolution of the Universe to the distribution of matter at the time when the Cosmic Microwave Background (CMB) was formed. Small distortions in the distribution of matter (baryon acoustic oscillations) should persist from the era of CMB formation until today. Tracking if and how these ripples change in size and spacing over cosmic time can then constrain the existing models for DE or indicating the way to new possible ideas. Deep all-sky SKA survey will detect HI emission from Milky Way-like galaxies out to $z \sim 1$. The galaxy observations will be sliced in different redshift (time) intervals and hence reveal a comprehensive picture of the Universe's history. The same data set will provide unique information about the evolution of galaxies, how the hydrogen gas was concentrated to form galaxies, how fast it was transformed into stars, and how much gas did galaxies acquire during their lifetime from intergalactic space. HI survey will simultaneously yield information on the synchrotron radiation intensity of the galaxies which is a measure of their star-formation rate, high-E particle content and magnetic field strength.

- **Tests of General Relativity and detection of gravitational waves**. Pulsars are ideal probes for experiments in the strong gravitational field. The SKA can detect almost all pulsars in the Milky Way (see, e.g., Beck 2011) and several 100 bright pulsars in nearby galaxies. The SKA will search for a radio pulsar orbiting around a black hole, measure time delays in extremely curved space with much higher precision than with laboratory experiments and hence probe the limits of General Relativity. Regular high-precision observations with the SKA of a network of pulsars with periods of milliseconds opens the way to detect gravitational waves with wavelengths of many parsecs, as expected for example from two massive black holes orbiting each other with a period of a few years resulting from galaxy mergers in the early Universe. When such a gravitational wave passes by the Earth, the nearby space-time changes slightly at a frequency of a few nHz. The wave can be detected as apparent systematic delays and advances of the pulsar clocks in particular directions relative to the wave propagation on the sky.

- **Origin and evolution of cosmic magnetism**. Synchrotron radiation and Faraday Rotation (FR) revealed magnetic fields in our Milky Way, nearby spiral galaxies, and galaxy clusters, but little is known about magnetic fields in the intergalactic medium. Furthermore, the origin and evolution of magnetic fields is still unknown. The SKA will measure FRs towards tens of million polarized background sources (mostly AGNs), allowing to derive the magnetic field structures and strengths of the intervening objects, such as, the Milky Way, distant spiral galaxies, clusters of galaxies, and the intergalactic space.

- **The cradle of life**. The SKA will be able to detect the thermal radio emission from centimeter-sized pebbles in protoplanetary systems which are thought to be the first step in assembling Earthlike planets. Biomolecules are also observable in the radio range. Prebiotic chemistry - the formation of the molecular building blocks necessary for the creation of life - occurs in interstellar clouds long before that cloud collapses to form a new solar system. Finally, the SETI (Search for Extra Terrestrial Intelligence) project will use the SKA to find hints of technological activities. Ionospheric radar experiments similar to those on Earth will be detectable out to several kpc, and Arecibo-type radar beams, like those that we use to map our neighbor planets in the solar system, out to ~ 10 kpc.

Two out of the five major science goals have been identified that drive the technical specifications for the first phase (SKA-1):

Origins: Understanding the history and role of neutral hydrogen in the Universe from the dark ages to the present-day.
Fundamental Physics: Detecting and timing binary pulsars and spin-stable millisecond pulsars in order to test theories of gravity.

There are however additional science cases for the SKA dealing with new discoveries and opportunities: the search for Dark matter and the understanding of its nature is certainly an important aspect in the exploration of the unknown with the SKA.

2 Probing the nature of Dark Matter with the SKA

Among the viable competitors for having a cosmologically relevant DM species, the leading candidate is the lightest particle of the minimal supersymmetric extension of the Standard Model (MSSM, see Jungman et al. 1996), plausibly the neutralino χ, with a mass M_χ in the range between a few GeV to a several hundreds of GeV. Information on the nature and physical properties of the neutralino DM can be obtained by studying the astrophysical signals of their interaction/annihilation in the halos of cosmic structures. These signals[a] involve, in the case of a χ DM, emission of gamma-rays, neutrinos, together with the synchrotron and bremsstrahlung radiation and the Inverse Compton Scattering (ICS) of the CMB (and other background) photons by the secondary electrons produced in the DM annihilation process (see Colafrancesco 2010 for a review). Neutralinos which annihilate inside a DM halo produce quarks, leptons, vector bosons and Higgs bosons, depending on their mass and physical composition. Electrons and positrons (hereafter refereed to as electrons for simplicity) are then produced from the decay of the final heavy fermions and bosons. The different composition of the $\chi\chi$ annihilation final state will in general affect the form of the electron spectrum.
Neutral pions produced in $\chi\chi$ annihilation decay promptly in $\pi^0 \to \gamma\gamma$ and generate most of the continuum spectrum at energies $E \gtrsim 1$ GeV.
Secondary electrons are produced through various prompt generation mechanisms and by the decay of charged pions, $\pi^\pm \to \mu^\pm \nu_\mu(\bar{\nu}_\mu)$, with $\mu^\pm \to e^\pm + \bar{\nu}_\mu(\nu_\mu) + \nu_e(\bar{\nu}_e)$ and produce $e^\pm$, muons and neutrinos.
Secondary electrons are subject to spatial diffusion and energy losses. Both spatial diffusion and energy losses contribute to determine the evolution of the source spectrum into the equilibrium spectrum of these particles, *i.e.* the quantity which is used to determine the multi-frequency spectral energy distribution (SED) induced by DM annihilation. The time evolution of the secondary electron spectrum is described by the transport equation:

$$\frac{\partial n_e}{\partial t} = \nabla\left[D\nabla n_e\right] + \frac{\partial}{\partial E}\left[b_e(E)n_e\right] + Q_e(E,r) \;, \tag{1}$$

where $Q_e(E,r)$ is the $e^\pm$ source spectrum, $n_e(E,r)$ is the $e^\pm$ equilibrium spectrum and b_e (given here in units of GeV/s) is the $e^\pm$ energy loss per unit time $b_e = b_{ICS} + b_{synch} + b_{brem} + b_{Coul}$, with $b_{ICS} \approx 2.5 \cdot 10^{-17}(E/GeV)^2$, $b_{synch} \approx 2.54 \cdot 10^{-18} B_\mu^2 (E/GeV)^2$, $b_{brem} \approx 1.51 \cdot 10^{-16}(n_{th}/cm^{-3})\,(\log(\Gamma/n_{th}) + 0.36)$, $b_{Coul} \approx 7 \cdot 10^{-16}(n_{th}/cm^{-3})\,(1 + \log(\Gamma/n_{th})/75)$. Here n_{th} is the ambient gas density and $\Gamma \equiv E/m_e c^2$.
The diffusion coefficient D in eq.(1) sets the amount of spatial diffusion for the secondary electrons: it turns out that diffusion can be neglected in galaxy clusters while it is relevant on galactic and sub-galactic scales (see discussion in Colafrancesco, Profumo & Ullio 2006, 2007). Under the assumption that the population of high-energy $e^\pm$ can be described by a quasi-stationary ($\partial n_e/\partial t \approx 0$) transport equation, the secondary electron spectrum $n_e(E,r)$ reaches

[a]Neutralino DM annihilation produces several types of particle and anti-particle fluxes, whose complete description is not discussed here for the sake of brevity. We refer the interested reader to Colafrancesco, Profumo & Ullio (2006) for the case of galaxy clusters and Colafrancesco, Profumo & Ullio (2007) for the case of dwarf galaxies.

its equilibrium configuration mainly due to synchrotron and ICS losses at energies $E \gtrsim 150$ MeV and to Coulomb losses at lower energies.
Secondary electrons eventually produce radiation by synchrotron in the magnetized atmosphere of cosmic structures, bremsstrahlung with ambient protons and ions, and ICS of CMB (and other background) photons (and hence an SZ effect, Colafrancesco 2010). These secondary particles also produce heating of the ambient gas by Coulomb collisions with the ambient plasma particles.

The Spectral Energy Distribution from DM annihilation

The astrophysical signals of neutralino DM annihilation computed in various DM models can be visible over the entire e.m. spectrum, from radio to γ-ray frequencies (see Fig.2).

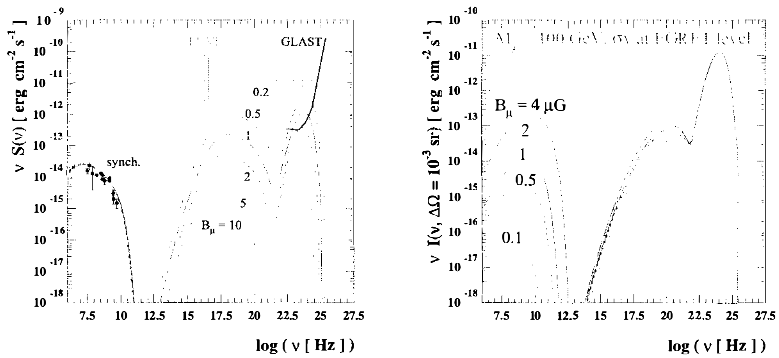

Figure 2: Left. Multi-frequency SED of the Coma cluster for a representative DM modelswith $M_\chi = 40$ GeV ($b\bar{b}$. The halo profile is a NFW profile with $M_{vir} = 0.9\,10^{15} M_\odot h^{-1}$ and $c_{vir} = 10$, with DM subhalo setup as given in Colafrancesco et al. (2006). The scaling of the multi-frequency SED with the value for the mean magnetic field B_μ in Coma is shown. The neutralino pair annihilation rate has been tuned to fit the radio halo data (figure from Colafrancesco et al. 2006). Right. Multi-frequency SED of Draco for a 100 GeV neutralino annihilating into $b\bar{b}$ and for a varying magnetic field strength. The neutralino pair annihilation rate has been tuned to give a gamma-ray signal at the level of the EGRET upper limit (figure from Colafrancesco et al. 2007).

As pointed by Colafrancesco et al. (2006), the relevant physical properties of DM which determine the features of the emitted radiation are the composition of the neutralino, its mass, and the value of the annihilation cross section.
A large amount of efforts have been put in the search for DM indirect signals at gamma-ray energies looking predominantly for two key spectral fetures: the $\pi^0 \to \gamma\gamma$ decay spectral bump, and the direct $\chi\chi \to \gamma\gamma$ annihilation line emission. Results from Fermi -LAT and other Cherenkov gamma-ray experiments are so far not conclusive and hopes are relegated to the next CTA experiment.
Here we alternatively discuss the impact of radio observations towards DM halos on large scales, i.e. from dwarf galaxies to clusters of galaxies.

Radio emission

Secondary $e^\pm$ produced by $\chi\chi$ annihilation can generate synchrotron emission in the magnetized atmosphere of galaxy clusters (as well as galaxies) which could be observed at radio frequencies as a diffuse radio emission (i.e. a radio halo or haze) centered on the DM halo. Observations of cluster radio-halos are, in principle, very effective in constraining the neutralino mass and composition (Colafrancesco & Mele 2001, Colafrancesco et al. 2006), under the hypothesis that DM annihilation provides a major contribution to the radio-halo flux. Under this hypothesis, a pure energy requirement requires that the neutralino mass is bound to be $M_\chi \geq 23.4 \mathrm{GeV}(\nu/GHz)^{1/2}(B/\mu G)^{-1/2}$ in order that the secondary $e^{\pm}$ emit at frequencies $\nu \geq 1$ GHz, as observed in cluster radio halos (see Fig.??). Soft DM models ($b\bar{b}$ with $M_\chi = 40 - 60$ GeV) are able to reproduce both the overall radio-halo spectrum of Coma and the spatial distribution of its surface brightness , while hard DM models (W^+W^- with $M_\chi = 81 - 500$ GeV) are excluded being the radio spectrum too flat to reproduce the Coma data (see Colafrancesco et al. 2006, 2011).

In dwarf galaxies, radio emission is strongly affected by propagation effects. [b] Fig.3 shows that for a propagation set up (Diff. set #1) with a Kolmogorov spectrum ($D \propto E^{1/3} B_\mu^{-1/3}$) there is a depletion of the electron populations with a significant fraction leaving the diffusion region, while for a propagation set up (Diff. set #2) with a steeper spectrum ($D \propto E^{0.6} B_\mu^{-0.6}$) they are more efficiently confined within the diffusion region but still significantly misplaced with respect to the emission region. As a consequence, also the spectral shape of the radio flux of Draco is affected by diffusion effects which produce a steeper spectral slope when the electron populations are more efficiently confined within the diffusion region (i.e. Diff. set #2) with respect to the case (i.e. Diff. set #1) where there is a depletion of the electron populations with a significant fraction leaving the diffusion region (see Colafrancesco et al. 2007 for details).

Predictions for the SKA

Deep observations of radio halos in DM halos are not yet available, and this limits in fact the capabilities of the available radio experiments to set relevant limits on DM models. Our program of deep search for DM radio emission in a sample of local dwarf galaxies has been recently approved with the ATCA observatory and the results of our analysis will be soon available to the community. The limits on χ DM radio signals obtainable with the available radio telescopes will be surpassed by far by the next coming large radio experiments like SKA and its precursor MeerKAT (in South Africa).

For the case of a typical dwarf galaxy, like e.g. Draco, the constraints on a typical DM model that has been already investigated will be at least a factor 100 more constraining than the limits obtained by Fermi-LAT in the gamma-rays (see Fig.3). This is mainly due to the unprecedent sensitivity of the SKA, even considering the decrease in the peak signal of DM-induced radio emission produced by the spatial diffusion effects. These limits scale with the value of the B field in dwarf galaxies following the SED behaviour shown in Fig.2.

Analogous searches for radio emission in large cosmological volumes of DM halos are being planned with the SKA and with the MeerKAT precursor. In this framework the SKA will be also able to set a reliable estimate of the magnetic field in the dwarf galaxy region by using both polarization measurements and Faraday Rotation measurements of background radio sources. In addition, the possibility to have an extended frequency coverage of the SKA in its Phase-2 reaching at least 25 GHz will allow to use both radio synchrotron observations and Inverse Compton observations of the same DM-produced secondary electrons to fully disentangle the magnetic field vs. electron degeneracy present in the synchrotron radio emission and thus determine at the same time both the magnetic field and the DM particle properties contributing

[b] For the diffusion coefficient we consider here the case of a Kolmogorov form $D(E) = D_0/B_\mu^{1/3}\ (E/1\ \mathrm{GeV})^{1/3}$, with $D_0 = 3 \cdot 10^{28}$ cm^2 s^{-1}, in analogy with its value for the Milky Way (here B_μ is the magnetic field in units of μG). The dimension of the diffusion zone is, consistently with the Milky Way picture, about twice the radial size of the luminous component, i.e. $\approx$ 102 arcmin for Draco (Diff. set #1). An extreme diffusion model in which the diffusion coefficient is decreased by two orders of magnitudes down to $D_0 = 3 \cdot 10^{26}$ cm^2 s^{-1} (implying a much smaller scale of uniformity for the magnetic field), and with a steeper scaling in energy, $D(E) = D_0\ (E/1\ \mathrm{GeV})^{-0.6}$ (this is the form sometime assumed for the Milky Way) is considered for comparison (Diff. set #2)

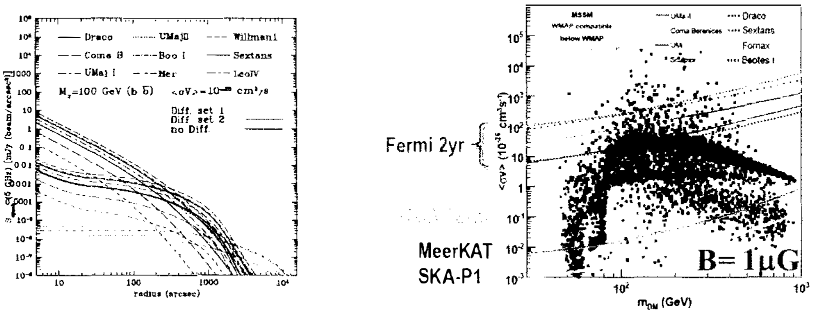

Figure 3: Left. DM-induced radio brightness for a sample of local dwarf galaxies without diffusion (black curves) and with diffusion (blue ad red curves). The SKA senitivity is expected to be $\sim 0.01 - 0.1$ μJy. Right. Limits in the $M_\chi - < \sigma V >$ plane obtainable with SKA-1 compared with the actual best limits obtained by the Fermi-LAT collaboration (2010) (Figures from Colafrancesco & Marchegiani (2012).

to the diffuse radio emission in a DM halo.

This possibility offered by the SKA will further allow to use radio observations of DM halos to probe the distribution of DM halos up to quite high redshifts (see Colafrancesco & Marchegiani 2012) and in principle up to the redshift range in which there is not a major content of baryons in DM halos associated with primordial galaxies (thus excluding the possibility to produce radio emission by other kind of mechanisms, like e.g. cosmic ray emission or HI line emission) but leaving the DM-induced radio emission like the minimum guaranteed source of radio emission (in the DM models we are considering here).

Acknowledgments

S.C. acknowledges support by the South African Research Chairs Initiative of the Department of Science and Technology and National Research Foundation and by the Square Kilometre Array.

References

1. Beck, R. preprint arXiv:1111.5802
2. Carilli C., Rawlings S., 2004, Science with the Square Kilometer Array, New Astr. Rev., 48, Elsevier, Amsterdam
3. Colafrancesco, S. 2010, invited lecture at the 4th Gamow International Conference on Astrophysics & Cosmology After Gamow (9th Gamow Summer School), AIPC, 1206, 5C
4. Colafrancesco, S. & Mele, B. 2001, ApJ, 562, 24
5. Colafrancesco, S., Profumo, S. and Ullio, P. 2006, A&A, 455, 21
6. Colafrancesco, S., Profumo, S. and Ullio, P. 2007, PhRvD, 75, 3513
7. Colafrancesco, S. et al. 2011, A&A, 527, 80
8. Colafrancesco, S. & Marchegiani, P. 2012, in press
9. Fermi-LAT Collaboration 2010, arXiv:1001.4531v1
10. Garrett M.A., Cordes J.M., Deboer D.R., et al., 2010, arXiv:1008.2871
11. Jungman, G., Kamionkowki, M. & Griest, K. 1996, Phys.rep, 267, 195

Intensity Mapping with the 21-cm and Lyman Alpha Lines

J. B. Peterson and Enrique Suarez
Department of Physics, Carnegie Mellon University, 5000 Forbes Avenue, Pittsburgh PA 15217, USA

The 21-cm and Lyman Alpha lines are the dominant line-emission spectral features at opposite ends of the spectrum of hydrogen. Each line can be used to create three dimensional intensity maps of large scale structure. The sky brightness at low redshift due to Lyman Alpha emission is estimated to be 0.4 Jy/Steradian, which is brighter than the zodiacal light foreground.

1 Introduction

This paper is about foregoing individual galaxy detections and, instead, directly mapping cosmic structure using the 21-cm and Lyman alpha (Ly_α) lines. For almost a century the *galaxy* has been the glowing test particle used to trace the cosmic expansion. A galaxy is a aggregation of as much as $\sim 10^{12}$ solar masses of dark matter and gas, concentrated to a density millions of times the cosmic average. This concentration stimulates star formation and the resulting increment of specific intensity on the sky can be detected with optical telescopes at redshifts that now approach eight. Although galaxies will continue to be of great value in tracing cosmic structure, we examine an alternative: using line emission of widely distributed gas as the tracer of cosmic density structure.

Previously, all studies of three dimensional large scale (cosmic-web) structure have used bright galaxies to carry out redshift surveys. In this type of study, individual galaxies are selected from images of the sky, a set of slit or fiber masks are fabricated, spectra are recorded, and each spectrum is examined. If spectral features are detected with sufficient signal to noise, usually about 5, an individual entry is made in a redshift catalog. Modern redshift surveys collect 100,000 or more redshift entries. The study of large scale structure then proceeds by examining the catalog. This is, clearly, a very laborious process, but also an insensitive one. Redshift surveys miss a great deal of information by recording spectra only on a sparse set of site lines and, in addition, the five sigma threshold means many spectra with substantial signal are discarded. In contrast, intensity mapping is a technique that requires no detection threshold, and therefore uses all the available spectral information on each line of sight. This technique also rapidly covers sky by using large beams, or pixels, leading to orders of magnitude improvement of mapping speed compared to traditional galaxy-based survey techniques.

The term Intensity Mapping (IM) is short for 'three dimensional mapping of the specific intensity due to line emission. To use this technique, one assumes the spectral density of the flux received along each line of sight is due to a single emission line (or a template of multiple lines), and the emissivity of the line is linearly related to mass density. Then, the received spectral density can be translated directly to cosmic density just by translating the received frequency to comoving distance, and the brightness to mass density.

One of the main advantages of intensity maps is that they need only 1-10 arc-minute angular resolution, which allows for rapid coverage of large comoving volumes. Such coarse resolution is allowed because much of cosmology focuses on the study of linearly evolving structure. The smallest linear scale is $\sim$ 10 Mpc which subtends a few arcminutes. Assuming a typical average spacing of galaxies around 1 Mpc, voxels resolving 10 Mpc would on average contain $\sim$1000 galaxies. Traditional redshift surveys would record spectra for only the brightest of these galaxies. An intensity mapping survey, on the other hand, includes the emission from all the galaxies.

As mentioned above, intensity mapping assumes that the spectral density of the flux received along each line of sight is due to a single emission line. In the spectrum of a typical spiral galaxy two lines stand out: both the 21-cm line and the Ly_α line (see Figure ??) are much brighter than neighboring continuum emission, and are well separated from other spectral lines. That means that each line can be used to directly create three dimensional maps of cosmic structure, via the intensity mapping technique.

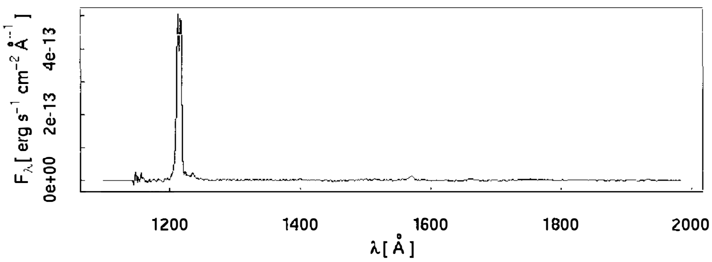

Figure 1: 9 **The line spectrum of the galaxy NGC 0262, at z $\sim$ 0.015.** The Ly_α emission line is very prominent and several orders of magnitude brighter than the small bumps in the spectrum due to the OVI doublet and CIV line. Image obtained from NASA/IPAC Extragalactic Database (NED)

2 21-cm Intensity Mapping

Intensity mapping is a natural extension of previous work in radio astronomy. Throughout the history of radio astronomy, instruments have been optimized either for brightness sensitivity (single dishes) or resolution (dilute aperture synthesis arrays), but not both. This limitation was due to the lack of signal processing computational power needed to allow focal plane or synthesis arrays with more than about 50 elements. Now, with the Moore's Law reduction of processing cost, 512 element systems are under construction, and 10,000 element arrays will be possible within a few years. This increased signal-processing bandwidth makes high-sensitivity 21-cm intensity mapping possible.

Several authors [? ? ? ? ?] have developed the idea of 21-cm intensity mapping at redshifts below six. At these redshifts, cosmic UV flux is high enough to keep most of the volume of intergalactic space ionized. Then, neutral gas can only survive in dense self shielded regions such as spiral galaxies. Thus, at low redshifts, with gas localized to galaxies, it is tempting to pursue the traditional redshift survey using the 21-cm line. Research teams using the Parkes and Arecibo telescopes have carried out surveys that detect the galaxies individually. Nevertheless, despite years of telescope time at large telescopes, these surveys do not extend beyond redshift

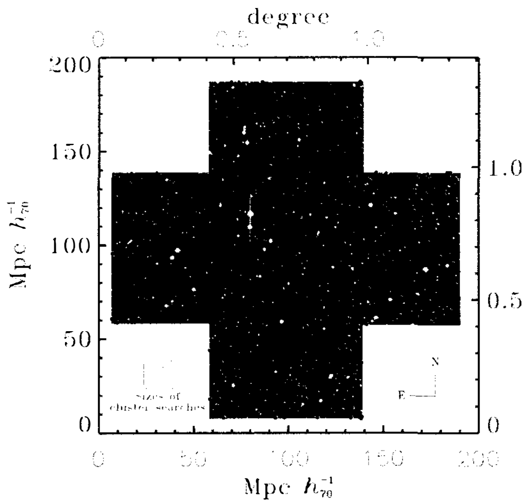

Figure 2: 9 **Lyman Alpha Emitters at redshift** $z = 5.9$ Red dots show the locations of Lyman Alpha Emitter candidates detected in narrowband-wideband image ratios. Large Scale Structure is apparent in the form of clusters and voids in the LAE locations. Plot from Ouchi et *al.* (2005) [?], adapted by Kevin Bandura

$z \geq 0.1$. One reason for this redshift limit is the 21-cm flux from an individual galaxy declines as $z^{-2}[1 + z]^{-2}$. In contrast, the sky brightness contrast due to the 21-cm line declines only as $[1 + z]^{-1/2}$, making intensity mapping the productive option as the redshift increases. At higher redshift, before reionization at $z \sim 10$, neutral gas clouds extend to sizes exceeding 1 Mpc, and 21-cm intensity mapping is a natural choice. In fact, the world-wide suite of 21-cm Epoch-of-Reionization telescopes [?] are all designed for intensity mapping.

Moving well beyond the redshift limit of traditional redshift surveys, Chang *etal.* [?] have used intensity mapping to detect emission of the 21-cm line at redshift $z = 0.8$, using the Green Bank Telescope. By stacking 21-cm emission from the regions surrounding 5000 bright galaxies in the optical DEEP2 redshift survey, they detected the 21-cm signal in just 12 hours of telescope time. An important part of this accomplishment is detection of 21-cm sky structure five orders of magnitude below the synchrotron glow of the Galaxy.

While 21-cm intensity mapping seems well on its way to becoming widely accepted, there are other spectral lines from hydrogen that are currently being used to detect galaxies at high redshift, and these lines might be useful for directly mapping linearly evolving structure. For example, in the ultra-violet end of the spectrum, Lyman Alpha (Ly_α; $\lambda_e = 1215\ \AA$), has not yet been used for intensity mapping. We will discuss below why it is also a worthy candidate.

3 Lyman Alpha Intensity Mapping

Figure ?? shows the positions of over one hundred Lyman Alpha Emitter (LAE) candidates detected in deep mosaic observations using Subaru/Suprimecam. These candidates were selected by finding five-sigma bright outliers in narrowband versus broadband flux. The narrow band filter was tuned to Ly_α redshifted by $z = 5.9$. In follow-up of similar observations [?], over 200 candidates were later confirmed as Ly_α-bright galaxies. Large scale structure is apparent in figure ?? (and confirmed statistically [?]), since it contains several tight concentrations of sources and voids. The Subaru LAE image gives confidence that Ly_α intensity mapping, which amounts to taking many narrowband wide-field images simultaneously, can be used to rapidly map cosmic structure.

As we suggested above, intensity mapping is much more efficient than the narrowband technique used for traditional LAE surveys. Rather than restricting the spectral range with a single narrowband filter, which discards $\sim$ 99 % of the observed spectrum, intensity mapping observations would collect a spectrum across a broad band for every pixel. The redshift slice shown by the red dots in Figure ?? and hundreds of other slices could be imaged simultaneously in each exposure, allowing a factor $\sim$ 100 in speed increase.

Unlike radio astronomy, optical/UV astronomy makes use of detector arrays with millions of simultaneously operating detectors. In addition, even small telescope apertures offer arc-second angular resolution. Therefore, astronomers operating at optical/UV wavelengths are used to detecting galaxies individually, and all of their equipment is designed to do so. Thus, the thought of abandoning individual galaxy detections in favor of improving mapping speed and bandwidth, may seem like a step backward. However, we argue below that the speed advantages are substantial and, by calibrating the IM technique using redshift surveys of small fields, one can gain confidence that these types of surveys will successfully map cosmic structure.

An additional efficiency factor in favor of intensity mapping comes from the high-pass filtering used to make the individual LAE detections using the narrowband images such as figure ??. At these high redshifts, this high-pass filtering is likely discarding substantial flux since Ly_α photons tend to diffuse by resonantly scattering off of neutral hydrogen. Clear evidence of this scattering comes from the study of quasar spectra. By redshift $z \sim 5.9$, most quasars spectra show substantial Gunn-Peterson decrements. However, photons taken out of the line of sight in the Gunn-Peterson effect are typically not absorbed, but are simply scattered to other lines of sight and surely present in the form of low surface-brightness extended halos around bright sources. Such halos would be discarded by high-pass filtering, and therefore would often be missed. However, in a few images extended Ly_α emission has recently been noticed and described as Lyman Alpha Blobs [?,?].

Diffuse emission is a subject where simulations are more advanced than observations. Zheng *etal.* [?] estimate that the random walk distances for Ly_α photons can be as large as 1 Mpc before the photons redshift out of the resonance. These simulations indicate that ratio of photon counts in the diffuse (arcminute-sized) halo compared to central (arcsecond-sized) LAE galaxy may be as high as 100. If this is correct, intensity mapping could capture 100 photons for each that survives the high pass filter of the traditional survey.

Returning to the Subaru image, figure ??, the Ly_α bright galaxies that meet the five sigma selection criterion to produce a red dot are in the high luminosity region of the luminosity function. It is important to remember that for each red dot there are surely hundreds of nearby dimmer LAE sources. The red dots are like tips of icebergs, each marking the position of a great mass of unseen sources.

We have described above several types of mapping-speed efficiency factor that favor intensity mapping versus the narrowband imaging technique. We now collect these to attempt a rough estimate of the total mapping-speed advantage. Counting orders of magnitude, for redshift $z \sim$ 6: a) recording spectra versus narrowband filtering–2, b) the use LAE flux from sources below the five sigma detection threshold–1, c) the use of the photons in resonant scattering halos–1-2. d) the use of arc-minute size pixels–2. Intensity mapping could therefore be six to seven orders of magnitude more efficient than the narrowband imaging technique. This means that expensive 10 meter class instruments like Subaru are not needed for an intensity mapping survey. Much smaller apertures can be considered.

The required aperture for a Ly_α intensity mapping telescope could be less than one meter, and this is small enough that the telescope can be placed on balloon-borne platforms or

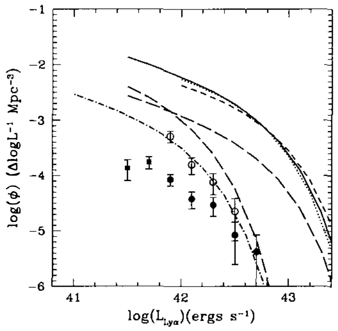

Figure 3: 9 **Ly$_\alpha$ luminosity functions.** Space density of Ly$_\alpha$ emitting galaxies ($0.2 < z < 0.35$) per $\log L_{Ly\alpha}$ both as measured (*filled circles*, all five fields; *filled squares*, CDFS, GROTH, and NGPDWS fields) and with an evaluation accounting for incompleteness (*open circles*). The lines represent comparisons with Ly$_\alpha$ LFs at high redshifts. *Solid line:* van Breukelen et al. (2005) [?] at $2.3 < z < 4.6$. *Dotted line*: Gronwall et al. (2007) [?] at $z \sim 3.1$. *Short – dashed line*: Ouchi et al. (2008) [?] at $z \sim 3.1$. The *dot – dashed* LF is derived from a least-squares fit on the 5 brightest points. The *long – dashed* lines show the impact of a factor of 5 decrease of L* (the nearest curve to the data points) or Φ^* in the LF of van Breukelen et al. (2005); this factor corresponds to the decrease of the UV LD from $z \sim 3$ to $z \sim 0.3$. Figure and caption taken from Deharveng, J-M. et al. (2008) [?], which analyzed data from GALEX

spacecraft. This opens the possibility that redshift ranges that are largely absorbed by the atmosphere, $0 \leq z \leq 3$, and $z > 10$ could be observed. At the low redshift end, an important target of an intensity mapping survey would be the detection of Baryon Acoustic Oscillation features. However, note that, at low redshift, LAEs are typically dimmer than at high redshift, and the resonant scattering halos are likely absent at low redshift. In turn, this would make the observations more challenging than at redshifts $z \geq 6$.

While we know of no research group that has so far conducted an intensity mapping Ly$_\alpha$ survey, several teams have estimated the luminosity functions (LF) of Lyman Alpha Emitters at various redshifts. For example, Deharveng *et al.* (2008) [?] constructed Figure **??**, which compares their estimate of the LF of LAEs to those of other researchers. The low-redshift measurements were made using the GALEX observatory. At higher redshift, the detections were made using ground-based telescopes. In either case, as described above, spatial and spectral high pass filters are used, and only the bright end of the luminosity function is detected. Unfortunately, then, the bulk of Ly$_\alpha$ emission may be missing from these luminosity functions. However, these LFs are the best measurements available of Ly$_\alpha$ source strengths, so we proceed to use them to calculate the sky brightness due to Ly$_\alpha$.

4 Ly$_\alpha$ Sky brightness

Integrating the GALEX luminosity function yeilds

$$\frac{dP}{dV} = 10^{39}\ erg\ s^{-1}\ Mpc^{-3} \tag{1}$$

which translated to Ly$_\alpha$ brightness

$$I_\nu = \left(4 \times 10^{-27}\right) \frac{1}{\left(\Omega_\Lambda + \Omega_m \left(1+z\right)^3\right)^{1/2}}\ W\ m^{-2}\ sr^{-1} \tag{2}$$

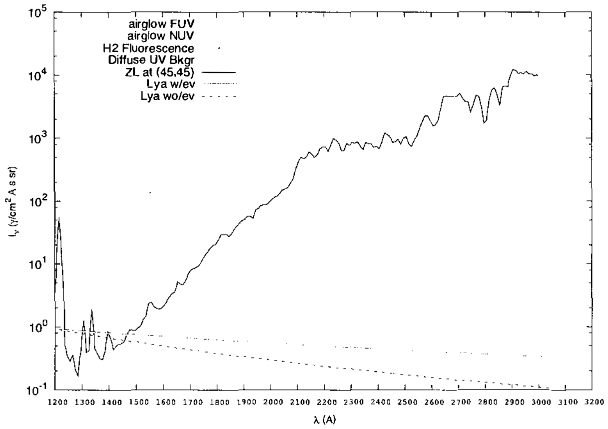

Figure 4: 9 **The Ly$_\alpha$ Sky Brightness.** The red curve show the estimated brightness due to Ly$_\alpha$ emission. Here modest luminosity function evolution has been assumed. The dashed black curve assumes no evolution. Additional sources of sky brightness include: Ariglow, H_2 fluorescence, Diffuse UV ?; the plotted values for these sources represent the maximum amount of emission detected by GALEX. Zodiacal light ?, is estimated for the direction (45°, 45°) in ecliptic coordinates, measured from the sun.

The Ly$_\alpha$ brightness is compared to other sources of sky brightness in figure ??. The zodiacal light (ZL) in the UV region is due to the sunlight scattered by interplanetary dust. The ZL brightness is a smooth function angle of observation with respect to the sun, and the ZL spectrum closely matches the solar spectrum. We estimate the ZL brightness using the solar spectrum of Leinert et *al.* (1997) ?. At low redshift, the brightness due to Ly$_\alpha$ actually exceeds the (ZL) foreground glow. As redshift increases, the zodiacal light exceeds the Ly$_\alpha$ glow, but the ZL is spatially very smooth and can likely be filtered or modeled out very precisely. Additionally, we also have to worry about the diffuse UV background emission, which in both *GALEX* bands, FUV and NUV, was observed ? to be 500 - 800 $\gamma\ cm^{-2}\ s^{-1}\AA^{-1}sr^{-1}$. The source of this emission is the subject of controversy, and some of it may be due to Ly$_\alpha$. We also plot the upper limit to the H_2 fluorescence emission, from data collected by *GALEX* which constrain the flux to the range 0 - 250 $\gamma\ cm^{-2}\ s^{-1}\AA^{-1}sr^{-1}$ in the FUV, with no contribution in the NUV ?. For balloon-borne telescopes or those in low earth orbit another competing source is Airglow, which is produced in the Ionosphere's E and F layers, at altitudes of $\sim$ 90 km, and above 150 km, respectively, as well as a contribution from the Geocorona. Observations by *GALEX* indicate Airglow emission to be 85 $\gamma\ cm^{-2}\ s^{-1}\AA^{-1}sr^{-1}$?. These are all the competing foregrounds we know of and the foreground brightness rises to exceed the Ly$_\alpha$ brightness by 10^4 at the high end of the plotted redshift range. This compares well to 21-cm, where the galactic synchrotron brightness is a factor $\sim 10^4$ brighter than the 21-cm brightness. The foregrounds should be easier to subtract for Ly$_\alpha$, since ZL is very smooth on the sky and sun-synchronous.

The Ly$_\alpha$ brightness structure can be estimated by assuming the Ly$_\alpha$ emission traces density. The usual bias factor $b = \frac{\delta I/I}{\delta\rho/\rho}$ will be needed to translate brightness structure to density structure and estimates of b will no doubt be the subject of lengthy discussion.

5 Techniques for Optical/UV Intensity Mapping.

While cosmological intensity mapping in the UV/optical has not been attempted, optical intensity maps of the Milky Way have been made using the Wisconsin H-alpha Mapper (WHAM).

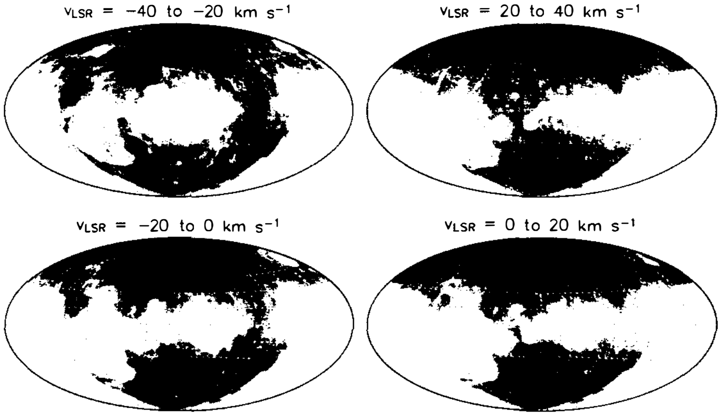

Figure 5: 9 **Intensity maps of the H_α emission in the Milky Way** Images made using the Wisconsin H-alpha Mapper, which uses a 0.6 m aperture. From Matsuda et *al.* (2004) ?

This system uses a tunable Fabre-Perot narrowband filter to select H_α emission at a variety of doppler shifts within the Galactic velocity profile. Images from WHAM ? are shown in Figure ??. The telescope aperture is only 0.6 m, but by using a wide field, three degrees, the instrument can rapidly map the volume brightness of the line. These images are rather encouraging, given that they show what is possible with a very small telescope specifically designed for intensity mapping. Furthermore, the images shown have angular resolution three arcminutes, similar to that needed for the study of cosmological large scale structure. The choice of a tunable narrow filter makes sense for this instrument since it is designed primarily to observe in the rather narrow velocity range of the Galaxy. For a survey of cosmological large scale structure, one would not want a narrow filter but instead would like to cover a much wider frequency range in each exposure.

For redshifts $0 \leq z \leq 3$, Ly_α observations must be carried out above the atmosphere, but at these short wavelengths optical elements have substantial attenuation. Optical system must be very simple at these wavelengths. One example of an instrument that may be capable of making Ly_α intensity maps is the GALEX spacecraft instrument, which is equipped with a slit-less spectroscopy mode using a Grism. It may be possible to use the GALEX grism, but also rotate the spacecraft through a set of paralactic angles. Each image is a projection of the intensity map, with the projection direction precessing along a cone. An inverse Radon transform of this set of observations should to allow tomography, essentially a CAT-scan of cosmic structure.

At optical wavelengths, Ly_α redshifts $3 \leq z \leq 7$, very high mapping speed can be achieved using an integral field spectrometer. Here, each lens of a microlens lens array defines a large pixel on the sky and collects the light from that pixel into an optical fiber. These fibers are then routed to populate the slit of a spectrometer allowing a fast wide field, three dimensional observation.

For redshift $7 \leq z \leq 9$, the late stages of reionization, Sliva *et al.* ? have thoroughly studied Ly_α IM and suggest that a sub-orbital or orbital instrument may be useful at these redshifts. Aiming at redshift $z \sim 15$, The Low Resolution Spectrometer on the CIBER sounding-rocket instrument produces spectra of 1280 pixels in each observation. It is impressive that an instrument with a 5 cm aperture, observing for just 8 minutes in an intensity mapping mode, has the potential to detect cosmological large scale structure. At redshift $z \sim 15$ stars are likely shrouded in neutral gas, so the Lyman-limit edge may produce more sky structure than the Ly_α line.

6 Line Confusion

A significant difference between 21-cm IM and Ly_α IM is the issue of linc confusion. The 21cm line is the strong line in the emission spectrum of a galaxy with the *longest* wavelength. While there are Rydberg lines of longer wavelength, these are much weaker than 21-cm. Because there is no longer-wavelength line to cause confusion as the redshift increases, some authors contemplate 21-cm intensity mapping at redshifts as high as 50. In contrast, Ly_α dominates the opposite cxtreme end of the spectrum of the hydrogen atom. Now, thcre is potential for confusion with other lines such as the rest of the Lyman series, H-alpha, and the lines of other species. However, the other Lyman series lines are at shorter wavelength, and are much weaker than Ly_α, validating the assumption that a single line dominates sky brightness. In deep intensity maps, though, the other Lyman series lines may be detectable by cross correlation at the appropriate lag in the spectrum. In this case, rathcr than causing confusion, the rest of the Lyman series serves to confirm the Ly_α structure. At redshift $z = 4.4$ Ly_α crosses the rest frame wavelength of H-alpha. Longward of this wavelength ($\lambda = 656$ nm), the two intensity maps will overlap in the data cube. However, most of the LAE candidates in narrowband images seem to be Ly_α rather than H_α sources, so the assumption of Ly_α dominance should be accurate.

References

1. Battye, R. A., Davies, R. D. , & Weller, J. 2004, MNRAS, 355, 1339
2. Sethi, S. K. 2005, MNRAS, 363, 830
3. Wyithe, S. B. & Loeb, A. 2009, MNRAS, 397, 1926W
4. Chang, T.-C., Pen, U.-L., Peterson, J. B., & McDonald, P. 2008, Phys. Rev. Lett., 100, 091303
5. Chang, T.-C., Pen, U.-L., Bandura, K., & Peterson, J. B. 2010, Nature, 466, 463
6. Peterson, J. B. *et al.* 2009, arXiv:0902.3091v1
7. Zheng, Z. et*al*., 2011, ApJ, 739, 62
8. Morales, M. F. & Wyithc, 2009, arXiv:0910.3010v1
9. Gong, Y., Cooray, A., Silva, M., ct al. 2012, ApJ, 745, 49
10. Gong, Y., Cooray, A., Silva, M. B., Santos, M. G., & Lubin, P. 2011, ApJ, 728, L46
11. Lidz, A., Furlanetto, S. R., Oh, S. P., et al. 2011, ApJ, 741, 70
12. Visbal, E., & Loeb, A. 2010, JCAP, 11, 16
13. Ouchi, M. et *al*., 2005, ApJ, 620, L1L4
14. Ouchi, M. ct *al*., 2010, ApJ, 713, 869
15. Silva, M.,Santos, M. G., Gong, Y., & Cooray, A. 2012, arXiv:1205.1493v1
16. Deharveng, J-M. et *al*., 2008, ApJ, 680, 1072D
17. van Breukelen, C., Jarvis, M. J., & Venemans, B. P. 2005, MNRAS, 359, 895
18. Gronwall, C., et *al*. 2007, ApJ, 667, 79
19. Ouchi, M., et *al*. 2008, ApJS, 176, 301
20. Steidel, C. C., Bogosavljevic, M., Shapley, A. E., et al. 2011, ApJ, 736, 160
21. L. M. Hafner *et al*, ApJ Supp. , 2003, 405
22. Matsuda et al., 2004, AJ, 128, 569
23. Steidel et al. 2000, ApJ., 532, 170.
24. Sujatha, N. V., Murthy, J., Karnataki, A., Henry, R. C., Bianchi, L., 2009, ApJ, 692, 1333-1338
25. Leinert, Ch. et *al*., 1998, Astron. Astrophys. Suppl. Ser. 127, 1-99

BINGO: a single dish approach to 21cm intensity mapping

R.A. Battye[1], M.L. Brown[1], I.W.A. Browne[1], R.J. Davis[1], P. Dewdney[2], C. Dickinson[1], G. Heron[1], B. Maffei[1], A. Pourtsidou[1,3], P.N. Wilkinson[1]

[1] *Jodrell Bank Centre for Astrophysics, University of Manchester, Oxford Road, Manchester, M13 9PL.*

[2] *SKA Organization, Alan Turing Building, Manchester, M13 9PL.*

[3] *Dipartimento di Astronomia, Università di Bologna, via Ranzani 1, I-40127 Bologna, Italy.*

BINGO is a concept for performing a 21cm intensity mapping survey using a single dish telescope. We briefly discuss the idea of intensity mapping and go on to define our single dish concept. This involves a ~ 30 m dish with an array of ~ 50 feed horns placed ~ 75 m above the dish using a pseudo-correlation detection system based on room temperature LNAs and one of the celestial poles as references. We discuss how such an array operating between 960 and 1260 MHz could be used to measure the acoustic scale to 2.4% over the redshift range $0.13 < z < 0.48$ in around 1 year of on-source integration time by performing a 10 deg$\times$200 deg drift scan survey with a resolution of $\sim 2/3$ deg.

1 21cm intensity mapping

The studies of dark energy [1] and modified gravity [2] are now a major area of research using a plethora of observational tests [3]. The baryonic acoustic oscillation (BAO) approach [4] is now well established. Originally applied to the SDSS LRG DR3 survey [5] subsequent detections have been reported by a number of groups analysing data from 2dF [6], SDSS DR7 [7], WiggleZ [8], 6dF [9]and BOSS [10] surveys. These surveys detect galaxies in the optical and construct a galaxy density contrast whose 2-point correlation function, or equivalent power spectrum, is then estimated. Under the assumption of simple biasing between the galaxy density field and that of the underlying matter density, one can infer the acoustic scale.

Galaxy redshifts obtained using the 21cm line of neutral hydrogen can also be used to perform redshift surveys [11,12] but this typically requires very large collecting areas to do this at high redshift - this was the original motivation for the SKA [14]. Radio telescopes with apertures ~ 100 m have sufficient surface brightness sensitivity to detect HI at high redshift if they have a filled or close to filled aperture, but they will preferentially detect objects of angular size comparable to their resolution [13] which will typically be clusters. The idea of 21cm intensity mapping [15,16,17,18,19,20] is to use the full intensity field $T(f,\theta,\phi)$ and measure the power spectrum directly, without ever detecting the individual galaxies. The average signal is expected to be $\sim 100\,\mu$K on degree scales with the band width of $\sim$ few MHz, with order one fluctuations. This will require exquisite subtraction of receiver bandpasses and the continuum emission from our own Galaxy and extragalactic sources. The latter of these two should be possible using the fact that the continuum emission should have a relatively smooth spectral signature relative the 21cm emission and designing a telescope to mitigate the former is the main topic of this paper.

Table 1: Summary of proposed BINGO telescope parameters

Main reflector diameter	30 m
Illuminated diameter	25 m
Resolution (at 30 cm)	~40 arcmin
Number of feeds	50
Instantaneous field of view	10 deg × 2 deg
Frequency range	960 MHz to 1260 MHz
Number of frequency channels	≥300

2 BINGO concept

A detailed analysis of the signal and possible observing strategies [21] suggests that a survey of 2000 $\deg^2$ with a resolution of 2/3 deg in the frequency band 960 – 1260 MHz is close to optimal in terms of measurement of the acoustic scale. We propose a static single dish telescope to achieve this by a drift scan survey at constant declination. A key issue is the size of the smallest dimension, $\theta_{\rm min}$, of the survey area since power spectrum, $P(k)$ needs to be binned with $\Delta k > \pi/\theta_{\rm min}r(z)$ where $r(z)$ is the coordinate distance to redshift z, so that the bandpowers are uncorrelated, but this bin width needs to be a factor of around 3 times the acoustic scale, $k_{\rm A} \approx (150\,{\rm Mpc})^{-1}$ since otherwise the BAOs would be washed out. This restricts $\theta_{\rm min} > 10$ deg for $z \approx 0.3$. If the drift scan is at moderate latitudes then the largest dimension of the survey will be ≈ 200 deg and hence a survey of $\approx 2000\,\deg^2$ will be possible with around 50 feedhorns in 3 rows giving an instantaneous field-of-view of 10 deg × 2 deg.

In order to achieve the desired resolution the feedhorns will need to illuminate an aperture of ≈ 25 m and the total dish size is proposed to be ≈ 30 m in order to reduce the sidelobe levels. It would be difficult to accommodate such a large feedhorn array in a standard focal arrangement since the focal area will be too small. Therefore, we propose to suspend the feedhorns > 75 m above the dish on a boom which is anchored to a cliff, or other steep slope. The basic arrangement is illustrated schematically in the in the left-hand panel of Fig. 1. This should allow a focal plane sufficiently large to allow 50 feedhorns in 3 rows to allow $\theta_{\rm min} > 10$ deg. The parameters of the proposed system are presented in table 1

We will use a pseudo-correlation receiver system in order to control $1/f$ fluctuations [23]. A block diagram for such a system is presented in the right-hand panel of Fig. 1. It uses hybrids to difference and add signals either side of the primary amplification. If the hybrids are perfect and the inputs are perfectly balanced then the $1/f$ noise due to gain fluctuations is completely removed in the difference spectrum. The receiver system will operate between 960 and 1260 MHz in order to avoid the mobile phone band between 900 and 960 MHz and will use room temperature LNAs with a conservative system temperature of $T_{\rm sys} = 50\,{\rm K}$. The reference beam of each pseudo-correlation system will be pointed at one of the celestial poles without going via the main dish in order to provide a stable, low resolution reference with the same spectrum as the sky.

3 Projected science reach

The projected error on a power spectrum measurement average over a radial bin in k-space of width Δk is

$$\frac{\sigma_P}{P} = \sqrt{2\frac{(2\pi)^3}{V_{\rm sur}}\frac{1}{4\pi k^2\Delta k}}\left(1 + \frac{\sigma_{\rm pix}^2 V_{\rm pix}}{[\bar{T}(z)]^2 W(k)^2 P}\right), \qquad (1)$$

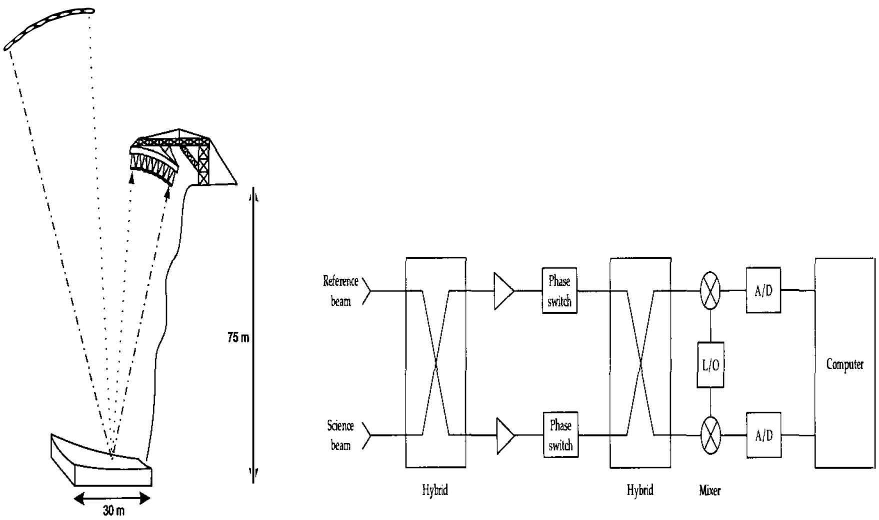

Figure 1: On the left schematic of the proposed design of the BINGO telescope. There will be an under-illuminated $\sim 30\,\mathrm{m}$ static parabolic reflector at the bottom of a cliff which is around $\sim 75\,\mathrm{m}$ high. A boom will be placed at the top of a cliff on which there is a receiver system of ~ 50 feed-horns. On the right a block diagram for the receiver chain for the proposed pseudo-correlation receiver system. The reference beam will point toward one of the celestial poles.

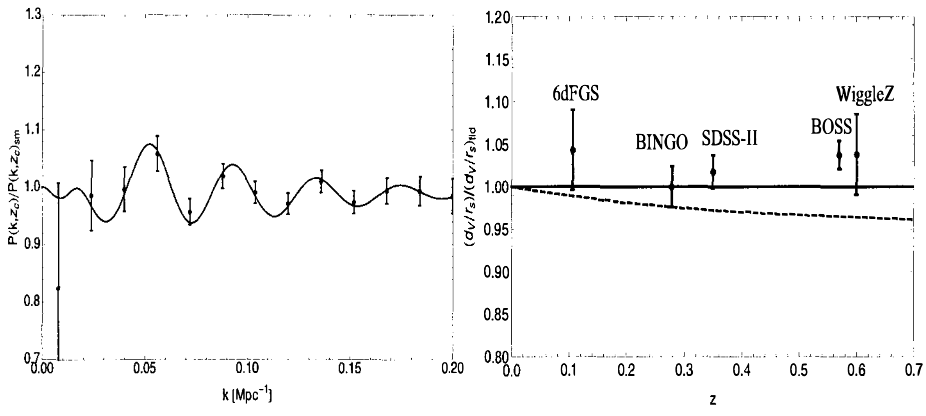

Figure 2: On the left projected errors on the power spectrum (divided by a smooth power spectrum) expected for the survey described in the text. We have used $\Delta k = 0.016\,\mathrm{Mpc}^{-1}$. The projected errors would lead to a measurement of the acoustic scale with a percentage fractional error of 2.4%. On the right, projected constraints on the residual Hubble diagram for the volume averaged distance, $d_V(z)$ from a fiducial model. Included also are the actual measurements made by 6dF, SDSS-II, BOSS and WiggleZ. The shaded region represents indicates the range of d_V allowed by the 1σ constraint $\Omega_m h^2$ from WMAP7. The dotted line is the prediction for $w = -0.84$.

where $V_{\rm sur}$ is the survey volume, $\sigma_{\rm pix}$ is the pixel noise over a nominal bandwidth of $\Delta f = 1\,{\rm MHz}$, $W(k)$ is the angular window function and $\bar{T}(z)$ is the average temperature

$$\bar{T}(z) = 44\,\mu{\rm K}\left(\frac{\Omega_{\rm HI}(z)h}{2.45\times 10^{-4}}\right)\frac{(1+z)^2}{E(z)}\,. \tag{2}$$

$\Omega_{\rm HI}$ is the HI density relative to the present day critical density and $E(z) = H(z)/H_0$. We have computed the projected errors on the measurement of the power spectrum at $z = 0.28$ for 1 year of on-source integration (which we would expect to be possible in around 2 years of observing), corresponding to the central redshift of the proposed survey, and they are presented on the power spectrum relative to a smooth spectrum in the left-hand panel of Fig. 2. It is clear from this that it should be possible to measure the acoustic scale. We note that these estimates ignore the possible effects of foreground removal.

Such a measurement will allow the acoustic scale to be measured to $\delta k_{\rm A}/k_{\rm A} \approx 0.024$. The science reach of such a measurement is illustrated in the right-hand panel of Fig. 2 where it is compared to the recent measurements. It is clear that this would lead to interesting constraints on the cosmological parameters. Assuming that the dark energy equation of state parameter, $w = P/\rho$, is constant and all the other cosmological parameters are constant, this would lead to $\delta w/w \approx 0.16$.

References

1. E. J. Copeland, M. Sami and S. Tsujikawa, Int. Journal. Mod. Phys. **D15**, 1753 (2006)
2. T. Clifton et al. (2011), `arXiv:1106.2476`
3. D.H. Weinberg et al. (2012), `arXiv:1201.2434`
4. D. J. Eisenstein (2003) in Dey, A. (Ed), Wide-field Multi Object Spectroscopy, ASP Conference Series
5. D. J. Eisenstein et al. Astrophys. J. **633**, 2 (2005)
6. S. Cole et al., Mon. Not. Roy. Astro. Soc. **362**, 505 (2005)
7. W. J. Percival, et al. Mon. Not. Roy. Astro. Soc. **401**, 2148 (2010)
8. C. A. Blake et al. (2011), `arXiv:1105.2862`
9. F. Beutler et al., Mon. Not. Roy. Astro. Soc. **416**, 3017 (2011)
10. L. Anderson et al. (2012), `arXiv:1203.6594`
11. F. B. Abdalla and S. Rawlings, Mon. Not. Roy. Astro. Soc. **360**, 27 (2005)
12. A. R. Duffy et al., Mon. Not. Roy. Astro. Soc. **383**, 150 (2008)
13. R. A. Battye, R. D. Davies and J. Weller, Mon. Not. Roy. Astro. Soc. **355**, 1339 (2005)
14. P. N. Wilkinson (1991) in *Proceedings of the* 131^{st} *IAU Colloquium, ASP Conference Series*, 19, 428
15. J. B. Peterson, K. Bandura and U.-L. Pen, (2006) in *proceedings of 41st Recontres de Moriond: Contents and Structure of the Universe*
16. A. Loeb and J.S.B Wyithe, Phys. Rev. Lett. **100**, 161301 (2008)
17. T. -C. Chang, U. L. Pen, J.B. Peterson and P. McDonald, Phys. Rev. Lett. **100**, 091303 (2008)
18. U.-L. Pen et al., Mon Not. Roy. Astro. Soc. **394**, L6 (2009)
19. T. -C. Chang, U. L. Pen, K. Bandura and J.B. Peterson Nature **466**, 463 (2010)
20. J.B. Peterson and E. Suarez (2012), `arXiv:1206.0143`, published in this volume
21. R.A. Battye et al. (2012), `to appear`
22. H.-J. Seo et al., Astrophys. J. **721**, 164 (2010)
23. K. Rohlfs and T. L. Wilson (2004), Tools of radio astronomy, Springer

LYMAN-α FOREST: BAO and neutrino mass

J.-M. LE GOFF
CEA-Saclay irfu/SPP, 91191 gif-sur-Yvette, France

The light from distant quasars is absorbed by intervening hydrogen clouds. The resulting absorption lines form the so-called Lyman-α forest, probing the density of the intergalactic medium along the lines of sight. The 3D correlation function of the absorption exhibits a peak around 100 Mpc/h comoving due to baryonic acoustic oscillations (BAO). This BAO scale is a standard ruler and its measurement constrains the dark energy equation of state. On the other hand Fourier transform of individual quasar spectra provides the 1D power-spectrum up to high k and constrains the sum of the neutrino masses. Preliminary results from the SDSS III / BOSS collaboration are presented.

1 introduction

Quasars can be used as backlights to illuminate the intergalactic medium (IGM). The IGM is made mostly of ionized hydrogen with a small fraction of neutral hydrogen (H1 in spectroscopist notation) in its ground state ($n = 1$). Fig. 1 presents an example of a quasar spectrum. This spectrum exhibits several emission lines, like Civ, and Hydrogen Lyman-α ($n = 2 \rightarrow n = 1$) and Lyman-β ($3 \rightarrow 1$). The Lyman-α peak is redshifted and appears at $(1 + z_{QSO}) \times 1216\AA$. Many absorption lines are present on the left of this peak. A line at wavelength λ corresponds to Lyman-α absorption ($1 \rightarrow 2$) by intervening H1 at a redshift such that $(1 + z) \times 1216 = \lambda$. On the right of the Lyman-β peak we have both Lyman-α and Lyman-β absorption lines. The Lyman-α analysis can therefore be performed in the region lying between the Lyman-α and Lyman-β peaks, the so-called Lyman-α forest. High z quasars, typically $z > 2$, are required for the Lyman-α forest to be redshifted in the optical window and observed from the ground. At $z = 2.5$ the Lyman-α forest corresponds to a range, $\Delta z \approx 0.3$, and its length is about 350 Mpc/h.

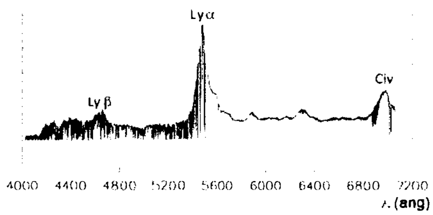

Figure 1: A QSO spectrum with high resolution and high signal-to-noise ratio.

The transmitted flux fraction F is the ratio of the actual flux to the flux in the unabsorbed quasar spectrum. In the absence of noise, $0 < F < 1$ and $F = \exp(-\tau)$, where τ is the optical depth of the absorber(H1), proportional to the square of the total hydrogen density, which is itself related to the baryon density. Finally, the power spectra of F and dark matter are related through $P_F(k) = b^2 P_{CDM}(k)$, where b is a bias factor.

2 BAO in 3D analysis

2.1 BAO

Fig. 2 depicts the evolution a single primordial overdensity. In the early Universe filled with dark matter, neutrinos, hadrons (mainly protons), electrons and photons, the electrons and baryons form a plasma coupled to the photons. Radiative pressure means that the overdensity is also an overpressure in the plasma. Therefore the plasma and photon overdensities propagate together like an acoustic wave, while the dark matter overdensity hardly moves. At $z \approx 1100$, the electrons recombine with the hadrons and the resulting neutral atoms decouple from the photons. The radiative pressure and the acoustic wave velocity drop to zero. The relativistic photon overdensity then spreads out while the hadron overdensity is frozen. At this point the latter has travelled a distance s = 150 Mpc comoving, which is the acoustic horizon at decoupling. The baryons then fall in the dark matter potential well, while the dark matter also fall in the well due to the hadron overdensity, resulting in very close density profiles in the recent Universe. The matter autocorrelation function therefore exhibits a peak around 150 Mpc comoving, at all z. This BAO scale represents a standard ruler which can be used to measure the expansion rate of the Universe and constrain the equation of state of the dark energy.

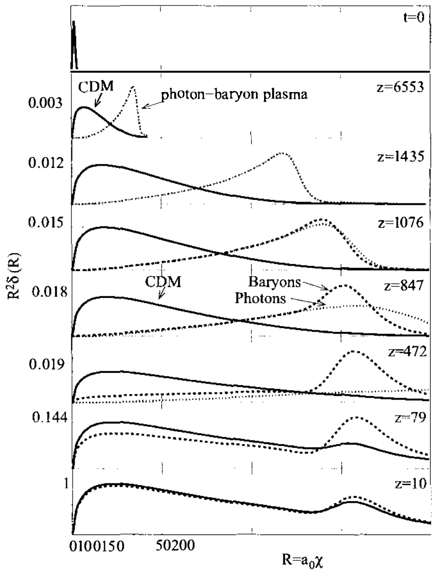

Figure 2: The evolution of a single overdensity with z. Distances are comoving distances in Mpc.

A BAO survey is a 3D survey with measurements of right ascension, declination and redshift. We can therefore measure correlation transverse to and along the lines of sight. In the transverse direction we measure an angular scale, $\Delta\theta = s/D_\perp(z)$, where $D_\perp(z) = (1+z)D_A(z) = \int_0^z cdz'/H(z')$ is the comoving angular distance. This is essentially the same information as obtained in supernovae measurements, which provide the luminosity distance $D_L(z) = (1+z)^2 D_A(z)$. In the radial direction we get $\Delta z = c/H(z)$. BAO survey require a spectrometric measurement of the redshift. Photometric redshifts result in an enlargement of the acoustic peak and therefore in a loss of statistics on the peak position by a factor 5 relative to the cosmic variance limit.

2.2 SDSS III / BOSS

The main Lyman-α BAO survey is carried out by the BOSS collaboration. BOSS is part of the Sloan Digital Sky Survey consortium, SDSS III, together with three other collaborations, Marvels looking for exo-planets, Segue and Apogee doing Galactic science. SDSS III includes many US universities, Brazil, France, Germany, Korea, Spain and UK. It uses a 2.5m telescope located at Apache point observatory in New Mexico. BOSS is a 10,000 deg^2 spectrometric survey of both Large Red Galaxies and Lyman-α forest of quasars. All dark nights for a five year period (2009 - 2014) are reserved for BOSS. The SDSS II photometry in the 5 optical bands u, g, r, i and z is used to define galaxy and quasar candidates. Holes are drilled in an aluminum plate corresponding to these targets and optical fibers are connected to the holes. The aluminum plate is set on the focal plane of the telescope and the fibers are sent to a set of two spectrographs. At the end each spectrum appears as a line on a CCD plane.

2.3 unabsorbed quasar spectra

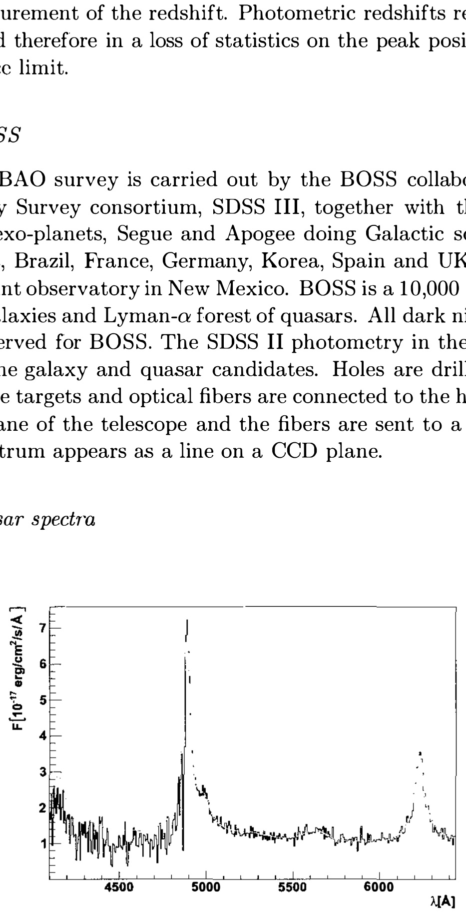

Figure 3: A mock quasar spectrum, typical of BOSS conditions, together with the true unabsorbed spectrum as a red continuous line.

The first step of the analysis is to define the unabsorbed quasar spectrum. This is easy for a high resolution and high signal-to-noise spectrum as shown in Fig. 1, but much more difficult for a typical BOSS quasar spectrum as illustrated in Fig. 3. Several methods are used. The simplest one consists in stacking all spectra to define the mean shape and fitting the observed spectrum with this mean shape, times a linear function in the wavelength to take into account part of the diversity between individual quasar spectra. More sophisticated methods include using principal component analysis of a sample of high resolution high S/N spectra to try to guess the unabsorbed spectrum blueward of the Lyman-α peak from the spectrum redward. In this case, however, the mean value of the predicted unabsorbed spectrum has to be corrected [1].

Simulations show, however, that this issue is not too serious. Using the simplest method discussed above results in a relative increase of the statistical error on the BAO scale of typically 10% and in a sub percent bias, quite smaller than the statistical error [2].

We compute the correlation function $\xi(r) = \langle\delta(x)\delta(x+r)\rangle$ of the field δ defined from

$$\phi(\lambda) = \bar{\phi}(\lambda^{rf}, z)(a + b\lambda)(1 + \delta) \; , \tag{1}$$

where $\bar{\phi}(\lambda^{rf}, z)$ is the mean stacked flux as a function of $\lambda^{rf} = \lambda/(1 + z_{QSO})$ and redshift. This procedure distorts $\xi(r)$ as illustrated in Fig. 4 left. However, the distortion is a monotonous function of r (Fig. 4 right) and should not affect the determination of the BAO peak.

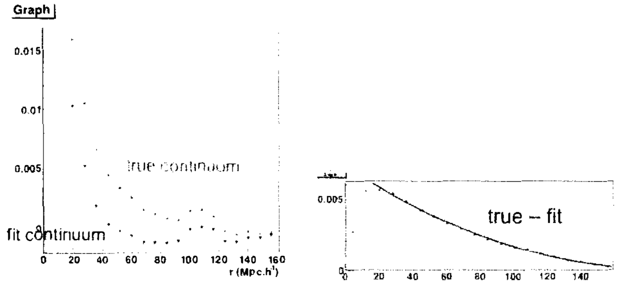

Figure 4: Left: the reconstructed $\xi(r)$ for mock data using either the true unabsorbed spectrum (red) or the procedure applied to the real data (blue). Right: the difference between the two, using the same vertical scale.

2.4 BAO analysis

In order to improve the determination of $\xi(r)$ from a statistical point of view, the field δ is weighted with $w = 1/\sigma_\delta^2$, where σ_δ^2 is the sum of the variance provided by the pipeline and the intrinsic variance due to the large scale structure which is determined by a fit to the data, $\sigma_\delta^2 = \sigma_{pipeline}^2 + \sigma_{LSS}^2$. The estimator is simply

$$\hat{\xi}(r, \mu) = \frac{\sum_{ij} w_i w_j \delta_i \delta_j}{\sum_{ij} w_i w_j} \; . \tag{2}$$

More sophisticated estimators are also being studied.

Since the same $\delta(x)$ enter $\xi(r)$ and $\xi(r')$, they are expected to be correlated. The full error matrix of the $\xi(r_i)$ was evaluated by splitting data in N subsamples and comparing the values of the $\xi(r_i)$ obtained for each subsample. This appears to be in fair agreement with an analytical calculation assuming Gaussian distributions and using Wick theorem. The correlation between $\xi(r)$ bins finally appears to be quite small (Fig.5), in particular in comparison to the galaxy case. This is due to noise and to the limited quasar density in the Lyman-α case, which increase the diagonal terms of the matrix.

The correlation is measured in bins in r and $\mu = \cos\theta$, where θ is the angle relative to the line of sight. In linear theory, it is decomposed using Legendre polynoms, $P_l(\mu)$, as

$$\xi(r, \mu) = b^2 \sum_{l=0,2,4} C_l(\beta)\xi_l(r)P_l(\mu) \; , \tag{3}$$

where b is the linear bias parameter, β the redshift distortion parameter, $C_0 = 1 + 2/3\beta + 1/5\beta^2$, $C_2 = 4/3\beta + 4/7\beta^2$ and $C_4 = 8/35\beta^2$. Fig.6 presents the resulting monopole $\xi_0(r)$ and quadrupole

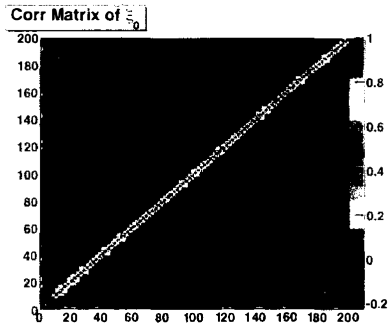

Figure 5: The error correlation matrix obtained by the jackknife method.

$\xi_2(r)$. The hexadecapole $\xi_4(r)$ is small and compatible with zero. A blind analysis is performed and the region around the expected BAO peak will be unblinded only when the analysis is frozen.

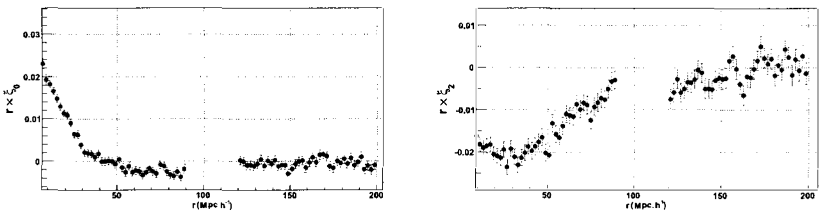

Figure 6: The monopole $\xi_0(r)$ (left) and the quadrupole $\xi_2(r)$ (right) correlation functions. The region around the expected BAO peak is hidden to allow for a blind analysis.

With the statistical accuracy provided by the BOSS Lyman-α forest survey it is not clear whether it will be possible to separately determine $D_A(z)$ and $H(z)$. A first goal is to make an isotropic analysis which provides the average $D_V(z) = [D_A^2(z)/H(z)]^{1/3}$. A Fisher matrix analysis combined with an analytical description of the power spectrum indicates [3] that for the full BOSS survey, 150,000 quasars over 10,000 deg^2, we can expect an error of 2% on $D_V(z)$ for $\langle z \rangle = 2.5$. This was confirmed with a full simulation of the survey using mock quasar spectra [2].

3 Neutrino mass in 1D analysis

The difference between the masses of neutrino species are known from neutrino oscillation experiments to be $\Delta m_{12}^2 = 7.5810^{-5}$ eV^2 and $\Delta m_{23}^2 = 2.4310^{-3}$ eV^2 and tritium β decay experiments yield $m(\nu_e) < 2$ eV (95% CL). This results in a constrain for the sum of the neutrino masses: $0.06 < \sum m_i < 6$ eV.

Concerning cosmological constrains, the Lyman-α data are interesting because they are the only data extending down to the Mpc/h scale. An analysis [6] of SDSS-II Lyman-α data combined with other cosmological data has provided the strong constrain, $\sum m_i < 0.17$ eV. However this depends on the relative normalization of Lyman-α forest and other data. It is safer to use only Lyman-α data, which results [7] in $\sum m_i < 0.9$ eV.

3.1 influence of neutrino mass on $P(k)$

At high temperature the neutrinos are in thermal equilibrium through electroweak interactions. When the temperature goes below about 1 MeV, they decouple and from this time on, the average number of neutrinos per comoving volume remains constant. They constitute the cosmic neutrino background. A little bit latter, when $T < m_e$, electron-positron annihilation heats up the photons. As a result their temperature is larger than that of the neutrinos, $T_\gamma = 1.40 T_\nu$ and they are more numerous, $n_\gamma = (11/3)n_\nu$. At $z = 0$, the density of each neutrino species is then 113 neutrinos or antineutrinos per cm^3.

We define the ratio of neutrino to matter energy densities, $f_\nu = \Omega_\nu/\Omega_m \approx \sum m_i/13.3$ eV. If $f_\nu < 0.1$, i.e. $\sum m_i < 1.3$ eV, the three neutrino species become non relativistic after photon-baryon decoupling at $z \approx 1100$ and there is no direct effect of the neutrino mass on the CMB spectrum. There is only an indirect effect through a change of the background evolution: for constant Ω_m when Ω_ν increases, Ω_{CDM} decreases and, since neutrinos where radiation and not matter at that time, the radiation-matter equality occurs latter. However, this effect is degenerate with other cosmological parameters, so that CMB data alone cannot constrain the neutrino mass below about 1.3 eV, which is actually the limit obtained by WMAP7[8]. Combining CMB data with H_0 and BAO measurements removes this degeneracy and WMAP7 obtains $\sum m_i < 0.58$ eV[8].

At high z the density fluctuations of the coupled baryons photons oscillate, while those of dark matter grow only logarithmically, due to radiation domination. The ultrarelativistic neutrinos can move freely from high density to low density regions, they "free-stream" over all scales, and there are essentially no neutrino density fluctuations. When the Universe reaches matter-radiation equality at $z \approx 3300$ the dark matter fluctuations start to grow linearly, while the baryon fluctuations start to grow at photon-baryon decoupling. At $z_{nr} = 1890(m_{\nu_i}/1 \text{ eV})$, neutrinos of species ν_i becomes non relativistic and their free-streaming is limited to a free-streaming length which depends on their kinetic energy. The neutrino do not free-stream on scales larger than this free streaming length and the matter fluctuations grow as $\delta_m \propto a$, where $a = 1/(1+z)$. On smaller scales the free streaming of the neutrinos smoothes the gravitational potential and reduces the growing of the matter fluctuations, $\delta_m \propto a^{1-0.6 f_\nu}$.

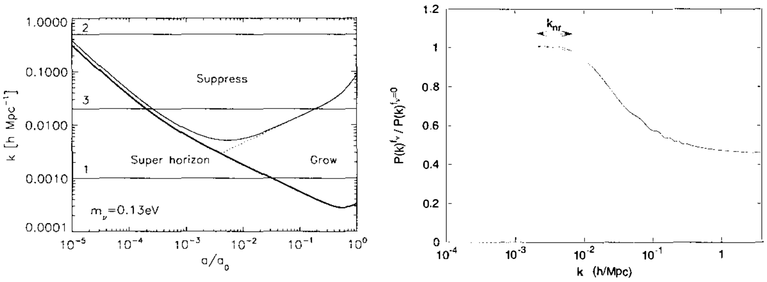

Figure 7: Left: the horizon scale (lower curve) and the neutrino free-streaming scale (upper curve) versus a in the case $f_\nu = 0.1$. The horizontal lines represent three different modes. The modes start to grow when they enter the horizon but their growth is suppressed if they are above the free-streaming scale. Right: The ratio $P(k, f_\nu)/P(k, f_\nu = 0)$ at $z = 0$, for $f_\nu = 0.1, 0.2, 0.3, ..., 1.0$ (from top to bottom).

Fig. 7 left shows what happens depending on the considered scale. When large scale modes (horizontal line 1 in the figure) enter the horizon, the neutrinos are already non relativistic. They behave as an additional type of cold dark matter, $\delta_\nu = \delta_{cdm}$, and the matter power spectrum is not affected by the neutrino mass. This is true for all modes such that $k < k_{nr}$, where k_{nr}

is the value of the free streaming scale when the neutrino becomes non relativistic. On the other hand the growth of a small scale mode (line 2) is suppressed over all z, resulting in a reduction of the power spectrum $\Delta P/P \approx 8f_\nu$ at $z = 0$. The growth of an intermediate scale mode (line 3) is suppressed, but not over all z, and the reduction of the power spectrum is less important. When the neutrino mass increases, the reduction of the power spectrum for small scales mode, $\Delta P/P = 8f_\nu$, becomes more important, but the neutrinos become non relativistic earlier, the value of k_{nr} becomes larger and more modes are unaffected by the neutrino mass. Heavier neutrinos have a stronger effect but over a smaller range. This is illustrated in Fig. 7 right, which shows the ratio $P(k, f_\nu)/P(k, f_\nu = 0)$ for different values of f_ν.

3.2 BOSS 1D analysis

The 1D power spectrum is obtained by performing the Fourier transform of individual spectra. Wavelength λ in a spectrum corresponds to Lyman-α absorption by H1 at a redshift such that $(1 + z) \times 1216\AA = \lambda$ and a separation $\Delta\lambda$ corresponds to a velocity difference $\Delta v = c\Delta z$. Therefore the spectra are usually presented in velocity units, which can be done independently of any fiducial cosmology. Such a fiducial cosmology is required to replace velocity by Mpc. The unit of the power spectrum is then also km/s, while k is in $(\mathrm{km/s})^{-1}$. The minimum scale to be probed is given by the spectrum pixel size. BOSS pixels are 69 km/s wide, which corresponds to about 0.7 Mpc/h. This is a much smaller scale than is obtained in galaxy redshift surveys. The following cuts are used in the BOSS analysis: signal-to-noise ratio $S/N > 2$, pixels with a wavelength such that $2.1 < z_{pixel} < 4.5$, and resolution < 85 km/s, which results in a sample of 16,000 QSO spectra.

The raw power spectrum is obtained with a fast Fourier transform (FFT) of the quasar spectra. The noise power spectrum must be subtracted from it and the result must be divided by the squared window function which includes the effect of the spectrometer resolution R and the pixel width $\Delta\lambda$ as

$$P^{1D}(k) = \frac{P^{1D}_{raw}(k) - P^{1D}_{noise}(k)}{\exp(-(kR)^2)\left[\frac{\sin(k\Delta\lambda/2)}{k\Delta\lambda/2}\right]^2} . \tag{4}$$

In this process sky lines had to be masked and detailed studies were required to correct the noise and resolution provided by BOSS pipeline.

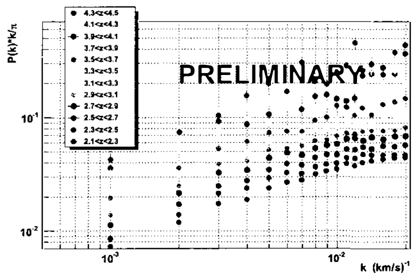

Figure 8: Preliminary 1D power spectra, $kP(k)/\pi$, obtained by BOSS in 12 bins in redshifts, from $z = 2.1$ (bottom) to $z = 4.5$ (top).

Fig. 8 presents the resulting $P^{1D}(k)$. The error bars are statistical only. At small z the systematic error bars are smaller or comparable to the statistical errors. At large z they are negligible relative to the statistical errors. This is the result of the analysis using FFT. A more sophisticated analysis is also performed using a maximum likelihood approach. This allows for the resolution to depend on the wavelength. The resulting $P^{1D}(k)$ are very close to those of the FFT analysis.

4 Conclusions

The 3D analysis of BOSS Lyman-α data is well advanced. This corresponds to data release 9, i.e. up to July 2010, representing less than 20 % of the final data set. The data will be unblinded soon but it is not sure whether we will get a significant BAO signal from these data. Data taking will go on up to July 2014 at which time a clear detection of the BAO peak is expected.

The analysis of the 1D power spectrum is nearly finished. Hydrodynamic simulations will be performed in order to be able to extract the sum of the neutrino masses from Lyman-α data alone.

The Lyman-α data can be used for several other science cases which were not discussed here. For instance strong absorption regions in the Lyman-α spectra, so called DLA, can be used to study the chemistry of denser regions in the IGM, like filaments or proto-galaxies.

References

1. K.G Lee, N. Suzuki and D.N. Spergel, arXiV:1108.6080.
2. J.-M. Le Goff et al., A&A **534**, A135 (2011).
3. P. McDonald and D. Eisenstein, *Phys. Rev.* D **76**, 063009 (2007).
4. J. Lesgourgues and S. Pastor, Phys. Rep. **429**, 307 (2006).
5. M. Shoji and E. Komatsu, arXiv:1003.0942.
6. U. Seljak et al., JCAP **10**, 014 (2006).
7. M. Viel, M.G. Haehnelt and V. Springel, JCAP **06**, 015 (2010).
8. E. Komatsu et al., ApJS **192**, 18 (2011).

Detectability of cold streams into high-z galaxies by absorption lines

Tobias Goerdt
Departamento de Física Teórica, Universidad Autónoma de Madrid,
28049 Madrid, España

Cold gas streaming along the dark-matter filaments of the cosmic web is predicted to be the major source of fuel for disc buildup, violent disk instability and star formation in massive galaxies at high redshift. I investigate to what extent such cold gas is detectable in the extended circum-galactic environment of galaxies via selected low ionisation metal absorption lines. I model the expected absorption signatures using high resolution zoom-in AMR cosmological simulations. In the postprocessing, I distinguish between self-shielded gas and unshielded gas. In the self-shielded gas, which is optically thick to Lyman continuum radiation, I assume pure collisional ionisation for species with an ionisation potential greater than 13.6 eV. In the optically thin, unshielded gas these species are also photoionised by the meta-galactic radiation. I compute the absorption line profiles of radiation emitted by the galaxy at the centre of the same halo. I predict the strength of the absorption signal for individual galaxies without stacking. I find that the absorption profiles produced by the streams are consistent with observations of absorption and emission profiles in high redshift galaxies. Due to the low metallicities in the streams, and their low covering factors, the metal absorption features are weak and difficult to detect.

1 Introduction

Cold gas is thought to flow into massive haloes $\sim 10^{12}$ M$_\bullet$ at $z = 2-3$ along filaments with velocities of $\gtrsim 200\,\mathrm{km\,s^{-1}}$. This phenomenon is predicted by simulations and theoretical analysis, where high-z massive galaxies are continuously fed by narrow, cold, intense, partly clumpy, gaseous streams that penetrate through the shock-heated halo gas into the inner galaxy [?]. Indeed, hydrodynamical cosmological simulations reveal that the rather smooth gas components, including mini-minor mergers with mass ratio smaller than 1:10, brings in about two thirds of the mass [?]. But it seems that only a small fraction of the LBGs exhibit redshifted absorption features, which was interpreted as an indication for the absence of cold streams in haloes with $4\times10^{11} < M_\mathrm{v} < 10^{12} M_\bullet$ [?][hereafter S10]. The goal of this study [?] is to predict the absorption-line signatures of the cold flows, for a detailed comparison with observations like S10.

[?] used cosmological hydrodynamical AMR simulations to predict the characteristics of Lyα emission from the cold gas streams. The Lyα luminosity in their simulations is powered by the release of gravitational energy as the gas is flowing with a rather constant velocity down the potential gradient toward the halo centre. The simulated Lyα-blobs (LABs) are similar in many ways to the observed LABs. Some of the observed LABs may thus be regarded as direct detections of the cold streams that drove galaxy evolution at high z. Observations seem to support this picture [?].

2 The Simulations

We use three simulated galaxies from a suite of simulations, employing Eulerian adaptive mesh refinement (AMR) hydrodynamics in a cosmological setting. These are zoom-in simulations in dark-matter haloes with masses $\sim 5 \times 10^{11}$ $M_{\odot}$ at $z = 2.3$, with a maximum resolution of 35 - 70 pc in physical coordinates [?](hereafter CDB).

3 Computing the ionisation states

In order to compute the ionisation states via post-processing we take the densities, temperatures and metallicities from the simulation. We assume a primordial helium mass fraction $Y = 0.24$, corresponding to a helium particle abundance of 1/12 relative to hydrogen. For the heavy elements we assume the [?] solar photosphere pattern.

We determine whether a given simulation cell is "self-shielded", i.e. optically thick to Lyman continuum radiation, via a simple density criterion. Cells with total hydrogen exceeding $n_{\mathrm{shield}} \equiv 0.01$ cm^{-3} are assumed to be self-shielded. For lower densities the cells are assumed to be optically thin. We calculate the atomic and ionic fractions x_{Ai} using CLOUDY [?], where x_{Ai} is defined as the fractions of element A in ionisation state i.

4 Central source

In this section we consider the Lyα and metal line absorption that occurs as UV light emitted by the central galaxy is absorbed by gas in the circum-galactic environment. As defined by S10, the circumgalactic medium is situated in the spherical zone from just outside the galactic disk to around the virial radius R_{v}. Observations of absorption against the central galaxy itself have the advantage of being able to discriminate between inflows and outflows because the absorptions may be assumed to occur in foreground material only. Radiation emitted or scattered from behind the galaxy is blocked by the galaxy itself. However, such absorptions do not provide spatial information about the distance from the galaxy centre as they are all by definition at an impact parameter $b = 0$ from the galaxy centre. S10 employed this technique of observing absorptions against the central galaxy by stacking a sample of 89 galaxies with $z = 2.3 \pm 0.3$ using both rest-frame far-UV and Hα spectra, to investigate the kinematics of the gas flows in the circumgalactic regions.

Along a given sight-line the gas has a varying density, temperature and radial velocity as function of radial position r from the central galaxy. The convolutions of the different densities and radial velocities in the gas along the line of sight are the main ingredients to compute an absorption line profile. This is done as follows: the radial velocity offset Δw relative to central source at rest of all the gas is measured. We assume Voigt profiles with a thermal Doppler broadening parameter

$$b = \sqrt{\frac{2\,k\,T}{m_{\mathrm{A}}}}, \tag{1}$$

where k is the Boltzmann constant, T is the temperature of the gas and m_{A} is the mass of the element A. So for angular position (ϕ,θ) we can compute the optical depth $\tau_{\nu}(\phi,\theta,\Delta w)$ at the velocity offset Δw as

$$\tau_{\nu}(\phi,\theta,\Delta w) = \frac{\sqrt{\pi}\,e^2\,f_{\lambda}\,\lambda_0}{m_{\mathrm{e}}\,c} \int_{\mathrm{r_i}}^{R_{\mathrm{v}}} \frac{n_{\mathrm{A}}(\vec{r})\,x_{\mathrm{Ai}}(\vec{r})}{b(\vec{r})}\,H\left[\frac{\gamma_{\lambda}\,\lambda_0}{4\,\pi\,b(\vec{r})}\,,\frac{\Delta w - v(\vec{r})}{b(\vec{r})}\right]\,dr, \tag{2}$$

where e is the electron charge, m_{e} is the electron mass, c is the speed of light, λ_0 is the transition wavelength, $n_{\mathrm{A}}(\vec{r})$ is the gas density of element A at position $\vec{r} = (\phi,\theta,r)$, x_{Ai} is the ionisation

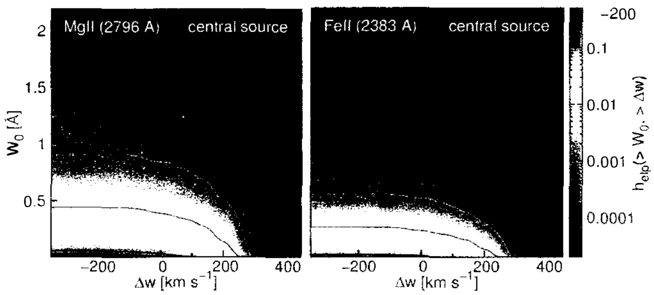

Figure 1: Fraction $h_{\rm elp}$ of all possible example line profiles in the central geometry whose EW is higher than W_0 and whose line centre is at a velocity offset indicating an inflow at least as fast as Δw. Here for the metal lines. Positive velocities are inflowing into the galaxy and negative velocities are out of the galaxy. Contour lines are at 0.1, 0.01, 0.001 and 0.0001 respectively. Note the different y-axis scalings from row to row. In C II one sees an inflow $> 150\,{\rm km\,s^{-1}}$ with an EW > 0.17 Å in 0.4 % of all observations. For Mg II one sees an inflow $> 150\,{\rm km\,s^{-1}}$ with an EW > 0.2 Å in 1.3 % of all observations. The line which has by far the strongest signal is the Mg II line followed by the Fe II line. These values should be achievable by future observations.

fraction of element A in state i, v is the velocity of the gas, f_λ is the oscillator strength of the absorption line and γ_λ is the sum over the spontaneous emission coefficients or the damping width. The Voigt profile is

$$H(a, u) = \frac{a}{\pi} \int_{-\infty}^{\infty} \frac{\exp(-y^2)}{(u-y)^2 + a^2}\, dy, \tag{3}$$

where a is the ratio of the damping width to the Doppler width and u is the offset from line centre in units of Doppler widths. Knowing $\tau_\nu(\Delta w)$ it is now possible to compute an absorption line profile $I(\Delta w)$ for a given direction which is simply the function

$$I(\Delta w) = \exp[-\tau_\nu(\Delta w)]. \tag{4}$$

For a fair comparison to the observations done by S10, we mimic a Gaussian point spread function. It has a beam-size (= FWHM η of the Gaussian) of 4 kpc. It is done by splitting up a cylinder with a radius of three times the beam-size into as many parallel fibres as the resolution permits, determining the absorption line profile for every individual fibre and then computing a Gaussian weighted average absorption line profile from all fibres.

Figure ?? is intended to give the likelihood of a detection of a cold stream while looking at a single galaxy from a single direction without averaging. It shows the fraction $h_{\rm elp}$ of all possible example line profiles in the central geometry whose EW is higher than W_0 and whose line centre is at a velocity offset indicating an inflow at least as fast as Δw. The example line profiles are integrated from $1.0\,R_{\rm v}$ down to $0.3\,R_{\rm v}$. Positive velocities are inflowing into the galaxy and negative velocities are out of the galaxy. For Mg II one sees an inflow $> 150\,{\rm km\,s^{-1}}$ with an EW > 0.2 Å in 1.3 % of all observations. These values should be achievable by future observations.

We produce stacked spectra using our simulations by summing up the line profiles of several thousand different directions for each of the three galaxies and stack them together. We determine the absorption line profile for a spherical shell between an outer radius and an inner radius $r_{\rm i}$. The outer radius is always kept constant at 1.0 $R_{\rm v}$ which corresponds roughly to 74kpc. The inner radius $r_{\rm i}$ however is varied between 0.3 $R_{\rm v}$ and 0.02 $R_{\rm v}$. In figure ?? the resulting profiles are shown for all the metal lines. The predicted metal line absorption profiles appear tiny compared to the corresponding lines presented in figures 6 or 10 of S10 having a line depth of 0.5 and $\eta \sim 1000$ km s^{-1} in metals. Probably the most suitable lines for the purpose

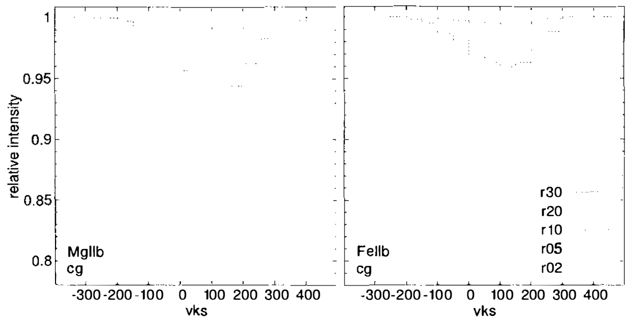

Figure 2: Metal line bsorption profiles for a central source geometry averaged over different viewing angles and all three galaxies. We integrated from 1.0 R_v down to different inner radii r_i. Positive velocities are inflowing into the galaxy and negative velocities are out of the galaxy. Note the different y-axis scaling from row to row. The metal lines are much weaker than the Lyα line, since the inflowing material is mainly unprocessed primordial gas with very low metallicity. These metal lines also appear tiny compared to the corresponding lines presented by S10. The profiles always peak in the positive, indicating inflow.

of detecting cold streams in absorption are C II and Mg II since they have the strongest signal. Out of those Mg II is closer to being observed with the needed sensitivity and resolution.

5 Conclusions

Here we addressed the expected absorption signature from these cold streams. We "observed" simulated galaxies for metal lines from low and medium ionisation ions. We focused on the absorption line profiles as observed by S10, using their set of ten different lines and mimicking their way of stacking data from several galaxies, for sources that are either in the background or at the centre of the absorbing halo itself. The simulations used are zoom-in cosmological simulations with a maximum resolution of 35-70 pc [?]. Self-shielding was accounted for by a simple density criterion.

We conclude that the signatures of cold inflows are subtle, and when stacked are overwhelmed by the outflow signatures. Our predicted Lyα line absorption profiles agree with the observations, while the stacked metal line absorption from the inflows is much weaker than observed in the outflows. The single-galaxy line profiles predicted here will serve to compare to single-galaxy observations.

References

1. Dekel A, Birnboin Y, Engel G. et al, 2009, Nature, 457, 451
2. Steidel C. C, Erb D. K, Shapley A. E, Pettini M, Reddy N. A, Bogosavljević M, Rudie G. C, Rakic O, 2010, ApJ, 717, 289, S10
3. Goerdt T, Dekel A, Sternberg A, Gnat O, Ceverino D, 2012, arXiv:1205.2021
4. Goerdt T, Dekel A, Sternberg A, Ceverino D, Teyssier R, Primack J. R, 2010, MNRAS, 407, 613
5. Erb D. K, Bogosavljević M, Steidel C. C, 2011, ApJ, 740L, 31
6. Ceverino D, Dekel A, Bournaud F, 2010, MNRAS, 404, 2151, CDB
7. Asplund M, Grevesse N, Sauval A. J, Scott P, 2009, ARA&A, 47, 481
8. Ferland G. J, Korista K. T, Verner D. A, Ferguson J. W, Kingdon J. B, Verner E. M, 1998, PASP, 110, 761

THREE TESTS OF ΛCDM

C. J. A. P. MARTINS

Centro de Astrofísica, Universidade do Porto, Rua das Estrelas, 4150-762 Porto, Portugal

The observational evidence for the acceleration of the universe demonstrates that canonical theories of gravitation and particle physics are incomplete, if not incorrect. The next generation of astronomical facilities must both be able to carry out precision consistency tests of the standard cosmological model and search for evidence of new physics beyond it. I describe some of these tests, and discuss prospects for facilities in which the CAUP Dark Side team is involved, specifically ESPRESSO, Euclid and CODEX.

1 The dark side of the universe

In the middle of the XIX century Urbain Le Verrier and others mathematically discovered two new planets by insisting that the observed orbits of Uranus and Mercury agreed with the predictions of Newtonian physics. The first of these—Neptune—was soon observed by Johann Galle and Heinrich d'Arrest. However, the second (dubbed Vulcan) was never found. The discrepancies in Mercury's orbit were a consequence of the fact that Newtonian physics can't adequately describe Mercury's orbit, and accounting for them was the first success of Einstein's General Relativity.

Over the past several decades, cosmologists have mathematically discovered two new components of the universe—dark matter and dark energy—which have so far not been directly detected. Whether the will prove to be Neptunes or Vulcans remains to be seen but even their mathematical discovery highlights the fact that the standard ΛCDM paradigm, despite its phenomenological success, is at least incomplete.

Something similar applies to particle physics, where to some extent it is our confidence in the standard model that leads us to the expectation that there must be new physics beyond it. Neutrino masses, dark matter and the size of the baryon asymmetry of the univserse all require new physics, and—significantly—all have obvious astrophysical and cosmological implications. Further progress in fundamental particle physics will increasingly depend on progress in cosmology.

One must therefore carry out explicit consistency tests of the standard cosmological model and search for evidence of new physics beyond it. For example fundamental scalar fields are crucial in the standard particle physics model (cf. the Higgs field) and are also invoked in several key cosmological contexts, including inflation, cosmological phase transitions and their relics (cosmic defects), dynamical dark energy powering the current acceleration phase, and varying fundamental couplings. Even more important than each of these paradigms is the fact that they don't occur alone: this will be crucial for future consistency tests.

2 Varying fundamental couplings

Nature is characterized by a set of physical laws and fundamental dimensionless couplings, which historically we have assumed to be spacetime-invariant. For the former this is a cornerstone of the scientific method, but for the latter it is only a simplifying assumption without further justification. These couplings determine the properties of atoms, cells, planets and the universe as a whole, so it's remarkable how little we know about them—we have no 'theory of constants'. If they vary, all the physics we know is incomplete. Such a detection would be revolutionary, but even improved null results are important and useful: natural scale for cosmological evolution would be Hubble time, but current bounds are 6 orders of magnitude stronger [1].

Recent astrophysical evidence from quasar absorption systems [2] suggests a parts-per-million spatial variation of the fine-structure constant α at low redshifts; although no known model can explain such a result without considerable fine-tuning, there is also no identified systematic effect that can explain it. One possible cause for concern (with these and other results) is that most of the existing data has been taken with other purposes, whereas this kind of neasurements needs customized analysis pipelines [3]. An ongoing UVES Large Programme dedicated to these tests should soon provide and independent test [4]. In the longer term a new generation of high-resolution, ultra-stable specrographs like ESPRESSO and CODEX will significantly improve the precision of these measurements.

At much higher redshifts, the CMB is an ideal, clean probe of varying α, which will impact the ionization history of the universe (energy levels and binding energies are shifted, and the Thomson cross-section is proportional to α^2). Having said this, bounds are relatively weak due to degeneracies, and the percent barrier has only recently been broken [5]. In any realistic model where α varies other couplings are also expected to vary, and such coupled variations can also be constrained [6]. One can also constrain the coupling between the putative scalar field and electromagnetism, independently (and on a completely different scale) from what is done in local tests [7].

The recent CMB measurements from WMAP and arcminute angular scales (from ACT and SPT) suggest that the effective number of relativistic degrees of freedom is larger than the standard value of $N_{\rm eff} = 3.04$, and inconsistent with it at more than two standard deviations. We have recently shown [8] that if one assumes this standard value this CMB data significantly improves previous constraints on α, with $\alpha/\alpha_0 = 0.984 \pm 0.005$, i.e. hinting also to a more than two standard deviation from the current, local, value. A significant degeneracy is present between α and $N_{\rm eff}$, and when variations in the latter are allowed the constraints on α are consistent with the standard value. Again it's worth stressing that deviations of either parameter from their standard values would imply the presence of new, currently unknown physics.

Many compact astrophysical objects can also be used to search for spacetime variations of fundamental couplings, including Population III stars [14], neutron stars [15] and solar-type stars [16].

3 Dynamical dark energy

Observations suggest that the universe is dominated by component whose gravitational behavior is similar to that of a cosmological constant. Its value is so small that a dynamical scalar field is arguably more likely. Such a field must be slow-rolling (which is mandatory for $p < 0$) and be dominating the dynamics around the present day. It follows [9] that couplings of this field to the rest of the model (which will naturally exist, unless an ad hoc symmetry is postulated to suppress them) lead to potentially observable long-range forces and time dependencies of the constants of nature.

Standard observables such as supernovae are of limited use as dark energy probes [10]. A clear detection of varying $w(z)$ is key, since $w \sim -1$ today. Since the field is slow-rolling when dynamically important, a convincing detection of $w(z)$ will be tough at low redshift, and we must probe the deep matter era regime, where the dynamics of the hypothetical scalar field is fastest. Varying fundamental couplings are ideal for probing scalar field dynamics beyond the domination regime[11]. We have recently shown[12] that CODEX can constrain dark energy better than supernovae (its key advantage being huge redshift lever arm), and even ESPRESSO can provide a significant contribution.

Dark energy reconstruction using varying fundamental constants requires an assumption on the field coupling, but there are in-built consistency checks, so that inconsistent assumptions can be identified and corrected[13]. On the other hand this analysis allows scalar field couplings to be measured and compared to local constraints. Interesting synegies also exist between these ground-based spectroscopic methods and Euclid, which need to be further explored.

4 The quest for redundancy

Whichever way one finds direct evidence for new physics, it will only be believed once it is seen through multiple independent probes. This was manifest in the case of the discovery of the recent acceleration of the universe (where the supernova results were only accepted by the wider community once they were confimed through CMB, large-scale structure and other data) and it is clear that history will repeat itself in the case of varying fundamental couplings and/or dynamical dark energy. It is therefore important to develop consistency tests—in other words, astrophysical observables whose behaviour will also be non-standard as a consequence of either or both of the above.

The temperature-redshift relation, $T(z) = T_0(1+z)$, is a robust prediction of standard cosmology; it assumes adiabatic expansion and photon number conservation, but is violated in many scenarios, including string theory inspired ones. At a phenomenological level one can parametrize deviations to this law by adding an extra parameter, say $T(z) = T_0(1+z)^{1-\beta}$. Measurements of the SZ effect at resdshifts $z < 1$, combined with spectroscopic measurements at redshifts $z \sim 2-3$ yield the direct constraint $\beta = -0.01 \pm 0.03$[17]. Forthcoming data from Planck, ESPRESSO and CODEX will lead to much stronger constraints[18,19].

The distance duality relation, $d_L = (1+z)^2 d_A$, is a robust prediction of standard cosmology; it assumes a metric theory of gravity and photon number conservation, but is violated if there's photon dimming, absorption or conversion. At a phenomenological level one can parametrize deviations to this law by adding an extra parameter, say $d_L = (1+z)^{2+\epsilon} d_A$. In this case, current constraints are $\epsilon = -0.04 \pm 0.08$[20].

In fact, in many models where photon number is not conserved the temperature-redshift relation and the distance duality relation are not independent. With the above parametrizations one can show[19] that $\beta = -2/3\epsilon$, but in fact a direct relation exists for any such model, provided the dependence is in redshift only (models where there are frequency-dependent effects are more complex). This link allows us[19] to use distance duality measurements to further constrain β, and we recently found $\beta = 0.004 \pm 0.016$ up to a redshift $z \sim 3$, which is a 40% improvement on the previous constraint. With the next generation of space and ground-based experiments, these constraints can be further improved by more than one order of magnitude.

5 Outlook

Observational evidence for the acceleration of the universe demonstrates that canonical theories of cosmology and particle physics are incomplete, if not incorrect. Several few-sigma hints of new physics exist, but so far these are smoke without a smoking gun; it's time to actively search for the gun.

The forthcoming generation of high-resolution ultra-stable spectrographs will play a key role in this endeavour, by enabling a new generation of precision consistency tests of the standard cosmological paradigm and its extensions. Further exciting possibiblites, not explicitly discussed in this contribution, include direct astrophysical Equivalence Principle tests and E-ELT measurements of the redshift drift (on the latter, see Pauline Vielzeuf's contribution to these proceedings). Finally, there are interesting synergies with space facilities, particularly Euclid, which should be further studied.

Acknowledgments

The work of CJM is supported by a Ciência2007 Research Contract, funded by FCT/MCTES (Portugal) and POPH/FSE (EC), with further support from grant PTDC/CTE-AST/098604/2008. Many interesting discussions with the rest of CAUP's Dark Side team and our collaborators elsewhere have shaped my views on this subject, and are gratefully acknowledged.

References

1. T. Rosenband *et al*, Science **319**, 1808 (2008).
2. J. K. Webb *et al*, PRL **107**, 191101 (2011).
3. R. I. Thompson, J. Bechtold, J. H. Black and C. J. A. P. Martins, New Astronomy **14**, 379 (2009).
4. P. Molaro *et al*, 2012, to appear.
5. E. Menegoni, S. Galli, J. G. Bartlett, C. J. A. P. Martins and A. Melchiorri, PRD **80**, 087302 (2009).
6. C. J. A. P. Martins, E. Menegoni, S. Galli, G. Mangano and A. Melchiorri, PRD **82**, 023532 (2010).
7. E. Calabrese, E. Menegoni, C. J. A. P. Martins, A. Melchiorri and G. Rocha, PRD **84**, 023518 (2011).
8. E. Menegoni, M. Archidiacono, E. Calabrese, S. Galli, C. J. A. P. Martins and A. Melchiorri, PRD **85**, 107301 (2012).
9. S. M. Carroll, PRL **81**, 3067 (1998).
10. I. Maor, R. Brustein and P. J. Steinhardt, PRL **86**, 6 (2001).
11. N. J. Nunes and J. E. Lidsey, PRD **69**, 123511 (2004).
12. L. Amendola, A. C. O. Leite, C. J. A. P. Martins, N. J. Nunes, P. O. J. Pedrosa and A. Seganti, arXiv:1109.6793.
13. P. E. Vielzeuf and C. J. A. P. Martins, PRD **85**, 087301 (2012).
14. S. Ekstrom *et al*, A. & A. **514**, A62 (2010).
15. M. A. Perez-Garcia and C. J. A. P. Martins, arXiv:1203.0399.
16. J. P. P. Vieira, C. J. A. P. Martins and M. J. P. F. G. Monteiro, 2012, to appear.
17. P. Noterdaeme, P. Petitjean, R. Srianand, C. Ledoux and S. Lopez, A. & A. **526**, L7 (2011).
18. I. de Martino, F. Atrio-Barandela, A. da Silva, H. Ebeling, A. Kashlinsky, D. Kocevski and C. J. A. P. Martins, arXiv:1203.1825.
19. A. Avgoustidis, G. Luzzi, C. J. A. P. Martins and A. M. R. V. L. Monteiro, J.C.A.P. **1202**, 013 (2012).
20. A. Avgoustidis, C. Burrage, J. Redondo, L. Verde and R. Jimenez., J.C.A.P. **1010**, 024 (2010).

On the physical origin of the dark energy component: a revival of the vacuum contribution.

A. BLANCHARD[1], A. DUPAYS[1], B. LAMINE[2]
[1]*Université de Toulouse, Paul Sabatier, IRAP, F-31400 Toulouse, France,* [2]*Université Pierre et Marie Curie, UPMC, ENS, Laboratoire Kastler Brossel, F-75252 Paris Cedex 05, France*

The acceleration of the expansion can now be regarded as established beyond reasonable doubt. However, the physical origin of this acceleration, the so-called dark energy, remains a puzzling problem in fundamental physics. The current explanations, quintessence and modified gravity, are based on a fundamental revision of known physics. Here we present a revival of an old proposition : that the origin of cosmic acceleration is due to the gravitational active vacuum. This possibility is generally belived to be plagued by a large discrepancy in order of magnitude which has lead to the conclusion that such possibility was excluded. However, the situation is very different in the presence of additional dimensions of space. In such case, a non vanishing contribution from the vacuum through a Casimir effect of the gravitational field can arise connecting the observed present day value of the dark energy density to high energy scale of the order of TeV. Furthermore, the equation of state of such a component is exactly those of a cosmological constant. The consequences of this model are briefly discussed.

1 Introduction

The evidence for the acceleration of the expansion of the universe has gained in strength since the first result from the Hubble diagram of distant type Ia supernovae [1,2]. The angular power spectrum of the fluctuations in the cosmic microwave background and the large scale properties of the galaxy distribution are all consistent with the accelerated expansion of an homogenous universe, while no alternative Friedmann-Lemaître model seems to be able to reproduce these three data sets [3,4]. Dark energy, the origin of the cosmic acceleration, is often qualified as one of the deepest mysteries of modern physics whose origin is hard to explain within the standard framework of high energy physics [5]. This issue is a tremendous stimulation for the community, producing a rich ensemble of theoretical approaches, while being the target of unprecedent efforts in astrophysical observational strategy, either in the form of ground projects [6] or ambitious space projects like EUCLID [7].

Historically, a cosmic acceleration was possible from a genuine Cosmological Constant (CC), as introduced by Einstein in 1917. In retrospect, most scientists agree on the lack of theoretical motivation for the introduction of such a term into the Einstein equations. A physical explanation came from the identification of the Cosmological Constant to a Lorentz invariant vacuumby Lemaître:1934. The possibility of a gravitationally active vacuum due to the contribution of zero-point energy has been discussed as early as in the 1920s by Nernst and Pauli and it was immediately realized that this possibility is plagued by a large discrepancy in estimate order of magnitude. The zero-point energy of vacuum in quantum field theory and its dramatic consequences in cosmology have been further emphasized in early time of the theory.

2 The zero-point energy contribution to the Vacuum

Considering the example of a massive scalar field, the bare contribution of zero-point energy to the density is obtained as the expectation value of the 00 component of the energy momentum $T^{\mu\nu}$

$$\rho_v = \langle 0|T^{00}|0\rangle = \frac{1}{2(2\pi)^3}\int_0^{+\infty} \sqrt{m^2+k^2}\, d^3k \tag{1}$$

This contribution is highly divergent. In the absence of any further knowledge, a first assumption is to assume the existence of some cutoff k_c at high energy, whose natural scale is the Planck scale. For a mass m much smaller than the Planck mass

$$\rho_v(k_c) = \frac{k_c^4}{16\pi^2}\left(1+\mathcal{O}\left(\frac{m^2}{k_c^2}\right)\right) \tag{2}$$

that is known to be $\sim 10^{120}$ larger than the observational limits on the present day cosmic density. This is the so called first cosmological constant problem or the vacuum catastroph. One can envisaged that some symmetry ensures cancellation of the total contribution at high energy, as in supersymmetry. Experimentally such a symmetry is broken at energy below 1 TeV, so the discrepancy remains as large as $\sim 10^{60}$ at least. At this stage, it is worth noting that for a massless scalar field in an isotropic space, the vacuum pressure can be computed in a similar way to the density

$$p_v = (1/3)\sum_i \langle 0|T^{ii}|0\rangle = \frac{1}{3}\frac{1}{2(2\pi)^3}\int_0^{+\infty} k\, d^3k \tag{3}$$

This expression is formally identical to one third of the expression of the density (equation (1) with $m=0$). These expressions have to be renormalized in order to get physical finite values. In the simplest case where the same regularization procedure is applied to p_v and ρ_v, the equation of state is

$$p_v = \frac{1}{3}\rho_v \tag{4}$$

while Lorentz invariance of the vacuum implies

$$p_v = -\rho_v \tag{5}$$

Therefore has the vacuum to follow the two equations of state simultaneously would guaranty $p_v = 0$ and $\rho_v = 0$. However the regularization procedure may not always lead to this conclusion. For instance, for massive fields and developping both the density and pressure terms in power of m/k Zeldovich[8] found an a priori non vanishing term that is Lorentz invariant. More recently, it has been argued that non covariant counterterms can lead to Lorentz invariant vacuum[9]. For a recent discussion of the quantum vacuum contribution to the density of the universe see[7].

Even if this specific consideration for a massless field does not stand for a general demonstration, the previous consideration corroborates the standard conclusion that some unknown mechanism sets the contribution of vacuum energy to exactly zero in a 4D isotropic spacetime. The origin of the acceleration of the expansion of the universe is then logically expected to happen from a distinct physical mechanism. The late domination of a scalar field or modifications to the Einstein-Hilbert action are the two options most investigated by now, subject of intensive research activities since the evidence for an accelerated expansion[10,11].

Even if the ground value of vacuum density energy is zero, a modification of the properties of quantum vacuum is known to lead to non trivial physical effects. The Casimir force between two infinite plates is a known example of a non zero contribution from the QED vacuum. In this configuration, isotropy of space has been obviously broken. The pressure in the direction normal to the plates satisfies $p_\perp = 3\rho$ (with $\rho < 0$). Remarkably enough, the Lorentz invariance in the 2 dimensions parallel to the plates ensures the equation of state $p_{\|} = -\rho$ with a non zero value of ρ: indeed the pressure parallel to the plates can be computed and satisfies $p_{\|} = -\rho$ [12], consistenly with the traceless nature of the electromagnetic field.

3 Casimir effect from higher dimension

The presence of additional space dimensions has been proposed with various motivations in modern physics [10], from the Kaluza-Klein scenario aiming at unification of interactions to the more recent braneworld paradigm dealing with the hierarchy issue [13,14]. In the braneworld picture, with one or several additional dimensions, matter is localized in a 4D spacetime (the brane) while gravity can propagate in all the dimensions (the bulk). In a 4+d isotropic spacetime the density and pressure of the vacuum will have similar expressions than before and the equation of state will be

$$p_v = \frac{1}{3+d}\rho_v \tag{6}$$

As in the 4D case, we still assume some unknown mechanism to set the gravitationally active vacuum energy to zero for fields which are confined to the brane as well as to those propagating in the bulk. However, in the case of compact additional dimensions as proposed originally in ADD model [13], the situation is different since the structure of the quantum vacuum is modified by the quantification along the additional dimension. This quantification of the gravitational field modes in the bulk leads to a Casimir energy that has been computed many years ago in [15] and later, using a zero-point energy calculation, Rohrlich [16] regularized the divergence by introducing a convergence factor $\exp(-\alpha\omega_n(k))$ in the summation, which leads to the following expression of the Casimir density energy [16]

$$\rho_v^{5\mathrm{D}} = \frac{15\hbar c}{2\pi^2\alpha^5} - \frac{15\hbar c\zeta(5)}{128\pi^7 R^5} \tag{7}$$

While the pressure can be derived from energy conservation condition for variation of the radius R:

$$p_v^{5\mathrm{D}} = -\frac{15\hbar c}{2\pi^2\alpha^5} - \frac{60\hbar c\zeta(5)}{128\pi^7 R^5} \tag{8}$$

The usual renormalization procedure consists in subtracting the divergent term in the previous expressions ($\alpha \to 0$). Equivalently, this imposes vanishing Casimir energy and pressure for an infinitely large radius R and an otherwise negative energy contribution, opposite to what would be needed to match the observed dark energy. Another equally sound solution is to renormalize the Casimir energy and pressure to zero for a finite value R_i, a scale at which the new physics occurs. In order to get the macroscopic terms of the energy-momentum tensor it is necessary to integrate along the fifth dimension, the energy density finally reads

$$\rho_v = \int_0^{2\pi R} \rho_v^{5\mathrm{D}}\, dx^5 = \frac{15\hbar c\zeta(5)}{64\pi^6 R^4}\left[\left(\frac{R}{R_i}\right)^5 - 1\right] \tag{9}$$

while the pressure term in the fifth dimension reads:

$$p_v^{5\mathrm{D}} = \int_0^{2\pi R} p_v^{5\mathrm{D}}\, dx^5 = \frac{60\hbar c\zeta(5)}{64\pi^6 R^4}\left[\left(\frac{R}{R_i}\right)^5 - 1\right] \tag{10}$$

The pressure term corresponds to the diagonal elements of the energy-momentum tensor on the usual space dimension and can be obtained from the fact that the 5D $T^{\mu\nu}$ is traceless:

$$p_v^i = -\frac{15\hbar c\zeta(5)}{64\pi^6 R^4}\left[\left(\frac{R}{R_i}\right)^5 - 1\right] \tag{11}$$

Thus we therefore recover the equation of state for vacuum in the usual 4D space:

$$p_v^i = -\rho_v \tag{12}$$

In the initial state $R = R_i$, $\rho_v = 0$ and for $R = R_f$ larger than R_i, the Casimir energy density becomes positive. Eq. (9) can thus be identified with the present day dark energy density 4 keV/cm^3 for appropriate (R_i, R_f) provided R_f is below present day experimental limits on the size of a 5th compact dimension, roughly in the range of $50\,\mu$m [17]. Taking the non dimensional quantity $[(R_f/R_i)^5 - 1]$ of the order of one, the previous identification leads to $R_i \sim R_f \sim 10\mu$m. A consequence is that gravitation law might be modified on scales of the order of tens of μm.

The isotropy of space will be broken when the size of the horizon reaches the size of the compact dimension. It is therefore natural to expect that the mechanism keeping the contribution of zero-point energy to exactly zero will break at this epoch. This allows to estimate the energy at which this breaking of the 5D Lorentz invariance is expected to occur : the corresponding Hubble time being $\sim 10^{-13}$ s, it corresponds to an energy of 1 TeV, a value close to anticipated unification scale in higher dimension scenarios [13].

4 Conclusion

In this work, we have shown that zero-point energy contribution from additional compact dimension can provide a small positive value to the density of the universe. Such a term is produced by a Casimir effect and is naturally Lorentz invariant in the usual 4D spacetime and therefore provides a natural explanation for the observed cosmological constant, whose effective value is related to the evolution of the size of the compact dimension. This mechanism provides a natural explanation for the origin of the observed cosmic acceleration which appears as a manifestation of the quantized gravitational field in higher dimensions. A first consequence is that the equation of state parameter of dark energy should be $w = -1$. A second consequence is that gravitation law is modified on scales of the order of the size of the compact dimension, which could be of the order of $10\,\mu$m, a value below the dimensional Dark Energy length scale $(\hbar c/\rho_v)^{1/4} \sim 85\,\mu$m [17].

References

1. Riess, A. G., Filippenko, A. V., Challis, P., et al. 1998, *Astron. Journal* , 116, 1009
2. Perlmutter, S., Aldering, G., Goldhaber, G., et al. 1999, *Astrophys. Journal* , 517, 565
3. Frieman, J. A., Turner, M. S., & Huterer, D. 2008, *Annual Rev. Astron. Astrophys.* , 46, 385
4. Blanchard, A. 2010, *Astron. Astrophys. Rev.* , 18, 595
5. Weinberg, S. 1989, *Reviews of Modern Physics*, **61**, 1
6. LSST Science Collaborations, Abell, P. A., Allison, J., et al. 2009, arXiv:0912.0201
7. Laureijs, R., Amiaux, J., Arduini, S., et al. 2011, arXiv:1110.3193
8. Zel'dovich, Y. B. 1968, Soviet Physics Uspekhi, 11, 381
9. Hollenstein, L., Jaccard, M., Maggiore, M., & Mitsou, E. 2011, arXiv:1111.5575
10. Martin, J. 2012, arXiv:1205.3365
11. Clifton, T., Ferreira, P. G., Padilla, A., & Skordis, C. 2012, *Phys. Reports* , 513, 1
12. Weinberg, D. H., Mortonson, M. J., Eisenstein, D. J., et al. 2012, arXiv:1201.2434
13. Brown L.S. & Maclay G. J., *Phys. Rev.* , 184, 1272 (1969).
14. Arkani-Hamed, N., Dimopoulos, S., & Dvali, G. 1998, *Phys. Lett.* B, 429, 263
15. Randall, L., & Sundrum, R. 1999, *Phys. Rev. Lett.*, 83, 3370
16. Appelquist, T., & Chodos, A. 1983, *Phys. Rev.* D, 28, 772
17. Rohrlich, D., 1984, *Phys. Rev.* D, 29, 330
18. Kapner, D. J., Cook, T. S., Adelberger, E. G., et al. 2007, *Phys. Rev. Lett.*, 98, 021101

Cosmological constraints from stacked voids in the SDSS

P.M. Sutter, G. Lavaux, B.D. Wandelt, D.H. Weinberg

Department of Physics, University of Illinois at Urbana-Champaign, Urbana, IL 61801
UPMC Univ Paris 06, UMR7095, Institut d'Astrophysique de Paris, F-75014, Paris, France
CNRS, UMR7095, Institut d'Astrophysique de Paris, F-75014, Paris, France
Center for Cosmology and Astro-Particle Physics, Ohio State University, Columbus, OH 43210
Department of Astronomy, University of Illinois at Urbana-Champaign, Urbana, IL 61801
Department of Astronomy, Ohio State University, Columbus, OH 43210

We discuss the application of the Alcock-Paczynski test to constrain cosmological parameters by measuring ellipticities of stacked voids. We use voids from the Sutter et al. (2012) void catalog, which was derived from the SDSS DR7 main sample and LRG spectroscopic catalogs. We apply the shape-fitting procedure presented in Lavaux & Wandelt (2011) to ten void stacks out to redshift $z = 0.36$. We use the void ellipticity measurements to constrain Ω_M at the $\sim 20\%$ level, with larger uncertainties on dark energy equation of state parameters. Our results are consistent with WMAP 7-year cosmological constraints.

1 Introduction

Characterizing the nature and history of dark energy is perhaps the greatest challenge in the near future of observational cosmology. Many complimentary probes now examine this cosmic acceleration by exploiting multiple cosmological distance measures and the growth of structure. Many reviews of past probes, current constraints, and future predictions are available, such as [1]. The Alcock-Paczynski (A-P) test [2], in which ratios of cosmological distance measures will deviate from an assumed cosmology as a function of redshift, is potentially a powerful direct probe of cosmology.

While there are many candidate structures available for applying the A-P test in the Universe, perhaps the best ones are cosmic voids. Voids are the large, underdense regions that occupy a large fraction of the volume of the Universe. Voids are potentially more powerful probes because of their small size compared to the BAO scale, allowing for better statistics, and their relative emptiness, reducing systematics due to galaxy peculiar velocities. [3] found that dense spectroscopic galaxy surveys such as EUCLID [4] are potentially capable of measuring stacked void ellipticities to such a high fidelity that the A-P test would significantly outperform BAO measurements, even for surveys not optimized for void detection.

For this work, we will apply the A-P test to stacked voids from the void catalog of [5], which is derived from the Sky Survey (SDSS) Data Release 7 [6]. While we don't expect the SDSS to provide significantly strong constraints due to its sparseness, this will allow us to compare to theoretical expectations and provide more accurate prospects for future missions.

Table 1: Data samples used in this work.

Sample Name	Catalog	$M_{r,\min}$	$z_{\min}$	$z_{\max}$	Mean Spacing (h^{-1}Mpc)
dim1	NYU VAGC	-18.9	0.0	0.05	3
dim2	NYU VAGC	-20.4	0.05	0.1	5
bright1	NYU VAGC	-21.35	0.1	0.15	8
bright2	NYU VAGC	-22.05	0.15	0.2	13
lrgdim	LRGs	-21.2	0.16	0.36	24
lrgbright	LRGs	-21.8	0.36	0.44	38

1.1 Measuring Ellipticity & The A-P Test

We follow the analysis of [3], which involves stacking voids, pixelizing the density to smooth fluctuations, and fitting to an ellipse assuming a radial profile using a Monte Carlo Markov Chain exploration. This process gives us an estimate of the stacked void ellipticity and its uncertainty.

At sufficiently low redshifts, the void ellipticity reduces to $e_v(z) = E(z)$, where $E(z)$ is the expansion rate at redshift z, and $e_v(z)$ as the measured void ellipticity. As we stack voids within redshift bins, we assume that the stack provides a measurement of the *average* ellipticity in that bin, and we will compare that to the average stretching in that bin:

$$\frac{1}{\bar{E}(z)} = \frac{1}{\Delta z}\int_z^{z+\Delta z} \frac{dz'}{E(z')}, \tag{1}$$

where the given bin starts at redshift z and has width Δz.

Throughout we will assume a dark energy equation of state as parameterized by [7, 8], which gives a Hubble equation at low redshifts of

$$E(z, w_0, w_a) = \left(\Omega_m(1+z)^3 + \Omega_\Lambda(1+z)^{3(1+w(z))}\right)^{1/2}, \tag{2}$$

where Ω_m and Ω_Λ are the matter and dark energy densities relative to the critical density.

2 Void catalogs

We take our void catalog from [5], which is based on volume-limited samples of the New York University Value-Added Galaxy Catalog [9]. We also use the LRG catalog of [10]. Table 1 gives a brief overview of the volume-limited samples used in this work. Additionally, to improve our statistics by using as many voids as possible, we merge the four samples within $z < 0.2$ into two samples: *dim1+dim2* and *bright1+bright2*.

[5] produced void catalogs using a modified version of the void finder ZOBOV [11]. To remove the bias due to the presence of the mask, we choose the "central" catalog of voids, which are selected such that they could not possibly intersect any boundary or mask in the survey.

3 Results

Figure 1 shows a Hubble diagram of the expansion rate $E(z)$ constructed via the identity discussed above. For the expected ellipticity we assume a fiducial cosmology of $\Omega_M = 0.27$, $\Omega_\Lambda = 0.73$, and $h_0 = 0.71$ [12]. We see a strong signal consistent with a positive measurement of steadily increasing ellipticity with redshift, consistent with expectations from the A-P test. Indeed, summed across all the ellipticity measurements we deviate from unity by over 14σ.

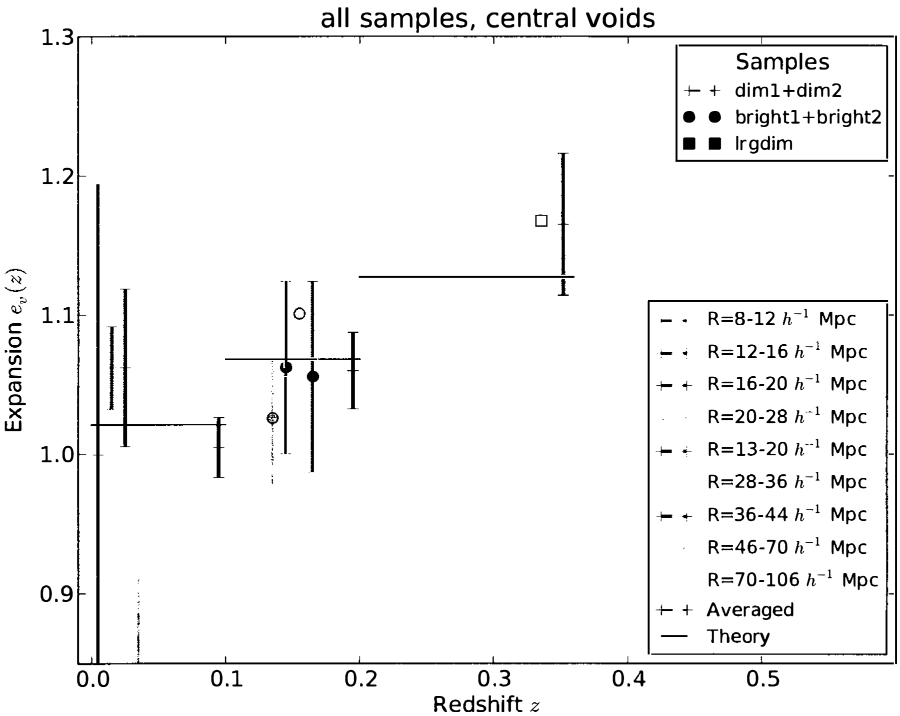

Figure 1: We show the measured ellipticity (points with error bars) of each stack for all samples versus the expected mean ellipticity in that redshift bin (black horizontal lines). We indicate each sample with a different point shape, and each radial bin with a unique color. Also, the bins are ordered left-to-right within each sample redshift range. Note that we distribute the individual points within the redshift range for clarity of plotting only. The black points with error bars indicate the weighted mean of the measurements in that redshift range. Error bars indicate 1σ uncertainty.

We use the calculated expansion rates derived from ellipticity measurements to produce cosmological constraints. For this example we perform a simplified analysis of only three parameters: Ω_M, w_0, and w_a. We thus assume a flat Universe ($\Omega_k = 0.0$) and a fixed Hubble parameter of $h_0 = 0.71$. Figure 2 shows our 1σ and 2σ likelihood contours for each two-dimensional marginalization of the three explored parameters. Overlaid on the $\Omega_M - w_0$ marginalization are the likelihood contours of the WMAP 7-year results plus supernovae measurements [12].

Since our measurements are at very low redshift ($z < 0.36$) we do not constrain the dark energy equation of state parameters strongly. However, our results at low redshift are still sensitive to Ω_M. Hence, our measurements here provide much stronger constraints, on the order of $\sim 20\%$. The single measurement in the *lrgdim* sample provides the anchor for these constraints, and since it is very uncertain we have very large contours. In all cases, our likelihoods overlap the preferred regions of the WMAP7+SN constraints.

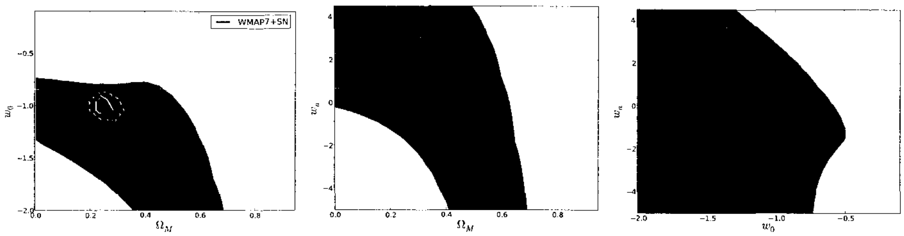

Figure 2: We show 1σ (dark red) and 2σ (light red) marginalized likelihood contours on the $w_0 - \Omega_M$ (left), $w_a - \Omega_M$ (middle), and $w_a - w_0$ (right) planes assuming $\Omega_k = 0.0$ and $h_0 = 0.71$. In the $w_0 - \Omega_M$ plane we also show the 1σ and 2σ contours (solid and dotted black lines) from the WMAP 7-year results combined with constraints from Supernovae.

4 Conclusions

We have performed the first successful application of the Alock-Paczynski test to stacked voids in observational data. While the SDSS is certainly not an optimal survey for voids due to its sparseness and limited redshift range, we are still able to use voids in this survey to provide cosmological constraints. After correcting for a systematic offset, we are able to constrain Ω_M at the 20% level. Our constraints on the dark energy equation of state parameters w_0 and w_a, while more uncertain, are consistent with current observations.

Our results are limited by the depth of currently available data. Future missions, such as EUCLID [4], will perform spectroscopic surveys of many more galaxies, over a wider range of sky, and out to higher redshifts. Future work, including more thorough analysis of LRG data from BOSS [13] and modeling of the underlying systematics will potentially make cosmological analysis with voids an essential future resource for probing the past history of the Universe.

References

[1] D.H. Weinberg et al. *arXiv e-prints: 1201.2434.*

[2] C. Alcock and B. Paczynski. *Nature*, 281:358–359, 1979.

[3] G. Lavaux and B. D. Wandelt. *eprint arXiv:1110.0345*, 2011.

[4] D. Schlegel et al. *ArXiv e-prints: 1106.1706*, 2011.

[5] P.M. Sutter et al. *Astrophys. J. (in prep)*, 2012.

[6] Kevork N. Abazajian et al. *Astrophys. J. Supp.*, 182:543–558, 2009.

[7] M. Chevallier and D. Polarski. *International Journal of Modern Physics D*, 10:213, 2001.

[8] E.V. Linder. *Phys. Rev. Lett.*, 90:091301, 2003.

[9] M. R. Blanton et al. *The Astronomical Journal*, 129:2562–2578, 2005.

[10] E. A. Kazin et al. *Astrophys. J.*, 710:1444–1461, 2010.

[11] M. C. Neyrinck. *MNRAS*, 386:2101–2109, 2008.

[12] E. Komatsu et al. *Astrophys. J.*, 192:18, 2011.

[13] S. E. Nuza et al. *ArXiv e-prints: 1202.6057*, 2012.

LSST PREDICTED SENSITIVITY TO DARK ENERGY WITH COSMIC MAGNIFICATION

A. BOUCAUD[a], J.G. BARTLETT, G. BLANC
AstroParticule et Cosmologie, Univ Paris Diderot, CNRS/IN2P3, CEA/Irfu, Obs de Paris, Sorbonne Paris Cité, France

We present expected cosmological constraints in the $w_0 - w_a$ plane from with tomographic cosmic magnification using the Fisher matrix formalism for an LSST-like survey. Our preliminary results presented here only take into account statistical errors. We find that cosmic magnification has the potential to give competitive constraints and provide a complementary cosmological probe with different systematics than cosmic shear.

1 Introduction

Weak gravitational lensing is becoming a powerful probe of the content of the Universe as it traces the mass and evaluates cosmological distances along the line-of sight. This paper focuses on cosmic magnification, an aspect of weak lensing less studied so far than cosmic shear. First magnification measurements were made in 2005 [2] and only a few have been released since then on the subject. If shear has a signal-to-noise ratio 2 to 5 times greater than magnification, it does require shape measurements. We can thus use many more objets with cosmic magnification and win back competitiveness, especially with upcoming wide and deep surveys such as LSST.

In this paper, we present preliminary predictions for the dark energy equation-of-state parameters constraints with cosmic magnification, in the framework of LSST.

2 Theory

2.1 Magnification bias

Gravitational lensing is mainly parametrized along a given line-of-sight $\vec{\theta}$ by the convergence $\kappa(\vec{\theta})$ and the shear $\gamma(\vec{\theta}) \equiv \gamma_1(\vec{\theta}) + \mathrm{i}\gamma_2(\vec{\theta})$ in complex notations. The angular distortions due to

[a] aboucaud@apc.univ-paris7.fr

lensing can be described by the Jacobian matrix $\mathcal{A}$:

$$\mathcal{A} = \begin{pmatrix} 1-\kappa-\gamma_1 & -\gamma_2 \\ \gamma_2 & 1-\kappa+\gamma_1 \end{pmatrix}$$

which leads to the magnification $\mu(\vec{\theta}) = (\det \mathcal{A})^{-1} = \left((1-\kappa(\vec{\theta}))^2 - \gamma^2(\vec{\theta})\right)^{-1}$.
In the weak lensing regime $\kappa, |\gamma| \ll 1$, the magnification reduces to first order to

$$\mu(\vec{\theta}) \simeq 1 + 2\,\kappa(\vec{\theta}) \,. \tag{1}$$

Gravitational light deflection preserves surface brightness of sources (Liouville's theorem) but changes their surface-density. This leads to an increase of the flux or magnification in the image of the source and objects that were too faint become visible ; while the source density is diluted because of sky enlargement behind the lens. Hence, for magnitude-limited survey, the number of images observed is related to the actual number of sources at that magnitude by the relation:

$$N(<m) = \mu^{\alpha(m)-1}\, N_0(<m) \,, \tag{2}$$

where $\alpha(m)$ is proportional to the slope of the galaxy number counts at magnitude m. That equation is referred to as the magnification bias. This physical process only (apart from dust extinction) can lead to a locally lower number density of objects.

2.2 Cross-correlations

We consider now two line-of-sight populations of galaxies $\delta^{\rm fg}$ and $\delta^{\rm bg}$ respectively at redshifts $z_{\rm fg}$ and $z_{\rm bg}$ with $z_{\rm fg} < z_{\rm bg}$. Assuming they are well separated in redshift, there is no cross-correlation between them $\langle \delta_g^{\rm bg} \delta_g^{\rm fg} \rangle = 0$. Because $\delta^{\rm fg}$ acts as a lens on $\delta^{\rm bg}$ and considering what was said in 2.1, we should find an excess or a lack of galaxies from the population at $z_{\rm bg}$ around each galaxy at $z_{\rm fg}$ depending on the magnitude cuts for the selection and the slope of the number counts (cf. Eq. (2)). In other words, the gravitational magnification creates a cross-correlation between the two independent populations of galaxies:

$$\begin{aligned} \langle \delta_{g,obs}^{\rm bg}\, \delta_g^{\rm fg} \rangle &= \langle (\delta_g^{\rm bg} + \delta_\mu^{\rm bg}) \delta_g^{\rm fg} \rangle \\ &= \cancel{\langle \delta_g^{\rm bg} \delta_g^{\rm fg} \rangle} + \langle \delta_\mu^{\rm bg}\, \delta_g^{\rm fg} \rangle \end{aligned} \qquad \text{with} \qquad \left| \begin{aligned} \delta_\mu &= \mu^{\alpha-1} - 1 \\ \delta_g &= b\,\delta \end{aligned} \right.$$

where b is the biasing parameter of the galaxies. Thus, the angular cross-correlation between two galaxy populations, for an angular separation $\theta = |\vec{\theta}|$ is given by

$$\begin{aligned} w_{\mu\delta_g}(\theta) &= \langle \delta_{g,obs}^{\rm bg}(\vec{\phi})\, \delta_g^{\rm fg}(\vec{\phi}+\vec{\theta}) \rangle = \langle \delta_\mu^{\rm bg}(\vec{\phi}) \delta_g^{\rm fg}(\vec{\phi}+\vec{\theta}) \rangle \\ &= 2\,(\alpha-1)\,\bar{b}\,\langle \kappa(\phi)\,\bar{\delta}(\phi+\vec{\theta}) \rangle \end{aligned} \tag{3}$$

where κ is the lensing convergence and δ a weighted projection of the density contrast whose expressions can be found in [1].

Using the Limber's equation for the statics of projected homogeneous Gaussian random fields as well going to Fourier space to retrieve the matter power spectrum $P_\delta(k)$, we introduce the magnification cross-power spectrum

$$w_{\mu\delta_g}(\vec{\theta}) = \int \frac{d^2 l}{(2\pi)^2}\, e^{-i\vec{l}\cdot\vec{\theta}}\, P_{\mu\delta}(l) \quad \text{with} \quad P_{\mu\delta}(l) = 2\,(\alpha-1)\,b \int d\chi\, \frac{p_\kappa(\chi)\, p_\delta(\chi)}{\chi^2}\, P_\delta\left(\frac{l}{\chi}, \chi\right) \tag{4}$$

where p_δ is the lens distribution function and p_κ the lensing kernel containing the source distribution.

2.3 Tomography

What stands here for tomography is the idea of probing several background slices with a given lens and then shift the lens to the first background bin and repeat the same schematic until there is only one bin left. The interest is that

1. by carefully tuning the range of the redshifts bins given photometric uncertainties, we make sure at first order there will not be any overlap between the sources and the lens plane when moving the lens to higher redshifts.
2. by cross correlating multiple background samples with the same lens, we can fit out the bias and the matter power spectrum at the lens redshift. This will be the purpose of future work.

Figure 1 shows LSST expected galaxy-redshift distribution when the depth of the survey reaches $i = 25$; and several redshift bins for the tomography pattern aforementioned. The blue bin is the starting point for the lens as the red bins for the background planes. The chosen space between background slices is enough to avoid contamination from one to another, especially when the lens will shift from one to another.

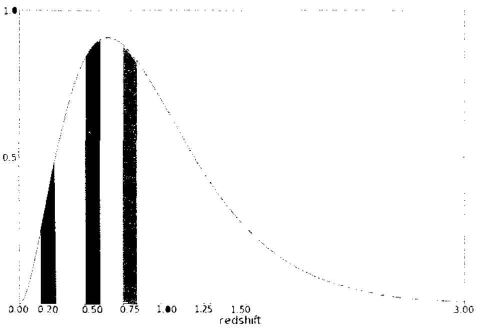

Figure 1: Normalised probability distribution of galaxies as seen by the LSST with a magnitude limit of $i = 25$. The colored slices represent redshift bins that account for lens and the background planes. The blue color only stands for the starting point for the lens in the tomography process. The lens will then move to the next redshift bin and the computation will proceed with the remaining background slices.

3 Fisher analysis

In those simulations, we used the Fisher matrix formalism to derive constraints on the dark energy equation-of-state:

$$\mathcal{F}_{\alpha\beta} = \sum_l \sum_{i,j} \frac{\partial P^{(i)}_{\mu\delta}(l)}{\partial p_\alpha} \, \mathcal{C}^{-1}_{ij}(l) \, \frac{\partial P^{(j)}_{\mu\delta}(l)}{\partial p_\beta} \tag{5}$$

where i and j denote the multiple backgrounds chosen to compute the cross power spectra (*eg.* $P^{(i)}_{\mu\delta} = P_{\mu_i\delta}$). In this preliminary study, we fix the value of the other cosmological parameters and choose the bias $b = 1$ and we use the code *NICAEA*[6] to compute the matter power spectrum $P_\delta(k)$.

The covariance matrix $\mathcal{C}$ we derived is composed of three terms[3] : the clustering term $\mathcal{C}^{\mathrm{C}}$, the lensing term $\mathcal{C}^{\mathrm{L}}$ and the shot noise term $\mathcal{C}^{\mathrm{S}}$. The first one stands for the intrinsic clustering inside the populations we are probing, the second one regroups first and second order lensing cross correlations, the first order being the signal we use in this analysis. The shot noise term refers to the sparse sampling of the matter density field by astrophysical sources. Whereas the shot noise dominates at high l, the clustering and the lensing term have a relative contribution at low l that depends on the redshift of the selected populations.

4 Preliminary results

Using the Fisher matrix formalism, we have computed the probability contours in the $w_0 - w_a$ plane to probe the power of tomographic magnification in constraining the evolution of dark energy. Figure 2 shows the results obtained with the background configuration described in Figure 1. The ellipses agree with the expected constraints from the tomographic weak lensing shear without systematic effects given in the *LSST Science Book* [7]. This tells us that with upcoming wide and deep surveys, cosmic magnification is becoming a powerful probe of dark energy.

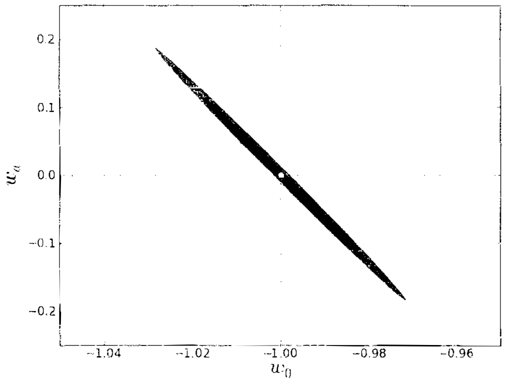

Figure 2: Preliminary constraints of the dark energy equation-of-state parameters with tomographic magnification for an LSST-like survey. Dark and light blue represent respectively $1-\sigma$ and $2-\sigma$ probability contours. These expected constraints have been derived using 5 backgrounds and account only for statistical uncertainties. The centered white dot shows the fiducial value used in the simulation.

This preliminary work does not yet include systematic errors like photometric redshift uncertainties that may affect the result. This will be addressed in a future paper [5] together with the addition of priors for the unconstrained cosmological parameters.

References

1. M. Bartelmann and P. Schneider, *Physics Reports* **340**, 291B (2001)
2. R. Scranton *et al.*, *Astrophys. J.* **633**, 589S (2005)
3. L. VanWerbaeke, *Mon. Not. R. Astron. Soc.* **401**, 2093-2100 (2010)
4. A. Heavens *et al.*, *Mon. Not. R. Astron. Soc.* **415**, 1681H (2011)
5. A. Boucaud *et al.*, *in prep.* (2012)
6. M. Kilbinger, http://www2.iap.fr/users/kilbinge/nicaea
7. LSST Science Book, http://www.lsst.org/lsst/scibook

The Hobby-Eberly Telescope Dark Energy Experiment

Martin Landriau (for the HETDEX collaboration[a])
Max-Planck-Institut für extraterrestrische Physik
Postfach 1312, Giessenbachstraße 1, 85741 Garching, Germany
and
Universitäts-Sternwarte München
Scheinerstraße 1, 81679 München, Germany

The Hobby-Eberly Telescope Dark Energy Experiment (HETDEX) is a blind spectroscopic survey to map the evolution of dark energy using Lyman-α emitting galaxies (LAEs) as tracers over the redshift range $1.9 < z < 3.5$. We will describe the survey instrument, VIRUS, which consists of 75 IFUs distributed across the 22" field of the upgraded 9.2m HET. We will then describe the main science goals of the baseline survey of 42x7 square degrees which is expected to start in early 2014 and to last 3 years and to deliver spectra of 0.75M LAEs in a 6 Gpc^3 volume. We will then discuss potential ancillary science and extensions of the survey currently under consideration. We conclude by discussing the current status of the project.

1 Introduction

Explaining the accelerated expansion of the Universe has become one of the main goals of modern cosmology. Accurately measuring the expansion rate as a function of redshift is thus an important endeavour that would provide something to which theoretical models can be compared to. Recently completed galaxy redshift surveys and data from type IA supernovae have measured this up to $z \simeq 1$; HETDEX aims to measure $H(z)$ at comparatively very high z, i.e $1.9 < z < 3.5$. In this contribution, I will describe the project and the survey instrument, our main science goals as well as ancillary science opportunities.

2 HETDEX

HETDEX will observe 294 sq. deg. centred at RA=13h and DEC= $+60°$ eventually expanded to 420 sq. deg. We also plan to observe an equatorial field of 140 sq. deg. centred at RA = 1h30m eventually expanded to 224 sq. deg. The volume of the baseline survey is 2.1(Gpc/h)^3, in which we expect to detect 0.75M LAEs.

2.1 The Hobby-Eberly Telescope

The Hobby-Eberly Telescope (HET) is located on Mount Fawlkes at the McDonald Observatory in west Texas. It has a 9.2m mirror which consists of 91 hexagonal segments. HETDEX has been guaranteed a sufficient fraction of the dark time for an initial period of 3 years. The HET

[a] `http://www.hetdex.org`

is a fixed elevation telescope and can thus only change azimuth, which means targets cannot be tracked in the conventional sense.

Part of the HETDEX budget is dedicated to upgrading the HET. Namely, a new tracker assembly will increase the field of view of from 4' to 22'; the survey instrument VIRUS; and an on-site mirror coating facility.

2.2 VIRUS

The survey instrument, the Visible Integral-field Replicable Unit Spectrograph, will consist of 75 IFUs each feeding 2 spectrographs, having a resolution of $R \simeq 750$ in the wavelength range 360nm – 540nm. It will cover the sky at a fill factor of 1/4.5 with 33500 fibres of 1.5" diameter. The 20 minute-observations will be dithered, so that the fill factor for a single IFU will be 1.

2.3 The Pilot Survey

As a proof of concept, a pilot survey was conducted at the H.J. Smith 2.7m telescope at the McDonald Observatory with a prototype spectrograph, VIRUS-P[b]. One of the main results – in preparation of HETDEX – is that LAEs can be confidently identified from other single emission line sources (see figure 17 from Adams *et al.*[2], which clearly shows that LAEs can be separated from OII emitters through an equivalent-width cut).

In order to apply this criterium for HETDEX, we need to conduct an imaging survey in parallel, down to g=25.1 in order to accurately measure the continuum level. This is currently underway and approximately 25% completed.

2.4 Cure

The data analysis pipeline for VIRUS, Cure, is being developed at MPE/USM and UNAM. After the achievement of a milestone in the development, an internal release – or *treatment* – is made. Treatment 1 was used to re-analyse the data from the Pilot Survey, which had been initially done with the VIRUS-P data analysis pipeline, Vaccine, developed in Austin. The agreement between the two independent pipelines gives us confidence in the robustness of our algorithms. The current version, Treatment 3, is fully parallelised and integrated into the Astro-Wise database system[4]. Benchmark tests have shown we could reduce a night's data (roughly 170Gb) the next day.

[b]VIRUS-P was renamed the Mitchell Spectrograph in January 2012.

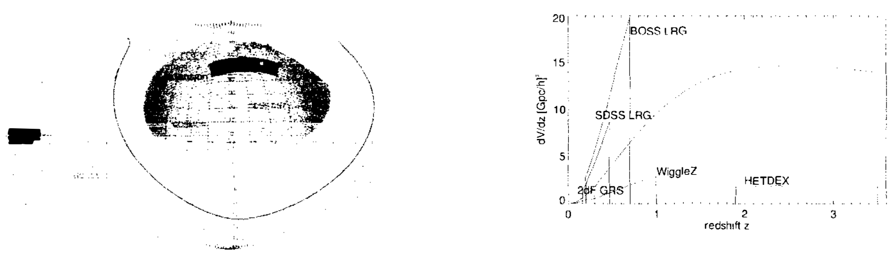

Figure 1: HETDEX survey footprint (left) and area, redshift range and volume of HETDEX in comparison to other surveys (right).

2.5 *Data Products*

We plan to have a data release 14 months after each of the following milestones: the completion of 1 and 3 years of observations and completion of all extensions.

Each data release will consist of all flux-calibrated spectra, their absolute positions on the sky to 1" and a timestamp. For each spectrum, we will provide an estimate of the spatial and spectral PSF, and the flux limit including transparency. Data access will be via a web interface in the Astro-Wise system, retrieving data from servers in Munich or Austin.

2.6 *Current Status*

The new tracker assembly has been built and tested and will be installed on the HET once the old tracker is dismantled in the late fall 2012. The installation of VIRUS will then follow. We expect to commission the instrument in early 2013 and the first science observations to take place soon after.

3 Main Science Goals

As the name of the project implies, HETDEX aims to constrain dark energy. More specifically, we aim to measure the expansion rate of the Universe and the energy density of dark energy at $z > 2$, which we will achieve by measuring the amplitude of the matter power spectrum $P(k)$ to better than 2% accuracy. Using the full shape of the 2D power spectrum, as opposed to using the baryonic acoustic oscillation (BAO) scale alone[5], HETDEX will make a joint measurement of $H(z)$ and $d_A(z)$ to better than 1% accuracy at $z = 2.3$. Given the measurement of the expansion rate, we can then measure $X(z)$, given by the last term in

$$H^2(z) = H_0^2\left[\Omega_m(1+z)^3 + \Omega_k(1+z)^2 + \Omega_{DE}X(z)\right] \tag{1}$$

to $3-\sigma$ even if it is a pure cosmological constant.

HETDEX will also be able to improve constraints on the primordial power spectrum $P_\zeta(k) \propto \left(\frac{k}{k_p}\right)^{n_s+\frac{1}{2}\alpha_s \log k/k_p}$. By combining our data with CMB data, we expect to significantly reduce the error bars on the spectral index n_s and the running parameter α_s compared to using CMB alone.

Measuring the power spectrum to high accuracy will also enable HETDEX data to constrain the summed neutrino masses Σm_ν because massive neutrinos affect the shape of the power

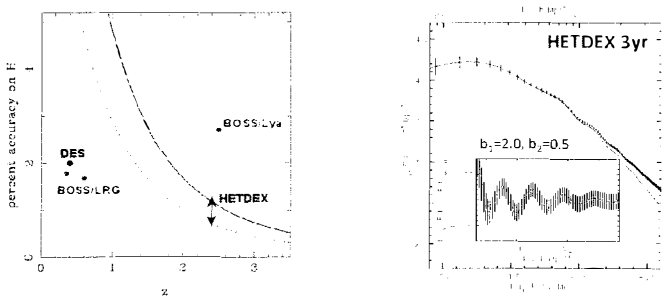

Figure 2: Expected error on the measurement of H(z) at 3 (..) and 5 (-) σ (left) and P(k) from HETDEX (right).

spectrum by suppressing power on small scales. We expect that $\Delta\Sigma m_\nu < 0.05$eV, which is the current lower limit obtained from neutrino oscillation experiments; hence HETDEX could make a measurement of, rather than put more stringent constraints on, Σm_ν.

As well as measuring the matter power spectrum, HETDEX will of course measure the matter bispectrum. The combination of the two will provide constraints on the non-linear field parameter f_{NL} of the same order as Planck for the baseline survey. This has the potential to eliminate or severely constrain inflation models.

4 Ancillary Science

The ancillary science possible with HETDEX falls in two broad categories. Firstly, because HETDEX is a blind survey, many objects aside from LAEs will be detected and this will open up many scientific opportunities. More specifically, HETDEX will detect 1M OII emitters ($0 < z < 0.5$), 0.4M other local galaxies, 0.25M stars, 2k Abell rich galaxy clusters and 10-50k AGNs ($z < 3.5$).

Secondly, combining HETDEX data with that of other projects surveying the same areas in other bands will also provide very valuable information. As an example, the Spitzer Hetdex Extragalactic Large Area (SHELA) survey, a successful proposal [3] for the last warm Spitzer cycle mapping a 28 sq. deg. subfield of the HETDEX equatorial field. The combined HETDEX and Spitzer data will allow us to connect star formation evolution to galaxy models and measure the growth of stellar mass as a function of halo mass and environment.

5 Summary

HETDEX will survey a volume of $2.1(\mathrm{Gpc/h})^3$ between $1.9 < z < 3.5$ and detect 0.75M LAEs emitters which we will use to accurately measure the full matter power spectrum, the expansion rate, the angular diameter distance and the energy density of dark energy at $z > 2$. We also expect to improve constraints on n_s, α_s, f_{NL} and Σm_ν.

First light is expected in mid-2013 and the baseline survey is expected to start soon afterwards and take 3 years to complete. The first data set will be released 14 months after our first completed observing season.

Acknowledgments

HETDEX is a consortium involving the University of Texas at Austin, the McDonald Observatory, Texas A&M University, Pennsylvania State University, the Max-Planck-Institut für extraterrstrische Physik, the Universitäts-Sternwarte-München, the Astrophysikalisches Institut Potsdam, the Institut für Astrophysik Göttingen and the University of Oxford. The project has received additional funding from the NSF, the US Air Force and many private benefactors.

References

1. G. J. Hill *et al*, SPIE Conference Series, 7775 (2010).
2. J. Adams *et al*, Astrophys. J. Supp. **192**, 5 (2011).
3. C. Papovich *et al*, Spitzer proposal ID #80100 (2011).
4. E. A. Valentijn and G. Verdoes Keijn, Highlights of Astronomy **14**, 607 (2007)
5. M. Shoji, D. Jeong and E. Komatsu, Astrophys.J. **693**, 1404 (2009)

Cosmic magnification as a probe of cosmology

Christopher Duncan, Alan Heavens, Benjamin Joachimi, Catherine Heymans
Scottish Universities Physics Alliance, Institute for Astronomy, University of Edinburgh, Royal Observatory, Blackford Hill, Edinburgh, EH9 3HJ, UK

With the wealth of upcoming data from wide-field surveys such as KiDS, Pan-STARRS, DES and Euclid, it is more important than ever to understand the full range of independent probes of cosmology at our disposal. With this in mind, we motivate the use of cosmic magnification as a probe of cosmology, presenting forecasts for the improvements to cosmic shear cosmological parameter constraints when cosmic magnification is included for a KiDS-like survey. We find that when uncertainty in the galaxy bias is factored into the forecasts, cosmic magnification is less powerful that previously reported, but as it is less likely to be prone to measurement error we conclude it is a useful tool for cosmological analyses.

1 Introduction

As light from distant galaxies propagates through the Universe, its path can be deflected by the local matter distribution, an effect called gravitational lensing. As a result, when we view images of distant galaxies we observe both a change in the shape of the image as well as a change in its size. The former of these effects is described by shear, and statistical analyses of cosmic shear have proven to be a very promising tool in constraining cosmology. However, as cosmic shear analysis requires accurate shape information of observed galaxies, its measurement has proven a particularly difficult task [1], with measurements sensitive to the Point Spread Function (PSF) and pixelisation, as well as physical contamination from intrinsic galaxy alignments.

The change in size of a body due to gravitational lensing is referred to as magnification. Whilst direct measurements of a change in sizes of a lensed galaxy population have been successful [3], these can suffer from similar measurement systematics to cosmic shear and are less frequently used for statistical analyses using magnification. Instead, magnification can also be studied via its effect on the observed number density of sources, known as magnification bias. Detections using number density effects have been performed using the cross-correlation between low redshift galaxies and high redshift quasars [4,5], and more recently with high redshift Lyman break galaxies [6,2]. Whilst weak magnification analyses via number density effects do not suffer from many of the systematics inherent in a shear analysis, they are affected however by their own set of systematics which have been less thoroughly studied.

2 Modelling Magnification Bias

By modelling the number counts of galaxies close to the survey flux limit (f) as a power law $N(>f) \propto f^{\alpha}$, it can be shown that the observed number density of galaxies on the sky is given as

$$n = n_0[1 + 2(\alpha - 1)\kappa + \delta n_g] \tag{1}$$

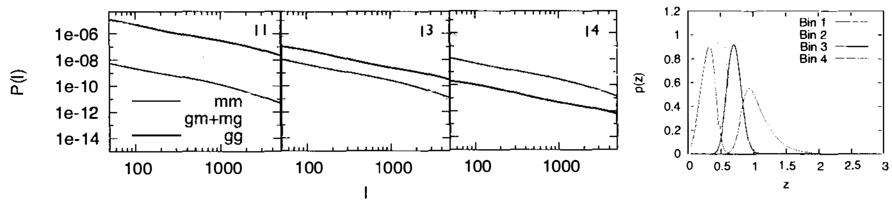

Figure 1: Contributions to Eqn. 2 using a KiDS-like survey with $\sigma_z = 0.05(1+z)$. Binned galaxy distributions are shown in the right panel, for redshift bin combinations (from left to right) of $i = 1$ with $j = 1$, 1-3, and 1-4.

where n_0 is the unlensed number density, κ the convergence and δn_g the number density fluctuation due to intrinsic clustering [7]. The number density contrast power spectrum is then

$$P^{(ij)}_{\delta_n\delta_n} = 4(\alpha^{(i)}-1)(\alpha^{(j)}-1)P^{(ij)}_{\kappa\kappa} + 2(\alpha^{(i)}-1)P^{(ij)}_{\kappa\delta n_g} + 2(\alpha^{(j)}-1)P^{(ij)}_{\delta n_g\kappa} + P^{(ij)}_{\delta n_g\delta n_g} \quad (2)$$

$$\equiv P^{(ij)}_{mm} + P^{(ij)}_{mg} + P^{(ij)}_{gm} + P^{(ij)}_{gg} \quad (3)$$

where superscript i denotes tomographic redshift bin, and $\delta_n = (n - n_0)/n_0$. The projected convergence $\kappa(\theta)$ and intrinsic clustering number density contrast $\delta n_g(\theta)$ can be related to the matter over-density [8]. The intrinsic clustering contribution is related to the matter over-density via the galaxy bias b, which can be redshift and scale dependent.

Figure 1 shows each contribution to the power spectra in Eqn. 2 for a variety of combinations of redshift bins for a KiDS-like survey with $b = 1$, non-redshift dependent $\alpha = 2$, and gaussian photometric redshift scatter with $\sigma_z = 0.05(1+z)$.

We obtain forecast parameter constraints using a Fisher information matrix [9], given by

$$F_{\alpha\beta} = \frac{1}{2} Tr[C^{-1}C_{,\alpha}C^{-1}C_{,\beta}] \quad (4)$$

where C is the covariance matrix for data vector $D = (\delta n, \kappa_s)$, assuming that all the shape information is contained in the convergence κ_s. The indices α, β run over a set of cosmological parameters $\Theta = (\Omega_{\mathrm{B}}, \Omega_{\mathrm{M}}, \Omega_\Lambda, w, \mathrm{H}_0, \mathrm{n}_{\mathrm{spec}}, \sigma_8)$, and derivatives are taken around a fiducial ΛCDM cosmology with dark energy equation of state w. The covariance matrix is given in block form, with each block giving the covariances $C_{\delta n\delta n}, C_{\kappa\kappa}$ and cross terms $C_{\delta n,\kappa}$ and $C_{\kappa,\delta n}$. The number density contrast covariance matrix is given by the power spectrum in Eqn. 2 with a shot noise term: $C^{ij}_{\delta n\delta n} = P^{ij}_{\delta_n\delta_n} + \delta_{ij}/\bar{n}^i$, and similarly $C^{ij}_{\kappa\kappa} = P^{ij}_{\kappa\kappa} + \sigma_e^2\delta_{ij}/\bar{n}^i$ with $\sigma_e = 0.4$. The matter power spectrum is modelled using an Eisenstein and Hu transfer function [10] with a non-linear correction [11].

We construct the Fisher matrix using the redshift dependent l-mode cuts from [7] given as $l_{max} = f_k(\chi(z_{med}))k_{max}(z_{med})$ for each redshift bin, with $k_{max} = 0.1$, beyond which any information from that bin is discarded. This removes non-linear scales such that we can assume linear galaxy bias. We then marginalised over N_z nuisance parameters, where N_z is the number of tomographic redshift bins used in the analysis.

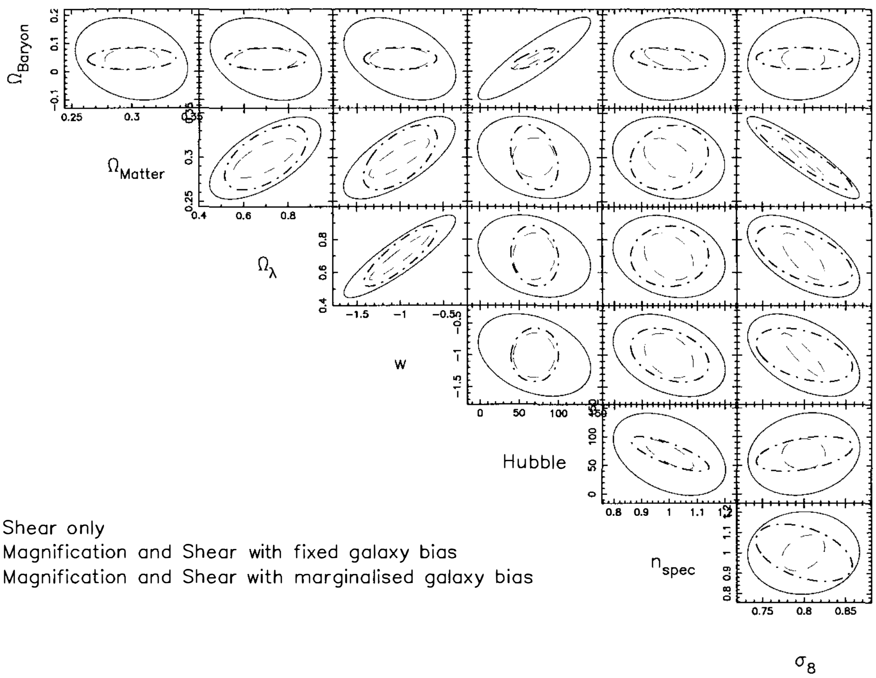

Figure 2: The 1σ marginal contours for pairs of cosmological parameters. Solid blue lines denote constraints using cosmic shear, dashed red lines are joint constraints with fixed galaxy bias $b = 1$, and dot-dashed green lines give constraints for a joint analysis using shear with cosmic magnification information with marginalised bias. Crosses mark the fiducial cosmology. This analysis assumed a KiDS like survey with with median redshift $z_{\rm med} = 0.6$, global number density of galaxies $n_{\rm gal} = 9$ for the shear signal and $n_{\rm gal} = 18$ for the magnification signal, survey area $A = 1500$ square degrees, and photometric redshift scatter $\sigma_z = 0.05(1 + z)$ using 10 tomographic bins. No priors have been applied.

3 Results

Figure 2 shows cosmological constraints for a KiDS-like survey. Considering the case with a known fixed bias parameter (shown red dashed), combining magnification and shear information gives much improved parameter constraints for nearly all cosmological parameters. In particular, constraints on both σ_8 and Ω_M are improved due to degeneracy lifting between the magnification and shear signal, as the shear signal varies $\propto \Omega_M^2$ whilst the dominant magnification signal (P_{gm} in Eqn. 2) varies $\propto \Omega_M$. This agrees well with the results presented in[12]. However, in the case of known fixed galaxy bias much of the information is expected to come from the intrinsic clustering signal, as knowledge of the bias allows the use of cosmological information from the matter power spectrum in the intrinsic clustering signal, despite using a conservative l-cut. If we compare these constraints to those when the galaxy bias is unknown and marginalised over (shown black dot-dashed), we find a degradation in the constraints on σ_8 and $\Omega_{\rm M}$ as information of the amplitude of the matter power spectrum is no longer accessible due to the linear dependence of P_{gm} on

b. As a result, much of the degeneracy lifting seen for fixed galaxy bias is lost, suggesting that parameter constraints presented using a fixed bias are overly optimistic.

The remaining parameters, $(\Omega_{\rm B}, \Omega_\lambda, w, {\rm H}_0, {\rm n}_{\rm spec})$ are robust to removal of information of the bias, as distance information is still accessible through the magnification signal, as well as the dependancy of the matter power spectrum on these parameters. Whilst improvements on constraints for $\rm H_0$ and Ω_B are promising, it should be noted that distance probes combined with CMB surveys such as Planck will constrain these values very well.

4 Conclusion

We confirm previous findings that including magnification bias with a cosmic shear analysis can significantly improve constraints on a large set of cosmological parameters, when the galaxy bias is fixed. However, in the more realistic case where the bias is marginalised over, we find only small improvement to constraints on Ω_M and σ_8. The remaining parameter errors seem less sensitive to the removal of information due to galaxy bias marginalisation. Improved knowledge of the galaxy bias can allow more information to be ascertained from the intrinsic clustering of galaxies. As the autocorrelation is dominated by intrinsic clustering (Figure 1) measurements of number density of galaxies may also glean information on the galaxy bias. Realistic measurements of magnification bias may therefore lie somewhere between the results presented for marginalised bias and fixed bias, however it should be noted that in any case a Fisher matrix analysis gives us the best constraints possible for a given experiment.

Future work will look further into the practical applications of magnification, taking into account catastrophic photometric redshift failures, the redshift dependence of the slope of the galaxy number counts (α in Eqn. 1) and other systematics such as the effect of spatially varying dust extinction and the effect of magnitude zero-point errors in a survey. The effect of catastrophic photometric redshift failures are particularly important as they can induce non-zero intrinsic clustering contamination from sources and lenses separated by a large photometric redshift, or contamination through non-vanishing P_{mg} in Eqn. 2, potentially limiting useable information from magnification.

As magnification bias is affected by different measurement and statistical errors to those affecting cosmic shear analyses, both are complementary probes of cosmology, suggesting that magnification could also be used to better control the systematics of a shear analysis. Moreover, as accurate photometry is already taken with many surveys, this information is obtained for free.

References

1. T. Kitching *et al*, Arxiv e-print , 1009.0779 (2010)
2. C. B. Morrison *et al* Arxiv e-print , 1204.2830 (2012)
3. F. Schmidt *et al*, ApJ **744**, L22 (2012)
4. R. Scranton *et al*, ApJ **633**, 589 (2005)
5. A.D. Myers *et al*, MNRAS **359**, 741 (2005)
6. H. Hildebrandt *et al*, A&A **507**, 683 (2009)
7. B. Joachimi, S. Bridle, A&A **523**, 1 (2010)
8. M. Bartelmann, P Schneider, Physics Reports **340**, 291 (1999)
9. M. Tegmark *et al*, ApJ **480**, 22 (1997)
10. D. Eisenstein, W. Hu, ApJ **496**, 605 (1998)
11. R.E. Smith *et al*, MNRAS **341**, 1311 (2003)
12. L. van Waerbeke, MNRAS **401**, 2093 (2010)

4.
Theory

INFLATION, OR WHAT?

William H. Kinney, Ghazal Geshnizjani, and Azadeh Moradinezhad Dizgah

Department of Physics, University at Buffalo, SUNY, Buffalo, NY 14260, United States of America

1 Introduction

Observations of both the Cosmic Microwave Background (CMB) and large-scale structure (LSS) are compatible with a spectrum of nearly scale-invariant and Gaussian primordial perturbations with correlations on super-Hubble length scales [1], in agreement with the predictions of the simplest inflationary models. However, inflation is not the only way to generate cosmological perturbations. Alternatives that have been put forward range from contracting scenarios where the universe needs to go through a singular or non-singular bounce (see [2] and references there), string gas cosmology, in which the universe is initially static [3], varying fundamental speed of light [4], or a rapidly varying speed of sound [5,6,7,8,9,10,11]. All of the alternatives so far suggest that to produce the observed primordial power spectrum, any route but inflation requires an understanding of gravity beyond general relativity. This is either due to violation of the Null Energy Condition, a singular bounce, or the breaking of Lorentz invariance due to a preferred frame of reference to explain varying speed of light or super-luminal sound speed [12]. (It is worth noting that inflation itself, while more successful than its alternatives on many fronts, still has its own challenges to overcome, ranging from setting the correct initial conditions [13] to relying on the existence of a scalar field which has not yet been confirmed by any fundamental theory.) It is interesting to ask: what is the most general conclusion that can be drawn from the observed spectrum of primordial perturbations in the universe?

In this contribution, we study general properties of the production of a scale-invariant two point function. We use the simple framework put forward in Ref. [14] and later used in Ref. [15] that makes it simple to study scenarios that have different background evolution but result in the same second-order gravitational action for quantum perturbations. The format of the paper is the following: In Section 2 we review the framework developed in Ref. [14]. In Section 3 we prove that to produce enough scale invariant modes on super-Hubble scales in an expanding universe one of the following conditions must be met: (1) accelerating expansion, (2) superluminal sound speed, or (3) super-Planckian energy density. Section 4 contains discussion and conclusions.

2 Action and solutions for scale-invariant curvature perturbations

The quadratic action for curvature perturbation ζ around a flat Friedmann-Robertson-Walker (FRW) background with a time dependent sound speed $c_s(\tau)$ in general can be written as[16,17] :

$$S_2 = \frac{M_{pl}^2}{2} \int dx^3 d\tau \; z^2 \left[\left(\frac{d\zeta}{d\tau} \right)^2 - c_s(\tau)^2 (\nabla\zeta)^2 \right], \tag{1}$$

where

$$z \equiv \frac{a\sqrt{2\epsilon}}{c_s},. \tag{2}$$

Here a and τ are the scale factor and conformal time, respectively, while ϵ is defined through Hubble parameter $\epsilon \equiv -\dot{H}/H^2$.

Note that for $\epsilon < 0$, which corresponds to phantom matter, we will have $z^2 < 0$. The overall sign of the action does not change the equation of motion and it leads to the same two-point function for ζ. However a problem arises, since in the presence of other fields, the kinetic term of ζ has an opposite sign. By quantizing those, we will end up with Hamiltonians which are unbounded in opposite directions, with ghost instabilities.

As was pointed out in [14], through a time transformation $dy = c_s d\tau$ one can re-express the action (1) in the new form:

$$S_2 = \frac{M_{pl}^2}{2} \int dx^3 dy \; q^2 \left[\left(\frac{d\zeta}{dy} \right)^2 - (\nabla\zeta)^2 \right], \tag{3}$$

where

$$q \equiv \frac{a\sqrt{2\epsilon}}{\sqrt{c_s}}. \tag{4}$$

Now introducing the canonically normalized scalar variable $v = M_{pl}\; q\; \zeta$, the equation of motion for v in Fourier space is given by

$$v_k'' + (k^2 - \frac{q''}{q}) v_k = 0, \tag{5}$$

where prime represents d/dy.

A scale-invariant spectrum is obtained if

$$\frac{q''}{q} \sim \frac{2}{y^2}, \tag{6}$$

in analogy with canonical inflation where $z_{,\tau\tau}/z \sim 2/\tau^2$. Eq. (6) has a general solution of the form

$$q = \frac{\alpha}{y} + \beta y^2, \tag{7}$$

for arbitrary α and β.

Production of superhorizon perturbations requires the following conditions: At early time, a mode with given comoving wavenumber k starts in an approximately Minkowski vacuum state with $k^2 \gg 2/y^2$, such that the WKB approximation is valid. At late time, the mode evolves such that $k^2 \ll 2/y^2$ and WKB breaks down, resulting in particle production. Since for increasing time $d\tau > 0$, $dy > 0$, we see that for particle production we must have $y \in [-\infty, 0]$. Therefore, at early times $\omega_k^2 \sim k^2$ and is almost constant, so that $|\omega_k'/\omega_k^2| \ll 1$ and WKB is correct. However, at late times $\omega_k^2 \sim -2/y^2$, $|\omega_k'/\omega_k^2| \sim \mathcal{O}(1)$ and WKB is no longer valid. This argument already enables us to see that at late time the α/y term is always an attractor solution and dominates over βy^2.

Applying the standard method of quantization for v and setting the adiabatic initial condition at early times, the familiar mode function[14] is obtained:

$$v_k(y) = \frac{1}{\sqrt{2k}}\left(1 - \frac{i}{ky}\right)e^{-iky}. \tag{8}$$

In long wavelength limit v_k behaves as

$$v_k \sim \frac{-1}{\sqrt{2k}}\left(\frac{i}{ky} + \frac{1}{2}k^2y^2\right) \qquad ky \ll 1. \tag{9}$$

Note that mode freezing occurs when $ky = 1$, which is not the same as when the mode crosses the Hubble horizon, $k = aH$. There are *three* horizons with independent dynamics: the Hubble horizon, $R_H \equiv 1/(aH)$, the sound horizon, $R_s \equiv c_s/(aH)$, and the "freezeout horizon"[a]

$$R_\zeta \equiv -y. \tag{10}$$

All three horizons are expressed in comoving units. As long as the freezeout horizon is shrinking, generation of perturbations occurs. Furthermore, modes can be generated on super-Hubble scales even if the Hubble horizon is growing, as long as the freezeout horizon is larger than the Hubble horizon[b]. We can now calculate the power spectrum $\mathcal{P}_k^\zeta \equiv k^3\zeta_k^2$ for different choices of α and β. First, taking $\beta = 0$ is the case very similar to inflation since for superhorizon modes we obtain:

$$k^3\zeta_k^2 \sim k^3\left(\frac{\nu_k}{M_p q}\right)^2 \sim \frac{1}{2M_p^2\alpha^2}, \tag{11}$$

which is the exact scale-invariant power spectrum. The amplitude of ζ is constant outside freezeout horizon, $R_\zeta \equiv \sqrt{q/q''} \sim y$. This solution leads to a stable solution for the background spacetime, since at $k \to 0$, a constant metric perturbation does not change the time evolution of the scale factor.

Next we consider $\alpha = 0$. Substituting for the power spectrum leads to:

$$k^3\zeta_k^2 \sim k^3\left(\frac{\nu_k}{M_p q}\right)^2 \sim \frac{1}{M_p^2\beta^2y^6}. \tag{12}$$

While this spectrum is scale invariant, the amplitude of ζ grows outside R_ζ which signals instability or a non-attractor behavior for the background.

Last, if neither of α or β are zero then

$$k^3\zeta_k^2 \sim k^3\left(\frac{\nu_k}{q}\right)^2 \sim \frac{1}{2M_p^2}\left(\frac{1}{\alpha + \beta y^3}\right)^2. \tag{13}$$

At late times, $y^3 \ll \alpha/\beta$, the α/y term will win over βy^2, and we regain the conserved ζ solution. Since we also have $ky \ll 1$ this condition is automatically satisfied if $k^3 > \beta/\alpha$. So in this case the amplitude is also well behaved and not divergent as $y \to 0$.

It is also worth noting that all these solutions correspond to exact scale invariance. In other words , even though applying the naive slow-roll result $n_s - 1 \sim 2(\epsilon + d\ln\epsilon/Hdt + d\ln c_s/Hdt)$ may suggest otherwise, calculating the spectral index n_s would result in

$$n_s - 1 = 0. \tag{14}$$

In practice, to obtain non-zero tilt, q must have deviations from these solutions. For example taking $\beta = 0$ and allowing for α to have small time dependence can lead to a small tilt[18].

[a]We use the terminology of freezeout horizon loosely to be consistent with literature. However, note that in the case where $\beta \neq 0$, then ζ is not conserved.

[b]For an example of an expanding scenario without super luminal speed of sound where the freezeout horizon is larger than the Hubble horizon see[15].

3 General conditions for scale invariance

This section contains the main result of the paper: In an expanding universe, in order to generate a scale-invariant spectrum of curvature perturbations on a range of scales compatible with observations, one of three conditions must be met: (1) accelerating expansion (*i.e.* inflation), (2) speed of sound faster than the speed of light, or (3) super-Planckian energy density. Current observations of CMB and LSS indicate that the spectrum of curvature perturbations must be nearly scale-invariant over *at least* three decades in wavelength, and we will take this to be the lower bound.

We first consider the simple case of $c_s = 1$ in an expanding background. Non-accelerating expansion implies that Hubble horizon measured in comoving units is always growing, since $\epsilon > 1$:

$$\frac{dR_H}{d\tau} = \epsilon - 1 > 0. \tag{15}$$

Following the framework described in Sec. 2, production of scale invariant modes for $c_s = 1$ leads to the freezeout horizon shrinking as $R_\zeta \equiv \sqrt{z/z_{\tau\tau}} \sim -\tau$. Note that the same argument that we used in that section for the range of y applies here to the range of conformal time τ such that $\tau \in [-\infty, 0]$.

Consider modes with comoving wavelengths $\lambda_f < \lambda < \lambda_i$ corresponding to the scale-invariant modes that we observe today in CMB and LSS. Observations of CMB and LSS require scale invariance over about three decades in wavelength,

$$\lambda_i \geq 1000\ \lambda_f. \tag{16}$$

Since the horizon is always growing, for the modes to be larger than the Hubble horizon at late time, they must also be superhorizon at early time, so that

$$\lambda_f(\tau_f) > R_H(\tau_f). \tag{17}$$

Here the conformal time τ is taken to be the time when a given mode crosses the freezeout horizon, $\lambda_i \sim |\tau_i|$, $\lambda_f \sim |\tau_f|$. Then the conditions (16) and (17) become:

$$\begin{aligned} |\tau_i| &\geq 1000\ |\tau_f|, && (18)\\ |\tau_f| &> R_H(\tau_f), && (19) \end{aligned}$$

which implies

$$\frac{\tau_f - \tau_i}{R_H(\tau_f)} > 1000. \tag{20}$$

Now, writing the continuity equation

$$\frac{\dot{\rho}}{\rho} = -2\epsilon H, \tag{21}$$

integrating from τ_i to τ_f leads to the inequality

$$\begin{aligned} \ln\frac{\rho_i}{\rho_f} &= 2\int_{t_i}^{t_f} \epsilon H dt \\ &= 2\int_{\tau_i}^{\tau_f} \epsilon R_H^{-1}(\tau)\, d\tau \\ &> 2R_H^{-1}(\tau_f)\int_{\tau_i}^{\tau_f} \epsilon\, d\tau \\ &> 2R_H^{-1}(\tau_f)\epsilon_{\min}(\tau_f - \tau_i), && (22) \end{aligned}$$

where $\epsilon_{\rm min}$ is the minimum value of ϵ, and we have used the fact that non-accelerating expansion requires $R_H(\tau) < R_H(\tau_f)$. Since non-accelerating expansion also means that $\epsilon_{\rm min} \geq 1$, the relation (20) results in the following inequality for the cosmological density:

$$\ln \frac{\rho_i}{\rho_f} > 2000, \tag{23}$$

or

$$\rho_i > 10^{868} \rho_f. \tag{24}$$

Taking the lower bound on ρ_f to be given by the lower bound on the reheat temperature, which is given by Big Bang nucleosynthesis, $\rho_f > \rho_r > (100 \text{ MeV})^4$, we have

$$\rho_i \gg M_{\rm Pl}^4. \tag{25}$$

This is purely the result of our two assumptions, non-accelerating expansion, and mode generation on a sufficiently large range of scales (16). Therefore, we have shown that to produce enough super-Hubble modes at reheating, the initial density of our scenario has to start larger than the Planck energy for decelerating expansion ($\epsilon_{\rm min} \geq 1$). For larger values of ϵ, the problem becomes more severe. Furthermore, if we want the range of modes (16) to be one order of magnitude larger we need e^{10} higher energy density ρ_i. It is also interesting that this problem can arise in a different form in contracting scenarios as well: even though the density is sub-Planckian the curvature still becomes exponentially greater than the Planck curvature [19].

Next, we repeat the same calculation allowing c_s to vary. The modes this time exit the freezeout horizon when $\lambda \sim |y|$. Therefore, the conditions (16) and (17) now yield:

$$\begin{aligned} |y_i| &\geq 1000\, |y_f| \qquad (26) \\ |y_f| &> R_H(\tau_f), \qquad (27) \end{aligned}$$

which implies

$$\frac{y_f - y_i}{R_H(\tau_f)} > 1000. \tag{28}$$

The inequality (22) is still valid and since

$$y_f - y_i = \int_{\tau_i}^{\tau_f} c_s d\tau = \bar{c}_s(\tau_f - \tau_i), \tag{29}$$

where $\bar{c}_s$ is the average sound speed, we obtain:

$$\ln \frac{\rho_i}{\rho_f} > 2R_H^{-1}(\tau_f)\epsilon_{\rm min} \frac{y_f - y_i}{\bar{c}_s}. \tag{30}$$

Combining above condition with (28), $\epsilon_{\rm min} > 1$, we have

$$\frac{2000}{\bar{c}_s} < \ln \frac{\rho_i}{\rho_f} < \ln \frac{M_{Pl}^4}{\rho_r} \sim 80 \ln 10, \tag{31}$$

where we take $\rho_r \sim (100 \text{ MeV})^4$. This results in a lower bound on the average sound speed,

$$\bar{c}_s > 10. \tag{32}$$

Therefore, we have shown that in a non-accelerating expanding universe, if the energy density starts sub-Planckian, producing the range of scale invariant modes consistent with observations requires super-luminal sound speed.

Could a small deviation from scale invariance as favored by the WMAP 7-year data [1] weaken these bounds? For a power-law spectrum $P(k) \propto k^{n-1}$, the freezeout horizon behaves as

$$R_\zeta^{-2} = \frac{q''}{q} = \frac{2 + (3/2)\,(1-n)}{y^2} \propto \frac{1}{y^2}, \tag{33}$$

so that the bound remains essentially unchanged even in the case of weakly broken scale invariance. The next section presents discussion and conclusions.

4 Concluding remarks

The universe is observed to have a spectrum of nearly scale-invariant density perturbations over about three decades in wavelength, which were at scales larger than the Hubble length at early times. In this contribution, we have shown that generating cosmological perturbations consistent with observation in an expanding universe requires at least one of: (1) accelerated expansion, (2) superluminal sound speed, or (3) super-Planckian energy density. We note that this applies to the curvaton mechanism [20] as well, since the freezeout horizon for a free scalar "spectator" field shrinks as τ ($a \propto 1/\tau$) to produce scale-invariant perturbations. Therefore super-Hubble curvaton fluctuations directly require inflation. It is important to note that scale invariance alone does not require inflation or "tachyacoustic" [10] evolution: a key point is that even with sub-luminal sound speed, super-Hubble perturbations can be generated with a growing Hubble horizon, as long as the freezeout horizon is shrinking and $R_\zeta > R_H$ [15]. However, one cannot generate three decades of modes in this fashion without super-Planckian energy densities. Perturbations could also be generated on sub-Hubble scales by a period of non-inflationary expansion [15,2], and only later redshifted to super-Hubble scales by a subsequent period of inflation. This would be consistent with our bound.

Acknowledgements

We thank Niayesh Afshordi, Justin Khoury and Sara Shandera for useful discussions. This research is supported in part by the National Science Foundation under grant NSF-PHY-0757693.

References

1. E. Komatsu *et al.* [WMAP Collaboration], Astrophys. J. Suppl. **192**, 18 (2011) [arXiv:1001.4538 [astro-ph.CO]].
2. J. Khoury and P. J. Steinhardt, Phys. Rev. D **83**, 123502 (2011) [arXiv:1101.3548 [hep-th]].
3. A. Nayeri, R. H. Brandenberger and C. Vafa, Phys. Rev. Lett. **97**, 021302 (2006) [hep-th/0511140].
4. A. Albrecht and J. Magueijo, Phys. Rev. D **59**, 043516 (1999) [astro-ph/9811018].
5. C. Armendariz-Picon and E. A. Lim, JCAP **0312**, 002 (2003) [astro-ph/0307101].
6. C. Armendariz-Picon, JCAP **0610**, 010 (2006) [astro-ph/0606168].
7. Y. -S. Piao, Phys. Rev. D **75**, 063517 (2007) [gr-qc/0609071].
8. J. Magueijo, Phys. Rev. Lett. **100**, 231302 (2008) [arXiv:0803.0859 [astro-ph]].
9. Y. -S. Piao, Phys. Rev. D **79**, 067301 (2009) [arXiv:0807.3226 [gr-qc]].
10. D. Bessada, W. H. Kinney, D. Stojkovic and J. Wang, Phys. Rev. D **81**, 043510 (2010) [arXiv:0908.3898 [astro-ph.CO]].
11. J. Magueijo and J. Noller, Phys. Rev. D **81**, 043509 (2010) [arXiv:0907.1772 [astro-ph.CO]].
12. E. Babichev, V. Mukhanov and A. Vikman, JHEP **0802**, 101 (2008) [arXiv:0708.0561 [hep-th]].
13. T. Vachaspati and M. Trodden, Phys. Rev. D **61**, 023502 (1999) [gr-qc/9811037].
14. J. Khoury and F. Piazza, JCAP **0907**, 026 (2009) [arXiv:0811.3633 [hep-th]].
15. J. Khoury and G. E. J. Miller, Phys. Rev. D **84**, 023511 (2011) [arXiv:1012.0846 [hep-th]].
16. R. H. Brandenberger, H. Feldman and V. F. Mukhanov, astro-ph/9307016.
17. J. Garriga and V. F. Mukhanov, Phys. Lett. B **458**, 219 (1999) [hep-th/9904176].
18. W. Hu, Phys. Rev. D **84**, 027303 (2011) [arXiv:1104.4500 [astro-ph.CO]].
19. A. Linde, V. Mukhanov and A. Vikman, JCAP **1002**, 006 (2010) [arXiv:0912.0944 [hep-th]].
20. D. H. Lyth and D. Wands, Phys. Lett. B **524**, 5 (2002) [hep-ph/0110002].

SELF-REGULARISATION OF IR-DIVERGENCES DURING INFLATION

BJÖRN GARBRECHT

Institut für Theoretische Teilchenphysik und Kosmologie, RWTH Aachen, 52056 Aachen, Germany

The propagator of a massless minimally coupled scalar field exhibits an infrared divergence. While it corresponds to the very same effect that leads to the generation of primordial perturbations during inflation, it must be regulated within loop diagrams. For $\lambda\phi^4$ theory, we show that the effect of self-energies can be described by an effective mass term, which in turn limits the infrared divergence. A self-consistent relation for determining this dynamical mass is given by the Schwinger-Dyson equations.

1 The Infrared Problem

Throughout this contribution, we consider $\lambda\phi^4$ theory that is given by the Lagrangian

$$\mathcal{L} = \sqrt{-g}\left\{g^{\mu\nu}(\partial_\mu\phi)(\partial_\nu\phi) - \frac{1}{2}m^2\phi^2 - \frac{\lambda}{4!}\phi^4\right\}. \tag{1}$$

In de Sitter space-time, $g_{\mu\nu} = a^2(\eta)\mathrm{diag}(1,-1,-1,-1)$, where $\eta \in]-\infty;0[$ is the conformal time and $a = -1/(H\eta)$ the scale factor. The relation to the comoving time is $dt = ad\eta$, such that $a = \exp(Ht)$. For $\lambda = 0$ and $m = 0$, the field equation and the equation for a momentum mode are

$$\nabla^2\phi(x) = 0 \;\Rightarrow\; \left(\partial_\eta^2 + \mathbf{k}^2 - \frac{a''}{a}\right)a\phi(\mathbf{k},\eta) = 0\,, \tag{2}$$

where the latter has the well-known solution

$$a\phi(\mathbf{k},\eta) = \frac{1}{\sqrt{2|\mathbf{k}|}}\left(1 - \frac{\mathrm{i}}{|\mathbf{k}|\eta}\right)\mathrm{e}^{-\mathrm{i}|\mathbf{k}|\eta}\,. \tag{3}$$

From the field operator and the commutation relation ($x^0 = \eta$),

$$\phi(x) = \int\frac{d^3k}{(2\pi)^3}\left(\mathrm{e}^{-\mathrm{i}\mathbf{k}\cdot\mathbf{x}}\phi(\mathbf{k},\eta)a(\mathbf{k}) + \mathrm{e}^{\mathrm{i}\mathbf{k}\cdot\mathbf{x}}\phi^*(\mathbf{k},\eta)a^\dagger(\mathbf{k})\right),\quad [a(\mathbf{k}),a^\dagger(\mathbf{k}')] = (2\pi)^3\delta^3(\mathbf{k}-\mathbf{k}')\,, \tag{4}$$

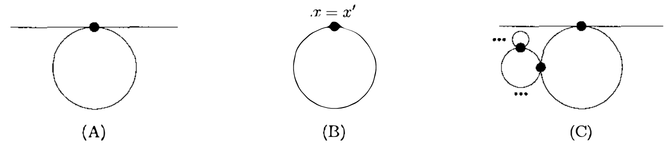

Figure 1: (A): One-loop correction to the propagator, (B): one-loop self-energy $\Pi(x;x')$, (C): diagrams that are resummed through the Schwinger Dyson approach.

we immediately obtain the power spectrum

$$\langle\phi(\mathbf{k})\phi(\mathbf{k}')\rangle \underset{|k|/a\gg H}{\approx} (2\pi)^3\delta^3(\mathbf{k}-\mathbf{k}')\frac{H^2}{2|\mathbf{k}|^3} =: (2\pi)^3\delta^3(\mathbf{k}-\mathbf{k}')\frac{2\pi^2}{|\mathbf{k}|^3}\mathcal{P}_\phi(\mathbf{k}) \Rightarrow \mathcal{P}_\phi(\mathbf{k}) = \frac{H^2}{(2\pi)^2}\,. \quad (5)$$

This tree-level observable is therefore finite, even though the two-point function $\langle\phi(\mathbf{k})\phi(\mathbf{k}')\rangle$ exhibits an infrared (IR) divergence for $|\mathbf{k}| \to 0$. The two-point function however enters as the propagator into Feynman diagrams at higher orders in perturbation theory, and the IR divergence would make these quantities ill-defined. This is the IR problem.

2 Position Space Propagator

Due to the curved background, it is useful to work with position space-propagators. The propagators are Green functions defined for different boundary conditions:

$$\begin{aligned} \mathrm{i}\Delta^{+-}(x;y) &= \langle\phi(y)\phi(x)\rangle\,, & \mathrm{i}\Delta^{-+}(x;y) &= \langle\phi(x)\phi(y)\rangle\,, \\ \mathrm{i}\Delta^{++}(x;y) &= \langle T[\phi(x)\phi(y)]\rangle\,, & \mathrm{i}\Delta^{--}(x;y) &= \langle \bar{T}[\phi(x)\phi(y)]\rangle\,, \end{aligned} \quad (6)$$

where T ($\bar{T}$) stands for (anti-) time-ordering, and the indices $\pm$ are referred to as the Closed-Time-Path indices. The tree-level propagators satisfy the equation

$$(-\nabla_x^2 - m^2)\mathrm{i}\Delta^{(0)fg}(x;x') = fg\delta^{fg}a^{-4}\mathrm{i}\delta^4(x-x')\,, \quad f,g=\pm\,. \quad (7)$$

For $m \ll H$, the solution is (note the IR divergence for $m \to 0$)

$$\mathrm{i}\Delta^{(0)}(y) = \frac{H^2}{4\pi^2}\left\{\frac{1}{y} + \frac{1}{2}\log(-y) - \frac{3}{2}\frac{H^2}{m^2} + \ldots\right\}\,, \quad (8)$$

where $y(x;x') = 4\sin^2(\frac{1}{2}H\ell(x;x')) = H^2(x-x')^2aa'$ is a de Sitter invariant distance function [$\ell(x;x')$ is the geodesic distance]. The various boundary conditions are enforced by appropriate ε prescriptions that are important for time like ($y>0$) coordinate separations[1].

3 Schwinger-Dyson Equation

The full propagator $\mathrm{i}\Delta$ satisfies the Schwinger-Dyson equation

$$a^4(-\nabla_x^2 - m^2)\mathrm{i}\Delta^{ab}(x;y) + \mathrm{i}c\int d^4z\mathrm{i}\Pi^{ac}(x;z)\mathrm{i}\Delta^{cb}(z;y) = \delta^{ab}\mathrm{i}\delta^4(x-y)\,. \quad (9)$$

Because the self-energy $\mathrm{i}\Pi$ functionally depends on $\mathrm{i}\Delta$, it is a non-linear integro-differential equation, that in practice cannot be solved exactly. For a Lagrangian mass $m=0$, we therefore choose the ansatz, that the full propagator is approximated by a free propagator with a dynamical mass $m_{\rm dyn}$. Eq. (9) then leads to a mass-gap equation that can be solved for $m_{\rm dyn}$.

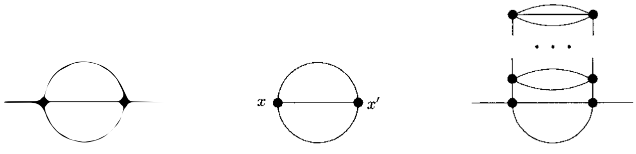

(A) (B) (C)

Figure 2: (A): Two-loop correction to the propagator, (B): two-loop self-energy $\Pi(x;x')$, (C): diagrams that are resummed through the Schwinger Dyson approach.

4 One-Loop Correction

Above ansatz is valid, provided the leading effect of the self-energies is indeed the one of a mass-term. Extracting only the leading contribution in $H^2/m_{\rm dyn}^2$, this becomes immediately clear for the one-loop contribution[2] [Figure 1(B)]:

$$\Pi^{fg}(x;y) = \frac{\lambda}{2}\sqrt{-g(\eta)}f\delta^{fg}\delta^4(x-y)\mathrm{i}\Delta^{fg}(x;y) \approx f\delta^{fg}\sqrt{-g}\lambda\frac{3H^4}{16\pi^2 m_{\rm dyn}^2}\delta^4(x-y)\,. \tag{10}$$

Substitution into the convolution term in Eq. (9) indeed yields a mass-square $3\lambda H^4/(16\pi^2 m_{\rm dyn}^2)$.

5 Two-Loop Correction

Setting the effective mass-square from Section 4 equal to $m_{\rm dyn}^2$ would give rise to a mass-gap equation. However, since the resulting effective mass-square is of order $\sqrt{\lambda}H^2$, we infer from Eq. (8), that the constant, IR-enhanced term in the propagator is $\sim H^2/\sqrt{\lambda}$. We might therefore expect that each propagator line gives an enhancement by $1/\sqrt{\lambda}$ and each vertex a suppression by a factor of λ. Consequently, the diagram in Figure 2(A) would be larger than the one in Figure 1(A), and the loop expansion would break down.

However, the dependence of the effective mass on λ is not given by this cursory power counting argument. Eq. (9) is non-diagonal in the Closed-Time-Path indices $\pm$. It is therefore useful to consider the retarded propagator

$$\mathrm{i}\Delta^R = \mathrm{i}\Delta^{++} - \mathrm{i}\Delta^{+-} = \mathrm{i}\Delta^{-+} - \mathrm{i}\Delta^{--}\,. \tag{11}$$

The retarded self-energy $\mathrm{i}\Pi^R$ follows from according linear combinations. From the Schwinger-Dyson equation (9), we then obtain a linear combination, that is homogeneous in $\mathrm{i}\Delta^R$ (up to the δ-function term):

$$-a^4\nabla_x^2\mathrm{i}\Delta^R(x;y) = \mathrm{i}\delta^4(x-y) - \mathrm{i}\int d^4z\mathrm{i}\Pi^R(x;z)\mathrm{i}\Delta^R(z;x)\,. \tag{12}$$

Now, from Eq. (11) we observe, that the constant, IR-enhanced term cancels within the retarded propagator. Therefore, in the leading contribution to $\mathrm{i}\Pi^R$, we can substitute only two of the IR-enhanced terms, while one of the propagators must be $\mathrm{i}\Delta^R$. Moreover, we can effectively reduce the convolution integral to a local term by acting once more with ∇_x^2 on Eq. (12) and using the relation

$$-(\nabla_x^2 - m_{\rm dyn}^2)\mathrm{i}\Delta^R(x;y) = \mathrm{i}\delta^4(x;y)\,. \tag{13}$$

Combining the one-loop and two-loop contributions, we obtain for $y \neq x$

$$\left(\nabla_x^4 - \frac{\lambda^2}{2}\left(\frac{3H^4}{8\pi^2 m_{\rm dyn}^2}\right)^2 - \lambda\frac{3H^4}{16\pi^2 m_{\rm dyn}^2}\nabla_x^2\right) {\rm i}\Delta^R(x;y) = 0\,. \tag{14}$$

Now, when using Eq. (13), we may replace $\nabla_x^2 \to m_{\rm dyn}^2$, such that we obtain a gap-equation for $m_{\rm dyn}^2$. We interpret the occurrence of higher orders in ∇_x^2 as an analogy with dispersion relations in finite-temperature field theory, that involve powers of the momenta beyond the quadratic order. The final result is

$$m_{\rm dyn}^2 = \frac{\sqrt{3\lambda}H^2}{2\sqrt{2}\pi}\,. \tag{15}$$

Notice that the Schwinger-Dyson equation as well resums the ladder diagrams in Figure 2(C). We have therefore found that the two-loop diagram contributes to the effective mass at the same order in $\sqrt{\lambda}$ as the one-loop term. One should therefore check, whether higher-loop diagrams render contributions of similar importance. One can however verify that these diagrams do not contribute to the effective mass at the leading order in the IR enhancement [1], such that the result (15) should include all contributions to leading order in $\sqrt{\lambda}$.

6 Summary and Further References

The two main results of the work presented here are first, that leading IR effects from non-local self-energies such as the two-loop diagram in $\lambda\phi^4$ theory can be described by an effective local mass term and second, the resulting effective mass-square (15) that is obtained from a mass-gap relation following from the Schwinger Dyson equation (9).

There are additional works that rely on the same underlying picture of self-regularisation of the IR-divergence due to the self-coupling. A technically different approach results from the stochastic-inflation formalism, where the fluctuation of the scalar field (the constant term in the propagator) is obtained from the solution of a Langevin equation. While the fluctuation is enhanced by a factor $1/\sqrt{\lambda}$ as well, the numerical coefficient turns out to be different.

The resummation of the one-loop self energy has been performed in Refs. [2,4]. In Euclidean de Sitter space, the resummation of all leading IR contributions is described in Ref. [5], with a result that agrees with Ref. [3], but differs in the coefficient from the one that is reported here.

The resolution of these discrepancies is of conceptual interest, as it will indicate whether the IR fluctuations during inflation may be described by a classical statistical ensemble or whether they exhibit quantum properties that cannot be described by a probability distribution.

Acknowledgments

This work is supported by the Gottfried Wilhelm Leibniz programme of the Deutsche Forschungsgemeinschaft.

References

1. B. Garbrecht and G. Rigopoulos, Phys. Rev. D **84** (2011) 063516 [arXiv:1105.0418 [hep-th]].
2. A. Riotto and M. S. Sloth, JCAP **0804** (2008) 030 [arXiv:0801.1845 [hep-ph]].
3. A. A. Starobinsky, J. Yokoyama, Phys. Rev. **D50** (1994) 6357-6368. [astro-ph/9407016].
4. J. Serreau, Phys. Rev. Lett. **107** (2011) 191103 [arXiv:1105.4539 [hep-th]].
5. A. Rajaraman, Phys. Rev. **D82** (2010) 123522. [arXiv:1008.1271 [hep-th]].

UNIVERSALITY IN MULTIFIELD INFLATION FROM STRING THEORY

S. RENAUX-PETEL
Department of Applied Mathematics and Theoretical Physics,
University of Cambridge, Wilberforce Road, Cambridge, U.K.

We develop a numerical statistical method to study linear cosmological fluctuations in inflationary scenarios with multiple fields, and apply it to an ensemble of six-field inflection-point models in string theory. The latter are concrete microphysical realizations of quasi-single field inflation, in which scalar masses are of order the Hubble parameter and an adiabatic limit is reached before the end of inflation. We find that slow-roll violations, bending trajectories and "many-field" effects are commonplace in realizations yielding more than 60 e-folds of inflation, although models in which these effects are substantial are in tension with observational constraints on the tilt of the scalar power spectrum.

1 Motivations and methodology

Inflation provides both a beautiful mechanism to solve the conceptual problems of the Hot Big-Bang model as well as an elegant explanation for the observed spectrum of cosmic microwave background anisotropies. The simplest models of inflation, involving a single field slowly rolling down its potential, generate primordial fluctuations in agreement with observational requirements: adiabatic, Gaussian and nearly scale-invariant. However, more complicated models involving multiple light fields and/or violations of slow roll are more natural from a theoretical point of view. In particular, generic scalar fields during inflation acquire masses of order the Hubble parameter H through gravitational-strength interactions, and therefore do not decouple from the inflationary dynamics. This general picture is well-attested in flux compactifications of string theory, in which lots of moduli are found with masses clustered around H. In cases where the moduli potential is computable, one generally finds a complicated, high-dimensional potential energy landscape with structure dictated by the spectrum of Planck-suppressed operators in the theory [?]. The nature of inflation in such a potential is the important problem that we address in McAllister *et al.* [?].

For definiteness, we study the primordial fluctuations generated in a class of six-field inflationary models in string theory, corresponding to a D3-brane moving in a conifold region of a stabilized compactification. We draw potentials at random from a well-specified ensemble and study realizations that inflate by chance (they add up to more than 18400). We build on prior work[?] characterizing the homogeneous background evolution in this system. There, it was shown that inflationary trajectories lasting more than 60 e-folds take a characteristic form: the D3-brane initially moves rapidly in the angular directions of the conifold, spirals down to an inflection point in the potential, and then settles into an inflating phase. It was also established that the inflationary phenomenology has negligible dependence on the detailed form of the statistical distribution for the coefficients characterizing the potentials: a sort of universality emerges in this complicated ensemble.

2 Mass spectrum and the adiabatic limit

A important aspect of our system is its mass spectrum, *i.e.* the distribution of the 6 eigenvalues of the mass matrix of cosmological perturbations. Details of it, in particular the splitting between the various mass eigenvalues, can be understood using a random mass matrix model of supergravity theories [?,?]. We refer the reader to these papers for more details, and only emphasize here its main characteristic and consequences: except the lightest direction, which can happen to be very light ($|m/H| \ll 1$)) because of accidental cancellations, all other directions have masses of order H (typical values are between H and $5H$). This implies both that each direction is light enough to fluctuate and have interesting observational consequences, and that an "adiabatic limit" is naturally reached before the end of inflation. To make this statement more precise, let us recall that cosmological fluctuations during N-field inflation are commonly divided into one instantaneous adiabatic perturbation and $N-1$ entropic perturbations, defined as fluctuations pointing respectively along and off the background trajectory [?,?]. The key-feature of inflation with multiple fields lies in the fact that entropic perturbations, absent in single-field models, can feed the adiabatic perturbation, even on super-Hubble scales, when the trajectory bends. As we will explain, we observe that such effects have to be taken into account in our system and can have a profound impact on observable predictions. However, it turns out that the entropic perturbations, with typical masses greater than H, gets gradually diluted after Hubble-crossing until becoming completely "exhausted" by the end of inflation, with an amplitude suppressed by several order of magnitudes (typically more than 10) compared to the adiabatic perturbation. This dynamical process implies that that the curvature perturbation, proportional to the adiabatic one, has becomes constant by the end of inflation. It therefore allows us to make definite predictions for observables without having to make a detailed description of the reheating scenario, as well as it guarantees the absence of remaining primordial isocurvature perturbations in the radiation era [a]. Put in another way, our ensemble provides concrete microphysical realizations of quasi-single field inflation [?], with the notable difference that self-couplings in our potentials are not large enough to generate observable non-Gaussianities [?].

3 Results on linear cosmological perturbations

For each of our inflationary realizations, we numerically solve the exact dynamics of linear perturbations for the pivot scale crossing the Hubble radius 60 e-folds before the end of inflation, imposing Bunch-Davies initial conditions. We deduce the corresponding amplitude $\mathcal{P}$ and spectral index of the curvature perturbation when it has become constant at the end of inflation. Eventually, to disentangle the different physical effects affecting the results, we cross-correlate the exact results with some relevant background quantities and the predictions of three approximate models of the cosmological perturbations: the `naive` (or slow-roll) model, which neglects multifield effects and assumes all fields are very light, gives the simple estimate $\mathcal{P}_{\rm naive} = \frac{H_\star^2}{8\pi^2\epsilon_\star}$ where the star denotes evaluation at Hubble crossing. In the `one-field` model, all entropic perturbations are set to zero but the full dynamics of the instantaneous adiabatic fluctuation is taken into account, including possible slow-roll violations. Finally, the `two-field` model additionally takes into account one particularly picked entropic mode (see below).

We observe that the amplitude of the curvature power spectrum generically differs significantly from its naive estimate. This should not come as a surprise as, even neglecting entropic perturbations, the adiabatic mass at Hubble crossing is typically of order H, implying a smaller amplitude of large-scale fluctuations than what the naive estimate suggests. The `one-field` power-spectrum $\mathcal{P}_1$, however, accurately describes, to the percent-level, 70 % of our realizations. These cases, that we call effectively one-field, generally have a complicated non slow-roll dynamics, but nonetheless have negligible multiple field effects. In the following, we concentrate on the other substantial fraction of our realizations, about 30 %, which are effectively multifield, *i.e.* in which entropic perturbations can not be neglected.

[a] [illegible]

We find that the impact of entropic perturbations is modest in the majority of these effectively multifield models, the ratio $\mathcal{P}/\mathcal{P}_1$ being less than 2 in about 65 % of them, but that there exists a long tail toward large multifield effects, 15 % (resp. 5 %) of them having $\mathcal{P}/\mathcal{P}_1 > 10$ (resp. > 100): *i.e.* models in which entropic perturbations affect the amplitude of the power spectrum by one or several orders of magnitude are not rare. One should also note that, due to our specific typical background evolution, the amplitude of the multifield effects is correlated with the duration of inflation: models with a large number of e-folds of expansion (> 100 for definiteness) generally already have reached their inflection point attractor 60 e-folds before the end of inflation, implying a modest degree of bending when our pivot scale is super-Hubble, and hence negligible conversion of entropic fluctuations into the curvature perturbation. Models with a shorter number of efolds, on the contrary, usually exhibit some bending around and after Hubble-crossing as remnants of their initial conditions, and are more liable to multifield effects. An even more remarkable fact though, which we believe has not been observed before, is the existence of a critical threshold of total turning (between Hubble-crossing and the end of inflation) to obtain a given amplitude of multifield effects, as measured by $\mathcal{P}/\mathcal{P}_1$ (see McAllister *et al.* [?] for more details).

In a general N-field model of inflation, one of the $N-1$ entropic fluctuation is usually picked: the one that instantaneously couples to the adiabatic perturbation [?], which we call the "first" entropic fluctuation. Most explicit studies of inflation with multiple fields have considered by simplicity 2-field models only, in which case the entropic subspace is one-dimensional and this distinction is unnecessary. In our system however, it is legitimate to assess the importance of *many*-field effects, *i.e.* to discriminate which models, amongst the effectively multifield ones, can be accurately described by the adiabatic and first entropic fluctuations only, which we call effectively two-field, and the ones in which the "higher-order" entropic modes affect the curvature perturbation, which we call effectively *many*-field. For that purpose, we compare the exact and the `one-field` power spectrum to the one in which all these higher-order entropic modes are set to zero. Our results are as follows: we find that non-negligible many-field effects are commonplace, with only 38% of effectively multifield models being effectively 2-field. There is also a clear pattern regarding the relative importance of 2-field versus many-field effects. We find that when multifield effects are modest in size, they are most often 2-field only. When they are large however, we find either large many-field effects, or large 2-field effects (in smaller proportion), but few models display both significant 2-field and many-field effects.

The above analysis was carried out without conditioning on obtaining a scalar spectral index in the observational window $0.93 < n_s < 0.99$ (95% CL) [?]. Once we impose this condition, we find that the overwhelming majority of viable realizations are effectively single-field and with small departures from slow-roll. In view of this, one might be inclined to brush off our findings as uninteresting. At least two reasons make us resist this inclination. First: although they are rare, there do exist models that would be naively ruled out from the naive estimate $n_s - 1 = -2\epsilon_\star - \eta_\star$ and that turn out to be consistent with the observational constraints because of large multifield effects. Second and more important: we find that non-negligible multifield effects most often (more than 80%) tend to reduce the spectral index significantly, by several factors of 0.1. This interesting and unexpected feature simply turns out to be not large enough in general to counterbalance the fact that the one-field spectral index is way too blue in the models with small duration of inflation which display significant bending in their last 60 e-folds. We find this trend nonetheless remarkable, and we think it leaves the interesting possibility that other classes of models, different from inflection point inflation, may generically display large multifield effects while meeting observational requirements.

4 Conclusions and perspectives

We have developed a statistical approach to the study of inflationary scenarios with multiple fields: it consists in comparing, in a large ensemble of realizations of a class of inflationary models, the exact dynamics of linear fluctuations to three approximate descriptions: `slow-roll`, `single-field`, and `two-field`, enabling us to characterize to which extent these simpler effective models are able to describe the physics of our class of models. We have applied this method to inflection-point inflationary models with multiple fields of masses of order the Hubble parameter, as expected in generic low-energy effective field theories. We have observed that this mass spectrum implies that cosmological perturbations dynamically reach an "adiabatic limit" by the end of inflation, thereby alleviating the need for a precise description of reheating. We found that slow-roll violations and strongly bending trajectories are common in realizations yielding more than 60 e-folds of inflation, although the majority of models with an observably acceptable spectral index turns out to be effectively slow roll single-field. We think however that this pessimistic conclusion regarding the likelihood of models displaying large multifield effects and consistent with observations should be tempered, as it might be particular to inflection point inflation, and as we found that multifield effects most often tend to significantly redden the spectrum. We also demonstrated the existence of a critical threshold of turning to generate a given amplitude of multifield effects. Eventually, we pointed out the generic importance on cosmological perturbations of *many* (beyond 2)-field effects, implying that the prevailing trend to study 2-field models of inflation may well be misleading to unveil the true nature of inflation with multiple fields. More generally, while a great deal of attention has been recently devoted to the study of the primordial non-Gaussianities generated during inflation, we think our study shows that many aspects of the *linear* dynamics of cosmological perturbations during inflation with multiple fields remain to be explored, and we hope our work and our methodology will pave the way for further developments in this direction.

Acknowledgments

I am supported by the STFC grant ST/F002998/1 and the Centre for Theoretical Cosmology. I would also like to thank the scientific committee of the Moriond conference for their financial support.

References

1. D. Baumann, A. Dymarsky, S. Kachru, I. R. Klebanov and L. McAllister, JHEP **0903**, 093 (2009)
2. L. McAllister, S. Renaux-Petel and G. Xu, in preparation.
3. N. Agarwal, R. Bean, L. McAllister, G. Xu, JCAP **1109** (2011) 002.
4. D. Marsh, L. McAllister and T. Wrase, JHEP **1203**, 102 (2012)
5. C. Gordon, D. Wands, B. A. Bassett and R. Maartens, Phys. Rev. D **63** (2001) 023506
6. S. Groot Nibbelink and B. J. W. van Tent, CQG **19** (2002) 613
7. X. Chen and Y. Wang, JCAP **1004** (2010) 027
8. D. Larson *et al.*, Astrophys. J. Suppl. **192** (2011) 16

SuperCool Inflation

Douglas Spolyar
FermiLab P.O. Box 500 ms 209
Batavia IL, 60510

SuperCool (SC) Inflation implements a thermal and technically natural graceful exit from old inflation. Initially, the Universe is hot and localized in the symmetric minima of the inflaton potential. As the Universe cools and the true vacuum appears, the Universe becomes stuck in the false vacuum and inflates. Eventually, a hidden non-Abelian gauge group freezes. Quark like fermions (charged under the non-Abelian group) form a condensate and generate a linear term in the inflaton potential which removes the barrier trapping the inflaton in the false vacuum. The field rapidly goes to the true vacuum. The model solves the standard inflationary problems and reheats the Universe. In addition, a spectator field creates perturbations which matches all CMB data and can generate non-Gaussianities observable by Plank. Finally, the model works at the TeV scale and below. Colliders also offer a handle on the model.

1 Introduction

In 1981, Guth [?] introduced an inflationary phase (old inflation) to explain the horizon, flatness, and monopole problems. Initially, the Universe is hot, cools, and becomes stuck in a false vacuum and begins to inflate. Eventually, the Universe transitions to the true vacuum and reheats. Unfortunately, Guth's model failed due to the Swiss cheese problem or lack of a graceful exit.

In fact, Guth and Weinberg [?] have shown that the tunneling rate (per unit time per unit volume) Γ compared to the Hubble 4-Volume

$$\beta = \Gamma/H^4 \gtrsim 9/4\pi = \beta_c, \tag{1}$$

must be larger than β_c for the Universe to transition from the false to the true vacuum, which requires that the universe can only be stuck in the false vacuum for at most a $1/3$ of an efold of inflation. Hence, the Universe either generates a sufficient amount of inflation (~ 60 efolds for GUT scale inflation) to solve the standard cosmological problems, or the universe never reheats.

Previous authors have introduced mechanism which have a graceful exit, such as double field inflation [?], a variant of hybrid inflation [?], and chain inflation [?,?] to name a few. These models with the exception of chain inflation use the dynamics of a rolling field to give old inflation a graceful exit. Instead, we introduce a thermal effect to generate a graceful exit (n.b. thermal inflation [?] is similar but does not solve the standard cosmological problems).

2 Particle Physics Model

As our model, we introduce a hidden sector, which is similar to the Standard Model (SM) except without E.M., $SU(2)_L$, and leptons (our particle physics model is also similar to [?]).

$$V(\phi) = (1/8)\,\mathrm{T}^2\,\phi^2 + \frac{3g_X^4}{32\pi^2}|\phi|^4\left(\ln\left(\frac{|\phi|}{\langle|\phi|\rangle}\right) - \frac{1}{4}\right) + \sum y_i\boldsymbol{\phi} * (q_R\bar{q}_L)_i + \text{h.c.} + \Lambda^4 + \ldots.. \tag{2}$$

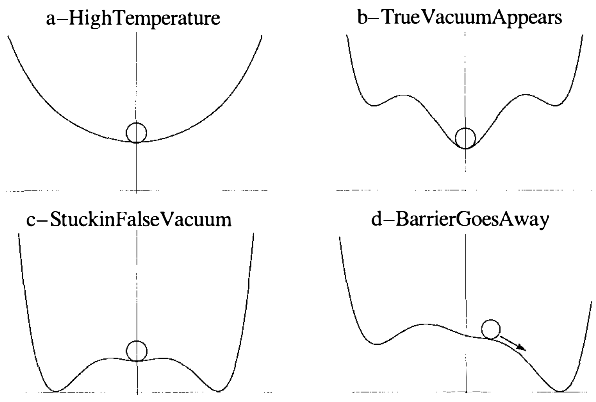

Figure 1: The effective potential at different temperatures: **a**–At high temperatures, only one vacuum state exist. **b**–Eventually, other vacuum states appear. **c**–As the temperature drops, the universe becomes stuck in the false vacuum and inflates. **d**–at T_c, the linear term removes the barrier. The Universe rapidly goes to the true vacuum.

The model contains a set of hidden QCD like quarks (Hquarks) $q_R\bar{q}_L$ (with $\mathcal{O}(1)$ Yukawa couplings y_i) charged under a QCD like gauge group (HQCD), which becomes strongly coupled at a critical temperature T_c. The model has an Abelian Higgs (our inflaton and a complex scalar) which has a Coleman-Weinberg potential? with a vev $|\langle\phi\rangle| \simeq 10$ TeV (the second term in Eq. **??**). The inflaton and Hquarks are charge under an Abelian gauge group $U(1)_X$ with a gauge coupling $g_X \simeq 0.4$. At finite temperature, the first term generates an effective mass. Λ accounts for the standard cosmological tuning and sets the scale of inflation, which we take to be $\Lambda \simeq 1$ TeV. We could have picked a larger or smaller scale of inflation. The ellipses account for non-renormalizable terms.

3 SuperCool (SC) Inflation

The Universe starts off hot. The first term of Eq. **??** dominates the inflaton potential (Fig. **??a**). As the temperature drops, the true vacuum appears (Fig. **??b**). Eventually, the universe begins to inflate in our model when the temperature is around 300 GeV (Fig. **??c**). The field is localized in the symmetric minima.

In fact, the Universe is stuck in the false vacuum to arbitrarily low temperatures. Next, we calculate the tunneling rate to the true vacuum. We have considered a variety of instantons, but find that a thermal instanton dominates the tunneling rate to the true vacuum. The tunneling rate? then goes like

$$\Gamma \simeq T^4\left(\frac{S_3}{2\pi T}\right)^{3/2}\exp\left[-\frac{S_3}{T}\right] \qquad S_3 = \frac{4\pi}{3}\frac{T}{g_X^3\ \ln(M_X/T)} \tag{3}$$

where M_X is the mass of the gauge boson associated with the $U(1)_X$ gauge group (in the true vacuum). We find that $\beta \ll \beta_c$ (See Eq. **??**) to arbitrarily low temperatures. Hence, the field is safe from tunneling to the true vacuum. The Universe then super cools and inflates solving the standard cosmological problems (flatness and horizon problems).

At this point, we are back to old inflation. We now introduce a graceful exit. After 30 efolds of inflation (which is sufficient to solve the standard cosmological problems at the TeV scale), the temperature of the Universe has dropped exponentially (the scale factor scales roughly inversely with temperature T) eventually reaching 10^{-2} eV. As the temperature of the Universe drops, the coupling constant for the hidden QCD like gauge group (HQCD) runs logarithmically. At the critical temperature $T_c = 10^{-2}$ eV, HQCD becomes strongly coupled. The Hidden quarks (Hquarks) form a condensate

$$|\Sigma_i(q_R\bar{q}_L)_i \star \phi| \to |\langle\Sigma_i(q_R\bar{q}_L)_i\rangle \star \phi| = \epsilon \star |\phi| \tag{4}$$

which generates a linear term in the inflaton potential. Near the origin, we can model the potential as

$$\epsilon \star |\phi + \frac{\mathrm{T}^2}{8}|\phi|^2 - \frac{3g_x^4}{32\pi^4}|\phi|^4\Big(\ln\left(\frac{\mathrm{M}_X}{\mathrm{T}}\right) + \mathcal{O}(1)\Big) \tag{5}$$

where ϵ is of the order of the critical temperature cubed following [?]. Upon substituting in values for the parameters chosen, we find that the linear term in ϕ removes the barrier once the temperature of the universe reaches the critical temperature (T_c). The field then rapidly transitions to the true vacuum ending inflation (Fig. **??d**). The vacuum energy is converted into inflaton particles which rapidly decay into standard model particles. We would like to emphasis that SC inflaton is technically natural since the end of inflation is due to the logarithmic running of a dimensionless coupling constant in the same way that the QCD scale is also technically natural compared to the Plank scale.

Eventually, the inflaton decays into standard model particles. In general, there are three different renormalizable and gauge invariant couplings to the Standard Model (SM), a scalar coupling to the SM Higgs, a SM Higgs fermion coupling, and kinetic mixing with hypercharge [?]. We will focus on the last case of kinetic mixing between hypercharge and $\mathrm{U(1)}_X$ with

$$\mathcal{L}_{\mathrm{KE}}^{BX} = -\frac{1}{4}B_{\mu\nu}B^{\mu\nu} - \frac{1}{4}X_{\mu\nu}X^{\mu\nu} + \frac{\chi}{2}B_{\mu\nu}X^{\mu\nu} \tag{6}$$

where $B_{\mu\nu}$ is hypercharge, $X_{\mu\nu}$ is the $\mathrm{U(1)}_X$ and χ is the mixing parameter. Upon diagonalization of the mass matrix into a Z and Z′ [?], the inflaton can then decay directly into a pair of Z bosons. Following [?,?,?], the decay rate goes like

$$\Gamma_{\phi\to ZZ} = \frac{\pi}{6}M_\phi(g_X\ \sin\theta_w\eta\Delta z)^4\frac{\sqrt{1-x}}{x^2}(3x^2 - 4x + 4) \tag{7}$$

where M_ϕ ($\sim 300\,\mathrm{GeV}$) is the mass of the SC inflaton, $\sin\theta_w$ is the Weinberg angle, $\Delta z = (M_{Z_0}/M_X)^2$, $x = 4M_Z^2/M_\phi^2$, $\eta = \chi/\sqrt{1-\chi^2}$ and $g_X = 0.4$. We find that $\Gamma_{\phi\to ZZ} = 0.03$ eV$\gg$ H $\simeq 10^{-4}$ eV, where we have taken $\chi = .9$ and $M_{Z'} \simeq M_X$ (~ 4 TeV). Also, SC inflaton avoids present collider constraints due to the large mass of the Z′ [?,?]. The Universe rapidly reheats to a few hundred GeV. Finally, we reheat to a sufficiently high temperatures to do baryogenesis via Electro-Weak Baryogenesis. The QCD axion is a viable DM candidate for SC inflation. Hence, the standard cosmology can be achieved.

4 Perturbations

We will require a new mechanism to generate perturbations. Standard adiabatic perturbations from a rolling field will be suppressed by the thermal background (See [?]). Silvia Mollerach [?] showed that if a matter component with an isocurvature component decays into radiation, the isocurvature perturbation becomes a real adiabatic density perturbation (for example the Curvaton [?,?]). Unfortunately, the Curvaton only works with inflation at 10^9 GeV or greater.

Instead, we introduce the Aulos (Greek for flute). A pseudo-scalar with a U(1) symmetry is broken with a mexican hat potential. The aulos field corresponds to the angular variable of the mexican hat. We can model the potential of the aulos field with a cosine function

$$\mathrm{V}(a) = \Lambda_a^4(1 + \cos(a/f_a)). \tag{8}$$

The width of the potential is set by the Spontaneous Symmetry Breaking (SSB) scale f_a and the height Λ_a by an explicit breaking from a constrained instanton [?,?] (the explicit breaking scale is proportionate to the

SSB scale for a constrained instanton). As a result, the mass of the aulos field m_a is also proportionate to the SSB scale. During inflation the mass m_a and decay constant f_a are small (sub-eV scale) and become large at the end of inflation (GeV scale) since we couple the inflaton field with the pseudo-scalar. At the end of inflation, the aulos field begins to oscillate generating a condensate of aulions. The energy density ρ_a of the aulos field goes like $\sim m_a^2 f_a^2$, which are the values set at the end of inflation (GeV scale). Hence, we effectively have transferred energy from the inflaton into the aulos field.

5 Predictions

We can now match WMAP data (see ?). The model can also generate non-Gaussianities observable by Plank with

$$f_{\rm NL} = \frac{5}{4r} \tag{9}$$

where r is the ratio of the energy density of the aulos over the total energy density of the universe before the aulos field decays into radiation, $r \geq 10^{-2}$. Furthermore, the low scale of the aulos field and the SC inflaton (TeV scale and below) allow for colliders to search for their signatures. In fact, there exists a non-trivial relationship between the aulos field and cosmological observations. The size of the soft breaking term of the aulos field (which can be measure in a lab)

$$\lambda_s = 6\pi^2(1 - n_s)\left(\frac{\Delta_\xi(k_0)\,\theta_0}{r \times q}\right)^2. \tag{10}$$

is given in terms of n_s, r, q and ($\theta_0 \simeq \pi$). $\Delta_\xi^2(k_0) = 2.43 \times 10^{-9}$?, which are measured cosmologically.

References

1. A. H. Guth, *Phys.Rev.*, vol. D23, pp. 347–356, 1981.
2. A. H. Guth and E. J. Weinberg, *Nucl.Phys.*, vol. B212, p. 321, 1983.
3. F. C. Adams and K. Freese, *Phys.Rev.*, vol. D43, pp. 353–361, 1991.
4. A. Linde, *Phys. Rev. D*, vol. 49, pp. 748–754, Jan 1994.
5. K. Freese and D. Spolyar, *JCAP*, vol. 0507, p. 007, 2005.
6. K. Freese, J. T. Liu, and D. Spolyar, *ArXiv e-prints*, 2006
7. D. H. Lyth and E. D. Stewart,*Phys.Rev.*, vol. D53, pp. 1784–1798, 1996.
8. M. J. Strassler and K. M. Zurek, *Phys. Lett.*, vol. B651, pp. 374–379, 2007.
9. S. R. Coleman and E. J. Weinberg,*Phys.Rev.*, vol. D7, pp. 1888–1910, 1973.
10. A. D. Linde, *Nucl.Phys.*, vol. B216, p. 421, 1983.
11. E. Witten, *Nucl.Phys.*, vol. B177, p. 477, 1981.
12. J. D. Wells, *ArXiv e-prints*, Sept. 2009.
13. B. W. Lee, C. Quigg, and H. Thacker, " *Phys.Rev.Lett.*, vol. 38, pp. 883–885, 1977.
14. B. W. Lee, C. Quigg, and H. Thacker, *Phys.Rev.*, vol. D16, p. 1519, 1977.
15. J. F. Gunion, H. E. Haber, G. L. Kane, and S. Dawson,*Front.Phys.*, vol. 80, pp. 1–448, 2000.
16. E. Accomando *et al.*,Phys. Rev. *D*, vol. 83, pp. 075012–+, Apr. 2011.
17. T. Appelquist, B. A. Dobrescu, and A. R. Hopper, *Phys.Rev.*, vol. D68, p. 035012, 2003.
18. D. Spolyar, arXiv:1111.3629 [astro-ph.CO].
19. S. Mollerach,*Phys.Rev.*, vol. D42, pp. 313–325, 1990.
20. D. H. Lyth and D. Wands, *Phys.Lett.*, vol. B524, pp. 5–14, 2002.
21. D. H. Lyth, C. Ungarelli, and D. Wands, *Phys.Rev.*, vol. D67, p. 023503, 2003.
22. G. 't Hooft, *Phys. Rev. D*, vol. 14, pp. 3432–3450, Dec 1976.
23. I. Affleck, *Nucl.Phys.*, vol. B191, p. 429, 1981.
24. E. Komatsu *et al.*,*Astrophys.J.Suppl.*, vol. 192, p. 18, 2011.

MAGNETIC FIELDS FROM INFLATION: THE TRANSITION TO THE RADIATION ERA

C. CAPRINI
CEA, IPhT & CNRS, URA 2306, F-91191 Gif-sur-Yvette, France

We compute the contribution to the scalar metric perturbations from large-scale magnetic fields which are generated during inflation. We show that apart from the usual passive and compensated modes, the magnetic fields also contribute to the constant mode from infiation. This is different from the causal (post inflationary) generation of magnetic fields where such a mode is absent, and it can strengthen the CMB constraint on the amplitude of inflationary magnetic fields by about one order of magnitude.

1 Introduction

The origin of the large scale magnetic fields observed in all astrophysical objects and even in voids (as recently shown using gamma-ray telescopes[1]) is still not clear. One possibility is generation in the primordial Universe, during phase transitions or during inflation[2]. In particular, inflationary magnetogenesis can provide magnetic seeds filling the entire Universe, possibly with significant amplitude also at very large scales. A term $\mathcal{L} \ni (1/4)f(\varphi)^2F^2$ in the Lagrangian[3], with a coupling function of the form $f(\varphi) \propto \eta^\gamma$, leads to electromagnetic fields at the end of inflation with power law power spectra which depend only on γ. For $\gamma > -2$ the magnetic field spectrum is blue, while for $\gamma \simeq -2$ it is scale invariant: a numerical estimate of the present day value of the magnetic field from slow roll inflation gives[3] $B_0 \sim 5\times 10^{-10}\mathrm{G}(10^5 H/m_{\mathrm{P}})$, where $m_P^2 = 1/(8\pi G)$.

The coupling $(1/4)f(\varphi)^2F^2$ is quite constrained[4], but it has the advantage to be simple. Moreover, the main features of the result here derived do not depend on the specific form of the coupling. We evaluate the effect on scalar metric perturbations of the electromagnetic field, generated during inflation by the presence of this coupling[a]. The electromagnetic field should not affect the evolution of the inflationary background, but its energy momentum tensor acts as a source of perturbations at first-order in perturbation theory (setting the electromagnetic field first order and its energy-momentum tensor second order[5] does not change the final result). To determine the metric perturbations we solve Bardeen equation on super-horizon scales during inflation, and match the inflationary solution to the solution during radiation domination. The matching has to be done at next to leading order in the slow roll expansion, and shows that the electromagnetic field contributes a constant term to the Bardeen potentials in the radiation era. This term adds to the 'passive' and 'compensated' modes[6,7], and it is specific to inflationary generated magnetic fields. We evaluate it by solving the evolution equation for the curvature perturbation in comoving gauge ζ.

[a]Note that the result given in this proceeding differs from what presented at the conference seminar: we have discovered and corrected an error in the calculations which led to different conclusions. The methodology of the calculation remains however the same as before.

In the following we use longitudinal gauge $ds^2 = a^2\left[-(1+2\Phi)d\eta^2 + (1-2\Psi)d\mathbf{x}^2\right]$ and work at first order in slow-roll inflation, with $a \simeq a_1 |\eta_1/\eta|^{1+\epsilon}$ and $\mathcal{H} \simeq -(1+\epsilon)/\eta$. The slow-roll parameters ϵ and ϵ_2 are defined by $\mathcal{H}^2 - \mathcal{H}' = \epsilon\mathcal{H}^2$ and $\epsilon' = 2\epsilon(3\epsilon_2 + 2\epsilon)\mathcal{H}$, where $' = d/d\eta$.

2 Metric perturbations from the inflationary electromagnetic field

The gravitational action of the inflationary electromagnetic field leads to a source term in the Bardeen equation for scalar metric fluctuations. At very large scales $x = |k\eta| \ll 1$ and at first order in the slow roll parameters, one has

$$\frac{d^2\Psi}{dx^2} + \frac{2(\epsilon+3\epsilon_2)}{x}\frac{d\Psi}{dx} + \left[1 - \frac{2(3\epsilon_2+2\epsilon)}{x^2}\right]\Psi \simeq \frac{3}{\rho_\varphi}\left[\frac{2(1+2\epsilon-3\epsilon_2)}{x^4}\Pi_S - \frac{1+3\epsilon}{x^3}\frac{d\Pi_S}{dx}\right] \equiv S_{\rm em}\,. \quad (1)$$

At lowest order in $x \ll 1$, the source term $S_{\rm em}(\mathbf{k},\eta)$ depends only on the scalar electromagnetic anisotropic stress $\Pi_S(\mathbf{k},\eta)$. $S_{\rm em}$ is a quantum operator acting on the electromagnetic vacuum, which can be calculated by exploiting the fact that the time dependence of Π_S is deterministic and the quantum creation and annihilation operators do not depend on time [8]. Using the time evolution of the electromagnetic potential $A_i(\mathbf{k},\eta)$, whose solutions are known in terms of Bessel functions[3], one finds $\Pi'_S = (\alpha+4\epsilon)\Pi_S/\eta$, with[8] $\alpha(\gamma) = \min(4-2|\gamma|, 3/2)$. This time dependence gives then $S_{\rm em}(\mathbf{k},\eta) = 3(2-\alpha-3\alpha\epsilon-6\epsilon_2)\,\Pi_S(\mathbf{k},\eta)/(x^4\rho_\varphi)$, where ρ_φ denotes the background energy density. Once $S_{\rm em}$ is known, the Bardeen equation (1) can be solved, and the resulting Bardeen potential is the sum of two uncorrelated quantum operators: $\hat{\Psi}_- = \hat{b}(k) - \beta(1+3\epsilon)\,\Pi_S/(x^2\rho_\varphi)$. $\hat{b}(k)$ is the usual inflationary solution at large scales, the homogeneous constant mode, and the rest is the contribution from the electromagnetic source, with $\beta = 3/(3-\alpha(\gamma))$ (the subscript $_-$ indicates that we evaluate the quantity in the inflationary era). Conventionally, the quantum to classical transition leads to the identification of these quantum operators with classical perturbations having stochastic amplitudes [10]. For simplicity we identify the quantum operators $\hat{\chi}$ with their r.m.s. amplitude: $\langle 0|\hat{\chi}^\dagger(\mathbf{q},\eta)\hat{\chi}(\mathbf{k},\eta)|0\rangle = (2\pi)^3 P_\chi(k,\eta)\delta(\mathbf{q}-\mathbf{k})$ and $\hat{\chi} \to \chi = \sqrt{k^3 P_\chi}$, where $\hat{\chi}$ can stand for $\hat{b}$, Π_S, $S_{\rm em}$ or $\hat{\Psi}_-$. For the electromagnetic anisotropic stress, we introduce the dimensionless ratio $\Omega_\Pi^- \equiv \sqrt{k^3 P_\Pi}/\rho_\varphi$. A lengthy calculation of the anisotropic stress power spectrum yields [8]

$$\Omega_\Pi^-(k,\eta) = \frac{H^2}{3m_P^2}C_\Pi(\gamma)\,x^\alpha\,, \quad (2)$$

where $C_\Pi(\gamma)$ is a dimensionless parameter of order unity (here H is taken at lowest order in slow roll: $H = \mathcal{H}/a \simeq 1/(a_1\eta_1)$, c.f. the definition at the end of the introduction). The classical Bardeen potential at lowest order $\mathcal{O}(x^{-2})$ in $x \ll 1$ and at first order $\mathcal{O}(\epsilon)$ in slow roll becomes then

$$\Psi_-(x) \simeq b(k) + \beta\left[1 + \left(1 + 2\log\left(\frac{\eta}{\eta_1}\right)\right)\epsilon\right]\frac{\Omega_\Pi^-}{x^2}\,, \quad (3)$$

(note that at first order in perturbation theory the electromagnetic contribution is not correlated with the inflationary one). Φ_- can be obtained from Ψ_- and the ij Einstein equation [8]. The logarithmic factor arises because Ω_Π^- is defined in terms of H at $\mathcal{O}(\epsilon^0)$.

We are aiming to find the Bardeen potentials the radiation era. The solution of the Bardeen equation during radiation domination gives [9]

$$\Psi_+(x) = \Psi_0 + \frac{\Psi_1}{x^3} + \frac{3\Omega_\Pi^+}{x^2} \quad \text{and} \quad \Phi_+(x) = \Psi_0 + \frac{\Psi_1}{x^3}\,, \quad (4)$$

where Ψ_0 and Ψ_1 are two arbitrary constants that have to be determined by matching the above solutions to those during inflation. The quantity $\Omega_\Pi^+ = \sqrt{k^3 P_\Pi^+}/\bar{\rho}_{\rm rad}$ is the dimensionless magnetic anisotropic stress in the radiation era, and it is constant in time. Note that during the radiation era, many charged particles are present and the conductivity of the Universe is high: we therefore may neglect the electric field in Ω_Π^+, which is rapidly 'short-circuited'. Consequently, the anisotropic stress is not necessarily continuous at the transition: if the value of γ in the coupling function $f(\eta)$ is such that the electric field dominates in Ω_Π^- during inflation, then Ω_Π^+ can be considerably smaller than Ω_Π^- because the electric field gets dissipated.

In order to determine Ψ_0 and Ψ_1, we match solutions (4) and (3) at the transition from inflation to the radiation era η_*. This instantaneous matching is a good approximation for all wavelengths which are much larger than the horizon scale at the moment of matching, $x_* = |k\eta_*| \ll 1$. To perform the matching we have to choose a physical hypersurface on which we require the induced 3-metric and the extrinsic curvature to be continuous [11]. The most natural surface is the one with constant inflaton energy density (since we assume inflation to stop when ρ_φ has dropped below a certain value). A convenient choice of coordinates for this hypersurface is to set the time coordinate $\tilde{\eta}$ to constant, and to relate it to the original one by a gauge transformation $\tilde{\eta} = \eta + T$, such that $T = -\delta\rho_\varphi/\rho'_\varphi$. The matching conditions then impose the continuity of Ψ and of the gauge transformation variable T at the transition. The resulting constants are $\Psi_0 \simeq 2/(3\epsilon)b(k)$ and $\Psi_1/x_*^3 \simeq -2/(3\epsilon)b(k) + \beta\,\Omega_\Pi^-/x_*^2 - 3\,\Omega_\Pi^+/x_*^2$.

We note that in Ψ_0 only the inflationary contribution remains, the electromagnetic field does not appear: thus, the matching conditions imply that there is no transfer of the electromagnetic mode to the constant mode in the radiation era at lowest order in the large scale expansion $\mathcal{O}(x^{-2})$. Since the decaying mode Ψ_1 can be neglected, we arrive to the result that the inflationary electromagnetic field contributes to the metric perturbation Ψ_+ in the radiation era through Ψ_0 only at $\mathcal{O}(x^0)$.

However, solving Bardeen equation analytically at next to leading order is higly non-trivial. To evaluate Ψ_0 at $\mathcal{O}(x^0)$, it turns out that the simplest way is to solve for the curvature perturbation[5,12] $\zeta = \Psi + 2(\mathcal{H}\Phi + \Psi')/[3\mathcal{H}(1+w)]$. Inserting solutions (4) in this definition, one obtains in fact that in the radiation era the curvature perturbation is simply $\zeta_+ = 3\Psi_0/2$. Furthermore, using the definition of ζ it is easy to demonstrate that the matching conditions imply that the curvature is continuous at the transition on the ρ_φ =const hypersurface. Hence, Ψ_0 is given by the value of the curvature at the end of inflation: $\zeta_-(x_*) = 3\Psi_0/2$. The evolution of ζ is governed by the following equation, at lowest order in the slow roll expansion[8]:

$$\frac{d^2\zeta}{dx^2} - \frac{2}{x}\frac{d\zeta}{dx} + \zeta = \frac{1}{\epsilon\, x^2 \rho_\varphi}\left[-6\rho_{\rm em} + x\frac{d\rho_{\rm em}}{dx} + x\frac{d\Pi_S}{dx}\right], \tag{5}$$

where $\rho_{\rm em}$ denotes the electromagnetic energy density. Comparing the source of the Bardeen equation (1) and the one of the above equation, we see that the former is by a factor x^{-2} larger than the latter; on the other hand, the source of (5) is larger in what concerns the slow roll expansion: it is of order ϵ^{-1}, while (1) is of order ϵ^0. Consequently, we expect $\zeta_-(x_*)$ to be of the order $\mathcal{O}(x^0)\cdot\mathcal{O}(\epsilon^{-1})$. This is the relevant contribution of the electromagnetic field to the metric fluctuations.

The electromagnetic energy density, which enters in the source of (5), has the same dependence on time and wavenumber of the electromagnetic anisotropic stress (as can be demonstrated by calculating its power spectrum $P_{\rm em}(k,\eta)$, in the same way[8] as P_Π). We therefore define, analogously to (2), the parameter $\Omega_{\rm em}^- \equiv \sqrt{k^3 P_{\rm em}}/\rho_\varphi \simeq H^2\, C_{\rm em}(\gamma)\, x^\alpha/(3m_P^2)$. The integration of (5) is then straightforward, leading to

$$\zeta_-(x) \simeq \frac{H^2}{9m_P^2}\frac{1}{\epsilon}\left[(\alpha-6)^2 C_{\rm em}^2 + 2\alpha(\alpha-6)C_{\rho\Pi} + \alpha^2\, C_\Pi^2\right]^{1/2} \left\{ \begin{array}{ll} -\log\left(x/x_{\rm in}\right) & \text{if } \alpha = 0 \\ x_{\rm in}^\alpha/\alpha & \text{if } \alpha \neq 0 \end{array} \right. \tag{6}$$

where $x_{\rm in} \simeq 1$ denotes horizon exit (when the source starts to act), and we have introduced the (order unity) coefficient $C_{\rho\Pi}$ denoting the amplitude of the cross term arising from the correlation $\langle 0|\rho^{\dagger}_{\rm em}\Pi_S|0\rangle$. Setting now $3\Psi_0/2 = \zeta_-(x_*)$, the Bardeen potentials in the radiation era Eq. (4) are completely determined.

3 Conclusions

We have demonstrated that an inflationary electromagnetic field leads to a constant mode in the Bardeen potential Ψ_+ in the radiation era: during inflation, the curvature is dynamically generated by the electromagnetic source and, at the end of inflation, it transfers into $\Psi_0 = 3\zeta_-(x_*)/2$. The constant mode in Ψ_+ remains unaltered until the recombination epoch, while the decaying mode sourced by the anisotropic stress in the radiation era $3\,\Omega^+_\Pi/x^2$ is compensated by neutrino free-straming [6,9]. This leads to the usual passive mode, which is present also for causally generated magnetic fields. The two modes give the full solution for the Bardeen potential in the matter era from an inflationary magnetic field:

$$\Psi^{\rm em}_+(\eta > \eta_{\rm eq}) \simeq \Psi_0 - \frac{3}{5}\Omega^+_\Pi \log\left(\frac{\eta_\nu}{\eta_*}\right)\,, \quad \text{where} \quad \Psi_0 \sim \left(\frac{H_*}{m_P}\right)^2 \frac{1}{\epsilon}\begin{cases} -\log\left(k\eta_*\right) & \text{if } \alpha = 0 \\ 1/\alpha & \text{if } \alpha \neq 0 \end{cases} \tag{7}$$

where $\eta_{\rm eq}$ is the time of equality, η_ν the time of neutrino decoupling, and we have used solution (6) neglecting numerical factors of order one. The term proportional to Ω^+_Π is the passive mode taken from Eq. (6.10) of [9]. We neglect the compensated mode, because it is subdominant with respect to both the passive and constant modes: it is of the form [9] $\Psi^{\rm em}_+ \sim \Omega^-_{\rm em}$.

To estimate the effect of the inflationary magnetic field on the CMB at large scales, we can set very roughly $\Delta T/T \sim \Psi^{\rm em}_+$. In the scale invariant case $\alpha = 0$, the logarithmic enhancement of the passive mode is $-3/5\,\log(T_*/T_\nu) \simeq -27$ if $T_* \simeq 10^{-2}\,m_P$. The enhancement of the new inflationary contribution, on very large scales $k \sim H_0$, is of the order of the number of e-folds of inflation after the present Hubble scale has exited the horizon: $-\log(H_0\,\eta_*) \simeq 64$. This is larger than the passive mode by about a factor $2/\epsilon$. We obtain then that the amplitude of the magnetic effect on the CMB is increased with respect to the naively expected amplitude $\simeq \Omega^-_{\rm em}$ by nearly two orders of magnitude due to the large logarithms. In other words, it might be possible to detect inflationary magnetic fields in the CMB down to about 10^{-10}G instead of the usual limit of 10^{-9}G. The nanoGauss limit was obtained for example in model independent analyses [7] which, in order to stay general and not assume a particular generation time for the magnetic field, only evaluate the effect of the compensated mode.

References

1. A. Neronov and I. Vovk, Science 328, 523 (2010)
2. A. Kandus, K. E. Kunze, C. G. Tsagas, Phys. Rept. 505 , 1-58 (2011) [arXiv:1007.3891].
3. M.S. Turner and L.M. Widrow, Phys. Rev. D37, 2743 (1988); B. Ratra, Astrophys. J. Lett. 391, L1 (1992); J. Martin, J. 'i. Yokoyama, JCAP 0801 (2008) 025 [arXiv:0711.4307]
4. V. Demozzi, V. Mukhanov, H. Rubinstein, JCAP 0908, 025 (2009) [arXiv:0907.1030].
5. N. Barnaby, R. Namba and Marco Peloso, [arXiv:1202.1469].
6. J. R. Shaw and A. Lewis, Phys. Rev. D81, 043517 (2010).
7. D. Paoletti and F. Finelli, Phys. Rev. D 83, 123533 (2011); D.G. Yamazaki et al, Phys. Rev. D 8, 023008 (2010).
8. C. Bonvin, C. Caprini and R. Durrer, [arXiv:1112.3901].
9. C. Bonvin and C. Caprini, JCAP 1005, 022 (2010).
10. D. Polarski and A. A. Starobinsky, Class. Quant. Grav. **13** (1996) 377 [gr-qc/9504030]
11. N. Deruelle and V.F. Mukhanov, Phys. Rev. D52, 5549 (1995)
12. D. Seery, JCAP 0908:018 (2009) [arXiv:0810.1617]

CONSTRAINING FAST-ROLL INFLATION

JOHANNES NOLLER
Theoretical Physics, Blackett Laboratory, Imperial College, London, SW7 2BZ, UK

We present constraints on how far single field inflation may depart from the familiar slow-roll paradigm. Considering a fast-roll regime while requiring a near-scale invariant power spectrum introduces large self-interactions for the field and consequently large and scale-dependent non-Gaussianities. Employing this signal, we use the requirement of weak-coupling together with WMAP constraints to derive bounds on generic $P(X, \phi)$ theories of single field inflation.

Introduction: Recently much progress has been made in understanding inflationary phenomenology beyond the slow-roll paradigm [1,2,3,4,5], i.e. where inflation is not almost de Sitter. An important question then poses itself: How far may we depart from the standard slow-roll regime without coming into conflict with observational and theoretical constraints? More specifically, what bounds can we place on "slow roll" parameters (which measure the "distance" from purely de Sitter expansion)? Here we present a number of such constraints for generic classes of inflationary single field models.

Departure from pure de Sitter expansion generically breaks the scale invariance of n-point correlation functions for the curvature perturbation ζ. However, present-day data constrain the 2-point function (the power spectrum) to be near scale-invariant [6]. Generic single field models can restore this observed behaviour via the introduction of non-canonical kinetic terms and hence a time-varying "speed of sound" c_s. In doing so, large interaction terms are produced at the level of the cubic action, leading to the generation of large levels of non-Gaussianity. These will be heavily constrained by CMB and large scale structure surveys in the near future and as such non-Gaussianity becomes an excellent tool for constraining slow-roll parameters.

The setup: We consider general single field inflation models described by an action

$$S = \int \mathrm{d}^4x\sqrt{-g}\left[\frac{R}{2} + P(X, \phi)\right] , \qquad (1)$$

where $X = -\frac{1}{2}g^{\mu\nu}\partial_\mu\phi\partial_\nu\phi$. It is useful to introduce a hierarchy of slow-roll parameters

$$\epsilon \equiv -\frac{\dot{H}}{H^2},\ \eta \equiv \frac{\dot{\epsilon}}{\epsilon H},\ldots \qquad \epsilon_s \equiv \frac{\dot{c}_s}{c_s H},\ \eta_s \equiv \frac{\dot{\epsilon}_s}{\epsilon_s H},\ldots \qquad \text{, where } c_s^2 = \frac{P_{,X}}{P_{,X} + 2XP_{,XX}} \qquad (2)$$

where a is the scale factor of an FRW metric and $H(t) = \dot{a}/a$ is the corresponding Hubble rate. c_s is the speed of sound with which perturbations propagate, essentially quantifying the non-canonical nature of (1). A near de Sitter expansion is associated with the slow-roll regime, where $\epsilon, \eta ... \epsilon_s, \eta_s ... \ll 1$ and accelerated expansion takes place as long as $\epsilon < 1$. We now wish to understand what constraints can be placed on these parameters. For simplicity we here focus

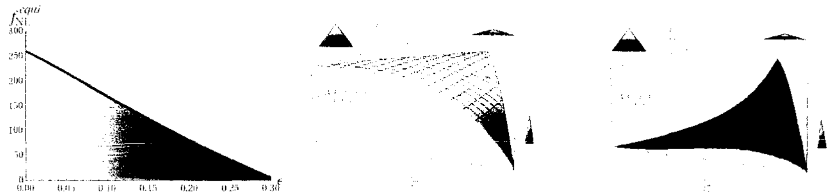

Figure 1: **Left**: $f_{\rm NL}^{equi}$ vs. ϵ for a horizon-crossing $\bar{c}_s = 0.1$ and $f_X = -70$. **Middle**: The dimensionless bispectrum $\mathcal{A}(k_1, k_2, k_3)/(k_1k_2k_3)$ plotted in the slow-roll limit $\epsilon \to 0$ for $\bar{c}_s = 0.07$ and $f_X = -53$. Triangular shapes denote the equilateral, enfolded and squeezed/local limit clockwise from top left. **Right**: Analogous plot for $\epsilon = 0.3$. Note how the overall amplitude is suppressed and the shape has changed, now peaking in the enfolded limit.

on the case where slow-roll is broken at the first level in the hierarchy, for ϵ and ϵ_s, but assume that slow-roll conditions still hold for higher order parameters, setting $\eta, \eta_s \sim 0$.

In deriving the constraints presented here we will firstly map present-day observational bounds, especially those coming from the WMAP experiment[6], onto the parameter space of fast-rolling models. As a second guidance principle we will impose a minimal theoretical constraint: The fluctuations described by (1) should remain weakly coupled for at least ~ 10 e-folds. This range corresponds to the observable window of scales where primordial non-Gaussianity may be measured (running from CMB, $k^{-1} \sim 10^3$ Mpc, to galactic scales, $k^{-1} \sim 1$ Mpc).

Why require weak coupling at all? Strong coupling scales are frequently associated with the appearance of new physics. In the standard model, for example, the would-be strong coupling scale lies around $\sim 1\ TeV$, before the Higgs is introduced. We may expect an analogue to be true for single field inflation models, especially given the generic presence of other massive degrees of freedom (dof) in UV completions of primordial physics. Such *dofs* may be integrated out at low energies, but can become relevant around the would-be strong coupling scale[7,8]. If so, predictions beyond this scale will depend on exactly how and which *dofs* enter. Flipping the argument around, even if we were able to calculate the dynamics for generic strongly coupled systems, one should remain cautious whether the effective field theory under consideration is valid anymore in such circumstances. As such we will require weak coupling to ensure that (1) is predictive over at least the observable window of scales where primordial fluctuations may be measured.

Non-Gaussian signals: The 2-point function of the curvature perturbation ζ is given by

$$\langle\zeta(\mathbf{k}_1)\zeta(\mathbf{k}_2)\rangle = (2\pi)^5\delta^3(\mathbf{k}_1 + \mathbf{k}_2)\frac{P_\zeta}{2k_1^3} \quad , \quad n_s - 1 \equiv \frac{d\ln P_\zeta}{d\ln k} = \frac{2\epsilon + \epsilon_s}{\epsilon_s + \epsilon - 1} \, , \tag{3}$$

where P_ζ is the power spectrum. We will focus on the case of an exactly scale-invariant 2-point function $n_s = 1$ here, requiring $\epsilon_s = -2\epsilon$. For $(n_s - 1)$-dependent corrections see[2,3,5]. The 3-point function then measures the strength of interactions of the field[a] which are described by the interaction vertices in the cubic action[9,3]

$$S_3 = \int d^3x\, d\tau\; a^2\left\{\frac{\Lambda_1}{a}\zeta'^3 + \Lambda_2\zeta\zeta'^2 + \Lambda_3\zeta(\partial\zeta)^2 + \Lambda_4\zeta'\partial_j\zeta\partial_j\partial^{-2}\zeta' + \Lambda_5\partial^2\zeta(\partial_j\partial^{-2}\zeta')(\partial_j\partial^{-2}\zeta')\right\}. \tag{4}$$

The 3-point function itself can be expressed through the amplitude $\mathcal{A}$

$$\langle\zeta(\mathbf{k}_1)\zeta(\mathbf{k}_2)\zeta(\mathbf{k}_3)\rangle = (2\pi)^7\delta^3(\mathbf{k}_1 + \mathbf{k}_2 + \mathbf{k}_3)P_\zeta^2\frac{1}{\Pi_j k_j^3}\mathcal{A} \quad , \quad f_{\rm NL}^{equi} = 30\frac{\mathcal{A}_{k_1=k_2=k_3}}{K^3}, \tag{5}$$

[a] A free field is Gaussian, hence the 3-point function captures the non-Gaussian statistics for ζ.

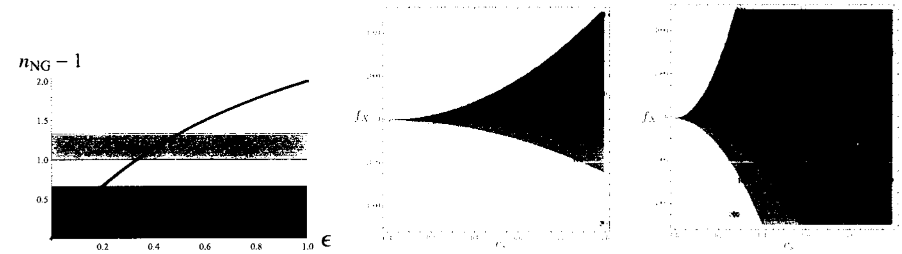

Figure 2: **Left**: $n_{\rm NG}-1$ plotted against ϵ in the small c_s limit. Green, yellow and orange ($< 2/3, < 1, < 4/3$) regions are those allowed by perturbative constraints assuming $f_{\rm NL}^{equi}(\text{CMB}) \sim \mathcal{O}(100), \mathcal{O}(10), \mathcal{O}(1)$ respectively. **Middle**: Contour plot showing the region in parameter space allowed by the WMAP 2σ constraint $f_{\rm NL}^{\rm equil} = 26 \pm 240$ in the slow-roll limit $\epsilon \to 0$. **Right**: Analogous plot for $\epsilon = 0.3$. Note how the allowed region widens.

where $f_{\rm NL}^{equi}$ serves as a convenient single number measure of the amplitude of non-Gaussianity in the equilateral limit $k_1 = k_2 = k_3$ and the power spectrum P_ζ is conventionally calculated for the mode $K = k_1 + k_2 + k_3$. The size of non-Gaussianities is then a function of the parameters $\{c_s^{-2}, f_X, \epsilon, n_s\}$, where $f_X{}^b$ essentially measures the strength of the first interaction vertex ζ'^3 and satisfies [3]

$$\Lambda_1 = \frac{2\epsilon}{3Hc_s^4}\left(1 - c_s^2 - f_X\right). \tag{6}$$

$f_{\rm NL}^{equi}$ can then be estimated by $f_{\rm NL}^{equi} \sim \mathcal{O}(c_s^{-2}) + \mathcal{O}(\frac{f_X}{c_s^2})$. Since requiring a scale-invariant 2-point function yields $\epsilon_s = -2\epsilon$, fast-roll models with $\epsilon \sim \mathcal{O}(1)$ lead to a rapidly decreasing c_s (as long as inflation is not ghost-like, i.e. $\epsilon \nless 0$). They therefore naturally yield regimes where c_s is small and the 3-point function is large. A useful fitting formula in this context is [1]

$$f_{\rm NL}^{equi} = 0.27 - \frac{0.164}{c_s^2} - (0.12 + 0.04 f_X)\frac{1}{c_s^2}\left(1 - \frac{4\epsilon}{1+\epsilon}\right). \tag{7}$$

This has three significant consequences for fast-roll phenomenology:

- **Fast-roll suppresses $f_{\rm NL}$.** Figure 1 and eqn. (7) show that for equilateral non-Gaussianity, $f_{\rm NL}^{equi}$ is generically reduced when departing from the slow-roll regime. This implies that models with a small speed of sound c_s, which violate observational constraints in the slow-roll limit, can still be allowed when considering fast-roll scenarios.

- **The shape of the bispectrum is modified.** Figure 1 also shows that fast-roll suppression is not an artefact of focusing on the equilateral limit, but that in fact the full bispectrum as described by $\mathcal{A}$ is fast-roll suppressed. Furthermore the shape of the amplitude is modified - full details are given in [1,2], but figure 1 illustrates a particular case where a predominantly equilateral shape is altered into an "enfolded" shape, peaking in the limit $2k_1 = k_2 = k_3$.

- **The allowed parameter-space for f_X, c_s becomes wider.** As a result of fast-roll suppression observational bounds, e.g. the WMAP result [6] $f_{\rm NL}^{\rm equil} = 26 \pm 240$ at 95% confidence, map onto weaker constraints for parameters f_X, c_s at the expense of enlarged ϵ. Figure 2 shows how constraints are altered, cf. [10].

[b] We concentrate on solutions for which f_X is constant here. Also note that for DBI models the first interaction vertex vanishes $\Lambda_1 = 0$.

Induced blue running of non-Gaussianities → strong coupling constraints: The dependence of the 3-point function on scale K can be described by the parameter $n_{\rm NG} - 1 \equiv \mathrm{d}\ln|f_{\rm NL}^{equi}|/\mathrm{d}\ln K$. Expanding around the phenomenologically motivated small c_s limit, we find

$$n_{\rm NG} - 1 = \frac{4\epsilon}{1+\epsilon} + \frac{4\epsilon(8\epsilon - 55)\mathrm{Sec}\left[\frac{2\epsilon\pi}{1+\epsilon}\right]c_s^2}{(55 + 8f_X + 2\epsilon(15\epsilon + 12\epsilon f_X - 47 - 16f_X))\Gamma\left[\frac{4}{1+\epsilon} - 3\right]} + \mathcal{O}(c_s^4), \quad (8)$$

which is an exact result in ϵ (the solution to all orders in c_s can be found in [2]). Interestingly this means we have a generically blue running of non-Gaussianities (as long as $\epsilon \nless 0$), resulting in larger interactions and hence enlarged signals on smaller scales. In other words, primordial non-Gaussianities measured on e.g. galaxy cluster scales would be larger than those measured at CMB scales. However, this also means interactions will eventually become strongly coupled for sufficiently small scales. Following [11] we take the ratio of cubic and quadratic Lagrangians as our measure of strong coupling, requiring

$$\frac{\mathcal{L}_3}{\mathcal{L}_2} \sim \mathcal{O}(1, \epsilon, f_X)\frac{\zeta}{c_s^2} \ll 1 \quad (9)$$

for fluctuations to be weakly coupled, roughly corresponding to $f_{\rm NL} \ll 10^5$. If this condition breaks (at horizon crossing, where n-point correlation functions are evaluated here), quantum loop corrections are no longer suppressed and a perturbative treatment is no longer applicable. We now impose a minimal constraint of at least $\sim$ 10 e-folds of weakly coupled inflation governed by action (1), corresponding to the window of scales where primordial non-Gaussianity may be observable (from CMB, $k^{-1} \sim 10^3$ Mpc, to galactic scales, $k^{-1} \sim 1$ Mpc).[c]

Depending on the size of $f_{\rm NL}^{equi}$ at CMB scales, this results in different bounds on $n_{\rm NG}$ as shown in figure 2. In terms of the scale K the appropriate range here corresponds to $K_{\rm gal}/K_{\rm CMB} \simeq 10^3$. For $f_{\rm NL}$ this means $f_{\rm NL}^{equi}(\mathrm{CMB}) \approx 10^{-3(n_{\rm NG}-1)}f_{\rm NL}^{equi}(\mathrm{Gal})$. If the bound on $n_{\rm NG}$ is satisfied, non-Gaussian interactions remain under perturbative control throughout the range of observable scales. In the optimistic scenario with detectable CMB non-Gaussianities, i.e. $f_{\rm NL}^{equi}(\mathrm{CMB}) \gtrsim \mathcal{O}(10)$, we can combine these constraints with equation (8) to put an upper bound on ϵ: $\epsilon \lesssim 0.3$.[1,2] If $f_{\rm NL}^{equi}(\mathrm{CMB}) \gtrsim \mathcal{O}(100)$ the bound is strengthened to $\epsilon \lesssim 0.2$. This shows how one can constrain the amount of slow-roll violation by requiring the action (1) to be a valid effective field theory over the observable range of scales for primordial fluctuations.[d]

References

1. J. Khoury and F. Piazza, JCAP **0907**, 026 (2009), [arXiv:0811.3633 [hep-th]].
2. J. Noller and J. Magueijo, Phys. Rev. D **83**, 103511 (2011) [arXiv:1102.0275 [astro-ph.CO]].
3. C. Burrage *et al*, JCAP **1107**, 032 (2011) [arXiv:1103.4126 [astro-ph.CO]].
4. T. Battefeld and J. Grieb, JCAP **1112**, 003 (2011) [arXiv:1110.1369 [astro-ph.CO]].
5. R. H. Ribeiro, arXiv:1202.4453 [astro-ph.CO].
6. E. Komatsu *et al.* [WMAP Collaboration], arXiv:1001.4538 [astro-ph.CO].
7. A. J. Tolley and M. Wyman, Phys. Rev. D **81**, 043502 (2010) [arXiv:0910.1853 [hep-th]].
8. D. Baumann and D. Green, JCAP **1109**, 014 (2011) [arXiv:1102.5343 [hep-th]].
9. D. Seery and J. E. Lidsey, JCAP **0506**, 003 (2005), [astro-ph/0503692].
10. L. Senatore *et al*, JCAP **1001**, 028 (2010) [arXiv:0905.3746 [astro-ph.CO]].
11. D. Baumann *et al*, JCAP **1105**, 004 (2011) [arXiv:1101.3320 [hep-th]].

[c] Beyond those 10 e-folds several options exist, depending on the UV-completion of the low-energy effective $P(X,\phi)$ theory [8,7]: new degrees of freedom may become important, resulting in an inflationary weakly coupled multi-field theory, the dispersion relation may change, a strongly coupled phase of inflation may take place,...

[d] Note that eqn. (8) shows that these bounds receive $\mathcal{O}(c_s^2)$ corrections. [2]

Large Scale Structures: pushing the non-linear frontier by semi-analytic methods

M. PIETRONI
INFN - Sezione di Padova, Via Marzolo 8
I-35131 Padova, Italy

The study of the Large Scale Structure of the Universe will provide a wealth of information on the nature of Dark Matter and Dark Energy in the near future, provided measurements and theoretical computations can attain accuracies at the percent level. We review semi-analytical methods, based on Eulerian perturbation theory, as a promising tool to follow the time evolution of cosmological perturbations at small redshifts and at mildly nonlinear scales. We discuss in particular a newly proposed resummation scheme, which agrees with N-body results up to $k \sim 1\,\mathrm{h}/Mpc$ at the percent level. Due to the extremely reduced computational time required by this method, it provides a very promising tool to explore a large wealth of cosmologies in the mildly non-linear range of scales.

1 Motivation

Understanding the statistical properties of matter inhomogeneities in the universe at the percent level is one the main goals for cosmology in the near future. A reliable description of the evolution of perturbations beyond the linear regime, i.e. at moderately high, and high wavenumbers is indeed a very active field of investigation, since future generation of observations, such as high redshift galaxy surveys are going to provide information on several aspects of the cosmological model, and with their unprecedented accuracy call for a detailed theoretical framework to compare with. As an example, the location and amplitude of the Baryon Acoustic Oscillations (BAO) in the wavelength range $k \simeq 0.05 - 0.25\ h\ \mathrm{Mpc}^{-1}$ are powerful probes of the expansion history of the universe and of the properties of the dark energy [1]. Furthermore, the yet unknown absolute neutrino mass scale will be also more efficiently constrained (or detected) by comparing data with a theoretically robust determination of the power spectrum (PS) in the high k range.

There are two approaches to deal with nonlinearities. The more established one is to use N-body simulations. However, in order to attain the required percent accuracy on such large scales very large volumes and high resolutions are needed. The resulting limitation in computer time makes it impossible to run simulations over the many thousands of cosmologies necessary for grid based or Markov Chain Monte Carlo (MCMC) estimation of cosmological parameters. One is therefore forced to develop interpolation methods for theoretical predictions, which limits the practical use of this approach to "vanilla" type ΛCDM models and a restricted set of their variants, as it was discussed thoroughly in [2,3].

The alternative approach is provided by Eulerian perturbation theory (PT), where the Euler-Poisson system of equations describing the self-gravitating dark matter fluid is solved perturbatively in the matter density fluctuations (for a review, see [4], for recent applications, see for instance [5,6,7,8]). After its first formulation in the nineties, this framework is now experiencing a renewed interest, mainly thanks to the work of Crocce and Scoccimarro [9,10], who showed that

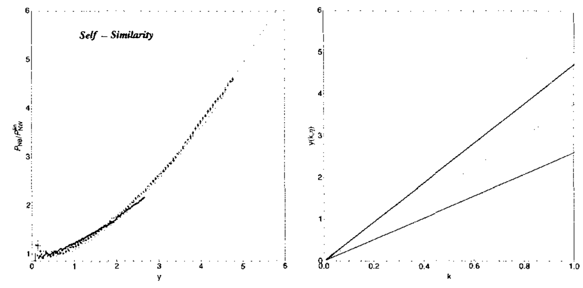

Figure 1: The nonlinear PS from N-body simulations plotted against the variable y defined in the text. The color-code is the following: green for $z = 0$, black for $z = 0.5$, red for $z = 1$, and purple for $z = 2$. Each PS has been truncated at $k = 1\,h/Mpc$ (left). The relation between y and k at different redshifts (right).

some classes of perturbative corrections can be resummed at all orders, enhancing the range of applicability of the approach towards lower redshifts and smaller scales. A number of different semi-analytic resummation methods have been proposed [11,12,8,13,14,15,16,17] and applied to the calculation of the matter PS mainly in the BAO range [18,13,19,20]. Using these methods, non-linear effects have been computed in a variety of non-ΛCDM cosmologies, such as those with massive neutrinos [21], with primordial non-gaussianity of different shapes [22], or with clusterizing dark energy [23,24]. The status of these methods to date can be summarized as follows: at $z \gtrsim 1$ the PS can be computed at a few percent accuracy (in comparison with state of the art N-body simulations) in the BAO range of scales ($0.05 \lesssim k \lesssim 0.25\,\mathrm{h/Mpc}$), the accuracy degrading quite rapidly at higher wave numbers (smaller scales) and smaller redshifts. Moreover, the computational time of these approaches, though much smaller than for N-body simulations, is still in the few hours range for a single PS, thereby making the implementations of MCMC's still quite problematic.

2 A new resummation scheme

In a recent paper [25] we have introduced a new computational scheme which overcomes the present limitations of resummed PT approaches in both respects: it greatly enlarges the range of scales in which it gives results accurate at the percent level, and it greatly reduces computational times. At $z = 1$ we can compute the PS up to $k \simeq 1\,\mathrm{h/Mpc}$ at the percent level, in a time comparable to that of a simple 1-loop computation, namely, $O(1)$ minutes. This opens the road both to parameter estimation via MCMCs, and to the extension of these methods from the BAO physics to weak lensing measurements.

At the technical level, our main result is a resummation of the dominant PT corrections to the PS in the range of scales mentioned above. In the CS resummation for the propagator the effective expansion parameter in the large k limit turns out to be [10]

$$y \equiv e^{\eta}\sigma_v k\,, \tag{1}$$

where $\eta = \log D(z)/D(z_{in})$ ($D(z)$ being the linear growth factor), and

$$\sigma_v^2 \equiv \frac{1}{3}\int d^3q\,\frac{P^0(q)}{q^2}\,, \tag{2}$$

with $P^0(q)$ the linear PS evaluated at the initial redshift, to be formally sent to infinity (in practice we use $z_{in} = 100$). Our starting point is the realization that. in the small scale limit, also the PS becomes a function of the variable y defined in eq. (1). In Fig. 1 we plot the PS from the N-body simulations of [26] at different redshifts, normalized by the smooth PS by Eisenstein and Hu [27], as a function of y. It is clear that, for $y > O(1)$, all the PS's can expressed as an universal function depending on y alone. Therefore our goal is to identify, at each order in PT, the leading large y corrections which, once resummed at all orders, give the y-function plotted in Fig. 1.

Our approach provides a very efficient way to reorganize the PT expansion, and is based on evolution equations in time which are exact at all orders in PT. A similar approach was already presented in ref. [28] for the propagator, where it was used to reproduce the CS result, and also to include next-to-leading corrections. We have derived the large k or, better, large y, limit of the evolution equation for the PS. At the same time, at low k, the equation is solved by the 1-loop PS, thereby providing an interpolation between the two correct behaviors in the two extremes of the physically interesting range of scales. It is important to keep in mind that the range of scales where the eulerian approach is applicable is limited in the UV (small scales) by multi streaming, *i.e.* by small scale velocity dispersion, a physical effect which is absent from the approach even at the non-perturbative level. Therefore the small-scale limit referred to in this paper will always correspond to momentum scales at most of order $k \sim 1\,\mathrm{h/Mpc}$.

As we have already anticipated, our resummation procedure works remarkably well: its performance degrades only for (low) redshifts and (small) scales where the effect of multi-streaming, the intrinsic limit of eulerian PT, is known to become relevant [29,30]. In other words, at the few percent level, our approach reproduces all the physics contained in the Euler-Poisson system on which eulerian PT is founded. As a consequence, it provides the best starting base for methods aimed at going beyond the single-stream approximation, as that proposed in [31].

We compared the nonlinear PS predictions against the data coming from high accuracy N-body simulations designed to predict the nonlinear PS at the percent accuracy around the BAO range of scales. The initial linear PS for the simulations we considered was obtained from the CAMB public code [32] and any primordial non–Gaussianity was neglected. Accordingly, we solved our evolution equations taking the initial PS from CAMB at $z_{in} = 100$, where the gravitational clustering is fully linear on the scales of interest.

We provide plots of the comparison between our approach and the N-body simulations presented by Sato and Matsubara in [26]. They considered a ΛCDM cosmology with the following parameters: $\Omega_m = 0.265$, $\Omega_b h^2 = 0.0226$, $h = 0.71$, $n = 0.963$ and $\sigma_8 = 0.8$. In order to check the possible dependence of our results on the cosmology or on the N-body simulations, we also compared our results with the independent set of simulations produced by Carlson, White and Padmanabhan in [33] for a different ΛCDM cosmology, and with the results from the cosmic Coyote emulator [2,3,34]. The latter is an interpolator built from a suite of many different N-body simulations which provides nonlinear PS's for different cosmological parameters chosen inside a certain range and for redshifts $z \leq 1$. In all these cases our comparison tests worked at the same quality level.

In Fig. 2 we plot the nonlinear PS computed in different approximations, divided by the smooth linear PS given in [27]. The blue dashed line corresponds to the small k approximation of the evolution equation, while the red solid line is obtained by interpolating betwwn the small k solution and the large k one. The results obtained in linear PT (grey dash-dotted) and 1-loop PT (been dotted) are also shown.

We notice that our evolution equation, in the small k limit, is able to reproduce the nonlinear PS at the percent level in the BAO range. Concerning the resummed and interpolated solution, *i.e.* the red line, we see that it performs at the 1% level in the BAO region at any redshift, including $z = 0$, where, due to the larger amount of nonlinearity, the last peak is at about 0.15 h/Mpc. At redshifts $z \geq 0.5$ it performs as the Coyote interpolator up to $k \simeq 0.35$ h/Mpc, namely, still in agreement with the N-body results of [26] at the 1% level.

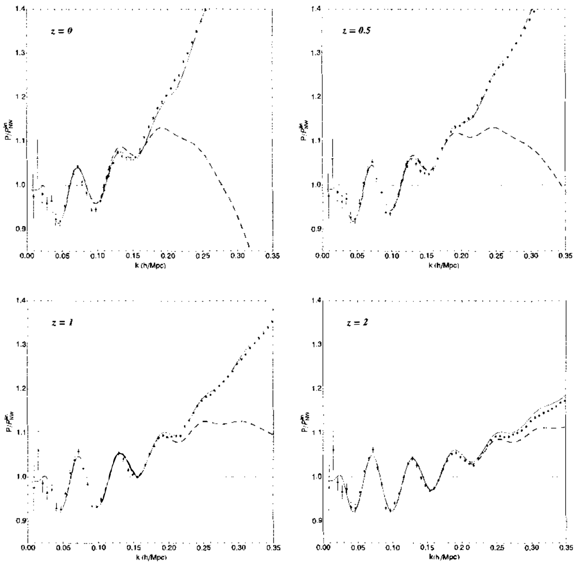

Figure 2: PS's at different redshifts. The color code is the following: the grey dash-dotted line is linear PT, the green dotted line is 1-loop PT, the blue dashed line corresponds to the solution of our evolution equation in the small k approximation, the red solid line is the solution of the evolution equation with the large k expansion included, and dots with error-bars are the N-body results of Sato and Matsubara. Also shown (thin grey line) is the output of the Coyote interpolator.

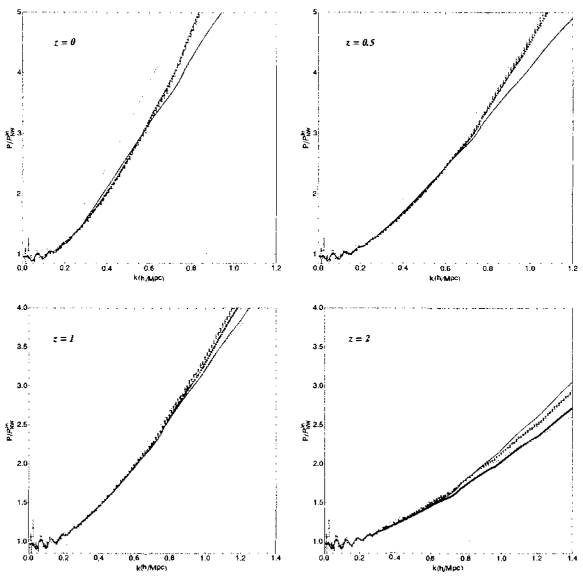

Figure 3: Comparison between the evolution equation discussed in the text (red solid line), and the N-body simulations of Sato and Matsubara: black dots are for the large volume simulation ($L = 1000\,\mathrm{Mpc/h}$), blue ones for the small volume one ($L = 500\,\mathrm{Mpc/h}$). Also shown are linear PT (grey dash-dotted line) and 1-loop PT (green dotted line).

The comparison with the nonlinear PS from the N-body simulations at large k is given in Fig. 3. In order to gauge the performance of the N-body results at large k, Sato and Matsubara performed runs with two different volumes, a large one ($L_{box} = 1000\,\mathrm{Mpc/h}$) and a small one ($L_{box} = 500\,\mathrm{Mpc/h}$), which we plot with black and blue points, respectively. We notice that the two sets of data are practically overlapped for $z < 1$, where we also checked that they agree with the Coyote emulator, but diverge significantly at $z \geq 2$ for $k \gtrsim 0.8\,\mathrm{h/Mpc}$. These transient effects therefore prevent us from considering the comparison for higher redshifts and scales, however, the trend from $z = 0$ up to $z = 2$ clearly shows a progressive improvement, as it should. Quantitatively, at $z = 1$ we measure an agreement at the 1% level between our results and the N-body simulations up to $k = 0.8\mathrm{h/Mpc}$ and at 2% on the same range of scales for $z = 0.5$.

3 Discussion and conclusions

The scheme introduced in [25] presents three main advantages with respect to alternative approaches to the nonlinear PS in the $k \lesssim 1$ h/Mpc scale, including N-body simulations: the accuracy (already discussed in the previous section), the computational time, and the range of cosmologies that can be dealt with. The computational time is the same as that required by a standard PT computation at 1-loop. Indeed, concerning momentum integrations, to obtain the three independent components of the PS, one needs to perform two one-dimensional integrals and three two-dimensional ones. Exactly the same integrals enter the 1-loop expression for the PS. In addition, the solution of our evolution equation requires only one more integration in time, or better, in η, which however takes a time of the order of a second. Therefore, any point in k takes at most a few seconds to be evaluated.

The extension from ΛCDM cosmology to more general ones is also greatly eased in this approach. In principle, all the cosmologies in which the fluid equations (i.e. the system composed by the continuity, Euler, and Poisson equations) are modified only in the linear terms, can be taken into account as it was discussed in [16]. Cosmologies of this type include, for instance, those with massive neutrinos [6,21,7], modifications of gravity of the scalar-tensor/f(R) type [35], or Dark Energy models with a non-relativistic sound speed [24]. Non-gaussian initial conditions can also be taken into account by the inclusion of new vertices in the diagrammatic rules of Fig. **??** and their impact on the propagator and on the PS can be analyzed [22,36].

Evolution equations for the nonlinear PS have been proposed also before [12,15,?,17]. The main step forward provided by the present analysis is, besides the computational speed, the improved treatment of the large k limit, in particular for the mode-mode coupling term.

As any other approach based on eulerian perturbation theory, also this one suffers from an intrinsic physical limitation, namely, the neglect of velocity dispersion and all higher order moments of the particle distribution function, which is at the basis of the derivation of the fluid equations from the Vlasov equation. This "single stream approximation" is known to hold at large scales and high redshifts, but it was estimated to fail at the percent level in the BAO range at $z \to 0$ [29,30]. The comparison between our results and N-body simulations exhibits the same trend. It will be interesting to investigate further the origin of this excellent agreement. A way to incorporate such effects in semi-analytical methods was recently proposed in [31], in which the feeding of the multi stream at small scales on the more perturbative intermediate scales was described in terms of effective source terms. The inclusion of such effects in the present approach will be studied elsewhere.

For the time being, the increase of the maximum k at which the nonlinear PS can be computed reliably, provided by our approach, opens the way to interesting cosmological applications, allowing a tighter extraction of cosmological parameters from the LSS relevant for topics such as the measurement of the acoustic scale from BAO's, the limit on the neutrino mass scale, and possibly, cosmic shear.

Acknowledgments

It is a pleasure to thank Stefano Anselmi for the exciting collaboration which lead to the original part of this talk. Partial support from the European Union FP7 ITN INVISIBLES (Marie Curie Actions, PITN- GA-2011- 289442) is acknowledged.

References

1. Daniel J. Eisenstein et al. Detection of the Baryon Acoustic Peak in the Large-Scale Correlation Function of SDSS Luminous Red Galaxies. *Astrophys. J.*, 633:560–574, 2005.
2. Katrin Heitmann, Martin White, Christian Wagner, Salman Habib, and David Higdon. The Coyote Universe I: Precision Determination of the Nonlinear Matter Power Spectrum. *Astrophys.J.*, 715:104–121, 2010.
3. Katrin Heitmann, David Higdon, Martin White, Salman Habib, Brian J. Williams, et al. The Coyote Universe II: Cosmological Models and Precision Emulation of the Nonlinear Matter Power Spectrum. *Astrophys.J.*, 705:156–174, 2009.
4. F. Bernardeau, S. Colombi, E. Gaztanaga, and R. Scoccimarro. Large-scale structure of the universe and cosmological perturbation theory. *Phys. Rept.*, 367:1–248, 2002.
5. Donghui Jeong and Eiichiro Komatsu. Perturbation Theory Reloaded: Analytical Calculation of Non-linearity in Baryonic Oscillations in the Real Space Matter Power Spectrum. *Astrophys. J.*, 651:619, 2006.

6. Shun Saito, Masahiro Takada, and Atsushi Taruya. Impact of massive neutrinos on nonlinear matter power spectrum. *Phys. Rev. Lett.*, 100:191301, 2008.
7. Shun Saito, Masahiro Takada, and Atsushi Taruya. Nonlinear power spectrum in the presence of massive neutrinos: perturbation theory approach, galaxy bias and parameter forecasts. *Phys. Rev.*, D80:083528, 2009.
8. Emiliano Sefusatti. 1-loop Perturbative Corrections to the Matter and Galaxy Bispectrum with non-Gaussian Initial Conditions. *Phys.Rev.*, D80:123002, 2009.
9. Martin Crocce and Roman Scoccimarro. Renormalized Cosmological Perturbation Theory. *Phys. Rev.*, D73:063519, 2006.
10. Martin Crocce and Roman Scoccimarro. Memory of Initial Conditions in Gravitational Clustering. *Phys. Rev.*, D73:063520, 2006.
11. P. Valageas. A new approach to gravitational clustering: a path- integral formalism and large-N expansions. *Astron. Astrophys.*, 421:23–40, 2004.
12. Patrick McDonald. Dark matter clustering: a simple renormalization group approach. *Phys. Rev.*, D75:043514, 2007.
13. Sabino Matarrese and Massimo Pietroni. Resumming Cosmic Perturbations. *JCAP*, 0706:026, 2007.
14. Takahiko Matsubara. Resumming Cosmological Perturbations via the Lagrangian Picture: One-loop Results in Real Space and in Redshift Space. *Phys. Rev.*, D77:063530, 2008.
15. A. Taruya and T. Hiramatsu. A Closure Theory for Nonlinear Evolution of Cosmological Power Spectra. *Astrophys.J.*, 674:617–635, February 2008.
16. Massimo Pietroni. Flowing with Time: a New Approach to Nonlinear Cosmological Perturbations. *JCAP*, 0810:036, 2008.
17. Takashi Hiramatsu and Atsushi Taruya. Chasing the non-linear evolution of matter power spectrum with numerical resummation method: solution of closure equations. *Phys. Rev.*, D79:103526, 2009.
18. Sabino Matarrese and Massimo Pietroni. Baryonic acoustic oscillations via the renormalization group. *Mod. Phys. Lett.*, A23:25–32, 2008.
19. M. Crocce and R. Scoccimarro. Nonlinear Evolution of Baryon Acoustic Oscillations. *Phys. Rev.*, D77:023533, 2008.
20. Atsushi Taruya, Takahiro Nishimichi, and Shun Saito. Baryon Acoustic Oscillations in 2D: Modeling Redshift- space Power Spectrum from Perturbation Theory. *Phys. Rev.*, D82:063522, 2010.
21. J. Lesgourgues, S. Matarrese, M. Pietroni, and A. Riotto. Non-linear Power Spectrum including Massive Neutrinos: the Time-RG Flow Approach. *JCAP*, 0906:017, 2009.
22. Nicola Bartolo, J. P. Beltran Almeida, Sabino Matarrese, Massimo Pietroni, and Antonio Riotto. Signatures of Primordial non-Gaussianities in the Matter Power-Spectrum and Bispectrum: the Time-RG Approach. *JCAP*, 1003:011, 2010.
23. Guido D'Amico and Emiliano Sefusatti. The nonlinear power spectrum in clustering quintessence cosmologies. *JCAP*, 1111:013, 2011.
24. Stefano Anselmi, Guillermo Ballesteros, and Massimo Pietroni. Non-linear dark energy clustering. *JCAP*, 1111:014, 2011.
25. Stefano Anselmi and Massimo Pietroni. Nonlinear Power Spectrum from Resummed Perturbation Theory: a Leap Beyond the BAO Scale. *ArXiv 1205.2235*, 2012.
26. Masanori Sato and Takahiko Matsubara. Nonlinear Biasing and Redshift-Space Distortions in Lagrangian Resummation Theory and N-body Simulations. *Phys.Rev.*, D84:043501, 2011.
27. Daniel J. Eisenstein and Wayne Hu. Power spectra for cold dark matter and its variants. *Astrophys.J.*, 511:5, 1997.
28. Stefano Anselmi, Sabino Matarrese, and Massimo Pietroni. Next-to-leading resummations

in cosmological perturbation theory. *JCAP*, 1106:015, 2011.
29. Sebastian Pueblas and Roman Scoccimarro. Generation of Vorticity and Velocity Dispersion by Orbit Crossing. *Phys.Rev.*, D80:043504, 2009.
30. Patrick Valageas. Impact of shell crossing and scope of perturbative approaches in real and redshift space. *Astron. Astrophys.*, 526:A67, 2011.
31. Massimo Pietroni, Gianpiero Mangano, Ninetta Saviano, and Matteo Viel. Coarse-Grained Cosmological Perturbation Theory. *JCAP*, 1201:019, 2012.
32. Antony Lewis, Anthony Challinor, and Anthony Lasenby. Efficient Computation of CMB anisotropics in closed FRW models. *Astrophys. J.*, 538:473–476, 2000.
33. Jordan Carlson, Martin White, and Nikhil Padmanabhan. A critical look at cosmological perturbation theory techniques. *Phys. Rev.*, D80:043531, 2009.
34. Earl Lawrence, Katrin Heitmann, Martin White, David Higdon, Christian Wagner, et al. The Coyote Universe III: Simulation Suite and Precision Emulator for the Nonlinear Matter Power Spectrum. *Astrophys.J.*, 713:1322–1331, 2010.
35. F. Saracco, M. Pietroni, N. Tetradis, V. Pettorino, and G. Robbers. Non-linear Matter Spectra in Coupled Quintessence. *Phys. Rev.*, D82:023528, 2010.
36. Francis Bernardeau, Martin Crocce, and Emiliano Sefusatti. Multi-Point Propagators for Non-Gaussian Initial Conditions. *Phys.Rev.*, D82:083507, 2010.

UNIVERSAL NON-GAUSSIAN INITIAL CONDITIONS AND EFFICIENT BISPECTRUM ESTIMATION IN N-BODY SIMULATIONS

M.M. SCHMITTFULL[1], D.M. REGAN[2], and E.P.S. SHELLARD[1]
[1] *Centre for Theoretical Cosmology, DAMTP, University of Cambridge, CB3 0WA, UK*
[2] *Department of Physics and Astronomy, University of Sussex, Brighton, BN1 9QH, UK*

We present an implementation of novel methods to generate general non-Gaussian initial conditions for N-body simulations and estimate the bispectrum of large scale structures. The methods are based on a separable decomposition of the bispectrum, which has been applied successfully to CMB bispectrum analyses, and are significantly faster than previously used techniques, allowing us to examine a wide range of scales. We explicitly demonstrate this by running N-body simulations with Gaussian and non-Gaussian initial conditions of the local, equilateral, orthogonal and flattened type. We measure the full matter bispectrum at different redshifts and disentangle primordial contributions from contributions due to non-linear gravity.

1 Introduction

Inflation predicts that quantum fluctuations in the early universe served as seeds for anisotropies of the cosmic microwave background (CMB) and the formation of the clustered distribution of dark matter. By studying the statistical properties of these observables we can potentially distinguish different models of inflation. Deviations from Gaussian statistics probe particle interactions during inflation. Such primordial non-Gaussianity (PNG) has not yet been detected, but on-going experiments are searching for it with ever higher sensitivity. The best current constraints on PNG come from CMB observations, exploiting the fact that linear cosmological perturbation theory is sufficient to model the observed CMB to great accuracy and astrophysical complications are well under control.

In contrast to the two-dimensional CMB observations, large scale structure (LSS) observations from galaxy surveys provide three-dimensional data, which are expected to improve CMB constraints on PNG if a sufficiently large sample of galaxies is observed. Additionally, PNG is found to modify the bias between dark matter halos and the underlying dark matter distribution in a scale dependent way, which can be exploited to tighten constraints significantly, especially for the squeezed limit of PNG which has the power to rule out all single field inflation models and can probe the mass content of inflationary models.[1,2]

Despite these great prospects, several complications arise in practice. Even for perfectly Gaussian primordial initial conditions, non-linear gravitational collapse generates large late-time non-Gaussianity, which must be modeled accurately to avoid confusion with a primordial signal. Additionally, the time evolution of PNG is influenced by non-linear gravity. Even though both effects can be modeled with perturbation theory (PT), this is only valid on very large scales and N-body simulations or phenomenological descriptions must be used on smaller scales. Here we present an implementation of separable expansion methods[3] which we use to run N-body simulations with general non-Gaussian initial conditions[4] and measure gravitational and primordial contributions to the matter bispectrum in a numerically efficient way. We can only summarise the results here and provide a more complete analysis elsewhere[5].

The primary diagnostic for non-Gaussianity is the three-point correlation function of the fractional density perturbation $\delta \equiv \delta\rho/\langle\rho\rangle$ in Fourier space, the matter bispectrum, which vanishes for perfectly Gaussian statistics and is defined by

$$\langle \delta(\mathbf{k}_1)\delta(\mathbf{k}_2)\delta(\mathbf{k}_3)\rangle = (2\pi)^3 \delta_D\left(\mathbf{k}_1 + \mathbf{k}_2 + \mathbf{k}_3\right) B_\delta(k_1, k_2, k_3), \tag{1}$$

assuming statistical homogeneity and isotropy. The Dirac delta function imposes a triangle constraint on the bispectrum arguments k_1, k_2, k_3. If we impose $k_i \leq k_{\max}$, the space of such triangle configurations is given by a tetrahedron with a cap, which is called a tetrapyd[6]

2 Non-Gaussian Initial Conditions

To study the impact of PNG on the late time matter distribution in N-body simulations, we need to sample the primordial potential Φ from a pdf with given primordial power spectrum P_Φ and bispectrum $f_{\rm NL}B_\Phi$, neglecting higher order correlation functions for simplicity. This can be achieved by generating a Gaussian field Φ_G and evaluating[7,6,8,3,4,9]

$$\Phi(\mathbf{k}) = \Phi_G(\mathbf{k}) + \frac{f_{\rm NL}}{2}\int \frac{d^3\mathbf{k}' d^3\mathbf{k}''}{(2\pi)^6} \frac{(2\pi)^3\delta_D(\mathbf{k}-\mathbf{k}'-\mathbf{k}'')B_\Phi(k,k',k'')\Phi_G(\mathbf{k}')\Phi_G(\mathbf{k}'')}{P_\Phi(k)P_\Phi(k') + P_\Phi(k)P_\Phi(k'') + P_\Phi(k')P_\Phi(k'')}. \tag{2}$$

The high computational cost required to evaluate this expression prohibits generation of initial conditions with arbitrary B_Φ for large N-body simulations. The problem becomes tractable if the integrand in Eq. 2 can be expressed by a sum of separable functions in k, k', k''. While this can be achieved analytically for some CMB bispectrum templates[8,9], we follow a more general approach by expanding the integrand in separable functions[3,4]

$$\frac{B_\Phi(k,k',k'')}{P_\Phi(k)P_\Phi(k') + P_\Phi(k)P_\Phi(k'') + P_\Phi(k')P_\Phi(k'')} = \sum_{rst} \alpha^{\rm IC}_{rst} q_r(k) q_s(k') q_t(k''), \tag{3}$$

where we choose $q_r(k) = k^r$ as basis functions. Substituting this expansion in Eq. 2 allows for an efficient generation of arbitrary non-Gaussian initial conditions if the separable expansion is truncated when the desired accuracy is achieved (after $\mathcal{O}(50)$ terms for our purposes and choice of q_r). We have presented an implementation of this method and a generalisation to trispectra in a separate paper[4], which confirmed unbiasedness and numerical efficiency. To get initial particle displacements and velocities for N-body simulations, a second order extension[10] of the Zeldovich approximation is used. Particles are displaced either from a regular grid or a glass distribution, which is obtained by evolving a random particle distribution with the sign of gravity reversed. While we find an excess bispectrum from the anisotropy of the regular grid at very early times, low redshift results are consistent with glass initial conditions at the few percent level.

3 Bispectrum Estimation

The maximum likelihood estimator for the amplitude $f^{\rm th}_{\rm NL}$ of a theoretical bispectrum $B^{\rm th}_\delta$ is

$$\hat{f}^{\rm th}_{\rm NL} \propto \int \frac{\Pi_{i=1}^3 d^3\mathbf{k}_i}{(2\pi)^9}(2\pi)^3\delta_D(\mathbf{k}_1+\mathbf{k}_2+\mathbf{k}_3)\frac{B^{\rm th}_\delta(k_1,k_2,k_3)[\delta_{\mathbf{k}_1}\delta_{\mathbf{k}_2}\delta_{\mathbf{k}_3} - 3\langle\delta_{\mathbf{k}_1}\delta_{\mathbf{k}_2}\rangle\delta_{\mathbf{k}_3}]}{P_\delta(k_1)P_\delta(k_2)P_\delta(k_3)}, \tag{4}$$

where weak non-Gaussianity and validity of the Edgeworth expansion are assumed. Again, this expression is computationally expensive for general bispectra but not for separable bispectra, whose amplitude can be computed $\mathcal{O}(N^3)$ times faster if $N = \mathcal{O}(1000)$ is the number of grid points per dimension. We can therefore estimate the bispectrum of the data by estimating $f_{\mathrm{NL}}^{\mathrm{th}}$ for a set of independent separable bispectra and then summing up the contributions. In practice, $\mathcal{O}(50)$ independent polynomial bispectra represent the theoretical bispectra examined in this study to good accuracy (with at least 96% integrated shape correlations between theoretical shapes and their expansions for the local, equilateral and orthogonal case). The speedup by a factor of $\mathcal{O}(N^3)$ with respect to the brute force evaluation of Eq. 4 makes the bispectrum estimation an almost negligible operation compared to the computational cost required to run N-body simulations. E.g. we estimated the bispectrum of a 1024^3 grid in less than one hour on 6 cores without aggressive code optimisation. Whenever power spectra of N-body simulations are computed, we can now also estimate the bispectrum, which can be used to quantitatively characterise the three-dimensional distribution of dark matter and study the effects of PNG.

4 Results

We have performed a suite of N-body simulations with Gaussian and non-Gaussian initial conditions of the local ($f_{\mathrm{NL}} = \pm 10, 20, 50$), equilateral ($f_{\mathrm{NL}} = \pm 100$), flattened ($f_{\mathrm{NL}} = 10$) and

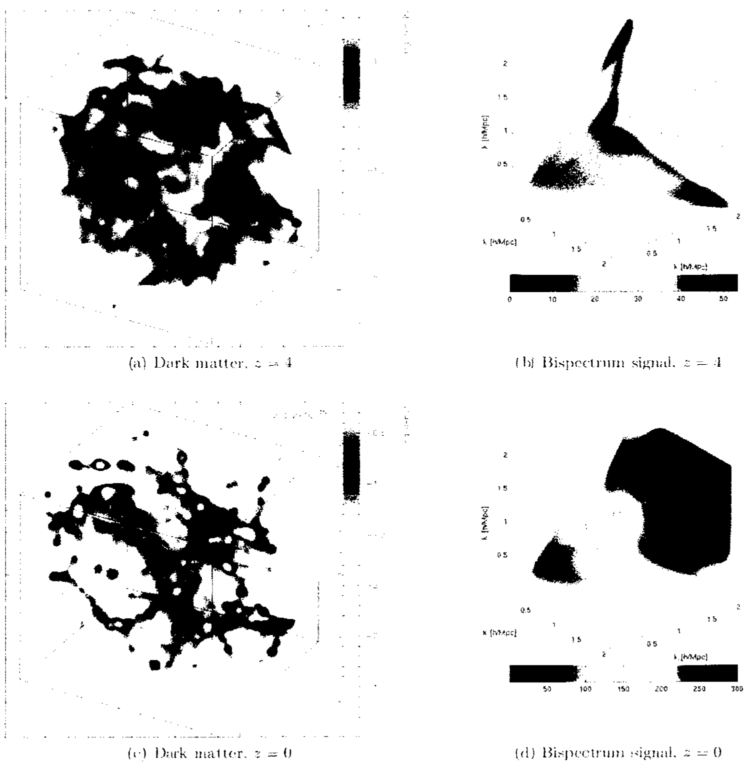

(a) Dark matter, $z = 4$

(b) Bispectrum signal, $z = 4$

(c) Dark matter, $z = 0$

(d) Bispectrum signal, $z = 0$

Figure 1: *Left:* Dark matter distribution in a $(40\mathrm{Mpc}/h)^3$ subbox of a Gaussian N-body simulation with 512^3 particles in a $(400\mathrm{Mpc}/h)^3$ box. *Right:* Estimated bispectrum signal $\sqrt{k_1 k_2 k_3/(P_\delta(k_1)P_\delta(k_2)P_\delta(k_3))}B_\delta(k_1,k_2,k_3)$ of the full simulation drawn on the tetrapyd domain. Axes show $k_1, k_2, k_3 \leq 2h/\mathrm{Mpc}$.

orthogonal ($f_{\rm NL} = \pm 100$) shape in boxes with side lengths between 2400Mpc/h and 100Mpc/h. While our fiducial simulations contain 512^3 particles, our largest simulations use 1024^3 particles. The simulations assume a flat ΛCDM cosmology with WMAP7 parameters and were run with the Gadget-3 code[11].

Fig. 1 shows the dark matter distribution in a simulation with Gaussian initial conditions and the measured bispectrum due to non-linear gravity, drawn in the full tetrapyd volume mentioned above. At early times, $z = 4$, the matter is in large scale clumps and the bispectrum can be described by leading order PT as expected[12]. At late times, $z = 0$, filaments and point-like clusters have formed, corresponding to a bispectrum with an enhanced signal for equilateral triangle configurations and a relatively suppressed signal for squeezed configurations.

We also follow the time evolution of the dark matter bispectrum in simulations with non-Gaussian initial conditions. On large scales and at early times the excess bispectrum compared to Gaussian simulations agrees well with the linearly evolved primordial bispectrum. However leading order PT breaks down at late times on small scales and the excess bispectrum due to non-Gaussian initial conditions receives additional contributions, changing the overall scale dependence as well as the bispectrum shape. A more detailed and quantitative analysis including three-dimensional shape correlations and comparisons of integrated bispectrum sizes will be provided in a separate paper[5]. We also leave it to future work to assess the validity of higher order PT or more phenomenological approaches in the non-linear regime.

5 Conclusions

We have demonstrated that universal non-Gaussian initial conditions for N-body simulations can be generated efficiently with a separable mode decomposition of the bispectrum (and trispectrum). A similar decomposition can be used to extract the bispectrum (and trispectrum) from N-body simulations efficiently and in a model-independent way, allowing us to take all possible triangle configurations into account on a wide range of scales. We have performed a suite of N-body simulations with Gaussian and non-Gaussian initial conditions and extracted gravitational and primordial contributions to the dark matter bispectrum. Future work will consider the distribution of halos, scale-dependent halo-bias for different primordial bispectrum shapes, inclusion of the trispectrum, different cosmologies and possibly analysis of real data.

Acknowledgements and References

We thank James Fergusson for his contributions to the separable expansion methods, its application to the CMB and for important help with modifications for the application to large scale structure. We are grateful to Hiro Funakoshi for his help with setting up initial conditions. We also thank Daniel Baumann, Francis Bernardeau, Anthony Challinor, Helge Gruetjen, Martin Haehnelt, Antony Lewis and Emiliano Sefusatti for discussion and Andrey Kaliazin for computer support. We acknowledge use of the COSMOS@DiRAC supercomputer funded by STFC and BIS. MMS thanks the organisers of the Moriond conference, STFC, DAMTP and St John's College Cambridge for their support.

1. N. Dalal, O. Doré, D. Huterer, and A. Shirokov, PRD **77**, 123514 (2008), 0710.4560
2. E. Sefusatti, J. R. Fergusson, X. Chen, and E. P. S. Shellard, ArXiv e-prints (2012), 1204.6318
3. J. R. Fergusson, D. M. Regan, and E. P. S. Shellard, ArXiv e-prints (2010), 1008.1730
4. D. M. Regan, M. M. Schmittfull, E. P. S. Shellard, and J. R. Fergusson, ArXiv e-prints (2011), 1108.3813
5. M. M. Schmittfull, D. M. Regan, and E. P. S. Shellard, *in prep.*
6. J. R. Fergusson, M. Liguori, and E. P. S. Shellard, PRD **82**, 023502 (2010), 0912.5516
7. K. M. Smith and M. Zaldarriaga, MNRAS **417**, 2-19 (2011), astro-ph/0612571
8. C. Wagner, L. Verde, and L. Boubekeur, JCAP **10**, 22 (2010), 1006.5793
9. R. Scoccimarro, L. Hui, M. Manera, and K. C. Chan, PRD **85**, 8 (2012), 1108.5512
10. M. Crocce, S. Pueblas, and R. Scoccimarro, MNRAS **373**, 369 (2006), astro-ph/0606505
11. V. Springel, MNRAS **364**, 1105 (2005), astro-ph/0505010
12. E. Sefusatti, M. Crocce, and V. Desjacques, MNRAS **406**, 1014 (2010), 1003.0007

MODIFIED NON-LOCAL GRAVITY: EXACT SOLUTIONS AND APPLICATIONS

A.S. KOSHELEV

Theoretische Natuurkunde, Vrije Universiteit Brussel and The International Solvay Institutes, Pleinlaan 2, B-1050, Brussels, Belgium

We consider non-local higher derivative modification of Einstein's gravity and show explicitly that this modification leads to a stable bouncing Universe.

1 Model

The model we examine is motivated by the String Field Theory [1] where one can easily find that all interactions acquire non-local higher derivative form-factors. Those factors appear in the kinetic terms one we do an expansion around a non-trivial vacuum. This is a general feature of String Field Theory and is characteristic to all interactions including higher order vertexes of the gravitational sector coming out of closed string. This motivation led to considering non-local higher derivative theories of scalar fields [2] and was also promoted as a modification of gravity by [3].

The model of interest is described by the following non-local action

$$S=\int d^4x\sqrt{-g}\left(\frac{M_P^2}{2}R+\frac{\lambda}{2}R\mathcal{F}(\Box)R-\Lambda\right) \tag{1}$$

Here the dimensionality is manifest and in the sequel all the formulae are written having 4 dimensions in mind, M_P is the Planckian mass, Λ is a cosmological constant and λ is a dimensionless parameter measuring the effect of the R^2 corrections. The most novel and crucial for our analysis ingredients are the functions of the covariant d'Alembertian $\mathcal{F}$. For simplicity to avoid extra complications we assume that these function are analytic with real coefficients f_n in Taylor series expansion $\mathcal{F}=\sum_{n\geq 0}f_n\Box^n/M_*^{2n}$. The new mass scale determines the characteristic scale of the gravity modification.

Equations of motion for action Eq. 1 can be derived by a straightforward variation and are as follows

$$\begin{gathered}[M_P^2+2\lambda\mathcal{F}_1(\Box)R]G^\mu_\nu=T^\mu_\nu-\Lambda\delta^\mu_\nu-\frac{\lambda}{2}R\mathcal{F}_1(\Box)R\delta^\mu_\nu+2\lambda(\nabla^\mu\partial_\nu-\delta^\mu_\nu\Box)\mathcal{F}_1(\Box)R+\\+\lambda\mathcal{K}^\mu_\nu-\frac{\lambda}{2}\delta^\mu_\nu\left(\mathcal{K}^\sigma_\sigma+\bar{\mathcal{K}}\right)\end{gathered} \tag{2}$$

where we have defined:

$$\mathcal{K}^\mu_\nu=\sum_{n=1}^{\infty}f_{1n}\sum_{l=0}^{n-1}\partial^\mu R^{(l)}\partial_\nu R^{(n-l-1)},\ \bar{\mathcal{K}}=\sum_{n=1}^{\infty}f_{1n}\sum_{l=0}^{n-1}R^{(l)}R^{(n-l)},$$

Here G^μ_ν is the Einstein tensor, $R^{(n)} = \Box^n R$, and T^μ_ν is the matter stress tensor if one is present in the system.

One would benefit considering first the trace equation

$$-M_P^2 R = T - 4\Lambda - 6\lambda\Box\mathcal{F}_1(\Box)R - \lambda(\mathcal{K}_1 + 2\bar{\mathcal{K}}_1) \tag{3}$$

where quantities without indices denote the trace and significant simplifications are obvious.

To find exact solutions we use quite intensively ideas and the knowledge accumulated in [3,4] where this model was considered and some solutions (and their construction) were discussed. To be more specific we are interested only in FRW type solutions and this simplifies the problem considerably.

Clearly those equations have as solutions Minkowski (if $\Lambda = 0$) and de Sitter (if $\Lambda = \text{const} > 0$) backgrounds. The question is however whether we can find other solutions especially focusing on the possible bouncing backgrounds. Equations are definitely highly non-trivial but a decent progress was achieved in [3] by employing the ansatz

$$\Box R = r_1 R + r_2 \tag{4}$$

This makes the system much simpler creating the recursive relation for $\Box^n$ and one can try to find exact solutions.

Note that it is almost enough to solve the trace equation Eq. 3 if we assume no or only traceless matter because for FRW type metrics we have only two independent equations which are moreover constrained by the Bianchi identity. It means that if the trace equation is solved, then all the system Eq. 2 would have the same solution perhaps supported by some amount of radiation.

Known exact solutions to the trace equation Eq. 3 (apart from M_4 and dS_4) include (saying solution we solve for the scale factor $a(t)$)

$$a(t) = a_0 \cosh(\sigma t) \text{ found in } ^3 \tag{5}$$

and

$$a(t) = a_0 \exp\left(\frac{\sigma}{2}t^2\right) \text{ found in } ^4. \tag{6}$$

The first one requires some radiation to be included and the second one is self-sufficient.

There are in fact other interesting solutions which include

$$a(t) = a_0 t, \ a(t) = a_0\sqrt{t}, \ a(t) = \sqrt{\cosh(\sigma t)} \tag{7}$$

2 Applications

Surely found solutions are not some outstanding new universes but rather well known configurations. What is new here is that equations of motion include higher derivative, most likely infinite number of them. Such a modification was proven in [3] to lead to an asymptotically-free gravity. This is why we have arrived to a non-singular bouncing behaviour. The question here is how stable is a background configuration and this is exactly where new structures play an important role. Their implication is crucial and solutions which are unstable or pathological in, say, $f(R)$ gravities become well behaved in this non-local higher-derivative modification. One can get more insight looking in [5] for a detailed analysis of these properties.

It is therefore the main purpose of the introduced gravity modification to smooth the singularities such as initial singularity or the Black Hole singularity. The answer for a possible question why we need infinite higher derivatives is simply because finite higher derivatives will generate extra degrees of freedom while infinite series may not. This is related to the Ostrogradski constraint [6] and mathematical properties of infinite higher derivative operators.

Presence of R^2 terms indicates that we modify gravity in UV and therefore we do not hesitate to include some cosmological constant. We are speaking about short distance or equivalently early times of our Universe. Thus the mentioned Λ is not our present day cosmological constant and it is not our goal to use this modification in application to the present day problems. Resolving puzzles of the present day cosmology does not seem to be easily combined together with the UV modification.

To see whether the obtained configurations are stable or not one has to do the full analysis of inhomogeneous perturbations. This is a very complicated task which was up to some extent accomplished in [5]. The general idea is to classify the perturbation modes according to perturbations of the ansatz. In other words let us denote ζ the perturbation of the ansatz Eq. 4. ζ is not supposed to be zero but it turns out to be a very special set of functions. This simplifies the rest of equations an one can come to a conclusion that all found bouncing solutions are in fact stable during bounce and do not blow up at zero time.

3 Next step

One however can recognize that initial model Eq. 1 is the non-local analogue of $f(R)$ gravity. Using the same logic as in $f(R)$ models we could pass to a new Lagrangian introducing a scalar field ψ and eliminate higher curvature terms.

$$S = \int d^4x\sqrt{-g}\left(\frac{M_P^2}{2}R(1+c\psi) - \frac{1}{2\lambda}\psi\frac{1}{\mathcal{F}(\Box)}\psi - \Lambda\right) \tag{8}$$

For instance, $\mathcal{F}(\Box) = \exp(\Box)$ is a very nice simple example of an invertible operator. Varying over ψ and substituting the solution to the corresponding equation of motion back we restore the initial model for a properly adjusted constant c.

We notice that defining $\mathcal{G}(\Box) \equiv 1/\mathcal{F}(\Box)$ we have arrived for the kinetic term of the scalar field to a form familiar from the p-adic string Lagrangian [1]. Usually p-adic strings have $\mathcal{G} = \exp(\Box)$ while we keep it general. The major difference here is the non-minimal coupling to gravity. Also a usual for p-adic strings potential is missing.

This non-minimal coupling can be eliminated by transforming to the Einstein frame $g_{\mu\nu} \to \bar{g}_{\mu\nu}$. Crucial in this transformation is that the $\Box$ operator from the initial frame can be expressed in the new variables as

$$\Box = F(\psi)\left(\Box_{\bar{g}} - \frac{F'}{F}\partial^\mu\psi\partial_\mu\right) \tag{9}$$

where $F(\psi)$ is the conformal rescaling function. This induces interacting terms for the scalar field ψ and all this vertices are dressed with the momentum-dependent form-factors. Expanding $\mathcal{G}(\Box)$ in the Taylor series we can find the lowest order interactions to be similar to so called galileon fields [7]. More similarities with those theories appear if we do an expansion around a constant stationary point $\psi = \psi_0 + \chi$. Also for the terms to be combined in some specific structures one would need to fix the taylor series coefficients g_n of the function $\mathcal{G}$. This has great importance because one can reverse the problem. As explained in the beginning the model in this note is inspired initially by strings and one can therefore make use of good cosmological properties to improve our knowledge of stringy motivated quantities.

Also as it is known already from the investigation of $f(R)$ models Λ turned out to be a coupling constant in front of a special potential. This would hide explicit Λ in the action.

This connection to non-local scalar-tensor theories is very important first because such theories were intensively studied and second because in our case we most likely to get a very specific and promising class of galileon type models. Developing this directions seems to be the most important continuation in analysis of such non-local higher derivative models.

Acknowledgments

A.K. is the postdoctoral researcher of "FWO-Vlaanderen" and is also supported in part by Belgian Federal Science Policy Office through the Interuniversity Attraction Pole P6/11, and in part by the "FWO-Vlaanderen" through the project G.0114.10N, and the RFBR grant 11-01-00894.

References

1. I. Ya. Aref'eva, D.M. Belov, A.A. Giryavets, A.S. Koshelev, P.B. Medvedev, hep-th/0111208.
2. A. S. Koshelev and S. Yu. Vernov, *Class. Quant. Grav.* **28**, 085019 (2011) [arXiv:1009.0746 [hep-th]].
3. T. Biswas, A. Mazumdar and W. Siegel, *JCAP* **0603**, 009 (2006) [hep-th/0508194].
4. A. S. Koshelev and S. Yu. Vernov, arXiv:1202.1289 [hep-th].
5. T. Biswas, A. S. Koshelev, A. Mazumdar and S. Y. .Vernov, arXiv:1206.6374 [astro-ph.CO].
6. M. Ostrogradski, *Mem. Ac. St. Petersburg* **VI 4**, 385 (1850).
7. C. de Rham, arXiv:1204.5492 [astro-ph.CO].

Effective field theory for perturbations in dark energy and modified gravity

Jonathan A. Pearson
Jodrell Bank Centre for Astrophysics, School of Physics and Astronomy,
The University of Manchester, M13 9PL

When recent observational evidence and the GR+FRW+CDM model are combined we obtain the result that the Universe is accelerating, where the acceleration is due to some not-yet-understood "dark sector". There has been a considerable number of theoretical models constructed in an attempt to provide an "understanding" of the dark sector: dark energy and modified gravity theories. The proliferation of modified gravity and dark energy models has brought to light the need to construct a "generic" way to parameterize the dark sector. We will discuss our new way of approaching this problem. We write down an effective action for linearized perturbations to the gravitational field equations for a given field content; crucially, our formalism does not require a Lagrangian to be presented for calculations to be performed and observational predictions to be extracted. Our approach is inspired by that taken in particle physics, where the most general modifications to the standard model are written down for a given field content that is compatible with some assumed symmetry (which we take to be isotropy of the background spatial sections).

1 Introduction

The standard cosmological model uses General Relativity (GR) as the gravitational theory, an FRW metric as the background geometry and a matter content of photons, baryons and cold dark matter. When this cosmological model is confronted with observational data of the Universe, a huge inconsistency arises: the observed acceleration[1] of the Universe is completely incompatible with the standard cosmological model. The standard "fix" for this is to include some mysterious substance into the matter content of the Universe, dark energy. One of the other "fixes" is to change the underlying gravitational theory for the Universe: perhaps GR is not the appropriate gravitational theory we should be applying on cosmological scales. Whether it is a modification to the gravitational theory or the addition of some dark energy, it is becoming clear that some as-yet unknown *dark sector* must be introduced into the cosmological model. In the literature there are a plethora of modified gravity and dark energy theories whose aim it is to provide some description for the dark sector: Λ, quintessence, k-essence, galileon, Horndeski, TeVeS, æther, $F(R)$, Gauss-Bonnet, Brans-Dicke are all such examples, to name but a few. The interested reader is directed to the extensive review[2].

All modified gravity and dark energy theories have gravitational field equations which can be written as

$$G_{\mu\nu} = 8\pi G T_{\mu\nu} + U_{\mu\nu} \tag{1}$$

where $G_{\mu\nu}$ is the Einstein curvature tensor and contains the metric and its derivatives, $T_{\mu\nu}$ is the energy-momentum tensor for the known matter species in the Universe: it contains information about the content of the known sector. The final term, $U_{\mu\nu}$, is the *dark energy-momentum tensor*, and parameterizes everything in the field equations that represents a deviation from the General Relativity + standard model particles picture. Equation (1) can be split up using perturbation theory: the unperturbed term provides an equation governing the time evolution of the scale factor, where the energy density and pressure of the dark sector fluid are given by $\rho_{\rm dark} = U^0{}_0, P_{\rm dark} = \frac{1}{3}U^i{}_i$. To linearized perturbations, the equation contains information governing the evolution of structures in the Universe,

$$\delta G^{\mu\nu} = 8\pi G \delta T^{\mu\nu} + \delta U^{\mu\nu}. \tag{2}$$

The quantity $\delta U^{\mu\nu}$ is the *perturbed dark energy momentum tensor* and parameterizes the deviation of the gravitational theory from GR at perturbed order. The salient question is, therefore, "*how do we write down the consistent and physically meaningful deviations from GR?*" How do we construct the allowed set of $\delta U^{\mu\nu}$? This has been studied by a number of authors, see e.g. [3].

Of course, known theories will provide prescriptions for what the $\delta U^{\mu\nu}$ could be. However, we would like a tractable approach which does not require a theory to be presented at all. Our approach [4] is to construct a Lagrangian for the perturbations, and use that to construct the perturbed dark energy-momentum tensor. The advantage of using a Lagrangian is that all the usual field theoretic techniques can be employed, and all freedom in the theory can be traced back to some interaction term in the Lagrangian. This is the same approach taken in particle physics. For example: the most general modifications to the standard model potential are written down under a very small number of assumptions (usually just a field content and some symmetries), all "new" mass and interaction terms are identified and then experiments are devised to constrain the values of these new terms.

We are able to identify the maximum number of free functions under a very general set of theoretical priors we impose on the theory (such as the field content). The number of free functions decreases as soon as extra theoretical priors are imposed (such as symmetries of the background spacetime).

2 The Lagrangian for perturbations: formalism

We will consider a dark sector which is constructed from some set of field variables $\{X^{(\mathrm{A})}\}$; this includes the metric, vector and scalar fields. In perturbation theory each of the field variables is written as a perturbation about some homogeneous background value: $X^{(\mathrm{A})} = \bar{X}^{(\mathrm{A})} + \delta X^{(\mathrm{A})}$. We will construct the Lagrangian for perturbations from *Lagrangian* perturbed field variables, denoted by $\delta_{\mathrm{L}} X^{(\mathrm{A})}$, and these are given in terms of the *Eulerian* perturbation of the field variable, $\delta_{\mathrm{E}} X^{(\mathrm{A})}$, via the Lie derivative of the field variable along some diffeomorphism generating vector field, ξ^μ, according to

$$\delta_{\mathrm{L}} X^{(\mathrm{A})} = \delta_{\mathrm{E}} X^{(\mathrm{A})} + \pounds_\xi X^{(\mathrm{A})}. \tag{3}$$

We must be provided with information as to whether the field variables $X^{(\mathrm{A})}$ are scalars, vectors, tensors etc, so that we can incorporate the correct combinations of the ξ^μ-field in the Lagrangian. For example, one can compute the relationship between the Eulerian and Lagrangian perturbations to the metric: $\delta_{\mathrm{L}} g_{\mu\nu} = \delta_{\mathrm{E}} g_{\mu\nu} + 2\nabla_{(\mu}\xi_{\nu)}$.

The Lagrangian which will give linearized field equations in the perturbed field variables is a quadratic functional of the Lagrangian perturbed field variables. The Lagrangian for perturbations, $\mathcal{L}_{\{2\}}$, is equivalent to the second measure-weighted variation of the action:

$$\delta^2 S = \int \mathrm{d}^4x\sqrt{-g}\left\{\frac{1}{\sqrt{-g}}\delta^2(\sqrt{-g}\mathcal{L})\right\} = \int \mathrm{d}^4x\sqrt{-g}\,\mathcal{L}_{\{2\}}. \tag{4}$$

The Lagrangian for perturbations will contribute towards the gravitational field equations via a perturbed energy momentum tensor, which is a linear functional in the Lagrangian perturbed field variables, $\delta_{\mathrm{L}} U^{\mu\nu} = \delta_{\mathrm{L}} U^{\mu\nu}[\delta_{\mathrm{L}} X^{(\mathrm{A})}]$, and is computed via

$$\delta_{\mathrm{L}} U^{\mu\nu} = -\frac{1}{2}\left[4\frac{\hat{\delta}}{\hat{\delta}\delta_{\mathrm{L}} g_{\mu\nu}}\mathcal{L}_{\{2\}} + U^{\mu\nu} g^{\alpha\beta}\delta_{\mathrm{L}} g_{\alpha\beta}\right]. \tag{5}$$

The perturbed dark energy momentum tensor also satisfies the perturbed conservation equation, $\delta(\nabla_\mu U^{\mu\nu}) = 0$. The perturbations relevant for cosmology are the Eulerian perturbations (because they are performed around the FRW background geometry).

3 Examples

We will now provide two examples. To begin, the simplest possible example, where the dark sector does not contain anything extra: only the metric is present. Hence, we are considering a dark sector theory with field content given by

$$\mathcal{L} = \mathcal{L}(g_{\mu\nu}). \tag{6}$$

The Lagrangian for perturbations is given by the quadratic functional

$$\mathcal{L}_{\{2\}} = \frac{1}{8}\mathcal{W}^{\mu\nu\alpha\beta}\delta_{\mathrm{L}}g_{\mu\nu}\delta_{\mathrm{L}}g_{\alpha\beta}. \tag{7}$$

We had to introduce one rank-4 tensor, $\mathcal{W}$, which is only a function of background field variables (for an FRW background, $\mathcal{W}$ is specified in terms of 5 time dependent functions). The perturbed dark energy momentum tensor is given by

$$\delta_{\mathrm{L}}U^{\mu\nu} = -\frac{1}{2}\left\{\mathcal{W}^{\mu\nu\alpha\beta} + U^{\mu\nu}g^{\alpha\beta}\right\}\delta_{\mathrm{L}}g_{\alpha\beta}. \tag{8}$$

This encompasses elastic dark energy and massive gravity models in GR, such as the Fierz-Pauli theory. As a second example, we consider a dark sector containing the metric, a scalar field ϕ and its first derivative

$$\mathcal{L} = \mathcal{L}(g_{\mu\nu}, \phi, \nabla_\mu\phi). \tag{9}$$

In this case, the Lagrangian for perturbations is given by the quadratic functional

$$\begin{aligned}\mathcal{L}_{\{2\}} &= \mathcal{A}(\delta\phi)^2 + \mathcal{B}^\mu\delta\phi\nabla_\mu\delta\phi + \frac{1}{2}\mathcal{C}^{\mu\nu}\nabla_\mu\delta\phi\nabla_\nu\delta\phi \\ &\quad + \frac{1}{4}\left[\mathcal{Y}^{\alpha\mu\nu}\nabla_\alpha\delta\phi\delta_{\mathrm{L}}g_{\mu\nu} + \mathcal{V}^{\mu\nu}\delta\phi\delta_{\mathrm{L}}g_{\mu\nu} + \frac{1}{2}\mathcal{W}^{\mu\nu\alpha\beta}\delta_{\mathrm{L}}g_{\mu\nu}\delta_{\mathrm{L}}g_{\alpha\beta}\right].\end{aligned} \tag{10}$$

We had to introduce 6 tensors, each of which is only a function of background field variables. These tensors describe the interactions of the field content in the Lagrangian. The perturbed dark energy momentum tensor is given by

$$\delta_{\mathrm{L}}U^{\mu\nu} = -\frac{1}{2}\left\{\mathcal{V}^{\mu\nu}\delta\phi + \mathcal{Y}^{\alpha\mu\nu}\nabla_\alpha\delta\phi\right\} - \frac{1}{2}\left\{\mathcal{W}^{\alpha\beta\mu\nu} + g^{\alpha\beta}U^{\mu\nu}\right\}\delta_{\mathrm{L}}g_{\alpha\beta}. \tag{11}$$

This model is similar to that studied in [5]. This encompasses quintessence, k-essence, and Lorentz violating theories. Notice that the generalized gravitational field equations at perturbed order will be entirely specified once the components of the three tensors $\mathcal{V}, \mathcal{Y}, \mathcal{W}$ are specified. If we do not impose any symmetries or theoretical structure upon the theory, then there are 74 free functions in these three tensors. As soon as we impose spatial isotropy of the background one finds that there are 10 free functions, and imposing the theoretical structure: $\mathcal{L} = \mathcal{L}(\phi, \mathcal{X})$ where $\mathcal{X} \equiv -\frac{1}{2}g^{\mu\nu}\nabla_\mu\phi\nabla_\nu\phi$ is the kinetic scalar, there are only 3 free functions. These three functions can conceivably be confronted with experimental data to constrain the possible values that they can take.

4 Cosmological perturbations and entropy

If we impose isotropy upon the spatial sections of the background we are able to split the background tensors which appear in $\mathcal{L}_{\{2\}}$ using an isotropic (3+1) decomposition using a time-like unit vector u^μ and a 3D metric $\gamma_{\mu\nu}$. This means that all tensors are immediately compatible with an FRW background, the relevant equations considerably simplify and the number of free functions dramatically decreases (each free function is now only a function of time).

The Eulerian perturbed dark energy-momentum tensor can be written as a fluid decomposition

$$\delta_{\mathrm{E}}U^{\mu}{}_{\nu} = (\delta\rho + \delta P)u^{\mu}u_{\nu} + \delta P\delta^{\mu}{}_{\nu} + (\rho + P)(v^{\mu}u_{\nu} + u^{\mu}v_{\nu}) + P\Pi^{\mu}{}_{\nu}, \tag{12}$$

where ρ, P are the density and pressure of the dark sector fluid and $\Pi^{\mu}{}_{\nu}$ is the anisotropic sources (u^{μ} is the time-like unit vector and v^{μ} is a space-like vector). The entropy perturbation $w\Gamma \equiv (\delta P/\delta\rho - \mathrm{d}P/\mathrm{d}\rho)\delta$, can also be identified. The perturbed conservation equations provide evolution equations for δ, v but not $\delta P, \Pi$; thus, once $\delta P, \Pi$ are provided by some means, the system of equations becomes closed and can be solved. Our formalism enables us to obtain general forms of Γ, Π. For a scalar field theory of the type $\mathcal{L} = \mathcal{L}(\phi, \mathcal{X})$, where $\mathcal{X} \equiv -\frac{1}{2}g^{\mu\nu}\nabla_{\mu}\phi\nabla_{\nu}\phi$ is the kinetic term of the scalar field (and can be thought of as a theoretical prior on how the metric and derivative of the scalar field combine in the theory) one finds that $\Pi = 0$ identically and the entropy perturbation can be written in terms of *two free functions of time*:

$$w\Gamma = (\alpha - w)\Big[\delta - 3\mathcal{H}\beta(1 + w)\theta\Big]. \tag{13}$$

This (α, β)-parameterization of the entropy perturbation (13) is more general than that given in[6], who had $\beta = 1$. For a general kinetic scalar field theory, one finds

$$\alpha = \left(1 + 2\mathcal{X}\frac{\mathcal{L}_{,\mathcal{X}\mathcal{X}}}{\mathcal{L}_{,\mathcal{X}}}\right)^{-1}, \qquad \beta = \frac{2a\mathcal{L}_{,\phi}}{3\mathcal{H}\mathcal{L}_{,\mathcal{X}}\sqrt{2\mathcal{X}}}\left[1 + \mathcal{X}\left(\frac{\mathcal{L}_{,\mathcal{X}\mathcal{X}}}{\mathcal{L}_{,\mathcal{X}}} - \frac{\mathcal{L}_{,\mathcal{X}\phi}}{\mathcal{L}_{,\phi}}\right)\right]\frac{\alpha}{\alpha - w}. \tag{14}$$

In quintessence models, $\mathcal{L} = \mathcal{X} - V(\phi)$, one finds that $(\alpha, \beta) = (1, 1)$ and in pure k-essence models, $\mathcal{L} = \mathcal{L}(\mathcal{X})$, one finds that $(\alpha, \beta) = (\alpha, 0)$.

5 Discussion

In this paper we have merely given a flavour of our formalism[4] and how we use it to construct the generalized perturbed gravitational field equations. The formalism provides a systematic way to isolate all the freedom within wide classes of models, and to obtain an understanding how this freedom translates into cosmologically observable quantities (such as the CMB, matter power and lensing spectra). At this stage, the most useful result of our formalism is given by equation (13).

In future work we will show how our formalism can be extended for use with theories with high derivatives (relevant for theories containing curvature tensors or galileons). We will also show what the observational signatures of our generalized theories are, where we will use current datasets to provide constraints on the free parameters.

This work was done in collaboration with R.A. Battye, and we acknowledge stimulating conversations with T. Baker, P. Ferreira, A. Lewis and R. Bean.

References

1. A.G. Riess et al *arXiv/9805201*, S. Permutter et al *arXiv/9812133*
2. T. Clifton et al *arXiv/1106.2476*
3. W. Hu and I. Sawicki *arXiv/0708.1190*, C. Skordis *arXiv/0806.1238*, T. Baker et al *arXiv/1107.0491*, J. Zuntz et al *arXiv/1110.3830*, T. Baker *arXiv/1111.3947*
4. R.A. Battye and J.A. Pearson *arXiv/1203.0398*
5. P. Creminelli et al *arXiv/0811.0827*
6. J. Weller and A. Lewis *arXiv/0307104*

Quantum and Classical Fluctuations in the Inflationary Universe — Laboratory quantum mechanics and cosmic density fluctuations —

Masahiro MORIKAWA
Department of Physics, Theoretical Physics, 1 Keble Road, Oxford OX1 3NP, England

We explore the faithful application of quantum mechanics on the origin of density fluctuations in the early Universe. This attempt turns out to be very similar to the analysis of the EPR measurement based on the physical model of measurement apparatus. Therefore we study both the processes in a consistent formalism. The amplitude of the primordial density fluctuations drastically depends on the inflaton potential and the reheating interaction models.

1 Introduction

Quantitative description of the Universe has greatly progressed in recent years due to the development of variety in observational methods including the precise measurement of the cosmic microwave background. Primordial density fluctuation spectrum is especially important to describe the detail dynamics of the early Universe. The very origin of this density fluctuation is considered to be the quantum squeezed state in the inflationary era. Actually many cosmology textbooks[1] [2] describe this derivation and the calculated power spectrum of the density fluctuation basically agrees with observations.

However, as many authors often claim[3], the standard naïve derivation of the density fluctuation is not valid; it confuses the quantum average and the statistical correlation. It is true that the de Sitter expansion yields strong squeezing of the scalar field mode $v_k \approx k^{-1/2}\left(1 + ik^{-1}He^{Ht}\right)$, but we cannot directly identify the quantum correlation $\left\langle \hat{\phi}(x)\,\hat{\phi}(y)\right\rangle\Big|_k$ as the classical fluctuation spectrum $|\delta\varphi(k)|^2 \to P(k)$, based on the principle of quantum mechanics. We have no idea how the mode becomes classical at the horizon crossing. This standard method never derive spatially inhomogeneous structures from the symmetric quantum fluctuations. Popular arguments of the decoherence or simple stochastic methods are still incomplete to derive spatial structures.

Therefore we shall reconsider this problem in a fundamental point of view. For this purpose we need to construct a physical description of the full dynamics of a set of the quantum system and the classical measurement apparatus in general. This method[4] is based on the generalized Schwinger-Keldysh effective action theory and describes dynamics of spontaneous symmetry breaking and statistical fluctuations.

2 Quantum measurement

It is important to notice that the origin of the above cosmic problem is common with that in laboratory. Usually, we cannot physically describe the dynamics of the measurement apparatus although it is definitely an objective device governed by quantum mechanics. The problem stems from the dualism in quantum theory; 'Schrödinger equation' + 'projection axiom'. The first part of the measurement process which establishes the entanglement between the system ($|\uparrow\rangle, |\downarrow\rangle, ...$) and the apparatus ($|A_0\rangle, ...$), $(\alpha|\uparrow\rangle + \beta|\downarrow\rangle)|A_0\rangle \Rightarrow \alpha|\uparrow\rangle|A_\uparrow\rangle + \beta|\downarrow\rangle|A_\downarrow\rangle$ is described by the former. On the other hand the second part to choose either the combination $|\uparrow\rangle|A_\uparrow\rangle$ or another combination $|\downarrow\rangle|A_\downarrow\rangle$ (and not both) is described by the latter.

Many world theory is not useful because it is exactly equivalent to the standard quantum mechanics. Decoherence theory is not sufficient because it does not select a single combination.

In order to apply quantum mechanics in the Universe, we need a fully physical description for quantum measurement process without relying upon the projection axiom. If this becomes possible, then the dualism in the theory disappears and quantum mechanics becomes an objective theory both in laboratory and in the Universe.

We propose that the quantum measurement is associated with a spontaneous symmetry breaking (SSB) process. The order parameter corresponds to the meter degrees of freedom in the apparatus. This SSB process is described by the generalized closed time path effective action (GCEA) method[5]; the effective action $\Gamma[\varphi]$ in GCEA yields a probabilistic differential equation for the order parameter or the mean classical field $\varphi(x)$.

The key observation is the similarity of the action and the entropy. The entropy is given by $S_{entropy} = -k_B \mathrm{Tr}(\rho \ln \rho)$ and the system tends to maximize it. The action is given by $S_{action} = -i\hbar \ln \Psi$ and the system tends to minimize it. Putting the latter expression into the former, we obtain the relation between the entropy and the action:

$$S_{entropy} \approx (k_B/\hbar)\, \mathrm{Im}\left[\sum \left(S_{action} - S_{action}^{*(time-reverse)}\right)\right] \approx (k_B/\hbar)\, \mathrm{Im}\tilde{\Gamma}. \tag{1}$$

Here appears the closed time path effective action $\tilde{\Gamma}$ naturally. This relation suggests that the imaginary part of the effective action should represent statistical properties of the system. The real part of it should describe the dynamics of the system as usual. The formalism of GCEA actually realizes these suggestions. The imaginary part of $\tilde{\Gamma}$ is familiar in Physics and generally arises from the environment of finite temperature or density, instability of the system, negative mass squared (Tachyon), time dependent background space-time, and so on. On the other hand, we can apply the least action principle for the real part of $\tilde{\Gamma}$. Then we obtain the probabilistic differential equation

$$(\Box + m^2)\varphi = -V' + \int_{-\infty}^{t} dt' \int dx' A(x-x')\varphi(x') + \xi, \tag{2}$$

for the classical order parameter $\varphi(x)$, where $\xi(x)$ represents the classical stochastic force whose property is fully described by $\mathrm{Im}\tilde{\Gamma}$.

Now we introduce a simplest model of quantum measurement, in which a scalar field ϕ measures a spin $\vec{S}$, through the SSB of ϕ. The Lagrangian of the whole system is

$$L = \frac{1}{2}(\partial_\mu \phi)^2 - \frac{m^2}{2}\phi^2 - \frac{\lambda}{4!}\phi^4 + \mu\phi\vec{S}\cdot\vec{B} + (\text{bath}), \tag{3}$$

where $\mu > 0$. From the method of GCEA, the equation for the order parameter is given in the over-damped limit as

$$\dot{\varphi} = \gamma\varphi - \frac{\lambda}{3!}\varphi^3 + \mu\left\langle\vec{S}\right\rangle\cdot\vec{B} + \xi, \quad \langle\xi(t)\xi(t')\rangle = \varepsilon\delta(t-t'), \tag{4}$$

where the stochastic force $\xi(x)$ triggers SSB. On the other hand, the equation for the spin density matrix in the environment becomes

$$\dot{\rho}(t) = -i\omega_0[\hat{S}_3, \rho(t)] + \left(a\left[\hat{S}_+\rho(t), \hat{S}_-\right] + b\left[\hat{S}_-\rho(t), \hat{S}_+\right] + c\left[\hat{S}_3\rho(t), \hat{S}_3\right] + h.c.\right), \tag{5}$$

where a, b and c are coefficients which depend on the order parameter $\varphi(x)$. If initially $\left\langle\vec{S}\right\rangle \cdot \vec{B} > 0$, then this linear bias forces φ to roll down toward the minimum position $\varphi_+ > 0$. From $a = \exp\left[-\hbar\mu\varphi(t) B/(kT)\right] b$, the effective temperature $T/\varphi(t)$ reduces and the spin approaches toward the pure up state (parallel to $\vec{B}$). This makes the original linear bias much stronger. This positive feedback establishes the firm correlation in spin and the order parameter. This model predicts an important time scale that is necessary for the completion of the measurement: $t_0 = \frac{1}{2\gamma}\ln\left[\frac{-\lambda}{\gamma}\left(\frac{\varepsilon}{\gamma}+\delta^2\right)\right]^{-1}$ where $\delta = (\mu/\gamma)\left\langle\vec{S}\right\rangle \cdot \vec{B}$.

3 EPR measurement in laboratory

The above formalism of quantum measurement can be applicable to the EPR spin measurement[6] by local apparatus ϕ_1, ϕ_2 with magnetic fields $\vec{B}_1, \vec{B}_2$. These two measurement apparatuses perform independent local measurements in spatially-separated locations.

The GCEA method yields the probabilistic differential equations for the order parameters for each detector:

$$\dot{\varphi}_1 = \gamma\varphi_1 - \frac{\lambda}{3!}\varphi_1^3 + \mu\mathrm{Tr}\left[\rho\vec{S}_1 \cdot \vec{B}_1\right] + \vec{\xi}_1 \cdot \vec{B}_1,\ \dot{\varphi}_2 = \gamma\varphi_2 - \frac{\lambda}{3!}\varphi_2^3 + \mu\mathrm{Tr}\left[\rho\vec{S}_2 \cdot \vec{B}_2\right] + \vec{\xi}_2 \cdot \vec{B}_2, \tag{6}$$

where the imaginary part of the effective action yields the statistical correlation for the classical stochastic forces: $\langle\xi_{1i}\xi_{2j}\rangle = Tr\left(\rho(t)\, S_i^{(1)} S_j^{(2)}\right)$. If the initial state is the most entangle state $|\psi\rangle = \frac{1}{\sqrt{2}}\left(|\uparrow\rangle_1 \otimes |\downarrow\rangle_2 - |\downarrow\rangle_1 \otimes |\uparrow\rangle_2\right)$, then we have the complete anti-correlation: $\langle\xi_{1i}\xi_{2j}\rangle = -\delta_{ij}$. For the system state $\rho(t) \equiv \rho_1 \otimes \rho_2$, the same equation (5) holds. This set of equations (5, 6) determines the full quantum mechanical time evolution including the measurement process as previously. It is possible to derive the violation of the Bell-inequality in this formalism[7]. Thus the present formalism does not belong to the category of hidden variable theories.

4 Density fluctuations in the early Universe

Generation process of the primordial density fluctuations is very similar to the above EPR measurement. In the inflationary model, a scalar field, called inflaton, is introduced to yield exponential cosmic expansion: $a(t) \propto e^{Ht}$, with H is almost constant. In this space-time, the scalar field fundamental mode $\nu_k(t)$ obeys $v_k'' + \left(k^2 - 2H^2e^{2Ht}\right)v_k = 0$. This solves as $v_k \approx k^{-1/2}\left(1 + ik^{-1}He^{Ht}\right)$, which represents a strongly squeezed state.

In the standard cosmology scenario, one simply adopts the identification: $\underbrace{\left\langle\hat{\phi}(x)\,\hat{\phi}(y)\right\rangle\Big|_k}_{quantum} = \underbrace{|\delta\varphi(k)|^2}_{cvlassical}$ assuming that the fluctuation modes become classical when they cross the horizon. Then, the power spectrum is given by $P_{\delta\varphi} = 4\pi k^3(2\pi)^{-3}|v_k/a|^2 \underset{k/(aH)\to 0}{\longrightarrow} (H/(2\pi))^2$, which becomes a scale invariant spectrum. The scale invariance stems from the fact that all the modes evolve analogously in de Sitter space.

Actually the above squeezed state is in the quantum state. Physical measuring process or its equivalent is necessary for the classical fluctuation pattern. The most probable process for this would be the nonlinear interaction at the reheating era just after the inflation. In the simple $\lambda\phi^4$ case, the mean field in k-mode φ_k reacts as order parameter of the measuring apparatus.

The effective action

$$\tilde{\Gamma} = \tilde{\Gamma}_0 + \int \lambda\bar{\varphi}_0^2\delta\bar{\varphi}(k)\left\langle\tilde{\phi}(x)\,\tilde{\phi}(y)\right\rangle\lambda\bar{\varphi}_0^2\bar{\varphi}(-k)\,dk \tag{7}$$

has a real kernel

$$Re\langle\phi(\vec{z})\phi(0)\rangle=\int_0^\infty dk\frac{\sin[kz]}{4\pi^2 z}\left[\left(\frac{\eta'^3-\eta^3}{3\eta'\eta}\right)+O\left(k^3\right)\right], \tag{8}$$

and an imaginary kernel

$$Im\langle\phi(\vec{z})\phi(0)\rangle=\int_0^\infty dk\frac{\sin[kz]}{4\pi^2 z}\left[\begin{array}{l}\frac{-1}{\eta'\eta k^2}-\frac{1}{2}\left(\frac{\eta}{\eta'}+\frac{\eta'}{\eta}\right)\\+O\left(k^2\right)\end{array}\right], \tag{9}$$

where $\eta\equiv-1/(aH)$. The real kernel is infrared finite and yields finite renormalization contribution disregarding the ultraviolet manipulation. On the other hand, the imaginary kernel that yields statistical correlation is infrared divergent. This does not affect the physical evolution of the order parameter since the stochastic force is always finite at each moment.

Applying the least action principle on $Re\bar{\Gamma}$, we have

$$\ddot{\varphi}(x)+V'(\varphi(x))+\int_{-\infty}^{t_x}dyG_{\text{ret}}(x-y)\varphi(y)=\xi(x), \tag{10}$$

where the real part of the effective action yields the infrared-finite renormalization. The stochastic force $\xi(x)$ has the correlation $\langle\xi(x)\xi(y)\rangle=G_C(x-y)\lambda^2\varphi_0(x)^2\varphi_0(y)^2$ derived from the imaginary part of the effective action. Since the most relevant part of the above equation becomes $\ddot{\varphi}_k\approx\xi_k$, we have

$$P_{\delta\varphi}=\frac{4\pi k^3}{(2\pi)^3}|\varphi_k|^2\underset{k/(aH)=1}{\longrightarrow}\lambda^2(\Delta t\,\varphi_0)^4\left(\frac{H}{2\pi}\right)^2, \tag{11}$$

where Δt is the time scale of the reheating and φ_0 is the typical amplitude of the order parameter.

In the present $\lambda\phi^4$ case at the reheating phase, $\Delta t\approx\varphi_0/\dot{\varphi}_0$, and $V(\varphi_0)\approx0$ yield

$$P_{\delta\varphi}=O(1)\left(\frac{H}{2\pi}\right)^2, \tag{12}$$

which is almost the same as the standard result. In this case. the large amplitude of the order parameter φ_0 exactly cancels the small time scale Δt (rapid process) to yield the factor of order one in front of the scale free power spectrum. On the other hand for example in the chaotic model, small field $\varphi_0\approx0$ at reheating may yield very small fluctuations. Although the scale free property of the power spectrum is robust, the amplitude generally depends on the interaction at reheating.

5 Conclusions

We developed a theory of quantum-classical transition in the inflationary Universe. This is directly important to calculate the correct amplitude of the primordial density fluctuations. This problem is common with the EPR measurement in laboratory. In both cases the role of the measurement apparatus is very important to obtain a statistical description of the system.

Acknowledgments

This work was supported by KAKENHI, Grant-in-Aid for Scientific Research (C23540291).

1. T. Padmanabhan, *Structure Formation in the Universe*, Cambridge University Press (1993).
2. S. Weinberg, *Cosmology*, Oxford University Press (2008).
3. G. Leon et al, arXiv:1107.3054v1 (2011).
4. M. Morikawa and A. Nakamichi, Prog. Theor. Phys. **116**, 679 (2006).
5. M. Morikawa, Prog. Theor. Phys. **93,** 685 (1995).
6. A. Einstein, B. Podolsky, and N. Rosen, Phys. Rev. **47** 777 (1935).
7. M. Morikawa, in preparation (2012).

5.
Lensing

PROSPECTS FOR WEAK LENSING STUDIES WITH NEW RADIO TELESCOPES

MICHAEL L. BROWN
Jodrell Bank Centre for Astrophysics, School of Physics & Astronomy, University of Manchester, Oxford Road, Manchester M13 9PL

I consider the prospects for performing weak lensing studies with the new generation of radio telescopes that are coming online now and in the future. I include a description of a proposed technique to use polarization observations in radio weak lensing analyses which could prove extremely useful for removing a contaminating signal from intrinsic alignments. Ultimately, the Square Kilometre Array promises to be an exceptional instrument for performing weak lensing studies due to the high resolution, large area surveys which it will perform. In the nearer term, the e-MERLIN instrument in the UK offers the high sensitivity and sub-arcsec resolution required to prove weak lensing techniques in the radio band. I describe the SuperCLASS survey -- a recently accepted e-MERLIN legacy programme which will perform a pioneering radio weak lensing analysis of a supercluster of galaxies.

1 Weak lensing in the radio band

Weak gravitational lensing is the coherent distortion in the images of faint background galaxies due to gravitational light deflection caused by intervening (dark) matter distributions. On the very largest scales, the effect traces the large scale structure of the Universe and is known as cosmic shear. The vast majority of weak lensing surveys to date have been conducted in the optical bands since large numbers of background galaxies are required in order to measure the small ($\sim$ a few %) distortions. However, a new generation of powerful radio facilities is now imminent which makes weak lensing in the radio band a viable alternative.

The only significant measurement of cosmic shear in the radio band to date is the work of Chang et al. (2004) who made a statistical detection in the Very Large Array (VLA) FIRST survey. Recently a further attempt to measure radio weak lensing has been applied to data from the VLA and old MERLIN telescopes (Patel et al. 2010). This latter work did not detect a significant lensing signal precisely because of the small number density of galaxies typically found in radio surveys. However, it was able to assess the feasibility of doing so and also proposed that systematic effects could be removed by observing the same patch of the sky in the radio and optical wavebands. The e-MERLIN and LOFAR facilities, along with the Square Kilometre Array (SKA) precursor telescopes, MeerKAT (Karoo Array Telescope) and ASKAP (Australian Square Kilometre Array Pathfinder), will be of sufficient sensitivity to achieve a comparable source galaxy number density to planned optical surveys. Ultimately, all of these facilities will act as pathfinders for the SKA itself which will conduct all-sky surveys with unprecedented sensitivity in the radio band towards the end of this decade.

Performing weak lensing in the radio band is particularly attractive for a number of reasons. For example, one of the main obstacles facing the optical lensing community is an issue of instrumental systematics: an exquisite deconvolution of the telescope point spread function (PSF) is required in order to return unbiased estimates of the galaxy shapes. In contrast to complicated and spatially varying optical PSFs, radio telescopes have highly stable and well understood beam shapes. In addition, a definitive weak lensing survey conducted with the SKA would yield precise redshifts for a large fraction of the source galaxies through the detection of their H1 emission line (e.g. Blake et al. 2007). Uncertainties and biases associated with photometric redshift errors would consequently be greatly reduced with an SKA lensing survey.

In addition to instrumental systematics, weak lensing surveys are also subject to serious astrophysical systematics — *intrinsic galaxy alignments.* Galaxies are expected to exhibit some degree of alignment in their orientations due to the tidal influence of large-scale structure during the galaxy formation process. These intrinsic alignments can mimic a cosmic shear signal and represent one of the biggest challenges for precision cosmology measurements using weak lensing.

With this in mind, a unique advantage offered by measuring lensing in the radio band is the polarization information which is usually measured in addition to the total intensity in radio surveys. Previous authors have exploited the fact that the polarization position angle is unaffected by lensing in order to measure gravitational lensing of distant quasars (Kronberg et al. 1991, 1996; Burns et al. 2004). In a recent paper with R. Battye (Brown & Battye 2011a), I showed how one could extend this idea to measure cosmic shear. The technique relies on there existing a reasonably tight relationship between the orientation of the integrated polarized emission and the intrinsic morphological orientation of the galaxy. The existence of this relationship needs to be established for the high-redshift star-forming galaxies which are expected to dominate the radio sky at the μJy flux sensitivities achievable with forthcoming instruments. However, such a relationship certainly exists in the local universe (Stil et al. 2009) and it is reasonable to assume that it persists to higher redshift. A key difference between the polarization technique and standard techniques for measuring lensing is that the former does not assume that the ensemble average of the intrinsic shapes of galaxies vanishes. It is thus, in principle, able to cleanly discriminate between a lensing signal and a possible contaminating signal due to intrinsic galaxy alignments (Brown & Battye 2011a).

Fig. 1 demonstrates the potential power of this technique in terms of its ability to mitigate intrinsic alignments. The figure shows the bias in the recovered weak lensing power spectra in simulations of a future SKA-like survey in the presence of a contaminating signal from intrinsic alignments. For these simulations, we assumed that the orientation of the polarized emission is an unbiased tracer of the intrinsic structural position angle with a scatter of 5 degs and that we can measure the polarization in 10% of the total galaxy sample.

2 The SuperCLASS survey

e-MERLIN, the UK's next generation radio telescope, has now been commissioned and has recently begun science operations. It consists of seven radio telescopes, spanning 217 km, connected by a new optical fibre network to Jodrell Bank Observatory near Macclesfield in the UK. Of the present (or soon to be available) radio instruments e-MERLIN has a number of advantages for detecting weak lensing in the radio band. Most significant of these is the fact that it has very high resolution (≈ 0.2 arcsec at L-band) making it possible to detect the ellipticity of individual sources since they have similar angular extent to that detected in the optical (Muxlow et al., 2005). The SuperCLuster Assisted Shear Survey (SuperCLASS; P.I. R. Battye) was recently approved as an e-MERLIN legacy project to pursue the objective of performing weak lensing analyses in the radio band. SuperCLASS will survey a 1.75 degs^2 region of sky with 0.2 arcsec at 1.4 GHz to an unprecedented r.m.s. sensitivity level of 4 μJy bm^{-1}. In addition to performing a standard weak lensing analysis, these data will allow us to perform the first demonstration of the polarization lensing techniques described above on real data.

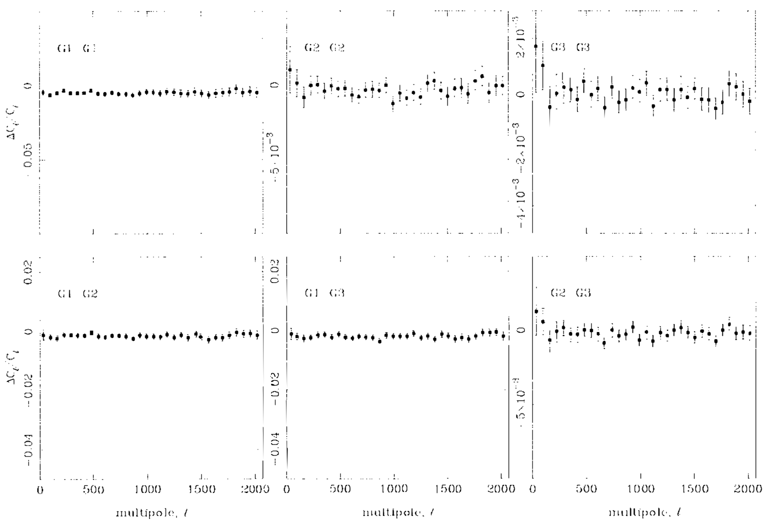

Figure 1: Fractional bias ($\Delta C_\ell/C_\ell$) in the simulated reconstruction of the shear auto- and cross-power spectra in three redshift bins in the presence of a contaminating signal from intrinsic alignments. The top panels show the residuals in the auto-power spectra in the three redshift bins (increasing in redshift from left to right). The bottom panels show the cross-power residuals. The light blue points show the result obtained using a standard lensing analysis and shows a clear bias due to the intrinsic alignment effect. The black points show the recovery obtained with an analysis using polarization information where the bias is reduced by an order of magniutde.

The presently chosen target is a region containing 5 Abell clusters at right ascension $\approx$ 14 hours and declination $\approx$ 68 degs with measured redshifts $\approx$ 0.2. All five clusters (A968, A981, A998, A1005, A1006) have been detected by ROSAT with luminosities compatible with them having masses in the range $(1-2)\times 10^{14}$ $M_\odot$. We expect to be able to detect the weak lensing effect of these clusters and also from some of the large-scale filamentary structure expected to permeate the regions between the clusters.

Fig. 2 shows a simulation of how well we might expect to recover the dark matter distribution in the region of the supercluster. It shows reconstructions of the dark matter distribution in a randomly chosen 1.75 deg^2 region of simulated sky as seen in the N-body simulations of White (2005). The projected mass reconstructions were performed using the algorithms described in Brown & Battye (2011b) which extended standard mass-reconstruction techniques to include potential information coming from polarization observations. The reconstructions are presented for sensitivity levels approximating the SuperCLASS survey and for a sensitivity level approximating what one might expect to achieve with the SKA.

3 Conclusion

I have given a brief summary of the status of the field of weak lensing in the radio band. While it currently lags well behind the field of optical weak lensing, the new radio instruments coming online now make radio weak lensing a viable alternative which is complementary to large scale optical surveys. In particular, radio polarization observations offer interesting possibilities for removing intrinsic alignments from radio lensing surveys. Over the course of the next few years, the SuperCLASS survey on the e-MERLIN telescope will act as a pathfinder experiment for more ambitious radio lensing surveys with future instruments.

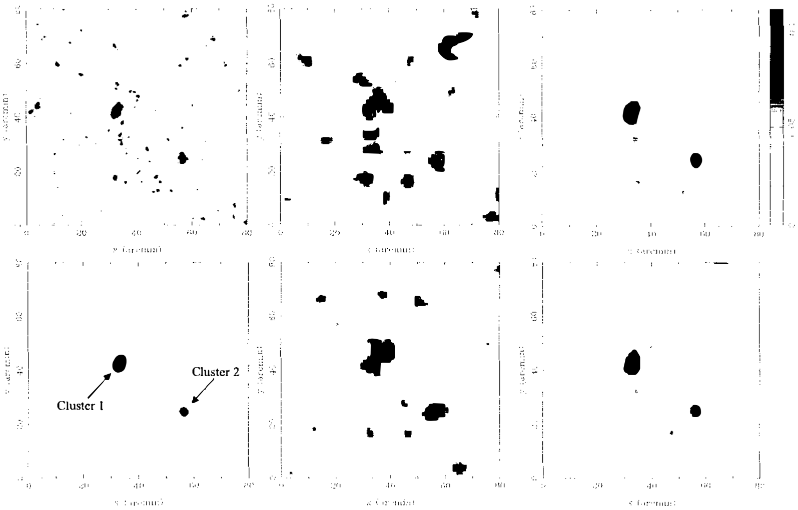

Figure 2: Simulation of the recovery of the dark matter distribution in a randomly selected simulation designed to mimic the SuperCLASS survey and a future SKA survey. The input distribution is shown in the top-left panel and shown smoothed in the bottom left. The middle panels show the recovery for a SuperCLASS-like survey with e-MERLIN and the right hand panels show the simulated recovery for future surveys with the SKA. The top panels show the recoveries obtained using a standard lensing analysis. The bottom panels show the recovery obtained using the polarization technique.

Acknowledgments

I thank the SuperCLASS collaboration, and in particular, the P.I. and my close collaborator Richard Battye, for their contributions to this work. I thank the STFC for an Advanced Fellowship (reference ST/I005129/1) and the ERC for the award of a Starting Independent Researcher Grant (No. 280127).

References

1. C. Blake *et al*, *SKADS Virtual Telescope Proposal* (available at http://www.skads-eu.org/p/svt/svt2007.php)
2. M. L. Brown and R. A. Battye, *MNRAS* **410**, 2057 (2011a)
3. M. L. Brown and R. A. Battye, *ApJL* **735**, 23 (2011b)
4. C. R. Burns *et al*, *ApJ* **613**, 672 (2004)
5. T. Chang *et al*, *ApJ* **617**, 794 (2009)
6. P. P. Kronberg *et al*, *ApJL* **367**, 1 (1991)
7. P. P. Kronberg *et al*, *ApJ* **472**, 115 (1991)
8. T. W. B. Muxlow *et al*, *MNRAS* **358**, 1159 (2005)
9. P. Patel *et al*, *MNRAS* **401**, 2572 (2010)
10. J. M. Stil *et al*, *ApJ* **693**, 1392 (2009)
11. M. White, *Astropart. Phys.* **23**, 349 (2005)

H-ATLAS: Strong gravitational lensing in the sub-mm universe

J. González-Nuevo
Instituto de Física de Cantabria, CSIC-Universidad de Cantabria, Avda. de los Castros s/n, 39005 Santander, Spain
SISSA, Via Bonomea 265, I-34136 Trieste, Italy

A. Lapi
Dipartimento di Fisica, Università di Roma 'Tor Vergata', Via Ricerca Scientifica 1, 00133 Roma, Italy
SISSA, Via Bonomea 265, I-34136 Trieste, Italy

Sub-millimeter surveys were predicted, and demonstrated, to be an especially effective route to efficiently detect strongly lensed galaxies at high redshift. We describe HALOS (the *Herschel*-ATLAS Lensed Objects Selection), a method for efficiently selecting candidate strongly lensed galaxies. HALOS will allow the selection of up to $\sim$ 1000 candidate strongly lensed galaxies (with amplifications $\mu \geq 2$) over the full H-ATLAS survey area. The counts of candidate strongly lensed galaxies are also in good agreement with model predictions. Due to the new era of large samples of galaxy-galaxy lenses, Lapi et al.(2012) proposed simple analytic solutions, assuming that the combination of dark matter and star distribution can be very well described by a simple power-law, allowing an easy insight into the role of the different ingredients that determine the lens cross section and the distribution of gravitational amplifications. They also ease the reconstruction of the lens mass distribution from the observed images and, vice-versa, allow a fast application of ray-tracing techniques to model the effect of lensing on a variety of source structures.

1 Introduction

The discovery rate of strong galaxy-galaxy lens systems has increased dramatically in recent years mostly thanks to spectroscopic lens searches and, most recently, to surveys of sub-millimeter galaxies. Spectroscopic searches, such as the Sloan Lens Advanced Camera for Surveys (SLACS) survey or the BOSS (Baryon Oscillation Spectroscopic Survey) Emission-Line Lens Survey (BELLS) or the optimal line-of-sight (OLS) lens survey or the Sloan WFC (Wide Field Camera) Edge-on Late-type Lens Survey (SWELLS), rely on the detection of multiple background emission lines in the residual spectra found after subtracting best-fit galaxy templates to the foreground-galaxy spectrum.

Sub-millimeter surveys were predicted,[1] and demonstrated,[2] to be an especially effective route to efficiently detect strongly lensed galaxies at high redshift because the extreme steepness of number counts of unlensed high-z galaxies implies a strong magnification bias so that they are easily exceeded by those of strongly lensed galaxies at the bright end. Also, gravitational lensing effects are more pronounced for more distant sources. But high-z galaxies are frequently in a dust-enshrouded active star formation phase and therefore are more easily detected at far-IR/sub-mm wavelengths, while they are very optically faint.

Samples of strongly lensed galaxies are further enriched by the, to some extent complementary, imaging surveys which look for arc-like features, and by radio surveys. All that holds the promise of a fast increase of the number of known strongly lensed sources, fostered by the forthcoming large area optical and radio (Square Kilometre Array; SKA) surveys. Therefore, simple, efficient, analytical tools applicable to the analysis of large samples of galaxy-galaxy lenses are therefore warranted.

2 The formation of Early Type Galaxies (ETG)

The 100 and 250 m LFs at different redshifts are quite well reproduced by the physical model of ETG formation and evolution by Granato et al.,[3] and the recently revised by Lapi et al.,[4] without any adjustment of the parameters. As discussed in these papers, the model is built in the framework of the standard hierarchical clustering scenario. Many simulations have shown that the growth of a halo occurs in two different phases: a first regime of fast accretion in which the potential well is built up by the sudden mergers of many clumps with comparable masses; and a second regime of slow accretion in which mass is added in the outskirts of the halo, only occasionally affecting the central region where the galactic structure resides. According to the model, the fast accretion phase triggers a burst of star formation that, in massive halos at $z \geq 1$, starts an evolutionary sequence that can be summarized as follows. There is an early, short phase of (almost) dust-free star formation when the galaxy shines as a bright UV source. It is followed by a dust-enshrouded star formation phase when the galaxy shines in the far-IR/submillimeter range. The duration of both the UV bright phase and the far-IR/submillimeter bright phase is shorter for the most massive galaxies, with the highest start formation rates (SFR); for these objects the UV phase lasts 10^7 yr and the far-IR/submillimeter phase lasts $< 10^9$ yr. Then there is a phase, lasting several 10^7 yr, when the nucleus shines as a bright QSO after having swept away most of the interstellar gas and dust. Finally, passive evolution of the stellar populations follows, and the galaxy evolves into a local ETG.

According to Lapi et al.[4] model, star-forming proto-spheroidal galax- ies account for a substantial fraction of the cosmic infrared back- ground and dominate the cosmic SFR at $z > 1.5$, while at lower-z the SFR is dominated by late-type (normal and starburst) galaxies. This model was the basis for the successful predictions of the submillimeter counts of strongly lensed galaxies by Negrello et al.[1] It also accurately reproduced the epoch-dependent galaxy LFs in dif- ferent spectral bands (Fig. 1), as well as a variety of relationships among photometric, dynamical, and chemical properties, as shown in previous papers.

3 Effective Strongly Lensed Galaxy (SLG) selection

Negrello et al.[1] predicted that about 50% of galaxies with 500 μm flux densities above $\simeq 100$ mJy would be strongly lensed, with the remainder easily identifiable as local galaxies or as radio-loud AGNs. This prediction was supported by the mm-wave SPT (South Pole Telescope) counts. But a spectacular confirmation came with the results of the *Herschel* Astrophysical Terahertz Large Area Survey [a] (H-ATLAS [5]) for the Science Demonstration Phase (SDP) field covering about 14.4 deg^2. Five out of the 10 extragalactic sources with $S_{500\mu m} \geq 100$ mJy were found to be strongly lensed high-z galaxies, four are $z < 0.1$ spiral galaxies and one is a flat-spectrum radio quasar [2]. Gonzalez-Nuevo et al.[6] presented a simple method, the Herschel-ATLAS Lensed Objects Selection (HALOS), aimed at identifying fainter strongly lensed galaxies. This method gives the prospect of reaching a surface density of $\sim 2\,\mathrm{deg}^{-2}$ for strongly lensed candidates, i.e., the detection of ~ 1000 high-z strongly lensed galaxies over the full H-ATLAS survey area ($\simeq 550\,\mathrm{deg}^2$).

[a] http://www.h-atlas.org/

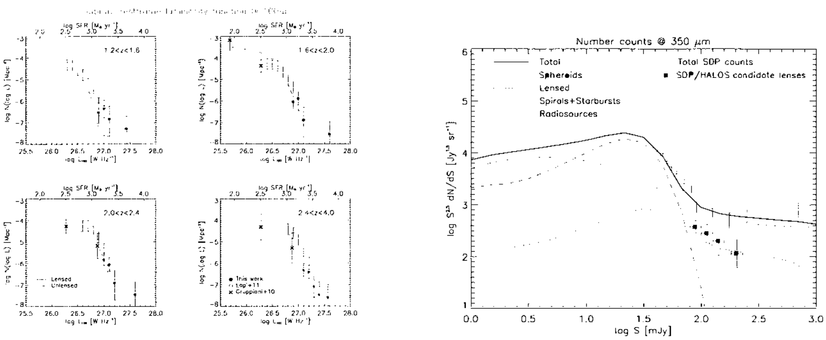

Figure 1: *Left panel*: Contributions of our bright objects (filled circles) to the 100 μm luminosity functions in different redshift intervals. The open circles show, for comparison, the estimates by Lapi et al.[4] The dashed lines, that coincide with the solid lines except at the highest apparent luminosities, show the model for unlensed proto-spheroidal galaxies described in Lapi et al.[4]. The solid lines include the contributions of strongly lensed galaxies (see text). *Right panel*: Euclidean normalized differential number counts, corrected for the flux density dependent purity, at 350μm of the SLG candidates (open red squares) compared with the total counts (filled squared). The purple dotted line shows the predictions from the SISSA model[9] strongly lensed proto-spheroidal galaxies.

3.1 HALOS

The method appeals to the fact that strongly lensed galaxies inevitably dominate the highest apparent luminosity tail of the high-z luminosity function. The first step is therefore to pick up high apparent luminosity and high-z galaxies. The primary selection, based on SPIRE photometry ($S_{350} \geq 85\,\mathrm{mJy}$, $S_{250} \geq 35\,\mathrm{mJy}$, $S_{350}/S_{250} > 0.6$, and $S_{500}/S_{350} > 0.4$), has yielded a sample of 74 objects in the H-ATLAS SDP field of $\simeq 14.4\,\mathrm{deg}^2$. After having rejected intruders of various types we are left with a sample of 64 objects, with estimated redshifts ≥ 1.2. This sample has allowed us to re-assess the brightest portion of the apparent 100 μm luminosity function in the same 4 redshift bins ($1.2 \leq z_{\mathrm{source}} < 1.6$, $1.6 \leq z_{\mathrm{source}} < 2.0$, $2.0 \leq z_{\mathrm{source}} < 2.4$, $2.4 \leq z_{\mathrm{source}} < 4.0$) of Lapi et al.,[4] whose sample was biased against SLGs because of the rejection of all objects with SDSS $R > 0.8$ counterparts, some of which may be the foreground lenses. The new estimate of the luminosity function shows indications of a flattening at the highest apparent luminosities as expected, on the basis of the Lapi et al.,[4] model coupled with the formalism by Perrotta et al.,[7] as the effect of the contribution of SLGs (Fig. 1). This flattening reflects the flatter slope of the sub-L$_*$ luminosity function, and confirms that our approach has the potential of allowing us to investigate more typical high-z star-forming galaxies.

To identify the candidate SLGs we have looked for close associations (within 3.5 arcsec) with VIKING galaxies[8] that may qualify as being the lenses. We found 34 such associations. The optical/near-IR data for 32 of these objects were found to be incompatible (or, in 4 cases, hardly compatible) with them being the identifications of the H-ATLAS objects. Another object has two close VIKING counterparts, one of which may be the identification and the other may be the lens. We kept this object as a candidate SLG. The VIKING data on the counterpart of the last of the 34 objects are insufficient to decide whether it is a likely lens, and we conservatively dropped it.

Again to be conservative we have further restricted the sample of candidate SLGs to objects whose VIKING counterparts have redshifts ≥ 0.2 since this seems to be a lower limit to lens redshifts found in previous surveys, although there is nothing, in principle, that prevents a

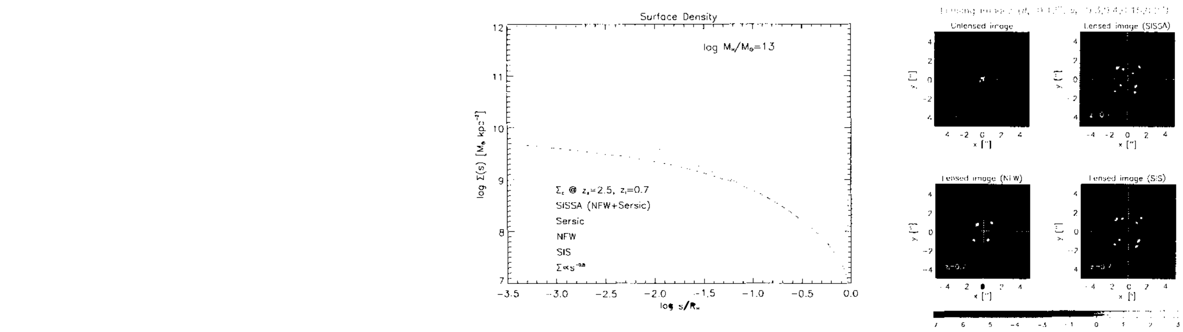

Figure 2: *Left panel*: Surface mass density of an early-type lens. (Blue) dashed line: NFW dark matter profile with $M_{\rm H} = 10^{13}\,M_{\odot}$ and concentration parameter $c = 5$; (cyan) dot-dashed line: Sérsic profile ($n = 4$) of the stellar component in the proportion $M_{\rm H}/M_{\star} = 30$; (red) solid line: SISSA model constituted by the sum of the two contributions; (green) triple-dot-dashed line: classical SIS model for the same DM mass; (magenta) dotted line: power law relation $\Sigma(s) \propto s^{-0.8}$, that provides a good approximation to the SISSA model in the radial range relevant for gravitational lensing (see text for details). The horizontal grey line represents the critical density for lensing for a source redshift $z_s = 2.5$ and a lens redshift $z_\ell = 0.7$. The projected radius s is normalized to the halo virial radius. *Right panel*: Example of a ray-tracing simulation of the gravitational lensing for four bright spots with impact parameters $\theta_b = 0.3, 0.4, 0.15, 0.2''$, respectively, at $z_s = 2.5$, and a lens at $z_\ell = 0.7$.

object at $z < 0.2$ from being a lens. Thus, the 2 objects with VIKING counterparts at $z < 0.2$ should also be taken into account for follow-up observations. In this way, we end up with at least 31 high apparent luminosity and high-z SDP objects, corresponding to a surface density of $\sim 2\,\rm deg^{-2}$, that appear to be physically associated with foreground galaxies that are most likely the lenses.

The number counts of candidate SLGs, corrected for the flux-density dependent purity are in well agreement with model predictions (Fig. 1). The model indicates that the counts of candidate SLGs with $S_{350} > 85$ mJy are mostly contributed by amplifications $\mu \geq 3$.

The estimated redshift distribution of our *candidate lensed galaxies* extends up to $z_{\rm source} \simeq 3.2$ and is similar to those of other searches for strongly lensed sources, like the Cosmic Lens All-Sky Survey (CLASS), the SDSS Quasar Lens Search (SQLS), and the COSMOS survey. On the other hand, our *lenses* are found up to $z_{\rm lens} \simeq 1.6$–1.8 (with a peak at $z_{\rm lens} \simeq 0.8$), while in the case of the other surveys they are confined to $z_{\rm lens} < 1$. We caution however that the redshift estimates are photometric, and need to be confirmed by spectroscopic measurements. If this lens redshift distribution will be validated, our selection will allow us to substantially extend the redshift range over which gravitational lensing can be exploited to study the lens galaxy mass and structure, and their evolution.

4 Revision of the strong lensing theory

In view of the large samples of strongly lensed galaxies that are being/will be provided by large area sub-mm, optical and radio (SKA) surveys Lapi et al.[9] have worked out simple analytical formulae that accurately approximate the relationship between the position of the source with respect to the lens center and the amplification of the images and hence the cross section for lensing. The approximate relationships are based on a lens matter density profile which is a combination of a Sérsic profile describing the distribution of stars with a NFW profile for the dark matter. We find that, for essentially the full range of parameters either observationally determined (for the Sérsic profile) or yielded by numerical simulations (for the NFW profile), the combination can be very well described, for lens radii relevant for lensing, by a simple power law (see Fig 2). Remarkably, the power law slope is very weakly dependent on the parameters characterizing the matter distribution of the lens (the dark matter to stellar mass ratio, the Sérsic index, the concentration of NFW profile). For the most common parameter choices, the slope is slightly sub-isothermal if we consider the projected profile and slightly super-isothermal if we consider the 3-dimensional profile, in good agreement with the results of detailed studies of individual lens galaxies. This very weak dependence of the amplification cross section on the parameters that control the density profiles of stars and DM implies that their variances do not hamper the possibility of exploiting gravitational lensing to probe cosmological parameters. Our approach implies slightly steeper slopes of the total matter density profile for the least massive systems. An indication in this direction has been reported by Barnabé et al.[10]

This simple analytic solutions provide an easy insight into the role of the different ingredients that determine the lens cross section and the distribution of gravitational amplifications. The maximum amplification depends primarily on the source size. Amplifications larger than $\simeq 20$, as found for some sub-mm and optical sources, are indicative of compact source sizes at high-z, in agreement with expectations if most of the stars formed during dissipative collapse of cold gas. Similarly, analytic formulae highlight in a transparent way the role of parameters characterizing the lens mass profile ($M_{\rm H}$, $M_{\rm H}/M_\star$ ratio, concentration of the DM component, Sérsic index of the stellar component), and of the source and lens redshifts. They also allow a fast application of ray-tracing techniques to model the effect of lensing on a variety of source structures (Fig. 2). We have investigated, in particular, the cases of a point-like or of an extended source with a smooth profile, and of a source comprising various emitting clumps (as frequently found for high-z active star-forming galaxies). Our formalism has allowed us to reproduce the counts of strongly lensed galaxies found in the H-ATLAS SDP field.

5 Summary and future

We have presented a simple method, that will be referred to as the *Herschel*-ATLAS Lensed Objects Selection (HALOS), that gives the prospect of identifying roughly 1.5–2 strong SLG candidates per square degree from the H-ATLAS survey, i.e. about 1000 over the full survey area. This amounts to a factor $\simeq 4$–6 increase compared to the surface density of SLGs brighter than $S_{500} = 100\,$mJy, whose selection has proven to be easy. Samples of thousands of strongly lensed systems are needed to make substantial progress on several major astrophysical and cosmological issues. Also, the extension to fainter flux densities is crucial to pick up galaxies representative of the bulk of the star-forming galaxy population at $z_{\rm source} \simeq 1$–3, that without the upthrust of strong lensing are fainter than the SPIRE confusion limit.

Excluding the candidate SLGs from the initial sample, we can constrain the bright end of the luminosity function of unlensed galaxies, which turns out to be extremely steep, as expected if these galaxies are indeed proto-spheroidal galaxies in the process of forming most of their stars in a single gigantic starburst.[3,4] The counts of candidate strongly lensed galaxies are also in good agreement with model predictions.[4,9]

Due to the new era of large samples of galaxy-galaxy lenses, simple, efficient, analytical tools applicable to the analysis of these sample are required. Lapi et al.[9] found that, for essentially the full range of parameters either observationally determined or yielded by numerical simulations, the combination of dark matter and star distribution can be very well described, for lens radii relevant for lensing, by a simple power-law whose slope is very weakly dependent on the parameters characterizing the global matter surface density profile and close to isothermal in agreement with direct estimates for individual lens galaxies. This simple analytic solutions allow an easy insight into the role of the different ingredients that determine the lens cross section and the distribution of gravitational amplifications. They also ease the reconstruction of the lens mass distribution from the observed images and, vice-versa, allow a fast application of ray-tracing techniques to model the effect of lensing on a variety of source structures.

The five brightest sources among the 31 best SLG candidates were already shown to be strongly lensed galaxies through an intense multi-instrument observational campaign.[2] As for the fainter ones, we envisage a follow-up strategy comprising several steps. First we need a spectroscopic confirmation that they are at the high redshifts indicated by our photometric estimates. Millimeter-wave spectroscopy of CO transitions proved to be very effective not only for redshift measurements but also for providing dynamical information and gas masses.[11] A comparison with expectations from the empirical relationship between CO luminosity and line-width for unlensed galaxies [11] provides a first indication for or against the presence of gravitational amplification and, in the positive case, an estimate of its amplitude. Deep high resolution imaging is obviously necessary to establish the lensing nature of the sources by revealing and mapping the lensed images (arcs). This has been done, although for brighter sources, in the optical/near-IR [12] and at (sub)-millimeter wavelengths.[13,14] The latter have the great advantage that the images are little affected by, or totally immune to the effect of the lensing galaxies (which, as mentioned above, are mostly passive, early type galaxies). ALMA overcomes the problem of the limiting sensitivity of earlier (sub)-mm instruments allowing one to make very deep, high resolution images, thus making possible a detailed study of the internal structure and dynamics of the lensed galaxies.

Acknowledgments

The authors acknowledge partial financial support by ASI/INAF Agreement I/072/09/0 for the Planck LFI activity of Phase E2, by INAF through the PRIN 2009 "New light on the early Universe with sub-mm spectroscopy", by MIUR PRIN 2009, and by the Spanish Ministerio de Economía y Competitividad projects AYA2010-21766-C03-01 and CSD2010-00064. JGN thanks the Spanish CSIC for a JAE-DOC fellowship. A.L. thanks SISSA for warm hospitality.

References

1. Negrello, M., Perrotta, F., González-Nuevo, J., et al., *MNRAS* **377**, 1557 (2007).
2. Negrello, M., Hopwood, R., De Zotti, G., et al., *Science* **330**, 800 (2010).
3. Granato, G. L., De Zotti, G., Silva, L., Bressan, A., & Danese, L., *ApJ* **600**, 580 (2004).
4. Lapi, A., González-Nuevo, J., Fan, L., et al., *ApJ* **742**, 24 (2011).
5. Eales, S., Dunne, L., Clements, D., et al., *PASP* **122**, 499 (2010).
6. González-Nuevo, J., Lapi, A., Fleuren, S., et al., *ApJ* **749**, 65 (2012).
7. Perrotta, F., Baccigalupi, C., Bartelmann, M., De Zotti, G., & Granato, G. L., *MNRAS* **329**, 445 (2002).
8. Fleuren, S., Sutherland, W., Dunne, L., et al., *MNRAS submitted* (2012; *eprint arXiv:1202.3891*).
9. Lapi, A., Negrello, M., González-Nuevo, J., et al., *ApJ* accepted , (2012).
10. Barnabè, M., Czoske, O., Koopmans, L. V. E., Treu, T., & Bolton, A. S., *MNRAS* **415**, 2215 (2011).
11. Harris, A. I., Baker, A. J., Frayer, D. T., et al., *ApJ accepted* (2012; *eprint arXiv:1204.4706*).
12. Fu, Hai, Jullo, E., Cooray, A., et al., *ApJ submitted* (2012; *eprint arXiv:1202.1829*).
13. Riechers, D.A., Cooray, A., Omont, A., et al., *ApJ* **733**, L12 (2011).
14. Bussmann, R. S., Dey, A., Armus, L., et al., *ApJ* **744**, 150 (2012).

HOW SENSITIVE IS THE CMB TO A SINGLE LENS?

B. RATHAUS, A. FIALKOV, N. ITZHAKI
Raymond and Beverly Sackler Faculty of Exact Sciences,
School of Physics and Astronomy, Tel-Aviv University,
Ramat-Aviv, 69978, Israel

We study the imprints of a single lens, that breaks statistical isotropy, on the CMB and calculate the signal to noise ratio (S/N) for its detection. We emphasize the role of non-Gaussianities induced by ΛCDM weak lensing in this calculation and show that typically the S/N is much smaller than expected. In particular we find that the hypothesis that a void is responsible for the WMAP cold spot can barely be tested via weak lensing of the CMB.

1 Introduction and Motivation

Within the framework of ΛCDM, which is statistically isotropic, the role of weak lensing (WL) is very well established. Nevertheless, although ΛCDM is an extremely successful paradigm, there still are quite a few large scale anomalies waiting to be resolved. [1,2] These include, among others, the alignment of the low l modes ("the axis of evil"), the anomalously large bulk flow, the WMAP cold-spot, the giant rings and the apparent oddity of space.

It has been suggested that some, if not all of these anomalies may be explained by the existence of a single "giant" structure. Perhaps the most famous example for this, is the WMAP cold-spot [3] which was shown to be a possible consequence of a cosmological void of ~ 1 Gpc radius.[4,5,6] Such a giant structure, however, would break statistical isotropy, and in addition would induce a signature on the CMB by means of WL. We therefore wish to find the S/N for its detection.

1.1 Weak Lensing of the CMB

According to ΛCDM the primordial temperature field is statistically isotropic and very nearly Gaussian, meaning that the temperature fluctuation's mean vanishes, that the entire information about the statistics followed by it is held in the two-point correlation function $C(l)$,

$$\langle T(\mathbf{l}_1)T^*(\mathbf{l}_2)\rangle = (2\pi)^2\delta(\mathbf{l}_1-\mathbf{l}_2)C(l_1), \tag{1}$$

and that the four-point correlation function is purely disconnected $\langle T(\mathbf{l}_1)T^*(\mathbf{l}_2)T(\mathbf{l}_3)T^*(\mathbf{l}_4)\rangle_c = 0$. Next we note that the CMB is further lensed by ΛCDM large scale structure, according to

$$\tilde{T}(\hat{\mathbf{n}}) = T(\hat{\mathbf{n}} + \nabla\psi^\Lambda(\hat{\mathbf{n}})), \tag{2}$$

where $\tilde{T}(\hat{\mathbf{n}}), \psi^\Lambda(\hat{\mathbf{n}})$ are the lensed temperature fluctuation and ΛCDM deflection potential in direction $\hat{\mathbf{n}}$. In ΛCDM ψ^Λ is also statistically isotropic and Gaussian, so

$$\left\langle \psi^\Lambda(\mathbf{l}_1)\psi^{\Lambda *}(\mathbf{l}_2)\right\rangle = (2\pi)^2\delta(\mathbf{l}_1-\mathbf{l}_2)C^\psi(l_1). \tag{3}$$

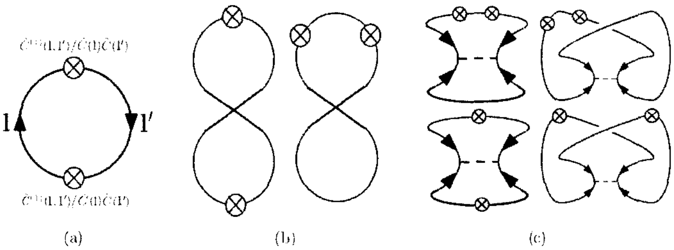

Figure 1: Representation of the S/N as Feynman diagrams. The 1-loop contribution to the S/N is plotted in (a), and the naive 2-loop diagrams in (b). Due to substructure of the 4-leg vertex, though, there are four diagrams which contribute in the 2-loop level, as in (c).

By using properly relations (1), (2), and (3) one finds that the resulting *lensed* temperature field $\tilde{T}$ is also statistically isotropic, but *no longer Gaussian*, a fact that will play a key role in the conclusions below.

2 An Anomalously Large Structure as a Lens

Consider an anomalously large structure (ALS), which is so large that it does not respect statistical isotropy. Due to its gravitational potential, it would modify the ΛCDM deflection potential

$$\psi^{\Lambda} \longrightarrow \psi' = \psi^{\Lambda} + \delta\psi, \tag{4}$$

where $\delta\psi$ is the deflection potential induced by the ALS. Since the ALS does not respect statistical isotropy ($\langle\delta\psi\rangle = \delta\psi$), ψ' has a non-vanishing mean, while its two-point correlation function stays intact

$$\langle\psi\rangle = 0 \longrightarrow \langle\psi'\rangle = \delta\psi \quad ; \quad \langle\psi\psi^*\rangle = C^{\psi} \longrightarrow \langle\psi'\psi'^*\rangle = C^{\psi}. \tag{5}$$

Due to the ALS, not only does $\psi^{\Lambda} \longrightarrow \psi'$, but also

$$\tilde{T}(\hat{\mathbf{n}}) \longrightarrow \tilde{T}'(\hat{\mathbf{n}}) = T(\hat{\mathbf{n}} + \nabla\psi^{\Lambda}(\hat{\mathbf{n}}) + \nabla\delta\psi). \tag{6}$$

By Taylor expanding (6) one concludes that in the case of the lensed temperature field the deformation satisfies

$$\langle\tilde{T}\rangle = 0 \longrightarrow \langle\tilde{T}'\rangle = 0 \quad ; \quad \langle\tilde{T}\tilde{T}^*\rangle = \tilde{C} \longrightarrow \langle\tilde{T}'\tilde{T}'^*\rangle = \tilde{C}' \neq \tilde{C}. \tag{7}$$

Comparison of (5) and (7) emphasizes the fact that even though the two deformations stem from the same ALS, they are essentially different. This difference must be taken into account when evaluating the S/N.

3 Evaluating Signal to Noise Ratios

3.1 Ideal S/N

The form of the S/N associated with the deformation (4) (of the mean value) is dictated by (5). Since we wish to be able to detect the ALS, $\delta\psi$ plays the role of the signal, while the noise is the background field ψ^{Λ}. In ΛCDM however, all we know about ψ^{Λ} is through its correlation function (3). Therefore the S/N we are after is

$$\left(\frac{\mathrm{S}}{\mathrm{N}}\right)^2_{\mathrm{Ideal}} = \int \frac{\mathrm{d}\mathbf{l}}{(2\pi)^2}\frac{|\delta\psi(l)|^2}{C^{\psi}(l)}. \tag{8}$$

We refer to this S/N as "ideal" for two reasons: (1) $\delta\psi$ carries the entire information of the lensing effect, and (2) we took the minimal possible noise. Practically speaking, however, the ideal S/N is not easy to use. ψ is not an observable field, and its reconstruction is noisy. Hence it is convinient as an upper bound on the realistic S/N, given a model.

3.2 Realistic S/N

The most direct observable field of the CMB is the temperature field. Therefore we seek the S/N for the detection of an ALS in terms of the deflected temperature field ("realistic" S/N). Owing to the fact that the deformations of ψ and of $\tilde{T}$ belong to two different types of deformations, the correct way to obtain this S/N is to expand the deformed covariance matrix $\tilde{C}'$ around the original covariance [7] $\tilde{C}$

$$\tilde{C}' = \tilde{C} + \epsilon \tilde{C}^{(1)} + \frac{\epsilon^2}{2}\tilde{C}^{(2)} + \dots \tag{9}$$

This way we find that to second order in the small parameter ϵ the realistic S/N is

$$\left(\frac{\mathrm{S}}{\mathrm{N}}\right)^2_{\mathrm{Real.}} = \int \frac{d\mathbf{l}}{(2\pi)^2}\frac{d\mathbf{l}'}{(2\pi)^2}\frac{|\tilde{C}^{(1)}(\mathbf{l},\mathbf{l}')|^2}{\tilde{C}^2(l)\tilde{C}^2(l')}\tilde{C}(l)\tilde{C}(l'). \tag{10}$$

At this point it is instructive to introduce a novel approach of writing a set for Feynman rules for a field theory of a propagating field $\tilde{T}$ which interacts with a non-dynamical field $\delta\psi$: [7]

- To Each leg assign a 2D momentum, $\mathbf{l}$, and a corresponding propagator $\tilde{C}(l)$.
- Integrate over all undetermined (loop) momenta.
- Represent lensing by the ALS as a vertex and multiply by $\tilde{C}^{(1)}(\mathbf{l},\mathbf{l}')/\tilde{C}(\mathbf{l})\tilde{C}(\mathbf{l}')$, where $\mathbf{l},\mathbf{l}'$ are the momenta that enter the vertex.

With these rules (10) looks like a vaccum energy diagram, as in the left panel of Fig. 1.

4 The Role of non-Gaussianities

Now that we have derived both ideal and realistic S/N, we are supposed to be in a pretty good shape. Given a model of an ALS, we can find an upper bound on the S/N for its detection via WL, and calculate the realistic S/N associated with this ALS. Trying to examine this, we encounter a problem, which is illustrated with the aid of a simple toy model ($\delta\psi(\mathbf{l}) = (2\pi)^2\delta(\mathbf{l}-\mathbf{l}_0)$, where $\mathbf{l}_0$ is some single mode) in Fig. 2. We find that not only does the realistic S/N cross the ideal S/N, it actually diverges, which is inconceivable.

As was already mentioned in the introduction, ΛCDM lensed temperature field is not Gaussian. It having a connected four-point correlation function is easily seen, if we consider, for example,

$$\begin{aligned}
\left\langle \tilde{T}\tilde{T}\tilde{T}\tilde{T} \right\rangle &\rightarrow \langle (T + \nabla\psi\cdot\nabla T)\,(T + \nabla\psi\cdot\nabla T)\,T\;T\rangle \\
&\rightarrow \langle (\nabla\psi\cdot\nabla T)\;(\nabla\psi\cdot\nabla T)\;\;T\;T\rangle \\
&\rightarrow \langle (\nabla\psi\cdot\nabla T)(\nabla\psi\cdot\nabla T)\;T\;T\rangle .
\end{aligned} \tag{11}$$

Therefore the Feynman rules must be supplemented with a 4-leg vertex, and consequently, the vaccum energy diagram must be corrected by higher-loop diagrams (center panel of Fig. 1). Here the calculation is more complicated, since the 4-leg vertex has substructure, which originates from various possible contractions of (11), so more topologically distinct diagrams contribute

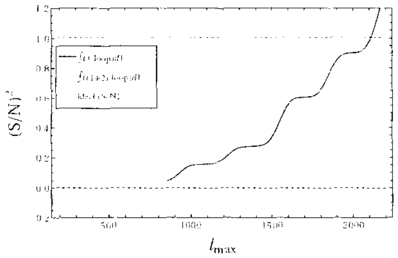

Figure 2: The S/N as a function of the cutoff $l_{\max}$ in the integral (10). The red line is the normalized ideal S/N, the blue line is the 1-loop contribution (10), and the cyan line includes 2-loop corrections (section 4).

to the S/N. There are four different diagrams which contribute to the 2-loop S/N (right panel of Fig 1). The overall leading non-Gaussian contribution to the S/N is *negative*. Therefore, it lowers $(S/N)^2$ (cyan line in Fig. 2), thus resolving the puzzle.

Fig. 2 shows that the leading non-Gaussian contribution becomes significant at $l \sim 900$ and that for $1000 < l_{\max} < 1500$ there is an approximated plateau in the accumulated S/N. The value of $(S/N)^2$ at this plateau is about 1/10 of the ideal $(S/N)^2$. These features are not sensitive to the toy-model's l_0. For $l_{\max} > 1500$ the accumulated S/N starts to drop. This is a nonphysical artifact of the fact that we keep only the first non-Gaussian correction. It should be emphasized that, irrespective of $l_{\max}$, one cannot exceed $\sim \frac{1}{\sqrt{10}} S/N_{\text{Ideal}}$ using the temperature data alone without performing higher loop calculation.

Physical situations, like the cosmic void as a candidate to explain the WMAP cold spot, can be viewed as a superposition of toy models with different l_0's. Therefore we expect them to behave in a similar way, namely

$$\left(\frac{S}{N}\right)_{\text{Real.}} \sim \frac{1}{\sqrt{10}} \left(\frac{S}{N}\right)_{\text{Ideal}} \tag{12}$$

to be a good approximation. Keeping the example of a cosmic void, with a density profile taken to be able to explain the WMAP cold spot, we find that its ideal S/N is ~ 4, and therefore the realistic S/N ~ 1.25, which is barely detectable.

Acknowledgements

We would like to thank A. Ben-David for useful discussions. This work is supported in part by the Israel Science Foundation (grant number 1362/08) and by the European Research Council (grant number 203247).

References

1. C. J. Copi *et al.*, *Adv. Astron.* **2010**, 847541 (2010).
2. C. L. Bennett *et al.*, *Astrophys. J. Suppl.* **192**, 17 (2011).
3. M. Cruz *et al.*, *Mon. Not. Roy. Astron. Soc.* **356**, 29 (2005).
4. M. Cruz *et al.*, [arXiv:0804.2904 [astro-ph]].
5. S. Das, D. N. Spergel *Phys. Rev.* D **D79**, 043007 (2009)
6. I. Masina and A. Notari, *JCAP* **0907**, 035 (2009)
7. B. Rathaus, A. Fialkov and N. Itzhaki *JCAP* **1106**, 033 (2011).

6.
Dark Matter: direct and indirect detection

DARK MATTER SEARCH WITH LIQUID NOBLE GASES

MARC SCHUMANN
Physik Institut, University of Zurich, Winterthurerstrasse 190, 8057 Zurich, Switzerland

Dark matter detectors using the liquid noble gases xenon and argon as WIMP targets have evolved rapidly in the last decade and will continue to play a major role in the field. Due to the possibility to scale these detectors to larger masses relatively easily, noble liquids will likely be the first technology realizing a detector with a ton-scale target mass. In this article, we summarize the basic concepts of liquid noble gas dark matter detectors and review the current experimental status.

1 Introduction

There is plenty of indirect cosmological evidence [1] that the vast majority of the Universe's energy content is dark, with about 25% being in the form of dark matter which builds large scale structures. Another 70% is the mysterious dark energy, responsible for the accelerated expansion of the Universe and only about 5% is "ordinary", baryonic matter which forms stars, planets, and eventually us.

There is no known particle in the Standard Model of Particle Physics which could be the dark matter particle, neutrinos for example are too light and fast, hence the dark matter particle must be from new physics and is yet unknown. One of the most favorite candidates is the weakly interacting massive particle (WIMP) [2], which arises naturally in several extensions of the Standard Model, such as Supersymmetry, Universal Extra Dimensions, and little Higgs models. Many experiments aim at the direct detection of these particles by measuring nuclear recoils of target nuclei after they interact with a WIMP [3]. Sensitive detectors are placed in deep underground laboratories in order to fight backgrounds induced by cosmic rays and their daughter particles. The expected WIMP interaction rate is less than 1 event per kg of target material and year, and the featureless recoil spectrum is exponentially falling with typical energies of tens of keV only.

These experiments use different targets and detection methods, which all have different pros and cons. Liquid noble gases such as xenon and argon, but possibly also neon, have started to play an important role in the field since about a decade and are currently placing the most stringent limits on spin-independent WIMP-nucleon cross-sections over a large range of WIMP masses [4,5]. This article gives a brief review on these detectors.

2 Noble Gases as WIMP Targets

The noble gases neon (Ne), argon (Ar), and xenon (Xe), which in liquid phase are all used or being considered as target materials for WIMP searches, have boiling points between 27.1 K (Ne) and 165.0 K (Xe), see Table 1. This makes operation easier than for cryogenic detectors

Table 1: Selected properties of noble gases being used as WIMP targets. W_{ph} and W are the average energies to create a scintillation photon or an electron-ion pair. Numbers taken from [6].

Element	Xenon	Argon	Neon
Atomic Number Z	54	18	10
Atomic mass A	131.3	40.0	20.2
Boiling Point T_b [K]	165.0	87.3	27.1
Liquid Density @ T_b [g/cm^3]	2.94	1.40	1.21
Fraction in Earth's Atmosphere [ppm]	0.09	9340	18.2
Price	$$$$	$	$$
Scintillator	✓	✓	✓
W_{ph} (α, β) [eV]	17.9 / 21.6	27.1 / 24.4	
Scintillation Wavelength [nm]	178	128	78
Ionizer	✓	✓	–
W (E to generate e-ion pair) [eV]	15.6	23.6	
Experiments [stopped, running, in preparation]	~ 5	~ 5	1/2

which have to be run at mK temperatures. Xe and Ar can be even liquefied using liquid nitrogen. All three elements are excellent scintillators with very high light yields, and liquid xenon (LXe) and liquid argon (LAr) are very good ionizers as well, allowing for a direct measurement of the ionization signal induced by particle interactions. For this reason, mainly LAr and LXe are employed in current and future experiments, while neon is currently only considered as one option for one experiment (see CLEAN in Sect. 4). Hence, we restrict this summary to these two elements.

More material properties are summarized in Table 1. In particular the possibility to build large, monolithic detectors make cryogenic noble liquids interesting for WIMP searches, as it is considered to be somewhat easier to scale these detectors up to the ton scale and beyond. Compared to the expensive Xe, the price of Ar is rather modest. However, while Xe is intrinsically clean from the radioactive point of view (there are no long-live Xe isotopes and contaminations of radioactive the ^{85}Kr can be removed by cryogenic distillation), radioactive ^{39}Ar is present in natural argon at the 1 Bq/kg level. This leads to background and pile-up problems. Finally, the wavelength of the scintillation light is at 178 nm for LXe which is observable with commercially available photocathodes, while LAr based detectors need to employ wavelength shifters (such as TPB) to detect the light. Fig. 1 (left) shows how scintillation light is generated in liquid noble gases.

The expected nuclear recoil energy E_{nr} spectra from spin-independent WIMP-nucleon scattering interactions are featureless exponentials, and the interaction rate is expected to scale with A^2, see Fig. 1 (right). Therefore, the much heavier Xe is preferred. However, since the nucleus is also larger coherence is lost for large momentum transfers, leading to a form factor suppression of the rate at higher E_{nr}. A low detector threshold is therefore more mandatory for LXe. This is not the case for LAr, however, its overall interaction rate is always smaller.

Background Discrimination If they exist, WIMPs are feebly interacting particles and their expected interaction rates are much lower than the omnipresent backgrounds from natural radioactivity and induced by cosmic rays. The latter can be decreased considerably (typically by factors $\sim 10^{-6}$) by placing the experiments in deep underground laboratories, protected by several km of rock overburden. Environmental radioactivity requires additional massive shields in which the detectors, built from selected radiopure materials, are being placed. The most critical background is from neutrons as these interact with the target nuclei and generate nuclear recoils, which makes them indistinguishable from WIMPs if they interact only once. However, neutrons

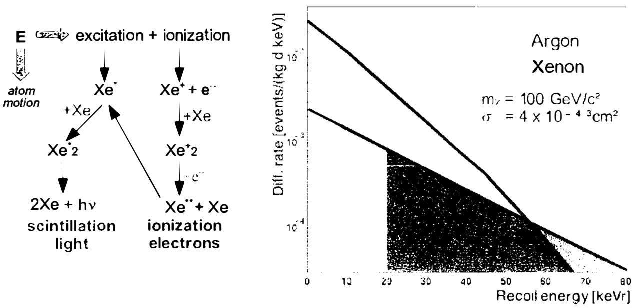

Figure 1: (left) Particle interactions excite and ionize the target (Xe in this example, but Ar works exactly the same way). Excited atoms Xe* combine with a neutral atom and form an excimer state Xe_2^* which decays under the emission of scintillation light. If ionization electrons are not removed from the interaction site (e.g., by an electric field in a TPC), they eventually recombine and also produce scintillation light. Therefore, the light and the charge signal are anti-correlated. (right) Expected nuclear recoil spectra from interactions of a 100 GeV/c^2 WIMP with LXe and LAr, assuming a cross-section of $\sigma = 10^{-43}$ cm^2. The expected rate is higher in LXe at low energies, but form factor suppressed at higher energies, which is not the case for LAr. A low detection threshold is therefore necessary if LXe is used. Experimentally achieved thresholds are indicated by the colored areas.

have a rather large probability to interact several times inside a detector what allows for their rejection if these individual interactions can be resolved. The liquids, in particular LXe, have a rather high stopping power which can be used for self-shielding if only the inner part of the detector is selected for analysis ("fiducialization"). This, however, requires that the interaction vertex can be fairly well reconstructed in 3 dimensions.

The most abundant background for almost all dark matter experiments is from gamma and beta backgrounds which generate electronic recoils. These have a different energy loss $\mathrm{d}E/\mathrm{d}x$ compared to nuclear recoils leading to detectable differences in their signals which can be used for signal/background discrimination. The first possibility for noble liquids is the pulse shape of the scintillation signal. The excimers (see Fig. 1) eventually emitting the light can be formed in singlet and triplet states which have different decay times. The individual population of the states depends on the particle interaction. In LAr, the lifetimes are about 3 order of magnitude different, with 0.005 μs and 1.6 μs for the singlet and triplet state, respectively, leading to a large slow component of the pulse for events from electronic recoil interactions. It has been demonstrated that this feature can be used to reject electronic recoils at the 3×10^{-8} level [7]. However, such high levels are mandatory in order to cope with the huge background from ^{39}Ar. With 4 ns and 22 ns, the singlet and triplet lifetimes are very similar in LXe and only very moderate rejection levels ($\sim$ 0.1) can be achieved [8], hence it is not used as default in any experiment.

If the charge and the light signal generated in an interaction are measured simultaneously for every event, one can exploit that the different $\mathrm{d}E/\mathrm{d}x$ for electronic recoil backgrounds and nuclear recoils signals produce a different charge/light ratio. The discrimination depends on the deposited energy and on the electric field strength applied to extract the charge signal. In LXe, it ranges between values of 5×10^{-3} and 1×10^{-4} at 50% nuclear recoil acceptance [9]. It is also used in LAr, however, its performance is much weaker than the pulse shape discrimination channel and would by itself not be sufficient to reduce the ^{39}Ar background to the required low levels.

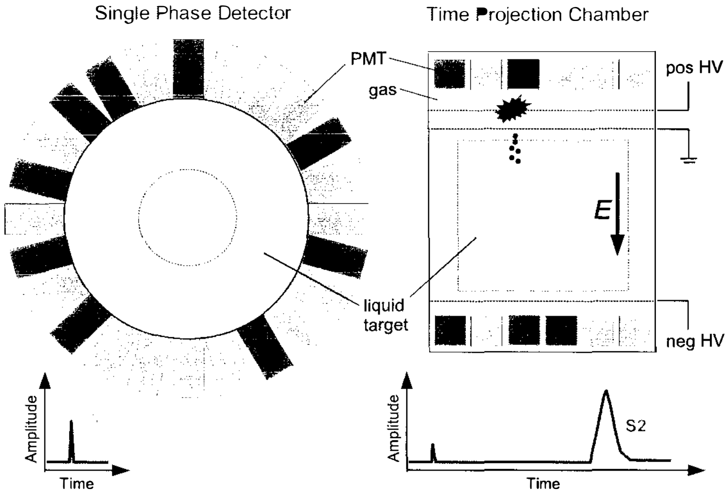

Figure 2: The two detector concepts currently used for dark matter detectors based on liquid noble gases. (Left) Single phase detectors are essentially a large volume of a noble liquid which is viewed by many photosensors, usually PMTs, in order to detect the scintillation light S1. (Right) In a double phase detector the S1 signal is also detected by photosensors, but the ionization charge signal is measured as well since the detector is operated as a time projection chamber (TPC). An electric field across the target volume removes the ionization electrons from the interaction site and drifts them towards the gas phase on top of the liquid. The electrons are extracted into the gas and generate proportional scintillation light S2, which is registered time-delayed by the drift time.

3 Detector Concepts

Detectors using liquid noble gases as WIMP targets are currently operated by using two different concepts, which are illustrated in Fig. 2 and are explained below.

Single Phase Detectors These detectors are conceptually very simple devices in which a large volume of a liquid noble gas is viewed by as many light sensors (usually PMTs) as possible in order to reduce the detection threshold, see Fig. 2 (left). Since only rather short scintillation light signals have to be detected, it also allows for rather high event rates since pile-up is almost no issue. The chosen geometry is usually spherical in order to exploit self shielding as much as possible. The 4π arrangement of the PMTs can be used for some rough event vertex reconstruction, with a resolution of typically several cm. The reconstruction performance, however, depends on the number of detected photons and deteriorates close to threshold. Since only the light is detected, background discrimination via the charge/light ratio is not possible. Hence experiments have to rely on pulse shape discrimination or, in case of LXe, on almost perfect background reduction by shielding. For this reasons, most experiments will only use the innermost part of the detector as WIMP target and the outer part (which can be almost up to 90% of the mass) as background shield.

Double Phase Detectors, Time Projection Chambers Time projection chambers (TPCs), see Fig. 2 (right), provide much better 3-dimensional vertex reconstruction, with demonstrated z-resolutions below 1 mm and a xy-resolution of ~ 3 mm [4]. This is achieved by measuring the scintillation light and the ionization charge signal simultaneously. A particle interaction leads to scintillation and liberates ionization electrons which are removed from the interaction site by a strong electric field E ("drift field", typically around 1 kV/cm). The electrons drift towards the top of the cylindrical detector, where they are extracted into the gas phase above the liquid and generate a secondary light signal which is proportional to the charge [10]. The lightpattern on the top PMT array is used to derive the xy-position and the time difference between light (S1) and charge (S2) signal to determine z. The excellent vertex detection capabilities allow for powerful background rejection via fiducialization and multi-scatter identification, accompanied by charge/light discrimination (plus pulse shape discrimination for LAr detectors). On the other hand, the optical coverage with photosensors is usually considerably smaller compared to single phase detectors, which might lead to an increased threshold. Additionally, one has to deal with the technical challenges related to the necessary high voltage system.

4 Current Experiments using Noble Liquids

In this section, we give a brief overview on most experimental efforts which currently employ liquid noble gases as WIMP targets or which will use them in the near future. We have collected this information to the best of our knowledge (using the experiment's presentations given recently [11]), it represents the status of May 2012. For space reasons, some projects have been omitted.

Experimentally achieved WIMP exclusion limits (at 90% CL) are shown as solid lines in Fig. 3 for spin-independent WIMP-nucleon scattering interactions. Projected sensitivities are indicated by dashed lines. The most stringent limit to date comes from the XENON100 experiment [4] excluding cross sections above 7.0×10^{-45} cm^2 for $m_\chi = 50$ GeV/c^2. Below $\sim$ 10 GeV/c^2, the best limit is from XENON10 [5].

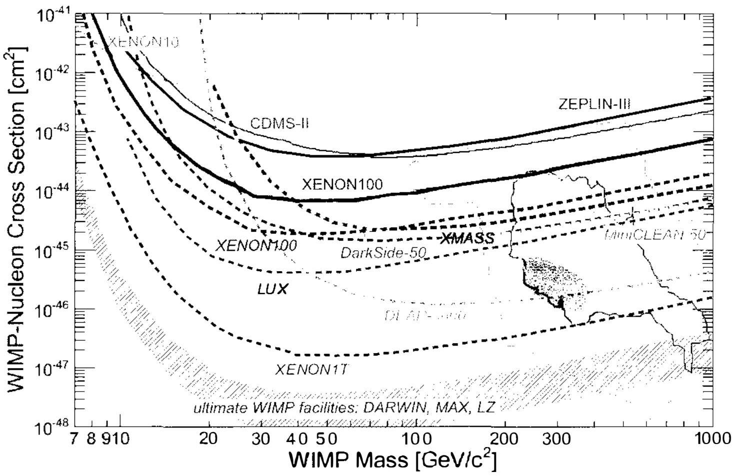

Figure 3: Achieved 90% exclusion limits (solid lines) and projected sensitivities (dashed) of various dark matter projects using liquid noble gases (with the exception of CDMS-II). Shown is the spin-independent WIMP-nucleon scattering cross section vs. the WIMP mass. Not all existing or planned experiments are shown, and most of the current experimental constraints are omitted. The closed areas indicate theoretically preferred SUSY regions [12].

ZEPLIN-III was a 12 kg double-phase LXe TPC out of which 5.1 kg were used as WIMP target. The experiment was installed in Boulby mine, UK. The extremely flat TPC geometry allowed for a very high drift field of 3-4 kV/cm and therefore a charge/light background rejection of $\sim 1 \times 10^{-4}$. In the last science run from 2010-2011 [13], 8 events were observed in the predefined WIMP search region which was compatible with the background expectation and therefore led to an exclusion limit. With this result, the long history of ZEPLIN experiments has come to an end.

XENON100 and XENON1T The current stage of the phased XENON program is XENON-100, a double-phase LXe TPC with a total mass of 161 kg, located at Laboratori Nazionali del Gran Sasso (LNGS), Italy. 62 kg are inside the TPC and the remaining xenon surrounding the target in 4π is used as active veto. In the last science run [4] of 100.9 days$\times$48 kg raw exposure, three events were observed, fully compatible with the expected background of (1.8 ± 0.6) events. A limit was placed which is currently setting the most stringent constraints for $m_\chi > 10$ GeV/c^2. The results of a new dataset with about twice the exposure, a lower background, and a lower trigger threshold will be published soon.

The collaboration is already working on the next phase, XENON1T, which aims to explore cross sections down to 2×10^{-47} cm^2 by 2017, after two years of data taking with a TPC of 1 ton LXe fiducial mass. XENON1T will be also installed at LNGS, inside a water shield of ~ 10 m diameter which is operated as Cerenkov muon veto and will suppress ambient gamma radiation and neutrons.

XMASS is a Japan-based single phase LXe detector, which aims for sensitivities around 2×10^{-45} cm for $m_\chi = 100$ GeV/c^2 [14]. It employs a total of 800 kg LXe and uses about 100 kg as WIMP target. Since end of 2010 it is installed and running in Kamioka mine. A very high light yield has been achieved due to the large coverage with photosensors ($\sim 60\%$). A first year of science data has been already collected, however, the collaboration has recently announced some issues with unexpected radioactive background from the PMTs [15]. XMASS is currently working to reduce the background.

LUX is a double-phase LXe TPC which will be installed at the Sanford Underground Research Facility (SURF, USA). The detector employs a total of 350 kg of LXe and aims for a 100 kg fiducial mass for the WIMP search [16]. It is currently operated above ground to have a fully working detector once the underground space is ready for occupation. It has already demonstrated a rather high light yield and underground science is expected to start end of 2012 aiming at 300 days of data taking.

DarkSide is a double-phase TPC which will use LAr as WIMP target [17]. The goal for the next years is to build and operate DarkSide-50 with about 50 kg target mass. It will be located at LNGS (Italy), inside the the Borexino counting test facility (CTF), a large water tank which is currently being refurbished for this purpose. Inside the water shield, DarkSide will be surrounded by a spherical boron-loaded liquid scintillator neutron veto and it will use Ar which is depleted in ^{39}Ar by a factor ~ 100. Commissioning is scheduled for end of 2012, and two years of data taking is necessary to reach the final sensitivity around 10^{-45} cm^2.

ArDM is a double-phase LAr detector [18] which has been installed and commissioned at CERN and is currently being moved underground to the Canfranc laboratory (Spain). It employs a large target mass of 850 kg of LAr in a TPC of 120 cm height and 80 cm diameter. The collaboration is developing novel ways to deal with the technical challenges of multi-ton LAr/LXe detectors. The high voltage to bias the TPC, e.g., is generated next to the field cage in a Greinacher circuit and ArDM's final goal is to detect the charge signal with sub-mm precision in large micro-machined charge amplification detectors (large electron multipliers, LEMs).

DEAP-3600 and MiniCLEAN is a large single phase detector using 3.6 tons of LAr, with about 1000 kg being used as WIMP target [19]. The LAr will be contained inside an acrylic vessel installed in a cryostat which itself is inside a water shield. Construction of the experiment is ongoing at SNOLab (Canada) and the first filling is expected around the end of 2013. The science goal is to reach the 10^{-46} cm^2 level after 3 years of operation. The large light collection in the single phase setup will allow for a very good rejection of electronic recoil background via pulse shape discrimination.

The "twin"-experiment MiniCLEAN [20] is being installed right next to DEAP-3600. With 150 kg LAr fiducial mass (500 kg total) it is considerably smaller, however, the experiment is being designed such that it can also be operated with liquid neon (LNe). Initially, this has been proposed in order to detect low energy neutrinos from the Sun and from supernovae [21]. However, if a signal is being seen in LAr it can be very useful to cross check this finding using the same detector (and the same systematics) with another target nucleus. MiniCLEAN is expected to run from end of 2012 to 2014.

Ultimate WIMP Facilities Even though experimental results with ton-scale detectors have not been realized yet, several collaborations have already started to study the ultimate WIMP facilities which will explore the parameter space around $\sigma_\chi = 10^{-48}$ cm^2, where neutrinos will be an homogeneously distributed irreducible background. The existing proposals DARWIN [22], MAX [23], and LZ [24] are all double phase TPCs. At the current stage, all these projects are just design and R&D studies for multi-ton LXe and LAr detectors, which will likely not being built before 2020.

5 Summary and Outlook

Many experiments aim to directly detect WIMP dark matter by searching for nuclear recoils from elastic WIMP collisions inside very sensitive detectors with ultra-low backgrounds. A large number of projects employs the noble gases xenon or argon, cooled down and liquefied in order to obtain high-density targets. We have detailed why these elements are excellent WIMP targets and have explained the most common detector concepts. These are either single phase detectors measuring the scintillation light signal only, or double-phase detectors measuring the light and the charge signal (from ionization) in a TPC setup.

At the time of writing, the most stringent exclusion limits for all WIMP masses are from LXe based detectors. We have presented the current status of more than 10 experiments using noble liquids which are all aiming to reach even higher sensitivities. Their goal is to explore new regions in the cross section vs. mass parameter space (see Fig. 3) and to finally detect the dark matter particle with detectors of 100-1000 kg target mass or even beyond.

Acknowledgments

We would like to thank the organizers of Rencontres de Moriond Cosmology 2012 for their kind invitation to this great conference.

References

1. N. Jarosik *et al.*, *Astrophys. J. Suppl.* **192**, 14 (2011);
   K. Nakamura *et al.* (Particle Data Group), *J. Phys. G* **37**, 075021 (2010).
2. G. Steigman and M. S. Turner, *Nucl. Phys. B* **253**, 375 (1985);
   G. Jungman, M. Kamionkowski, and K. Griest, *Phys. Rept.* **267**, 195 (1996).
3. M. W. Goodman and E. Witten, *Phys. Rev.* D **31**, 3059 (1985).

4. E. Aprile *et al.* (XENON100), *Phys. Rev. Lett.* **107**, 131302 (2011).
5. J. Angle *et al.* (XENON10), *Phys. Rev. Lett.* **107**, 051301 (2011).
6. E. Aprile and L. Baudis, in *Particle Dark Matter*, ed. G. Bertone (Cambridge University Press, 2010).
7. M.G. Boulay *et al.*, arXiv:0904.2930;
   H. Lippincott *et al.* PRC **78**, 035801 (2008).
8. J. Kwong *et al.*, *Nucl. Instrum. Methods* A **612**, 328 (2010);
   K. Ueshima *et al.* (XMASS), NIMA **659**, 161 (2011).
9. E. Aprile *et al.*, *Phys. Rev.* D **72**, 072006 (2005);
   V. Lebedenko *et al*, *Phys. Rev.* D **80**, 052010 (2009).
10. B. Dolgoshein, V. Lebedenko, B. Rodionov, *JETP Lett.* **11**, 513 (1970);
    A. Bolozdynya *et al.*, *IEEE Trans. Nucl. Sci.* **42**, 565 (1995).
11. Presentations given at UCLA Dark Matter 2012:
    `https://hepconf.physics.ucla.edu/dm12/agenda.html`.
12. A. Fowlie *et al.*, *Phys. Rev.* D **85**, 075012 (2012);
    O. Buchmueller *et al.*, arXiv:1112.3564;
    C. Strege *et al.*, *JCAP* **1203**, 030 (2012).
13. D. Akimov *et al.* (ZEPLIN-III), *Phys. Lett.* B **709**, 14 (2012).
14. H. Sekiya (XMASS), arXiv:1006.1473.
15. XMASS, presentation at the Japanese Physical Society (JPS) meeting, March 30, 2012.
16. D.S. Akerib *et al.* (LUX), *Nucl. Instrum. Methods* A **668**, 1 (2012).
17. D. Akimov *et al.* (DarkSide), arXiv:1204.6218.
18. A. Marchionni *et al.* (ArDM), arXiv:1012.5967.
19. M.G. Boulay (DEAP-3600), arXiv:1203.0604.
20. A. Hime (MiniCLEAN), arXiv:1110.1005.
21. D.N. McKinsey, K.J. Coakley, *Astropart. Phys.* **22**, 355 (2005).
22. L. Baudis (DARWIN), arXiv:1201.2402;
    M. Schumann (DARWIN), arXiv:1111.6251.
23. `www.fnal.gov/pub/max`.
24. D.C. Malling *et al.* (LZ), arXiv:1110.0103.

Constraints on Dark Matter and Supersymmetry from LAT Observations of Dwarf Galaxies

Alex Drlica-Wagner on behalf of the Fermi LAT Collaboration
Kavli Institute for Particle Astrophysics and Cosmology, Department of Physics and SLAC National Accelerator Laboratory, Stanford University, Stanford, CA 94305, USA

Due to a large mass-to-light ratio and low astrophysical backgrounds, dwarf spheroidal galaxies (dSphs) are considered to be one of the most promising targets for dark matter searches via γ rays. The *Fermi* LAT Collaboration has recently reported robust constraints on the dark matter annihilation cross section from a combined analysis of 10 dSphs. These constraints have been applied to experimentally valid, super-symmetric particle models derived from a phenomenological scan of the Minimal Supersymmetric Standard Model (the pMSSM). Additionally, the LAT Collaboration has searched for spatially extended, hard-spectrum γ-ray sources lacking counterparts in other wavelengths, since they may be associated with dark matter substructures predicted from simulations.

1 Introduction

It has been well-established that non-baryonic cold dark matter (DM) makes up approximately 85% of the matter density of the Universe. A popular DM candidate is a weakly interacting massive particle (WIMP) that could pair-annihilate to produce γ rays. The γ-ray flux from WIMP annihilation is given by $\phi(E,\psi) = \langle\sigma v\rangle/(8\pi m_W^2) \times N_W(E) \times J(\psi)$, where $\langle\sigma v\rangle$ is the velocity averaged pair annihilation cross section, m_W is the WIMP mass, $N_W(E)$ is the γ-ray energy distribution per annihilation, and $J(\psi) = \int_{l.o.s.,\Delta\Omega} dl\, d\Omega \rho^2[l(\psi)]$ is the line-of-sight (l.o.s.) integral of the squared DM density, ρ, toward a direction of observation, ψ, integrated over a solid angle, $\Delta\Omega$. Local enhancements in the DM density with large $J(\psi)$, or J-factors, and little astrophysical contamination are potentially good targets for DM searches in γ rays.

The LAT, the primary instrument on board the *Fermi* observatory, is a pair-conversion telescope with unprecedented sensitivity to γ rays in the energy range from 20 MeV to > 300 GeV. Scanning the entire sky every three hours, the LAT is an ideal instrument to search for faint new γ-ray sources. Here we report on the recent LAT searches for Galactic DM substructures that have led to some of the tightest constraints on DM annihilation into γ rays.[1,2,3]

2 Combined Analysis of Dwarf Spheroidal Galaxies[1]

The Milky Way dSphs are promising sources for the indirect detection of DM via γ rays. Stellar velocity data from these galaxies suggests large DM content, while observations at other wavelengths show no signs of astrophysical signals.[4,5] With two years of LAT observations, we constrained the γ-ray signal from ten dSphs using a joint likelihood analysis.[1]

To set limits on the DM annihilation cross section, we calculated the integrated J-factor within a cone of solid angle $\Delta\Omega = 2.4 \times 10^{-4}$ sr centered on each dSph assuming that the DM

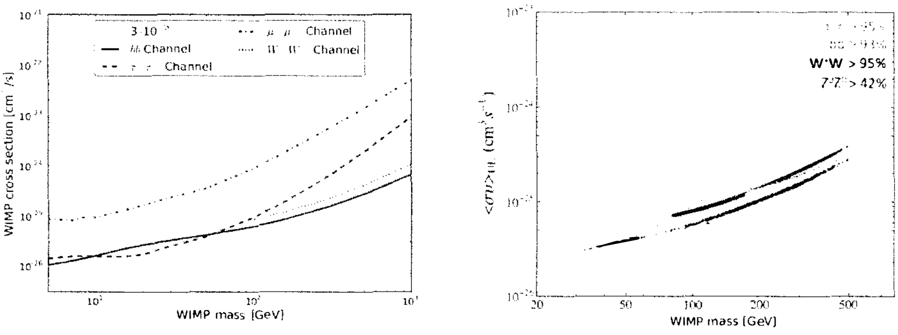

Figure 1: Left: Derived 95% C.L. upper limits on a WIMP annihilation cross section for the $b\bar{b}$, $\tau^+\tau^-$, $\mu^+\mu^-$, and W^+W^- channels from Ackermann et al. (2011). The generic annihilation cross section ($\sim 3 \times 10^{-26}\,\mathrm{cm}^3\mathrm{s}^{-1}$) is plotted as a reference. Uncertainties in the J factor are included. Right: Similar to the left plot but with each point corresponding to a specific pMSSM model. Colored points denote nearly pure annihilation channels corresponding to the lines in the left plot.

distribution follows a NFW profile.[6] For many of the dSphs, significant statistical uncertainty in the integrated J-factor exists due to limited stellar kinematic data. We incorporated this statistical uncertainty as nuisance parameters in our likelihood formulation:

$$L(D \,|\, \mathbf{p_m}, \{\mathbf{p_k}\}) = \prod_k L_k^{\mathrm{LAT}}(D_k \,|\, \mathbf{p_m}, \mathbf{p_k}) \times \frac{1}{\ln(10) J_k \sqrt{2\pi}\sigma_k} e^{-(\log_{10}(J_k) - \overline{\log_{10}(J_k)})^2 / 2\sigma_k^2}. \tag{1}$$

where k indexes the dSphs, L_k^{LAT} denotes the standard LAT binned Poisson likelihood for the analysis of a single dSph, D_k represents the binned γ-ray data, $\{\mathbf{p_m}\}$ represents the pMSSM model parameters shared across the dSphs, and $\{\mathbf{p_k}\}$ are dSph-dependent model parameters.

In Fig. 1, we show combined limits assuming DM annihilation through the $b\bar{b}$, $\tau^+\tau^-$, W^+W^-, and $\mu^+\mu^-$ channels. For the first time, γ-ray data are able to constrain models possessing the most generic cross section ($\sim 3 \times 10^{-26}$ cm^3 s^{-1} for a purely s-wave cross section), without assuming additional boost factors. This strong constraint extends up to a mass of $\sim$ 27 GeV for the $b\bar{b}$ channel and up to a mass of $\sim$ 37 GeV for the $\tau^+\tau^-$ channel.

In addition to statistical uncertainties, systematic uncertainties arise from the choice of DM profile. We recalculated our combined limits using the J-factors presented in Charbonnier et al. (2011),[7] which allow for shallower profiles than we assumed. We find that the systematic uncertainty resulting from the choice of profile is subdominant, and the combined constraints agree within $\sim$ 10%.

3 Constraints on the pMSSM from Dwarf Spheroidal Galaxies[2]

Supersymmetry (SUSY) is one of the most widely-studied theoretical frameworks for physics beyond the Standard Model (SM). Generic predictions of SUSY are difficult to obtain, and we examined the impact of the dSph limits on a phenomenological subset of the MSSM, the pMSSM.[10] The pMSSM models obey existing experimental constraints and exhibit a much broader array of phenomenology than can be seen in highly-constrained (mSUGRA/CMSSM) models. The Lightest Supersymmetric Particles (LSPs) of the pMSSM are viable candidates to comprise some or all of DM, and they may be probed through a variety of experimental approaches.

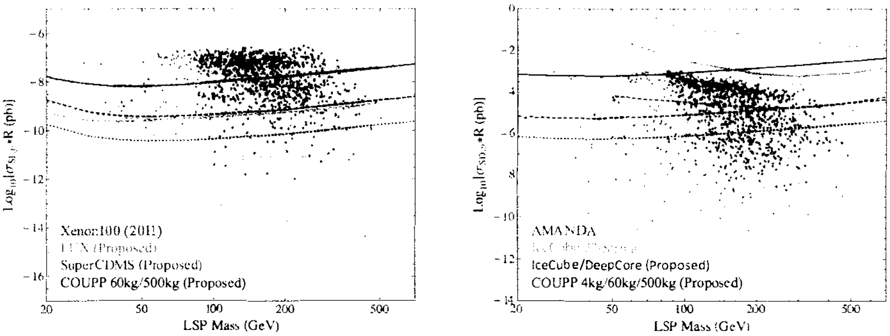

Figure 2: Comparison of direct detection limits and LAT dSph constraints from Cotta, et al. (2012). Spin-independent (left) and spin-dependent (right) direct detection cross sections for the pMSSM models are displayed as the gray points, highlighting those within reach of the LAT in red. Limits from current and near-future experiments are displayed as colored lines. Current spin-dependent scattering limits from the AMANDA and IceCube-22 collaborations are displayed with the assumption of soft (dashed) or hard (solid) channel annihilations.

We model the putative γ-ray emission from the dSphs having spectra generated from $\sim$ 71k pMSSM models rather than from prototypical annihilation channels (i.e., $b\bar{b}$, $\tau^+\tau^-$, $\mu^+\mu^-$, and W^+W^-). We calculated a joint likelihood for each pMSSM model by tying the pMSSM model parameters across the analysis regions surrounding the ten dSphs and incorporating statistical uncertainties in the J-factors of the dSphs. We found no significant γ-ray signal from any of the dSphs when analyzed individually or jointly for any of the pMSSM models.

Within the time frame of an extended mission, the LAT has the potential to constrain many of the pMSSM models. In Fig. 2, we display the set of pMSSM models in the spin-independent (left panel) and spin-dependent (right panel) scattering cross section vs. LSP mass planes, highlighting the models within reach of future LAT dSph analyses. We observe that many models are expected to be discovered or excluded by both direct detection experiments and the LAT. This could allow for a more detailed characterization of the DM particle. Additionally, we observe that there exist a number of models that will only be accessible to the LAT. These are models whose LSPs are dominantly bino and whose particle spectrum is somewhat hierarchical. These models include a light bino and one or more light sleptons, making them essentially invisible to both direct detection experiments and the LHC due to a lack of accessible colored production channels.

4 Search for Unassociated Dark Matter Satellites[3]

Cosmological N-body simulations predict the existence of many more DM satellites than are observed as dSphs.[8,9] These satellites may be detected as γ-ray sources having hard spectra, finite angular extents, and no counterparts at other wavelengths. We selected unassociated, high-Galactic-latitude γ-ray sources from both the First LAT Source Catalog (1FGL)[11] and from an independent list of source candidates created with looser assumptions on the source spectrum. Using the likelihood ratio test, we distinguished extended sources from point sources and WIMP annihilation spectra from conventional power-law spectra. No candidates were found in either the unassociated 1FGL sources or our additional list of candidate sources. This null detection is combined with the Via Lactea II[8] and Aquarius[9] simulations to set an upper limit on the annihilation cross section for a 100 GeV WIMP annihilating through the $b\bar{b}$ channel.

Using the detection efficiency of our selection, the absence of DM satellite candidates can be combined with the Aquarius and Via Lactea II simulations to constrain a conventional 100 GeV WIMP annihilating through the $b\bar{b}$ channel. We calculated the probability of detecting no satellites from the individual detection efficiency of each simulated satellite. By increasing the satellite flux until the probability of detecting no satellites drops below 5%, we set a 95% confidence upper limit on $\langle\sigma v\rangle$ to be less than $1.95 \times 10^{-24}\,\mathrm{cm}^3\,\mathrm{s}^{-1}$ for a 100 GeV WIMP annihilating through the $b\bar{b}$ channel.[3]

5 Conclusion

LAT observations of Galactic DM substructure have placed some of the most robust constraints on the annihilation cross section to date. Observations of known dSphs place tight constraints that can be extended to a broader category of supersymmetric models presented by the pMSSM. Additionally, the null detection of DM substructures as unassociated, spatially-extended, hard-spectrum γ-ray sources can be combined with predictions from simulations to place independent limit on DM annihilation to $b\bar{b}$. In the future, each of these studies will benefit from increased observation time and improvements to the LAT performance.

Acknowledgments

The *Fermi* LAT Collaboration acknowledges support from a number of agencies and institutes for both development and the operation of the LAT as well as scientific data analysis. These include NASA and DOE in the United States, CEA/Irfu and IN2P3/CNRS in France, ASI and INFN in Italy, MEXT, KEK, and JAXA in Japan, and the K. A. Wallenberg Foundation, the Swedish Research Council and the National Space Board in Sweden. Additional support from INAF in Italy and CNES in France for science analysis during the operations phase is also gratefully acknowledged.

ADW is supported in part by the Department of Energy Office of Science Graduate Fellowship Program (DOE SCGF), made possible in part by the American Recovery and Reinvestment Act of 2009, administered by ORISE-ORAU under contract no. DE-AC05-06OR23100.

References

1. Fermi LAT Collaboration. Phys. Rev. Lett. **107**, 241302 (2011)
2. Cotta, R.C. *et al.*, JCAP **04**, 16 (2012)
3. Fermi LAT Collaboration. Ap. J. **747**, 121 (2012)
4. Mateo, M. Ann.Rev.Astron.Astrophys. **36** 435 (1998)
5. Grcevich, J. *et al.*, Ap.J. **696** 385 (2009)
6. J. F. Navarro *et al.*, Ap. J. **490**, 493 (1997)
7. Charbonnier, A. *et al.*, MNRAS **418**, 1526 (2011)
8. J. Diemand *et al.*, Ap. J. **657**, 262 (2007)
9. V. Springel *et al.*, MNRAS **391**, 1685 (2008)
10. Berger, C.F., *et al.*, JHEP, 0902, 23 (2009)
11. Fermi LAT Collaboration. Ap. J. Supp. **188**, 405 (2010)

The Quest for Dark Matter Signals and the gamma-ray sky

ALDO MORSELLI
INFN Roma Tor Vergata,
Via della Ricerca Scientifica 1, Roma, Italy

The energy range between 10 and 50 MeV is an experimentally very difficul range and remained uncovered since the time of COMPTEL. Here we propose a possible mission to cover this energy range.

One of the major scientific objectives of γ-ray instruments is the indirect search for dark matter (DM), by means of the production of secondary γ-rays after the annihilation (or decay) of the DM particle candidates. The search strategy, which was assessed with a detailed study [1], comprises the study of targets with an expected relatively large γ-ray signal (such as the Galactic Center [2, 3, 4],which was previously studied with EGRET data [5]), or with a very low foreseen conventional γ-ray emission [6, 7], the search for annihilation lines [8,9] and also the search of possible anisotropies generated by the DM halo substructures [11]. The indirect DM searches with γ rays are complemented with those performed with the detection of cosmic-ray electrons by the LAT [12, 13, 10].

All these searches and limits were possible thanks to the extraordinary performances of the Fermi-Lat [16, 17] that allowed the Fermi collaboration to compile the Second Fermi-LAT catalog (2FGL) [15] that is the deepest catalog ever produced in the energy band between 100 MeV and 100 GeV. Compared to the First Fermi-LAT (1FGL) [14], it features several significant improvements: it is based on data from 24 (vs. 11) months of observation and makes use of the new Pass 7 event selection. The energy flux map is shown in figure 1. In the catalog 127 sources of the 1873 sources are firmly identified, based either on periodic variability (e.g. pulsars) or on spatial morphology or on correlated variability. In addition to that 1170 are reliably associated with sources known at other wavelengths, while 576 (i.e. 31% of the total number of entries in the catalog) are still unassociated. The association is particulary difficult in the Galactic plane region (see figure 2) where many sources are condensed in small regions of the sky. The task of source association as well as the search for dark matter coud have a great benefit from an instrument with better angular resolution and effective area in the energy range centered near 10 MeV. This energy range is notoriously difficult to study, and since COMPTEL on board of CGRO there has been no space instrument devoted to the 5- 50 MeV energy range. The main problem is the multiple scattering of the electron and positron pair that ruin the reconstruction of the direction of the incoming gamma. In figure 3 it is shown the effect of Multiple Scattering on the angular distribution of electrons for different thickness of material traversed (in Radiation Lengths (X_0)) and from this figure it is clear that a tracker sistem without passive converter is the only way to minimize the multiple scattering effects. The importance of the 5- 50 MeV energy range the search for dark matter can be seen in figure 4 where the differential γ-ray

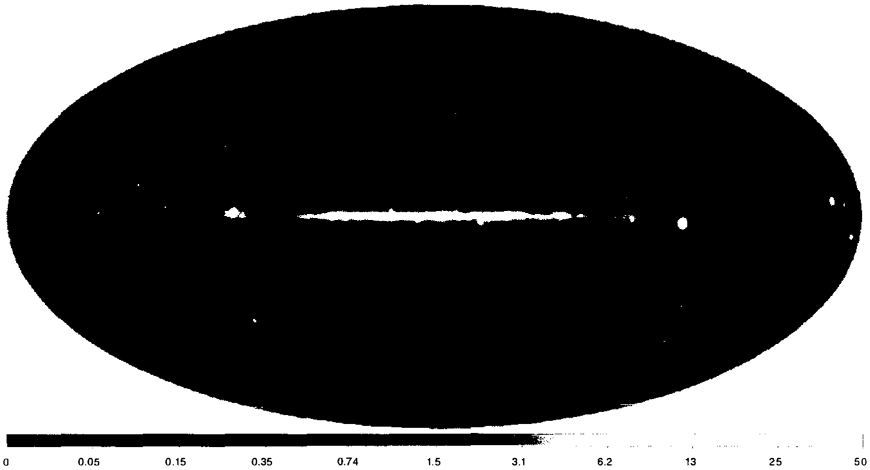

Figure 1: Sky map of the energy flux derived from 24 months of observation. The image shows γ-ray energy flux for energies between 100 MeV and 10 GeV, in units of 10^{-7} erg cm^{-2} s^{-1} sr^{-1}.

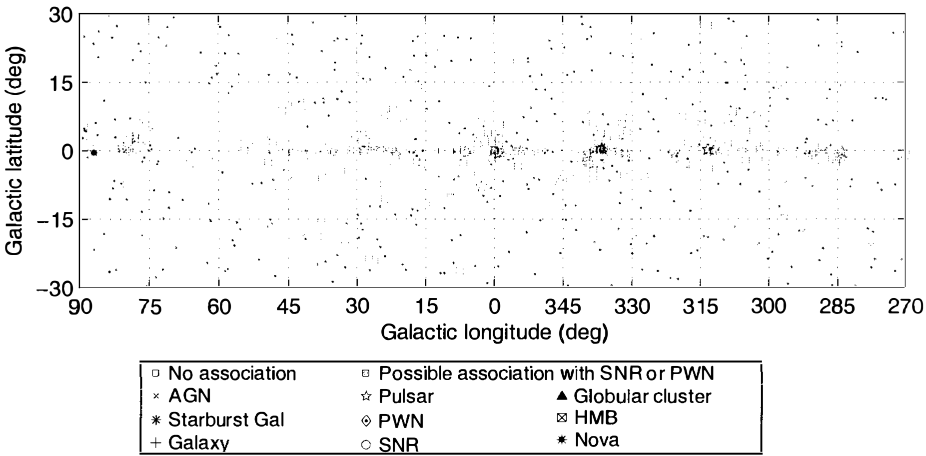

Figure 2: Map of the Inner Galactic region in the 100 MeV to 100 GeV energy range showing sources by source class. Identified sources are shown with a red symbol, associated sources in blue. Sources with no flag set are shown as small dots.

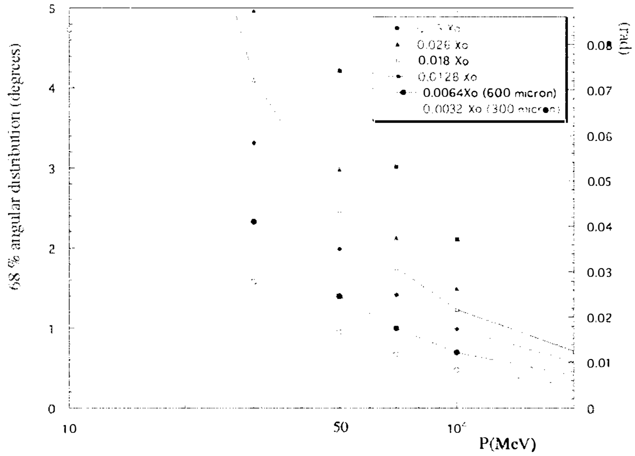

Figure 3: Effect of Multiple Scattering on the angular distribution of electrons for different thickness of material traversed (in Radiation Lengths (X_0)

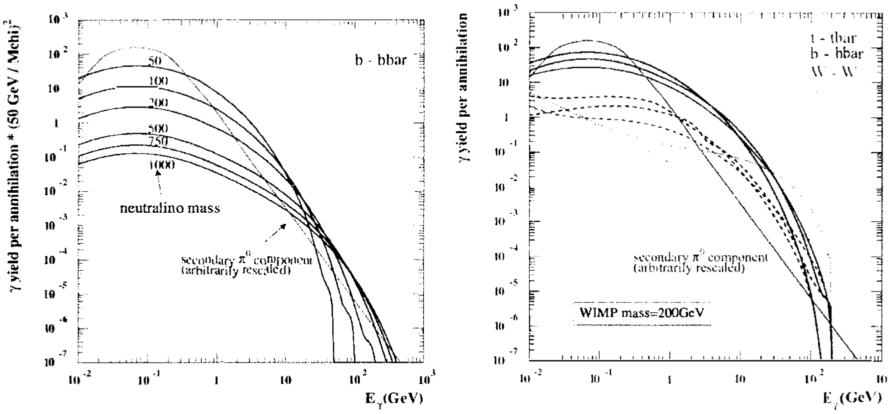

Figure 4: In the left panel: differential γ-ray energy spectra per annihilation for a fixed annihilation channel (b bar) and for a few sample values of WIMP masses. For comparison we also show the emissivity, with an arbitrarily rescaled normalization, from the interaction of primaries with the interstellar medium. In the right panel: differential energy spectra per annihilation for a few sample annihilation channels and a fixed WIMP mass (200 GeV). The solid lines are the total yields, while the dashed lines are components not due to π^0 decays.

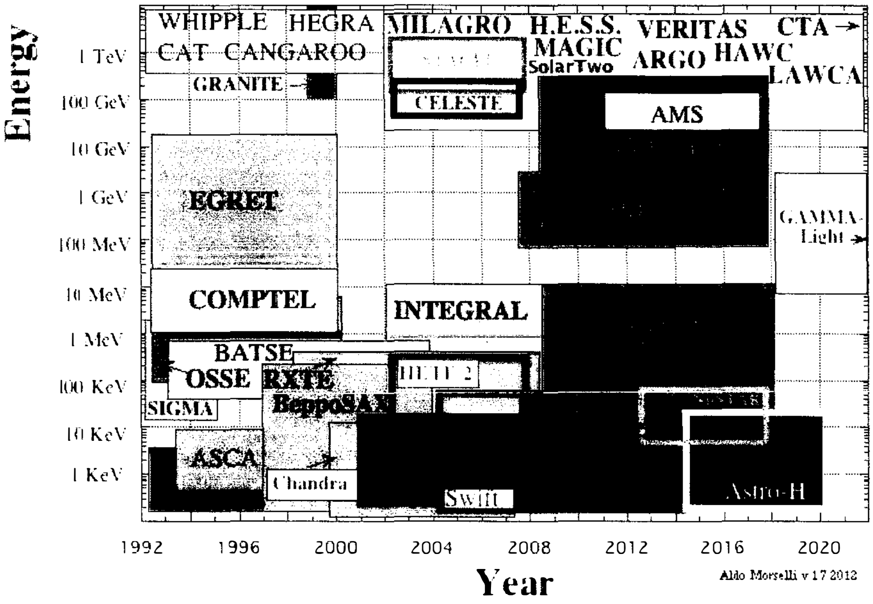

Figure 5: Energy range versus time for past and future X and γ-ray experiments

energy spectra per annihilation of Weakly Interacting Massive elementary Particle (WIMP) are plotted [5]. As one can see the bulk of the emission even for high WIMP masses is in the energy range 5 MeV - 100 MeV. To cover this energy range we are proposing to the Small Mission GAMMA-LIGHT in response to the ESA S-Mission call.

GAMMA-LIGHT is designed for a breakthrough new gamma-ray astrophysics in the range 10 MeV - 10 GeV obtained by an optimal effective area and a PSF substantially better than the current generation. Diffuse emission across the Galaxy can be completely resolved and correlated with radio, optical and CO surveys. Diffuse gamma-ray sources (SNRs, PWNe, star forming regions, gamma-ray bubbles, the Galactic Center region) can be studied with unprecedented accuracy. Extragalactic sources can be detected with great accuracy and sensitivity. Galactic and extragalactic source emission from 10 MeV up to 100 MeV can be studied for the first time with a sensitivity larger than COMPTEL by more than one order of magnitude. Several astrophysical issues can be addressed such as the properties of Galactic micro-quasars, exotic transients and MeV-blazars. In figure 5 is shown the energy range versus time for past and future X and γ-ray experiments and the range that GAMMA-LIGHT can cover with a benefit for all multi-wavelenth studies.

References

1. E. Baltz *et al.* , JCAP07 (2008) 013 [arXiv:0806.2911]
2. V.Vitale and A. Morselli for the Fermi/LAT Collaboration, 2009 Fermi Symposium [arXiv:0912.3828]
3. A.Morselli, B.Cañadas, V.Vitale, Il Nuovo Cimento Vol. 34 C, N. 3 (2011) [arXiv:1012.2292]
4. V.Vitale, A.Morselli , for the Fermi Coll. NIM A 630 (2011) 147150
5. A.Cesarini, F.Fucito, A.Lionetto, A.Morselli, P. Ullio, Astropart. Phys. 21 (2004) 267 [astro-ph/0305075]
6. A.Abdo *et al.* [Fermi Coll.] ApJ 712 (2010) 147-158 [arXiv:1001.4531]
7. M.Ackermann *et al.* [Fermi Coll.] 2011, PRL 107, 241302 (2011) [arXiv:1108.3546]
8. A.Abdo *et al.* [Fermi Coll.], Phys.Rev.Lett.104, 091302-08 (2010) [arXiv:1001.4836]
9. M.Ackermann *et al.* [Fermi Coll.], PRD accepted [arXiv:1205.2739]
10. M.Ackermann *et al.* [Fermi Coll.], Physical Review D 82, 092003 (2010) [arXiv:1008.5119]
11. M.Ackermann *et al.* [Fermi Coll.], Physical Review D 85, 083007 (2012) [arXiv:1202.2856]
12. A.A.Abdo *et al.* [Fermi Coll.], PRL 102, 181101 (2009) [arXiv:0905.0025]
13. M.Ackermann *et al.* [Fermi Coll.], PRD 82, 092004 (2010) [arXiv:1008.3999]
14. A.Abdo *et al.*[Fermi Coll.] Astrophys. J. Suppl. Series 188, 405 (2010) [arXiv:1002.2280]
15. A.Abdo *et al.* [Fermi Coll.] Astrophysical Journal Supplement Series (2012) 199, 31 [arXiv:1108.1435]
16. W.B.Atwood *et al.* [Fermi Coll.] ApJ 697 No 2 (2009 June 1) 1071-1102 [arXiv:0902.1089]
17. A.Abdo *et al.* [Fermi Coll.] Astroparticle Physics 32 (2009) 193-219 [arXiv:0904.2226]

Search for dark matter at the LHC using missing transverse energy

Sarah Alam Malik
1230 York Avenue New York, NY 10065, USA

Results are presented for a search for dark matter at the LHC using the signatures of a monojet plus missing transverse energy and a monophoton plus missing transverse energy. The data were collected by the CMS detector at the LHC with pp collisions at a centre-of-mass energy of 7 TeV and an integrated luminosity of 5 fb^{-1}. In the absence of an excess of events in the data compared to the Standard Model prediction, limits are set on the dark matter-nucleon scattering cross section which can be directly compared with bounds from the direct detection experiments.

1 Introduction

There is strong evidence from numerous cosmological observations, such as the rotational speed of galaxies and gravitational lensing, that approximately 25% of the matter-energy density of the universe is made up of dark matter.

One of the most popular class of candidates for dark matter are Weakly Interacting Massive Particles (WIMPs). Pairs of these particles can be produced at the LHC if the partonic centre-of-mass energy is above the energy threshold for a WIMP pair. When accompanied by the emission of a jet or a photon from the initial state, these processes lead to the signature of a jet plus missing transverse energy [10] and a photon plus missing transverse energy [9]. This article will describe searches for dark matter performed at the Large Hadron Collider (LHC) using data collected by the Compact Muon Solenoid (CMS) detector corresponding to an integrated luminosity of 5 fb^{-1}.

Searches for dark matter at colliders have previously been performed in the context of new physics models such as Supersymmetry (SUSY) where the lightest SUSY particle is neutral, stable, and thus a good candidate for dark matter. Recently, more model-independent approaches have been considered in which no assumptions are made about the new physics model that is producing the WIMPs. This is achieved by working within the framework of an effective field theory and assuming that the dark matter particle is the only new state that is accessible to the LHC. The mediator that couples the dark matter particles to the Standard Model (SM) states is assumed to be very heavy such that it can be integrated out and the interaction can be treated as a contact interaction. This approach is described in [1,2,3,4,5,6].

Working with one of these models [5,6], we assume that the dark matter particle(χ) is a Dirac fermion and the contact interaction is characterized by a scale $\Lambda = M/\sqrt{g_\chi g_q}$ where M is the mass of the mediator and g_χ and g_q are its couplings to χ and quarks, respectively. Operators that describe the nature of the coupling of the mediator can be defined and two possibilities are considered [5,6], a vector operator and an axial-vector operator, which proceed via an s-channel exchange of a new heavy gauge boson and translate to bounds on the spin independent and spin dependent dark matter-nucleon interactions, respectively.

2 Monojet search

The data used in the study of events with a monojet and missing transverse energy is recorded by a trigger that requires $\not\!\!E_{\mathrm{T}} > 80(95)$ and atleast one jet with $p_T > 80$ GeV. The trigger is found to be fully efficient for $\not\!\!E_{\mathrm{T}} > 200$ GeV and jet $\mathrm{p_T} > 110$ GeV. Particles in an event are individually identified as either charged hadrons, neutral hadrons, photons, muons, or electrons, using a particle-flow reconstruction [7]. The reconstructed particles are fully calibrated and clustered into jets using the anti-k_T algorithm [8] with a distance parameter of 0.5. The $\not\!\!E_{\mathrm{T}}$ in this analysis is defined as the magnitude of the vector sum of all particles reconstructed in the event excluding muons. This definition allows the use of a control sample of $\mathrm{Z}(\rightarrow \mu\mu)$+jets events to estimate the $\mathrm{Z}(\rightarrow \nu\nu)$ background. A Monte Carlo study of the optimization of the $\not\!\!E_{\mathrm{T}}$ cut found the optimal cut producing the best limits on the dark matter signal to be $\not\!\!E_{\mathrm{T}} > 350$ GeV. The signal sample is therefore selected by requiring $\not\!\!E_{\mathrm{T}} > 350$ GeV and the jet with the highest transverse momentum to have $\mathrm{p_T} > 110$ GeV and $|\eta| < 2.4$. A second jet is allowed, as signal events typically contain an initial or final state radiated jet, provided its angular separation in azimuth from the highest $\mathrm{p_T}$ jet satisfies $\Delta\phi < 2.5$ radians. This angular requirement suppresses QCD dijet events. Events containing more than two jets with $\mathrm{p_T} > 30$ GeV are vetoed. This requirement suppresses $t\bar{t}$ and QCD multijet events. To reduce background from electroweak processes and top-quark decays, events with isolated muons and electrons with $\mathrm{p_T} > 10$ GeV are rejected. Events with an isolated track with $\mathrm{p_T} > 10$ GeV are also removed as they come primarily from the decay of τ-leptons. A track is considered isolated if the scalar sum of the transverse momentum of all tracks with $\mathrm{p_T} > 1$ GeV in the annulus of radius $0.02 < \Delta R < 0.3$ around its direction is less than 1% of its $\mathrm{p_T}$.

The dominant backgrounds to this search are from Z+jet and W+jet events, where the Z boson decays to a pair of neutrinos and the W decays leptonically. These backgrounds are estimated from a control sample of μ+jet events, where $\mathrm{Z}(\rightarrow \mu\mu)$+jets events are used to estimate $\mathrm{Z}(\rightarrow \nu\nu)$ and $\mathrm{W}(\rightarrow \mu\nu)$ events are used to estimate the remaining W+jets background. The $\mathrm{Z}(\rightarrow \nu\nu)$ background is estimated by correcting the observed $\mathrm{Z}(\rightarrow \mu\mu)$+jets event yield by the detector acceptance, the selection efficiency and the ratio of the branching fractions. It is estimated to be 900 ± 94 events, where the uncertainty includes statistical and systematic contributions. The dominant uncertainty is from the statistical size of the $\mathrm{Z}(\rightarrow \mu\mu)$+jets control sample. The remaining W+jets background is estimated by selecting a control sample of $\mathrm{W}(\rightarrow \mu\nu)$ events and correcting for the inefficiencies of the electron and muon selection requirements. The W+jets background is estimated to be 312 ± 35 events.

Background contributions from QCD multijet events, $t\bar{t}$ and $\mathrm{Z}(\rightarrow ll)$+jets production are small and are obtained from the simulation. A 100% uncertainty is assigned to these backgrounds.

Table 1 shows the estimated contributions to the monojet sample from the SM backgrounds and the total number of observed events. The observed event yield is consistent with the number of events expected from SM backgrounds.

3 Monophoton search

The final state containing a photon and $\not\!\!E_{\mathrm{T}}$ is also a signature of many new physics scenarios, including the production of dark matter particles. The dataset is collected by single-photon triggers that are fully efficient for the selected signal region. A photon candidate is selected by requiring $\mathrm{p_T} > 145$ GeV and $|\eta| < 1.44$, to ensure it is in the central barrel region of the detector where purity is highest. The ratio of the energy deposited in the hadronic calorimeter

Table 1: Event yields for SM background predictions and the observed number of monojet events in the data.

Source	Estimate
Z($\to \nu\nu$)+jets	900 $\pm$ 94
W+jets	312 $\pm$ 35
$t\bar{t}$	8 $\pm$ 8
Z($\to ll$)+jets	2 $\pm$ 2
Single top	1 $\pm$ 1
QCD Multijets	1 $\pm$ 1
Total background	1224 $\pm$ 101
Observed candidates	1142

Table 2: Event yields for SM background predictions and the observed number of monophoton events in the data.

Source	Estimate
Z($\to \nu\nu$) + γ	45.3 $\pm$ 6.9
Jet mimics photon	11.2 $\pm$ 2.8
Beam halo	11.1 $\pm$ 5.6
Electron mimics photon	3.5 $\pm$ 1.5
$W\gamma$	3.0 $\pm$ 1.0
$\gamma\gamma$	0.6 $\pm$ 0.3
γ+jet	0.5 $\pm$ 0.2
Total background	75.1 $\pm$ 9.5
Observed candidates	73

(HCAL) to that in the electromagnetic calorimeter (ECAL) within a cone of $\Delta R = 0.15$ is required to be less than 0.05, where $\Delta R = \sqrt{(\Delta\phi)^2 + (\Delta\eta)^2}$ is defined relative to the photon candidate and the azimuthal angle ϕ is measured in the plane perpendicular to the beam axis. Photon candidates are also required to be isolated and have a shower distribution in the ECAL that is consistent with that expected for a photon. The $\not{E}_{\mathrm{T}}$ is defined as the magnitude of the vector sum of the transverse energies of all the reconstructed objects in the event, as computed using the particle-flow algorithm and is required to be $\not{E}_{\mathrm{T}} > 130$ GeV. To reduce instrumental background arising from showers induced by muons in the beam halo or cosmic rays, the energy deposited in the crystal containing the largest signal within the photon is required to be within ± 3 ns of the time expected for particles from a collision. Spurious signals in the ECAL are eliminated by requiring the energy deposition times for all crystals within an electromagnetic shower to be consistent. Events are also vetoed if they contain significant hadronic activity[9].

Backgrounds processes contributing to the photon plus $\not{E}_{\mathrm{T}}$ topology include; Z+γ production where the Z decays to neutrinos, $W + \gamma$ production where the W decays leptonically, W($\to e\nu$) events where the electron is misidentified as a photon, diphoton production, QCD multijet events where one of the jets mimics a photon and another is mismeasured, and events from out of time collisions.

Backgrounds from out of time collisions, W($\to e\nu$) events and QCD multijet events are estimated from the data. Other backgrounds from Z($\to \nu\nu$) + γ, W($\to l\nu$) + γ, γ+jet and diphoton events are estimated from simulation. Table 2 shows the estimated contributions to the signal sample from the various SM processes and the observed candidate events. The number of events observed in the data are consistent with the expected number of events from SM backgrounds.

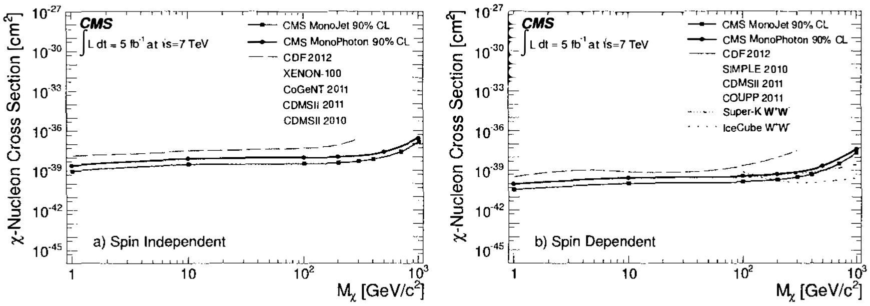

Figure 1: The 90% CL upper limits on the dark matter-nucleon cross section as a function of M_χ for (a) spin independent and (b) spin dependent interactions. Also shown are the bounds from other experiments.

4 Interpretation

Since there is no observed excess of events in the data over those expected from SM backgrounds, limits are set on the production of dark matter particles. The observed limit on the cross section is dependent on the mass of the dark matter particle and the nature of its interactions with the SM particles. The upper limits on the dark matter production cross sections, as a function of M_χ, for the vector and axial-vector interactions can be converted to lower limits on the effective contact interaction scale λ. These are then translated to an upper limit on the dark matter-nucleon scattering cross section, within the effective theory framework [6]. Figure 1 shows the 90% CL upper limits on the dark matter-nucleon scattering cross section as a function of the mass of the dark matter particle for the spin dependent and spin independent interactions. Also shown are the results from other experiments, including the CDF monojet analysis [11]. For spin dependent interactions, the bounds from the CMS monojet and monophoton analyses surpass all previous constraints for the 1−200 GeV mass range. For spin independent interactions, these limits extend the excluded M_χ range into the previously inaccessible region below 3.5 GeV.

In summary, results are presented for searches for dark matter at CMS using the monojet and monophoton plus $\not\!\!E_T$ signatures. The observed event yields are consistent with those expected from SM backgrounds. Hence, limits are set on the dark matter-nucleon scattering cross section as a function of M_χ and represent a significant extension to those from previous experiments.

References

1. M. Beltran *et al JHEP* **09**, 037 (2010).
2. J. Goodman *et al Phys. Rev. Lett.* **B695**, 185 (2011).
3. J. Goodman *et al Phys. Rev.* D **82**, 116010 (2010).
4. A. Rajaraman *et al* arXiv:1108.1196.
5. Y. Bai *et al JHEP* **12**, 048 (2010).
6. P.J. Fox *et al*, *Phys. Rev.* D **85**, 056011 (2012).
7. CMS Physics Analysis Summary CMS-PAS-PFT-09-001 (2009).
8. M. Cacciari *et al* JHEP **04**, 063 (2008).
9. CMS Collaboration, arXiv:1204.0821.
10. CMS Collaboration, *Phys. Rev. Lett.* **107**, 201804 (2011).
11. CDF Collaboration, *Phys. Rev. Lett.* **108**, 211804 (2012).

SUPERSYMMETRIC DARK MATTER IN LIGHT OF RECENT RESULTS FROM LHC, XENON100 AND FERMI DATA

LESZEK ROSZKOWSKI[a]
National Centre for Nuclear Research,
Hoża 69, 00-681 Warsaw, Poland

Recent LHC results, most notably the discovery of a Higgs boson with mass close to 125 GeV, as well as improved limits on BR $\left(B_s \to \mu^+\mu^-\right)$ and on direct supersymmetry searches, have led to a considerable shift in the pattern of high probability regions of the Constrained Minimal Supersymmetric Standard Model. Here I will present results of a recent Bayesian analysis of the model in which we include these and several other relevant experimental constraints. Ensuing predictions for spin-independent cross section of neutralino dark matter now at 1σ favor $\sigma_p^{\rm SI} \lesssim 10^{-9}$ pb, with WIMP mass of ~ 600 GeV to ~ 850 GeV, over an order of magnitude below the recently announced currently best limit from XENON100. Exploring this range of $\sigma_p^{\rm SI}$ will require one-tonne detectors. An upper limit on γ-ray flux from dwarf spheroidal satellite galaxies of the Milky Way published last year by the FermiLAT Collaboration could previously be used to exclude the $m_\chi \lesssim 160$ GeV part of a high-probability 1σ posterior region with $\sigma_p^{\rm SI} \gtrsim 10^{-8}$ pb, but this has now been superseded by the much improved LHC results, and, over the whole neutralino mass range, also by the new XENON100 limit.

1 Framework

In this writeup I will summarize several results presented in my talk which was based on some recent papers and ongoing work of the BayesFITS group [1,3,2], where more details and references to the literature can also be found. Since from the time of the conference some results were updated and strongly modified, and also a tantalizing announcement of the discovery of a Higgs boson with mass close to 125 GeV was recently made, to the extent possible I will present them in the up-to-date form.

In a pursuit to narrow down the choice of a correct model of "new physics" beyond the Standard Model (SM), we are guided both by theory and experimental data. In particular, effective models based on softly-broken global supersymmetry (SUSY) have been at the center of attention in light of rapidly improving limits from the LHC.

Here I will present results obtained in the framework of the Constrained Minimal Supersymmetric Standard Model (CMSSM) - the most popular and economical effective SUSY model of phenomenological interest. Since SUSY can contribute to a number of observables, available data can be used to constrain its parameters. The way to go is to compare various experimental input in a statistical way. In our work we have mostly employed the Bayesian approach, although we have also computed minimum χ^2, and have identified the corresponding best fit (BF) point. Below I will make some comments about it.

[a] On leave of absence from the University of Sheffield.

Table 1: Priors for the parameters of the CMSSM and for the SM nuisance parameters used in our scans. Masses and A_0 are in GeV.

CMSSM parameter	Description	Prior Range	Prior Distribution
m_0	Universal scalar mass	100, 4000	Log
$m_{1/2}$	Universal gaugino mass	100, 2000	Log
A_0	Universal trilinear coupling	-7000, 7000	Linear
$\tan\beta$	Ratio of Higgs vevs	3, 62	Linear
$\mathrm{sgn}\,\mu$	Sign of Higgs parameter	$+1$ or -1	Fixed
Nuisance	Description	Central value $\pm$ std. dev.	Prior Distribution
M_t	Top quark pole mass	172.9 ± 1.1	Gaussian
$m_b(m_b)^{\overline{MS}}_{\mathrm{SM}}$	Bottom quark mass	4.19 ± 0.12	Gaussian
$\alpha_s(M_Z)^{\overline{MS}}$	Strong coupling	0.1184 ± 0.0007	Gaussian
$1/\alpha_{\mathrm{em}}(M_Z)^{\overline{MS}}$	Reciprocal of electromagnetic coupling	127.916 ± 0.015	Gaussian

In the CMSSM, three of its defining parameters are set at the scale of grand unification. These are the universal scalar mass m_0, the universal gaugino mass $m_{1/2}$, and the universal trilinear coupling A_0. Additionally, $\tan\beta$ (the ratio of the expectation values of the two Higgs doublets), is defined at the electroweak scale, while the sign of the Higgs/higgsino parameter μ remains undetermined.

Space limitations do not allow me to enter into a longer discussion of the procedure used and the whole range of our results. Below I will therefore only briefly summarize the main points and refer the reader to our papers for a detailed presentation of our analysis and a list of references.

Table 2: The experimental measurements that we apply to constrain the CMSSM's parameters. Masses are in GeV.

Measurement	Mean or Range	Exp. Error	Th. Error	Likelihood Distribution
CMS Razor (4/invfb)	See text	See text	0	Poisson
SM-like Higgs mass m_h	125	2	2	Gaussian
$\Omega_\chi h^2$	0.1120	0.0056	10%	Gaussian
$\sin\theta_{\mathrm{eff}}$	0.23116	0.00013	0.00015	Gaussian
m_W	80.399	0.023	0.015	Gaussian
$\delta(g-2)^{\mathrm{SUSY}}_\mu \times 10^{10}$	28.7	8.0	1.0	Gaussian
$\mathrm{BR}\left(\overline{B} \to X_s\gamma\right) \times 10^4$	3.60	0.23	0.21	Gaussian
$\mathrm{BR}(B_u \to \tau\nu) \times 10^4$	1.66	0.66	0.38	Gaussian
ΔM_{B_s}	17.77	0.12	2.40	Gaussian
$\mathrm{BR}\left(B_s \to \mu^+\mu^-\right)$	$< 4.5 \times 10^{-9}$	0	14%	Upper limit – Error Fn

2 Procedure and Results

In our analysis we simultaneously scan over wide ranges of the four CMSSM parameters and, in addition, over four SM nuisance parameters, as specified in Table 1. Random scans are done with a new numerical code BayesFITS that we have developed for the purpose. The physical constraints that we impose are listed in Table 2. They are all defined and discussed in our recent paper [1].

The physical constraints, along with their respective experimental and theoretical errors, if available, are all incorporated in the analysis via a likelihood function. Positive measurements (e.g., the relic density $\Omega_\chi h^2$of neutralino assumed to be dark matter (DM)) are all approximated by a Gaussian distribution, while experimental limits are smeared out by an error function.

Three recent results from the LHC play a particularly important role in the analysis: (i) a new upper limit on $\mathrm{BR}(B_s \to \mu^+\mu^-)$ from LHCb; (ii) a lower limit on the plane $(m_0, m_{1/2})$ placed by a recent CMS analysis, with the razor method applied to 4.7/fb of data, for which

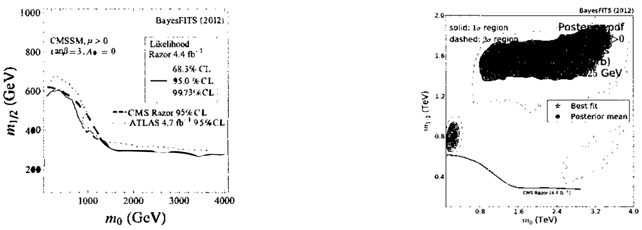

Figure 1: Left: Our approximation of the CMS razor 4.4/fb likelihood map. The thick solid line shows the 95.0% CL (2σ) bound. It approximates the CMS 95% CL exclusion contour, shown by the black (dashed) line. The thin solid line and the thin dashed line show our calculations of the 68.3% CL (1σ) and the 99.73% CL (3σ) exclusion bound, respectively. The grey dotted line shows the ATLAS 95% CL exclusion bound. Right: Marginalized 2-dim. posterior pdf in the (m_0, $m_{1/2}$) plane of the CMSSM for $\mu > 0$, constrained by the experiments listed in Table 2. The black (solid) line shows the CMS razor 95% CL exclusion bound which is included in the likelihood. We assume a light Higgs mass of 125 GeV, also implemented in the likelihood.

we derived an approximate but very accurate likelihood function (see the left panel of Fig. 1 in Ref. [1]), and a comparable one obtained by ATLAS using 0-lepton search; and finally (iii) following the recent announcement, information about SM-like Higgs with mass 125 GeV, which we approximate with a Gaussian function; see Table 2. (The now obsolete case with ATLAS and CMS limits on the SM-like Higgs boson mass considered in Ref. [1] gives almost identical results.)

We performed scans for four cases: with and without the $(g-2)_\mu$ constraint for $\mu > 0$ and separately for $\mu < 0$. In each case we derived maps of Bayesian posterior probability density function (pdf). A result of marginalizing it over all CMSSM and SM nuisance parameters, except for m_0 and $m_{1/2}$, is shown in the right panel of Fig. 1 for the most popular case of $\mu > 0$ and with the $(g-2)_\mu$ constraint included. The other cases are presented in Ref. [1].

The posterior features a bimodal behavior, with two prominent 1σ posterior (credible) regions. One mode, at small m_0, which is smaller in size, is the $\tilde{\tau}$-coannihilation region, whereas a much more extended mode at large $m_{1/2}$ is the A-funnel region. At 2σ both regions are enlarged, as expected, and in addition the focus point (FP)/hyperbolic branch (HB) region appears at large m_0 and $m_{1/2} \lesssim 1\,\text{TeV}$. The FP/HB region is now disfavored relative to our previous analysis [2,3], as a result of mostly the improved limit on BR ($B_s \to \mu^+\mu^-$) and identifying the light Higgs mass, as well as, to a lesser extent, by improved SUSY mass limits from CMS and ATLAS. Generally, a similar pattern is preserved in all the other cases considered [1].

For each scan one can derive a whole spectrum of implications for physical observables [1]. The resulting 2-dim. marginalized posterior pdf of the spin-independent cross section $\sigma_p^{\rm SI}$ of neutralino DM and its mass m_χ is shown in the left window of Fig. 2. The 1σ posterior region has now been pushed down compared to our previous studies [2,3] by improved LHC limits and the Higgs discovery. The 1σ pdf region is still considerably below the currently best upper limit on $\sigma_p^{\rm SI}$ from XENON100 (solid red), which improved the limit of 2011 (dash-dot green) by about a factor of four. One-tonne detectors will be needed (with a projected sensitivity of XENON shown in dash grey for illustration) in order to access that range.

At 2σ there remain two other regions at smaller m_χ. One, just above the 2011 XENON100 limit (corresponding to the FP/HB region), would not be excluded even if the XENON100 limit were added to the list of constraints in the likelihood function because of a large theory error ($\sim 5 - 10\,\sigma_p^{\rm SI}$) that would smear it out by a great deal [3]. With earlier LHC data, from last year, before the mass of the light Higgs boson close to 125 GeV was identified, and with weaker direct limits on $(m_0, m_{1/2})$ based on $\sim$ 1/fb of data, the FP/HB region featured a large 1σ region and extended to significantly lower $m_\chi \gtrsim 100\,\text{GeV}$ [2,3]. One could then exclude [3] a low m_χ part ($m_\chi \lesssim 160\text{GeV}$) of the 1σ region, after taking into account the upper limit on γ-ray flux

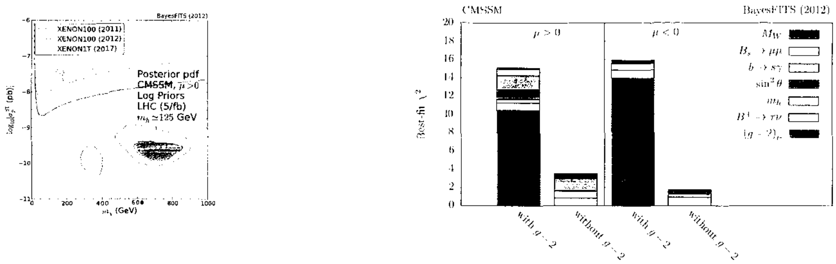

Figure 2: Left: A 2-dim. marginalized posterior pdf in the $(m_\chi,\ \sigma_p^{\rm SI})$ plane. The XENON100 previous (dash-dot green), current (solid red) and projected 1-tonne (dash grey) limits are shown but not imposed. Right: A bar-chart showing the breakdown of the main contributions to the χ^2 of the best-fit points of our four different likelihood scans.

from dwarf spheroidal satellite galaxies of the Milky Way (dSphs) obtained by the FermiLAT Collaboration [4]. However, with the 2012 data from the LHC, the FP/HB region is now reduced to the 2σ and, in addition, a bigger chunk the low-m_χ part of it is excluded. In addition, the whole FP/HB region of that scan is now in conflict with the 2012 XENON100 limit, as one can see in the right window of Fig. 1, although one cannot forget about the large theory error in the predictions of $\sigma_p^{\rm SI}$ mentioned above.

For $\mu < 0$ favored ranges of $\sigma_p^{\rm SI}$ are generally not larger, both at 1σ and 2σ. In fact, they can be much lower [1]. Dropping $\delta\,(g-2)_\mu^{\rm SUSY}$ has almost no effect on the posterior for either sign of μ since the claimed excess in the observable is anyway only very poorly fitted in the high posterior regions (at either 1σ or 2σ), as it requires low $M_{\rm SUSY}$ scale.

Unsurprisingly, an overall fit in terms of χ^2 is in fact mostly spoiled primarily by $\delta\,(g-2)_\mu^{\rm SUSY}$. After removing it from the list of constraints $\chi^2_{\rm min}$ improves enormously. This can be seen in the right panel of Fig. 2.

We have found that in both 1σ posterior regions in the $(m_0, m_{1/2})$ plane; compare the right panel of Fig. 1 there are quite large areas (especially in the A-funnel region at large m_0) where the lowest values of χ^2 are similar, and in fact comparable to $\chi^2_{\rm min}$, and actually to lowest values of χ^2 found in the stau coannihilation region. That implies that the location of the best fit point in the CMSSM can be quite sensitive to minor changes in the adopted methodology (scanning procedure, modeling of the likelihood for different observables, etc). Therefore, the position of the best fit point in comparable global analyses done by different groups can, and has been found to, vary a lot. In contrast, high probability posterior regions are relatively stable.

In conclusion, within the CMSSM one will need to wait until one-tonne detectors are operational before one can explore the currently most favored ranges of $\sigma_p^{\rm SI}$. As regards superpartner and heavy Higgs masses, only the stau coannihilation region will be fully explored, while a large chunk of the A-region corresponding to large m_0 and $m_{1/2}$ will in fact remain outside of the reach of the LHC.

References

1. A. Fowlie, et al., arXiv:1206.0264.
2. A. Fowlie, et al., *Phys. Rev.* D **85**, 075012 (2012), arXiv:1111.6098.
3. L. Roszkowski, E. M. Sessolo, Y.-L. S. Tsai, arXiv:1202.1503.
4. M. Ackermann, et al., The Fermi-LAT Collaboration, *Phys. Rev. Lett.* **107**, 241302 (2011), arXiv:1108.3546.
5. E. Aprile, et al., The XENON100 Collaboration, arXiv:1207.5988.

THE CONSISTENT INTERPRETATION OF FEATURES OF THE GALACTIC CENTER GAMMA RAY SPECTRUM AT HIGH ENERGIES TOGETHER WITH ELECTRON AND POSITRON DATA AS DARK MATTER

ALEXANDER BELIKOV
Institut d'Astrophysique de Paris, UMR 7095 CNRS, Université Pierre et Marie Curie, 98 bis Boulevard Arago, Paris 75014, France

GABRIJELA ZAHARIJAS
Abdus Salam International Centre for Theoretical Physics, Strada Costiera 11, 34151, Trieste, Italy

JOSEPH SILK
Institut d'Astrophysique de Paris, UMR 7095 CNRS, Université Pierre et Marie Curie, 98 bis Boulevard Arago, Paris 75014, France

Beecroft Institute of Particle Astrophysics and Cosmology, 1 Keble Road, University of Oxford, Oxford OX1 3RH UK

Department of Physics and Astronomy, 3701 San Martin Drive, The Johns Hopkins University, Baltimore MD 21218, USA

The spectrum of the source in the Galactic Center region was measured at TeV energies by the HESS collaboration and at GeV by the Fermi-LAT (only outside of the collaboration spectra are available for the latter spectrum . We perform a joint study of these two spectra, in terms of an astrophysical power law and a DM annihilation spectrum. Marginalizing over the astrophysical signal in our model, we find that a dark matter particle of mass of approximately 18 TeV can provide a good fit to the signal, and we determine the branchings ratios of such candidates. Prompted by a similarity in the DM mass between DM candidates needed for gamma rays and those that provide a good fit to the independent measurement of electrons and positrons (by the Fermi-LAT, PAMELA and HESS collaborations), we also explore whether the same DM candidate can fit both data sets.

1 Introduction

In the last few years a number of new generation cosmic ray detectors were able to collect data on gamma-rays, electrons and positrons, as well as protons and antiprotons in an extensive range of energies from 100 MeV to about 6 TeV for charged particles and up to 50 TeV with unprecedented precision. The newly acquired data are especially important for indirect dark matter searches, which might help to establish the nature of dark matter. The theory of cold dark matter supported by numerous evidence (structure formation, N-body simulations, etc) has a candidate for the dark matter particle with the mass in the range of few GeV - tens of TeV. If it were to decay of annihilate to Standard Model particles, such as photons and electrons/positrons, the spectrum of cosmic gamma-rays and electrons/positrons would have features in the range 100 MeV to 10 TeV.

On the one hand the strongest signal from annihilating or decaying dark matter is expected from a nearby source with the highest density. Such a source would be the galactic center or the source associated with the black hole at the center of the galaxy source 1FGL J1745.6-2900. The gamma-ray data for this source are available from HESS [1,2] in the range 200 GeV through 55 TeV and were first interpreted as multi-TeV dark matter in [6]. The analysis of the same region at lower energies (100 MeV - 100 GeV), based on FERMI data has been done by several authors

[3,5,4]. On the other hand a prospective dark matter candidate might also produce features in the spectrum of electrons and positrons in cosmic rays. The data on electrons and positrons are available (separately for positrons, electrons and combined) from PAMELA [7] in the range 1-625 GeV, from Fermi-LAT [8] in the range 20 GeV-1 TeV and HESS [9] in the range 370 GeV - 4.5 TeV. Data on electrons and positrons are available separately for PAMELA [10] and Fermi-LAT [11] in the range 20-200 GeV.

2 Fitting gamma rays from the galactic center

The total flux for a source observed in a solid angle $\Delta\Omega$ is

$$\phi_\chi(E) = \int_{\Delta\Omega} d\Omega\, \Phi_\chi(E,\psi) = \frac{dN}{dE_\gamma}(E)\frac{\langle\sigma v\rangle}{8\pi M_\chi^2}\int_\Delta \Omega \int_{los} \rho^2(r) dl\, d\Omega = \Phi_\chi(E) \times J \qquad (1)$$

The particle physics (and energy dependence) is contained in factor $\Phi_\chi(E)$, while the astrophysics is contained in J. We assume $\frac{dN}{dE_\gamma}$ to be a sum over annihilation channels $\frac{dN}{dE_\gamma} = \sum_i \frac{dN}{dE_i}$. In our analysis the sum runs over $\mu^+\mu^-$, $\tau^+\tau^-$ and $b\bar{b}$ annihilation channels. For the annihilation spectra of dark matter above 1 TeV we employ the spectra with electroweak corrections [12].

We try a few different models in order to find the best fit of the gamma ray flux of the source 1FGL J1745.6-2900. We try a power law of the form $Ae^{-\Gamma}$, a combination of a power law with a spectrum produced by annihilating dark matter $Ae^{-\Gamma} + \phi_\chi(E)$. We also try to fit the spectra dark matter annihilation spectra and a power-law $Ae^{-\Gamma} + \phi_{\chi_1}(E) + \phi_{\chi_2}(E)$. It is natural to assume a power-law as component of the spectrum associated with the synchrotron radiation. In each case we minimize χ^2 over the mass the dark matter candidate as well as normalization of the flux, the exponent of and the normalization of the power-law. We also minimize over the branching ratios to $\mu^+\mu^-$, $\tau^+\tau^-$ and $b\bar{b}$.

Just the power-law provides a fit with $A = 6.97 \times 10^{-8}$ and $\Gamma = 2.5$, $d.o.f. = 29+11-2 = 38$, $\chi^2/d.o.f. = 9.58$, see Fig.1. The power-law and a dark matter annihilation spectrum $Ae^{-\Gamma} + \phi_\chi(E)$ with $M = 18.2$ TeV and $B_{NFW} = 1.1 \times 10^3$ with the power-law described $A = 6.5 \times 10^{-8}$ and $\Gamma = 2.57$, $d.o.f. = 29 + 11 - 5 = 35$, and branching ratios of 60% to $\tau^+\tau^-$ and 40% to $b\bar{b}$ provides a fit with $\chi^2/d.o.f. = 4.76$. The power-law and a dark matter annihilation spectrum $Ae^{-\Gamma} + \phi_\chi(E)$ with $M = 37$ GeV with $A = 5.92 \times 10^{-8}$ and $\Gamma = 2.48$, $d.o.f. = 29 + 11 - 5 = 35$, and branching ratios of 40% to $\mu^+\mu^-$ and 60% to $b\bar{b}$ provides a fit with $\chi^2/d.o.f. = 8.94$.

In the case $M = 17.86$ TeV dark matter a boost factor of 1100 is required over the standard NFW profile, assuming $\Delta\Omega = 3 \times 10^{-6}$, corresponding to the definition of a point source given 0.1° resolution of HESS (we use $M_{MW} = 1.6 \times 10^{12} M_{Sun}$ [13] and $\rho(r = r_{Earth}) = 0.3\frac{GeV}{cm^3}$), in the case of $M = 38$ GeV dark matter the required boost factor is only 31.9. The spectra are plotted in figure 1.

The best fit with two dark matter spectra and a power-law provides $\chi^2/d.o.f. = 1.1$, ($d.o.f. = 29 + 11 - 10 = 30$). The parameters of the fit are $M_1 = 28$ GeV with $b_{\mu^+\mu^-} = 56\%$, $b_{\tau^+\tau^-} = 6\%$ and $b_{b\bar{b}} = 38\%$, and $M_2 = 18.2$ TeV $b_{\mu^+\mu^-} = 0\%$, $b_{\tau^+\tau^-} = 43\%$ and $b_{b\bar{b}} = 57\%$. The boost factors required to multiply the flux over the standard NFW profile defined above are $B_1 = 65$ and $B_2 = 1.6 \times 10^3$. The parameters of the power-law are $A = 4.06 \times 10^{-8}$ and $\Gamma = 2.6$. As there is no confirmation of the analysis of the galactic center region from Fermi team one should use them cautiously. We use the annihilation spectrum of dark matter of mass of about 30-40 GeV to model the corresponding feature in the spectrum, which could be a pulsar contribution.

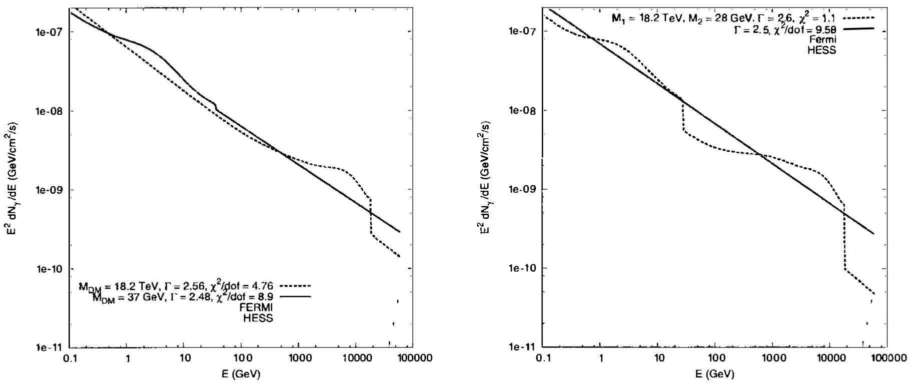

Figure 1: The fits to the gamma ray spectrum of the source 1FGL J1745.6-2900 (Fermi + HESS data). In the left inset the data are fit with the power law and a light dark matter annihilation spectrum (solid), possibly modeling a pulsar contribution, and with the power law and a heavy dark matter annihilation spectrum (dashed). In right inset the data are fit with just a power law (solid)and a power law and two dark annihilation spectra (dashed). See text for details.

3 Fitting electons and positrons

Since HESS measures the charged particles at highest energies, it does not discriminate between positive and negative charges. Therefore we perform the analysis on the flux of positrons and electrons, deriving the total flux for lower energies (Fermi and PAMELA) by adding up the fluxes of electrons and positrons. Henceforth we refer to "electrons and positrons" as to "electrons". We fit the spectrum of electrons and positrons by a combination of a power-law and the spectrum of electrons, produced by dark matter annihilating in the galactic halo with NFW profile. The propagation of electrons in the galaxy was handled by GALPROP [14].

We found that in accordance with previous research the spectrum of electrons can be well fitted with 3 TeV dark matter annihilating to $\tau^+\tau^-$.

We have also found that the damping of the spectrum below 10 GeV due to solar modulation [15,16] can be well modelled by $J_{TOA}(E) = \frac{E^2-m^2}{(E+|Z|e\phi)^2-m^2} J_{IS}(E+|Z|e\phi)$, where J_{TOA} is the flux at the top of the atmosphere and J_{IS} is the interstellar flux.

The electron spectra can be well fit by the annihilation spectra of 3 TeV dark matter going to $\tau^+\tau^-$ or 20 TeV dark matter going predominantly to $b_{b\bar{b}}$, when we marginalize over the potential of solar modulation ϕ, see Fig.2.

Conclusion

We have shown that the multi-TeV spectral feature in gamma rays from the galactic center as well as the feature in the electron flux can be both explained by spectra of dark matter of mass 18-20 TeV annihilating to a combination of $\tau^+\tau^-$ and $b_{b\bar{b}}$. The best fits however are achieved for different combinations of channels. Further studies are required to answer definitively if the same dark matter model can explain both phenomena: the uncertainties having an effect on the electron flux, such as, the distribution of dark matter (smooth halo vs. clumps) and the propagation of charged particles in the galaxy, as well as the uncertainties in the modeling of gamma-ray flux, need to be addressed. The considered model evades the Fermi constraints from dwarf galaxies, the antiproton constraints due to high mass of the dark matter particle. On the

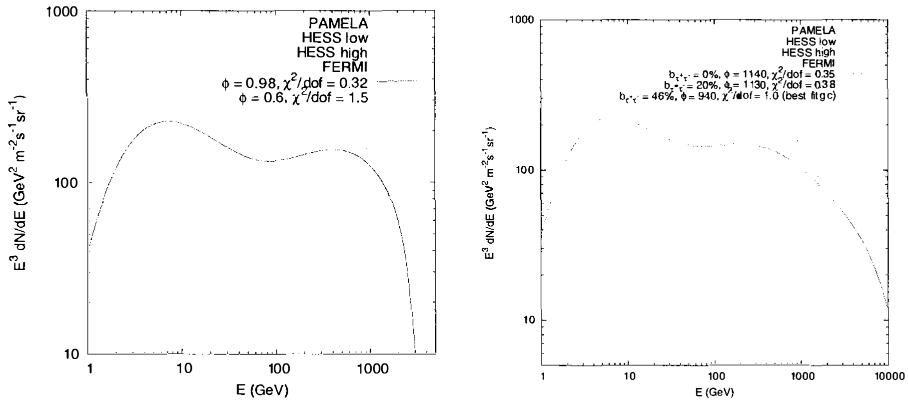

Figure 2: In the left inset the spectra are fitted by a power law and an electron/positron spectrum due annihilation of dark matter of mass 3 TeV into $\tau^+\tau^-$. In the first case the potential ϕ is kept fixed to a standard value 600 MV and $\chi^2 = 1.52$, in the second case the fit is optimized with $\phi = 980$ MV and delivers $\chi^2 = 0.32$. In the right inset the black, green and blue dotted lines correspond the electron spectra derived from 20 TeV dark matter annihilation spectra going to $b\bar{b}$ and $\tau^+\tau^-$ in different proportions. Higher value of ϕ (around 1000 MV) are required to obtain a reasonable fit compared to 3 TeV case.

other hand it consistent with the positron data.

Acknowledgments

We thank Marco Cirelli and Kathrin Egberts. AB was supported by a grant of 47th Rencontres de Moriond meeting.

References

1. F. Aharonian, et al., *Astron.Astrophys.* **425**, L13 (2004).
2. F. Aharonian, *Astron.Astrophys.* **503**, 817 (2009).
3. M. Chernyakova et al., *Phys. Lett.* B **726**, 60 (2011).
4. J. Cohen-Tanugi, talk given at 2nd Fermi symposium 2009; V. Vitale et al., Proceedings of the 2009 Fermi Symposium, 6 pages, eConf Proceedings C091122; C.Meurer, Heidelberg, GAMMA08 Proceedings.
5. D. Hooper et al., *Phys. Rev.* D **123005**, (2011).
6. S. Profumo, *Phys. Rev.* D **103521**, (2005).
7. O. Adriani et al., *Phys. Rev. Lett.* **201101**, (2011).
8. A. Abdo et al., *Phys. Lett.* B **62**, 183 (1976).
9. K. Egberts, Nucl.Instrum.Meth **A630**, 36 (2011).
10. O. Adriani et al., Nature **458**, 697 (2009).
11. M. Ackermann et al., *Phys. Rev. Lett.* **108**, 011103 (2012).
12. P. Ciafaloni et al., *JCAP* **1103**, 19 (2011).
13. O. Gnedin et al., *Astrophys. J.* **720**, L108 (2010).
14. A.W. Strong, arXiv:0907.0559.
15. L.J. Gleeson et al., *Astrophys. J.* **720**, L108 (2010).
16. P. Mertsch, PhD thesis, 2010.

Present and future dark matter searches with Imaging Atmospheric Cherenkov Telescopes

J-F. Glicenstein
DSM/IRFU, Service de Physique des Particules
CEA-Saclay, 91191 Gif-sur-Yvette, France

This paper gives a review of indirect dark matter searches with present and future Imaging Atmospheric Cherenkov Telescopes (IACT). Recent results published by H.E.S.S. towards the Galactic Halo and the Fornax cluster of galaxies, and by MAGIC and VERITAS towards the Segue 1 dwarf galaxy are given. Prospects for discovery or exclusion of dark matter annihilations with the planned CTA array are discussed.

1 Introduction

Imaging Atmospheric Cherenkov Telescopes (IACT) detect atmospheric gamma ray showers initiated by photons of energy between ~ 30 GeV and ~ 50 TeV. At present, there are 3 major IACT arrays: H.E.S.S., MAGIC and VERITAS. H.E.S.S. has started taking data in 2003 with four 107 m^2 reflectors. The HE.S.S array is located in the Khomas Highlands in Namibia. The telescopes are equipped with 960-pixel cameras in their focal planes. The field of view of the cameras is 5° and the effective energy threshold is ~ 100 GeV for a γ ray shower at zenith. A fifth telescope, with a 596 m^2 reflective area has been installed in 2012 and is in the commissioning phase. It is equipped with a 2048-pixel camera with a 3° field of view. The fifth telescope should lower the effective energy threshold of the H.E.S.S. array down to ~ 30 GeV. The MAGIC array started taking data in 2004 with a single 236 m^2 reflector located on the La Palma Canary island. A second telescope was installed in 2009. The showers are imaged by 576-pixel cameras located in the focal plane of the telescopes. The field of view is 3.5°. MAGIC telescopes can detect γ rays down to an energy of 60 GeV. The VERITAS collaboration operates an array of four 106 m^2 reflectors located in Arizona (USA). The telescopes are equipped with 499-pixel cameras in their focal planes. The field of view of the cameras is 3.5°, and the VERITAS array has an effective energy threshold of 100 GeV.

More than 100 high energy γ ray sources have been detected by present IACTs[a]. The largest fraction of the detected galactic sources are pulsar wind nebulae or supernova remnants. These objects are the likely birthplaces of galactic cosmic rays. The extragalactic sources are generally blazars, with some notable exceptions (Centaurus A, M87). Several "exotic" types of sources have also been detected such as starbust galaxies (NGC253). More informations on the goals and results of "Teraelectronvolt astronomy" can be found in the review by Hinton and Hofmann [1]. Observations by Very High Energy gamma ray instruments may also have some relevance to astroparticle physics and cosmology. Tests of fundamental laws such as Lorentz

[a] A catalog is avalaible online at address http://tevcat.uchicago.edu

invariance have been performed. Very strong constraints have been set on the spatial density of infrared extragalactic background light. Finally, WIMP (Weakly Interacting Massive Particles) dark matter models have been constrained. These constraints are the topic of the present review.

2 Dark matter searches with IACTs

The motivations for WIMPs models and the main WIMP candidates are given in the review by Bertone, Hooper and Silk[2]. The photon flux Φ_γ from dark matter annihilations in a cosmic target can be factorized as the product of a "particle physics dependent" factor times an "astrophysics dependent factor"

$$\frac{\mathrm{d}\Phi_\gamma(\Delta\Omega, E_\gamma)}{\mathrm{d}E_\gamma} = \frac{1}{8\pi}\left(\frac{\langle\sigma v\rangle}{m_{\mathrm{DM}}^2}\frac{\mathrm{d}N_\gamma}{\mathrm{d}E_\gamma}\right) \times \left(\bar{J}(\Delta\Omega)\Delta\Omega\right) , \tag{1}$$

with $\bar{J}$ defined as

$$\bar{J}(\Delta\Omega) = \frac{1}{\Delta\Omega}\int_{\Delta\Omega}\mathrm{d}\Omega\int_{\mathrm{los}}\rho^2[r(s)]\mathrm{d}s\,. \tag{2}$$

In equations (1) and (2), $\Delta\Omega$ is the solid angle of observation, ρ the dark matter density, m_{DM} the WIMP mass and $\langle\sigma v\rangle$ the velocity weighted cross-section for annihilation.

The particle physics term has to be estimated in the context of a specific model. Experimental groups often assume that that annihilating WIMPs are neutralino from the MSSM or $B^{(0)}$ bosons from Universal extra-dimension models. Other popular models are decaying dark matter and leptophilic models. Equation (1) is used to set limits on $\langle\sigma v\rangle$. Model independent limits can be obtained by assuming that pair of WIMPs annihilate with a branching ratio of 100% into pair of standard model particles such as W^+W^- or $b\bar{b}$.

Equation (2) shows that the dark matter clumpiness can increase the annihilation flux by several orders of magnitude, since $\bar{J} \propto \rho^2$. This effect has been studied with cosmological N-body simulations such as Via Lactea II[3] or Aquarius[4]. The enhancement effect as function of the observation angle was calculated by Abramovski et al[30] for the observation of the Fornax cluster of galaxies. It depends strongly on the free streaming mass M_{lim}. The boost factor due to clumpiness is $\sim$ 100 for wide field observations of the Fornax cluster of galaxies, assuming $M_{lim} = 10^{-6}\ M_\odot$. By constrast, the enhancement factor due to clumpiness is expected to be just a factor of a few for observations of dwarf galaxies.

Several other boosts can increase the annihilation flux. An example is the Sommerfeld effect[5]. The Sommerfeld is important for annihilations of cold dark matter particles in certain channels (e.g. to gauge bosons). Very high enhancement factors can be obtained for some specific values of the WIMP mass (see figure 2 of Lattanzi and Silk[5]). The Sommerfeld enhancement obtained at small WIMP relative velocities can reach $\sim$ 100 outside resonances. Radiative effects such the internal brehmstrahlung[6] are another potential source of annihilation flux boosts.

Annihilations of WIMPs into very high energy gamma rays have been searched towards massive cosmic objects such as the Galactic Center, the Galactic Halo, neighboring dwarf galaxies, globular clusters and clusters of galaxy. More speculative targets such as (resolved) dark matter clumps predicted by galactic formation simulations have also been searched for. The most recent results of these searches are given in the following sections.

3 The Galactic Center and the Galactic Halo

The Galactic Center and the Galactic halo are natural targets for indirect dark matter searches. A strong source, HESS J1745-290, has been observed at the Galactic Center by the major IACT collaborations. It is coincident with the SgrA* super massive black hole, but could be associated to other objects such as the the G359.95-0.04 pulsar wind nebula [8] . The spectrum of HESS J1745-290 is not compatible with the γ ray spectrum from the annihilation of a pair of WIMPs[7]. 99 % C.L. upper limits on the velocity weighted annihilation cross section of $\langle \sigma v \rangle \sim 10^{-23}$ $\mathrm{cm}^3\mathrm{s}^{-1}$ were obtained by the H.E.S.S. collaboration. However, these limits are very model dependent, since the dark matter density profile is not very well measured near the center of our galaxy. Less model dependent limits are obtained by studying the diffuse emission of the galactic halo close to the central region. The H.E.S.S. collaboration [9] has used data taken in a region of one degree around the Galactic center, with an exclusion zone in latitude $b \geq 0.3°$ to avoid the contamination by the diffuse emission of the galactic plane. A total of 112 hours were collected between 2004 and 2008. Figure 1 (left) shows the differential flux of observed γ ray candidates in the Galactic Halo region and the estimated background, which are in perfect agreement. The dark matter halo in the observation region was fitted by an Einasto profile. The results would not be affected by taking a NFW profile instead, however the choice of a cored profile would raise the limits by 3-4 orders of magnitude. The 95% C.L. limits on $\langle \sigma v \rangle$ as function of the WIMP mass are shown on figure 1 (right). They are the best currently available exclusion limits obtained by the IACT arrays.

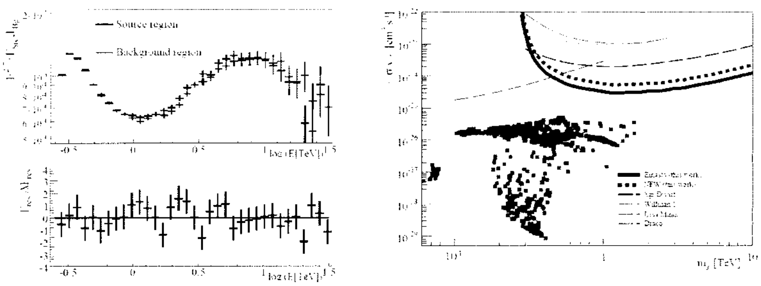

Figure 1: Left panel: Differential flux of gamma rays candidates from the Galactic Center halo and estimated background from misidentified hadrons, right panel: H.E.S.S. exclusion limits on dark matter from the analysis of the GC halo. Also shown are MSSM models and limits obtained by observations of dwarf galaxies (taken from F.Aharonian et al (2011) [9]

4 Dwarf Galaxies

The dynamics of dwarf galaxies is known to be dominated by dark matter. The dwarf galaxies are thus natural targets for dark matter searches. Their mass density profile is extracted from luminosity and velocity dispersion data by solving Jeans equation (see e.g Binney and Tremaine[10]). Unfortunately, in most cases several density profiles (cusped or cored) are allowed by a given set of data and result in $\bar{J}$ values which can differ by several order of magnitudes. The Canis Major[15], Sagittarius[16], Sculptor[17] and Carina dwarf galaxies have been observed by H.E.S.S., Draco[18], Segue 1[21,22], Ursa minor, Willman1[19] and Böotes by the MAGIC and VERITAS[20] collaborations.

4.1 Globular clusters

Globular clusters are massive objects which are not always easyly distinguished from dwarf galaxies, as seen on the left hand side of figure 2. This figure shows the distribution of nearby dwarf galaxies and galactic globular clusters in the (r_h, M_V) plane, where r_h is the half light radius and M_V the total visible magnitude. In the (r_h, M_V) plane, the separation of the two types of objects is obviously not clear-cut. In particular, the Segue 1 dwarf galaxy was classified as a globular cluster by Belokurov et al. [23]. However, recent observations [11] seems to favor the classification of Segue 1 as a dwarf galaxy.

Globular clusters are dynamic objects which evolve on a relaxation timescale smaller than the Hubble time. The stellar dynamics of globular clusters does not require a significant amount of dark matter. However, it has been argued [12] that metal-poor globular clusters were formed in dark matter minihaloes before galaxies. The Whipple collaboration [13] has searched for dark

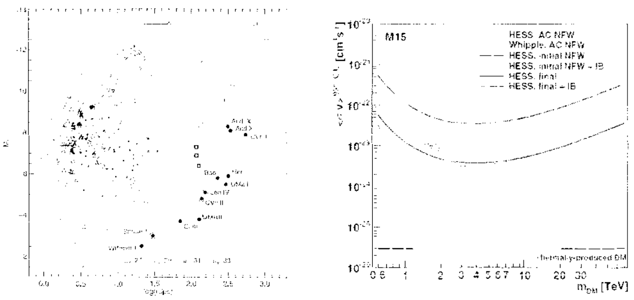

Figure 2: Left panel: Distribution of nearby dwarf galaxies and galactic globular clusters in the (r_h, M_V) plane (taken from Belokurov et al. [23]). Right panel: exclusion limits on $\langle \sigma v \rangle$ obtained on the M15 globular cluster by the H.E.S.S. collaboration. The various steps of the modelling and the Whipple-[13] upper limits are shown (taken from Abramovski et al. [14]).

matter annihilations in the M15 globular cluster. M15 is a metal-poor galactic globular cluster undergoing core collapse. The Whipple collaboration has argued that the dark matter halo of M15, if it exists, would have contracted adiabatically during the collapse of the stellar core. The contraction of the dark matter halo in turn leads to very large values of $\bar{J}$. M15 was also observed by the H.E.S.S. collaboration[14] during 15.2 hours. The model used by the H.E.S.S. collaboration takes into account the scattering of dark matter particles by stars in addition to the adiabatic compression of dark matter. The scattering of WIMPs occurs on the relaxation timescale of the M15 core and leads to a depletion of dark matter in the center. The exclusion limits obtained by H.E.S.S. are shown on the right hand side of figure 2. They are comparable to (but not better than) the limits obtained on dwarf galaxies.

4.2 Segue 1 dwarf galaxy

The Segue 1 dwarf galaxy was discovered in 2007 by Belokurov et al.[23] with the Sloan Digital survey. It is located at a distance of 23 ± 2 kpc from the Sun, at the intersection of 2 stellar streams: the Sagittarius and the Orphan stellar streams. It is one of the closest dwarfs, together with the Sagittarius and Canis Major dwarf. Only 71 stars of Segue 1 have been resolved. The limited stellat statistics impacts on the measurement of the central velocity dispersion σ, which is known with only a 50% uncertainty. This translates into uncertainties in the mass of Segue 1 of 100% and in $\bar{J}$ of a factor of at least 4. The MAGIC collaboration has taken 29.5 hours of high quality, single telescope data on Segue 1 in 2008-2009. The effective energy threshold for the observations was 100 GeV. The VERITAS collaboration has taken 48.7 hours of observations in 2010 and 2011 on the same target, with an effective energy threshold of 300 GeV. No signal was seen by either MAGIC or VERITAS. Both collaborations model the Segue 1 dark matter halo by an Einasto profile, as suggested in Essig et al [24]. The 95% exclusion limits obtained are shown on figure 3. The limit obtained by MAGIC is shown on the left panel.

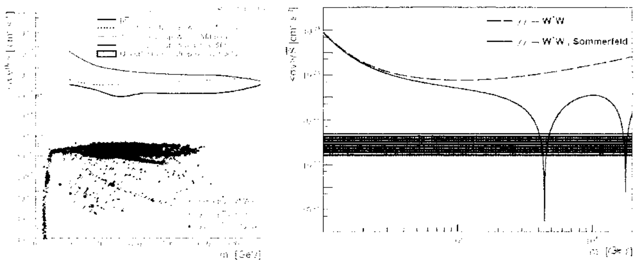

Figure 3: Left panel: 95% C.L. exclusion limits on $\langle\sigma v\rangle$ obtained by the MAGIC collaboration towards Segue 1. The hatched area shows the estimated astrophysical uncertainties (taken from Aleksić et al. [21]), right panel: 95% C.L. exclusion limits on $\langle\sigma v\rangle$ obtained by the VERITAS collaboration towards Segue 1. The solid line shows the effect of the Sommerfeld enhancement. The hatched area shows the thermal annihilation region (taken from Aliu et al [22]).

4.3 Sagittarius dwarf galaxy

The Sagittarius dwarf galaxy is located at a distance of 24 kpc in the Galactic plane. Because of its proximity to the sun, it was long thought to be one of the best target for indirect dark matter searches[27]. However, Sagittarius dwarf galaxy is experiencing strong tides from the Milky Way. This complicates its modelling. Constraints on a dark matter annihilation signal towards Sagittarius have been reported by the H.E.S.S. collaboration[16]. However these constraints were based on early, somewhat optimistic galactic models. Recently, several groups have published models of Sagittarius dwarf based on the study of the Sagittarius stellar stream. The dark matter constraints were revised in the light of these new models by Viana et al.[28]. The updated limits are shown on the l.h.s part of figure 4. The comparison with figure 1 (left) shows that the limits obtained are at the level of other dwarf galaxies. Viana et al.[28] study for the first time the astrophysical backgrounds to dark matter searches in dwarf galaxies. The M54 globular cluster at the center of Sagittarius dwarf is likely to harbor a population of millisecond pulsars. The collective emission of these pulsars could give a very high energy signal similar to that detected by the H.E.S.S. collaboration on the Terzan 5 globular cluster[29]. This signal could be detected by the future CTA array.

5 Galaxy clusters

Compared to dwarf galaxies, the galaxy clusters have the advantage of having less astrophysical uncertainties in their modelling, since the dark matter mass profile can be reconstructed with several tracers. Indeed, one can use stars (close to the center of the cluster), globular clusters, X-rays tracing the temperature of the gas in equilibrium in the gravitational potential, galaxies. Unfortunately, most clusters are too distant to give a signal detectable by IACTs.

The two closest galaxy clusters are the Virgo and Fornax clusters, both located at $\sim$ 15 Mpc. However, the Virgo cluster has the drawback of harboring the very high energy γ ray source M87 in its center. The H.E.S.S. collaboration has taken 14.5 hours of data towards the Fornax cluster in 2005. The energy threshold of observations was 260 GeV. The data were analyzed using three integration angles: 0.1°, 0.5° and 1°. The latter integration angle allows to take full advantage of the clumpiness boost factor.

The Fermi collaboration [31] has modelled the dark halo of Fornax with a NFW mass density profile with parameters fitted to the X-ray measurements. The corresponding model is called RB02 on figure 4 (right). Other dark halo models, based on the motion of dwarf galaxies (DW01) and globular clusters (RS08,SR10) have been investigated by the H.E.S.S. collaboration. The 95% exclusion limits on $\langle\sigma v\rangle$ obtained with the various models is shown on figure 4 (right).The integration angle is $0.1°$, appropriate for point sources. The uncertainty on the astrophysical factor $\bar{J}$ from the halo model is a factor 100, much smaller than for other targets.

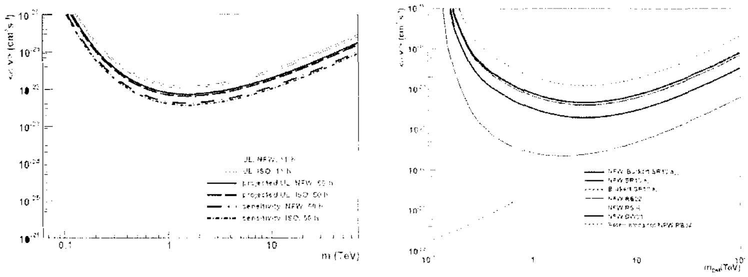

Figure 4: Left panel: Updated 95% C.L. exclusion limits on $\langle\sigma v\rangle$ obtained by A.Viana et al [28] towards the Sagittarius dwarf galaxy, using H.E.S.S. published data. The expected limit from CTA observation is also shown. Two different halo models of Sagittarius dwarf are used. Right panel: 95% C.L. exclusion limits on $\langle\sigma v\rangle$ obtained by the H.E.S.S. collaboration towards the Fornax cluster of galaxies. The integration angle is $0.1°$. Several dark halo models are shown. The limit obtained by the Fermi-LAT collaboration is also shown (taken from Abramovski et al [30]).

The upper limits on $\langle\sigma v\rangle$ can be improved by taking a larger integration radius of $1°$. The larger background of misidentified hadrons is more than compensated by the boost factor from unresolved clumps, as illustrated on figure 5. For the annihilation channels boosted by the Sommerfeld effect, the upper limits obtained by H.E.S.S. on the Fornax galaxy cluster are only one order of magnitude above the value $\langle\sigma v\rangle = 3\ 10^{-26}\ \mathrm{cm^3 s^{-1}}$ relevant for thermally produced WIMPs.

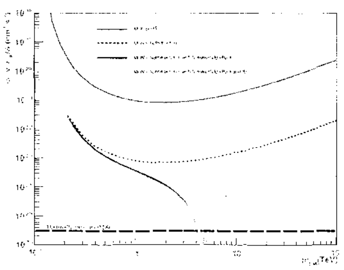

Figure 5: 95% C.L. exclusion limits on $\langle\sigma v\rangle$ obtained by the H.E.S.S. collaboration towards the Fornax cluster of galaxies.The integration angle is $1°$. The effect of the luminosity boost by substructures and the Sommerfeld enhancement are shown (taken from Abramovski et al [30])

6 Indirect dark matter search with CTA

The Cherenkov Telescope Array (CTA) is a proposed Very High Energy γ ray observatory. It will consist of two IACT arrays in the northern and southern hemisphere. Each of these arrays will have telescopes of several diameters to span the 30 GeV to 100 TeV energy range. The conceptual designs and the physics goals of CTA are described in Actis et al. [32]. CTA will achieve a 10 times better flux sensitivity compared to the previous generation of IACTs. The angular resolution will improve by a factor of 3.

Nieto et al. [33] have calculated the boost factor required for a CTA detection of the dark matter annihilation flux from dwarf galaxies. The result is shown on the left hand side of figure 6. For most dwarf galaxies, the detection of the photon flux from WIMP pair annihilations requires a boost factor of > 100. Unresolved clumps can only enhance the annihilation flux by a factor of a few in the case of dwarf galaxies. If the annihilation is boosted by the Sommerfeld effect, the total enhancement may reach a few tens outside resonances. If both enhacements are combined, a signal from Segue 1 or Willman 1 may be observed for values of $\langle\sigma v\rangle \sim 3\ 10^{-26}$ $\mathrm{cm^3s^{-1}}$ typical of thermally produced WIMPs.

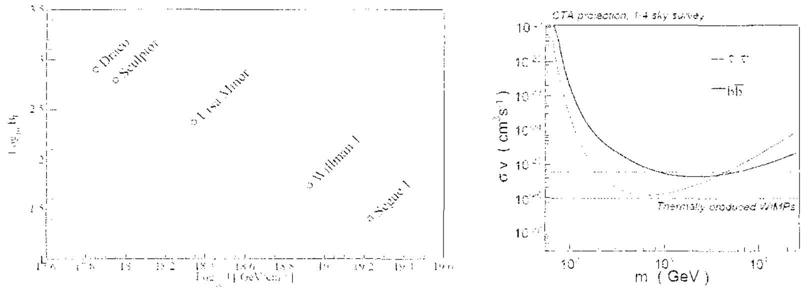

Figure 6: Left panel: Boosts factors required for a CTA detection of the annihilation flux of WIMPs in dwarf galaxies as a function of the astrophysical factor $J = \bar{J}\Delta\Omega$ (taken from Nieto et al [33]). Right panel: Exclusion limits on $\langle\sigma v\rangle$ from the survey of one fourth of the sky with CTA (taken from Brun et al [34])

It seems more promising to look for resolved dark matter clumps, as advocated by Brun et al [34]. The CTA observation program will include surveys of several regions of the sky. Brun et al. have assumed that one of these surveys will be similar to the H.E.S.S. galactic plane survey. The Via Lactea II [3] simulation was used to find the number of resolved clumps expected in the H.E.S.S. galactic plane survey. The Via Lactea II simulation finds a total of $\sim 10^4$ resolved halos with masses above 10^5 $M_\odot$ in the Milky Way. Only 168$\pm$44 of these clumps are in the fields covered by the H.E.S.S. galactic plane survey. Based on the observation of the galatic plane clumps, CTA should exclude velocity weighted cross-sections of respectively 2 10^{-25} and 10^{-24} $\mathrm{cm^3s^{-1}}$ for WIMP annihilations into $\tau^+\tau^-$ and $b\bar{b}$. These limits can be improved with a survey of one fourth of the sky. The sensitivity to the thermal annihilation region can be obtained by a survey of one fourth of the sky. Via Lactea II predicts that one fourth of the sky contains 3907 $\pm$ 324 clumps. With CTA, surveying one fourth of the sky would need only a few hundred hours of data taking. If no signal is seen, velocity weighted cross-sections at the level of $\langle\sigma v\rangle = 10^{-26}$ $\mathrm{cm^3s^{-1}}$ will be excluded. The corresponding 95% C.L. upper limits on $\langle\sigma v\rangle$ are illustrated on figure 6 (right).

7 Conclusion

IACT arrays have been searching for dark matter annihilations towards a large variety of targets. The best present upper limits on $\langle\sigma v\rangle$ have been achieved towards the Galactic halo [9]. The local group dwarf galaxies have the advantage of being neighboring objects whose dynamics is dominated by dark matter. However, their modelling is subject to large uncertainties. The best present upper limits on dwarfs are coming from the observation of Segue 1 [21,22]. The planned CTA array may observe a dark matter annihilation signal from Willman 1 or Segue 1 under favorable circumstances [33]. The observations of galaxy clusters such as Fornax [?] are promising since they lead to upper limits on the annihilation cross-section that have less astrophysical uncertainties than those obtained with dwarfs. For the annihilation channels which are affected by the Sommerfeld effect, the upper limit on $\langle \sigma v \rangle$ obtained with the observation of Fornax is only one order of magnitude above the thermal annihilation region. Last, the survey of a fourth of the sky by CTA may discover dark matter clumps [34] or put strong constraints on the dark matter annihilation cross-section.

References

1. J.Hinton and W.Hofmann, ARAA **47**, 523 (2009)
2. G.Bertone, D. Hooper and J.Silk, Phys. Report **405**, 279 (2005)
3. J. Diemand, M. Kuhlen, P. Madau, *et al.*, Nature **454**, 735 (2008)
4. V. Springel, S.D.M.White, C.S. Frenk, *et al.* nature **456**, 73 (2008)
5. M. Lattanzi and J. Silk, *Phys. Rev.* D **79**, 083523 (2009)
6. T.Bringmann, L. Bergström and J. Edsjö, JHEP **01**, 49 (2008)
7. F.Aharonian *et al,* (H.E.S.S. collaboration), *Phys. Rev. Lett.* **97**, 221102 (2006)
8. J.Hinton and F.Aharonian, ApJ **657**, 302 (2007)
9. A.Abramovski *et al.* (H.E.S.S. collaboration), *Phys. Rev. Lett.* **106**, 161301 (2011)
10. J.Binney and S.Tremaine, "Galactic dynamics",Princeton Series in astrophysics (2008)
11. G.D. Martinez *et al.*, ApJ **738**, 55 (2011)
12. P.J.E.Peebles, ApJ **277**, 470 (1984)
13. M.Wood *et al.* (Whipple collaboration) ApJ **678**, 594 (2008)
14. A.Abramovski *et al.* (H.E.S.S. collaboration), ApJ **735**, 12 (2011)
15. F.Aharonian *et al.* (H.E.S.S. collaboration), ApJ **691**, 175 (2009)
16. F.Aharonian *et al.* (H.E.S.S. collaboration) Astroparticle Physics **29**, 55 (2008), erratum Astroparticle Physics **33**, 274 (2010)
17. A. Abramovski *et al.* (H.E.S.S. collaboration) Astroparticle Physics **34**, 608 (2011)
18. J.Albert *et al.* (MAGIC collaboration) ApJ **679**, 428 (2008)
19. E.Aliu *et al.* (MAGIC collaboration) ApJ **697**, 1299 (2009)
20. V.A.Acciari *et al.* (VERITAS collaboration) ApJ **720**, 1174 (2010)
21. J.Aleksić *et al.* (MAGIC collaboration), *JCAP* **06**, 35 (2011)
22. E.Aliu *et al.* (VERITAS collaboration), *Phys. Rev.* D **85**, 062001 (2012)
23. V.Belokurov *et al.* ApJ **654**, 897 (2007)
24. R. Essig, N.Sehgal, L.E. Strigari, M.Geha and J.D.Simon, *Phys. Rev.* D **82**, 123503 (2010)
25. M. Niederste-Ostholt, V. Belokurov, N.W. Evans, G. Gilmore, R.F.G. Wyse and J.E Norris, MNRAS **398**, 1771 (2009)
26. J.D.Simon, M. Geha, Q.E.Minor *et al.*, ApJ **7 33**, 46 (2011)
27. N.W.Evans, F.Ferrer and S.Sarkar, *Phys. Rev.* D **69**, 123501 (2004)
28. A. Viana *et al.* ApJ **746**, 77 (2009)
29. A.Abramovski *et al.* Astron. Astrophys. **531**, L18 (2011)
30. A. Abramovski *et al.* (H.E.S.S. collaboration), ApJ **750**, 123 (2012)
31. M.Ackermann *et al.* (Fermi-LAT collaboration) JCAP **05**, 25 (2010)
32. M.Actis *et al.* (CTA consortium) Experimental Astronomy **32**, 193 (2011)
33. D.Nieto, T.Hassan, N.Mirabal, J-A. Barrio, J-L Contreras and the CTA consortium, proceedings of the 32nd International Cosmic Ray Conference, Beijing (2011)
34. P. Brun, E. Moulin, J. Diemand, J.F Glicenstein, *Phys. Rev.* D **83**, 015003 (2011)

Constraints on the Galactic Halo Dark Matter from Fermi-LAT Diffuse Measurements

G. Zaharijas
Institut de Physique Théorique, CEA/Saclay, F-91191 Gif sur Yvette, France

International Center for Theoretical Physics, Trieste, Italy

J. Conrad, A. Cuoco, Z. Yang
Department of Physics, Stockholm University, AlbaNova, SE-106 91 Stockholm, Sweden

The Oskar Klein Centre for Cosmoparticle Physics, AlbaNova, SE-106 91 Stockholm, Sweden

(for the *Fermi* LAT collaboration)

We have performed an analysis of the diffuse gamma-ray emission with the Fermi Large Area Telescope in the Milky Way Halo region searching for a signal from dark matter annihilation or decay. We consider both gamma rays produced directly in the dark matter annihilation/decay and produced by inverse Compton scattering of the e^+/e^- produced in the annihilation/decay. Conservative limits are derived requiring that the dark matter signal does not exceed the observed diffuse gamma-ray emission. A second set of more stringent limits is derived based on modeling the foreground astrophysical diffuse emission. The resulting limits impact the range of particle masses over which dark matter thermal production in the early Universe is possible, and challenge the interpretation of the PAMELA/Fermi-LAT cosmic ray anomalies as annihilation of dark matter.

1 Introduction

The Milky Way halo has long been considered a good target for searches of indirect signatures of dark matter (DM). WIMP DM candidates are expected to produce gamma rays, electrons and protons in their annihilation and decays and such emission, in our halo would appear as a diffuse signal. The majority of the Galactic diffuse emission is produced through radiative process of cosmic-ray (CR) electrons and nucleons injected by energetic astrophysical sources and represents a strong background for DM searches.

In this analysis we test the diffuse LAT data for a contribution from the DM signal by performing a fit of the spectral and spatial distributions of the expected photons at the intermediate Galactic latitudes. In doing so, we take into account the most up-to-date modeling of the diffuse signal of astrophysical origin, adapting it to the problem in question [1]. Efficient modeling of the diffuse gamma-ray emission needs an accurate description of both the interstellar gas and radiation targets as well as the distribution of CRs in the Galaxy. Those parameters are typically correlated with the assumed DM content and it is thus important to consider them since they affect directly the DM fit. Besides this approach, we will also quote conservative upper limits using the data only (i.e. without performing any modeling of the astrophysical background).

We follow[2] in using the GALPROP code v54[3], to calculate the propagation and distribution of CRs in the Galaxy the whole sky diffuse emission. In[2] various standard parameters of the CR propagation were studied in a fit to CR data and it was shown that they represent well the gamma-ray sky, although various residuals (at a $\sim$ 30% level[2]), remain. In our work, we use the results of the fits to the CR data from[2] but we allow for more freedom in certain parameters governing the CR distribution and astrophysical diffuse emission and constrain these parameters by fitting the models to *the LAT gamma-ray data.* Despite the large freedom we leave in the models we see residuals in our ROI at the $\pm 30\%$ level and at $\sim 3\,\sigma$ significance. These residuals can be ascribed to various limitations of the models: imperfections in the modeling of gas and ISRF components, simplified assumptions in the propagation set-up, unresolved point sources, and large scale structures like Loop I[4] or the Galactic Bubbles[5]. Since residuals do not seem obviously related to DM, we decide to focus in the following on setting limits on the possible DM signal, rather than *searching* for a DM signal.

2 DM maps

We parametrize the smooth DM density ρ with a NFW spatial profile $\rho(r) = \rho_0\, R_s/r\ (1 + r/R_s)^{-2}$ and a cored (isothermal-sphere) profile: $\rho(r) = \rho_0\, (R_\bullet^2 + R_c^2)\ /\ (r^2 + R_c^2)$. For the local density of DM we take the value of $\rho_0 = 0.43$ GeV cm^{-3}, and the scale radius is assumed to be $R_s =$ 20 kpc (NFW) and $R_c = 2.8$ kpc (isothermal profile). We also set the distance of the solar system from the center of the Galaxy to the value $R_\bullet = 8.5$ kpc. For the annihilation/decay spectra we consider three channels with distinctly different signatures: annihilation/decay into the $b\bar{b}$ channel, into $\mu^+\mu^-$, and into $\tau^+\tau^-$. In the first case gamma rays are produced through hadronization and pion decay and the resulting spectra are similar for all channels in which DM produces heavy quarks and gauge bosons in the energy range considered here. The choice of leptonic channels is motivated by the PAMELA positron fraction[6] and the *Fermi* LAT electrons plus positrons[7] measurements. In this case, gamma rays are dominantly produced through radiative processes of electrons, as well as through the Final State Radiation (FSR). We produce the DM maps with a version of GALPROP slightly modified to implement custom DM profiles and injection spectra (which are calculated by using the PPPC4DMID tool described in[8]).

3 Approach to set DM limits

We use 24 months of LAT data in the energy range between 1 and 100 GeV (but, we use energies up to 400 GeV when deriving DM limits with no assumption on the astrophysical background). We use only events classified as gamma rays in the P7CLEAN event selection and the corresponding P7CLEAN_V6 instrument response functions (IRFs)[a]. Structures like Loop I and the Galactic Bubbles appear mainly at high Galactic latitudes and to limit their effects on the fitting we will consider a ROI in Galactic latitude, b, of $5^\circ \leq |b| \leq 15^\circ$, and Galactic longitude, l, $|l| \leq 80^\circ$. Furthermore, we mask the region $|b| \lesssim 5$ deg along the Galactic Plane, in order to reduce the uncertainty due to the modeling of the astrophysical and DM emission profiles.

DM limits with no assumption on the astrophysical background: To set these type of limits we first convolve a given DM model with the Fermi IRFs to obtain the counts expected from DM annihilation. The expected counts are then compared with the observed counts in our ROI and the upper limit is set to the *minimum* DM normalization which gives counts in excess of the observed ones in at least one bin, i.e. we set 3σ upper limits given by the requirement $n_{iDM} - 3\sqrt{n_{iDM}} > n_i$, where n_{iDM} is the expected number of counts from DM in the bin i, and n_i the actual observed number of counts.

[a]http://fermi.gsfc.nasa.gov/ssc/

DM limits with modeling of astrophysical background: We use a combined fit of DM and of a parameterized background model and we consider the uncertainties in the background model parameters through *the profile likelihood method.* The linear part of the fit is performed with `GaRDiAn`, which for each fixed value of DM normalization θ_{DM} finds the $\vec{\alpha}$ parameters which maximize the likelihood and the value of the likelihood itself at the maximum.

CR source distributions (CRSDs) are modeled from the direct observation of tracers of SNR and can be observationally biased. As this is a critical parameter for DM searches, we define a parametric CRSD as sum of *step functions* in Galactocentric radius R, and treat a normalization of each step as a free parameter in R, *in a fit to gamma rays.* In order to have conservative and robust limits we set to zero the e, p CRSDs in the inner Galaxy region, within 3 kpc of the Galactic Center. In this way, potential e and p CR sources which would be required in the inner Galaxy will be potentially compensated by DM, producing conservative constraints. The linear part of the fits is then performed by combining the sky maps produced in each ring of CRSD of the main components of the diffuse emission: the emission from π^0 decay, bremsstrahlung and inverse Compton. Additionally an isotropic component arising from the extragalactic gamma-ray background and misclassified charged particles needs to be included to fit the *Fermi* LAT data. The outlined procedure is then repeated for each set of values of the non-linear propagation and injection parameters to obtain the full set of profile likelihood curves. We scan over the three parameters: electron injection index, the height of the diffusive halo and the gas to dust ratio which parametrizes different gas column densities. In this way we end up with a set of k profiles of likelihood $L_k(\theta_{DM})$, one for each combination of the non-linear parameters. The envelope of these curves then approximates the *final* profile likelihood curve, $L(\theta_{DM})$, where all the parameters, linear and non-linear have been included in the profile. Limits are calculated from the profile likelihood function by finding the $\theta_{DM,lim}$ values for which $L(\theta_{DM,lim})/L(\theta_{DM,max})$ is $\exp(-9/2)$ and $\exp(-25/2)$, for 3 and 5 σ C.L. limits, respectively.

4 Results

Despite the various conservative choices described above, the resulting limits are quite stringent. Upper limits on the velocity averaged annihilation cross section into various channels are shown in Fig. 1, for isothermal profile of the DM halo, together with regions of parameter space which provide a good fit to PAMELA (purple) and *Fermi* LAT (blue) CR electron and positron data[9]. They are comparable with the limits from LAT searches for a signal from DM annihilation/decay in dwarf galaxies [10]. In particular, as shown in Figure 1 for masses around 20 GeV the thermal relic value of the annihilation cross section is reached, both for the $b\bar{b}$ and $\tau^+\tau^-$ channels.

References

1. M. Ackermann *et al.* [The Fermi-LAT collaboration], arXiv:1205.6474v1[astro-ph.CO].
2. M. Ackermann *et al.* [The Fermi-LAT collaboration], arXiv:1202.4039 [astro-ph.HE].
3. A. W. Strong, I. V. Moskalenko and O. Reimer, Astrophys. J. **537**, 763 (2000)
4. J. -M. Casandjian, I. Grenier [The Fermi-LAT collaboration], [arXiv:0912.3478 [astro-ph.HE]].
5. M. Su, T. R. Slatyer, D. P. Finkbeiner, Astrophys. J. **724**, 1044-1082 (2010).
6. O. Adriani *et al.* [PAMELA Collaboration], Nature **458**, 607 (2009)
7. A. A. Abdo *et al.* [The Fermi LAT Collaboration], Phys. Rev. Lett. **102**, 181101 (2009)
8. M. Cirelli *et al.*, JCAP **1103** (2011) 051
9. M. Cirelli, P. Panci, P. D. Serpico, Nucl. Phys. **B840** (2010) 284-303.
10. M. Ackermann *et al.* [Fermi-LAT Collaboration], Phys. Rev. Lett. **107**, 241302 (2011)

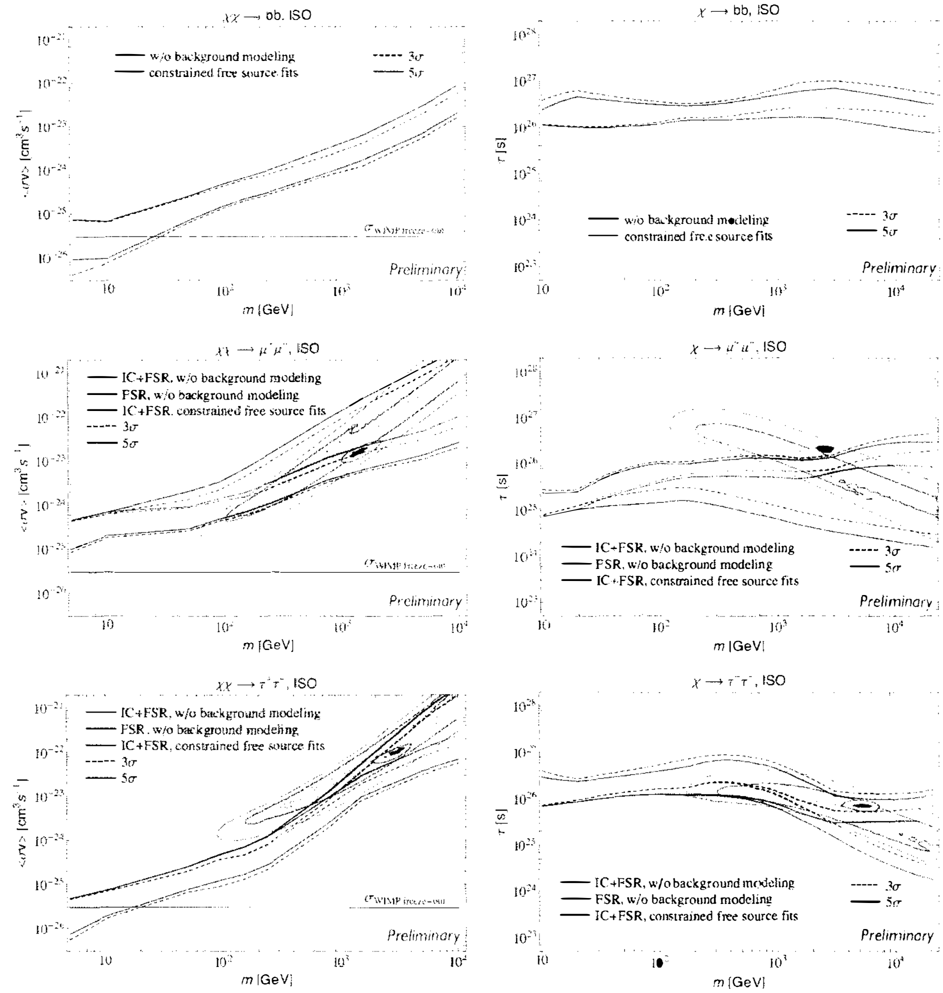

Figure 1: Upper limits on the velocity averaged DM annihilation cross-section (left) and decay time (right) including a model of the astrophysical background compared with the limits obtained with no modeling of the background. Limits are shown for $b\bar{b}$ (upper), $\mu^+\mu^-$ (middle) and $\tau^+\tau^-$ (lower panel) channels, for a DM distribution given by the isothermal distribution. The horizontal line marks the thermal decoupling cross section expected for a generic WIMP candidate. The regions of parameter space which provide a good fit to PAMELA (purple) and *Fermi* LAT (blue) CR electron and positron data are also shown.

Indirect searches for dark matter particles at Super-Kamiokande

P. MIJAKOWSKI
FOR THE SUPER-KAMIOKANDE COLLABORATION
National Centre For Nuclear Research, 00-681 Warsaw, Poland

This work presents indirect searches for dark matter as WIMPs (Weakly Interacting Massive Particles) using atmospheric neutrino data of Super-Kamiokande-I, -II and III (1996-2008). The results of two analyses are discussed: (1) search for WIMP annihilations in the Sun and (2) search for WIMP-induced neutrinos from the Milky Way halo. We looked for an excess of WIMP-induced neutrino signal from the Sun/Milky Way as compared to the expected atmospheric neutrino background. No excess of the neutrino signal was observed in any of the analyses. Corresponding limit (1) on the spin-depenedent WIMP-nucleon cross section $\sigma_{\chi N}$ and limit (2) on the WIMP self-annihilation cross section $\langle\sigma_A V\rangle$ were derived as a function of the mass of relic particles.

1 Search for dark matter from the Sun

There is a compelling evidence that ordinary baryonic matter composes only 4% of the total mass-energy of the Universe which is dominated by dark energy (73%) and dark matter (23%) components of the unknown nature. [1] Some well motivated candidates for the dark matter (DM) particle are provided by supersymmetric theories. [2] They belong to a collective group of particles referred to as WIMPs (Weakly Interacting Massive Particles). WIMPs may be attempted to observe directly or indirectly through detection of the products of their annihilations.

It is expected that heavy celestial objects like the Sun can gravitationally bound WIMPs. [4] Relic particles could accumulate in its core and effectively annihilate there. Neutrinos, as one of the annihilation products, can escape from dense matter region of the Sun's core and could be detected using neutrino telescopes, like Super-Kamiokande (SK) detector. [3]

In the following analysis, the Sun is assumed to be a point source of neutrinos and the search is conducted for the limited angular range around its position on the sky. We look for an excess of neutrino events from direction of the Sun as compared to the expected atmospheric neutrino background in the same angular range (Fig. 1). The data set used in this analysis consists of upward-going muons which are produced in $\nu_\mu/\bar{\nu}_\mu$ interactions below the SK detector [a]. The upward-going muons are categorized into (1) through-going associated with showers or (2) non-showering or (3) muons which stops inside the detector. The search is sensitive to WIMP masses (M_χ) in a range from 10 GeV/c^2 to 10 TeV/c^2.

Various half-cone angles around the Sun were examined and no excess of events was found above expected atmospheric background (Fig. 2). The size of the investigated cone-half angle was determined for each considered M_χ in a way that it should contain 90% of the flux of neutrinos from WIMP annihilations either into $b\bar{b}$ (soft channel) or into W^+W^- (hard channel).

[a] Upward-going muons are due to $\nu_\mu/\nu_{\bar{\mu}}$ interactions which take place outside the detector. On the contrary, downward-going muons are dominated by muons produced in cosmic ray showers. Flux of cosmic ray muons is not entirely suppressed by the rock above the detector, while it is effectively reduced from the directions below the horizon.

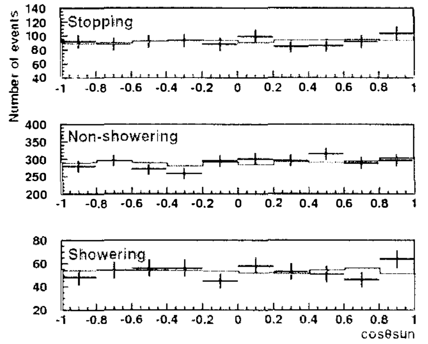

Figure 1: Angular distribution of upward-going muons with respect to the Sun ($\cos\theta_{Sun} = 1$ corresponds to direction of the Sun). Crosses indicate the observed data along with statistical uncertainties (livetime: 3109.6 days). Solid lines indicate atmospheric neutrino Monte Carlo normalized to the total number of data events in each category and after taking into account neutrino oscillations with $\sin^2 2\theta_{23} = 1$ and $\Delta m^2_{23} = 0.0025$ eV^2. See Tanaka *et al.* [4]

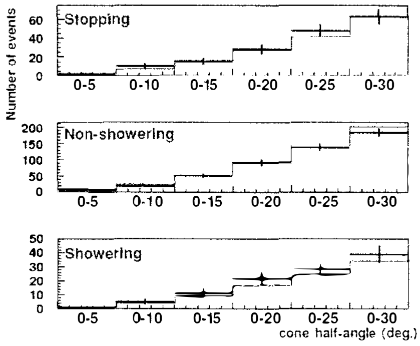

Figure 2: The expanded view of the angular distribution of upward-going muons around the Sun. Here, 0 degrees corresponds to the direction of the Sun. All symbols are the same as in Fig. 1.

Based on the null contribution of DM-induced neutrinos from the Sun, the upper limit on the flux of upward-going muons induced by WIMPS was derived. [4] It is often assumed in literature that capture rate of WIMPs in the Sun and their annihilation rate are in equilibrium. Therefore, the obtained limit on upward-going muon flux can be related to the limit on spin-dependent WIMP-nucleon cross section due to expected interactions of WIMPs on hydrogen in the Sun. [4] Constrains on the spin-dependent cross section are presented in Fig. 3 for the soft and hard annihilation channels. Obtained limit can be compared against results of direct detection experiments. In particular, this constraint excludes DAMA allowed region. [6]

2 Search for dark matter from the Galactic Halo

This analysis is focused on the search for a signal arising from a diffuse source of dark matter annihilation in the Milky Way halo. Maximum intensity of the signal is expected from the region of the Galactic Center (GC) according to the most common DM halo models. [12] Therefore, the expected angular distribution of DM-induced neutrino events should be sharply peaked from the GC direction.

The energy spectrum of WIMP-induced neutrinos is model dependent. We consider various DM annihilation modes: direct WIMP annihilation into pair of neutrinos, $\chi\chi \dashrightarrow \nu\bar{\nu}$, which lead to equal flux of neutrinos of every flavor; annihilations into $b\bar{b}$; and into W^+W^-. In soft and hard annihilation channels neutrinos are mainly created in decays of mesons produced during hadronization of primary quarks. In $\nu\bar{\nu}$ mode DM-induced neutrinos are monoenergetic and their energy equals the mass of the annihilating relic particles. DarkSUSY [5] simulator package was used to obtain neutrino energy spectra for different DM annihilation modes. We take into account neutrino oscillations over galactic scales and simulated expected WIMP-induced neutrino signal in the detector. The data set of Super-Kamiokande-I, -II, -III was investigated for the presence of expected signal signatures. The data set corresponds to 2805.9 live-days for contained neutrino events and 3109.6 live-days for upward-going muons.

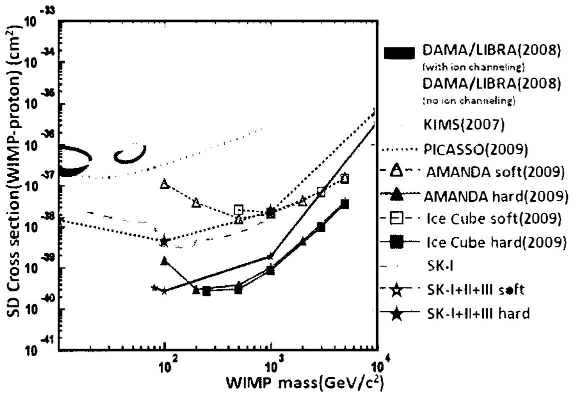

Figure 3: Upper 90% CL limits on the WIMP-proton spin-dependent cross section as a function of the WIMP mass (above lines is excluded). Limits from direct detection experiments: DAMA/LIBRA allowed region [6] (dark red and light red filled, for with and without ion channeling, respectively), KIMS [7] (light blue crosses), and PICASSO [8] (grey dotted line). Limits from indirect detection experiments (neutrino telescopes): AMANDA [9] (black line with triangles), IceCube [10] (blue line with squares), and this analysis (red line with stars). The previous limit from Super-Kamiokande [11] (green dashed line) is also shown.

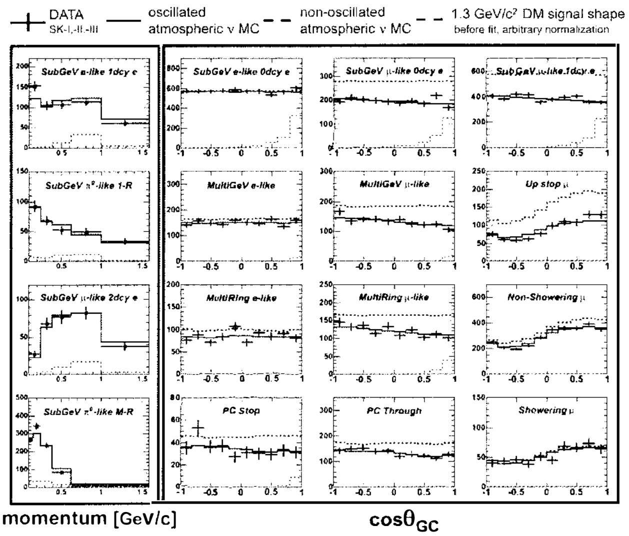

Figure 4: Illustration of a signal from direct annihilation of DM particles of $M_\chi = 1.3$ GeV/c^2 into pair of $\nu\bar{\nu}$. SK samples used in a fit are presented. SK data (black points with errors), best fit atmospheric MC with and without oscillations (blue solid and black dotted lines, respectively) and DM signal (red dashed lines) are shown with respect to the direction of the Galactic Center ($\cos\theta_{GC} = 1$ corresponds to the direction of the Galactic Center) or using the distributions of lepton momentum. Equal flux of all neutrino flavors is expected for the DM-induced neutrinos. The signal contribution is shown before fit and its normalization is enhanced for the illustration purpose. In a fit, the angular distributions shown in the figure are also binned using the lepton momentum information and relative contribution of samples is conserved during χ^2 minimization.

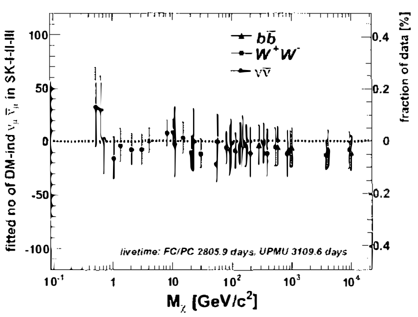

Figure 5: Fitted number of $(\nu_\mu + \bar{\nu}_\mu)$ events from DM annihilation into $\nu\bar{\nu}$ (red circles), $b\bar{b}$ (black triangles), W^+W^- (blue squares) as a function of the mass of DM particles.

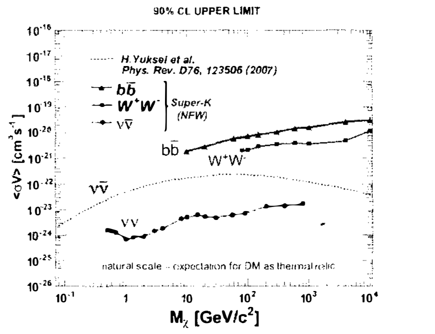

Figure 6: 90% CL upper limit on DM self-annihilation cross section $\langle \sigma_A V \rangle$ (above lines is excluded). SK limit for $\nu\bar{\nu}$ (red circles), $b\bar{b}$ (black triangles), W^+W^- (blue squares) annihlation modes is based on expected signal intensity (DM density) from NFW halo profile. [12] The limit obtained by Yuksel *et al* [13] is indicated as black dotted line (*Halo Average*).

It is assumed that collected data could be described by two components: DM-induced neutrinos (signal) and atmospheric neutrinos (background). We try to find the best combination of signal and background that would fully explain the data. We allow to vary estimation of atmospheric neutrino background as well as the hypothetical contribution from simulated DM signal. Fit is based on momentum and angular information of all collected neutrino events. Angular distributions refer to cosine of the angle between reconstructed lepton direction and direction of the GC. The effect of 119 systematic uncertainty terms is included in the procedure. The signal was simulated for a wide range of DM particle masses and is simultaneously fitted in all neutrino flavors. The illustration of the samples used in a fit is shown in Fig. 4.

No significant signal contribution is allowed by the data in addition to the atmospheric neutrino oscillation effect as shown in Fig. 5. Therefore, corresponding limit on DM-induced diffuse neutrino flux and DM self-annihilation cross section $\langle \sigma_A V \rangle$ were derived as a function of M_χ. The upper 90% CL limit on $\langle \sigma_A V \rangle$ is shown in Fig. 6.

References

1. D. Larson *et al*, *Astrophys. J. Suppl.* **192**, 16 (2011).
2. G. Bertone, D. Hooper, J. Silk, *Phys. Rept.* **405**, 279-390 (2005).
3. S. Fukuda *et al*, *Nucl. Instrum. Methods* A **501**, 418 (2003).
4. T. Tanaka *et al*, *Astrophys. J.* **742**, 78 (2011).
5. P. Gondolo, J. Edsjo, P. Ullio, L. Bergstrm, M. Schelke and E. A. Baltz, *J. Cosmology Astropart. Phys.* **07**, 008 (2004).
6. C. Savage *et al*, *J. Cosmology Astropart. Phys.* **04**, 010 (2009).
7. H. S. Lee *et al*, *Phys. Rev. Lett.* **99**, 091301 (2007).
8. S. Archambault. *et al*, *Phys. Lett.* B **682**, 185 (2009).
9. J. Braum and D. Hubert, *Proceedings of the 31st ICRC, Lodz, Poland* (2009).
10. G. Wikstrom and J. Edsjo, *J. Cosmology Astropart. Phys.* **04**, 009 (2009).
11. S. Desai *et al*, *Phys. Rev.* D **70**, 083523 (2004).
12. J. F. Navarro, C. S. Frenk and S. D. M. White, *Astrophys. J.* **462**, 563 (1996).
13. H. Yuksel, S. Horiuchi, J.F. Beacom, S. Ando, *Phys. Rev.* D **76**, 123506 (2007).

INDIRECT DARK MATTER SEARCHES WITH ICECUBE

E. STRAHLER for the ICECUBE COLLABORATION[a]
Interuniversity Institute for High Energies, Vrije Universiteit Brussel,
Pleinlaan 2, Brussels 1050, Belgium

IceCube is a cubic kilometer scale neutrino detector buried deep in the Antarctic ice. The detector consists of 5160 optical modules deployed on 86 strings between 1450 m and 2450 m of depth. Of these, 8 strings comprise a densely packed subarray in the deepest, clearest ice called DeepCore, which extends the sensitivity of neutrino searches below 100 GeV. Data taken with partial detector configurations have been used to search for neutrino signals of dark matter annihilations in the Sun, halo, and galactic center. We present the latest results of these searches as well as the projected sensitivity of the full detector.

1 Introduction

Weakly Interacting Massive Particles (WIMPs) are one of the most promising dark matter candidates. [1] In the Minimally Supersymmetric Standard Model (MSSM), the WIMP can take the form of the lightest neutralino [2]. These neutralinos accumulate in the center of massive objects and self-annihilate to standard model particles, including neutrinos. Event rates and energies depend on the specific model of dark matter under consideration and the astrophysics of the environment. Taking these variables into consideration leads to an expectation of a few to a few 10^2 neutrinos per year between GeV and TeV energies.

2 The IceCube Telescope

IceCube is located in the glacial ice at the geographic South Pole, and consists of an array of digital optical modules (DOMs), designed to collect the Cherenkov radiation produced by high energy, neutrino-induced leptons traveling through the detector volume. By recording the arrival times and intensities of these photons, the direction and energy of the parent neutrino may be reconstructed.

IceCube consists of 86 'strings', each containing 60 DOMs, deployed between 1450 m and 2450 m in the ice[3]. Of these, 8 strings at the center of IceCube comprise the DeepCore subarray, consisting of more densely instrumented strings and DOMs with higher light collection efficiency, intended to lower the energy threshold of IceCube below 100 GeV. In total, approximately one cubic kilometer is instrumented. Each DOM consists of a 25 cm photomultiplier tube and associated digitization and communication electronics, enclosed in a glass pressure sphere [4].

While the large ice overburden provides a shield against downward going, cosmic ray induced muons, most analyses use the Earth as a veto and focus on upward going neutrinos. Additionally, low energy analyses may focus on DeepCore as a fiducial volume and use the surrounding

[a]see http://icecube.wisc.edu/collaboration/authors/current for full author list

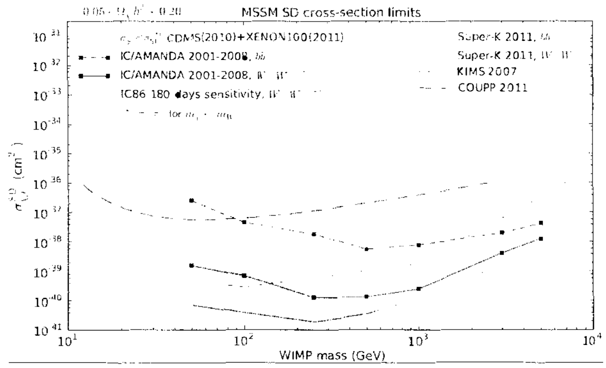

Figure 1: Limits on the spin-dependent $\chi - p$ scattering cross section. Results from the 8 year combined IceCube-AMANDA analysis are shown along with the predicted sensitivity for the completed detector. The shaded region depicts the model space allowed by direct detection experiments.

IceCube strings as an active veto to reduce penetrating muon backgrounds. Further background reduction is achieved by topological signatures that differentiate well-reconstructed neutrinos from misreconstructed muons.

3 Dark Matter from the Sun

As the Sun passes through the galaxy, dark matter particles from the halo may become bound in the gravitational potential of the solar system. These particles may then scatter weakly with solar nucleons and lose energy, becoming trapped by the Sun. Over time, this leads to a steady accumulation of dark matter in the center of the Sun where it may then self-annihilate, generating a flux of neutrinos which is spectrally dependent on the annihilation channel and neutralino mass.

Several such searches for WIMP annihilation in the center of the Sun have been performed using partial configurations of IceCube as well as its predecessor AMANDA. Recently, the results of these searches have been combined in a unified likelihood analysis [5]. All observations are in agreement with the background-only hypothesis, and upper limits have been set on both the spin-dependent (SD) and spin-independent (SI) WIMP-nucleon scattering cross sections. While SI cross sections are well constrained by direct dark matter searches, solar capture is dominated by SD processes, and thus this IceCube-AMANDA result represents the most stringent SD limit to date over a wide energy range. These SD limits are shown in Fig. 1. With this analysis, we are beginning to probe the still-allowed supersymmetry parameter space, and the full 86-string detector will be able to constrain a wide range of models.

4 Dark Matter from the Earth

Similarly to the Sun, dark matter may concentrate and annihilate in the center of the Earth. This will produce a unique signature of directly vertical neutrino-induced muons in IceCube. Model predictions for WIMP capture in the Earth favor low masses, which means that the DeepCore detector will play an important role in a search for such a signal. While this is a low background analysis, there are several notable difficulties. Primarily, the unique directionality of the signal, while creating a highly restricted data region, makes it impossible to create an off-source data sample for background determination. For this reason, simulation must be used to

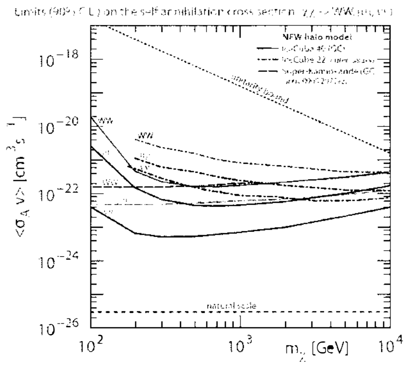

Figure 2: Limits on the dark matter self-annihilation cross-section, shown for an average (NFW) galactic density profile. Limits derived from Super-K data are shown for comparison.

understand the background, necessitating a detailed understanding of systematic uncertainties. An analysis using data taken with the full 86 string detector is underway, and it is expected that the sensitivity will improve on previous results [6] by at least an order of magnitude.

5 The Galactic Halo

The expected neutrino flux from self-annihilation in the galactic halo can be derived from an assumed dark matter halo density profile integrated along the line of sight, convolved with a channel-dependent dark matter annihilation spectrum. A search was conducted using the 22-string configuration of IceCube for such annihilations. [7] This search focused on the outer halo and looked for a large scale anisotropy in the neutrino event rate from the region surrounding the galactic center, and a region diametrically opposite. No such anisotropy was observed, and limits were set on the self-annihilation cross-section for various potential annihilation channels. With the 40-string IceCube detector, a veto was developed allowing to select downgoing neutrino events starting within the detector volume, opening up searches to the direction of the galactic center. As in the 22-string search, observations were in agreement with the expected backgrounds and limits were set, shown in Fig. 2. [8] The results of these analyses are competitive with limits derived from Super-Kamiokande data. [9] It is expected that the IceCube limits will improve substantially when using the full detector and the improved vetoing capabilities introduced with DeepCore.

6 Dwarf Spheroidals

Dwarf spheroidal galaxies are attractive targets for indirect dark matter searches due to their proximity, compact nature, and high dark matter mass fraction. We have performed a sensitivity study for several dwarf galaxies in the northern hemisphere using data taken with the 59-string configuration of IceCube. For this study, the dark matter distribution in these galaxies has been assumed to follow a Navaro-Frenk-White (NFW) profile. [10] Sensitivities have been derived for individual galaxies, as well as a combined sensitivity from a stacking of those sources with the highest expected neutrino fluxes. [8] Results for the $\tau^+\tau^-$ decay channel can be seen in Fig. 3. While we see that γ-ray observatories are significantly more sensitive at low energies, IceCube has the advantage that data is collected continuously, and that our analyses extend to higher WIMP masses.

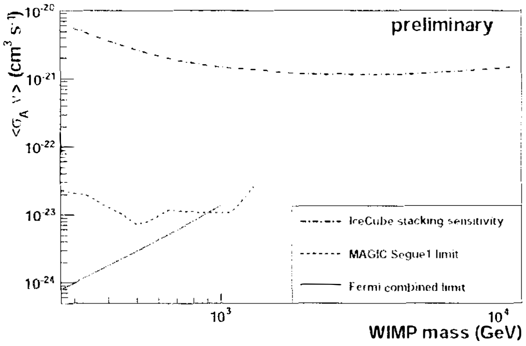

Figure 3: Sensitivity to the dark matter self-annihilation cross-section in the $\tau^+\tau^-$ channel, shown for a stacking of 4 dwarf spheroidal galaxies. Limits from MAGIC [11] and Fermi [12] for similar sources are shown for comparison.

7 Outlook

The IceCube detector has been fully deployed since December 2010, with 86 strings in the ice, and datataking with the full array began in May 2011. Included is the DeepCore subarray of 8 densely instrumented strings , which will reduce the energy threshold of IceCube to around 10 GeV. DeepCore should increase the sensitivity of IceCube to low WIMP masses as well as allowing the measurement of neutrino oscillation. In addition, by using the surrounding IceCube strings as a veto, it is possible to extend searches to the southern sky, including the galactic center.

We have performed several searches for dark matter annihilations using partial IceCube configurations. To date, no dark matter signal has been detected from any source and limits have been placed on both the spin-dependent and spin-independent WIMP-nucleon scattering cross sections as well as on the self annihilation cross section. It is anticipated that within the next few years IceCube will strongly improve these limits, constraining a variety of dark matter models, or will observe indirect evidence of dark matter annihilation.

References

1. J.P. Ostriker *et al.*, *Astrophys. J. Lett.* **193**, L1 (1974).
2. M. Drees and M.M. Nojiri, *Phys. Rev.* D **47**, 376 (1993).
3. A. Achterberg *et al.* (IceCube Collaboration), *Astropart. Phys.* **26**, 155 (2006).
4. R. Abbasi *et al.* (IceCube Collaboration), *Nucl. Inst. Meth.* **A601**, 294 (2009).
5. R. Abbasi *et al.* (IceCube Collaboration), *Phys. Rev.* D **85**, 042002 (2012).
6. J. Ahrens *et al.* (AMANDA Collaboration), *Phys. Rev.* D **66**, 032006 (2002)
7. R. Abbasi *et al.* (IceCube Collaboration), *Phys. Rev.* D **84**, 022004 (2011).
8. IceCube Coll, 32nd ICRC, Beijing 2011, *arXiv* 1111.2738.
9. J. Hisano, K. Nakayama, M.J.S. Yang, *Phys. Lett.* B **678**, 101 (2009).
10. J. F. Navarro, C. S. Frenk and S. D. M. White, *Astrophys. J.* **462**, 563 (1996).
11. J. Aleksic *et al.* (MAGIC Collaboration), *JCAP* **1106**, 035 (2011).
12. M. Ackermann *et al.* (Fermi-LAT Collaboration), *Phys. Rev. Lett.* **107**, 241302 (2011)

Status and results from the ANTARES neutrino telescope

C. RIVIÈRE*, for the ANTARES collaboration
*CPPM, Aix-Marseille Université, CNRS/IN2P3, Marseille, France

ANTARES is the largest neutrino telescope in the Northern hemisphere. Located in the Mediterranean Sea, it is operating in its full 12 lines configuration since 2008. We report here recent results on the search for magnetic monopole, the measurement of the neutrino oscillation parameters and the indirect search for dark matter.

1 Introduction

The ANTARES neutrino telescope[1] is composed of 12 detection lines of 75 photosensors each. It is located at about 40 km from the French coast at a depth of 2475 m in the Mediterranean Sea, and was completed in May 2008. Since then, the effective maintenance of the detector has assured a continuous data taking. The first goal of ANTARES is the search for high energy neutrino of cosmic origins, observing the Cherenkov light emitted by the muon produced by the interaction of up-going neutrinos at the vicinity of the detector. ANTARES presents assets such as the low light diffusion of deep sea water and a low energy threshold which makes it interesting for also other searches, such as the ones presented here.

2 Relativistic magnetic monopoles

Magnetic monopoles have not been observed so far but arise in many models of spontaneous symmetry breaking[2]. For velocities above the Cherenkov threshold, they would emit at least 8000 times more photons that a muon of the same velocity. Below the Cherenkov threshold, they would still produce measurable indirect light produced by δ-rays for velocities $\beta > 0.5$.

A track reconstruction algorithm where the velocity β is a free parameter was developed for this analysis. The ratio λ of the reconstruction qualities Q, $\lambda = log(\frac{Q(\beta=1)}{Q(\beta=free)})$ was used as a discriminative variable in this search, together with the total charge of the reconstructed track. The distributions of these variables are represented in Fig. 1.

The data from 2008 have been analysed looking for up-going monopole events. The cuts of the analysis were optimized blindly based on Monte Carlo. After unblinding of the data, no

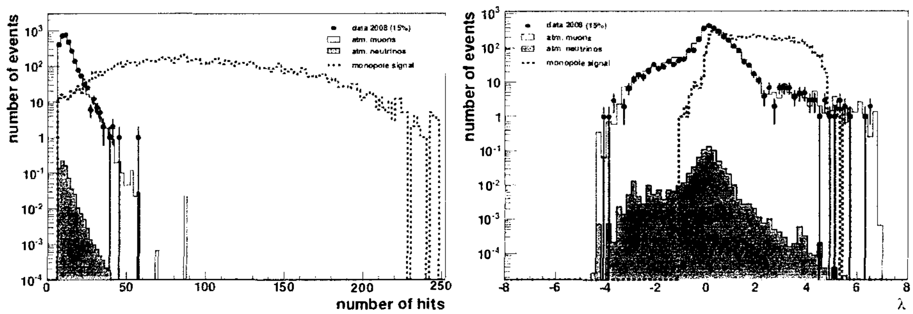

Figure 1: Distributions of the number of hits per event (left) and of the discriminant variable λ (right). The black points represent the data, the dashed line the simulated signal while the green and blue histograms represent the background from atmospheric muons and neutrinos.

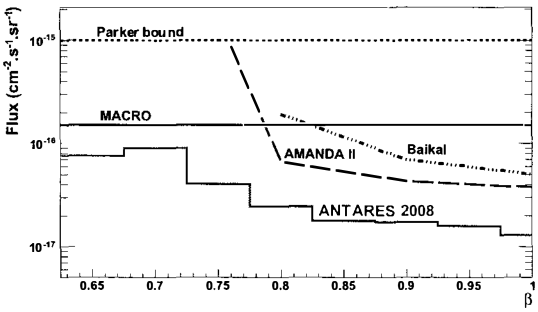

Figure 2: The ANTARES 90% C.L. upper limit on an up-going magnetic monopole flux obtained by this analysis.

significant excess of signal-like events was found. The limits obtained, presented on Fig. 2, are the most stringent obtained in this β range. Details of this analysis can be found in ref.[3].

3 Neutrino oscillations

The low energy threshold of ANTARES ($E_\nu > 15$ GeV) makes it sensitive to neutrino oscillations. Most of the observed neutrinos are ν_μ created by the interaction of cosmic rays in the atmosphere on the other side of the Earth. The survival probability of atmospheric ν_μ in the two flavour approximation is given by

$$P(\nu_\mu \rightarrow \nu_\mu) = 1 - \sin^2 2\theta_{32} \sin^2 \left(\frac{1.27 \Delta m_{32}^2 L}{E_\nu} \right) = 1 - \sin^2 2\theta_{32} \sin^2 \left(\frac{16200 \Delta m_{32}^2 \cos\Theta}{E_\nu} \right) \quad (1)$$

where E_ν is the neutrino energy and $L = D_{Earth} \cdot \cos\Theta$ is the travel path of the neutrino through Earth in km. With $\Delta m_{32}^2 = 2.43 \cdot 10^{-3}$ eV^2 and $\sin^2 2\theta_{32} = 1$ (world average values[2]), the vertical up-going ν_μ are completely suppressed for an energy of 24 GeV, which is close to the ANTARES threshold.

The neutrino energy is approximated in this analysis by the following formula

$$E_R = 0.2 \cdot (z_{max} - z_{min}) / \cos\Theta_R \text{ GeV} \quad (2)$$

where the highest and lowest hits of the track are used together with the reconstructed zenith to estimate the muon range.

Figure 3 left represents the expected distribution of $E_\nu / \cos\Theta$ obtained from Monte Carlo in the no-oscillation scenario and in the oscillation scenario. As the azimuth angle is not used and low energy events are of particular interest for this analysis, single-line events were used in addition to the multi-line events.

The measured distribution of $E_R / \cos\Theta_R$ is depicted on Fig. 3 right. The scenario with no oscillation is rejected with a confidence level around 98%. The best fit is obtained for $\Delta m_{32}^2 = 3.1 \cdot 10^{-3}$ eV^2 and $\sin^2 2\theta_{32} = 1.00$. The 68% C.L. contour for this measurement is represented on Fig. 4, and the measurement is compatible with other experiments. Details of the analysis can be found in ref.[4].

This measurement also confirms that ANTARES is sensitive to neutrinos with energies down to a few tens of GeV and that systematic errors are under control, making it interesting for dark matter searches.

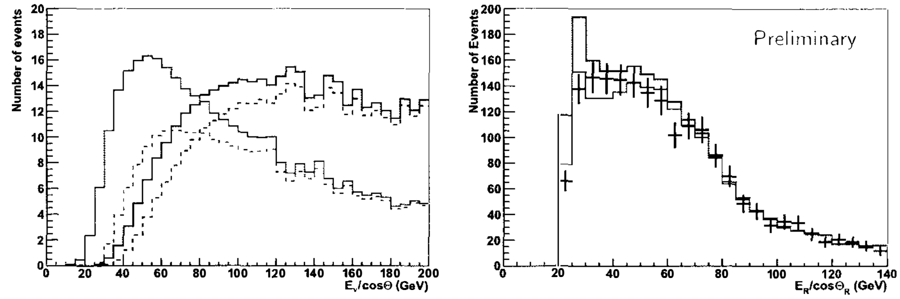

Figure 3: ***Left:*** Distribution of true $E_\nu/\cos\Theta$ for the atmospheric neutrino simulation. The solid lines are without neutrino oscillations, the dashed lines with oscillations assuming world average values[2]. The single-line sample is in red histograms, the multi-line in blue. ***Right:*** Distribution of reconstructed $E_R/\cos\bullet_R$ for selected single and multi-line events. Black crosses are data, whereas the blue histogram shows simulations without oscillations. The red histogram shows the result of the fit of the oscillation parameters Δm^2_{32} and θ_{32}.

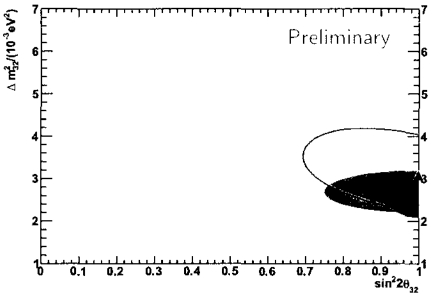

Figure 4: 68% C.L. contour (red) of the neutrino oscillation parameters as derived from the fit of the $E_R/\cos\bullet_R$ distribution. The best fit point is indicated by the triangle. The solid filled regions show results at 68% C.L. from K2K (green), MINOS (blue) and SuperK (magenta) for comparison.

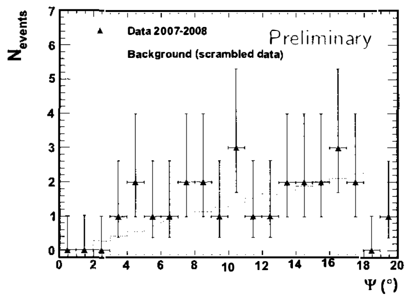

Figure 5: Blue: expected number of background events as a function of the distance from the Sun, obtained from scrambled data. Black: Number of events observed in data after unblinding.

4 Indirect dark matter search in the Sun

Massive objects such as the Earth, the Sun or the Galactic centre have the possibility to trap dark matter, enhancing its local density and thus increasing the annihilation rate. Such annihilations should produce neutrinos which can be used to track dark matter.

An analysis of the ANTARES data from 2007 to 2008 has been performed recently. An excess of neutrino events is searched in a cone around the Sun direction, while it is below the horizon. The cone radius and event selection criteria have been optimized using a blind strategy, using only off-zone data for the background and Monte Carlo for the signal, for different values of WIMP mass and various annihilation channels.

After unblinding, no significant excess of event was observed, as seen in Fig. 5, allowing to derive upper limits on the neutrino flux induced by dark matter annihilation.

We present here the limits on the spin-dependent cross-section $\sigma_{H,SD}$ of the WIMP with proton. These limits are computed assuming equilibrium between the capture rate and the annihilation rate in the Sun. A conservative model of halo was used, with an isothermal bubble

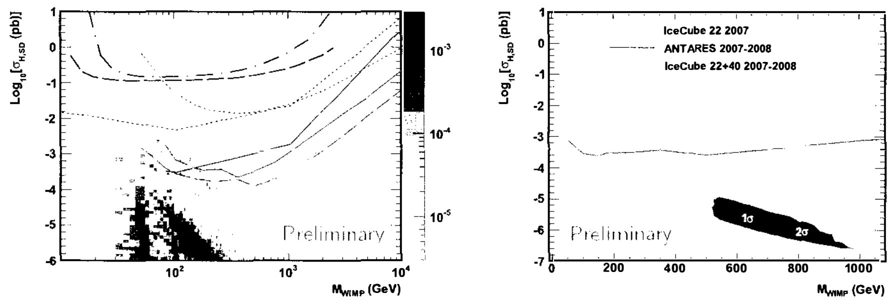

Figure 6: ***Left:*** 90% C.L. upper limits on the spin-dependent cross-section in the CMSSM model, as a function of the WIMP mass. Limits from other experiments are shown for comparison. Results of this analysis are in red ($\tau^+\tau^-$ channel: dashed, W^+W^-: continuous, $b\bar{b}$: dotted). Limits from IceCube (green), SuperK (Blue), KIMS and COUPP (black) are shown for comparison. Part of the allowed parameter space is also shown in grey scale[5]. ***Right:*** 90% C.L. upper limits on the spin-dependent cross-section in the mUED model, as a function of the WIMP mass. Limits from IceCube are shown for comparison. The allowed parameter space is also shown in grey scale[6].

around the galaxy with a local density of 0.3 GeV/cm^3. No extra disk was added in the galaxy, and diffusion in the solar system by Jupiter was taken into account.

On Fig. 6 left, the red curves represent the 90% C.L. upper limits on the $\sigma_{H,SD}$ cross section, for the soft channel $b\bar{b}$ in dotted line, for the hard channels W^+W^- and $\tau^+\tau^-$ in plain and dashed line. Thanks to the low energy threshold of ANTARES, the limits set using 2007–2008 data are similar to the one set by AMANDA/IceCube40 using 2001–2008 data. Some of the allowed parameter space of CMSSM can be excluded.

On Fig. 6 right, similar limits are shown for mUED model. ANTARES can extend IceCube limits in the low energy range, but the limits are still not testing the currently favoured parameter space.

5 Outlook

Some recent results of the ANTARES neutrino telescope were presented. The limit on the flux of magnetic monopoles of velocity $\beta \in [0.6, 1[$ are the best to date. The low energy threshold of ANTARES also allows observing neutrino oscillation, the measured value being compatible with measurement from other experiments. No significant signal have been found in the indirect search of dark matter signal from the Sun with the 2007–2008 data, and limits have been put which are the best to date in some regions of the parameter space. With increased data set and further analysis, these results will improve in the future.

References

1. M. Ageron *et al.*, *Nucl. Instrum. Methods* A **656**, 11–38 (2011) (arXiv:1104.1607).
2. K. Nakamura *et al.*, (Particle Data Group), *J. Phys.* G **37**, 075021 (2010).
3. S. Adrián-Martínez *et al.*, Astropart. Phys **35**, 634–640 (2012) (arXiv:1110.2656).
4. S. Adrián-Martínez *et al.*, submitted to *Phys. Lett.* B (arXiv:1206.0645).
5. F. Feroz *et al.*, *Journal of High Energy Phys.* **6**, 1029–8479 (2011) (arXiv:1101.3296).
6. G. Bertone *et al.*, *Phys. Rev.* D **83**, 036008 (2011) (arXiv:1010.2023).

Constraining Dark Matter annihilation cross-sections with the Cosmic Microwave Background

Silvia Galli
UPMC Univ Paris 06, UMR7095, Institut d'Astrophysique de Paris, F-75014, Paris, France.
CNRS, UMR7095, Institut d'Astrophysique de Paris, F-75014, Paris, France

The injection of secondary particles produced by dark annihilation around redshift $\sim$ 1000 would inevitably affect the process of recombination, leaving an imprint on cosmic microwave background (CMB) temperature and polarization anisotropies. We show that the most recent CMB measurements provided by the WMAP satellite mission and the ACT telescope place interesting constraints on DM self-annihilation rates. Our analysis includes an accurate treatment of the time-dependent coupling of the DM annihilation energy with the thermal gas. We present constraints for specific models of dark matter annihilation channels, as well as a model-independent approach to calculate constraints with future experiments, based on a principal components analysis. We show that current data place already stringent constraints on light DM particles, ruling out thermal WIMPs with mass $m \lesssim$ 10GeV annihilating into electrons and WIMPs with mass $m \lesssim$ 4GeV annihilating into muons. Finally, we argue that upcoming CMB experiments such as Planck, will improve the constraints by at least 1 order of magnitude, thus providing a sensitive probe of the properties of DM particles.

1 Introduction

The measurements of the Cosmic Microwave Background (CMB) flux provided by a number of different experiments, such as WMAP [1] and ACT [2] , have confirmed several aspects of the cosmological standard model and improved the constraints on several cosmological parameters. A key ingredient in the CMB precision cosmology is the accurate computation of the recombination process, occurring at redshift $z_r \sim 1000$. Recombination modeling, while not simple, involves only well-understood conventional physics, and the latest models are thought to be accurate at the sub-percent level required for the future Planck [3] satellite mission [4 5]. While the attained accuracy on the recombination process is impressive, it should be noticed that non-standard mechanisms could produce percent level modifications that are potentially observable in CMB data.

Dark Matter (DM) annihilation is one of these possible mechanisms, as it produces extra-Lyman-α and ionizing photons that can change the evolution of recombination. This kind of process has received particular attention in the last years as it could be one of the possible origins of the excess of positrons and electrons measured in cosmic rays by different experiments, such as PAMELA [7], ATIC [8] and FERMI [9].

Annihilation of dark matter particles during the epoch of recombination produces high-energy photons and electrons, which heat and ionize the hydrogen and helium gas as they cool. The result is an increased residual ionization fraction after recombination, giving rise to a low-redshift tail in the last scattering surface. The broader last scattering surface damps correlations

$p_{ann}[cm^3/s/GeV]$ at 95% c.l.	
WMAP5	$< 3.6 \times 10^{-27}$
WMAP7	$< 2.5 \times 10^{-27}$
WMAP7+ACT	$< 2.2 \times 10^{-27}$
Planck	$< 3.1 \times 10^{-28}$
CVI	$< 1.1 \times 10^{-28}$

Table 1: Upper limit on p_{ann} at 95% c.l. from current WMAP observations and future upper limits achievable from the Planck satellite mission and from a cosmic variance limited experiment.

between temperature fluctuations, while enhancing low multipole correlations between polarization fluctuations. With the WMAP results and the future Planck[3] data, it becomes conceivable these deviations may be detected.

2 Annihilating Dark Matter and CMB

The interaction of the shower produced by dark matter annihilation with the thermal gas has three main effects: i) it ionizes the gas, ii) it induces Ly-α excitation of the Hydrogen and iii) it heats the plasma. The first two modify the evolution of the free electron fraction x_e, the third affects the temperature of baryons. The imprint of self-annihilating dark matter in CMB angular power spectra can be quantified with the annihilation parameter $p_{ann} = f(z) < \sigma v > /m_\chi$ where $< \sigma v >$ is the effective self-annihilation rate, m_χ the mass of our dark matter particle and $f(z)$ indicates the fraction of energy which is absorbed *overall* by the gas, under the approximation that the energy absorption takes place locally. The fraction $f(z)$ depends on redshift, on the dark matter model and on the annihilation channel, and has been calculated by e.g. Slatyer et al.[10] for different cases.

2.1 Constraints with a constant f

In Galli et al. [11] and Galli et al. [12] we reported constraints on the p_{ann} parameter obtained using WMAP data, WMAP plus ACT data and using simulated data for the Planck experiment and for a hypotetical cosmic variance limited experiment, under the simplifying assumption that the fraction $f(z)$ is constant with redshift. This approach has the advantage of being model independent, but is clearly less accurate than implementing the whole redshift dependence of the $f(z)$ parameter, as we will show in the next section. Results for the constant $f(z) = f$ case are reported in Tab. 1. As one can notice, WMAP7 data improve the constraint of a factor ~ 1.4 compared to WMAP5 data, due to a better measurement of the third peak of the temperature power spectrum at $l \sim 1000 - 1200$ and of the second dip in the temperature-polarization power spectrum at $l \sim 450$. Furthermore, Planck is expected to improve constraints of about an order of magnitude. This is due to the high precision measurement of the CMB polarization that Planck is expected to deliver, and that will be able to break several degeneracies between the annihilation parameter and other cosmological parameters such as the scalar spectral index n_s.

2.2 Constraints with a model dependent $f(z)$

In Galli et al.[12] we also considered the more accurate case where the fraction f is not just a constant, but it varies with redshift according to the calculations of Slatyer et al. [10]. We chose specific values of the mass, model and annihilation channel of the dark matter particle we wanted to test, selected the corresponding $f(z)$ and then calculated the constraints on the annihilation cross-section $< \sigma v >$ with WMAP7 and ACT data. Results for different masses of dark matter particles annihilating in an electron/positron pair are reported in Table 2. Although

$< \sigma v >$ in [cm^3/s] with Variable f				
m_χ[GeV]	channel	WMAP7	WMAP7+ACT	
1 GeV	e^+e^-	$< 2.90 \times 10^{-27}$	$< 2.41 \times 10^{-27}$	
100 GeV	e^+e^-	$< 3.95 \times 10^{-25}$	$< 3.55 \times 10^{-25}$	
1TeV	e^+e^-	$< 4.68 \times 10^{-24}$	$< 3.80 \times 10^{-24}$	
$< \sigma v >$ in [cm^3/s] with Constant $f = f(z = 600)$				
m_χ[GeV]	channel	WMAP7	WMAP7+ACT	$f(z = 600)$
1 GeV	e^+e^-	$< 2.78 \times 10^{-27}$	$< 2.41 \times 10^{-27}$	0.87
100 GeV	e^+e^-	$< 3.87 \times 10^{-25}$	$< 3.35 \times 10^{-25}$	0.63
1TeV	e^+e^-	$< 4.02 \times 10^{-24}$	$< 3.48 \times 10^{-24}$	0.60

Table 2: Upper limits on self-annihilation cross section at 95% c.l. using WMAP7 data and a combination of WMAP7 and ACT data . On the top part of the table we show the results obtained using the proper variable $f(z)$ for each model. On the bottom part, for sake of comparison, we show the results obtained by taking the constraints for a constant generic f reported in Table 1, and then calculating $< \sigma v >$ for each case imposing that f is equal to the corresponding $f(z = 600)$ for each model. We show results for particles annihilating in an electron/positron pair only.

the implementation of the z-dependence of f clearly leads to more accurate results, we found that taking a simplified analysis with constant f, such that $f(z = 600) = f_{const}$, leads to a difference with respect to the full $f(z)$ approach of less than $\sim 15\%$, depending on the annihilation channel considered.

2.3 A principal component approach

The constraints obtained in the previous section are precise only for specific models of dark matter. In Finkbeiner et al. [13] we proposed an approach to obtain precise model independent constraints, that could however take into account the redshift dependence of the fraction f. The method exploits the fact that the effects of energy deposition by dark matter annihilation at different redshifts on the CMB spectra are not uncorrelated. Any arbitrary energy deposition history can be decomposed into a linear combination of orthogonal basis vectors, with orthogonal effects on the observed CMB power spectra (C_ℓ's). For a broad range of smooth energy deposition histories, the vast majority of the effect on the C_ℓ's can be described by a small number of independent parameters, corresponding to the coefficients of the first few vectors in a well-chosen basis. These parameters in turn can be expressed as (orthogonal) weighted averages of the energy deposition history over redshift. We employ principal component analysis (PCA) to derive the relevant weight functions, and the corresponding perturbations to the C_ℓ spectra. In Fig.1 we show the first three principal components for WMAP7, Planck and a CVL experiment, both before and after marginalization over the cosmological parameters.

For generic energy deposition histories that are currently allowed by WMAP7 data, we find up to 3 principal component coefficients are measurable by Planck and up to 5 coefficients are measurable by an ideal cosmic variance limited experiment. Fig. 2 shows the contraints on the coefficients of the first 3 principal components obtainable from the WMAP7 data, and from simulated data for Planck and a cosmic variance limited experiment, assuming no dark matter annihilation.

1. Larson, D., Dunkley, J., Hinshaw, G., et al. 2011, APJS, 192, 16
2. Fowler, J. W., et al. 2010, *Astrophys. J.*, 722, 1148.

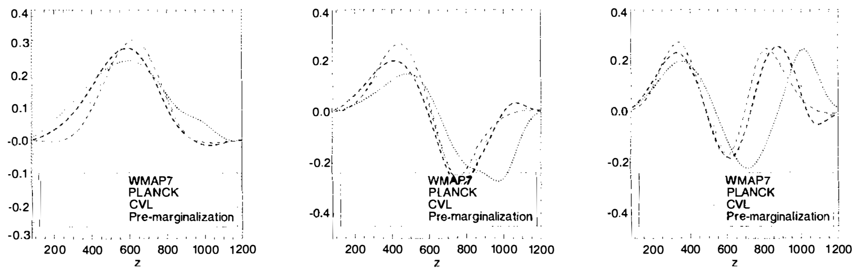

Figure 1: The first three principal components for WMAP7, Planck and a CVL experiment, both before and after marginalization over the cosmological parameters.

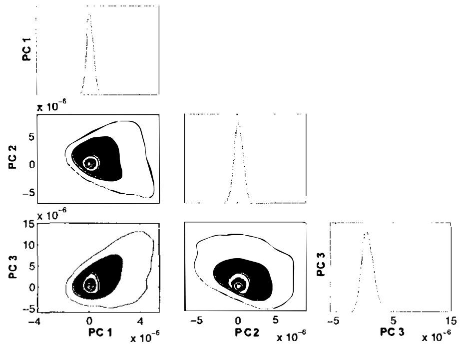

Figure 2: Constraints from the seven-year WMAP7 data (red), and from simulated data for Planck (blue) and a cosmic variance limited experiment (green). The plot shows marginalized one-dimensional distributions and two-dimensional 68% and 95% limits. The mock data for Planck and the CVL experiment assumed no dark matter annihilation. Three Principal Components were used in each run to model the energy deposition from dark matter annihilation. The units of the PC coefficients here are in $m^3/s/kg$, with $1\times10^{-6}m^3/s/kg = 1.8\times10^{-27}$ $cm^3/s/GeV$.

3. Planck Collaboration, Ade, P. A. R., Aghanim, N., et al. 2011, AAP, 536, A1
4. Chluba, J., & Thomas, R. M. 2011, MNRAS, 412, 748.
5. Ali-Haïmoud, Y., & Hirata, C. M. 2011, PRD, 83, 043513 .
6. Porter, T. A., Johnson, R. P., & Graham, P. W. 2011, ARAA, 49, 155
7. O. Adriani *et al.* [PAMELA Collaboration], Nature **458**, 607 (2009).
8. J. Chang *et al.*, Nature **456**, 362 (2008).
9. Abdo, A. A., et al. 2009, Physical Review Letters, 102, 181101.
10. Slatyer, T. R., Padmanabhan, N., & Finkbeiner, D. P. 2009, PRD, 80, 043526
11. Galli, S., Iocco, F., Bertone, G., & Melchiorri, A. 2009, Phys. Rev. D, **80**, 2.
12. Galli, S., Iocco, F., Bertone, G., & Melchiorri, A. 2011, PRD, 84, 027302
13. Finkbeiner, D. P., Galli, S., Lin, T., & Slatyer, T. R. 2012, PRD, 85, 043522

THE COSMIC HISTORY OF THE SPIN OF DARK MATTER HALOES *

Holly E. Trowland, Geraint F. Lewis and Joss Bland-Hawthorn
Sydney Institute for Astronomy, School of Physics A28, The University of Sydney, NSW 2006, Australia

The spin angular momentum of a dark matter halo is a relic of its past. It is the culmination of mergers, slow accretion and torquing by the surrounding landscape early on in the halo's life. To investigate how these different factors affect halo spin, N-body simulations are used to go back in time to see how the direction and magnitude of spin has evolved since z=3. Alignments between halo spins and the axis of filaments have been found as well as an alignment between neighbouring dark matter halo spins which is consistent with observation. Dark matter haloes start life with their spins predominantly orthogonal to the axis of filaments but over time the alignment becomes parallel. These changes over time indicate a complex history in the build up of angular momentum where mergers and accretion play a key role.

1 Introduction

The large scale structure of the universe observed today has formed by a long history of gravitational collapse, gradual accretion and mergers. The distribution of galaxies and their motions provides clues on how they formed, and together with galactic angular momentum data, the emergence of the intricate large scale structure can begin to be explained.

The initial spin of dark matter haloes is given through a mechanism known as "tidal torque theory" [2]. This theory proposes that the initial spin of a proto-halo early in its formation in the linear regime of structure formation depends on its shape and the tidal forces exerted from the surrounding structure, so the spin is dependent on the local dark matter landscape. A halo that was torqued in this manner should retain some memory of the tidal field where it formed. The cosmic web is the manifestation of the tidal field, filaments in particular are regular, symmetric morphologies which on large scales exhibit a uniform tidal field. Thus it is expected that the orientation of halo spin today should retain some correlation with the direction of filaments and haloes should be aligned with each other over short distances.

In N-body simulations, it has been shown that spins lie preferentially in the plane of sheets [3] and along the axis of filaments [4]. In observations there has been a tentative detection of some weak correlation with filaments [5] but no significant detection has been found to date. The evolution of halo spin with respect to filaments and sheets was explored by Hahn et el. [6] who found no significant change in the orientation of spin over cosmic time. More recently Codis et al. [7] found a redshift and halo mass dependant alignment of halo spin.

*This is based off work by Trowland et al. submitted to ApJ [1].

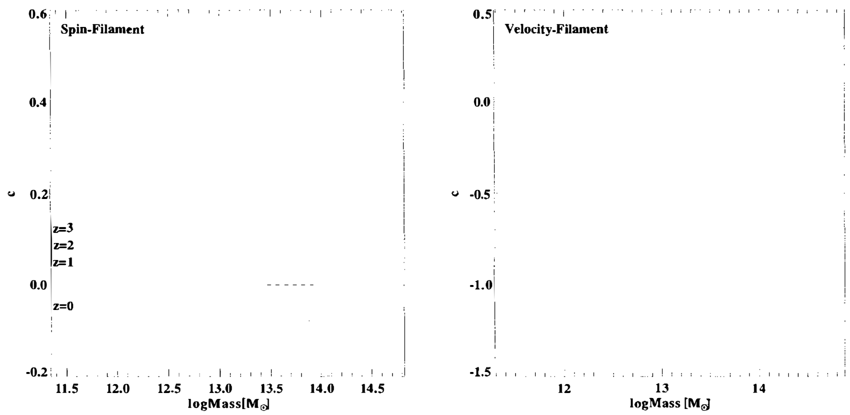

Figure 1: The alignment of dark matter halo spin (LEFT) and velocity (RIGHT) with filaments. Alignment is characterized by the c parameter of Equation 1 and $c > 0$ indicates orthogonal alignment whereas $c < 0$ indicates parallel alignment. At z=0 halo spin for low mass haloes is parallel and for high mass haloes it is orthogonal. For high redshift all haloes spin orthogonal to filaments but high mass haloes have a stronger orthogonal preference. For all redshifts, halo velocity aligned parallel with filaments which demonstrates a streaming motion of haloes down bulk flows. Lines are colored according to redshift.

2 Method

The halo catalogue of the Millennium simulation [8] was used to calculate the density field using the DTFE method [9,10]. The DTFE method is useful when looking for geometrical features in the density field because it automatically adapts to variations in density and geometry, which is useful in a sparse data set.

To find filaments in the density field, the field was smoothed using a Gaussian filter and the Hessian of second spatial derivatives was found. The eigenvalues of the Hessian quantify the curvature of density at a particular point, in the direction of the corresponding eigenvector. A filament region is a saddle shape where there are two negative and one positive eigenvectors and the direction of the axis of the filament is the direction of the positive eigenvalue.

The features discussed in this paper have all been found coosing the smoothing scale of 2Mpc/h. This scale has been chosen because it matches most closely with the visual classification of structure as postulated in Hahn et al. [11].

3 The behavior of haloes in filaments

The degree of alignment between the halo spin and filament axis can by characterized by the parameter c in the probability density function (see [1] for a derivation);

$$P(\cos\theta) = (1-c)\sqrt{1+\frac{c}{2}}\left[1-c\left(1-\frac{3}{2}\cos^2\theta\right)\right]^{-3/2}. \tag{1}$$

where c is the correlation parameter introduced by Lee & Pen [12] to measure the strength of the intrinsic spin($\hat{J}$)-shear($\hat{T}$) alignment.

$$\langle \hat{J}_i \hat{J}_j | \mathbf{T} \rangle \equiv \frac{1+c}{3}\delta_{ij} - c\hat{T}_{ik}\hat{T}_{kj}, \tag{2}$$

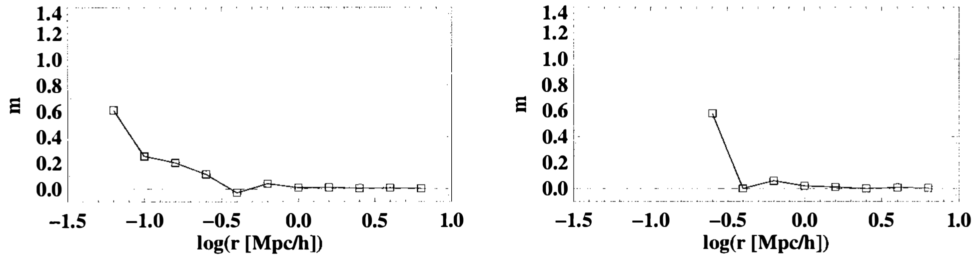

Figure 2: The alignment of neighbouring halo's spins (m), for haloes separated by distance r. The left panel is for the entire FOF+subhalo sample and the right panel is just including the FOF haloes. The dashed lines are random halo alignments and the shaded regions are the 1σ errors.

If halo spins are oriented completely randomly then $c = 0$ and the PDF is flat. If halo spins are preferentially orthogonal to filaments then $c > 0$ and the function increases with $\cos\theta$. Although tidal torque theory restricts c to positive values, other effects could be in play that cause halo spins to be aligned parallel with filaments, which would cause a negative value of c.

The alignment of halo spin vectors with filaments is shown in the left hand panel of Figure 1. The alignment distribution has been fitted to find c for haloes in bins of mass and for different redshifts. It can be seen that at z=0 the alignment is weakly parallel (negative c) for low mass halos in filaments ($M < 10^{13}M_\bullet$) and orthogonal (positive c) for high mass haloes. At higher redshifts the alignment becomes more orthogonal for all halo masses. There are less haloes in the high mass bins at high redshift because the high mass haloes have not had time to form yet. The result of [11] and [4] that halo spins generally lie along the axis of filaments is driven by the low mass haloes at z=0.

Although the c parameter was introduced in the context of spin alignments with the tidal field (manifested by filaments in the large scale structure), it can also be used as a more general measure of alignment. The alignment of centre of mass velocity with filament direction does not change over time, as seen in the right hand side of Figure 1 shows a parallel alignment which is stronger for high mass haloes. This means that for all halo masses, haloes are streaming coherently down filaments toward massive clusters. The highest mass haloes are streaming the most coherently because they are closest to the massive clusters which are the nodes of filaments.

4 The spin-spin alignment

Tidal torque theory predicts that as well as being aligned with the large scale structure, halo spins should be aligned with each other. This is tested by using the shape of the distribution of $|\hat{\mathbf{J}}(x) \cdot \hat{\mathbf{J}}(x+r)|$ (the number of halo pairs for values of $\cos\theta \in [0, 1]$). It is not a peaked distribution and best fit by a straight line:

$$P(|\hat{\mathbf{J}}(x) \cdot \hat{\mathbf{J}}(x+r)|) = m|\hat{\mathbf{J}}(x) \cdot \hat{\mathbf{J}}(x+r)| + c. \quad (3)$$

A positive slope (m) of the best fit line means there are more parallel aligned halo pairs, a negative m means they are more orthogonal and $m = 0$ means the haloes have random alignment.

The subhaloes can be excluded from the halo set by taking only the most massive subhalo in each Friends-of-Friends group (hereafter called the FOF haloes). When only the FOF haloes are regarded, there is no alignment on any scale (the right hand panel of Figure 2 is consistent with random halo orientations). However, an alignment has been seen in galaxy surveys, for example Galaxy Zoo [13] for galaxies closer than 0.5Mpc. This kind of alignment is seen in the simulation only when the subhaloes are included in the set (the left hand panel of Figure 2). The alignment exists on the scale of substructure within clusters. Only the subhaloes within large clusters exhibit any halo-halo spin alignment, although it is weak.

5 Conclusions

We found that angular momentum vectors of dark matter haloes since z=3 are generally orthogonal to filaments but high mass haloes have a stronger orthogonal alignment than low mass haloes. At z=0 the spins of low mass haloes have become parallel to filaments, whereas high mass haloes keep their orthogonal alignment.

An interpretation of this is that at early times all halo spins were aligned by tidal torque theory orthogonally to filaments. High mass haloes especially are well aligned because they have had their maximal expansion more recently and so will have been tidally torqued for longer. They usually exist close to clusters where the infall of dark matter is almost isotropic and so the nett effect from mergers and accretion is minimal. Low mass haloes, however, are vulnerable to being disturbed by mergers and accretion which is usually assumed to have the effect of randomizing the spin orientation. This leaves unexplained why low mass haloes at low redshift exhibit a parallel alignment with filaments.

There is an alignment between the spins of neighbouring haloes that is consistent with observation. This alignment is only over small scales ($<$ 0.5 Mpc) and is seen in the substructure of massive clusters.

Acknowledgments

We would like to thank the Virgo Consortium for making public the Millennium simulation data, Erwin Platen and Rien van de Weygaert for providing us with the DTFE code. HET would like to acknowledge the support of an Australian Postgraduate Award and a Denison Merit Award. GFL gratefully acknowledges the Australian Research Council for support through DP0665574 and DP110100678, and for his Future Fellowship (FT100100268). JBH is supported by a Federation Fellowship from the Australian Research Council.

References

1. H. E. Trowland, G. F. Lewis, and J. Bland-Hawthorn. *ArXiv e-prints*, January 2012.
2. Y. B. Zel'Dovich. A&A, 5:84–89, March 1970.
3. J. F. Navarro, M. G. Abadi, and M. Steinmetz. ApJ, 613:L41–L44, September 2004.
4. Y. Zhang, X. Yang, A. Faltenbacher, et al. ApJ, 706:747–761, November 2009.
5. B. J. T. Jones, R. van de Weygaert, and M. A. Aragón-Calvo. MNRAS, 408:897–918, October 2010.
6. O. Hahn, C. M. Carollo, C. Porciani, and A. Dekel. MNRAS, 381:41–51, October 2007.
7. S. Codis, C. Pichon, J. Devriendt, et al. *ArXiv e-prints*, January 2012.
8. V. Springel, S. D. M. White, A. Jenkins, et al. Nature, 435:629–636, June 2005.
9. R. van de Weygaert and W. Schaap. *ArXiv e-prints*, August 2007.
10. W. E. Schaap and R. van de Weygaert. A&A, 363:L29–L32, November 2000.
11. O. Hahn, C. Porciani, C. M. Carollo, and A. Dekel. MNRAS, 375:489–499, February 2007.
12. J. Lee and U.-L. Pen. ApJ, 532:L5–L8, March 2000.
13. A. Slosar, K. Land, S. Bamford, et al. MNRAS, 392:1225–1232, January 2009.

NEUTRON STARS AS LABORATORIES FOR COSMOLOGY

M ÁNGELES PÉREZ GARCÍA[a]
Department of Fundamental Physics and IUFFyM, University of Salamanca, Plaza de la Merced s/n 37008 Salamanca, Spain

Neutron stars can be considered a useful and interesting laboratory for Cosmology. With their deep gravitational potential they may accrete dark matter from the galactic halo and subsequent self-annihilation processes could induce an indirect observable signal this type of matter. In addition, the large densities in the interior of these objects may constitute a test-bench to study hypothesized deviations of fundamental constant values complementary to existing works using constraints at low density from BBN.

1 Introduction

Neutron stars (NS) are astrophysical objects where matter is subject to extreme conditions. They were hypothesized on theoretical grounds early in the 1930s by Baade, Zwicky and Landau and later discovered by Hewish and Bell [1]. They are born in the aftermath of a supernova event and typically have a mass less than $M \approx 2M_\odot$ and a radius $r \approx 12$ km. Based on their internal structure the estimated central densities may be about a few times nuclear saturation density $n_0 \approx 0.145\ fm^{-3}$, that is a mass density $\rho \approx 2\,10^{14}\ g/cm^3$. Zero temperature scenarios are usually assumed since in the interior they are in the few keV range while the Fermi energies of the degenerate baryonic species are in the MeVs. Its constituents vary according to a density distribution from a low density myriad of nuclei to, at larger densities, a hadronic sector composed of neutrons and to a less extent of protons and heavier particles. Leptons keep electrical charge neutrality in the system. In addition to the extreme densities some of them have large magnetic fields with strengths ranging $B \simeq 10^9 - 10^{15}$ G on the surface. These may power electromagnetic emission that can be detected on Earth, with periods $P \approx 10^{-3} - 1$ s due to a misalignement of the rotation and magnetic axis.

[a] mperezga@usal.es

2 Neutron stars as accretors of dark matter

Due to their compact size their gravitational potential well $\Phi \approx -GM^2/r$ is able to capture dark matter (DM) from the galactic distribution. Also the sun, other evolved stars and planets may accrete DM. Profiles, ρ_{DM}, are not yet fully determined but some of the most popular include work performed by Navarro et al [2] or those based on simulations [3]. Currently, DM interaction cross sections with matter in the Standard Model are not known and there is a large experimental effort to try to constrain them. Roughly speaking, indirect detection techniques try to obtain the gamma-ray outcome from the self-annihilation of DM particles while in direct detection they focus on nuclear recoiling from the scattering of the galactic flow of DM as it traverses the Earth [4]. Additionally, collider searches try to produce and detect SUSY DM candidates by missing transverse energy [5] in reactions involving Standard Model particles. The DM-nucleon

Figure 1: Ratio of spark to strangelet binding energy in the nuclear medium as a function of $B^{1/4}$.

scattering cross sections are, in principle, mass and energy dependent, but the usual approach in astrophysical scenarios is to assume S-wave scattering since at low energy Maxwellian distributed DM particles in a galactic halo will hit the experimental observer setting on Earth with mean velocities $v \simeq 270$ km/s= $10^{-3}c$. Considering coherence effects in the cross sections for DM and due to the fact that scaling with the nuclear target chiefly grows with mass number A, one can deduce the spin-independent (SI) cross section values $\sigma_{XN} \simeq 10^{-40}$ cm^2 [6]. In a NS most of the matter is concentrated in the inner core and estimations for the capture rates of DM particles with mass m_X at the maximum of the galactic plane pulsar distribution at about 3 kpc are given by[7] $F = \frac{3.042\,10^{25}}{m_X(GeV)} \frac{\rho_{DM}}{\rho_{DM,0}}\ s^{-1}$ where $\rho_{DM,0} = 0.3$ GeV/cm^3 is the DM density at the solar circle. Current indications from DAMA/LIBRA and CoGeNT seem to fit well with a light particle $\approx 4-12$ GeV/c^2 although other experiments give null results [6]. The mean free paths for these particles in NSs can be estimated as $\lambda = 1/(\sigma_{XN} n_0) \approx 0.7$ m. The number of in-medium scatterings would be on average $r/\lambda \simeq 1.7\,10^4$ times constituting an efficient capture. One of the possible models for DM is that where the particle candidate is of Majorana type and, therefore, self-annihilates with a probability per unit volume V given by $d\Gamma/dV \approx <\sigma v> (\rho_{DM}/m_X)^2$. At sufficiently high density these self-annihilation processes are removing part of the DM from the accreted distribution that is building up inside the NS. In this approximation the number of particles, $N(t)$, in the interior at time t can be obtained solving the equation $\frac{dN(t)}{dt} \approx F - \Gamma$. Let us consider that the energy deposit in the nuclear medium could be producing a series of *sparks* of the order of a fraction f of the X mass in the few GeV range as $\Delta E_{spark} = 2 f m_X c^2$. This seeding mechanism may produce one or multiple sparks that may help partially deconfine the hadronic quark content at large densities in the center of those objects [7]. These aggregates of quarks are known as *strangelets* and are currently under search in the CASTOR calorimeters at the CMS experiment in the LHC or AMS in the ISS. The binding energy (BE) of such a strangelet can be calculated and it is given in the MIT model by[8] $E_A(\mu_i, m_i, B) + E_{Coul}$ where μ_i and m_i are the chemical potential and mass of the *ith*-type quark, respectively. B is the MIT bag constant and E_{Coul} is the correction due to electrical charge. In Fig.1 we show the ratio of spark to strangelet binding energy with baryon number $A = 10$ in the nuclear medium for $m_X = 1, 10, 100$ GeV/c^2 as a function of $B^{1/4}$ for $f = 0.1$ at a central density of $2n_0$ compatible with NS observations. Even in this very conservative case where only 10% on the energy is deposited in the medium may indeed be larger than the strangelet binding. Thus,

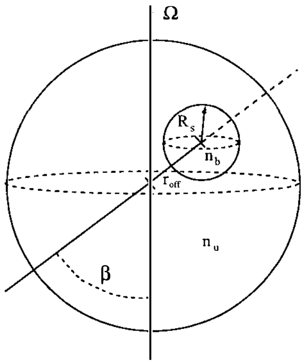

Figure 2: Simplified scheme of one bubble of quark matter proceeding through NS matter.

DM seeding may act as a 'Trojan Horse' liberating energy inside the central regions and cause a dramatic change in the internal structure of the object.The off-center energy release may have a kinematical signature from a velocity kick and change in the rotation pattern [7]. More exotic possibilities include the LSP in the SUSY theories as the DM candidate. If they are accelerated enough towards a gravitational compact object like a black hole or NS they could annihilate to an slepton and then radiate out a SM lepton and another LSP, provided the mass difference between the NSLP and LSP are up to a few GeV [9].

2.1 Kinematical implications of DM seeding in NS

Once the seeding mechanism has taken place at distance r_{off} from the NS center, then the quark bubbles (with density n_b and radius R_s) in the hadronic medium of density n_u, may coalescence [7]. In this way the progression of a burning front may proceed in direction β, for a simplified scheme of this see Fig. 2. NS burning has been partially studied [10] although the physical mechanisms for this are not yet clear and the hadron to quark star (QS) transition was only hypothesized in the context of very large central densities or temperature fluctuations. Observationally, the signature for this transition could be the emission of a gamma-ray-burst (GRB) due to the change in the gravitational and baryonic energy density. Both are of the same order and depend on the radial structure change $\Delta E_G \approx \frac{\Delta r}{r} 10^{53}$ erg. This is in agreement with order of magnitude of some of the Fermi measurements but further analysis is needed. If certain, this induced NS to QS conversion could provide an *internal engine* in these events where NS crust ejection is supposed to happen.

3 Testing variations of the fundamental couplings in extreme conditions

The extreme pressure and energy density attained in the interior of NSs can be also used to test some models in grand unification theories (GUT). Following GUT prescription [11] the set of fundamental forces: electroweak, strong and gravitational could be unified at some unspecified large energy scale. If we consider that the electromagnetic coupling constant α may vary with density contrasts, one could use some low density constraints from BBN [12] and, accordingly, NSs seem to be a good test-bench for trying to understand the large density counterpart. Using current information from either terrestrial [13](Heavy ion collisions, low density simulations of pure neutron matter, etc) and astrophysical sources [14] the equation of state (EOS) of nuclear matter constrains possible variations of the couplings that are not consistent with supporting the interplay of these three forces in a realistic NS. Using a physically motivated relativistic mean field lagrangian model parametrization, combined variation of couplings can be studied [15] since the expressions of pressure and energy density in the EOS consistently modify. The variations in $\Delta\alpha/\alpha$ relate to those in the gravitational constant G and meson masses for the strong interaction. We consider an input spatial variation in the allowed range by CMB constraints [16], $\Delta\alpha/\alpha \simeq \pm 10^{-2}$. We take for example $\Delta\alpha/\alpha = 0.005$ and what we find[15] is that the corresponding allowed regions, from an initial square L^2 centered at origin and side $L = 900$, for R, S parameters lie in the triangular shape between,

$$S \approx 450 - 3.8(R + 100); \;\; S \approx 450 - 0.145\, R. \tag{1}$$

The relative variations for particle masses are[11] $\frac{\Delta m_e}{m_e} = 0.5(1+S)\frac{\Delta\alpha}{\alpha}$, $\frac{\Delta m_p}{m_p} = [0.8R + 0.2(1+S)]\frac{\Delta\alpha}{\alpha}$, $\frac{\Delta m_n}{m_n} = \left[(0.1 + 0.7S - 0.6R) + \frac{m_p}{m_n}(0.1 - 0.5S + 1.4R)\right]\frac{\Delta\alpha}{\alpha}$. In a 'canonical' case where $R = 20$, $S = 160$ and imposing isospin symmetry we have $\frac{\Delta m_i}{m_i} = (0.201, 0.201, 0.5025)$ for $i = p, n, e$. Further work is needed to check for EOS model dependence. However we do not expect a change the general trend obtained. So fr the only constrains that exist come from a low density environment and our approach is, therefore, complementary. In this contribution we have discussed on the role of NSs as laboratories for extreme conditions of matter where some of the most interesting current issues in Cosmology can be tested to provide complementary insight to other existing constraints.

Acknowledgments

We would like to acknowledge support under ESF-COMPSTAR and MICINN Consolider MULTIDARK and FIS-2009-07238 projects.

References

1. A. Hewish et al, Nature 217, 709 (1968).
2. J. Navarro et al. , MNRAS, 349, 1039 (2004).
3. V. Springel, Mon.Not.Roy.Astron.Soc. 364 1105 (2005).
4. D. Hooper, C. Kelso and M. Buckley, arXiv: 1110.5338.
5. H. Baer et al, New J. Phys. 11 105024 (2009).
6. Z. Ahmed et al, arXiv:1203.1309v1.
7. M. A. Perez-Garcia, J. Silk, Phys. Rev. Lett. 105, 141101 (2010),arXiv:1108.5206, Phys. Lett. B 711 (2012), arXiv: 1111.2275.
8. A. Chodos et al, Phys Rev. D 10 2599 (1974), J Madsen, Phys. Rev. D 47, 5156 (1993).
9. M.Cannoni, M. E. Gomez, M. A. Perez-Garcia, J. Vergados, arXiv:1205.1709
10. A. Bhattacharyya et al, Phys. Rev. C, 74, 065804 (2006), B. Niebergal, R. Ouyed and P. Jaikumar, Phys. Rev. C, 82, 062801 (R) (2010).
11. A. Coc et al., Phys. Rev. D 76 023511 (2007).
12. Barrow J. D., Phys. Rev. D, 35, 1805 (1987).
13. P. Danielewicz, R. Lacey and W. G. Lynch, Science 298, 1592 (2002).
14. A. Steiner, J. M. Lattimer and E. Brown, ApJ 722, 1, 33 (2010).
15. M. A. Perez-Garcia, C. J. A. P. Martins, arXiv:1203.0399.
16. E. Menegoni et al, arXiv: 1202.1476.

7. Neutrinos and Cosmology

NEUTRINO MASSES

C. GIUNTI
INFN, Sezione di Torino, Via P. Giuria 1, I–10125 Torino, Italy

We review the status of three-neutrino mixing after the recent measurement of ϑ_{13} and discuss the implications for the absolute values of neutrino masses. Then, we discuss the possible explanation of short-baseline neutrino oscillation anomalies in the framework of 3+1 neutrino mixing.

1 Introduction

The results of several solar, atmospheric and long-baseline neutrino oscillation experiments have proved that neutrinos are massive and mixed particles [1]. There are two groups of experiments which measured two independent squared-mass differences (Δm^2) in two different neutrino flavor transition channels:

- Solar neutrino experiments (Homestake, Kamiokande, GALLEX/GNO, SAGE, Super-Kamiokande, SNO, BOREXino) measured $\nu_e \to \nu_\mu, \nu_\tau$ oscillations generated by [2] $\Delta m^2_{\rm S} = 6.2^{+1.1}_{-1.9} \times 10^{-5}\,{\rm eV}^2$ and a mixing angle $\tan^2\vartheta_{\rm S} = 0.42^{+0.04}_{-0.02}$. The KamLAND experiment confirmed these oscillations by observing the disappearance of reactor $\bar{\nu}_e$ at an average distance of about 180 km. The combined fit of solar and KamLAND data leads to [2]

$$\Delta m^2_{\rm S} = (7.6 \pm 0.2) \times 10^{-5}\,{\rm eV}^2, \qquad \tan^2\vartheta_{\rm S} = 0.44 \pm 0.03. \tag{1}$$

- Atmospheric neutrino experiments (Kamiokande, IMB, Super-Kamiokande, MACRO, Soudan-2, MINOS) measured ν_μ and $\bar{\nu}_\mu$ disappearance through oscillations generated by [3] $\Delta m^2_{\rm A} \simeq 2.3 \times 10^{-3}\,{\rm eV}^2$ and a mixing angle $\sin^2 2\vartheta_{\rm A} \simeq 1$. The K2K and MINOS long-baseline experiments confirmed these oscillations by observing the disappearance of accelerator ν_μ at distances of about 250 km and 730 km, respectively. The MINOS data give [4]

$$\Delta m^2_{\rm A} = 2.32^{+0.12}_{-0.08} \times 10^{-3}\,{\rm eV}^2, \qquad \sin^2 2\vartheta_{\rm A} > 0.90\,(90\%\ {\rm CL}). \tag{2}$$

2 Three-neutrino mixing

The two independent solar (S) and atmospheric (A) squared-mass differences in Eqs. (1) and (2). are nicely accommodated in the standard framework of three-neutrino mixing in which the three active flavor neutrinos ν_e, ν_μ, ν_τ are unitary linear combinations of three neutrinos ν_1, ν_2, ν_3 with masses m_1, m_2, m_3:

$$\Delta m^2_{\rm S} = \Delta m^2_{21}, \qquad \Delta m^2_{\rm A} = |\Delta m^2_{31}| \simeq |\Delta m^2_{32}|, \tag{3}$$

Ref.	$\Delta m^2_{21}\,[10^{-5}\,\mathrm{eV}^2]$	$\sin^2\vartheta_{12}$	$\Delta m^2_{31}\,[10^{-3}\,\mathrm{eV}^2]$	$\sin^2\vartheta_{23}$	$\sin^2\vartheta_{13}$
5	$7.58^{+0.22}_{-0.26}$	$0.306^{+0.018}_{-0.015}$	$2.35^{+0.12}_{-0.09}$	$0.42^{+0.08}_{-0.03}$	$0.021^{+0.007}_{-0.008}$
6	$7.59^{+0.20}_{-0.18}$	$0.312^{+0.017}_{-0.015}$	$2.50^{+0.09}_{-0.16}$	$0.52^{+0.06}_{-0.07}$	$0.013^{+0.007}_{-0.005}$
			$(2.40^{+0.08}_{-0.09})$	(0.52 ± 0.06)	$(0.016^{+0.008}_{-0.006})$

Table 1: Values of the neutrino mixing parameters obtained with global analyses of solar, atmospheric and long-baseline neutrino oscillation data.

with $\Delta m^2_{kj} = m^2_k - m^2_j$. There are two possible three-neutrino mixing schemes: the normal spectrum with $m_1 < m_2 < m_3$ and the inverted spectrum with $m_3 < m_1 < m_2$.

The values of the neutrino mixing parameters obtained in the global analyses of solar, atmospheric and long-baseline neutrino oscillation data of Refs.[5,6] are listed in Tab. 1. One can see that the results approximately agree and show that the mixing angle ϑ_{23} is close to maximal ($\vartheta_{23} \approx 45°$), the mixing angle ϑ_{12} is large but smaller than maximal ($\vartheta_{12} \approx 34°$), and the mixing angle ϑ_{13} is small. Recently, the Daya Bay[7] and RENO[8] collaborations have measured with high precision the mixing angle ϑ_{13}: $\sin^2\vartheta_{13} = 0.024 \pm 0.004$ (Daya Bay) and $\sin^2\vartheta_{13} = 0.029 \pm 0.006$ (RENO). The weighted average is

$$\sin^2\vartheta_{13} = 0.025 \pm 0.004. \tag{4}$$

Hence, we have a robust evidence of a non-zero value of ϑ_{13} which confirms the previous indications of the T2K [9], MINOS [10] and Double Chooz [11] experiments. These results are very important, because the measured value of ϑ_{13} opens promising perspectives for the observation of CP violation in the lepton sector and matter effects in long-baseline oscillation experiments, which could allow to distinguish the normal and inverted neutrino mass spectra [12].

An open problem in the framework of three-neutrino mixing is the determination of the absolute scale of neutrino masses, which is not resolved by neutrino oscillations, which depend on the differences of neutrino masses. However, the measurement in neutrino oscillation experiments of the neutrino squared-mass differences allows us to constraint the allowed patterns of neutrino masses. A convenient way to see the allowed patterns of neutrino masses is to plot the values of the masses as functions of the unknown lightest mass, which is m_1 in the normal mass spectrum and m_3 in the inverted spectrum, as shown in Figs. 1(a) and 1(b). We used the squared-mass differences obtained in the global analysis of neutrino oscillation data of Ref.[6] (see Tab. 1). Figures 1(a) and 1(b) show that there are three extreme possibilities:

A normal hierarchy $m_1 \ll m_2 \ll m_3$. In this case

$$m_2 \simeq \sqrt{\Delta m^2_{\mathrm{S}}} \approx 9 \times 10^{-3}\,\mathrm{eV}, \qquad m_3 \simeq \sqrt{\Delta m^2_{\mathrm{A}}} \approx 5 \times 10^{-2}\,\mathrm{eV}. \tag{5}$$

An inverted hierarchy $m_3 \ll m_1 \lesssim m_2$ In this case

$$m_1 \lesssim m_2 \simeq \sqrt{\Delta m^2_{\mathrm{A}}} \approx 5 \times 10^{-2}\,\mathrm{eV}. \tag{6}$$

Quasi-degenerate spectra $m_1 \lesssim m_2 \lesssim m_3 \simeq m_\nu$ in the normal scheme and $m_3 \lesssim m_1 \lesssim m_2 \simeq m_\nu$ in the inverted scheme, with

$$m_\nu \gg \sqrt{\Delta m^2_{\mathrm{A}}} \approx 5 \times 10^{-2}\,\mathrm{eV}. \tag{7}$$

There are three main sources of information on the absolute scale of neutrino masses:

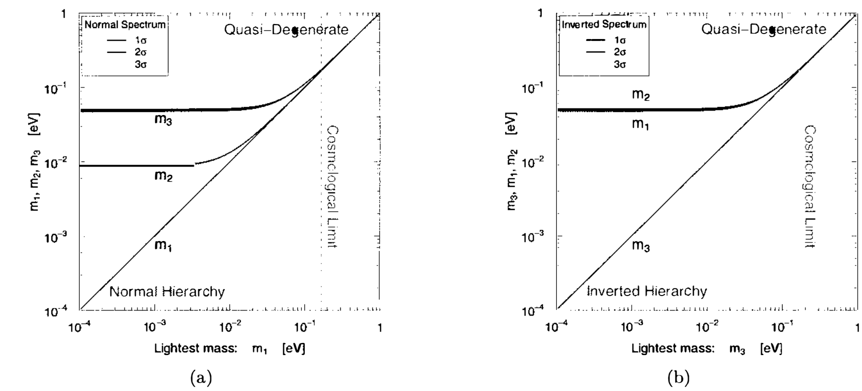

Figure 1: (a) Values of the neutrino masses as functions of the lightest mass m_1 in the normal mass spectrum obtained with the squared-mass differences of Ref.[6] (see Tab. 1). (b) Corresponding values of the neutrino masses as functions of the lightest mass m_3 in the inverted mass spectrum.

Beta decay The spectrum of electrons emitted in β decay is affected by neutrino masses through energy-momentum conservation. Hence, the β decay information on neutrino masses is very robust. Tritium β-decay experiments obtained the most stringent bounds on the neutrino masses by limiting the effective electron neutrino mass m_β given by [1]

$$m_\beta^2 = \sum_{k=1}^{3} |U_{ek}|^2 m_k^2. \tag{8}$$

The most stringent limits have been obtained in the Mainz [13] and Troitsk [14] experiments:

$$m_\beta \leq 2.3\,\mathrm{eV} \quad \text{(Mainz)}, \qquad m_\beta \leq 2.1\,\mathrm{eV} \quad \text{(Troitsk)}, \tag{9}$$

at 95% CL. The KATRIN experiment [15], which is scheduled to start data taking in 2014, is expected to have a sensitivity to m_β of about 0.2 eV.

Figure 2(a) shows the allowed value of m_β as a function of the lightest mass in the normal and inverted schemes. One can see that the current bound and the KATRIN sensitivity probe the quasi-degenerate region. Future β-decay experiments can distinguish between a normal and an inverted hierarchy only if $m_\beta \lesssim 4 \times 10^{-2}$ eV.

Neutrinoless double-beta decay This process occurs only if massive neutrinos are Majorana fermions and depends on the effective Majorana mass [1]

$$m_{\beta\beta} = \sum_{k=1}^{3} U_{ei}^2 m_k. \tag{10}$$

The most stringent limits have been obtained in the Heidelberg-Moscow [16], Cuoricino [17] and NEMO3 [18] experiments:

$$|m_{\beta\beta}| \lesssim (0.22 - 0.64)\,\mathrm{eV} \quad \text{(H-M)}, \tag{11}$$
$$|m_{\beta\beta}| \lesssim (0.30 - 0.71)\,\mathrm{eV} \quad \text{(Cuoricino)}, \tag{12}$$
$$|m_{\beta\beta}| \lesssim (0.47 - 0.96)\,\mathrm{eV} \quad \text{(NEMO3)}, \tag{13}$$

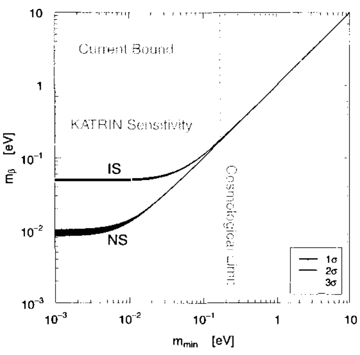

(a)

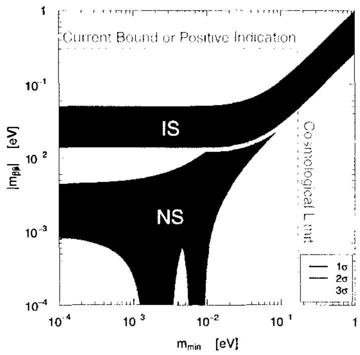

(b)

Figure 2: (a) Value of the effective electron neutrino mass m_β in β decay (see Eq. (8)) as function of the lightest mass $m_{\min} = m_1$ in the normal spectrum (NS) and $m_{\min} = m_3$ in the inverted spectrum (IS), obtained with the mixing parameters of Ref.[6] (see Tab. 1) and $\sin^2 \vartheta_{13}$ in Eq. (4). (b) Corresponding value of the effective Majorana mass $m_{\beta\beta}$ in neutrinoless double-β decay (see Eq. (10)).

with the interval determined by nuclear physics uncertainties [19]. Several experiments are running and planned in order to improve the sensitivity by one or two orders of magnitude [20].

Figure 2(b) shows the allowed value of $m_{\beta\beta}$ as a function of the lightest mass in the normal and inverted schemes. The large size of the allowed bands is due to our total lack of knowledge of the Majorana phases in the mixing matrix, which can generate cancellations between the different mass contributions. These cancellations cannot be large in the inverted scheme, in which $m_{\beta\beta} \gtrsim 10^{-2}\,\text{eV}$. On the other hand, in the normal scheme the cancellations can even zero out $m_{\beta\beta}$. From Fig. 2(b), one can also see that the current bound on $m_{\beta\beta}$ probes the quasi-degenerate region. Future neutrinoless double-β-decay experiments can distinguish between a normal and an inverted hierarchy only if $m_{\beta\beta} \lesssim 10^{-2}\,\text{eV}$.

Cosmology Since light massive neutrinos are hot dark matter, cosmological data give information on the sum of neutrino masses [1]. The analysis of cosmological data in the framework of the standard Cold Dark Matter model with a cosmological constant (ΛCDM) disfavors neutrino masses larger than some fraction of eV. The value of the of the upper bound on the sum of neutrino masses depends on model assumptions and on the considered data set [21], ranging from about 1.5 eV to a very stringent 0.28 eV (at 95% CL) [22]. In Figs. 1 and 2 we illustrate the effect of the cosmological bound considering the rather robust limit [23,21]

$$\sum_{k=1}^{3} m_k \lesssim 0.5\,\text{eV}. \tag{14}$$

3 Beyond three-neutrino mixing

The completeness of the three-neutrino mixing paradigm was challenged in 1995 by the observation of a signal of short-baseline $\bar{\nu}_\mu \to \bar{\nu}_e$ oscillations in the LSND experiment [24], which would imply the existence of one or more squared-mass differences much larger than Δm^2_{S} and

Δm^2_{A}. The MiniBooNE experiment was made in order to check the LSND signal with about one order of magnitude larger distance (L) and energy (E), but the same order of magnitude for the ratio L/E from which neutrino oscillations depend. The first results of the MiniBooNE experiment in neutrino mode [25] did not show a signal compatible with that of LSND, but the results in antineutrino mode [26], presented in the summer of 2010, show an excess of events over the background approximately at the same L/E of LSND. This result revived the interest in the possibility of existence of one or more neutrinos with masses at the eV scale which can generate squared-mass differences for short-baseline oscillations.

In this review we consider the so-called 3+1 neutrino mixing scheme which is the simplest extension of three-neutrino mixing with the addition of a fourth massive neutrino ν_4 such that $|\Delta m^2_{41}| \gg |\Delta m^2_{31}|$ (the more complicated 3+2 scheme has been recently considered in Refs.[27,28]). In the flavor basis the additional massive neutrino corresponds to a sterile neutrino, which does not have standard weak interactions. The existence of a sterile neutrino which has been thermalized in the early Universe is compatible with Big-Bang Nucleosynthesis data [29]. It is also compatible with cosmological measurements of the Cosmic Microwave Background and Large-Scale Structures if m_4 is limited below about 1 eV [30]. Therefore, we consider a neutrino mixing schemes in which the three standard neutrinos ν_1, ν_2, ν_3 have masses much smaller that 1 eV and ν_4 has a mass at the eV scale.

A further indication in favor of short-baseline oscillations came from new calculations of the reactor $\bar{\nu}_e$ flux [31,32], which obtained an increase of about 3% with respect to the previous value adopted in the analysis of the data of reactor neutrino oscillation experiments. The measured reactor rates are in agreement with those derived from the old $\bar{\nu}_e$ flux, but show a deficit of about 2.2σ with respect to the rates derived from the new $\bar{\nu}_e$ flux. This is the "reactor antineutrino anomaly" [33], which may be an indication in the $\bar{\nu}_e \to \bar{\nu}_e$ channel of a signal corresponding to the $\bar{\nu}_\mu \to \bar{\nu}_e$ signal observed in the LSND and MiniBooNE experiments. Finally, there is a "Gallium neutrino anomaly" [34], consisting in a short-baseline disappearance of electron neutrinos measured in the Gallium radioactive source experiments GALLEX [35] and SAGE [36].

In 3+1 neutrino mixing, the effective flavor transition and survival probabilities in short-baseline (SBL) experiments are given by [37]

$$P^{\text{SBL}}_{\overset{(-)}{\nu}_\alpha \to \overset{(-)}{\nu}_\beta} = \sin^2 2\vartheta_{\alpha\beta} \sin^2\left(\frac{\Delta m^2_{41} L}{4E}\right), \qquad P^{\text{SBL}}_{\overset{(-)}{\nu}_\alpha \to \overset{(-)}{\nu}_\alpha} = 1 - \sin^2 2\vartheta_{\alpha\alpha} \sin^2\left(\frac{\Delta m^2_{41} L}{4E}\right), \tag{15}$$

for $\alpha, \beta = e, \mu, \tau, s$ and $\alpha \neq \beta$, with

$$\sin^2 2\vartheta_{\alpha\beta} = 4|U_{\alpha 4}|^2 |U_{\beta 4}|^2, \qquad \sin^2 2\vartheta_{\alpha\alpha} = 4|U_{\alpha 4}|^2 \left(1 - |U_{\alpha 4}|^2\right). \tag{16}$$

Therefore:

1. All effective SBL oscillation probabilities depend only on the absolute value of the largest squared-mass difference $\Delta m^2_{41} = m^2_4 - m^2_1$.

2. All oscillation channels are open, each one with its own oscillation amplitude.

3. The oscillation amplitudes depend only on the absolute values of the elements in the fourth column of the mixing matrix, i.e. on three real numbers with sum less than unity, since the unitarity of the mixing matrix implies that $\sum_\alpha |U_{\alpha 4}|^2 = 1$.

4. CP violation cannot be observed in SBL oscillation experiments, even if the mixing matrix contains CP-violation phases, because neutrinos and antineutrinos have the same effective SBL oscillation probabilities. Hence, 3+1 neutrino mixing cannot explain the indication of a difference between neutrino [25] and antineutrino [26] oscillations obtained in the MiniBooNE experiment.

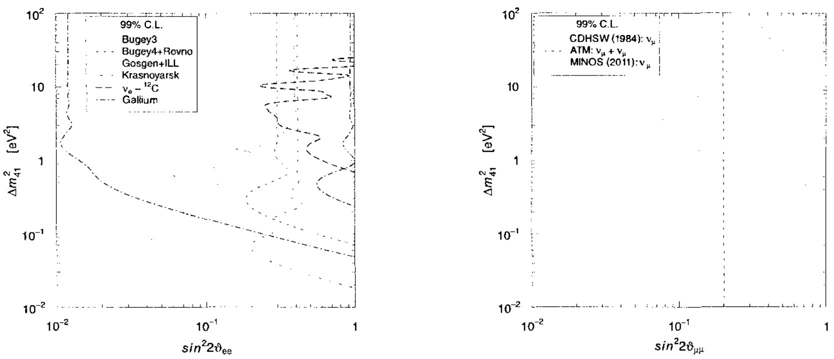

(a) (b)

Figure 3: Exclusion curves obtained from the data of disappearance experiments [28,38,39].

The dependence of the oscillation amplitudes in Eq. (16) on three independent absolute values of the elements in the fourth column of the mixing matrix implies that the amplitude of $\overset{(-)}{\nu}_\mu \to \overset{(-)}{\nu}_e$ transitions is limited by the absence of large SBL disappearance of $\overset{(-)}{\nu}_e$ and $\overset{(-)}{\nu}_\mu$ observed in several experiments.

The results of reactor neutrino experiments constrain the value $|U_{e4}|^2$ through the measurement of $\sin^2 2\vartheta_{ee}$. Even taking into account the reactor antineutrino anomaly [33] discussed above, the $\bar{\nu}_e$ disappearance is small and large values of $\sin^2 2\vartheta_{ee}$ are constrained by the exclusion curves in Fig. 3(a). Since values of $|U_{e4}|^2$ close to unity are excluded by solar neutrino oscillations (which require large $|U_{e1}|^2 + |U_{e2}|^2$), for small $\sin^2 2\vartheta_{ee}$ we have

$$\sin^2 2\vartheta_{ee} \simeq 4|U_{e4}|^2. \tag{17}$$

The value of $\sin^2 2\vartheta_{\mu\mu}$ is constrained by the curves in Fig. 3(b), which have been obtained from the lack of ν_μ disappearance in the CDHSW ν_μ experiment [40], from the requirement of large $|U_{\mu1}|^2 + |U_{\mu2}|^2 + |U_{\mu3}|^2$ for atmospheric neutrino oscillations [41] and from MINOS neutral-current data [42,38]. Hence, $|U_{\mu4}|^2$ is small and

$$\sin^2 2\vartheta_{\mu\mu} \simeq 4|U_{\mu4}|^2. \tag{18}$$

From Eqs. (16), (17) and (18), for the amplitude of $\overset{(-)}{\nu}_\mu \to \overset{(-)}{\nu}_e$ transitions we obtain

$$\sin^2 2\vartheta_{e\mu} \simeq \frac{1}{4} \sin^2 2\vartheta_{ee} \sin^2 2\vartheta_{\mu\mu}. \tag{19}$$

Therefore, if $\sin^2 2\vartheta_{ee}$ and $\sin^2 2\vartheta_{\mu\mu}$ are small, $\sin^2 2\vartheta_{e\mu}$ is quadratically suppressed [37,43]. This is illustrated in Fig. 4(a), where one can see that the separate effects of the constraints on $\sin^2 2\vartheta_{ee}$ and $\sin^2 2\vartheta_{\mu\mu}$ exclude only the large-$\sin^2 2\vartheta_{e\mu}$ part of the region allowed by $\overset{(-)}{\nu}_\mu \to \overset{(-)}{\nu}_e$ appearance data, whereas most of this region is excluded by the combined constraint in Eq. (19). Hence, there is a tension between appearance and disappearance data, which is quantified by a 0.3% parameter goodness-of-fit.

However, in spite of the low value of the parameter goodness-of-fit we consider the 3+1 neutrino mixing for the following reasons:

A. It is the simplest scheme beyond the standard three-neutrino mixing which can partially explain the data.

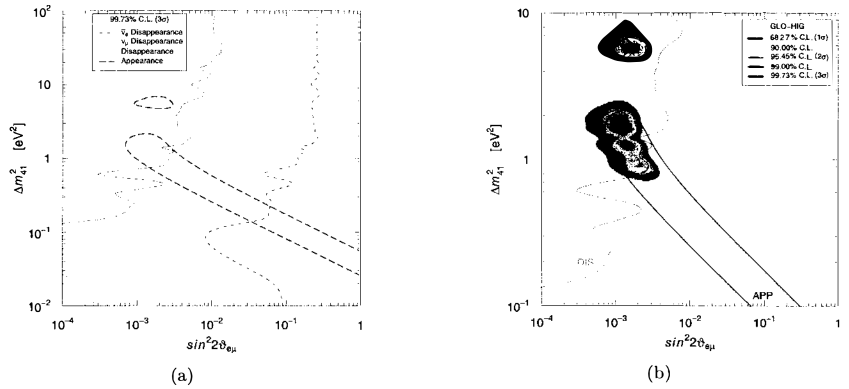

Figure 4: (a) Exclusion curves in the $\sin^2 2\vartheta_{e\mu}$–Δm^2_{41} plane obtained from the separate disappearance constraints in Fig. 3 (blue and green lines) and the combined constraint given by Eq. (19) (red line). (b) Allowed regions in the $\sin^2 2\vartheta_{e\mu}$–Δm^2_{41} plane obtained from the global fit in 3+1 neutrino mixing, confronted with the regions allowed at 3σ by appearance (APP) and disappearance (DIS) data. The best-fit point is indicated by a cross.

B. It corresponds to the natural addition of one new entity (a sterile neutrino) to explain a new effect (short-baseline oscillations). Better fits of the data require the addition of at least another new entity (in any case at least one sterile neutrino is needed to generate short-baseline oscillations).

C. The introduction of more than one sterile neutrino can resolve the MiniBooNE neutrino-antineutrino tension, but cannot resolve the more statistically significant appearance-disappearance tension.

D. 3+1 mixing is favored with respect to schemes with more than one sterile neutrino by the Big-Bang Nucleosynthesis limit $N_{\text{eff}} \lesssim 4$ at 95% CL obtained in Ref.[29].

Therefore, we consider the global fit of all data in the framework of 3+1 neutrino mixing, which yields the best-fit values

$$\Delta m^2_{41} = 1.62\,\text{eV}^2, \qquad |U_{e4}|^2 = 0.036, \qquad |U_{\mu 4}|^2 = 0.0084, \tag{20}$$

with $\chi^2_{\text{min}} = 137.5$ for 138 degrees of freedom, corresponding to an excellent 50% goodness of fit. Figure 4(b) shows the allowed regions in the $\sin^2 2\vartheta_{e\mu}$–Δm^2_{41} plane.

4 Conclusions

The current status of our knowledge of three-neutrino mixing is very satisfactory after the recent determination of the smallest mixing angle ϑ_{13}: the two squared-mass differences and the three mixing angles are known with good precision. Future experiments must determine the Dirac CP-violating phase in the mixing matrix, the mass hierarchy and the absolute scale of neutrino masses. It is also very important to find if neutrinos are Majorana particles and in that case what are the values of the Majorana CP-violating phases.

Anomalies which cannot be explained in the framework of three-neutrino mixing have been observed by some short-baseline neutrino oscillation experiments. A possible explanation in terms of neutrino oscillations requires the existence of light sterile neutrinos in a model beyond three-neutrino mixing. In the framework of 3+1 neutrino mixing, which is the simplest extension of three-neutrino mixing which can fit the data, there is a tension between appearance and disappearance data and a tension between MiniBooNE neutrino and antineutrino data. Hence, new experiments arc needed in order to check the current indications and resolve the tensions in favor of 3+1 mixing or a more complicated model.

1. C. Giunti and C. W. Kim, *Fundamentals of Neutrino Physics and Astrophysics* (Oxford University Press, Oxford, UK, 2007), ISBN 978-0-19-850871-7.
2. Super-Kamiokande, K. Abe *et al.*, Phys. Rev. **D83**, 052010 (2011).
3. Super-Kamiokande, Y. Ashie *et al.*, Phys. Rev. **D71**, 112005 (2005).
4. MINOS, P. Adamson *et al.*, Phys. Rev. Lett. **106**, 181801 (2011).
5. G. L. Fogli *et al.*, Phys. Rev. **D84**, 053007 (2011).
6. T. Schwetz, M. Tortola, and J. W. F. Valle, New J. Phys. **13**, 109401 (2011).
7. DAYA-BAY, F. P. An *et al.*, Phys. Rev. Lett. **108**, 171803 (2012).
8. RENO, S.-B. Kim *et al.*, arXiv:1204.0626.
9. T2K, K. Abe *et al.*, Phys. Rev. Lett. **107**, 041801 (2011).
10. MINOS, P. Adamson *et al.*, Phys. Rcv. Lctt. **107**, 181802 (2011).
11. DOUBLE-CHOOZ, Y. Abe *et al.*, Phys. Rev. Lctt. **108**, 131801 (2012).
12. M. Mezzetto and T. Schwctz, J. Phys. **G37**, 103001 (2010).
13. C. Kraus *et al.*, Eur. Phys. J. **C40**, 447 (2005).
14. Troitsk, V. Aseev *et al.*, Phys. Rev. **D84**, 112003 (2011).
15. KATRIN, F. Fraenkle *et al.*, arXiv:1110.0087.
16. H. V. Klapdor-Kleingrothaus *et al.*, Eur. Phys. J. **A12**, 147 (2001).
17. CUORICINO, E. Andreotti *et al.*, Astropart. Phys. **34**, 822 (2011).
18. NEMO-3, M. Bongrand *et al.*, arXiv: 1105.2435.
19. J. D. Vergados, H. Ejiri, and F. Simkovic, arXiv:1205.0649.
20. J. Gomez-Cadenas *et al.*, Riv. Nuovo Cim. **35**, 29 (2012).
21. Y. Y. Y. Wong, Ann. Rev. Nucl. Part. Sci. **61**, 69 (2011).
22. S. A. Thomas, F. B. Abdalla, and O. Lahav, Phys. Rev. Lett. **105**, 031301 (2010).
23. M. C. Gonzalez-Garcia, M. Maltoni, and J. Salvado, JHEP **08**, 117 (2010).
24. LSND, A. Aguilar *et al.*, Phys. Rev. **D64**, 112007 (2001).
25. MiniBooNE, A. A. Aguilar-Arevalo, Phys. Rev. Lett. **102**, 101802 (2009), 0812.2243.
26. MiniBooNE, A. A. Aguilar-Arevalo *et al.*, Phys. Rev. Lett. **105**, 181801 (2010).
27. J. Kopp, M. Maltoni, and T. Schwetz, Phys. Rev. Lett. **107**, 091801 (2011).
28. C. Giunti and M. Laveder, Phys.Rev. **D84**, 073008 (2011).
29. G. Mangano and P. D. Scrpico, Phys. Lctt. **B701**, 296 (2011).
30. J. Hamann *et al.*, JCAP **1109**, 034 (2011).
31. T. A. Mueller *et al.*, Phys. Rev. **C83**, 054615 (2011).
32. P. Huber, Phys. Rev. **C84**, 024617 (2011).
33. G. Mention *et al.*, Phys. Rev. **D83**, 073006 (2011).
34. C. Giunti and M. Lavcdcr, Phys. Rev. **C83**, 065504 (2011).
35. F. Kaether *et al.*, Phys. Lett. **B685**, 47 (2010).
36. SAGE, J. N. Abdurashitov *et al.*, Phys. Rev. **C80**, 015807 (2009).
37. N. Okada and O. Yasuda, Int. J. Mod. Phys. **A12**, 3669 (1997).
38. C. Giunti and M. Lavcder, Phys.Rev. **D84**, 093006 (2011).
39. C. Giunti and M. Laveder, Phys. Lett. **B706**, 200 (2011).
40. CDHSW, F. Dydak *et al.*, Phys. Lctt. **B134**, 281 (1984).
41. M. Maltoni and T. Schwetz, Phys. Rev. **D76**, 093005 (2007).
42. MINOS, P. Adamson *et al.*, Phys. Rev. Lett. **107**, 011802 (2011).
43. S. M. Bilenky, C. Giunti, and W. Grimus, Eur. Phys. J. **C1**, 247 (1998).

COSMOLOGICAL NEUTRINO MASS CONSTRAINT FROM THE WIGGLEZ DARK ENERGY SURVEY

S. RIEMER-SØRENSEN and the WiggleZ collaboration
School of Mathematics and Physics, University of Queensland, 4072 Brisbane QLD, Australia

The absolute neutrino mass scale is currently unknown, but can be constrained from observations of the large-scale structure. We use the WiggleZ Dark Energy Survey to obtain an upper limit on the sum of the neutrino masses of $\sum m_\nu < 0.60$eV (95% confidence) when combining with data from the Wilkinson Microwave Anisotropy Probe (WMAP), and $\sum m_\nu < 0.29$eV when also including priors on the Hubble parameter and the baryon acoustic oscillation scale. The WiggleZ high redshift star-forming blue galaxy sample is less sensitive to systematic effects from non-linear structure formation, pairwise galaxy velocities, redshift-space distortions, and galaxy bias than previous surveys. Through exhaustive tests using numerical dark matter simulations, we demonstrate that common modelling approaches lead to systematic errors in the recovered cosmological parameters, and we use the simulations to calibrate a new non-linear fitting formula extending to small scales.

1 Introduction

In the Standard Model of particle physics the neutrinos are treated as exactly massless despite neutrino oscillation experiments having measured mass differences between the three species. No current experiment has the sensitivity to measure the absolute neutrino mass but it can be inferred from observations of the galaxy distribution today because massive neutrinos suppress the gravitational collapse of halos on small scales.[1] The cosmic microwave background (CMB) provides an upper limit of $\sum m_\nu < 1.3\,\mathrm{eV}$ (all limits are 95% confidence).[2] Combining with large-scale structure measurements such as the galaxy power spectrum,[3,4,5,6] galaxy luminosity function,[7] cluster mass function,[8,9] or the baryon acoustic oscillations[3,2] (BAO) tightens the constraints to $\sum m_\nu < 0.3\,\mathrm{eV}$ by breaking parameter degeneracies. We use the galaxy power spectrum from the WiggleZ Dark Energy Survey to constrain the sum of neutrino masses.

2 The WiggleZ Dark Energy Survey

The WiggleZ Dark Energy Survey[10] contains 238,000 galaxies with redshifts $z < 1$ in a total volume of $1\,\mathrm{Gpc}^3$. The Gigaparsec WiggleZ Survey (GiggleZ) simulations[a,12] were designed to probe the low-mass haloes traced by WiggleZ galaxies, whilst providing an equivalent survey volume. They provide a powerful means for testing and calibrating our modeling algorithms. WiggleZ has several potential advantages over previous surveys: 1) The neutrino suppression of the galaxy power spectrum is degenerate with effects from non-linear structure formation. Non-linearities increase with time so for the distant galaxies probed by WiggleZ, the contamination

[a] $\Omega_b = 0.049$, $\Omega_m = 0.297$, $h = 0.7$, $n_s = 1.0$, $\sigma_8 = 0.8$[11]

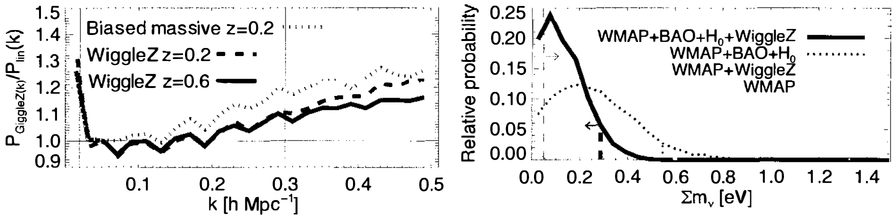

Figure 1: *Left:* The ratio between a simulated WiggleZ halo power spectrum and corresponding linear power spectrum. The vertical lines are our fitting range. Non-linear corrections are clearly less significant for the high-redshift, low-bias WiggleZ halos than at lower redshifts. *Right:* The relative probability distribution of $\sum m_\nu$ from fitting model F) with $k_{\rm max} = 0.3\,h\,{\rm Mpc}^{-1}$. The dashed grey line is the lower limit from oscillation experiments, and the vertical lines are 95% confidence upper limits.

from non-linearities is smaller than for previous surveys. This is illustrated in Fig. 1 where we show the ratio between a simulated WiggleZ power spectrum and the linear power spectrum for $z = 0.2$ (dashed blue) and $z = 0.6$ (solid black). For comparison we also show the ratio for simulated highly-biased massive haloes at $z = 0.2$ (dotted red). 2) The relationship (bias) between the observed galaxy distribution and the dark matter distribution, which is influenced by massive neutrinos, depends on the observed galaxy type. Previous studies[13,3] measured red galaxies, which tend to cluster in the centers of dark matter halos, whereas the star-forming blue WiggleZ galaxies avoid the densest regions leading to a lower overall bias, reducing any systematics that could arise from the bias. The GiggleZ simulations show that over the range of scales and halo masses relevant for this analysis, the galaxy bias is scale-independent to within 1% whereas the neutrino scale dependent effect is of the order of 5% for $\sum m_\nu = 0.3$ eV.[14]

3 Method and modelling

Large-scale structure alone cannot determine all cosmological parameters, so we include data from WMAP (7 year). To compute the parameter likelihoods, we use importance sampling[15,16] of the Markov Chain Monte Carlo (MCMC) chains[b] from fitting to WMAP alone as well as to the chains combining WMAP with the BAO scale from SDSS Luminous Red Galaxies[13] and a $H_0 = 74.2 \pm 3.6\,{\rm km\,s^{-1}\,Mpc^{-1}}$ prior on the Hubble parameter[17] (BAO+H_0). We assume a standard flat ΛCDM cosmology with no time variation of w and $N_{\rm eff} = 3.04$, and fit over the parameters: Ω_c (cold dark matter density), Ω_b (baryon density), Ω_Λ (dark energy density), Ω_ν (neutrino density), h (Hubble parameter), n_s (spectral index), $\Delta^2_{\mathcal{R}}$ (amplitude of primordial density fluctuations).

Massive neutrinos suppress the power spectrum on all scales smaller than their free-streaming length at the time the neutrinos become non-relativistic. For $\sum m_\nu = 0.3$ eV the most significant suppression happens for $k = 0.3 - 1.3\,h\,{\rm Mpc}^{-1}$, but the k-dependence of the suppression is more pronounced for $k < 0.3\,h\,{\rm Mpc}^{-1}$ and consequently easier to disentangle from other cosmological parameters and systematics.[1,14] At low redshift structure formation is no longer linear[1,18,19,20] for $k < 0.1\,h\,{\rm Mpc}^{-1}$ and simulations show that redshift-space distortions become k-dependent at low redshift and consequently are degenerate with neutrino mass[21,22]. By fitting to simulated power spectra from GiggleZ, we tested six different models for the non-linear effects: A) Linear structure formation with linear bias. B) Non-linear structure formation with linear bias. C) Non-linear structure formation and fitting formula for redshift space distortions and pairwise galaxy velocities. D) Same as C) but with zero pairwise velocities. E) Non-linear structure

[b] `http://lambda.gsfc.nasa.gov/product/map/dr4/parameters.cfm`

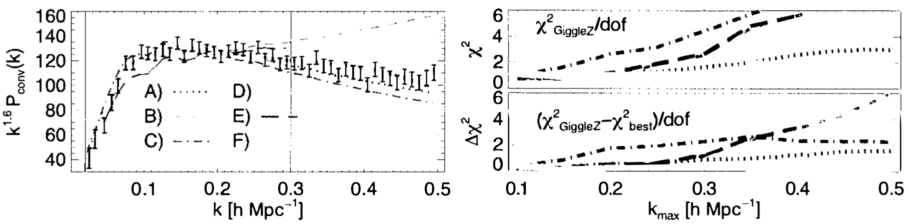

Figure 2: *Left:* The observed WiggleZ power spectrum, and the six models for the best fit cosmology of model F). The vertical lines are our fitting range. The divergence between the models at large k is clear and demonstrates the importance of careful modeling. *Left upper:* Reduced χ^2 of models A)-F) fitted to the N-body simulation halo catalogue for the GiggleZ fiducial cosmology values. In absence of systematic errors the models should recover the input cosmology with $\chi^2/\text{dof} = 1$. *Left lower:* Difference in reduced χ^2 values when using the GiggleZ fiducial cosmological parameters and the best fit values.

formation with pairwise galaxy velocity damping. F) Simulation calibrated model.

The details of the models are given in Riemer-Sørensen et al. 2012[23] and they are shown in Fig. 2 for a fixed cosmology. They are similar at low k, where the large-scale clustering is linear and the theory is robust, but for $k > 0.2\,h\,\text{Mpc}^{-1}$ the differences increase. The right part of Fig. 2 shows the the reduced χ^2 from fitting each of the models to simulated power spectra. The upper panel is the χ^2 for the simulation parameters. It is clear that model B), C), E) are unable to provide a good fit for the correct parameter values for $k_{\text{max}} > 0.2\,h\,\text{Mpc}^{-1}$. The lower panel shows the distance in χ^2 between the best fitting parameters and the simulation ones, which is a measure of how well the models recover the simulated parameter values. It is clear that at small scales models A)-E) are insufficient, and the complexity of model F) is necessary.

Model F: The non-linear effects are present in an N-body simulation for a fiducial cosmology and can be implemented following the approach of Reid et al. 2010.[3] For each trial cosmology:

$$P_{\text{gal}}^{\text{trial}}(k) = b^2 P_{\text{hf,nw}}^{\text{trial}}(k) \frac{P_{\text{damped}}^{\text{trial}}(k)}{P_{\text{nw}}^{\text{trial}}(k)} \frac{P_{\text{GiggleZ}}^{\text{fid}}(k)}{P_{\text{hf,nw}}^{\text{fid}}(k)}, \tag{1}$$

where $P_{\text{damped}}^{\text{trial}}(k) = P_{\text{lin}}^{\text{trial}}(k) f_{\text{damp}}(k) + P_{\text{nw}}^{\text{trial}}(k)(1 - f_{\text{damp}}(k))$ and $f_{\text{damp}}(k) = \exp(-(k\sigma_v)^2)$ with σ_v given by $\sigma_v^2 = 1/(6\pi^2) \int dk' P_{\text{lin}}(k')$. $P_{\text{GiggleZ}}^{\text{fid}}(k)$ is a 5$^{\text{th}}$ order polynomial fit to the power spectrum of a set of halos in the GiggleZ simulations chosen to match the clustering amplitude of WiggleZ galaxies. $P_{\text{lin}}(k)$ and $P_{\text{nw}}(k)$ are the linear and non-linear power spectra from CAMB[c], where the latter implements Halofit.[24] P_{nw} and $P_{\text{hf,nw}}$ are the same power spectra but without the acoustic peaks. The factor of b^2 in Eqn. 1 is related to galaxy bias. The second factor represents the smooth power spectrum of the trial cosmology. The third factor defines the acoustic peaks and their broadening caused by the bulk-flow motion of galaxies from their initial positions in the density field, and the fourth factor describes all additional non-linear effects in the N-body simulation.

Throughout the analysis we have fixed the lower limit to be $k_{\text{min}} = 0.02\,h\,\text{Mpc}^{-1}$, which corresponds to the largest modes observed in each of the WiggleZ regions and we present all results as a function of k_{max}.

4 Results and discussion

When fitting model F) to the observed WiggleZ power spectra we obtain a limit of $\sum m_\nu < 0.60\,\text{eV}$ for WMAP+WiggleZ with $k_{\text{max}} = 0.3\,h\,\text{Mpc}^{-1}$. Combining with BAO+$H_0$ reduces the

[c] `http://camb.info`

uncertainty in Ω_m and H_0, leading to a stronger neutrino mass constraints of $\sum m_\nu < 0.29\,\mathrm{eV}$.

The relative probability distributions of $\sum m_\nu$ for model F) with $k_{\max} = 0.3\,h\,\mathrm{Mpc}^{-1}$ are shown in Fig. 1. It is clear how adding WiggleZ data to the analysis narrows the distributions (dotted to solid) both with (orange) and without (black) the inclusion of BAO+H_0. This is the strongest neutrino mass limit so far derived from spectroscopic redshift galaxy surveys. The advantages of WiggleZ are a higher redshift for which the structure formation is linear to smaller scales, and a simple galaxy bias for the strongly star-forming blue emission line galaxies.

Our result is comparable to that obtained using independent methods[4,6,8,9], but with different systematics. Since the data sets are all independent, they can potentially be combined in the future to provide even stronger constraints. This is particularly interesting in light of recent results[2,25] that hint at the existence of additional neutrino species ($N_{\mathrm{eff}} > 3.04$). Allowing for additional neutrino species degrades the constraining power of large scale clustering alone, and the combination of N_{eff} and $\sum m_\nu$ is therefore poorly constrained with current data.

In the future, galaxy surveys such as the Baryon Acoustic Oscillation Survey, Dark Energy Survey and Euclid will be far more sensitive, however, as demonstrated in this paper, the small details of the modelling of non-linear effects become very important, so robust modelling either theoretically or calibrated to simulations with massive neutrinos will be necessary.

Acknowledgments

SRS thanks the organisers for financial support for participation in the cosmology section of the 47th Rencontres de Moriond.

1. J. Lesgourgues and S. Pastor. Phys. Reports, 429:307, 2006.
2. E. Komatsu et al. ApJ Supp., 192:18, 2011.
3. B. A. Reid et al. JCAP, 1:3, January 2010.
4. S. A. Thomas et al. Phys. Rev. Lett., 105(3):031301, 2010.
5. M. C. Gonzalez-Garcia et al. JHEP, 4:56, 2010.
6. R. de Putter et al. *ArXiv:1201.1909*, 2012.
7. C. Jose et al. Phys. Rev. *D*, 83(12):123518, 2011.
8. A. Mantz et al. MNRAS, 406:1805, 2010.
9. B. A. Benson et al. *ArXiv:1112.5435*, 2011.
10. M. J. Drinkwater et al. MNRAS, 401:1429, 2010.
11. C. Blake et al. MNRAS, 406:803, 2010.
12. G. B. Poole and The WiggleZ Collaboration. *In preparation*, 2012.
13. W. J. Percival et al. MNRAS, 401:2148, 2010.
14. S. Bird et al. *ArXiv:1109.4416*, 2011.
15. A. Lewis and S. Bridle. Phys. Rev. *D*, 66(10):103511, 2002.
16. M. E. C. Swanson et al. MNRAS, 409:1100, 2010.
17. A. G. Riess et al. ApJ, 699:539, 2009.
18. M. Takada et al. Phys. Rev. *D*, 73(8):083520, 2006.
19. S. Saito et al. Phys. Rev. Lett., 100(19):191301, 2008.
20. R. Scoccimarro. Phys. Rev. *D*, 70(8):083007, 2004.
21. E. Jennings et al. MNRAS, page 1572, 2010.
22. F. Marulli et al. MNRAS, 418:346, 2011.
23. S. Riemer-Sørensen et al. *ArXiv:1112.4940*, 2011.
24. R. E. Smith et al. MNRAS, 341:1311, 2003.
25. J. Kopp et al. Phys. Rev. Lett., 107(9):091801, 2011.

Measurement of θ_{13} by neutrino oscillation experiments

Tomoyuki Konno
Department of Physics, Tokyo Institute of Technology, Tokyo, Japan

Measurement of θ_{13} is one of the most important tasks in neutrino physics since the detectability of CP violation by future experiments depends on the value of θ_{13}. To measure the mixing angle θ_{13}, short baseline reactor experiments and long baseline accelerator experiments are currently accumulating data. Reactor experiments such as Double Chooz, Daya Bay and RENO are measuring disappearance of electron anti-neutrinos from reactor cores. On the other hand, accelerator experiments, such as MINOS and T2K, aim to detect appearance of electron neutrinos from muon neutrino beams with detectors placed at several hundred kilometers away from the accelerators. In addition to θ_{13}, accelerator experiments have sensitivities to θ_{23}, CP violation phase and mass hierarchy. Therefore, there is strong complementary between reactor and accelerator experiments. The status and prospects for reactor and accelerator neutrino oscillation experiments are reported.

1 Introduction

1.1 Neutrino oscillation

Neutrino oscillation is one of new phenomena beyond the standard model in the particle physics, which is described with a mixing of the neutrino mass eigenstates with non-zero masses. In the current model, there are three flavor and mass eigenstates; ν_e, ν_μ, ν_τ and ν_1, ν_2, ν_3 and mixing between the flavor and mass eigenstates are explained by Pontecorvo-Maki-Nakagawa-Sakata (PMNS) matrix [1] as Eq (1) shows:

$$\begin{pmatrix} \nu_e \\ \nu_\mu \\ \nu_\tau \end{pmatrix} = \begin{pmatrix} 1 & 0 & 0 \\ 0 & c_{23} & s_{23} \\ 0 & -s_{23} & c_{23} \end{pmatrix} \begin{pmatrix} c_{13} & 0 & s_{13}e^{-i\delta_{\rm CP}} \\ 0 & 1 & 0 \\ -s_{13}e^{i\delta_{\rm CP}} & 0 & c_{13} \end{pmatrix} \begin{pmatrix} c_{12} & s_{12} & 0 \\ -s_{12} & c_{12} & 0 \\ 0 & 0 & 1 \end{pmatrix} \begin{pmatrix} \nu_1 \\ \nu_2 \\ \nu_3 \end{pmatrix} \tag{1}$$

where, $c_{ij} = \cos\theta_{ij}, s_{ij} = \sin\theta_{ij}$. θ_{ij} $(i, j = 1, 2, 3)$ are mixing angles between ν_i and ν_j. $\delta_{\rm CP}$ shows the CP violation phase in lepton sector.

Assuming two neutrino flavor system, neutrino oscillation is simply described and the survival probability, which is a probability that a neutrino flavor ν_α with energy of E is detected as the same flavor at distance of L from generated point, is shown in Eq (2).

$$P(\nu_\alpha \to \nu_\alpha) = 1 - \sin^2 2\theta \sin^2\left(\frac{\Delta m^2 L}{4E}\right) \tag{2}$$

where Δm^2 is a difference of mass squares between the two neutrino flavors. Therefore, the mixing angle θ gives amplitude of the oscillation and $1/\Delta m^2$ is proportional to the maximum point of the amplitude.

1.2 Measurement of oscillation parameters

Several experiments were performed to measure oscillation parameters. θ_{12} and Δm^2_{21}, parameters related to solar neutrinos, are constrained by the combined analysis [2] of various solar neutrino experiments and the KamLAND experiment [3] as: $\sin^2\theta_{12} = 0.31 \pm 0.01$ and $\Delta m^2_{21} = (7.6 \pm 0.2) \times 10^{-5}\,\mathrm{eV}^2$. θ_{23} and Δm^2_{32}, parameters related to atmospheric neutrinos, are measured by the Super-Kamiokande experiments[4] and MINOS experiment[5] as: $\sin^2 2\theta_{23} > 0.90$ at 90% C.L. and $|\Delta m^2_{32}| = (2.32^{+0.12}_{-0.08}) \times 10^{-3}\,\mathrm{eV}^2$. While the absolute value of Δm^2_{32} are well measured, the sign is still unknown.

On the other hand, only an upper limit of θ_{13} was given by the CHOOZ short-baseline reactor neutrino experiment [6] as $\sin^2 2\theta_{13} < 0.15$ at $|\Delta m^2_{31}| = 2.5 \times 10^{-3}\mathrm{eV}^2$ as of early 2011. The current best constraint to $|\Delta m^2_{31}|$ is given by the MINOS experiment since $|\Delta m^2_{31}|$ can be substituted by $|\Delta m^2_{32}|$. The leptonic CP violation phase δ_{CP} is completely unknown. And there are still two possibilities of the neutrino mass hierarchy: normal ($m_3 > m_2 > m_1$) and inverted ($m_2 > m_1 > m_3$), which is not determined yet.

1.3 Approaches to θ_{13}

There are two approaches with neutrino oscillation to measure the mixing angle θ_{13}; short-baseline reactor experiment and long-baseline accelerator experiment. Reactor experiments aim to observe disappearance of electron anti-neutrino generated at nuclear reactors at the distance of $1 \sim 2$ km from the cores. The survival probability of $\bar{\nu}_e$ is a function of distance L from the sources (reactor cores) and the energy of neutrino E as Eq (3):

$$P(\bar{\nu}_e \to \bar{\nu}_e) = 1 - \sin^2 2\theta_{13} \sin^2\left(\frac{1.27 \times \Delta m^2_{31}[\mathrm{eV}^2] \times L[\mathrm{m}]}{E[\mathrm{MeV}]}\right) + O(10^{-3}) \tag{3}$$

The oscillation related to θ_{13} is maximized around $L = 1 \sim 2$ km with a few MeV energy which is an average value of $\bar{\nu}_e$ from reactors. The reactor experiment can obtain pure information of θ_{13}.

On the other hand, accelerator experiments focus on appearance of ν_e ($\bar{\nu}_e$) fromν_μ ($\bar{\nu}_\mu$) beams. The probability of ν_e appearance is written as a function of distance L and neutrino energy E as:

$$P(\nu_\mu \to \nu_e) \cong \sin^2 2\theta_{13} \sin^2\theta_{23} \sin^2\left(\frac{1.27 \times \Delta m^2_{32}[\mathrm{eV}^2] \times L[\mathrm{km}]}{E[\mathrm{GeV}]}\right) \tag{4}$$

While reactor experiments can measure pure θ_{13}, results of accelerator experiments have possibility to measure not only θ_{13} but also to test the CP violation in the lepton sector and to determine the neutrino mass hierarchy. However, there are potentially parameter degeneracies leading to the following ambiguities: 1) the $\delta_{\mathrm{CP}} - \theta_{13}$ ambiguity; 2) the ambiguity in the sign of Δm^2_{23}; 3) the θ_{23} ambiguity because only $\sin^2 2\theta_{23}$, not θ_{23}, is known. In addition to these ambiguities, Earth-matter effects also must be taken into account in the determination of θ_{13}.

The survival probability of $\bar{\nu}_e$ in reactor experiments is independent of δ_{CP}, θ_{12} and Δm^2_{21} and contribution of the matter effect is negligible due to the short distance. In other words, reactor experiments are ideal methods to measure θ_{13} without the degeneracy problem. If θ_{13} is measured unambiguously and found to be large enough by reactor experiments, then the $\delta_{\mathrm{CP}} - \theta_{13}$ ambiguity is solved and accelerator experiments can measure δ_{CP} and determine the sign of Δm^2_{32}. Therefore, strong complementarity exists between reactor and accelerator experiments.

2 Reactor experiments

The principle of short-baseline reactor neutrino reactor experiment is to measure $\bar{\nu}_e$ flux precisely at distance of $1 \sim 2$ km from the reactor cores and detect disappearance. In order to reduce the uncertainties related to neutrino flux estimation, the reactor experiments have a concept of placing identical detectors at near (before oscillation) and far locations from the sources. The Double Chooz, Daya Bay and RENO experiments are taking data since 2011 and they have opened the first results of neutrino oscillation.

Fission reactors are producers of $\bar{\nu}_e$ (about 10^{20} $\bar{\nu}_e$ s^{-1} per reactor core). The fission of ^{235}U produces elements and beta decays of the elements produce approximately six electron anti-neutrinos. There are also significant contribution from ^{238}U, ^{239}Pu and ^{241}Pu to the neutrino flux. The expected anti-neutrino spectrum is calculated as the convolution of the measurement of beta spectra of the fission products and cross sections of anti-neutrino interaction.

For the detection of $\bar{\nu}_e$, the reactor experiments use inverse-β decay (IBD) ($\bar{\nu}_e + p \to e^+ + n$). Due to the kinematics, there is a energy threshold: ~ 1.806 MeV $=: E_{\mathrm{thr}}$. Detectors of the experiments consist of organic liquid scintillator target doped with gadolinium (Gd). Gd has a large neutron absorption cross section. The positron deposits its kinetic energy and annihilates in the target, giving rise to a prompt signal. The neutrino energy can be measured from the prompt signal as:

$$E_{\mathrm{prompt}} = E_{e^+} + m_e \cong E_\nu - E_{\mathrm{thr}} + 2m_e. \tag{5}$$

The neutron thermalizes in the target and is absorbed by Gd, emitting a few γ rays with a total energy of 8 MeV as the delayed signal. This signal occurs about 30 μs after the prompt signal on average. Making timing correlation of the two signals (delayed coincidence) enables to reduce largely backgrounds from environment γ rays and cosmic muons.

To suppress background contamination, the three experiments have adapted a concept of detector design in which the inner detector consists of three region; ν-target, γ-catcher and buffer. The ν-target is filled with Gd-loaded liquid scintillator to observe IBD signals. the scintillator works not only as light emitter but also as the anti-neutrino target thanks to the richness of free protons. The γ-catcher, which surrounds the ν-target, contains liquid scintillator without Gd to detect γ rays escaping from the target. The buffer is filled with non-scintillating mineral oil, in which the PMTs are installed. The purpose of the buffer is to shield γ rays mainly from the radioactive impurities of the PMT glasses. In addition, the three experiments cover the inner detectors by optically separated muon veto detectors based on liquid scintillator (Double Chooz) or water cherenkov detectors (Daya Bay and RENO). In Figure 1, the drawing of the Double Chooz detector is shown as an example of the detector concept.

2.1 Double Chooz experiment

The Double Chooz experiment [7] is located in Ardenne, France to observe electron anti-neutrino from Chooz nuclear power plant, which has two reactor cores with 4.25 GW_{th} of thermal power per core. They have designed to place two detectors at distances of 1.05 km and 400 m from the cores. Data taking has started with only the far detector since April of 2011 and the near detector will start its operation from 2013.

As shown in Figure 1, the inner detector of the Double Chooz experiment contains the 10.3 m^3 target volume with 6.747×10^{29} free protons. The scintillator light is monitored by 390 10-inch PMTs mounted in the buffer region. In addition to the liquid scintillator based inner muon veto, the Double Chooz experiment has also installed outer muon detector made of plastic scintillator strips to cover large area over the main detector. The far detector is installed at 300 m.w.e underground and the near detector will be installed at 120 m.w.e underground to suppress cosmic muons.

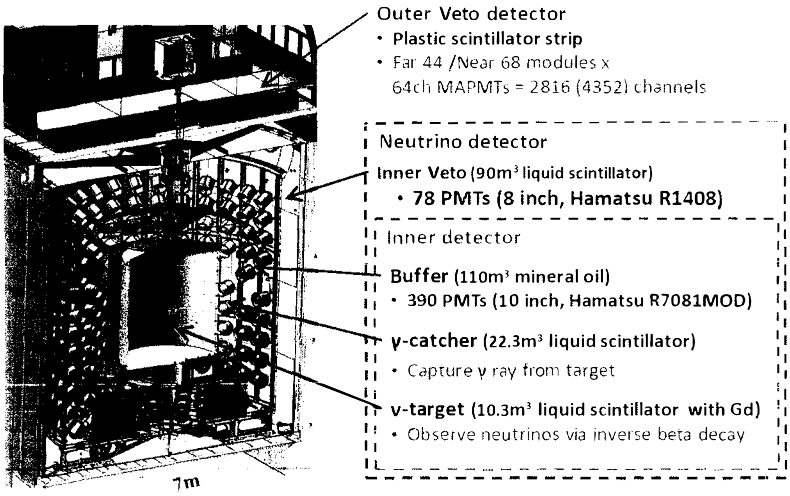

Figure 1: Drawing of the Double Chooz far detector

The Double Chooz experiment has operated only the far detector so that systematic uncertainties related to the neutrino ux prediction is not canceled. To suppress the uncertainties from reactors, the Double Chooz experiment used neutrino production per fission measured by the Bugey4 [8] experiment as an anchor point, reducing the uncertainties of reactor neutrino flux from 2.7% to 1.8%.

Energy measurements are based on the total charge collected by the inner detector PMTs, scaling by a constant corresponding to about 200 photo-electrons per MeV, which is calibrated with 2.2 MeV of neutron-hydrogen capture signals. Systematics of energy response are estimated from energy calibration with radioactive sources deployed inside the detector to be 1.7%. The total systematic uncertainty from detector response is estimated to be 2.1%.

The Double Chooz experiment has succeeded analyzing data of 101.5 DAQ days run time and obtained 4121 IBD candidates while 4344±165 events were predicted with no oscillation. Three types of the remaining backgrounds are considered in neutrino oscillation analysis: accidental, fast neutron and cosmogenic backgrounds. The estimated rates of the backgrounds are 0.33 ± 0.03, 0.83 ± 0.38 and 2.3 ± 1.2 events per day. Therefore, systematic uncertainty from the backgrounds is estimated to be 3.0% to the signal.

In order to improve the sensitivity to θ_{13}, the Double Chooz experiment has performed not only comparison of IBD rates but also comparing the shapes of the prompt energy spectrum to its prediction. For the shape analysis, they used χ^2 minimization with the covariance matrices to account for systematic uncertainty. The shapes of expected IBD spectrum and the three backgrounds were compared with observed data. Finally they got $\sin^2 2\theta_{13} = 0.086 \pm 0.041(\text{stat}) \pm 0.030(\text{syst})$ and excluded no oscillation hypothesis at 94.6% C.L.

The Double Chooz experiment has also performed combined analysis with the accelerator experiments (MINOS and T2K) on θ_{13} and CP violation phase δ_{CP} v.s. $\sin^2 2\theta_{13}$ plane for normal mass hierarchy as shown in Figure 3.

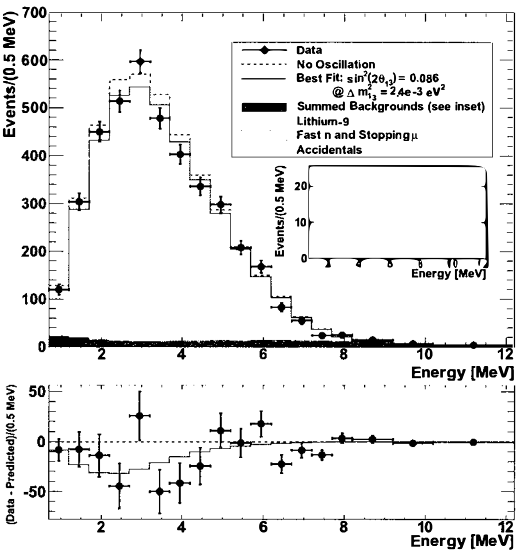

Figure 2: (Upper): Observed (dots) and predicted positron energy spectra for the best fit $\sin^2 2\theta_{13}$ (red solid) and no-oscillation expectation (blue dashed) with stacked background spectrum. (Lower): Difference between data and no-oscillation (dots) and difference between the best fit $\sin^2 2\theta_{13}$ and no-oscillation expectation (red line).

2.2 Daya Bay experiment

The Daya Bay experiment [9] is a reactor experiment located in the Guang-Dong Province, the south of China, on the site of the Daya Bay power station. The site is made up of three pairs of twin reactors, Daya Bay, Ling Ao I and Ling Ao II. Each of the reactor cores has a thermal power of 2.9 GW. The experiment has constructed three experimental halls: the Daya Bay near hall (experimental hall-1 (EH-1), 360 m away from Daya Bay), the Ling Ao near hall (EH-2, 481 m away from Ling-Ao)and the far hall (EH-3, 1980 m and 1600 m away from Daya Bay and Ling-Ao, respectably) and six 20 tons identical anti-neutrino detectors have been located to three sites.

The Daya Bay experiment started data taking from September 2011 and operation of the three experimental sites are on going since December 2011. They have analyzed data of about 50 days of DAQ live time from 24 December to 17 February 2012. They have observed 28935 and 28975 events at EH-1, 22466 events at EH-2, and 3528, 3436 and 3452 events at EH-3 to measure a deficit in the far hall, expressed as a ratio of observed to expected events: $R = 0.940 \pm 0.011(\text{stat}) \pm 0.004(\text{syst})$.

Finally, the Daya Bay experiment has performed rate-only comparison of observed data with expectation to obtain $\sin^2 2\theta_{13} = 0.092 \pm 0.016(\text{stat}) \pm 0.005(\text{syst})$ and to exclude no-oscillation hypothesis at 5.2 standard deviations.

2.3 RENO experiment

The RENO (Reactor Experiment for Neutrino Oscillation) experiment [10] aims to measure θ_{13} by using anti-neutrinos from Yonggwang unclear power plant in Korea with world-second largest thermal power output of 16.4 GW. The six pressurized water reactors are lined up in roughly

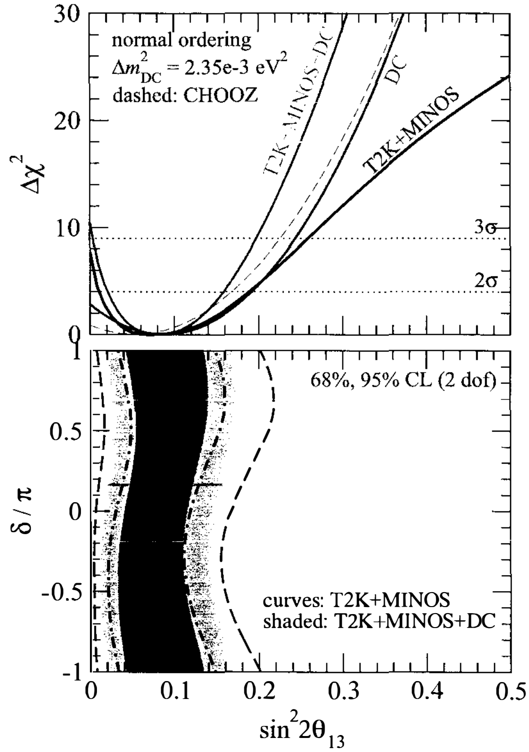

Figure 3: Combined analysis with Double Chooz, T2K and MINOS assuming normal mass hierarchy. (Upper): The χ^2 distribution for $\sin^2 2\theta_{13}$, (Lower): allowed region in 2D plane of δ_{CP} v.s. $\sin^2 2\theta_{13}$.

same distance of about 1.3km span. The near and far detector are located at distances of 290 and 1380 m from the center of the reactor line under 120 and 450 m.w.e., respectively. The inner detector contains 18.6 m^3 of target volume and 16 tons of 0.1% Gd-loaded liquid scintillator with 1.189×10^{30} free protons.

The RENO experiment has taken data for 229 days (live time near: 192.42, far: 222.06 days) from 11 August 2011 to 26 March 2012 with both the near and far detectors, obtaining 154088 and 17102 IBD candidates in the near and far detectors, respectively. The ratio of measured to expected events in the far detector is calculated to be $R = 0.920 \pm 0.009(\mathrm{stat}) \pm 0.014(\mathrm{syst})$. From the rate comparison of observed events with expectation in both the far and near detectors, the best fit value is obtained: $\sin^2 2\theta_{13} = 0.113 \pm 0.013(\mathrm{stat}) \pm 0.019(\mathrm{syst})$ excluding the no-oscillation hypothesis at 4.9 standard deviations.

3 Accelerator experiments

Thanks to the improvement of accelerator techniques, high intensity neutrino beam can be produced by accelerators. For generation of neutrino beam, accelerated proton hits graphite targets to produce pion, which decays into muon with muon neutrino: $\pi^+ \rightarrow \mu^+ + \nu_\mu$. To measure θ_{13} with accelerator neutrino beam, it is focused on the observation of appearance of electron neutrinos from the muon neutrino beam : $\nu_\mu \rightarrow \nu_e$.

Currently, several ten to one hundred GeV proton beams arc used to generate muon neutrino beams with a few hundred MeV to a few GeV of energy, which are observed at a distance of several hundred km from the accelerators. For the observation of neutrino beams, the accelerator experiments use charged current (CC) interactions: $\nu_e(\nu_\mu) + n \rightarrow e(\mu) + p$ as signal since flavor of outgoing lepton from thcse intcractions arc associated with the flavor of incming neutrinos while, neutral current (NC) interaction can be background.

3.1 MINOS experiment

The Main Injector Neutrino Oscillation Search (MINOS) experiment [11] started its operation with neutrino beam in 2005 at Fermilab in Chicago, USA and is currently under operation. The MINOS experiment uses 120 GeV proton injector to produce neutrino beam. The neutrino beam has a few GeV of energy (3GeV at peak) and are detected by the near detector (1km away) and far detector (735km away in the Soudan mine). Both detectors are steel and scintillator tracking calorimeters of 1 kton target mass (27 ton fiducial) for the near detector and 5.4 kton (4.0 kton fiducial) for the far detector.

With exposure of 8.2×10^{20} protons on the NuMI target at Fermilab, the MINOS experiment has performed search for electron neutrino appearance. Based on data of the near detector, the expected number of events in the far detector was calculated to be 49.6$\pm$7.0(stat)$\pm$2.7(syst) with assumption of $\theta_{13} = 0$. On the other hand, 62 events were observed in the far detector. Assuming $\delta_{\rm CP} = 0$ and $\Delta m^2_{32} = 2.32 \times 10^{-3}{\rm eV}^2$, thc uppcr limit of θ_{13} is obtained: $2\sin^2\theta_{23}\sin^2 2\theta_{13} < 0.12(0.20)$ at 90% C.L. with normal (inverted) hierarchy. and the $\theta_{13} = 0$ hypothesis is disfavored by the MINOS data at the 89% C.L.

3.2 T2K experiment

The Tokai-to-Kamioka (T2K) experiment [12] uses 30 GeV proton beam from J-PARC at Tokai, Japan, to generate muon neutrino beam with 0.6 GeV of energy. The neutrino beam is detected by the near detector based on fine grained detector (FGD) and time projection chamber (TPC) 280m away from the proton target at J-PARC and the far detector, Super-Kamiokande 295km away from the proton target. The T2K experiment is the first experiment to make use of an off-axis beam (2.5° off from the direction of proton beam) to make narrow band neutrino beam with the peak at thc maximum of the oscillation probability. Thc Supcr-Kamiokande detector is a water Cherenkov detector equipped with 11,129 of 20-inch PMTs, which has 22.5 kton fiducial volume and can separate electron and muon by Cherenkov ring patterns.

The T2K experiment has achieved to collect data with 1.4×10^{20} proton on the target until March 2011, when the big earthquake hit Eastern Japan. The oscillation analysis is based entirely on comparison of the number of ν_e candidates with prcdictions, varying $\sin^2 2\theta_{13}$ for each $\delta_{\rm CP}$ value. Including systematic uncertainties, the expectation of electron-like events is 1.5 ± 0.3 (5.5 ± 1.0) events with $\sin^2 2\theta_{13} = 0$ (0.1) while 6 single ring electron-like events were observed. The probability to observe six or more electron-like candidates with a three-flavor neutrino oscillation scenario with $\sin^2 2\theta_{13} = 0$ is only 0.7%. The results were converted into a confidence interval: 0.03 (0.04) $< \sin^2 2\theta_{13} <$ 0.28 (0.34) at 90 % C.L. for $\delta_{\rm CP} = 0, \sin^2 2\theta_{23} = 1$ and $\Delta m^2_{32} = 2.4 \times 10^{-3}{\rm eV}^2$ and for normal (inverted) hierarchy.

4 Conclusion

The neutrino mixing angle θ_{13} was the last unknown mixing angle to describe neutrino oscillation, which is a key parameter to search for the CP violation in the lepton sector. To measure θ_{13}, two types of approaches; short baseline reactor and long baseline accelerator experiments are currently taking data. The MINOS and T2K experiment have detected the indication of electron neutrinos from muon neutrino beams to exclude the hypothesis of $\sin^2 2\theta_{13} = 0$ at 89 % C.L. and 99.3% C.L., respectably. The Double Chooz reactor experiment has succeeded presenting the first indication of disappearance of electron anti-neutrino from reactors with 94.6% C.L. which has been followed by Daya Bay and RENO experiments within half a year. The Daya Bay has revealed $\sin^2 2\theta_{13} = 0.092 \pm 0.016(\mathrm{stat}) \pm 0.005(\mathrm{syst})$ with exclusion of $\theta_{13} = 0$ at 5.2 standard deviations. The RENO experiment has also observed $\sin^2 2\theta_{13} = 0.113 \pm 0.013(\mathrm{stat}) \pm 0.019(\mathrm{syst})$, excluding the no-oscillation hypothesis at 4.9 standard deviations.

The results of both reactor and accelerator experiments suggest that the value of neutrino mixing angle θ_{13} is large enough to start discussion for next plans of neutrino oscillation accelerator experiments to search for the CP violation phase and neutrino mass hierarchy. With well measured value of θ_{13}, the unknown parameters of neutrino oscillation are expected to be determined in future.

References

1. B. Pontecorvo, *Sov. Phys. JETP* **6**, 429 (1957) and **26**, 984 (1968);
   Z. Maki, N. Nakagawa, and S. Sakata, *Prog. Theor. Phy.* **28**, 870 (1962).
2. K. Abe et al. (Super-Kamiokande Collaboration), *Phys. Rev.* D**83**, 052010 (2011).
3. S. Abe *et al.* (KamLAND Collaboration), *Phys. Rev. Lett.* **100**, 221803 (2008).
4. J. Hosaka *et al.* (Super-Kamiokande Collaboration), *Phys. Rev.* D**74**, 032002 (2006).
5. P. Adamson *et al.* (MINOS Collaboration), *Phys. Rev. Lett.* **106**, 181801 (2011).
6. M. Apollonio *et al.* (CHOOZ Collaboration), *Eur. Phys. J.* C**27**, 331 (2003).
7. Y. Abe *et al.* (Double Chooz Collaboration), *Phys. Rev. Lett.* **108**, 131801 (2012).
8. Y. Declais *et al.*, *Phys. Lett.* B **338**, 383 (1994).
9. F. P. An *et al.* (Daya Bay Collaboration), *Phys. Rev. Lett.* **108**, 171803 (2012).
10. J. K. Ahn *et al.* (RENO Collaboration), *Phys. Rev. Lett.* **108**, 191802 (2012).
11. P.Adamson *et al.* (MINOS Collaboration), *Phys. Rev. Lett.* **107**, 181802 (2011).
12. K. Abe *et al.* (T2K Collaboration), *Phys. Rev. Lett.* **107**, 041801 (2011).

PROBING THE NEUTRINO MASS HIERARCHY WITH CMB WEAK LENSING

ALEX C. HALL
Institute of Astronomy, Madingley Road,
Cambridge CB3 0HA, United Kingdom

We investigate the ability of future cosmological experiments to determine simultaneously the absolute mass scale of cosmological neutrinos and their mass hierarchy. We discuss the signatures of light neutrinos in the CMB weak lensing deflection angle power spectrum, and consider a non-parametric description of the hierarchy with neutrino oscillation data as a prior. We forecast constraints on cosmological parameters with a future post-*Planck* CMB experiment, the *Cosmic Orgins Explorer (COrE)*.

1 Introduction

In the most recent extension to the Standard Model of particle physics, neutrino oscillation experiments have established that at least two of the three neutrino mass eigenstates possess non-zero mass [1]. The oscillation experiments not only reveal that neutrinos have mass, but that the three species have *different* masses.

However, these experiments are only sensitive to differences in the mass-squared of the three neutrino species, and are not sensitive to the absolute mass-scale. Specifically, oscillation data imply [2]:

$$\begin{aligned} m_2^2 - m_1^2 &= 7.9^{+1.0}_{-0.8} \times 10^{-5}\mathrm{eV}^2 \\ |m_3^2 - m_1^2| &= 2.2^{+1.1}_{-0.3} \times 10^{-3}\mathrm{eV}^2, \end{aligned} \tag{1}$$

with 3σ confidence levels indicated. Since the sign of $m_3^2 - m_1^2$ is unconstrained, these results imply that the neutrino masses are arranged in one of two 'hierarchies'; 'normal' ($m_1 < m_2 \ll m_3$) and 'inverted' ($m_3 \ll m_1 < m_2$). Note that Equation 1 implies a lower limit on the total mass for each hierarchy: 0.095 eV for inverted, and 0.056 eV for normal.

Cosmological experiments provide a different aspect on this problem, essentially by measuring the gravitational effect of the neutrinos on matter and radiation density fields across cosmic time. Cosmic Microwave Background (CMB) measurements can go some way to constraining absolute neutrino masses, but are fairly insensitive to realistic mass scales compared to the influence of baryons and cold dark matter. Current 95% confidence limits from *WMAP* imply $\Sigma m_\nu < 0.58$ eV when combined with SDSS7 BAO and an H_0 prior of 4% for fixed dark energy equation of state w and assuming a flat universe [3]. The ESA *Planck* Surveyor is expected to tighten these limits even further.

In this paper, we consider the ability of a post-*Planck* CMB experiment, the European-led *Cosmic Origins Explorer* (*COrE*) [4] to determine not only the absolute neutrino mass scale, but also the individual neutrino masses. *COrE* will provide precision measurements of the weak lensing deflection field of CMB photons, which probes both the matter distribution and geometry of the universe[5]. Since neutrino masses affect the growth of structure at late times, we would expect measurements of the weak lensing signal to place strong constraints on the masses, independently of measurements of the primary CMB anisotropies. For example, MCMC forecasts in the *COrE* white paper show that *COrE* will be able to bound the lightest neutrino mass to $m_1 < 0.034$eV for the normal hierarchy, and $m_3 < 0.045$eV for the inverted hierarchy at 95% confidence.

Since structure formation is actually sensitive to the masses of the individual neutrino species, it may be possible to constrain the individual masses with future high-quality CMB data. In combination with the oscillation results, this would determine the mass hierarchy.

In this work we forecast for the sum of the neutrino masses in each hierarchy with a combination of forecast CMB data from *COrE*, and geometric information from future BAO constraints from SDSS-III *BOSS*, and a Type 1a supernovae survey with *WFIRST*.

2 Cosmological Signatures of Neutrino Masses

2.1 Massive Neutrinos

Massive neutrinos have a small, but measurable effect on both the primary anisotropies of the CMB and the growth of structure (for a review, see Lesgourgues & Pastor 2006[7]). Neutrinos with a summed mass of ≤ 1.6 eV are still relativistic at the epoch of recombination, and so their primary effect is on the background through the angular diameter distance, since the universe is matter dominated at this epoch.

Since neutrinos contribute to the energy density of the universe, they affect the Hubble expansion parameter via the Friedmann equation, and thus affect the angular diameter distance to last scattering, $d_A(z^*)$. The ratio of this distance to the scale of the sound horizon sets the angular scale of the acoustic peaks. In the absence of spatial curvature, increasing the density of massive neutrinos today decreases $d_A(z^*)$, whilst the the sound horizon $r_s(z^*)$ has only a weak dependence on the neutrino sector. The last scattering surface therefore appears closer, and the acoustic peaks are shifted to larger scales. This effect is degenerate with a change in both the Hubble constant and the dark energy equation of state parameter w[6]. This degeneracy is partially broken on large scales due to the early ISW effect and the late ISW effect, caused by potential decay after the dark energy begins to dominate the energy budget of the (flat) universe. However, cosmic variance is large on these scales, so the degeneracy remains a problem for parameter estimation.

The matter power spectrum is also affected by the presence of massive neutrinos due to their free-streaming effect. On scales smaller than the horizon size at the epoch when the neutrinos become non-relativistic, the power spectrum is damped relative to that with massless neutrinos by a factor of $\approx -8f_\nu$ in linear theory, as the massive neutrinos increase the expansion rate and stream away from potential wells, suppressing the growth of structure.

One of the key observables we consider is the reconstruction of the CMB weak-lensing (WL) deflection field from the lensed primary anisotropies (for a review, see Lewis & Challinor 2006[5]). In linear theory, the power spectrum of the lensing deflection angle is a convolution over the matter power spectrum, and thus the effect of massive neutrinos is similar to their effect on the growth of large-scale structure. The effects are more subtle however, since the lensing power spectrum, C_l^{dd} is an integration over the conformal time elapsed since last scattering[5]

2.2 Individual Masses

Massive neutrinos affect the CMB anisotropies almost entirely through their combined effect on the angular diameter distance. The CMB power spectra are thus sensitive primarily to the total summed mass:

$$\sum m_\nu \approx 93.14\Omega_\nu h^2. \tag{2}$$

The signature of mass differences amongst the individual neutrino masses is thus felt mainly in the matter power spectrum. Different masses have different free-streaming wavenumbers, and each has their own unique signature on the structure formation history of the universe. These signatures also show up in the CMB WL power spectrum, which is itself a convolution over the matter power spectrum.

It should therefore be possible, at least in principle, to determine the mass hierarchy from a combination of CMB primary and anisotropy and CMB WL observations. Including the oscillation measurements as prior information significantly ameliorates this task, as we only have to determine a single model from a choice of two, rather than deduce the mass splittings purely from cosmology.

3 Results

3.1 MCMC Forecasts

We ran Markov Chain Monte Carlo (MCMC) to derive forecast constraints on the cosmological parameters in each of the two neutrino mass hierarchies. We assumed *COrE* noise levels [4], and calculated weak lensing statistical noise using the prescription of Okamoto & Hu 2003 [8]. Chains were run using the publicly available CosmoMC package[9], modified to include the effects of neutrino mass splitting. We use a modified version of the FUTURCMB lensing add-on for CosmoMC [10] including the small correlation between the polarisation E-mode and the lensing deflection. We assume spatial flatness, but allow the dark energy equation of state w to vary. We take fiducial values for our parameter set from the WMAP 7-year maximum likelihood results[3], and take the summed neutrino mass to be at its lowest posibble value consistent with the oscillation results in each hierarchy.

We also include forecast measurements of Type 1a supernovae from the Wide-Field InfraRed Survey Telescope ($WFIRST$). Expected survey characteristics were taken from the $WFIRST$ Interim Report[a]. We assume their 'conservative' Figure of Merit forecast, but double the survey time to 12 months. We also include forecast measurements of the BAO scale from Baryon Oscillation Spectroscopic Survey (BOSS), with expected survey charactersitics taken from the SDSS-III project description [b]. In addition, we impose a 2% prior on the Hubble constant.

Our results are displayed in Table 1.

3.2 Bayesian Model Selection

To determine which hierarchy is favoured by the data, we should use the tools of Bayesian Model Selection. We can quantify our relative degree of belief in different models by use of the Bayes' Factor B, defined as the ratio of Bayesian evidences in two models M and M'. We assume that our likelihoods are well-described by a multi-variate Gaussian distribution, and integrate over the prior volume. The results are displayed in Table 2. Jeffreys [11] proposed model selection criteria depending on the value taken by B. If $\ln B > 5$, evidence for model M' is 'decisive' over model M, if $2.5 < \ln B < 5$ the evidence is 'strong', and if $1 < \ln B < 2.5$ it is 'substantial'.

[a] http://wfirst.gsfc.nasa.gov/science/WFIRST_Interim_Report.pdf
[b] http://www.sdss3.org/collaboration/description.pdf

Table 1: 68% upper limits on $\Omega_\nu h^2$ and w for inverted (top) and normal (bottom) hierarchies, combining different prior datasets (see text for details).

	No priors	H_0	WFIRST	BOSS	Combined
$\sum m_\nu$(eV)	0.136	0.131	0.131	0.119	0.118
$\sum m_\nu$(eV)	0.098	0.095	0.095	0.082	0.080

Table 2: Values of $\ln \langle B \rangle$ between the hierarchies for different combinations of prior.

No priors	H_0	WFIRST	BOSS	Combined
-1.08	2.66	2.53	2.53	2.51

4 Discussion

It is should be noted that there are in principle two ways to discern the neutrino mass hierarchy. Firstly, cosmology could possess no sensitivity to the mass splittings, but have sufficiently accurate constraints on the total mass that a measurement of $\sum m_\nu$ sufficiently below the minimum mass of the inverted hierarchy excludes the inverted hierarchy. Secondly, if cosmology could be sensitive to the individual mass splittings, which is quantified by the deviation of the Bayes' Factor from unity.

Our Bayes' Factor results indicate that future cosmological experiments will be able to discern the hierarchy with 'substantial' evidence in the language of Jeffreys[11], although this results is driven mainly by the Bayesian 'Occam Factor', and does not indicate a strong sensitivity of cosmology to the individual mass splittings. With the inclusion of prior geometric information, the Bayes Factor increases, although this is again due to relative volume changes of the posterior ellipsoids. Further results are presented in Hall & Challinor 2012[12].

Acknowledgments

This work presented here was conducted in collaboration with Anthony Challinor. I acknowledge financial support from an Isaac Newton Studentship from the University of Cambridge and the Isle of Man Government. I thank the organizers for an enjoyable and fruitful conference.

References

1. Y. Ashie *et al*, *Phys. Rev. Lett.* **93**, 101801 (2004).
2. M. Maltoni *et al*, New Journal of Physics, 6, 122, (2004).
3. E. Komatsu *et al*, The Astrophysical Journal Supplement Series, 192, 18, (2011).
4. The COrE Collaboration, Armitage-Caplan *et al*, 2011, ArXiv e-prints 1102.2181
5. A. Lewis & A. Challinor, Physics Reports, 429, 1, (2006).
6. G. Efstathiou & J. R. Bond, Monthly Notices of the Royal Astronomical Society, 304, 75, (1999).
7. J. Lesgourgues & S. Pastor, Physics Reports, 429, 307, (2006).
8. T. Okamoto & W. Hu, Phys. Rev. D, 67, 083002, (2003).
9. A. Lewis & S. Bridle, Phys. Rev. D, 66, 103511, (2002).
10. L. Perotto *et al*, Journal of Cosmology and Astroparticle Physics, 013, (2006).
11. H. Jeffreys, Theory of Probability, 3rd edn. Oxford University Press (1961).
12. A. Hall & A. Challinor, in prep. (2012).

8.
Posters

Observational constraints on $r \equiv T/S$ in cosmological ΛMDM models

N.A. Arkhipova
Astrospace Center of Lebedev Physical Institute RAS, Moscow

The normalization of the spectrum of density perturbations in spatially flat Friedmann Universe with nonzero Λ-term on temporary galaxy cluster abundance (σ_8) has been used to calculate numerically the value of the large scale CMB anisotropy ($\ell \simeq 10$) and the relative contribution of cosmological gravitational waves $r \equiv T/S$.

1 Introduction

It is clear that a cosmological model should fit both the COBE data $(\Delta T/T)_{10^0}$ and $\sigma(8h^{-1}Mpc)$ data. From the agreement in the normalization of the two scales, one of which depends on the amount of tensor and scalar modes, and the other solely on the normalized scalar mode it is possible get a limit on the T/S, depending on the parameters of cosmological model [1].

2 Cross normalization of density perturbation spectrum on $8h^{-1}Mpc$ and COBE scale

Currently there are a set of articles on the determination of σ_8 by galaxy clusters data: $\sigma_8 = 0.813(\frac{\Omega_M}{0.25})^{-0.47} \pm 0.011$ by Vikhlinin *et al.* [2]; $\sigma_8 = 0.832(\frac{\Omega_M}{0.25})^{-0.41} \pm 0.033$ by Rozo *et al.* [3]; $\sigma_8\Omega_M^{\frac{1}{3}} = 0.49 \pm 0.006$ by Campanelli *et al.* [4].

The dispersion of density contrast σ_8 was calculated for these approximations for different Ω_M and Ω_ν. Then the Anisotropy of Cosmic Microwave Background Radiation were calculated by CAMB [5] and normalazed on COBE signal with some introduced $r \equiv T/S$ to get the same σ_8 as on approximation formulas. So we get the dependence of r from Ω_M with other parameters fixed: $n = 0.968, h = 0.734, \Omega_b h^{-2} = 0.223$ Komatsu [6] and Vikhlinin [7].

The results for LCDM model ($\Omega_\nu = 0$) for different approximations of σ_8 is shown on Fig.1. The results for LMDM model for different $m_\nu \neq 0$ (Ω_ν) is shown on Fig.2.

3 Conclusions and discussion

- ΛCDM model

  If Planck will measure constraint on $T/S \equiv r$, then we get upper independent limit on Ω_M) from approximation $\Omega_8 = f(\Omega_M)$, whereas lower limit is obtained by the requirement of $r \geq 0$.

  As the set of the observant data says that $\Omega_M < 0.25$, so to not contradict a condition that $r \geq 0$, the preferable $\sigma_8 = f(\Omega_M)$ to reach minimal Ω_M with $r \geq 0$ is the Campanelli approximation.

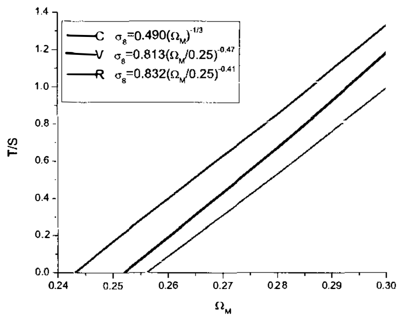

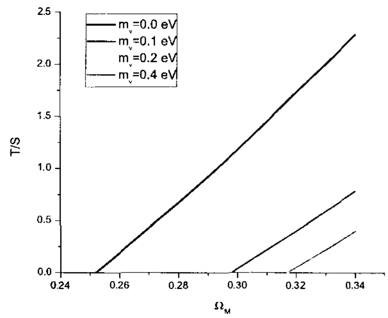

Figure 1: Dependence of T/S from Ω_M for different approximation of σ_8.

Figure 2: Dependence of T/S from Ω_M for different m_ν in Vikhlinin's approximation of σ_8.

- ΛMDM

  From the Fig 2. it is seen that for more size of $\Omega_\Lambda = 1 - \Omega_M$ a smaller value m_ν is needed for matching the normalizations and from requirements $r \leq 0$. The same effect of dependence m_ν and Ω_Λ have been found by Arkhipova *et al.*[8] on analysis of mass function evolution in ΛMDM models.

  And moreover, the demand $r \geq 0$, for example, m_ν=0.4 eV is allowed only for $\Omega_M > 0.288$ in the Vikhlinin's approximation of σ_8.

  But this effect may be related with that it's need to take into account that the dependence of $\sigma_8 = f(\Omega_M)$ is more complicated function of cold and hot dark matter $\sigma_8 = f(\Omega_{CDM}, \Omega_\nu)$ as it was done in the article by Malinovsky *et al.*[9] on mass function of galaxy clusters.

Acknowledgments

I acknowledge for financial support by the grant no. NSh 2915.2012.2 from the President of Russia and the grant ARISF from organization of the Rencontres de Moriond covering my living expenses on participation of the Conference.

References

1. N.A. Arhipova, E.V.Mikheeva, V.N.Lukash, Gravitation and Cosmology **5**, 159-163 (1999).
2. A. Vikhlinin *et al*, ApJ. **692**, 1033-1059 (2009).
3. E. Rozo *et al*, ApJ **708**, 645 (2010).
4. L. Campanelli *et al*, arXiv:1110.2310v1 [astro-ph.CO].
5. http://www.camb.info/.
6. E. Komatsu *et al*, Astrophys.J.Suppl. **192**, 18 (2011).
7. R.A. Burenin, A.A. Vikhlinin, arXiv:1202.2889 [astro-ph.CO].
8. N.A. Arhipova, T. Kahniashvilli, V.N. Lukash, Astronomy and Astrophysics **386**, 775-783 (2002).
9. A.M. Malinovsky, V.N. Lukash, E.V. Mikheeva, Astronomy Reports **Volume 52**, Issue 8 (pp.607-615)2008.

SECOND-ORDER RELATIVISTIC CONTRIBUTIONS TO THE COSMIC SHEAR BISPECTRUM

N. VAN DE RIJT[a], C. BONVIN[b,c]

[a]*CEA, Institut de Physique Théorique, 91191 Gif-sur-Yvette cédex, France*
CNRS, URA-2306, 91191 Gif-sur-Yvette cédex, France

[b]*Kavli Institute for Cosmology Cambridge and Institute of Astronomy, Madingley Road, Cambridge CB3 OHA, UK*

[c]*DAMTP, Centre for Mathematical Sciences, Wilberforce Road, Cambridge CB3 OWA, UK*

Future lensing surveys will be nearly full-sky and reach an unprecedented depth. This motivates the study of the cosmic shear beyond the small-angle approximation and including general relativistic corrections that are usually suppressed on sub-Hubble scales. Here we discuss the second-order contributions to the reduced cosmic shear and we compute the resulting bispectrum. We find that in the squeezed limit and at small redshift the relativistic corrections become relevant. We then compare the second-order signal with primordial non-Gaussianity of the local type and we show that relativistic corrections can contaminate the search for a primordial local signal by $f_{\rm NL}^{\rm loc} > 10$.

1 Introduction

With the advent of future wide-field surveys, weak gravitational lensing will become a powerful probe of the laws of gravity up to cosmological scales. In order to fully exploit the potentiality of the cosmic shear, it will be important to use its whole statistics. In particular, the lensing bispectrum represents a complementary probe to the power spectrum. The bispectrum receives not only contribution from non-gaussian initial conditions, but also from second-order couplings generated by the intrinsic non-linear nature of general relativity. At small scales, these couplings are well understood: they include the Born correction, the lens-lens coupling and the reduced shear correction. At large scales however, a plethora of new couplings come into play, allowing us to test the details of our understanding of the origin and formation of the large-scale structure. In this work we compute the cosmic shear bispectrum when all these effects are properly taken into account and we compare it to primordial non-Gaussianity of the local type.

2 Cosmic shear bispectrum

The second-order corrections to the shear are quadratic in Ψ and are conveniently (though not gauge invariantly) decomposed into [1]

$$\gamma = \gamma_{\rm geom}^{\rm (stan)} + \gamma_{\rm geom}^{\rm (corr)} + \gamma_{\rm geom}^{\rm (z)} + \gamma_{\rm dyn}^{\rm (stan)} + \gamma_{\rm dyn}^{\rm (corr)} \,.$$

The geometrical contributions refer to the second-order contributions from the Sachs equation. They are split into: the standard contributions which dominates at small scales, the relativistic

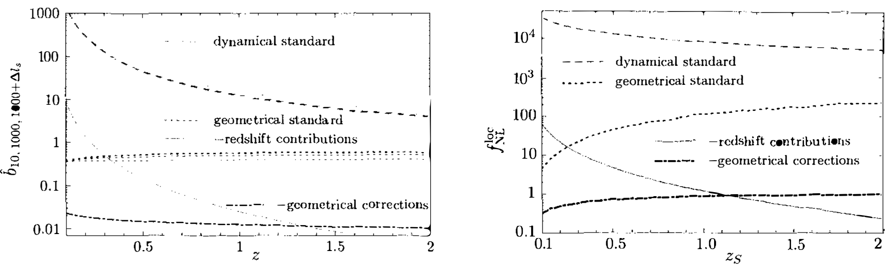

Figure 1: *Left panel*: The weighted bispectrum in the configuration $l_l = 10$ and $l_s = 1000$, plotted as a function of the redshift of the source z_S. *Right panel*: The contamination to a primordial local non-Gaussian signal.

corrections, and the redshift contributions generated by couplings between the perturbed redshift source plane and the shear. The dynamical contributions are generated by the non-linear dynamical evolution of the gravitational potentials. The standard dynamical contributions refer to the non-linear Newtonian evolution that governs the evolution of the potential at small scales, whereas the dynamical corrections come from the relativistic part of the evolution, that generates second-order scalar, vector and tensor modes.

Since the shear is a spin-2 field we can expand it on spin-weighted spherical harmonics as

$$\gamma(\hat{n}) = \sum_{lm} {}_2a_{lm}\ {}_2Y_{lm}(\hat{n}).$$

Contrary to the first-order shear, that contains only E-modes, the second-order shear contains both E and B-modes (for more details see [2]). Here we concentrate on the E-modes, that are related to ${}_2a_{lm}$ as $a_{E,lm} \equiv -({}_2a_{lm} + {}_{-2}a_{lm})/2$ where ${}_{-2}a_{lm}$ is the expansion coefficient of γ^*. From this we compute the electric reduced bispectrum

$$\hat{b}_{l_1l_2l_3} \equiv \langle a_{E,l_1m_1}\, a_{E,l_2m_2}\, a_{E,l_2m_2}\rangle (\mathcal{G}^{m_1m_2m_3}_{l_1l_2l_3})^{-1}/(C_{l_1}C_{l_2} + C_{l_2}C_{l_3} + C_{l_3}C_{l_1})\ , \qquad (1)$$

where $\mathcal{G}$ is a Gaunt integral and C_l is the angular power spectrum.

In Fig. 1 (left panel) we plot the reduced bispectrum in a squeezed configuration as a function of the redshift. We see that even though the signal is dominated by the standard dynamical and geometrical contributions, the relativistic corrections become relevant as the redshift decreases. The dominant effect among these non-standard corrections is due to the inhomogeneity of the source redshift. For redshift below 0.5 its amplitude become of the order of the standard couplings. We then compute the contamination from the second-order contributions to primordial non-Gaussianity of the local type. In the right panel of Fig. 1 we plot the effective $f_{\rm NL}^{\rm loc}$ from second-order corrections as a function of redshift. As expected the geometrical corrections lead to an $f_{\rm NL}^{\rm loc}$ of order 1 and roughly constant with z_S. The redshift corrections on the other hand are enhanced at small redshift and the contamination to $f_{\rm NL}^{\rm loc}$ becomes surprisingly large $f_{\rm NL}^{\rm loc} > 10$ for $z_S < 0.3$.

Acknowledgments

CB is supported by a Herchel Smith Postdoctoral Fellowship and by King's College Cambridge.

References

1. F. Bernardeau, C. Bonvin and F. Vernizzi, Phys. Rev. **D81**, 083002 (2010).
2. F. Bernardeau, C. Bonvin, N. Van de Rijt and F. Vernizzi, arXiv:1112.4430 (2011).

The VLT 5 year data set from the SuperNova Legacy Survey : redshifts and types of SNIa candidates

F. CELLIER-HOLZEM
LPNHE Laboratoire de Physique Nucléaire et des Hautes Énergies, Université Paris 6
4 place Jussieu, 75252 Paris Cedex 05, France

I present the spectral analysis of 81 Type Ia supernova candidates from the SuperNova Legacy Survey 5 year data set measured at the Very Large Telescope between august 2006 and september 2007. 54 objects are identified as Type Ia supernovae and their redshifts are estimated.

1 Cosmological context and aim

Using Type Ia supernovae (SNeIa) as standardisable candles permits to constrain the cosmological parameters governing the accelerated expansion of the universe (e.g., Perlmutter et al [1]). Based on a Hubble diagram built with high, intermediate and low redshift SNeIa and combining with other cosmological probes (BAO+WMAP7), Sullivan et al [2] obtain (assuming a flat universe) : $w = -1.061^{+0.069}_{-0.068}$ where w is the equation of state parameter of the dark energy. The SNeIa used in this analysis come from large spectro-photometric programs such as the SuperNova Legacy Survey (SNLS). In these programs, spectroscopy is essential to estimate redshifts and confirm the SNIa nature of the candidates. I present here a preliminary analysis of the SNLS 5 year spectroscopic data set, restricted to the spectra measured at the Very Large Telescope (VLT).

2 The SuperNova Legacy Survey experiment and the VLT 5 year spectral data

The SNLS is a 5 year experiment aiming at measuring the luminosity distance of a large number of SNeIa at intermediate to high redshift ($0.15 < z < 1.1$) in order to constrain cosmological parameters. Conducted from 2003 to 2008, this experiment is split in two surveys : 1) an imaging survey with the Canada-France-Hawaii Telescope in Hawaii to detect SNIa candidates and monitor their light curves in several photometric bands, and 2) several spectroscopic programs at the VLT, Gemini and Keck telescopes to confirm the nature of the SNIa candidates and measure their redshifts. SNLS measured 252 SNeIa during the first three years of operation [3]. Extending this set, spectra of 81 SNIa candidates have been obtained between august 2006 and september 2007 at the VLT in MOS (Multi-Object Spectroscopy) mode. These spectra have been wavelength and flux calibrated and are studied in the present work.

3 Spectral analysis : redshift estimates and SNeIa identification

The redshift determination is based on the presence, in the SN spectrum, of one or several host lines (e.g., [OII], CaH&K, H_β, [OIII]). An error of 0.001 is assigned to the redshift value, typical of redshift errors drawn from galactic emission/absorption lines. If no apparent host line is present, the redshift is estimated from the broad SN features (Si II, S II, Ca II) by fitting the SN spectrum with the spectro-photometric model SALT2 [4]. A typical uncertainty on the redshift in this case is 0.01.

To assess the nature of the candidates, a combined fit of the observed light curves and spectrum is done using SALT2. A galactic component is added and a wavelength tilt of the model is allowed. This procedure is illustrated for SN 06D4jh in figure 1. On the left panel, the full (SN+host) spectrum is shown in black. The best fit model is overlapped in red lines with (solid line) and without (dashed line) allowing for a wavelength tilt. The best fit host template (a Sd sunthetic template from PEGASE2) is shown in blue. On the right panel, the host model has been subtracted from the full spectrum (SN spectrum in black) and from the best fit model (SN model in red). We follow Balland et al [5] and classify the spectrum in one of the following categories : **SNIa** (typical SNIa features present and good overall fit), **SNIa⋆** (probable SNIa but other types (SNIb/Ic) can not be excluded), **SN?** (candidate of unclear type) and **other** (clearly not a SNIa).

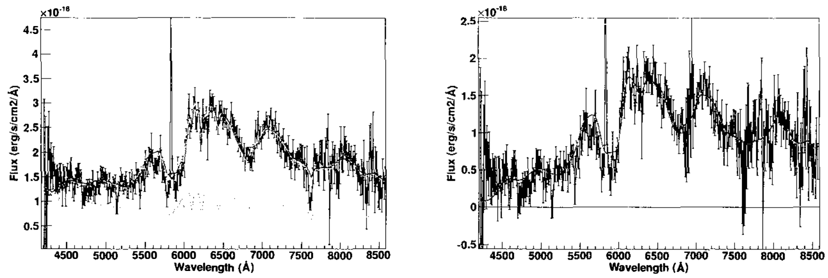

Figure 1: SN 06D4jh measured on 2006-11-14 at z=0.566 (redshift estimated from the [OII] galactic emission line visible at 5800Å) - **Left** : Full (SN+host) observer frame spectrum (black) with best fit model (red) overlapped. Dashed and solid lines are respectively without and with a wavelength tilt. The galactic component (a PEGASE2 spiral galaxy Sd) is shown in blue. - **Right** : Host subtracted SN spectrum (black) with the SN best fit model overlapped (red).

4 Results

Among the 81 SNeIa candidates of the SNLS VLT 5 year sample, 38 are classified as SNIa and 16 as SNIa⋆ (7 as SN? and 20 as others). The average redshift is $\langle z \rangle_{SNIa} = 0.56 \pm 0.03$ for SNeIa and $\langle z \rangle_{SNIa\star} = 0.77 \pm 0.03$ for SNeIa⋆. As expected, the SNIa⋆ sample has a higher average redshift than the SNIa sample (higher redshift means noisier spectra). Provided sufficient photometric information exist, the spectra falling into the SNIa and SNIa⋆ categories will be added to the spectroscopic sample for the SNLS 5 year cosmological analysis.

References

1. S. Perlmutter, G. Aldering, G. Goldhaber et al., ApJ **517**, 565 (1999)
2. M. Sullivan, J. Guy, A. Conley et al., ApJ **737**, 102 (2011)
3. J. Guy, M. Sullivan, A. Conley et al., A&A **523**, A7 (2010)
4. J. Guy, P. Astier, S. Baumont et al., A&A **466**, 11 (2007)
5. C. Balland, S. Baumont, S. Basa et al., A&A **507**, 85 (2009)

INFLECTION POINT QUINTESSENCE COSMOLOGIES AND THE CASE FOR DARK ENERGY

HUI-YIING CHANG
in collaboration with
ROBERT J. SCHERRER
Department of Physics and Astronomy
Vanderbilt University
6301 Stevenson Center
Nashville, TN 37235
U.S.A.

We examine several different cosmologies where the scalar field potentials are power law functions. They end up with slow-roll behavior, tunneling or oscillating based on particular variances in the potential and other factors. The examples of tunneling are Inflection Point Quintessence models of the universe. Accelerated expansion occurs in these models, which presents the case for dark energy.

The Inflection Point Quintessence (IPQ) cosmology has been explored as a model for inflation. The Euler-Lagrange equation of motion of the field ϕ is:

$$\ddot{\phi} + 3H\dot{\phi} + \frac{dV}{d\phi} = 0 \tag{1}$$

The total energy density in this cosmology is

$$\rho = \rho_{\phi} + \rho_M \tag{2}$$

where the dark energy density

$$\rho_\phi = V(\phi) + \frac{1}{2}\dot{\phi}^2 \tag{3}$$

and its scalar field potential

$$V(\phi) = V_0 + V_1\phi^n \tag{4}$$

When slow-roll conditions

$$(\frac{1}{V}\frac{dV}{d\phi})^2 \ll 1; \frac{1}{V}\frac{d^2V}{d\phi^2} \ll 1 \tag{5}$$

are satisfied, inflation happens. In the slow-roll limit,

$$\dot{\phi}^2 \ll V(\phi) \tag{6}$$

Since

$$\omega_\phi = \frac{p_\phi}{\rho_\phi} = \frac{\frac{\dot{\phi}^2}{2} - V(\phi)}{\frac{\dot{\phi}^2}{2} + V(\phi)} \tag{7}$$

$$\omega_\phi \approx -1 \tag{8}$$

which is the case for dark energy.

In the scalar field potential, we set $V_0 \approx 0.7$, which is the cosmological constant. For $n = 3$, when $V_1 \leq 0.80488$, ϕ slow rolls. When $V_1 \geq 0.8048825$, ϕ tunnels. We name such cosmologies the IPQ models of the universe. For $n = 4$, when $V_1 = 1$, ϕ slow rolls. When $V_1 = 1000$, ϕ oscillates. These are some representative behaviors of the scalar field.

MONTE CARLO PHOTOMETRY SIMULATION

P. EL-HAGE
LPNHE - Barre 12-22, 1er tage - 4 place Jussieu
75252 PARIS CEDEX 05

The Supernova Legacy Survey (SNLS) seeks to construct Hubble diagrams using Type Ia Supernovae. This has led to the most precise constraints on the equation of state of dark energy to date (*Astier et al 2006, Guy et al 2010, Sullivan et al 2011, Conley et al 2011*). The light curves of distant Supernovae are extracted using PSF photometry. In the analysis of the 3 year data set, the photometry method employed (dubbed **A06**) realigned and subsequently resampled the images, leading to pixel-to-pixel correlations. Since then, a new method has been developped (dubbed **WNR**) that avoids resampling the data. To this end, we aim to compare both methods and validate WNR prior to its use in the analysis of the 5 year data set.

1 Method Overview

1.1 Description

The first step of the simulation consists in creating images with so called *fake stars* added to them. These fake stars are constructed by Cutting aNd Pasting (*CNP*) bright, high quality stars, dubbed model stars, onto a nearby galaxy after being appropriately dimmed. In a few simple steps, this consists of selecting a vignette around a model star and a corresponding one around a galaxy, looping over values in the model star vignette, multiplying each value by a fixed factor while adding appropriate Poisson noise, then finally adding the value to the corresponding pixel in the galaxy vignette.

The idea, then, is to test a photometry by its ability to reproduce the photometric factor used above. To obtain a large sample of data for each model and fake star pairing, the same procedure is applied for each pair on a large set of images. For the A06 method, there exists a collection of images for which the data has already been aligned and resampled. During the CNP, therefore, one can always translate the pixels of the model star by a fixed amount and is guaranteed to always land on the same position in the sky. For the original images, we obviously do not have this guarantee. However, the shift from model to fake star must always be the same integer translation, otherwise we would be required to resample the data, thus defeating the purpose of the simulation. To get around this, we must be careful to select unaligned (and therefore un-resampled) images that are, by sheer happen stance, very nearly aligned up to a translation. During the simulation we assume that the images chosen are such that for the same translation, going from the same point, we will land on the same position in the sky.

1.2 Expected Bias

An important element of PSF photometry we wish to test is a flux estimation bias with respect to the S/N ratio. The bias is due to the fact that an error in the determination of the position of the star always leads to an underestimation of its flux. It is expected to take the form :

$$E[\hat{f}] = f\left\{1 - \frac{1}{S/N^2}\right\} \tag{1}$$

Because the fake and model stars differ greatly in S/N, we must take this bias into account when comparing the reconstructed photometric factor with its real value.

2 Results

2.1 Photometric Accuracy

We begin by comparing the results of A06 and WNR directly. To do this, we look at the difference between the two in terms of the ratio of the measured fake star flux to its actual flux. We look at the average difference between the two and find that:

$$\frac{F_{fake,A06}}{F_{model,A06} \times \text{photometric factor}} - \frac{F_{fake,WNR}}{F_{model,WNR} \times \text{photometric factor}} = 7.45 \times 10^{-4} \pm 6.49 \times 10^{-4} \tag{2}$$

We also compare the estimated photometric factor with the real one as a function of the S/N ratio. To detect any remaining bias, we fit equation 1 with an additional constant offset term (i.e. equation 1 becomes $E[\hat{f}] = f\left\{1 - \frac{1}{S/N^2} + b\right\}$). The fitted offset value for the WNR photometry is found to be $4.43 \times 10^{-04} \pm 3.69 \times 10^{-04}$.

2.2 Error Model

We also use the light curves of the model stars to fit an error model to the photometry method. We assume that the variance of the measurements as a function of flux takes the form :

$$V_{flux} = V_{sky} + \alpha F + \beta^2 F^2 \text{ where } \alpha = \frac{1}{G} \text{ and } G \text{ is the gain} \tag{3}$$

To find the value of beta, we look at the difference between the real variance of a star, as calculated numerically, and the known contributions from the Poisson noise of the sky and the star itself. The resulting value for β is $\sim 5 \times 10^{-03}$, which is consistent with past results, and is negligible at fluxes typical of Supernovae.

3 Conclusion

In conclusion, we find that the photometry method induces no systematic error beyond the per mil level. In addition, we find that the variance estimate output by the photometry is valid at the low fluxes typical of Supernovae in the SNLS survey.

DARK MATTER PRIMORDIAL BLACK HOLES AND INFLATION MODELS

MANUEL DREES, ENCIEH ERFANI
Physikalisches Institut and Bethe Center for Theoretical Physics, Universität Bonn
Nussallee 12, 53115 Bonn, Germany

A broad range of single field models of inflation are analyzed in light of all relevant recent cosmological data, checking whether they can lead to the formation of long-lived Primordial Black Holes (PBHs) as candidate for dark matter. To that end we calculate the spectral index of the power spectrum of primordial perturbations as well as its first and second derivatives. PBH formation is possible only if the spectral index $n_S(k_0)$ increases significantly at small scales. Since current data indicate that the first derivative α_S of the spectral index is negative at the pivot scale, PBH formation is only possible in the presence of a sizable and positive second derivative ("running of the running") β_S. Among the three small-field and five large-field models we analyze, only the "running-mass" model allows PBH formation, for a narrow range of parameters.

1 Introduction

Inflation dynamically resolves many cosmological puzzles of the big bang model. On the other hand, the generation of a spectrum of primordial fluctuations in the early universe is a crucial ingredient of all inflationary models. These fluctuations can explain the generation of all (classical) inhomogeneities that can be seen in our universe. In addition, each inflationary scenario makes accurate predictions to discriminate between the various candidate models. One such prediction is the possible formation of PBHs. For this generation mechanism to be efficient, one typically needs a "blue" spectrum. In this way, one can hope that the density contrast is sufficiently large that the resulting PBH production is significant and can be used as a powerful constraint on the spectrum of inflationary primordial fluctuations. On the other hand, since the production of PBHs take place on scales much smaller than those probed by the CMB anisotropy and LSS formation, they are also a unique cosmological probe.

For single-field inflation models, the relevant parameter space for distinguishing among models is defined by the scalar spectral index n_S, the ratio of tensor to scalar fluctuations r, the running of the scalar spectral index α_S and we introduce a new parameter as "running of running of the spectral index", β_S. The goal of this paper is to make use of the recent observational bounds derived from the combined data of WMAP7 data, Baryon Acoustic Oscillations, H_0, South Pole Telescope and *Clusters* [1] to discriminate among the wide range of inflationary models, by checking if they can produce high density fluctuations at the scale relevant for long-lived PBHs.

2 Primordial Black Holes and Inflation Models

PBHs are black holes that result from the collapse of density fluctuations in the early universe where a lower threshold for the amplitude of such homogeneities is $\delta_{\rm th} \approx 1/3$ at the time of radiation domination (RD). We have focused in our study [2,3] on PBHs which form in the RD era after inflation and we also considered the standard case of PBHs formation, which applies to scales which have left the horizon at the end of inflation. We only consider gaussian and spherically symmetric perturbations and we use Press–Schechter formalism. We study the possibility of PBH formation in two different categories of inflation models; small-field models and large-field models which their potentials are given as following:

2.1 Small-field models

$$\begin{aligned}
V(\phi) &= V_0\left[1-\left(\frac{\phi}{\mu}\right)^p\right], && (1)\\
V(\phi) &= V_0+\frac{1}{2}m_\phi^2(\phi)\phi^2, \quad \text{Running}-\text{mass} \quad \text{inflation} && (2)\\
V(\phi) &= V_0+\frac{\Lambda_3^{p+4}}{\phi^p}+\ldots, && (3)
\end{aligned}$$

2.2 Large-field models

$$\begin{aligned}
V(\phi) &= \Lambda^4\left(\frac{\phi}{\mu}\right)^p, \quad \text{chaotic} \quad \text{inflation} && (4)\\
V(\phi) &= \Lambda^4 e^{(\phi/\mu)^p}, && (5)\\
V(\phi) &= V_0\left(1-e^{-q\phi/M_P}\right), && (6)\\
V(\phi) &= \Lambda^4\left[1+\cos\left(\frac{\phi}{f}\right)\right], \quad \text{Natural} \quad \text{inflation} && (7)\\
V(\phi) &= V_0\left[1+\frac{2}{\pi}\arctan\left(\frac{\phi}{\mu}\right)\right], && (8)
\end{aligned}$$

3 Summary and Conclusions

The formation of PBHs with mass larger than 10^{15} g, whose lifetime exceeds the age of the Universe, will be produced at sufficient abundance to form the cold Dark Matter if the spectral index at scale $k_{\rm PBH}$ is about 1.37 for the threshold value $\delta_{\rm th} = 1/3$. This spectral index is much above the value measured at much larger length scales in the CMB. PBH formation therefore requires significant positive running of the spectral index when k is increased. We compared this with the values of the spectral index and its running derived from current data on large scale structure. At the pivot scale of the data set one finds $n_S(k_{\rm pivot}) = 0.9751$ as central value. The first derivative $\alpha_S(k_0)$ would then need to exceed 0.020 if it alone were responsible for the required increase of the spectral index; this is more than 3σ above the current central value of this quantity. However, the second derivative (the "running of the running") of the spectral index is currently only very weakly constrained. We showed in a model–independent analysis that this easily allows values of $n(k_{\rm PBH})$ large enough for PBH formation, even if the first derivative of the spectral index is negative at CMB scales. We applied this formalism [2] to a wide class of inflationary models, under the constraints imposed by the data. We classified the inflation models in small–field and large–field models. We have shown that only one small-field model, the running mass model [3], allows sizable positive running of running of the spectral index, and is thus a good candidate for long-lived PBHs formation. In contrast, all the large–field models we studied predict small or negative values for the second derivative of the spectral index, and thus predict negligible PBH formation due to the collapse of overdense regions seeded during inflation.

References

1. E. Komatsu *et. al.*, *Astrophys. J. Suppl.* **192** (2011) 18; R. Keisler *et. al.*, *Astrophys. J.* **743** (2011) 28; W. J. Percival *et al.*, *MNRAS* **401** (2010) 2148; A. G. Riess *et al.*, *ApJ* **730** (2011) 119; A. Vikhlinin *et. al.*, *ApJ* **692** (2009) 1060.
2. M. Drees and E. Erfani, *Primordial Black Holes in Single-Field Inflation Models*, *JCAP* **1201** (2012) 035.
3. M. Drees and E. Erfani, *Running–Mass Inflation Models and Primordial Black Holes*, *JCAP* **1104** (2011) 005.

COSMIC MICROWAVE BACKGROUND: HOW TO SEPARATE E- AND B-MODES?

AGNÈS FERTÉ
Institut d'Astrophysique Spatiale, Université Paris-Sud 11, Bâtiments 120-121, 91405 Orsay Cedex, France

The Cosmic Microwave Background (CMB) polarization is a promising source of information for a better understanding of the early Universe since *e.g.* polarized anisotropies of B-type, would give us a look to primordial gravitational waves. Nevertheless, its future detection is challenging. Because of the incomplete sky coverage of all CMB observations, E-modes leak into B-modes. Since B-modes amplitude is ten times less powerfull than E, the uncertainties on the reconstructed B-modes power spectrum are large due to extra sampling variance coming from leaked E-modes. Three different methods filtering out E-modes leaking into B have been realized. We propose to compare their relative efficiency on B-modes reconstruction.

1 Filtering out E-modes

Among many sources of uncertainties, extra sampling variance due to partial sky coverage, inherent to all CMB experiments, is a major source of error to be corrected. Because of the incomplete sky coverage, E-modes leak into B-modes and completely dominate it. If such a leakage is not corrected, the sampling variance on C_ℓ^{BB} is dominated by E-modes and prevent us from a measurement of C_ℓ^{BB} from Stokes parameters (Q, U) maps.

The standard method to reconstruct B-modes power spectrum –unfortunately plagued by E-to-B leakage– consists in decomposing the masked polarization field on the ${}_{\pm 2}Y_{\ell m}$. Due to the mask, E/B decomposition is not orthogonal anymore: the mean and the variance of pseudo-C_ℓ estimators of C_ℓ^{BB} are therefore affected by E-modes leaking into B, thus drastically increases uncertainties. In the standard method, such leakage can be corrected on average but not in the variance, thus preventing us from a detection of B-modes.

To correct for E-to-B leakage, E-modes leaking into B have to be filtered out at any momentum of the statistics of $\tilde{a}_{\ell m}^B$'s. This can be achieved by reconstructing the $\chi^{E/B}$ field on the observed part of the sky. Three different methods have been proposed:

• **SZ Method: Harmonic Filtering** [1 2 3] Multipoles of the $\chi^{E/B}$ field are directly computed from the (Q, U) maps where the sky apodization W has to verify Dirichlet and Neumann boundary conditions on the observed part of the sky replace the binary mask.

• **ZB Method: Pixel Filtering** [4] The map $W^2\chi^B$ can be directly computed from Q and U (see [3] for the complete expression in function of Q, U and their derivatives). W also has to satisfy the Dirichlet and Neumann conditions. This second technique can be viewed as a pixel implementation of the SZ method.

• **KN Method: Pixel Filtering** [5] This approach consists in removing the pixels which are mostly affected by E-to-B leakage. For that purpose, a first set of simulations is made with an input spectrum containing E-modes only: the resulting polarization map contains "aliased"

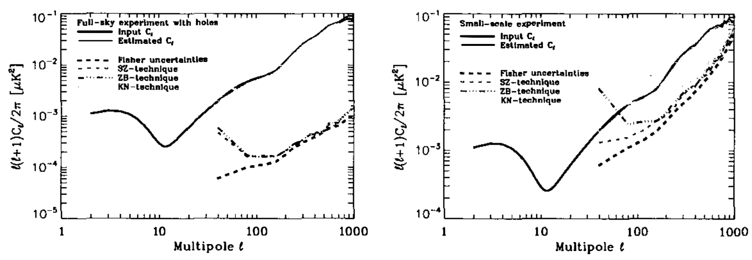

Figure 1: BB power spectra and the variance on their reconstruction via SZ, ZB and KN methods with the variance calculated via the f_{sky} approximation (under-estimation of the variance).

pixels only made of E-to-B leakage from which we define a mask removing these aliased pixels. Applying this new mask to measured (Q, U) maps allows us to estimate C_ℓ^B free of E-to-B leakage.

For each technique we have evaluated their efficiency first to solve E-to-B leakage examining the behaviour of the pseudo-C_ℓ^B and second to provide the most accurate estimation of C_ℓ^{BB}.

2 Numerical results and discussion

The estimated power spectrum of B-modes and their statistical uncertainties has been reconstructed using MC simulations for two kinds of experimental set up: 1) Small sky survey with an observed fraction of the sky $f_{sky} \simeq 1\%$ and a RMS of the noise of $\sigma_P = 5.75\mu K * arcmin$; 2) Full sky survey with $f_{sky} \simeq 71\%$ and $\sigma_P = 2.2\mu K * arcmin$. Both of them have a beam FWHM of $8arcmin$. Those uncertainties are shown in Fig. 1. For a full sky experiment, SZ and ZB perform the same and the error bars are lower than the signal, allowing for a reconstruction of C_ℓ^{BB}. The KN method does not performed as well as the SZ and ZB ones for ℓ lower than 60 as the uncertainties overwhelm the signal. For a small sky survey, the SZ technique performs the best and allows for a reconstruction of C_ℓ^{BB} for $\ell \sim 20$ to ~ 1000. The ZB method performs slightly worse since uncertainties are larger than the signal for $\ell < 80$. For the KN technique this dilution of the signal due to high error bars goes up to $\ell \sim 110$. These last results suggest that the SZ technique is at least for the small scale experiment the most efficient pseudo-C_ℓ technique for estimating BB angular power spectrum [6].

Acknowledgments

This work has been done with J. Grain (CNRS, IAS), M. Tristam (CNRS, LAL) and R. Stompor (CNRS, APC).

References

1. K. Smith, *Phys. Rev.* D **74**, 083002 (2006).
2. K. Smith and M. Zaldarriaga, *Phys. Rev.* D **76**, 043001 (2007).
3. J. Grain and M. Tristram and R. Stompor, *Phys. Rev.* D **79**, 123515 (2009).
4. W. Zhao and D. Baskaran, *Phys. Rev.* D **82**, 023001 (2010).
5. J. Kim and P. Naselsky, A&A **519**, A104 (2011).
6. A. Ferté and J. Grain and M. Tristram and R. Stompor, Deconstructing E/B separation methods for CMB polarized anisotropies, article in prep.

CLASSIC DARK MATTER THEORY WITH EXPERIMENTAL CONFIRMATIONS, EXACT SOLUTIONS AND PRACTICAL APPLICATIONS

M.Ja. Ivanov
Central Institute of Aviation Motors (CIAM)
Moscow, 111116, 2 Aviamotornaya St., Russia

Classic mechanical simulation of Dark Matter (DM) is considered. Proposed DM model bases on the Newtonian approach of gaseous compressible medium. As confirmation of our simulation we present the special experimental results on the temperature dependence for propagation velocity of electromagnetic fronts. The main conclusion of this experimental study is marked exceed of the speed value $2.998 \cdot 10^8$ m/s for electromagnetic front, which went inside a hot tube. The velocity propagation of electromagnetic front was increasing with temperature growth. Theoretical part of our study contains dimensional analysis, thermodynamically compatible conservation laws and some exact solutions. We demonstrate also practical application of this simulation for air breathing engines design.

Introduction. The π - theorem by E. Buckingham [1] and accurate application of the physics dimensional analysis [2-4] allow additionally getting good confirmations of the classic Dark Matter (DM) theory, which was developed in [5-8]. The main result of the dimensional analysis is the presence in a free space, containing the equilibrium radiation with the temperature $T = 2.735\ K$, material medium with the particle of non-zero mass $m = 5.6 \cdot 10^{-40}\ kg = 3 \cdot 10^{-4}\ eV$. This medium may consider as the classic ether, or the mass "photon" gas, or the DM medium. With the point of our view these different media may seeing as the same medium. By that the week perturbation velocity in this medium should be proportional to the square root from its temperature. This fact withdraws the limitation on a propagation velocity of week perturbations and allows the superluminal motion (without violation of the causality principle). Here relevantly one gives the analogy with the classic gas dynamics, which allows the motion with supercritical velocities.

Dimensional analysis. Discovery of the finite dimensional value $T = 2.735\ K$ in a free space with the characteristic speed $c=2{,}998 \cdot 10^8\ m/s$ leads automatically from the dimensional analysis [1-4] to a new dimension characteristic value, namely, the finite rest mass m of cosmic space particles. Write three dimensionless parameters by Buckingham π_1, π_2 and π_3 as

$$\pi_1 = \frac{kT}{mc^2} \sim 1\ , \quad \pi_2 = \frac{p}{\rho c^2} \sim 1\ , \quad \pi_3 = \frac{\pi_2}{\pi_1} = \frac{p}{nkT} = 1\ ,$$

where $k = 1.38 \cdot 10^{-23}\ kg/(m/s)^2/K$ is the Boltzmann constant p-pressure, ρ-density, $n=\rho/m$-concentration. The parameter π_1 gives the finite rest mass m of DM particles, π_2 is the correct relation for positive (no negative) cosmic pressure and π_3 presents the state equation of the DM medium. For the adiabatic constant $\kappa=4/3$ the exact value $m= \kappa kT/c^2=5.6 \cdot 10^{-40} kg=3 \cdot 10^{-4} eV$ [5-8].

The dimensional analysis shows us also that $c \sim sqrt(T)$.

Ground experiment. In our talk we present results of the special ground experiments for confirmation of our analysis, where study the temperature dependence for propagation velocity of electromagnetic front [9]. Modulated laser impulse is created in laboratory conditions by gas charge He-Ne laser LGN-207A on wave length λ=632,8 nm. The impulse propagates in an air medium in hollow metal tube of circular cross section with temperature up to 550 K. The initial impulse was divided on two rays by optical prism and after these rays were registries by the two laving photodiodes LFD-2-A with signal transfer on two channel oscilloscope GDS-710042. The time shift is fixed for ray fronts, which propagated in hot hollow metal tube with length 1.5 m. The main results of this study are marked exceed on 10-40% of velocity value $2.998 \cdot 10^8$ m/s for electromagnetic front, which went inside the hot tube. The velocity propagation of electromagnetic front was increasing with temperature growth.

Hidden mass boson. An important next step is to postulate the structure of DM particles, which allows explaining the large number of nature effects. Following [5-8], we consider a whole electrically neutral DM particle in the form of a dipole consisting of two parts with positive and negative charge equaled to about $5 \cdot 10^{-29}$ Coulomb. Thus, we actually introduce the new hidden mass boson (HMB) [10] with some analogy of the Higgs boson [11]. In this case the issue of physical vacuum polarization is extremely clear. In an external electric field orientation of the HMBs takes on power lines of the electric field, partly compensating for the external field. Thus, we obtain a physical interpretation of the Maxwell's displacement current in a free space. Further, the energy flux vector of the electromagnetic field – the Umov-Pointing vector indicates the direction of the HMB polarization under the influence of an external electromagnetic field. In particular, when a capacitor without insulator between plates is charging HMBs are moving from outer space in the capacitor plate space, providing in this case the displacement current. Also we get nature interpretation electric induction and self-induction phenomena. Another important process of electron-positron pair birth in the physical vacuum in the collision of two sufficiently intense electromagnetic pulse should be interpreted as a break in a certain (sufficiently large) number of dipoles – HMBs and followed concentration of their parts with the same sign of charge at the centers of the electron and positron under the influence of forces including non-electromagnetic nature. When implementing this scenario the HMBs will determine the birth mass of baryonic matter in the physical vacuum.

The poster presented the full system of conservation laws for the medium motion [10, 12] and their some exact solutions [13]. We demonstrated also a few practical applications of this simulation for air breathing engines design [12, 14].

References

1. Buckingham, E. On physically similar systems; the use of dimensional equations. Phys. Rev., 1914, 4.
2. Bridgmen P.W. Dimensional analysis. New Haven. Yale Univ. Press, 1932, 120p.
3. Sedov L.I. Methods of similarity and dimension in mechanics. M., "Nauka", 1967, 428 p.
4. Birkhoff G. Hydrodynamics. A study in logic, fact and similitude. Princ. Univ. Press, 1960, 244p.
5. Ivanov M.Ja. Dynamics of vector fields in a free space. Math. Model. 1998, т. 10, № 7, pp. 3-20.
6. Ivanov M.Ja. Accurate Dark Matter Theory and Exact Solutions. Proc. on IV Int. Symp. on DM&DE, Marina del Rey, CA, USA. Ed by D. B. Cline. Springer, 2001, pp. 281-289.
7. Ivanov M.Ja. Newtonian dark matter identification and search. Proc. on III Int. Workshop on the Identification of DM. Ed. N.J.C. Spooner, V. Kudryavtsev. World Scientific. 2001. pp. 324-330.
8. Ivanov M.Ja. Dark Matter Quo Vadis? 13th ICATPP Conf. Vila Olmo, Italia, Oct. 2011, p. 68.
9. Malakhov Ju.I., Ivanov M.Ja., Shi N.Q., Schaulov V.V. Registration of temperature dependence for electromagnetic front velocity with theoretical support and demonstration examples. Proc. XI Int. Conf. (ZST-2012), RFNC-VNIITF, Snezhinsk, Apr. 16-20, 2012.
10. Ivanov M.Ja., Zestkov G.B. Dimensional analysis, thermodynamics and conservation laws in a problem of radiation processes simulation. J. of Math. Research, 2012, 4, 2. pp.10-19.
11. Higgs P.W. Broken symmetries and the masses of gauge bosons. Phys. Rev. Let., 1964. Vol. 13.
12. Ivanov M.Ja. Thermodynamically compatible conservation laws in the model of heat conducting radiating gas. Comp. Mathematics and Mathematical Physics, 2011, Vol. 51, No. 1, pp. 133-142.
13. Ivanov M.Ja., Terentieva L.V. Exact solutions of two-fluid approach equations in aerospace plasmadynamics. AIAA Paper No. 2003-0843, 8p.
14. Ivanov M.Ja. Close system of thermodynamic coordinated conservation laws in working precess theory of high temperature turbojet engenes. ISABE Paper No. 2011-1337, 9p.

A NEW METHOD FOR DETECTING BARYON ACOUSTIC OSCILLATIONS

A. LABATIE, J.-L. STARCK and M. LACHIEZE-REY
Laboratoire AIM (UMR 7158), CEA/DSM-CNRS-Université Paris Diderot, IRFU, SEDI- SAP, Service dAstrophysique, Centre de Saclay, F-91191 Gif-Sur-Yvette cedex, France.

Baryon Acoustic Oscillations (BAOs) are a feature imprinted in the galaxy distribution by acoustic waves traveling in the plasma of the early universe. Their detection at the expected scale in large-scale structures strongly supports current cosmological models with a nearly linear evolution from redshift $z \approx 1000$ and the existence of dark energy. Besides, BAOs provide a standard ruler for studying cosmic expansion. We study BAO detection methods using the correlation function measurement $\hat{\xi}$ which can be formulated as an hypothesis test between $\mathcal{H}_0$ (no-BAO hypothesis) and $\mathcal{H}_1$ (BAO hypothesis). We describe problems with the classical method based on the $\Delta\chi^2$ statistic and we propose a new method, the Δl method, to overcome these difficulties.

1 BAOs in the correlation function

BAOs are relic of acoustic waves which traveled in the plasma before recombination. They stopped to propagate around the time of recombination, leaving a small excess of power at the sound horizon scale ($r_s \approx 150$ Mpc) in the matter distribution. As a consequence, BAOs can be detected as a peak around 150 Mpc in the correlation function of the galaxy distribution. Note that the BAO peak in the correlation function and its whole shape has a dependence on cosmological parameters. It is also possible to construct correlation functions without BAOs, by artificially erasing the BAO peak using a 'no wiggles' form[2] or setting a baryon density $\Omega_b h^2 = 0$. In order to estimate the correlation function we will use the Landy-Szalay[5] estimator $\hat{\xi}$.

2 A new method for BAO detection

BAO detection can be formulated as an hypothesis test

$$\mathcal{H}_0 \;:\; \exists\theta \in \Theta \text{ s.t. } \hat{\xi} \sim \mathcal{N}\left(\xi_{noBAO,\theta}, C_{noBAO,\theta}\right) \quad (1)$$

$$\mathcal{H}_1 \;:\; \exists\theta \in \Theta \text{ s.t. } \hat{\xi} \sim \mathcal{N}\left(\xi_{BAO,\theta}, C_{BAO,\theta}\right) \quad (2)$$

The classical BAO detection method makes the assumption that covariance matrices are constant ($C_{noBAO,\theta} = C_{BAO,\theta} = C$). It is based on the $\Delta\chi^2$ statistic, which can be thought as a generalized likelihood ratio (the optimal statistic to test between simple hypotheses is the likelihood ratio according to the Neyman-Pearson lemma)

$$\Delta\chi^2 = \min_\theta \chi^2_{noBAO,\theta}(\hat{\xi}) - \min_\theta \chi^2_{BAO,\theta}(\hat{\xi}) \quad (3)$$

$$= -2\log\left[\frac{\max_\theta \mathcal{L}_{noBAO,\theta}(\hat{\xi})}{\max_\theta \mathcal{L}_{BAO,\theta}(\hat{\xi})}\right] \quad (4)$$

Table 1: Expected significance averaged over all $\mathcal{H}_1$ models in the two different cases of constant C and model-dependent C_θ.

	Classical $\sqrt{\Delta\chi^2}.\sigma$ (wrong)	$\Delta\chi^2$ with correct significance using Eq. 5	Δl method
Constant C	2.21σ	2.0σ	2.0σ
Model-dependent C_θ	2.32σ	1.59σ	1.96σ

Given some regularity assumptions, one can show[4] that the BAO detection significance (i.e. the rejection of the $\mathcal{H}_0$ hypothesis) can be estimated as $\sqrt{\Delta\chi^2}.\sigma$. However these assumptions are usually wrong, so that the classical method can overestimate the detection significance. Another problem is that it only works for hypotheses with a constant covariance matrix which can be a poor estimation of the real hypotheses $\mathcal{H}_0$ and $\mathcal{H}_1$ of Eq. (1) and (2).

For these reasons we propose a new method, that we call the Δl method. First we modify the procedure to obtain the significance of the BAO detection, in order to make it rigorous. For a constant covariance matrix, the significance of the detection as a p-value $p(x)$ is computed as the p-value of $\Delta\chi^2 = x$ in the 'worst-case' $\mathcal{H}_0$ model

$$p(x) = \max_{\theta\in\Theta} P(\Delta\chi^2 \geq x \,|\, \mathcal{H}_0, \theta) \tag{5}$$

The second modification that we propose is to extend the statistic $\Delta\chi^2$ in the case of varying covariance matrices $C_{noBAO,\theta}$ and $C_{BAO,\theta}$ in (1) and (2). We call the new statistic the Δl statistic, as it is a difference of generalized log-likelihoods

$$\Delta l = -2\left[\max_\theta \log \mathcal{L}_{noBAO,\theta}(\hat{\xi}) - \max_\theta \log \mathcal{L}_{BAO,\theta}(\hat{\xi})\right] \tag{6}$$

3 Results

We test our new method and compare it to the classical method using lognormal simulations of the Luminous Red Galaxies sample of the Sloan Digital Sky Survey Data Release 7[4]. We estimate a covariance matrix C from 2000 simulations with realistic parameters. As a toy example we only take into account a model-dependent covariance matrix of the form $C_\theta = b^4 C$ (i.e. we only take into account a approximate dependence on b).

We show in Table 1 the average significances under $\mathcal{H}_1$ in the 2 different cases of constant C and model-dependent C_θ for different methods.

We obtain the following results:

- $\sqrt{\Delta\chi^2}.\sigma$ slightly overestimates the significance for hypotheses with constant C
- $\sqrt{\Delta\chi^2}.\sigma$ grossly overestimates the significance for hypotheses with model-dependent C_θ
- Δl largely outperforms $\Delta\chi^2$ for hypotheses with model-dependent C_θ

References

1. C. Blake *et al*, MNRAS **415**, 2892 (2011).
2. D.J. Eisenstein and W. Hu, ApJ **496**, 605 (1998).
3. D.J. Eisenstein *et al*, ApJ **633**, 560 (2005).
4. A. Labatie *et al*, ApJ **746**, 172 (2012)
5. S.D. Landy and A.S. Szalay, ApJ **412**, 64 (1993).

Inflation and stagflation
- Robust inflation and cosmological constant problem without fine tuning -

Akika NAKAMICHI & Masahiro MORIKAWA

A simple introduction of a small negative region of the inflaton potential often yields a sudden stop of the inflation, at the vanishing energy density, followed by a strong instability of the homogeneous mode of inflaton field (stagflation). This stagflation may provide us a unified termination mechanism of inflation and the subsequent autonomous vanishing of the effective cosmological constant without any fine tuning on the potential. We study how extent the stagflation is common in various potentials.

1 Introduction

Recent progress in cosmological observations have confirmed the basic idea of inflation in the early Universe. Variety of inflationary models have been proposed to explain the cosmological data and the inflationary scenario has phenomenologically achieved a big success. On the other hand, we do not have a principle of the inflation mechanism which guarantees the robustness of the inflationary scenario although many theoretical models of inflation have flooded at present. A phenomenological selection of one particular Lagrangian which best fits data does not provide us with any insight into the inevitability of the inflation and the cosmological constant problem.

Here in this paper, we take a different approach and argue a possibility of the robust inflationary model based on a simple idea. We look for a universal instability in the inflationary models. This guarantees the autonomous termination of the inflation and possibly the autonomous adjustment of the cosmological constant to vanish. A model of the inflation based on the Bose-Einstein condensation [1] is one such type. We continue this idea in a wider context.

2 Stagflation model

Stagflation is easily realized in the standard model of inflaton simply provided a negative potential region. A set of basic equations for the scale factor $a(t)$ and the energy densities of the gas ρ_g and the inflaton ρ_ϕ becomes

$$H^2 = \left(\frac{\dot{a}}{a}\right)^2 = \frac{8\pi G}{3c^2}\left(\rho_{gas} + \rho_\phi\right),\ \dot{\rho}_{gas} = -4H\rho_{gas} + \kappa\dot{\varphi}^2,\ \dot{\rho}_\phi = -6H\left(\rho_\phi - V\right) - \kappa\dot{\varphi}^2. \quad (1)$$

The gas particle production and the back reaction effects, $-\kappa\dot{\varphi}^2$, are taken into account. This allows an approximate analytical solution for the inflaton $\phi_{inf} \propto (t_0 - t)^{-1/2}$, in a simple potential model $\lambda\phi^4$ if $\lambda < 0$, which properly yields the power spectrum for the primordial density fluctuations consistent with the present observations[1].

The relevant contributions in the above equation during inflation, neglecting the gas component, yield $\dot{H} = -3H^2 + \left(8\pi G/c^2\right)V$. Therefore, if the potential V reduces in time toward 0 from above, then the term $-3H^2$ behaves as a simple friction and $H \to 0$ from the above. However if the potential V can be negative, then H can change its signature and the cosmic expansion stops at some finite moment: $\rho_\phi = 0$, $\dot{\rho}_\phi = 0$, $H = 0$. This is the stagflation which often appears when V can be negative. Suddenly after the stagflation, the Universe, with uniform distribution of the inflaton, collapses $a \to 0$ within some finite time. However this extreme behavior is actually taken place by the strong instability of the uniform mode of the inflaton and its decay into localized objects. At the same time, strong particle production (reheating) effect yields the radiation dominant Universe. Thus the inflation terminates with vanishing cosmological constant provided the inflaton potential V has negative region. We have numerically checked this behavior in various cases.

3 Variety of stagflation

Some attempts have been made to clarify the stagflation by using approximate analytical calculations before [1]. However, it was quite poor to establish the universality of the stagflation. Therefore we have decided to study the stagflation Eq.(1) numerically for various potentials which have negative regions. All the models we have checked this time turn out to show the stagflation followed by strong instability as in the figure: Results of new, chaotic, and linear type inflation models are shown in row, respectively. The columns are, from left to right, the potential $V(\phi)$, the time evolution of the inflaton $\phi(t)$, a scale factor $a(t)$ and densities (solid line for ρ_ϕ, broken line for ρ_g). Arrows show the stagflation point. The produced gas of particles dominate the Universe just after the stagflation. This guarantees the Big Bang and the subsequent radiation-dominant expansion of the Universe as well as vanishing effective cosmological constant.

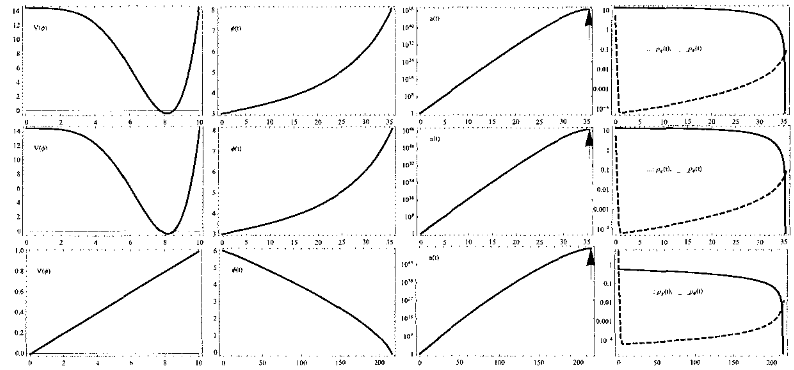

4 Conclusions

In order to show the universality of the stagflation to some extent, we have numerically studied various potential models which has negative region. Then we have found that stagflation phase appears for all cases we calculated. However, we would need some hybrid approach of analytic and numerical methods in order to show the full universality of the stagflation and the subsequent reduction of the cosmological constant. This will be reported in our future research.

Acknowledgments

This work was supported by MEXT of Japan, C21540287, C23540291, and S0801061.

1. T. Fukuyama and M. Morikawa, *Phys. Rev. D* **80** 063520 (2009).

Long Range Forces in Direct Dark Matter Searches

Paolo Panci
CP^3-Origins and DIAS, University of Southern Denmark,
Odense, Denmark

We study the effect of a long–range DM-nuclei interaction occurring via the exchange of a light mediator. We consider the main direct detection experiments: DAMA, CoGeNT, CRESST, CDMS and XENON100. We find that a long–range force is a viable mechanism, which can provide full agreement between the various experiments, especially for masses of the mediator in the 10–30 MeV range and a light DM with a mass around 10 GeV. The relevant bounds on the light mediator mass and scattering cross section are then derived.

1 Generalization of the pointlike cross section to long-range interactions

A specific realization of long–range interactions between DM particles χ and target nuclei N is provided by models in which ordinary photons possess a kinetic mixing ϵ with light dark photons ϕ (see e.g. [1,2,3]). In non relativistic limit this interaction is governed by a Yukawa potential $V(r) = \epsilon/(4\pi)(Ze\,Z_\chi e_\chi)/r\, e^{-m_\phi r}$, whose scale is determined by the mass of the mediator m_ϕ. In order to have a rough comparison with the "standard" picture (spin independent contact interaction), the differential cross section derived from the Yukawa potential above can be cast in the following form

$$\frac{d\sigma(v, E_R)}{dE_R} = \frac{m_N}{2\mu_{\chi p}^2}\frac{1}{v^2}\, A^2 \sigma^p_{\phi\gamma} F^2_{\rm SI}(E_R)\mathcal{G}(E_R), \tag{1}$$

where $\sigma^p_{\phi\gamma} = \mu^2_{\chi p}/\pi \cdot (e\,\epsilon\, Z_\chi e_\chi)^2/m_p^4$ is a normalized total cross section, $F_{\rm SI}(E_R)$ denotes the nuclear form factor and $\mu_{\chi p}$ is the DM-proton reduced mass. The function

$$\mathcal{G}(E_R) = (Z/A)^2 \left[m_p^2 / \left(q^2 + m_\phi^2\right)\right]^2, \quad \text{where } q^2 = 2 m_N E_R, \tag{2}$$

measures the deviations of the allowed regions and constraints respect to the "standard" picture. Here the factor $(Z/A)^2$ is due to the fact that the DM only couples with protons, while the factor in the square brackets accounts for the energy dependence of the differential cross section and exhibits two limits:

- ◇ Point–like limit ($q \ll m_\phi$): In this regime $\mathcal{G}$ is independent on E_R, and therefore the interaction is of contact type.
- ◇ Long–range limit ($q \gg m_\phi$); In this regime one has a E_R^{-2} drop–off of the cross section (Rurtherford scattering). Experiments with low energy thresholds and light target mass (e.g. DAMA) are more sensitive than the ones with high threshold and heavy targets (e.g. XENON100). The compatibility among the experiments could therefore be improved.

Considering typical nuclei ($m_N \sim 100$ GeV) and recoil energies (few keV) in the range of interest of the experiments, the transition between the two limits is obtained for $m_\phi \sim \mathcal{O}(10)$ MeV.

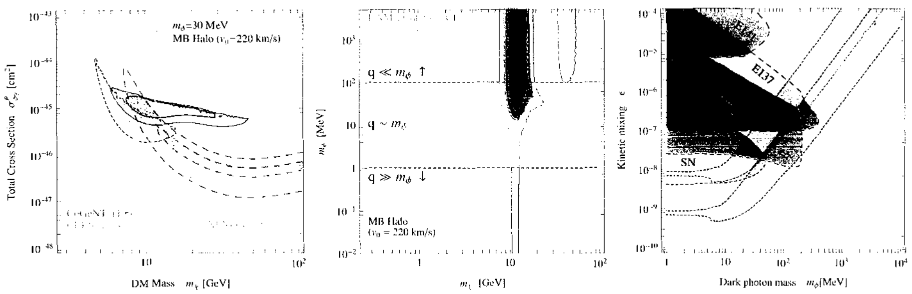

Figure 1: *left-panel*: Allowed regions compatible with DAMA (solid green regions), CoGeNT (dotted blue regions), and CRESST (dashed brown regions) as well as the constraints coming from null results experiments (magenta and gray dashed lines for XENON100 and CDMS), considering a dark photon mass of 30 MeV; *central-panel*: Bounds on the light-mediator mass m_ϕ as a function of the DM mass m_χ, as obtained by the analysis of the DAMA annual-modulation result; *right-panel*: Bounds and interpretation for DAMA and CoGeNT data in the (ϵ, m_ϕ) plane. A summary of the constraints is discussed e.g. in [4] and they are depicted as (blue) regions.

2 Results

In the left–panel of Fig. 1 we show the allowed regions and constraints coming from direct dark matter experiments, considering a dark photon mass of 30 MeV which falls in the transition between point-like and long-range interactions. One can see that:

◇ A large overlapping between DAMA, CoGeNT and CRESST is observed at $m_\chi \sim 10$ GeV, especially in the long–range scenario ($m_\phi \to 0$). For a conservative choice of the XENON100 constraints, the overlapping regions are allowed by all the experiments.

◇ Heavy targets (I for DAMA, W for CRESST), which account for the fit at large $m_\chi > 30$ GeV, reach the long–range limit earlier respect to the light ones (Na for DAMA, O and Ca for CRESST). The function $\mathcal{G}$ gets therefore suppressed and, to yield the measured event rate, an increase in $\sigma^p_{\phi\gamma}$ at high m_χ occurs. For this reason, the CRESST favorite region flattens respect to the point–like scenario. This also happens in DAMA, but the large $1/E_R^2$ enhancement of the cross section close to the low energy threshold rapidly overshoots the total rate, that is treated as a constraint; therefore, getting closer to the long–range limit, the DAMA-I region disappears.

◇ Approaching the long–range limit, the agreement among the various experiments increases, but the significance of the DAMA fit gets lower for the reason outlined in the previous item, this time applied to scattering on Na.

3 Constraints

In the central–panel of Fig. 1 we show a first class of constraints in the (m_ϕ, m_χ) plane, coming from the fact that long–range forces rapidly overshoots the total rate being the cross section strongly enhanced. We adopt the DAMA dataset and we find that long-range forces are only viable for light DM. Nevertheless, the best agreement is obtained for mediator masses larger than 20 MeV. A 99% C.L. lower bound on m_ϕ is about 10 MeV.

In the right–panel of Fig. 1 we show instead a second class of bounds in the (ϵ, m_ϕ) plane. One can see that in the "totally symmetric" case ($k = Z_\chi e_\chi / e = 1$), light mediators are excluded and only dark photons with $m_\phi > 100$ MeV can satisfy the constraints and provide a suitable interpretation for DAMA and CoGeNT data. However, for $k > 10$ ("composite" DM models), the whole range of light-mediator masses is allowed.

Another complementary class of bounds which are dependent on $Z_\chi e_\chi$ and m_ϕ, while independent on ϵ, arises from DM self–interaction. The most famous of them comes from the Bullet Cluster [5], which points towards collisionless DM ($\sigma/m_\chi \leq 1.25$ cm^2/g). Considering $m_\chi \sim 10$ GeV (to fit direct detection observations) and again two values of the parameter $k = 1\,(10)$, we get that the bound on the self–interaction is exceeded for $m_\phi < 1\,(20)$ MeV.

References

1. N. Fornengo, P. Panci, M. Regis, *Phys. Rev.* D **84**, 115002 (2011).
2. B. Holdom, *Phys. Lett.* B **166**, 196 (1986).
3. R. Foot, *Phys. Rev.* D **78**, 043529 (2008).
4. J. D. Bjorken *et al*, *Phys. Rev.* D **80**, 075018 (2009).
5. D. Clowe *et al*, *Astrophys. J.* **648**, L109-L113, (2006).

TRUE CMB POWER SPECTRUM ESTIMATION

P. PAYKARI[1], J.-L. STARCK[1], M. J. FADILI [2]
[1]*Laboratoire AIM, UMR CEA-CNRS-Paris 7, Irfu, SAp/SEDI, Service d'Astrophysique, CEA Saclay, F-91191 GIF-SUR-YVETTE CEDEX, France*
[2]*GREYC CNRS UMR 6072, ENSICAEN, 6 Bd du Maréchal Juin, 14050 Caen Cedex, France*

Having access to only one sky, the CMB power spectrum measured by our experiments is only a realization of the true underlying angular power spectrum. In this paper we aim to recover the true underlying power spectrum from the one realization we have without a need to know the cosmological parameters; the CMB spectrum is very sparse in two dictionaries; Discrete Cosine Transform (DCT) and Wavelet Transform (WT). Using the two dictionaries, we develop a technique that estimates the true underlying CMB power spectrum from data alone. The developed IDL code, **TOUSI**, for Theoretical pOwer spectrUm using Sparse estImation, will be released with the next version of ISAP (Interactive Sparse astronomical data Analysis Packages) `http://jstarck.free.fr/isap.html`.

1 Introduction

Measurements of the cosmic microwave background (CMB) anisotropies are powerful cosmological probes. The CMB angular power spectrum depends on the cosmological parameters through an angular transfer function $T_\ell(k)$ as $C[\ell] = 4\pi \int \frac{dk}{k}\, T_\ell^2(k)P(k)$, where k defines the scale, ℓ is the multipole moment, which is related to the angular size on the sky as $\ell \sim 180°/\theta$ and $P(k)$ is the primordial matter power spectrum.

We use the sparsity of the CMB spectrum as a key ingredient to estimate the theoretical power spectrum directly from the data, without having to know the cosmological parameter.

2 Sparsity of the CMB power spectrum; TOUSI Algorithm

A signal X considered as a vector in $\mathbb{R}^N$, is sparse if most of its entries are equal to zero. Generally signals are not sparse in direct space, but can be sparsified by transforming them to another domain; for eg, $\sin(x)$ is 1-sparse in the Fourier domain. In the so-called sparsity synthesis model, a signal can be represented as the linear expansion $X = \Phi\alpha = \Sigma_{i=1}^{T}\phi_i\alpha[i]$, where $\alpha[i]$ are the synthesis coefficients of X and ϕ_i are called the atoms (elementary waveforms) of the dictionary $\Phi = (\phi_1, \ldots, \phi_T)$; such as Fourier (FT), wavelet (WT) and discrete cosine transforms (DCT). The CMB power spectrum is very sparse in both the DCT and WT dictionaries, although their sparsifying capabilities are different; DCT recovers global features of spectrum (i.e. the peaks and troughs) while WT recovers localized features. These complementary capabilities of DCT and WT transforms are combined to propose a versatile way for adaptively estimating the theoretical power spectrum from a single realization. Having $X = C[\ell]$ and $\widehat{S}_N[\ell]$ as the noise power spectrum, we minimize equation 1 iteratively (equation 2);

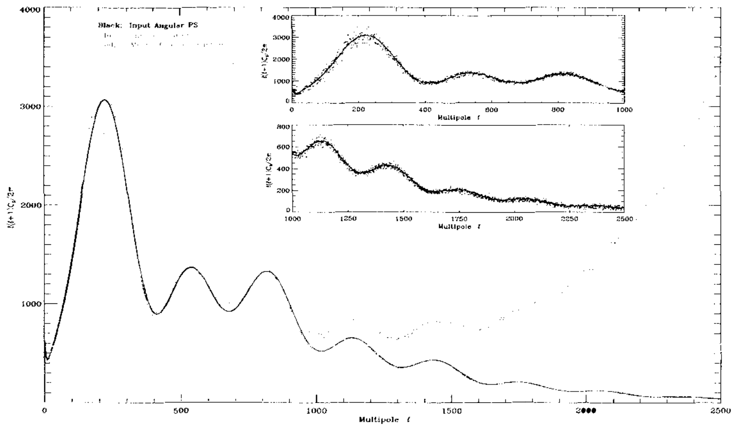

Figure 1: TOUSI reconstructed spectrum. Blue dots show the empirical power spectrum of one realization with instrumental noise. Yellow dots show the estimated noise spectrum of one of the simulated noise maps. Green dots show the the spectrum with the noise power spectrum removed. Black and red solid lines are the input and reconstructed power spectra, respectively. The inner plots show a zoomed-in version.

$$\min_X \|\Phi^T X\|_1 \quad \text{s.t.} \quad \begin{cases} X \geqslant 0 \\ M_d \odot \left(\Phi_d^T \mathcal{T}(X + \widehat{S}_N)\right) = M_d \odot \left(\Phi_d^T C^s\right), \; d \in \{1, \cdots, D\}, \end{cases} \tag{1}$$

$$\begin{aligned} \widetilde{X} &= \mathcal{R}\left(\mathcal{T}\left(X^{(n)} + \widehat{S}_N\right) + \Phi M \bullet \left(\Phi^T \left(C^s - \mathcal{T}\left(X^{(n)} + \widehat{S}_N\right)\right)\right)\right) - \widehat{S}_N \\ X^{(n+1)} &= \mathcal{P}_+\left(\Phi \; \mathrm{ST}_{\lambda_n}(\Phi^T \widetilde{X})\right) . \end{aligned} \tag{2}$$

3 Application to Monte Carlo simulations

We simulated 100 maps from a theoretical CMB power spectrum that was calculated by camb[1]. We added Planck level noise to the maps. The power spectra of these maps were run through the TOUSI algorithm, with the aim of recovering the theoretical spectrum from which these 100 spectra were simulated (i.e., the one that was calculated by camb).

Figure 1 shows the reconstruction of the theoretical CMB spectrum in the presence of noise. The reconstruction of the peaks and troughs by this algorithm is very impressive. This is very important because these features define the cosmological parameters. The theoretical power spectrum can be reconstructed up to the point where the structure of the spectrum has not been destroyed by the instrumental noise. In our case this goes to ℓ up to 2500.

Acknowledgments

The authors thank Marian Douspis, Olivier Doré, and Amir Hajian for useful discussions. This work is supported by the European Research Council grant SparseAstro (ERC-228261)

References

1. A. Lewis *et al*, *Astrophys J* L **538**, 473–476 (2000).

NEW COSMOLOGICAL TEST FROM PROPER MOTIONS OF GALAXIES

S.V. PILIPENKO, V.N. LUKASH
Astrospace Center, Lebedev Physical Institute, Profsojuznaja 84/32, Moscow 117997, Russia

We develop a new method of extracting valuable cosmological information from measurements of proper motions of galaxies in the Local Universe (at distances $< 50Mpc$). Such motions could be observed with the new generation of telescopes. The required precision is $\sim 10^{-6}$ arcsecond/year. With the experiment we propose the 3D peculiar velocity field and the mass distribution can be extracted and this does not require high precision distances and Hubble constant.

1 Introduction

In the near future a giant leap in the observational astrophysics will take place with the development of millimeter band radiointerferometers such as ground-based ALMA and space-based Millimetron. The new generation of telescopes in principle can achieve an extremely high angular resolution of the order of micro arcseconds [1]. With this precision measurements of proper motions of galaxies caused by their peculiar velocities (velocities relative to the Relic Radiation) may become available up to distances of tens Mpc. The goal of our work is to find out if such measurements can bring new information for cosmology.

Measuring peculiar velocity field is desirable since it contains the information on the power spectrum of cosmological perturbations, allows to extract the full (non-luminous + luminous) matter distribution, the evolution of structure [2], it allows to measure the "bulk motions" [3] and also to run constrained simulations [4].

Up to now the main method of finding the velocity field was measuring distances r to target galaxies with high precision and their full radial velocities, V_r. Then knowing the Hubble constant H one can find the radial peculiar velocity $v_r = V_r - Hr$. This method was used in many projects, e.g. in the POTENT project [5,6], where radial components of peculiar velocities were used to reconstruct the 3D peculiar velocity field using the potential nature of the velocity field in cosmology. The main disadvantage of this method is the requirement to know the distance and the Hubble constant with high precision.

We show that from measurements of proper motions of galaxies it is possible to reconstruct the 3D peculiar velocity field without requirements of knowing r and H with high precision (and it's enough to assume $r = V_r/H$).

2 Results and Discussion

We check the possibility of reconstruction of 3D peculiar velocity field from proper motions of galaxies using a catalogue of dark matter halos (their positions and peculiar velocities) from a

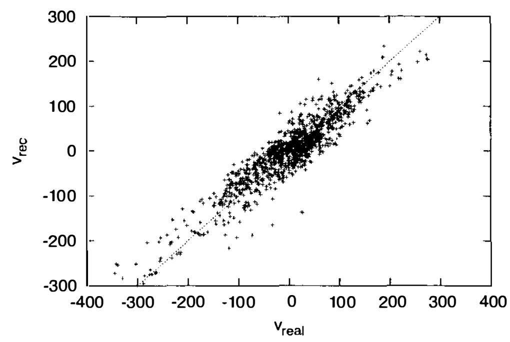

Figure 1: Reconstructed radial components of peculiar velocities of halos v_{rec} vs. real ones v_{real} (in km/s). The dashed line corresponds to equal velocities.

simulation with 50 Mpc box (thanks to S. Gottlöber). The velocity field in linear theory should be potential, so the 3D velocity field can be found from proper motions of galaxies by solving the Poisson equation. The details of the algorithm we use is described in Lukash & Pilipenko, 2011 [7]. In the real Universe at present time some structures are already nonlinear and in them peculiar velocities of galaxies are not potential (and they are not described in terms of field but rather a distribution function). This leads to errors in the reconstruction results and to decrease them one should exclude regions such as galaxy clusters, so our algorithm also takes this into account.

The input parameters for the algorithm are the proper motions (in angular units per time units) and redshifts of galaxies. The outputs are three components of the velocity field at any set of points, e.g., at the positions of input galaxies. The distances to these galaxies are also found by the algorithm. The comparison of real radial velocities of halos with reconstructed ones is shown in Figure 1. The dispersion of $v_{rec} - v_{real}$ is about 30 km/s. For the comparison, the 1D velocity dispersion in the Universe from the linear theory is 310 km/s. This result shows that radial velocities can be reconstructed from the proper motions of galaxies with the precision of 10%. Thus our method allows to separate peculiar motions from the Hubble flow without precise a priori knowledge of distances.

Acknowledgements

This work is supported by RFBR grant 11-02-12168 and Federal program "Scientific and pedagogical personnel of innovative Russia" contract N 16.740.11.0460 by 13 May 2011.

References

1. Millimetron project web site: *http://radioastron.ru/index2.php?engdep=20*
2. P. J. E. Peebles, Astrophys. J. Lett. **344**, L53 (1989).
3. R. Watkins *et al*, MNRAS **392**, 743 (2009).
4. S. Gottlöeber *et al*, *e-Print arXiv*:1005.2687 [astro-ph] (2010).
5. E. Bertschinger *et al*, Astrophys. J. **364**, 370 (1990).
6. A. Dekel *et al.*, Astrophys. J. **522**, 1 (1999).
7. V. N. Lukash, S. V. Pilipenko, Astron. Rep. **55**, 561 (2011).

The SkyMapper Southern Sky Survey and the SkyDice Calibration System

P. Rocci[1a], P. Bailly[1], E. Barrelet[1], H. Lebbolo[1], L. Le Guillou[1], N. Regnault[1], P. Repain[1], K. Schahmanèche[1], A. Vallereau[1], D. Vincent[1]
(1) - Laboratoire de physique nucléaire et des hautes énergies - UPMC, 4 Place Jussieu 75005 Paris (France)

SkyMapper is a 5.7 deg^2 imager mounted on a dedicated 1.35 m telescope installed at the Siding Spring Observatory (NSW, Australia). Among the core goals of SkyMapper are the Southern Sky Survey (S3), a 9-epoch survey of the entire southern sky, and a large nearby supernova survey (S5). S5 aims at producing a nearby SN Ia sample comparable in quality to those gathered by SNLS and SDSS. The SkyDice (SkyMapper Direct Illumination Calibration Experiment) system is a dedicated photometric calibration device that will be installed in the SkyMapper enclosure in the summer of 2012. Here we describe the design of the system, optical model simulation and the test bench with our first results from the calibration pipeline.

1 SkyDice System Design

SkyDice is an evolution of the SNDice system[1], re-designed to adapt it to the SkyMapper imager and telescope enclosure[2,3]. The SkyDice system is composed of a LED head with 24 LEDs covering the spectral response of the imager (350 nm - 900 nm). Each LED emits a lambertian beam that results in a quasi-uniform illumination of the focal plane. An additional "planet" channel generates a quasi-parallel beam.

The flux delivered by each LED is monitored in real time by control photodiodes located in the illumination system. A CLAP (Cooled Large Area Photodiodes) module installed within the optical path of the telescope allows one to monitor the flux emitted by the LEDs in real time. A DAQ system controls and monitors the LED and CLAP subsystems.

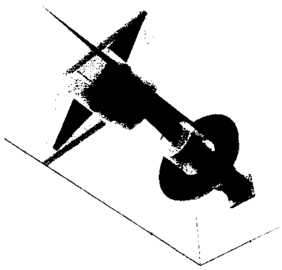

Figure 1: 3D model of the SkyMapper Optics. In blue the primary and secondary mirror, in gray the lenses system and the window. The SkyDice beam is represented in red.

2 Optical Model Simulation

We have developed a simple model of the SkyMapper optics[3] to predict the focal plane illumination for each SkyDice exposure. The model comprises two main components: a set of geometrical routines that allow one to compute the relative position and direction of SkyDice - SkyMapper system and an optical model of SkyMapper that allows us to track any ray emitted by the SkyDice source with its own position on the focal plane (figure

[a]mail: procci@in2p3.fr

1). The optical model will help us to disentangle the direct light and the reflections within the optics. The simulation we have developed can predict the focal plane illumination from direct light as well as from all potential reflections.

3 The SkyDice Calibration Test-Bench

Before the system will be installed it is essential to map the LED beams with a relative precision of $\sim 0.01\%$ and to determine the spectrum of each LED, as a function of the temperature. The beam maps are measured using a Hamamatsu S2281 Si photodiode calibrated by the National Institute of Standard and Technology (NIST), mounted on a motorized $X - Y$ axis. The spectra are determined using the same photodiode and a monochromator. The bench temperature can be varied from 0 to 25 °C, the temperature on site ranging from 0 °C to 15 °C.

4 First Calibration Data

The radiant intensity of each beam is mapped using the Hamamatsu S2281 photodiodecalibrated at NIST. We have implemented a procedure that performs scans at various distances, checks the projectivity of the maps, the temperature and measures potential variations of the LED emission pattern. This is used by the team to produce a theoretical model for the beam of every LED. The aim of the second set of measurements has been the check of all control photodiodes installed at the top of the SkyDice head. We have measured the relation between the intensity of each LED as a function of its current. We took a series of 33 independent measurements at different values of current for the LED and for the control photodiodes using a step function controlled by the electronics of SkyDice. As expected, the relation is linear in a large range, and displays non-linearities at low currents (figure 2).

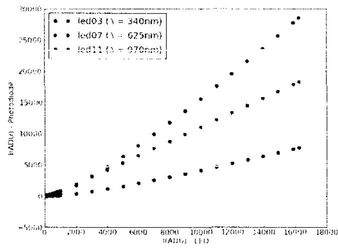

Figure 2: Photodiode current versus LED current (unit is in ADU) for three of 24 + 9 LEDs of the SkyDice head. The plot shows the relation between the LED and photodiode response.

5 Conclusions and Future Works

SkyDice is now ready for installation. The system has been extensively calibrated in flux and wavelength, at temperatures ranging from 0 °C to 25 °C. The installation and commissioning of the system will take place in June and July 2012. The system will be used routinely to measure the SkyMapper throughput as a function of the wavelength, and monitor its variations.

References

1. Barrelet E., Juramy C., 2008, Direct illumination LED calibration for telescope photometry, *Nuclear Instruments and Method in Physics Research A* 585, 93-101.
2. Keller S.C., Schmidt B.P. et al., 2007, The SkyMapper Telescope and the Southern Sky Survey, *Publications of the Astronomical Society of Australia* 24, 1-12.
3. Keller S.C., Schmidt B.P., Bessel M.S., 2007, SkyMapper and the Southern Sky Survey - a resource for the southern sky, *Proceedings of ESO Calibration Workshop 2007*.

GRAVITATIONAL LENS STATISTICS WITH *HERSCHEL*-ATLAS

J. SHORT

School of Physics & Astronomy, Cardiff University, 5 The Parade, Cardiff, CF24 3AA, United Kingdom

Whilst the identification of strong gravitational lenses has historically been a rather a laborious exercise, early data from the *Herschel*-ATLAS demonstrate that lenses can be identified efficiently at submillimetre wavelengths using a simple flux criteria. Motivated by that development, this work considers the statistical properties of the lenses found by *Herschel*-ATLAS.

1 Introduction

The *Herschel* Space Observatory is the only space-based submillimetre observatory and therefore provides a unique window through which to study large scale structure. It has long been thought that submillimetre flux would yield an effective way of identifying lenses [5] and this has now been successfully demonstrated using data from the *Herschel* Astrophysical Terahertz Large Area Survey (*Herschel*-ATLAS [1]). Using this technique, the *Herschel*-ATLAS team expect to find 100-1000 strongly lensed sources [2]. We therefore take a fresh look at the analytical theory behind predicting strong gravitational lens statistics and apply it to the lenses already identified.

The probability of a source being lensed is described by the lensing optical depth [7]: $\tau(z_s) = \int\int \frac{dD_l}{dz_l}(1+z_l)^3\, n(m,z_l)\, \sigma(m,z_l)\, dm\, dz_l$. This depends on: the size of the co-moving volume element; the mass function (n); and the lensing cross-section (σ) which is the area in the lens plane where strong lensing occurs [a]. It can be shown that:

- Increasing Ω_Λ (for a flat universe) increases the co-moving volume element but decreases the density perturbation growth rate. Combined, these decrease the overall optical depth.
- Where one mass function [6] over/under estimates at small/large m compared to the other, this results in an underestimate of τ as well as a preference to smaller z_l.
- SIS density profiles produce more lenses than the NFW [4] profile because they have a steeper inner density gradient, and the NFW gives a higher mean magnification μ [3].

2 *Herschel*-ATLAS SDP Lenses

Five new lensed sources were found in the *Herschel*-ATLAS Science Demonstration Phase (SDP) data. Figure 1 shows $P(\mu) = d\tau(\mu)/\tau d\mu$ and $P(z_l) = d\tau(z_l)/\tau d\mu$, or the conditional probability of a lens being at a given z_l or μ given that lensing has occurred, for two different estimates of the lens density profile (SIS and NFW). The likelihood of the data is given by $\mathcal{L}(\mu_i/z_{l\,i}|\,\rho_{\mathrm{SIS/NFW}}) = \prod P(\mu_i/z_{l\,i})$. The magnification results, $\mathcal{L}(\mu_i \mid \rho_{\mathrm{SIS}}) = 3\times10^{-3}$ and $\mathcal{L}(\mu_i \mid \rho_{\mathrm{NFW}}) < 5\times10^{-6}$,

[a] D_l is the lens angular diameter distance, z_l is the lens redshift, and m is the lens mass.

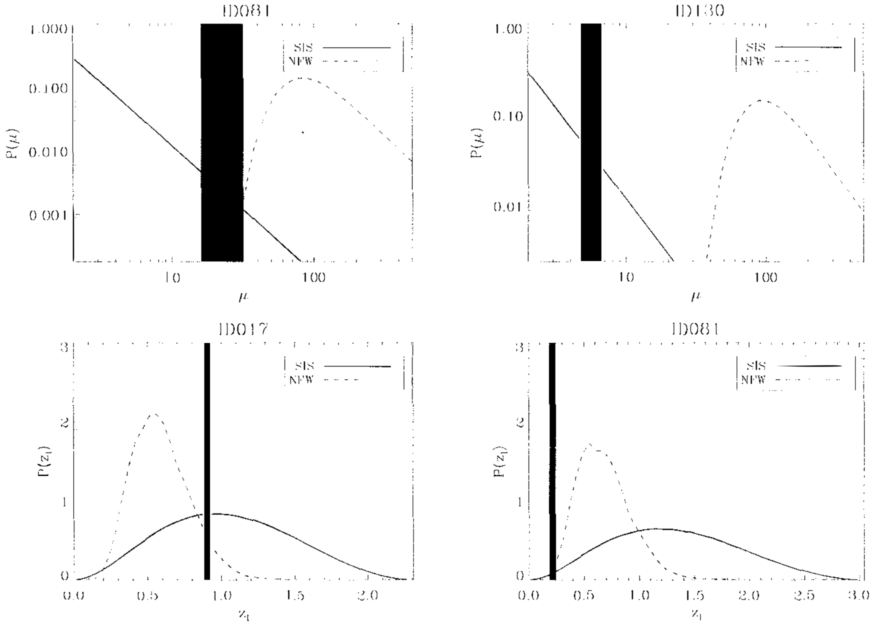

Figure 1: Conditional probability of a lens at a given magnification/lens redshift. Solid blue (dashed red) lines use the SIS (NFW) lens density profile. Shading indicates 68% confidence intervals. Green vertical lines show the estimated location of the H-ATLAS SDP lenses.

suggest the SIS density profile is preferred overall. Whereas the lens redshift results, $\mathcal{L}(\mathrm{SDP}\ z_{li} \mid \rho_{\mathrm{SIS}}) = 0.014$ and $\mathcal{L}(\mathrm{SDP}\ z_{li} \mid \rho_{\mathrm{NFW}}) = 0.026$, suggest the NFW profile is preferred over the SIS. Simulations suggest around 20 lenses are required for a definitive result. Using a similar approach to constrain Ω_Λ results in an estimate of $\Omega_\Lambda = 0.81 \pm 0.05$. Simulations suggest around 100 lenses are needed to provide constraints competitive with other current methods.

The dominant uncertainties in gravitational lens statistics are astrophysical; they involve understanding the nature of the lensing objects. Whilst the full *Herschel*-ATLAS data set should be able to constrain this robustly to provide competitive cosmological constraints, further investigation is needed to fully exploit this unprecedented data set [8].

References

1. Eales S. et al., 2010, PASP, 122, 499.
2. González-Nuevo J., et al., 2012, arXiv:1202.0402;Negrello M., et al., 2010, Science, 330:800.
3. Li L. -X., Ostriker J. P., 2002, ApJ, 566:652; Wyithe J. S. B., et al., 2001, ApJ, 555:504.
4. Navarro J. F., Frenk C. F., White S. D. M., 1997, ApJ, 490, 493.
5. Negrello M., et al., 2007, MNRAS, 377, 1557-1568.
6. Press W. H., Schechter P., 1974, ApJ, 187:425; Tinker J. L., et al., 2008, ApJ, 688:709.
7. Schneider P., Ehlers J., Falco E. E., 1993, Gravitational lenses, Springer
8. Short J., Pearson E., Coles P., Eales S., 2012, in preparation

MEASUREMENT OF THE EXPANSION RATE OF THE UNIVERSE BY USING PASSIVELY EVOLVING GALAXIES

THOMAS, R[1] ; LE FÈVRE, O[1]; SCODEGGIO, M[2]
[1] *Laboratoire de physique de Marseille,* [2] *Istituto Nazionale Di Astrofisica, Milan*

I present here the work that we are doing to study the evolution of the expansion rate when the universe was younger. We plan to use the ages of the oldest most massive galaxies in VVDS and VUDS spectroscopic surveys out to the highest possible redshifts z>2 to constrain the evolution of the Hubble constant H(z).

We have known for almost 15 years that the expansion of the universe is accelerating. To explain this acceleration, we have to consider an unknown component of the Universe, the 'Dark energy". There are a number of models of the universe which take into account this dark energy, for instance, the Lambda-CDM model, where the dark energy is represented by the cosmological constant. Other representation use quintessence where, for instance, the equation of state of the dark energy is redshift-dependant, while others such as the Einstein-de-Sitter model does not contain any dark energy representation .

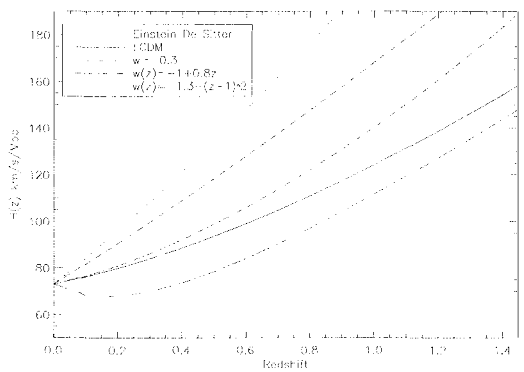

Figure 1: Different models of expansion history.

The aim of the on-going work presented here is the estimation of the evolution of the expansion rate of the universe ($H(z)$). To do so we plan to use the ages of the oldest most massive galaxies in the VIMOS VLT Deep Survey (VVDS 1), and VIMOS Ultra Deep Spectroscopic Surveys (VUDS), and others (like zCosmos, VIPERS) out to the highest possible redshifts z>2.

1 Up to $z \sim 2$

In a first approach we aim to calculate the Hubble parameters up to $z \sim 2$ using passively evolving galaxies to select old, massive and non star-forming galaxies. We eliminate galaxies with on-going star formation, e.g. selecting those with [OII]3727 equivalent width $EW(OII) < 5$ Å, or selecting galaxies with a low Star Formation Rate as estimated by SED-fitting, or passive galaxies using the BzK criterion [1]. In order to select the most massive galaxies we select galaxies with $M > 10^{11} M_{\odot}$ at the low redshift end $z \simeq 0.4$, and allow for mass evolution (following the evolution of the mass function) to select galaxies at higher redshifts.

We use age-sensitive spectroscopic features which are present in the spectra of the galaxies. A key feature is the break at 4000 Å(known as the D4000 break), resulting from an accumulation of metallic absorption lines. Given that this features is visible in optical spectra up to $z \sim 1.4$, at higher redshifts we use the MgUV feature at around 2800Å[2] which can be used from $z \sim 1.1-1.4$ and up to $z \sim 2$. The evolution of those indices can be related to the ages of the galaxies and it becomes possible to get a measurement of the Hubble constant as a function of z (using the method recently revived by Moresco et al. 2012,[3]):

$$H(z) = \frac{-1}{1+z}\frac{dz}{dt} \Longrightarrow H(z) = \frac{-A(Z,SFH)}{(1+z)}\frac{dz}{dD4000},$$

where $A(Z)$ is the slope of the relationship between the D4000 break and the age of the stellar population, and is estimated from stellar population synthesis models. This method is relevant up to $z \sim 2$. We are also exploring the robustness of age determinations using a more direct method of SED and spectra fitting with well calibrated templates.

2 From $z \sim 2$

We plan to extend this investigation beyond $z = 2$. We will aim to find the oldest galaxies at each redshift, as those passively evolving from an early burst of star formation (progenitors of early-type galaxies observed at $z \sim 1$ and below. At these redshifts, observed spectra are looking at the UV rest-frame from Lyα to 2800Å. We are investigating whether age-sensitive spectral indices can be defined and use these to infer $H(z)$.
Moreover, using galaxy ages derived as described above, we will be able to infer the formation epoch of those galaxies, as the epoch of the first starburst and its duration.

3 Prospects

This study of the evolution of $H(z)$, which is not based on any cosmological model, could set an improved constraint and help discriminate amongst different cosmologies.

Acknowledgments

This work is supported by the European Research Council through the Advanced grant contract ERC-2010-AdG-268107-EARLY.

References

1. Daddi, E. et al, ApJ.626, 680, 2005.
2. Alvio Renzini, 2004, Astrophysics and Space Science Proceedings.
3. Moresco M. et al, JCAP submitted, 2012.
4. Freedman, W.L, 2010, The Hubble constant, ARA&A, 48, 673.

Probing dark energy beyond $z = 2$ with CODEX

P. E. Vielzeuf, C. J. A. P. Martins
Centro de Astrofísica da Universidade do Porto, Rua das Estrelas, 4150-762 Porto, Portugal
Faculdade de Ciências, Universidade do Porto, Rua do Campo Alegre 687, 4169-007 Porto, Portugal
Université Paul Sabatier—Toulouse III, 118 route de Narbonne 31062 Toulouse Cedex 9, France

We summarize work recently published in Phys. Rev. D85, 087301 (2012), discussing CODEX's unique role in probing dynamical dark energy models deep in the matter era.

1 The observational tools

In any realistic dynamical dark energy scenario, the scalar field should be coupled to the rest of the model. The key assumption made is that the dark energy and the varying α are due to the same dynamical field. We will further assume a flat FRW universe with $\Omega_m + \Omega_\phi = 1$. The evolution of α and the scalar field evolution are given by:

$$\frac{\Delta\alpha}{\alpha} = \zeta\kappa(\phi - \phi_0), \qquad w + 1 = \frac{(\kappa\phi')^2}{3\Omega_\phi}, \tag{1}$$

The Sandage-Loeb test is a measurement of the evolution of the redshift drift of extragalactic objects by measuring the spectroscopic velocity, with no model-dependent assumptions beyond those of homogeneity and isotropy.

$$\Delta z = (1+z)\frac{\Delta v}{c} = \Delta t\left[H_0(1+z) - H(z)\right], \tag{2}$$

2 A consistency test

We assumed a BSBM model for which the variation of α is due to some other field which has a negligible contribution to the universe's energy density and dynamics. In these kind of models, we can in fact find an analytic solution for the behavior of α:

$$\frac{\Delta\alpha}{\alpha} = 4\epsilon N = -4\epsilon \ln{(1+z)}. \tag{3}$$

Hence, one can reconstruct the equation of state and apply the Sandage-Loeb test to this kind of model. (Fig 1)

3 Early dark energy

In this section we will consider the case of "early dark energy models", in which the dark energy density parameter behaves as follows

$$\Omega_\phi(a) = \frac{\Omega_{\phi 0} - \Omega_e\left(1 - a^{-3w_0}\right)}{\Omega_{\phi 0} + \Omega_{m0}a^{3w_0}} + \Omega_e\left(1 - a^{-3w_0}\right), \tag{4}$$

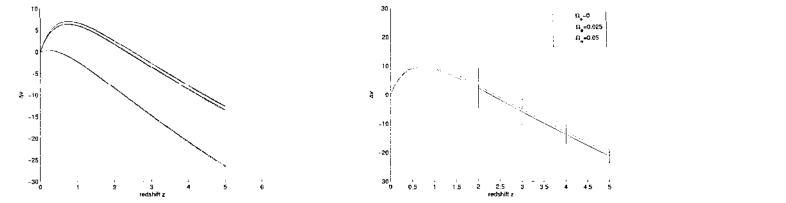

Figure 1: Sandage-Loeb test for reconstructed BSBM models (left) compared to the standard ΛCDM case (top band), and for early dark energy models (right).

One can assume that the dynamical field responsible of dark energy is coupling to electromagnetism and thus yielding a varying α.For this kind of model, the Sandage-Loeb test is unable to distinguish it from the standard ΛCDM scenario (Fig 1). But applying the local bound coming from atomic clocks one can verify the ability of CODEX in measuring the variation of α.(Fig 2)

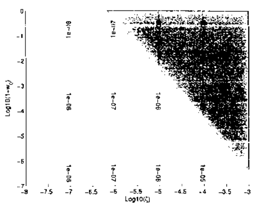

Figure 2: The relative variation of the fine-structure constant, $\Delta\alpha/\alpha$, at redshift $z = 4$, assuming an early dark energy model with Ω_e.

4 Conclusions

We have discussed examples illustrating the ability of CODEX to probe the nature of dark energy. Specifically, we have highlighted the importance of being able to carry out both the Sandage-Loeb test and highly accurate measurements of nature's fundamental couplings. Given the current absence of strong indications for what this new physics is and where it can be found, it is important to search for it in multiple places, and CODEX will have a key role to play, consolidating the importance of the $2 < z < 5$ redshift range in these searches.

Acknowledgements

This work was done in the context of the joint Master in Astronomy of the Universities of Porto and Toulouse, and supported by project AI/F-11, funded under the CRUP/Portugal–CUP/France cooperation agreement (F-FP02/11). We also acknowledge the support of Fundação para a Ciência e a Tecnologia (FCT), Portugal, in the form of the grant PTDC/FIS/111725/2009. The work of C.M. is funded by a Ciência2007 Research Contract, supported by FCT/MCTES (Portugal) and POPH/FSE (EC).

The instrumental calibration of MegaCam with SNDice

Francesca Villa
LPNHE, IN2P3/CNRS, Universities UPMC and Paris-Diderot

Photometric calibration is becoming a crucial issue in various cosmological measurements, such as the measurement of the cosmological parameters with Type Ia Supernovae (SNe Ia). To achieve the accuracy level of $\sim 0.1\%$ required by future surveys, several collaborations are studying new instrumental calibration strategies. We report on the SNDice project, which is an innovative and very stable illumination system installed at the Canada-France-Hawaii Telescope (CFHT). The goal is to demonstrate the feasibility of an instrumental photometric calibration with an accuracy of 0.1% or better.

1 Introduction

The next generation of very large surveys (DES, Euclid, LSST) will detect and study thousands of SNe Ia in order to reach a statistical precision of 1% on the measurement of the Dark Energy Equation of State [1]. The challenge is now to reduce systematic uncertainties to a comparable level. The dominant contribution to the systematic error budget is the photometric calibration of the imagers [2]. Future surveys will require a flux calibration accurate at the per-mil level. However, traditional techniques relying on observations of stellar calibrators will probably not permit to achieve this goal. Therefore, SN Ia surveys are exploring alternative methods to reach this accuracy target. The SNDice project is the result of the effort undertaken by the SNLS collaboration to explore new calibration techniques. SNDice is a demonstrator, designed and built at the LPNHE laboratory in Paris, which is installed since 2008 in the enclosure of the CFHT in Mauna Kea (Hawaii) [3] to study the wide field imager MegaCam [4]. In what follows, we present the design of the SNDice instrument. We briefly discuss the analysis of the SNDice dataset.

2 Design of the instrument

The instrument consists in a calibrated orientable light source composed of 24 narrow spectrum LEDs ($\delta\lambda/\lambda \sim 7\%$) chosen to cover the MegaCam bandwidth from the UV ($\sim$ 350 nm)to the near-IR ($\sim$ 950 nm). LEDs have been chosen for the stability of their emission and their spectral properties. Each LED emits a 1° wide conical beam yielding a nearly flat illumination on the focal plane. Finally, a 25th LED generates a collimated beam parallel to the light source axis, which allows one to align the SNDice and MegaCam optical axes.

3 Test bench activities at LPNHE

Prior to its installation, the SNDice instrument has been characterized and calibrated on a precision spectrophotometric test bench at LPNHE. The main products of these studies are: 1) maps of the radiant intensity of each LED beam, accurate at the 0.1% level, 2) spectra of each LED, measured with a similar precision in flux, and a wavelength accuracy of about 1 Å. All flux measurements have been performed using a NIST (National Institute of Standard of Technology) photodiode. Since the emission properties of LEDs are known to vary with temperature, all studies have been performed at different values of temperature, varying from 0°C (typical of Mauna Kea site) to 25°C (room temperature) Finally, repeatability studies have shown that the device is stable at the 0.01% level.

4 Analysis of the SNDice calibration frames

The flat field illumination delivered by a SNDice LED provides information on the imager optics. The exposure does not only integrate the direct light, but also the light coming from internal refections within the optics (up to 20% of the direct light intensity depending on the wavelength and on the focal plane position). For example, figure 1(b) shows the "pincushion" shaped reflection caused by the reflection on the lens 4 curved surface.

4.1 Simulating the imager

The focal plane illumination depends on the shape of the LED beam (characterized on the test bench[5]) and on its propagation through the optics. In order to disentangle the direct light from the stray light, it is necessary to simulate the propagation of the light through the instrument. The main tool developed for this goal is a simple ray-tracer software (based on `CERN ROOT` libraries). It allows one to simulate the light paths through the wide field corrector and to compare predicted and real SNDice exposures.

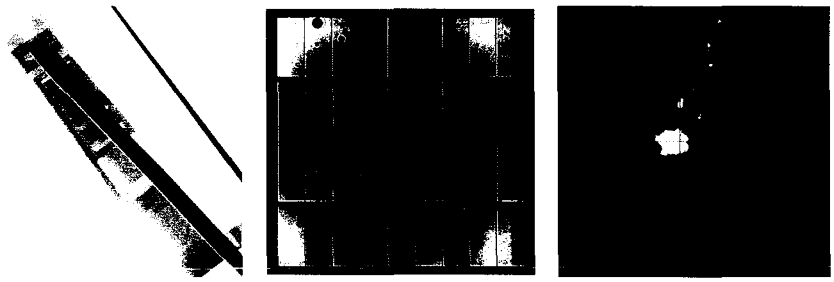

(a) MegaCam optical model (b) SNDice exposure: `GD4` filter r_M (c) SNDice exposure: planet beam

Figure 1: On figure (a) is shows the model of the MegaCam wide field corrector. On figure (b) an example of SNDice flat illumination of the focal planet (LED `GD4`). On figure (c), example of SNDice exposure taken with the planet collimated beam: the central spot and the reflection (aka ghosts) positions are well predicted by the simulation (green circles).

4.2 Validation of the simulation

The simulation has been validated using dedicated exposures taken with the collimated beam LED. This kind of exposures are characterized by a central spot (direct light) and a reflection pattern. The positions of these reflections have been used to constrain the parameters of the optical and geometrical model of the MegaCam-SNDice system. As shown on figure 1(c), the software is able to predict accurately the reflections on the focal plane. Once the instrument model is well determined, it is possible to disentangle the direct and indirect contributions of the illumination to get rid from reflections. Hence, from the comparison between the LED radiant intensity maps and the CCD flux measurements, it is possible to obtain an estimation of the imager photometric response.

5 Conclusion and perspectives

The analysis of SNDice flat field exposures is an ongoing work. The test bench studies continue on a spare light source to control SNDice performances and aging.

We are currently exploring the several application of the simulation tools and the SNDice exposures, such as the study of the instrument electronics, the monitoring of the telescope optics and the optimization of the flat-fielding procedure.

References

1. LSST Science Collaborations, ArXiv e-prints, 2009.
2. A. Conley, J. Guy, M. Sullivan, *et al.*, *Astrophysical Journal Supplement Series* **192**, 1 (2011).
3. C. Juramy, E. Barrelet, K. Schahmaneche, *et al.*, *Society of Photo-Optical Instrumentation Engineers (SPIE) Conference Series* **7014**, (2008).
4. O. Boulade, X. Charlot, P. Abbon, *et al.*, *Society of Photo-Optical Instrumentation Engineers (SPIE) Conference Series* **4841**, (2003).
5. K. Schahmaneche, *et al.* (2012) (in prep.).

List of Participants

Family name	First Name	Institution	Country	Email address
Abdalla	Filipe	University College	UK	fba@star.ucl.ac.uk
Amblard	Alexandre	NASA - Ames Research Center	USA	alexandre.amblard@nasa.gov
Ansari	Réza	Université Paris Sud, LAL	France	ansari@lal.in2p3.fr
Arkhipova	Natalia	Lebedev Physical Inst.	Russia	arfe@yandex.ru
Artymowski	Michal	University of Warsaw	Poland	artymowski@fuw.edu.pl
Astier	Pierre	LPNHE	France	pierre.astier@in2p3.fr
Aumont	Jonathan	Institut d'Astrophysique Spatiale	France	jonathan.aumont@ias.u-psud.fr
Balakishiyeva	Durdana	University of Florida	USA	dbalakis@phys.ufl.edu
Balland	Christophe	LPNHE	France	balland@lpnhe.in2p3.fr
Battye	Richard	Jodrell Bank Centre for Astrophysics	UK	Richard.Battye@manchester.ac.uk
Baxter	Eric	University of Chicago	USA	ebaxter@uchicago.edu
Belikov	Alexander	Institut d'Astrophysique de Paris	France	belikov@iap.fr
Ben-David	Assaf	Tel-Aviv University	Israel	bd.assaf@gmail.com
Benson	Bradford	University of Chicago	USA	bbenson@kicp.uchicago.edu
Berge	David	CERN	Switzerland	berge@cern.ch
Bernardeau	Francis	CEA Saclay	France	francis.bernardeau@cea.fr
Betoule	Marc	LPNHE	France	marc.betoule@lpnhe.in2p3.fr
Bielewicz	Pawel	IRAP	France	Pawel.Bielewicz@irap.omp.eu
Bigot-Sazy	Marie-Anne	APC	France	mabigot@apc.univ-paris7.fr
Blanchard	Alain	IRAP	France	alain.blanchard@irap.omp.eu
Bonvin	Camille	University of Cambridge	UK	cbonvin@ast.cam.ac.uk
Bordier	Guillaume	APC	France	bordier@apc.univ-paris7.fr
Bottai	Sergio	INFN Florence	Italy	bottai@fi.infn.it
Boucaud	Alexandre	APC	France	aboucaud@apc.univ-paris7.fr
Bourdin	Hervé	Univ. Roma "Tor Vergata"	Italy	herve.bourdin@roma2.infn.it
Brown	Michael	Jodrell Bank Centre for Astrophysics	UK	mbrown@jb.man.ac.uk
Busha	Michael	University of Zurich	Switzerland	mbusha@physik.uzh.ch
Canto	Arnaud	LPNHE	France	canto@lpnhe.in2p3.fr
Caprini	Chiara	CEA Saclay	France	chiara.caprini@cea.fr
Cellier-Holzem	Flora	LPNHE	France	cellier@lpnhe.in2p3.fr
Chang	Clarence	University of Chicago	USA	clchang@kicp.uchicago.edu
Chang	Hui-Yiing	Vanderbilt University	USA	hui-yiing.chang@vanderbilt.edu
Chluba	Jens	CITA, University of Toronto	Canada	jchluba@cita.utoronto.ca
Choi	Ami	University of Edinburgh	UK	choi@roe.ac.uk
Colafrancesco	Sergio	University of the Witwatersrand	South Africa	sergio.colafrancesco@wits.ac.za
Crowe	Christopher	Institute of Astronomy	UK	cmc60@cam.ac.uk
Daverio	David	Université de Genève	Switzerland	david.daverio@unige.ch
Diego	Jose M.	Instituto de Fisica de Cantabria	Spain	jdiego@ifca.unican.es
Drlica-Wagner	Alex	Stanford University - SLAC	USA	kadrlica@stanford.edu
Dumarchez	Jacques	LPNHE	France	jacques.dumarchez@cern.ch
Duncan	Christopher	Royal Observatory	Scotland	cajd@roe.ac.uk
El-Hage	Patrick	LPNHE	France	patrickelhageuniv@gmail.com
Erfani	Encieh	Universität Bonn	Germany	erfani@th.physik.uni-bonn.de
Errard	Josquin	Laboratoire APC	France	josquin@apc.univ-paris7.fr
Fabbian	Giulio	Laboratoire APC	France	gfabbian@apc.univ-paris7.fr
Ferté	Agnès	IAS-Institut d'Astrophysique Spatiale	France	agnes.ferte@ias.u-psud.fr
Foley	Ryan	Harvard-Smithsonian CfA	USA	rfoley@cfa.harvard.edu
Galli	Silvia	IAP- Inst. d'Astrophysique de Paris	France	silviagalli84@gmail.com
Garbrecht	Bjorn	RWTH Aachen University	Germany	garbrecht@physik.rwth-aachen.de
Giraud-Héraud	Yannick	APC	France	ygh@apc.univ-paris7.fr
Giunti	Carlo	INFN	Italy	giunti@to.infn.it
Glicenstein	Jean-François	CEA Saclay	France	glicens@cea.fr
Goerdt	Tobias	Universidad Autónoma de Madrid	Spain	tobias.goerdt@uam.es
Gonzalez-Nuevo	Joaquín	Instituto de Fisica de Cantabria	Spain	gnuevo@ifca.unican.es
Gubitosi	Giulia	IPhT, CEA/Saclay	France	giulia.gubitosi@gmail.com
Guy	Julien	LPNHE	France	guy@lpnhe.in2p3.fr
Guzzo	Luigi	INAF - Osservatorio di Brera	Italy	luigi.guzzo@brera.inaf.it
Hall	Alex	Inst Astronomy / Kavli Inst Cosmology	UK	ach74@ast.cam.ac.uk
Hamilton	Jean-Christophe	APC	France	hamilton@apc.univ-paris7.fr
Harrison	Ian	Cardiff University	UK	ian.harrison@astro.cf.ac.uk
Helbig	Phillip		Germany	helbig@astro.multivax.de
Huang	Zhiqi	CEA Saclay	France	zhiqi.huang@cea.fr
Ilic	Stéphane	IAS-Institut d'Astrophysique Spatiale	France	stephane.ilic@ias.u-psud.fr

Family name	First Name	Institution	Country	Email address
Ivanov	Mikhail	Central Institute of Aviation Motors	Russia	ivanov@ciam.ru
Jaccard	Maud	Université de Genève	Switzerland	maud.jaccard@unige.ch
Jasche	Jens	Institut d'Astrophysique de Paris	France	jasche@iap.fr
Kilbinger	Martin	CEA	France	kilbinger@iap.fr
Kinney	William	University at Buffalo, SUNY	USA	whkinney@buffalo.edu
Konno	Tomoyuki	Tokyo Institute of Technology	Japan	konno@hep.phys.titech.ac.jp
Kopp	Michael	Universitäts-Sternwarte München	Germany	michael.kopp@physik.lmu.de
Koshelev	Alexey	Vrije Universiteit Brussel	Belgium	alexey.koshelev@vub.ac.be
Kouvaris	Chris	Institute CP3-Origins	Denmark	kouvaris@cp3.dias.sdu.dk
Labatie	Antoine	CEA Saclay	France	antoine.labatie@cea.fr
Landriau	Martin	MPI fuer extraterrestrische Physik	Germany	landriau@mpe.mpg.de
Langer	Mathieu	Institut d'Astrophysique Spatiale	France	mathieu.langer@ias.u-psud.fr
Lapi	Andrea	Universita di Roma "Tor Vergata"	Italy	lapi@roma2.infn.it
Le Goff	Jean-Marc	CEA-Saclay	France	jmlegoff@cea.fr
Levy	Jean-Michel	LPNHE	France	jmlevy@in2p3.fr
Lewis	Antony	University of Sussex	UK	antony@cosmologist.info
Lopez Honorez	Laura	Max-Planck-Institut fuer Kernphysik	Germany	llopezho@mpi-hd.mpg.de
Magneville	Christophe	CEA Saclay	France	christophe.magneville@cea.fr
Malik	Sarah	The Rockefeller University	USA	smalik@cern.ch
Mangilli	Anna	IAP	France	mangilli@iap.fr
Martino	Joseph	APC	France	martino@apc.univ-paris7.fr
Martins	Carlos	Centro de Astrofisica Univ. do Porto	Portugal	Carlos.Martins@astro.up.pt
Maurin	Loïc	APC	France	lmaurin@in2p3.fr
McEwen	Jason	University College London	UK	jason.mcewen@ucl.ac.uk
Metcalf	Robert Benton	University of Bologna	Italy	robertbenton.metcalf@unibo.it
Mijakowski	Piotr	National Ctre For Nuclear Research	Poland	Piotr.Mijakowski@fuw.edu.pl
Mitsou	Ermis	Université de Genève	Switzerland	ermis.mitsou@unige.ch
Mohr	Joe	Ludwig-Maximilians Universitaet	Germany	jmohr@usm.lmu.de
Morikawa	Masahiro	Ochanomizu University	Japan	hiro@phys.ocha.ac.jp
Morselli	Aldo	INFN Roma Tor Vergata	Italy	aldo.morselli@roma2.infn.it
Mueller	Volker	Leibniz Institut fuer Astrophysik	Potsdam	vmueller@aip.de
Nakamichi	Akika	Koyama Astronomical Observatory	Japan	nakamichi@cc.kyoto-su.ac.jp
Newburgh	Laura	Princeton University	USA	newburgh@princeton.edu
Nishino	Haruki	University of California	USA	nishino@berkeley.edu
Noller	Johannes	Imperial College	UK	johannes.noller08@imperial.ac.uk
Nuss	Eric	LUMP	France	eric.nuss@univ-montp2.fr
Panci	Paolo	CP3-origins & DIAS	Denmark	panci@cp3-origins.net
Paykari	Paniez	CEA Saclay	France	paniez.paykari@cea.fr
Pearson	Jonathan	Jodrell Bank Ctre for Astrophysics	UK	jp@jb.man.ac.uk
Perez-Garcia	M. Angeles	University of Salamanca	Spain	mperezga@usal.es
Perrott	Yvette	Cavendish Laboratory	UK	ycp21@mrao.cam.ac.uk
Peterson	Jeffrey	Carnegie Mellon	USA	jbp@cmu.edu
Pietroni	Massimo	INFN	Italy	pietroni@pd.infn.it
Pilipenko	Sergey	Lebedev Physical Institute	Russia	spilipenko@asc.rssi.ru
Pointecouteau	Etienne	IRAP	France	etienne.pointecouteau@irap.omp.eu
Pryke	Clement	University of Minnesota	USA	pryke@physics.umn.edu
Rathaus	Ben	Tel Aviv University	Israel	ben.rathaus@gmail.com
Renaux-Petel	Sébastien	Dpt Appl. Mathematics & Th. Physics	UK	S.Renauxpetel@damtp.cam.ac.uk
Ricol	Jean-Stéphane	LPSC	France	ricol@lpsc.in2p3.fr
Riemer-Sørensen	Signe	University of Queensland	Australia	signe.riemer@gmail.com
Rivière	Colas	CPPM	France	riviere@in2p3.fr
Rocci	Pier-Francesco	LPNHE	France	procci@in2p3.fr
Rodriguez-Espinosa	J.Miguel	Instituto de Astrofisica de Canarias	Spain	jmr.espinosa@iac.es
Roszkowski	Leszek	Nat. Centre for Nuclear Research	Poland	L.Roszkowski@sheffield.ac.uk
Sadoyan	Avetis Abel	Astronomical Rechen Institute	Germany	asadoyan@ari.uni-heidelberg.de
Schammel	Michel	University of Cambridge	UK	mps54@mrao.cam.ac.uk
Schmid	Christoph	ETHZ	Switzerland	chschmid@itp.phys.ethz.ch
Schmittfull	Marcel	Centre for Theoretical Cosmology	UK	ms865@cam.ac.uk
Schumann	Marc	Physik Institut University of Zurich	Switzerland	marc.schumann@physik.uzh.ch
Serra	Paolo	IAS-Institut d'Astrophysique Spatiale	France	paoloserr@gmail.com
Shaw	John Richard	Canadian Inst. Th. Astrophysics	Canada	jrs65@cita.utoronto.ca
Shaw	Laurie	Yale University	USA	laurie.shaw@yale.edu
Short	Jo	Cardiff University	UK	joanna.short@astro.cf.ac.uk

Family name	First Name	Institution	Country	Email address
Sievers	Jonathan	Princeton University	USA	jsievers@princeton.edu
Simpson	Fergus	University of Edinburgh	UK	frgs@roe.ac.uk
Sliwa	Krzysztof	Tufts University	USA	krzysztof.sliwa@tufts.edu
Sloth	Martin	CP3-Origins and DIAS	Denmark	sloth@cern.ch
Soumagnac	Maayane	University College	UK	mts@star.ucl.ac.uk
Spolyar	Douglas	Fermilab	USA	dspolyar@fnal.gov
Strahler	Erik	Vrije Universiteit Brussels	Belgium	erik.strahler@vub.ac.be
Sutter	Paul	Univ. of Illinois at Urbana-Champaign	USA	sutter@iap.fr
Thomas	Romain	Lab. d'Astrophysique de Marseille	France	romain.thomas@oamp.fr
Trincherini	Enrico	Scuola Normale Superiore	Italy	enrico.trincherini@sns.it
Trowland	Holly	The University of Sydney	Australia	h.trowland@physics.usyd.edu.au
Vernizzi	Filippo	CEA/Saclay IPhT	France	filippo.vernizzi@cea.fr
Vielzeuf	Pauline	Centro de Astrofísica Univ. do Porto	Portugal	pauline.vielzeuf@gmail.com
Villa	Francesca	LPNHE	France	villa@lpnhe.in2p3.fr
Virkajärvi	Jussi	CP3-Origins, Univ. Southern DK	Denmark	virkajarvi@cp3.sdu.dk
Wagstaff	Jacques	Lancaster University	UK	j.wagstaff@lancaster.ac.uk
Wandelt	Benjamin	Institut d'Astrophysique	France	wandelt@iap.fr
Watanabe	Masaaki	Kyoto University	Japan	mwatanabe@tap.scphys.kyoto-u.ac.jp
Weller	Jochen	Ludwig-Maximilians University	Germany	jochen.weller@usm.lmu.de
Zaharijas	Gabrijela	ICTP, Trieste	Italy	gzaharij@ictp.it

COPYMEDIA IMPRIM'VERT®
Achevé d'imprimer en novembre 2012
par **www.copy-media.net**
CS 20023 - 33693 MÉRIGNAC CEDEX